SİNOP ÜNİVERSİTESİ REKTÖRLÜĞÜ

Adres: Korucuk Mahallesi Üniversite Caddesi 15 Temmuz Yerleşkesi No:21B 57010 – SİNOP / TÜRKİYE
Telefon: 0 368 271 57 57 - **Faks:** 0 368 271 57 63 - **Mail:** sufbd@sinop.edu.tr

e-ISSN 2564-7873

Sinop Üniversitesi Fen Bilimleri Dergisi & Sinop University Journal of Natural Sciences

Cilt
(9)
Sayı
(2)
2024

Sinop Üniversitesi Fen Bilimleri Dergisi
&
Sinop University Journal of Natural Sciences

Cilt / Volume 9
Sayı / Number 2
2024

SİNOP ÜNİVERSİTESİ YAYINLARI

SİNOP ÜNİVERSİTESİ
FEN BİLİMLERİ DERGİSİ

SİNOP UNIVERSITY
JOURNAL OF NATURAL SCIENCES

Cilt/Volume 9
Sayı/Number 2
2024

***e-ISSN** 2564-7873*

SİNOP ÜNİVERSİTESİ FEN BİLİMLERİ DERGİSİ

Sinop University Journal of Natural Sciences

SAHİBİ/PUBLISHER
Prof. Dr. Şakir TAŞDEMİR (Sinop Üniversitesi Rektörü/Rector)

EDİTÖR/EDITOR
Prof. Dr. Türkay ÖZTÜRK

YARDIMCI EDİTÖR/ CO EDITOR IN CHIEF
Doç. Dr. Sevda YILDIZ

EDİTÖR KURULU/EDITORIAL BOARD *(in alphabetical order - surname)*

Doç. Dr. Oylum GÖKKURT BAKİ *Sinop University, Türkiye*

Dr. Mustafa Kemal BALKİ *Sinop University, Türkiye*

Prof. Dr. Carlo BARDARO *University of Perugia, İtalya*

Prof. Dr. Levent BAT *Sinop University, Türkiye*

Prof. Dr. Emel ÇANKAYA *Sinop University, Türkiye*

Prof. Dr. Şükrü ÇELİK *Sinop University, Türkiye*

Prof. Dr. Kamil DEMİRCİ *Sinop University, Türkiye*

Prof. Dr. Cem Cüneyt ERSANLI *Sinop University, Türkiye*

Dr. Munish Kumar GUPTA *Opole University of Technology, Polonya*

Doç. Dr. Selda GÜNEY *Başkent University, Türkiye*

Doç. Dr. Jakrapong KAEWKHAO *Nakhon Pathom Rajabhat University, Tayland*

Dr. Julia KORNYYCHUK *A.O. Kovalevsky Institute of Biology of the Southern Seas of RAS, Rusya*

Doç. Dr. Fatma Sevinç KURNAZ *Yıldız Technicaly* University, Türkiye

Dr. Kulwinder Singh MANN *D.A.V. College Bathinda, Hindistan*

Dr. Levent ÖNCEL *Sinop University, Türkiye*

Prof. Dr. Ahmet ÖZER *Sinop University, Türkiye*

Doç. Dr. Muge EREL-OZCEVİK *Manisa Celal Bayar University, Türkiye*

Prof. Dr. Hülya ÖZLER *Sinop University, Türkiye*

Prof. Dr. Richard F. PATTERSON *University of North Florida, Amerika Birleşik Devletleri*

Prof. Dr. Meryem SEFERİNOĞLU *Sinop University, Türkiye*

Dr. Vishwanath P. SİNGH *Karnatak University, Hindistan*

Dr. Kremena STEFANOVA *Institute Of Oceanology– BAS, Bulgaristan*

Prof. Dr. Ahmet TABAK *Ondokuz Mayıs Üniversitesi, Türkiye*

Dr. Bahaeddine TAOUFİK *University of Lynchburg, Amerika Birleşik Devletleri*

Prof. Dr. Hülya TURAN *Sinop University, Türkiye*

ADRES/ADDRESS

Sinop Üniversitesi Rektörlüğü, Korucuk Mahallesi Üniversite Caddesi 15 Temmuz Yerleşkesi No:21B 57010–SİNOP/TÜRKİYE

Tel: 0 368 271 31 12 **Faks:** 0 368 271 57 63

https://dergipark.org.tr/sinopfbd

e-Posta: sufbd@sinop.edu.tr

İçindekiler/Contents

e-ISSN 2564-7873

Araştırma Makaleleri/Research Articles

Sayfa/Page

Sinopfbd, 2024; 9(2): 266-286 **https://doi.org/10.33484/sinopfbd.1460421**

Sinop Üniversitesi Fen Bilimleri Dergisi
Sinop Uni J Nat Sci

E-ISSN: 2564-7873

https://dergipark.org.tr/tr/pub/sinopfbd

Regional Analysis of Earthquakes and Earthquake Magnitude Estimation with Machine Learning Techniques

Gül Cihan HABEK[1] and Humar KAHRAMANLI ÖRNEK[2]

How to cite: Habek, G. C., & Kahramanli Örnek, H. (2024). Regional analysis of earthquakes and earthquake magnitude estimation with machine learning techniques. *Sinop Üniversitesi Fen Bilimleri Dergisi, 9*(2), 266-286. https://doi.org/10.33484/sinopfbd.1460421

Research Article

Corresponding Author
Gül Cihan HABEK
gulhabek@kmu.edu.tr

ORCID of the Authors
G.C.H: 0000-0003-1748-3486
H.K.Ö: 0000-0003-2336-7924

Received: 28.03.2024
Accepted: 10.06.2024

Abstract

Natural disasters, which have been increasing in recent years due to the impact of climate change, pose a significant threat worldwide. Natural disasters, which can cause a large number of human losses and material damages due to their uncertain nature and sudden effects, vary depending on the location and natural environment of the countries. Türkiye located in the Alpine-Himalayan Earthquake Zone, is one of the countries most exposed to earthquake disasters. Although timely prediction of earthquakes is of vital importance in minimizing the destructive effects that may occur during the disaster and increasing resistance to the destructive effects of the disaster, it cannot yet be predicted successfully due to its non-linear chaotic behavior. However, many researchers continue to work on the subject, and earthquake prediction models are actively used in some countries where earthquake disasters occur frequently and cause great destruction. In this study, the magnitudes of future earthquakes were predicted using various machine learning models: Long Short-Term Memory (LSTM), Recurrent Neural Network (RNN), Random Forests (RF), Gradient Boosting Algorithm (GB), Extreme Gradient Boosting Algorithm (XGBoost), 2-hidden-layer Artificial Neural Networks (ANN), and an ANN-KNN hybrid learning model. The performances of the established models were evaluated with MSE, MAE, RMSE, and R^2 metrics; and the ANN-KNN model showed that it was more effective than other models by exhibiting the highest performance with 0.0418 MSE, 0.0030 MAE, 0.0552 RMSE, and 0.7138 R^2 values. Additionally, unlike other studies, seven regions of Türkiye were considered separately and earthquakes were analyzed in detail according to their geography. The analysis results aim to add a new perspective to the literature.

Keywords: Earthquake prediction, machine learning, regression, earthquake analysis, regional analysis

Makine Öğrenmesi Teknikleriyle Depremlerin Bölgesel Analizi ve Deprem Büyüklüğü Tahmini

[1]Karamanoğlu Mehmetbey University, Faculty of Engineering, Institute of Science, Department of Computer Engineering, Karaman, Türkiye

Öz

İklim değişikliğinin etkisiyle son yıllarda artan doğal afetler dünya çapında önemli bir tehdit oluşturuyor. Belirsiz doğası ve ani etkileri nedeniyle çok sayıda insan kaybına ve maddi hasara neden olabilen doğal afetler, ülkelerin bulunduğu konuma ve doğal ortamlarına göre değişiklik göstermektedir. Alp-Himalaya Deprem Bölgesi'nde yer alan Türkiye, deprem felaketlerine en fazla maruz kalan ülkelerden biridir. Depremlerin

[2]Selçuk University, Faculty of Technology, Institute of Science, Department of Computer Engineering, Konya Turkiye

zamanında tahmini, afet sırasında oluşabilecek yıkıcı etkilerin en aza indirilmesi ve afetin yıkıcı etkilerine karşı direncin arttırılması açısından hayati öneme sahip olmasına rağmen, doğrusal olmayan kaotik davranışı nedeniyle henüz başarılı bir şekilde tahmin edilememektedir. Ancak pek çok araştırmacı konu üzerinde çalışmaya devam etmekte ve deprem felaketlerinin sıklıkla yaşandığı ve büyük yıkımlara neden olduğu bazı ülkelerde deprem tahmin modelleri aktif olarak kullanılmaktadır. Bu çalışmada gelecekte meydana gelebilecek depremlerin büyüklükleri Uzun Kısa Süreli Bellek (LSTM), Tekrarlayan Sinir Ağı (RNN), Rastgele Ormanlar (RF) ve Gradient Boosting Algoritması (GB) kullanılarak ölçülmektedir. Extreme Gradient Boosting Algoritması (XGBoost), 2 gizli katmanlı Yapay Sinir Ağları (ANN) ve ANN-KNN hibrit öğrenme modeli kullanılarak tahmin edilmeye çalışıldı. Kurulan modellerin performansları MSE, MAE, RMSE ve R^2 metrikleri ile değerlendirilmiş; ANN-KNN modeli ise 0.0418 MSE, 0.0030 MAE, 0.0552 RMSE ve 0.7138 R^2 değerleri ile en yüksek performansı sergileyerek diğer modellere göre daha etkili olduğunu göstermiştir. Ayrıca diğer çalışmalardan farklı olarak Türkiye'nin yedi bölgesi ayrı ayrı ele alınmış ve depremler coğrafyalarına göre detaylı bir şekilde analiz edilmiştir. Elde edilen analiz sonuçlarının literatüre yeni bir bakış açısı kazandırması amaçlanmaktadır.

Anahtar Kelimeler: Deprem tahmini, makine öğrenmesi, regresyon, deprem analizi, bölgesel analiz

Introduction

Natural disasters, which have increased in frequency due to climate changes in recent years, pose a significant threat in Türkiye and the world; they cause inevitable losses and destruction due to their unpredictable nature and sudden effects. According to the definition of Disaster made by the Disaster and Emergency Management Presidency, natural disasters; are events that may arise from various reasons such as nature, technological events, or human factors, affecting a part or all of the society, causing physical, economic and social losses, disrupting normal life or stopping it completely [1]. EM-DAT (Emergency Events Database), an international disaster database, examines disasters by dividing them into two groups: natural and technological [2]. When we look at the Türkiye data of the EM-DAT database, 216 of the 389 disasters that occurred between 1900 and 2023 occurred due to nature and 173 due to technological reasons. As seen in Figure 1, the most common disaster type among natural disasters is 53%. There have been earthquakes.

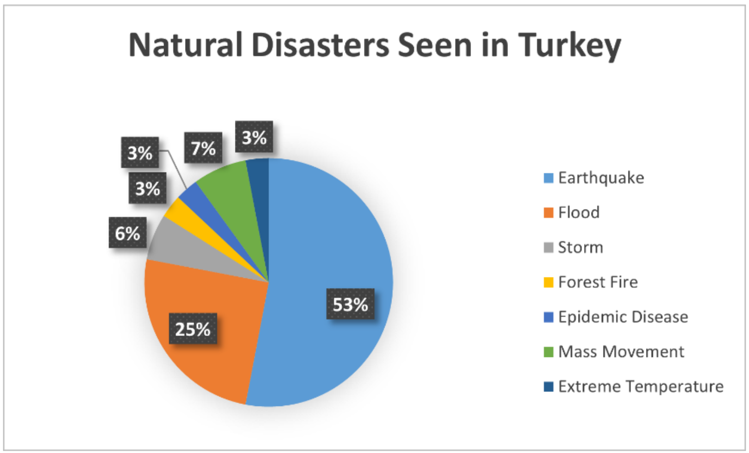

Figure 1. *Distribution of natural disasters that occurred between 1900-2023*

The types and frequencies of natural disasters vary depending on the geographical location and natural environment of countries. Floods, which can be seen all over the world and can easily turn into disasters due to different reasons, are seen in China due to extreme rainstorms, Volcanic Eruptions, and Earthquakes frequently occur in Pacific Ring of Fire countries such as Japan, Indonesia, the Philippines, and New Zealand [3, 4]. Due to frequent and destructive earthquakes, a large number of human and property losses occur in Türkiye, which is located in the Alpine-Himalayan Earthquake Zone. [5]. When we look at the natural disaster statistics of the last 20 years in our country, which is a 1st-degree earthquake zone, it is seen that a total of 50,999 people lost their lives and 2,827,859 dollars of damage were caused in the earthquakes that occurred [2]. Being able to predict earthquakes that societies are likely to encounter in the future may enable them to be prepared for disasters and develop coping strategies [6]. Timely and acceptable predictions are vital to be able to take strategic measures to determine and minimize the devastating effects that may occur during a disaster and to increase resilience to disasters [7]. Although no successful results regarding earthquake prediction can be achieved due to the non-linear chaotic behavior of the earthquake, studies continue to be carried out and discussed by many researchers [8]. When we look at the studies in the literature on the prediction of earthquakes, Çam and Duman [9] study four different regions with intense seismic activity in the west of Türkiye: Gölhisar Çameli Region, Burdur Fault Region, Büyük and Küçük Menderes Graben Region, and Gediz and Alaşehir Grabens. They aimed to predict future earthquakes. In this direction, he developed a feed-forward back-propagation ANN using the "b" value used in earthquake predictions based on the Gutenberg-Richter relationship; They trained the developed network using earthquake data. While the trained network gave successful results in predicting earthquakes that will not occur for 4 regions, it gave unsuccessful results in predicting earthquakes that will occur. In another study, Mallouhy et al. [10] aimed to predict earthquakes using a single time series data set obtained from an earthquake data center in Northern California. Each data point in the considered data set represents hourly average readings taken between 1967 and 2003 and only data from a single time series of a particular earthquake center were used in each forecast. In the analysis, earthquakes were classified as negative magnitude and positive magnitude earthquakes. Aftermath earthquakes that occurred in the same region after major earthquakes and were below 5 on the Rictor scale were ignored, and earthquakes that exceeded 5 on the scale were taken into account. This study aims to classify earthquakes as negative magnitude, which are less than 4, and are followed by at least 20 earthquakes that are not 0 in the last 512 hours~~;~~. Major earthquakes that occur 512 hours or more after another major earthquake are classified as positive major earthquakes. Random Forests (RF), Support Vector Machine (SVM), Logistic Regression (LR), Naive Bayes (NB), K-Nearest Neighbors (KNN), and Multilayer Perceptron, When the classification accuracy results obtained from the models established with eight machine learning algorithms, including AdaBoost and Classification and Regression Trees (CART), were compared, the highest result was obtained as 76.97% with the RF algorithm. Wang et al. [11] used machine learning techniques in their study to investigate whether earthquakes with magnitudes less than 4.0 can be used to predict earthquakes with magnitudes greater than 6.0. The data set used in the study consists of earthquakes greater than 3.0 that occurred in the Sichuan-Yunnan region between 1970 and 2021, taken from CEDC (China Earthquake Data Center). During the testing phase, the Chuandian region of Southwest China was preferred because there were many earthquakes in the region. There are two questions that the study focuses on. The first of these is whether an earthquake greater than 6.0 will occur next year, and four types of traditional machine learning algorithms were used to classify this: RF, Decision Tree (DT), SVM, and LR. In this part, the highest success was achieved at 97.5% with the RF algorithm. The second question that the study focuses on is what the maximum magnitude of the earthquake that will occur next year will be, and the LSTM network was used to predict this. At the end of the study, it was concluded that the network used showed sufficient success in predicting the earthquake magnitude and that small earthquakes can be used to predict large earthquakes. Demirelli et al. [12] aimed to predict earthquakes by combining geological and geodetic data in their studies. The data set consists of earthquakes that occurred between 1970 and 2021, recorded by the Kandilli Observatory and Earthquake Research Institute (KRDAE). Data on fault lines were taken from the Mineral Research and Exploration (MTA) and Active Fault Database of Türkiye [13]. When the prediction models created using RF, XGBoost, DT, and KNN regression algorithms were evaluated using MSE (Mean Squared Error) and RMSE (Root Mean Squared Error) performance metrics, the highest success was achieved when the KNN algorithm was used. In the last study discussed, Karcı and Şahin [14] developed two types of prediction models: earthquake magnitude prediction and prediction of earthquakes that will occur within a certain date range. The data set used in the study is earthquakes with a magnitude of 3.5 and above that occurred between 1970 and 2021 in the Kandilli Observatory and Earthquake Research Institute Regional Earthquake-Tsunami Monitoring and Evaluation Center (BDTİM) Earthquake Inquiry System. A deep learning architecture consisting of 3 hidden layers and 1 input layer was developed using the Keras library for earthquake magnitude estimation. For time estimation, the LSTM model consisting of 3 UKSB layers, 1 Dropout layer, and 1 output layer was designed. It has been concluded that the proposed models provide more accurate results in earthquake magnitude estimation when compared to traditional machine learning methods such as Multiple Linear Regression, Polynomial Regression, DT, and RF. In this study, a dataset was created using the main earthquakes that occurred in Türkiye between 2000 and 2023, obtained from the Kandilli Observatory and Earthquake Research Institute. The dataset was divided into geographical regions of Türkiye based on the location of occurrence, and the tables for each region were analyzed according to the total number of earthquakes and average magnitudes every month; the depth-magnitude relationship of earthquakes was examined. In the second stage, a hybrid learning model was employed, integrating LSTM, RNN, RF, GB, XGBoost, 2 hidden-layer ANN, and ANN with KNN algorithms, to attempt to predict the magnitudes of future earthquakes. The performance of the models was compared using MSE, MAE, RMSE, and R² evaluation metrics. In the continuation of the study, the created dataset and preprocessing steps are described in detail in the Materials and Methods section. Additionally, general information about the machine learning algorithms and evaluation metrics used in earthquake prediction is provided. The comparative results obtained from regional analysis and earthquake prediction models are discussed in the Results section. The comparison of the results with other studies and their contributions to science are discussed in detail in the Conclusion section.

Material and Method

In this section, after describing the data set created for the study in detail, general information about the machine learning algorithms and evaluation metrics used in prediction is included.

Dataset

The data set to be used in the study was created by taking the earthquakes between 2020 and 2023 in the earthquake catalog of Kandilli Observatory and Earthquake Research Institute (KRDAE) [15]. The captured data includes 94935 earthquake data that occurred at 35.00-42.00 latitude and 26.00-45.00 longitude. “earthquake_ID”, “code”, “occurrence date”, “occurrence time”, “latitude”, “longitude”, “der(km)”, “xM”, “MD”, “ML”, “Mw”, “ From the data set consisting of "Ms", "Mb", "type", "location" information, unnecessary columns were deleted and "occurrence date", "occurrence time", "latitude", "longitude", "depth (km)", "xM" and “location” information continued to work. A new column named "time" was created by combining the "occurrence date" columns, which contain the date information when the earthquake occurred, and the "occurrence time" columns, which contain the time it occurred. To be processed later, the time column was converted to the DateTime object of the pandas library and made ready for regression by converting it into a Unix timestamp, which is a numerical representation of seconds. The data includes main earthquakes with magnitudes ranging from 0 to 9 and minor earthquakes, that is, aftershocks, that occur after the main earthquakes. Aftershocks do not have a specific duration and can continue for a period ranging from 1 month to 2 years after the main earthquake [16]. Since it is thought to negatively affect learning, earthquakes that occurred in the same region within 3 months after the main earthquake and whose magnitude was smaller than the main earthquake were considered aftershocks and were removed from the data set. In addition, major earthquakes with magnitudes below 3 and considered very mild earthquakes by the USGS [17] were also removed from the data set, and the final data set was created with the remaining 7043 data, the first five examples of which are given in Table 1.

Table 1. *The first five rows in the Data Set*

Earthquake id	Time	Latitude	Longitude	Depth (km)	xm
0	1609518981	35.9273	27.8658	26.1	3.9
1	1609353912	36.4918	28.7092	5.0	3.9
2	1609335612	37.796	26.4165	14.4	4.4
3	1609196128	36.4522	26.7882	120.2	3.3
4	1609151401	35.8905	32.5063	5.6	3.3

For the models used to perform better, the values in the data set were scaled to a certain range using the MinMaxScaler class in the SciKit-Learn library; The data set was divided into 80% training and 20% test data, making it ready for the models to learn on the training data and then evaluate their generalization ability on the test data.

Machine Learning Techniques

Machine learning is a method that improves the ability of computer systems to make automatic decisions when faced with similar situations based on their previous experiences [18]. With the rapid advancement of technology, various machine learning methods have been developed and started to be widely used in classification and regression studies, thanks to the ability of computer systems to analyze and learn complex data sets [19]. In the study, earthquake magnitude predictions were made using a hybrid model created using machine learning methods from the ensemble learning category such as RF, GB, XGBoost algorithms, deep learning methods including LSTM and RNN, 2 hidden-layer ANN, and ANN with the K-nearest neighbor algorithm.

Gradient Boosting Algorithm (GB): It is an ensemble learning technique that aims to create a stronger learner by combining weak learners, that is, models with generally low accuracy [20]. The algorithm works by adding a new model that tries to correct the errors of the previous model at each step until it reaches a predetermined goal [21]. The success of the algorithm often depends on the hyperparameter settings and the type of weak learner used.

Extreme Gradient Boosting Algorithm (XGBoost): The XGBoost algorithm, published by Chen and Guestring [22], is one of the widely used applications of GB. Similar to GB, the model is trained iteratively by adding new trees, focusing on correcting errors produced by previous trees. As a base classifier, it focuses only on decision trees and thus creates a powerful classification model by controlling the structure of the trees using a special loss function and regularization terms [23].

Random Forests Algorithm (RF): The method introduced by Leo Breiman in 1997 was developed as an alternative to the Boosting method [24]. Unlike Boosting, which aims to create a strong learner by combining weak learners, it brings together different decision trees by creating random sub-feature subsets. Each tree is trained on randomly selected subsets of data points, thus adding diversity to the model. These trees are then combined to make an overall prediction. This multi-tree approach provides the advantages of being resistant to overfitting, obtaining a model with high performance and increased generalization.

Artificial Neural Network (ANN): These are mathematical models inspired by biological neural networks [25]. It is designed to consist of an input layer, an output layer, and one or more hidden layers. ANNs, which lack the correlation approach, produce the output by multiplying the input data with weights through the neurons in their layers and passing them through an activation function [26]. The disadvantage of this network is that it does not effectively handle time dependencies and historical information between input data and output data, but performs direct mapping. RNNs are used to eliminate this disadvantageous situation.

Recurrent Neural Network (RNN): RNNs are designed to handle connections in a time series and dependencies over time [26]. The output of each neuron is fed by the input from the previous steps and its previous output. During the training of RNNs, which are extremely effective in modeling complex dependencies over time, difficulties such as sudden growth (exploding gradients) or decrease (vanishing gradients) of backpropagating gradients over time are experienced [27, 28]. Such situations can limit the ability of RNNs to effectively learn long-term dependencies and negatively impact their performance. To cope with such difficulties, LSTMs are used that contain modifications designed to learn long-term dependencies more effectively.

Long Short-Term Memory (LSTM): A special type of RNN designed to cope with the challenges of RNNs. It uses memory units with input, output, and forget gates [29]. These gates control how much information the cell retains and how much it forgets. LSTMs can generally handle long-term dependencies better and learn more effectively than RNNs.

ANN-KNN Hybrid Model: The hybrid model is the integration of two models to create a more comprehensive and powerful prediction model by combining ANN's deep learning capabilities and KNN's example-based similarity measurement. The k-Nearest Neighbors (KNN) algorithm, which was introduced to the literature in the book "Pattern Classification and Scene Analysis" [30], is an easy-to-use and popular supervised learning algorithm. It makes a prediction based on the relationship between the sample to be predicted and its closest neighbors in the training set. Neighborhood relationships are usually determined using the Euclidean distance, which directly measures the distance between two points. Alternatively, Manhattan, Minkowski, and Chebyshev functions can also be used [31]. Once the distance is calculated, the nearest neighbors are ranked and then the sample to be predicted is appropriately assigned to the classes of its nearest neighbors based on this ranking [32].

Evaluation Metrics

In the study, MSE (Mean Squared Error), MAE (Mean Absolute Error), RMSE (Root Mean Squared Error), and R² metrics, which are frequently preferred in literature studies, were used to compare the performances of the models. MSE is a metric that measures how far the predictions of regression models are from the true values [33]. As seen in the formula given in Equation 1, the error at each data point is found by squaring the difference between the actual value and the prediction, and MSE is calculated by adding the squares of the obtained values and taking their average. The closer the MSE value is to zero, the better the model performs. The advantage of MSE is that it eliminates the differences between negative and positive errors by squaring the errors. However, it may cause major errors to be highlighted more.

$$MSE = \frac{1}{n}\sum_{i=1}^{n}(y_i - y_i')^2 \tag{1}$$

MAE is the average of the absolute differences between the real values and the values produced by the models, as seen in Equation 2 [34]. Unlike the MSE metric, since errors are not squared, it is resistant to outliers and the best-case scenario is that the MAE value is zero.

$$MAE = \frac{1}{n}\sum_{i=1}^{n}|y_i - y_i'| \tag{2}$$

RMSE is the square root of MSE, and the closer RMSE is to zero, the better the performance of the model [33]. As seen in Equation 3, the squares of the errors are summed, their average is calculated and the square root is taken. Similar to MSE, this metric emphasizes large errors, but the values become smaller as they get closer to correct predictions.

$$RMSE = \sqrt{\frac{1}{n}\sum_{i=1}^{n}(y_i - y_i')^2} \tag{3}$$

R² measures how close the actual values are to the values predicted by the model. The R² value varies between 0 and 1, and the best-case scenario is an R² value of 1. As given in Equation 4, the R² value is obtained by subtracting the Residual Sum of Squares (SSres) and Total Sum of Squares (SStot) ratio from 1. SSres is the sum of the squares of the differences between the values predicted by the model and the actual values, and SStot is the sum of the squares of the deviations of the actual values from the mean.

$$\mathrm{R2} = 1 - \frac{SS_{res}}{SS_{tot}} = \frac{\sum_{i=1}^{n}(y_i - y_i')^2}{\sqrt{\sum_{i=1}^{n}(y_i - y_i')^2}} \tag{4}$$

In the formulas given in Equation 1, Equation 2, Equation 3, and Equation 4, n represents the number of data points, y_i represents the actual values, and y_i' represents the predicted values of the model.

Results

In this section, regional analyses of earthquakes that occurred in the seven geographical regions of Türkiye are discussed under the heading "Earthquake Analysis", while the results obtained from earthquake prediction models are addressed under the title "Earthquake Prediction Model".

Earthquake Analysis

The data obtained by the Kandilli Observatory provides an important resource for evaluating Türkiye's earthquake activity. When we look at the earthquake map of Türkiye in Figure 2, which was created using the earthquake data in the Kandilli Observatory database; It is seen that earthquake disasters have been intense in the Marmara Region and its surroundings, where the North Anatolian Fault line passes, in the Eastern Anatolia region, where the Eastern Anatolian Fault line passes, and in the regions where the Western Anatolian Fault line extending from the Aegean region to the Southeast passes, in the last 23 years. These regions represent the main tectonic structures at earthquake risk in Türkiye.

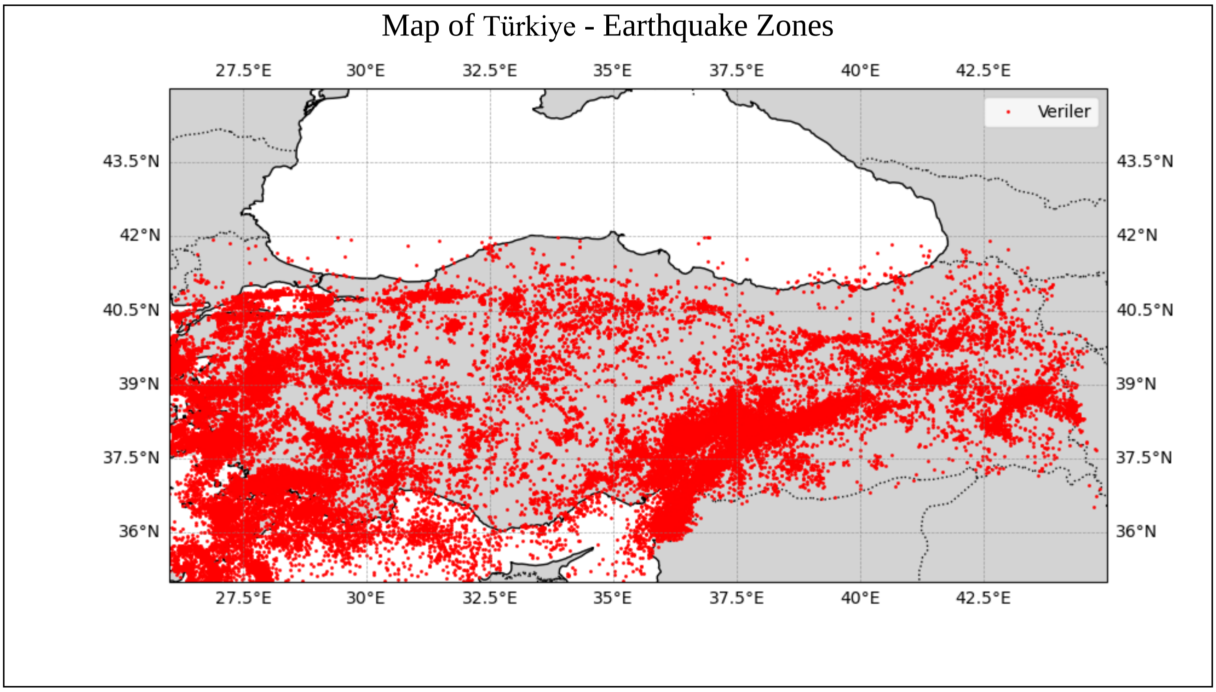

Figure 2. *Map of earthquakes occurring between 2020-2023*

To analyze the number and magnitude of earthquakes that occurred in the 7th region of Türkiye every month by region, the data to obtain the location information in the location column is based on 7 sub-tables. Table 2 shows an example of regular subtables for the Mediterranean Region. Other tables consist of earthquake data with the same columns, and the "occurrence date" column in the tables has been converted to date format and made ready for analysis.

Table 2. *Earthquakes occurring in the Mediterranean Region*

Earthquake id	Date	Time	Latitude	Longitude	Depth (km)	xm	Location	Region
0	2023-02-06 00:00:00	10:24:47	38.0818	37.1773	5	7.6	Kahramanmaras	Akdeniz
1	2021-01-01 00:00:00	16:36:21	35.9273	27.8658	26.1	3.9	Akdeniz	Akdeniz
2	2020-12-25 00:00:00	22:35:24	37.6125	30.6683	5	3.3	Burdur	Akdeniz
3	2020-12-18 00:00:00	9:24:10	37.1175	31.0832	104.9	3.7	Antalya	Akdeniz
4	2020-01-28 00:00:00	21:44:57	35.1688	27.9028	6.4	4.5	Akdeniz	Akdeniz

For the analysis, the monthly total number of earthquakes and average earthquake magnitude of each region were calculated and the values obtained are shown in the graphs given in Figure 3.

Upon examining the graphs provided in Figure 3, it can be observed that moderate-sized earthquakes have generally occurred in the seven geographical regions of Türkiye. The region where earthquakes are least observed is the Southeastern Anatolia Region, where the South Anatolian Fault passes through. When comparing earthquakes every month across regions, it is observed that, except for the Marmara Region, in the remaining six regions, earthquake frequencies and magnitudes generally change seasonally. It has been concluded that there is an increase in earthquakes during the winter months and fewer earthquakes during the summer months. According to their depth, earthquakes that occur between 0 and 60 km deep can be classified as "shallow earthquakes", those between 70 and 300 km as "medium depth earthquakes", and those with a depth of more than 300 km as "deep earthquakes" [35]. When the depths of the earthquakes occurring in the 7 geographical regions given in Figure 4 are examined, it is seen that the earthquakes occurring in Türkiye are generally shallow earthquakes that are felt in a narrow area but can cause great damage. In the Mediterranean and Aegean Regions, medium-sized earthquakes, which were felt over a wide area and whose damage was limited, although rare, occurred.

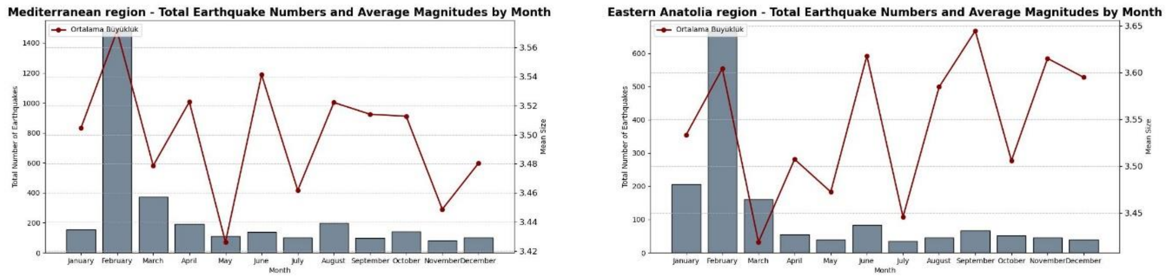

a. Mediterranean region *b. Eastern Anatolia region*

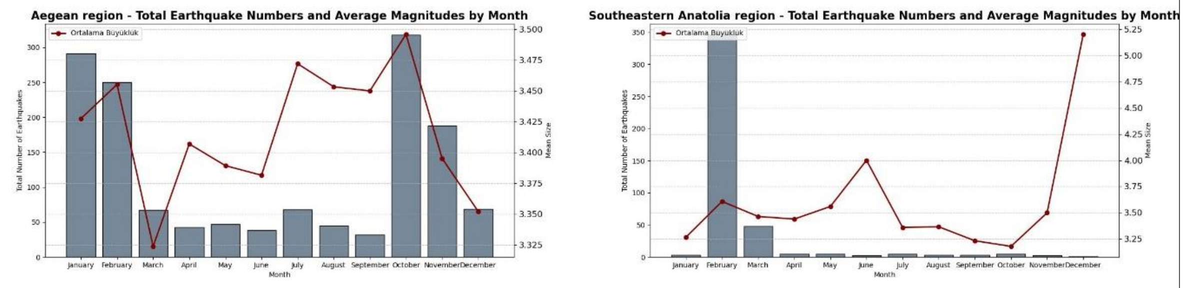

c. Aegean region *d. Southeastern Anatolia region*

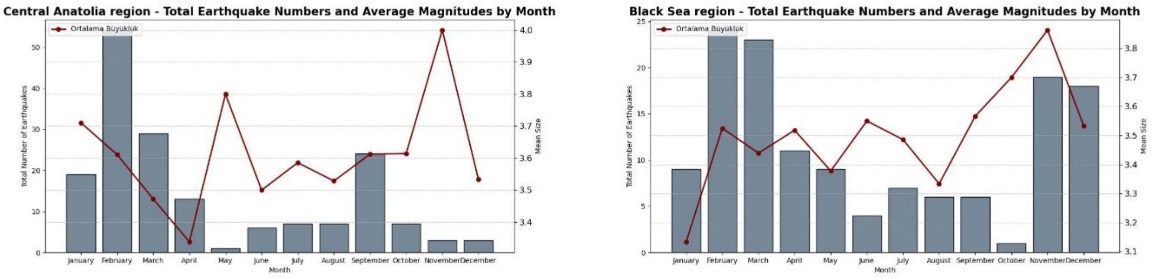

e. Central Anatolia region *f. Black Sea region*

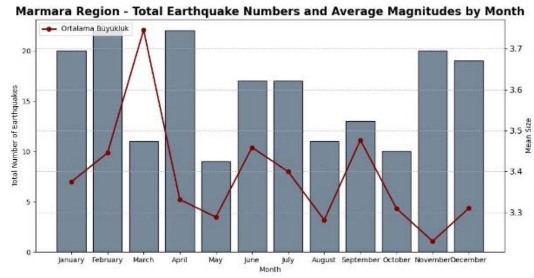

g. Marmara region

Figure 3. *Total number of earthquakes and average magnitudes by month*

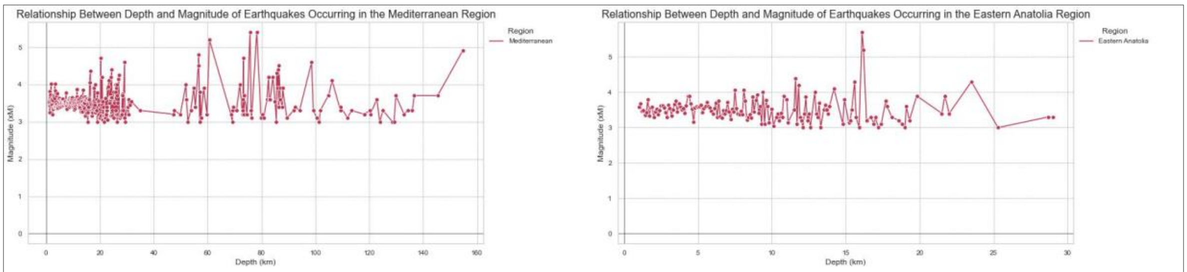

a. Mediterranean region *b. Eastern Anatolia region*

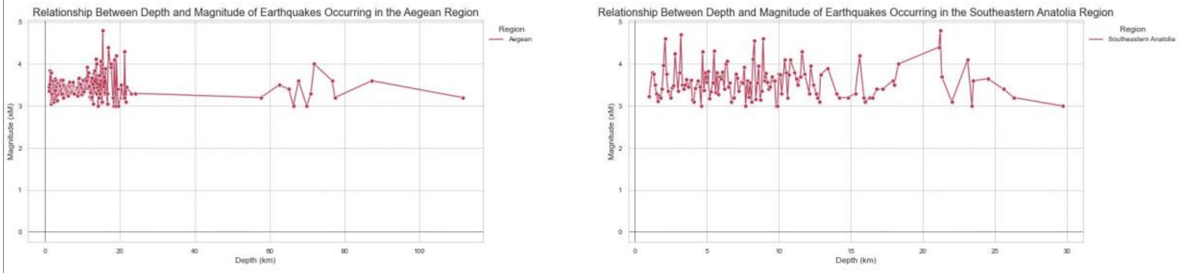

c. Aegean region *d. Southeastern Anatolia region*

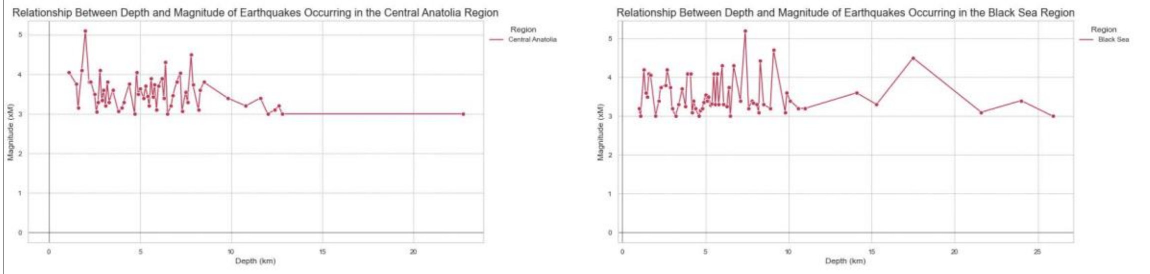

e. Central Anatolia region *f. Black Sea region*

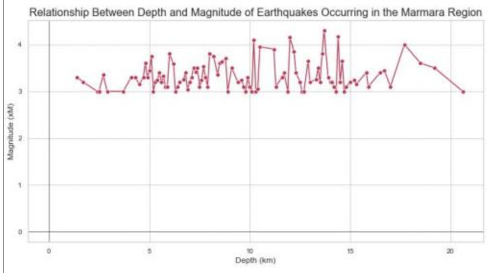

g. Marmara region

Figure 4. *Depth-magnitude relationship of earthquakes*

When the relationship between the depths and magnitudes of earthquakes was examined, it was observed that there was no significant relationship between these parameters. This shows that earthquake events are a complex and multifactorial process and that it is not possible to explain them with a single parameter.

Earthquake Prediction Model

In the second part of the study, a hybrid learning model in which machine learning algorithms LSTM, RNN, RF, GB, an attempt was made to estimate the magnitude of possible earthquakes. The testing phase of the created models was carried out using the SciKit-Learn library, which offers a wide set of machine learning tools and is widely preferred, especially in the Python programming language. LSTM, RNN, and ANN models are four-layered models with an input layer of 128 neurons with ReLU activation function, two hidden layers of 64 and 32 neurons with ReLU activation function, and an output layer with linear activation function. The first two layers of the models are configured with "return_sequences=True" to pass output to the subsequent layers. To prevent overfitting during training, 20% of the training data is reserved as the validation set. Adam’s optimization algorithm is preferred for optimization, combining adaptive learning rate and momentum for faster and more effective optimization. The mean squared error loss function is used to minimize the average squared differences between predictions and actual values. Finally, the batch size is set to 10, and the models are trained for 100 epochs. For the RF ensemble learning algorithm, hyperparameters are set as n_estimators: 200 and max_depth: 10 to provide a certain balance and stability during the training process to improve performance. In the GB model, n_estimators is set to 100. In the XGBoost model, which is an application of the GB algorithm, n_estimators is set to 50 and max_depth is set to 5. The hybrid model is an integration of two models to create a more comprehensive and powerful prediction model by combining ANN's deep learning capabilities and KNN's example-based similarity measurement. As depicted in Figure 5, an ANN consisting of an input layer with 128 neurons and ReLU activation function, two hidden layers with 64 and 32 neurons respectively, both using ReLU activation function, and an output layer with 1 neuron and linear activation function, has been trained on the dataset. The model uses the Adam optimizer function and mean squared error (MSE) loss function. The model will be trained for 50 epochs, and training data will be arranged into mini-batches of 32 samples each. To find similar examples in the dataset using the representations learned by the ANN model, these representations are given as input to the KNN model. The KNN model performs similarity measurement for n_neighbors=5 based on the learned representations.

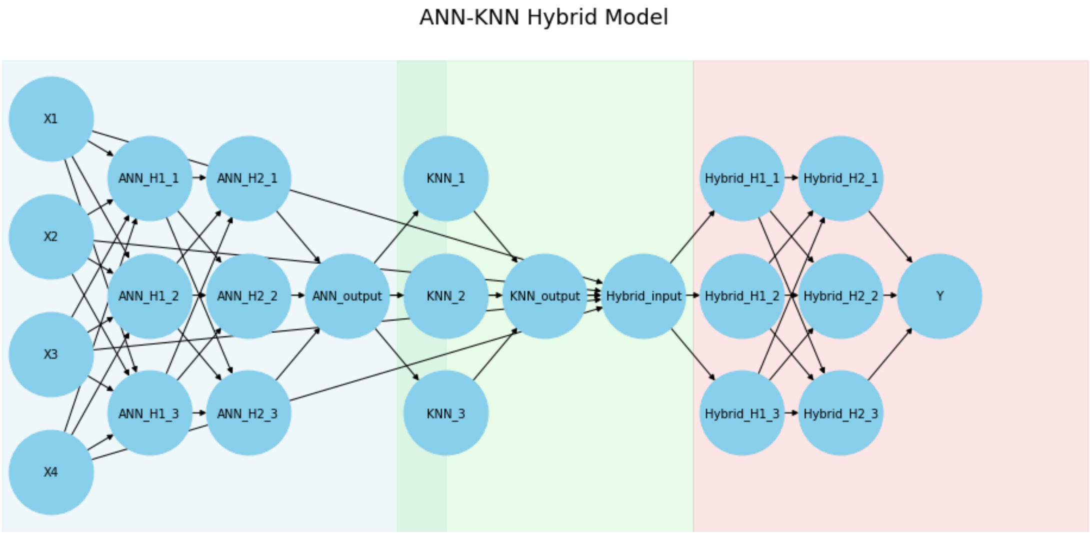

Figure 5. *Proposed model*

The prediction success of the models was evaluated using MSE, MAE, RMSE, and R² evaluation metrics as presented in Table 3.

Table 3. *Results obtained*

	MSE	**MAE**	**RMSE**	**R²**
LSTM	0.0762	0.01030	0.1015	0.03132
RNN	0.0769	0.0102	0.1009	0.0428
RF	0.06280	0.0068	0.0823	0.3636
GB	0.07320	0.0093	0.09629	0.1283
XGBoost	0.0763	0.0100	0.1000	0.0605
ANN	0.07711	0.01026	0.1013	0.0357
ANN-KNN	**0.0418**	**0.0030**	**0.0552**	**0.7138**

The results obtained using MSE, MAE, RMSE, and R² metrics were analyzed to evaluate the predictive abilities of the models. Figure 6-7-8-9 shows the MSE, MAE, RMSE, and R² results obtained from the models used in the study. When evaluating the predictive abilities of the models based on error criteria, generally lower error values were obtained from RF, GB, XGB, ANN, and ANN-KNN models. Among them, the ANN-KNN model showed the highest performance with 0.0418 MSE, 0.0030 MAE, 0.0552 RMSE and 0.7138 R². On the other hand, LSTM, RNN, XGBoost, and ANN models gave high error rates and low R² values compared to other models. This means that these models show lower predictive performance in the context of a particular problem compared to others.

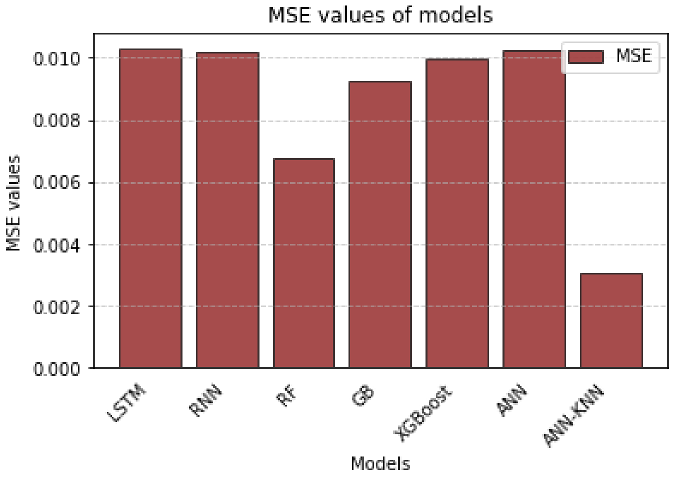

Figure 6. *Comparison of MSE values of the models*

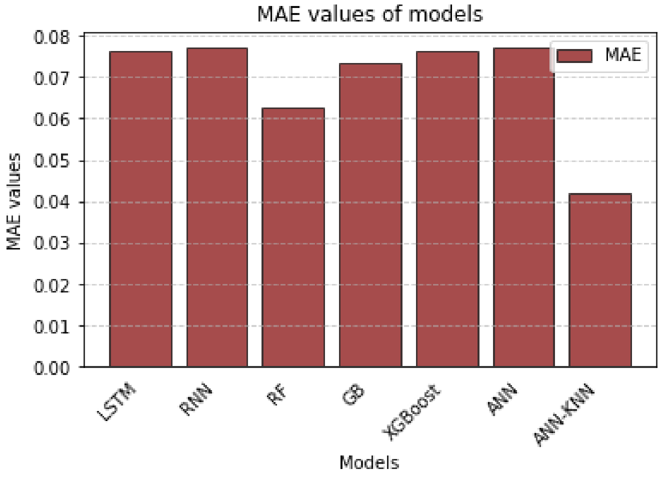

Figure 7. *Comparison of MAE values of the models*

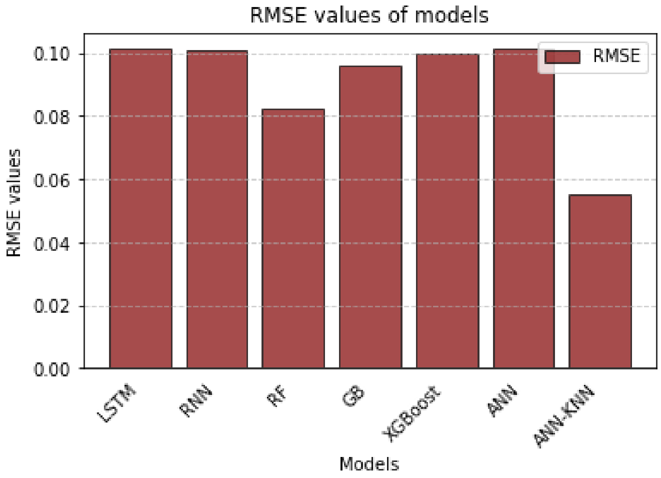

Figure 8. *Comparison of RMSE values of the models*

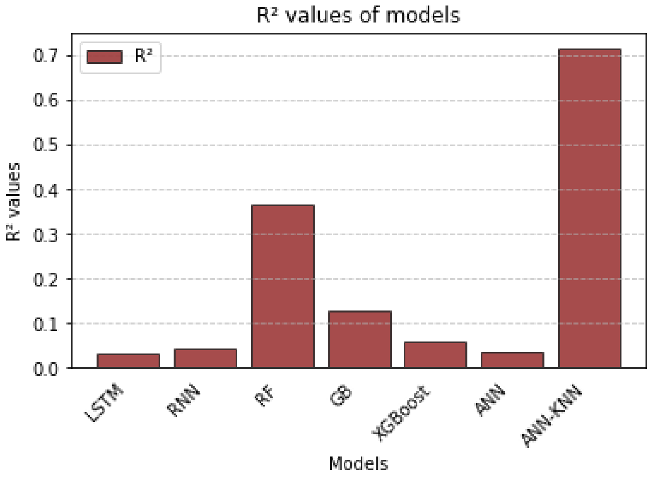

Figure 9. *Comparison of R^2 values of the models*

To visualize the results obtained from the models established in the study, scatter plots of the actual values and the predicted values produced by these models are presented in Figure 10. In these scatter plots, the x-axis represents the actual values, and the y-axis represents the predicted values. The distribution graphs created for each model are compared with the y=x line that runs through the center of the graph. Points that are close to the y=x line indicate good model performance, while points that are far from the line indicate poor performance.

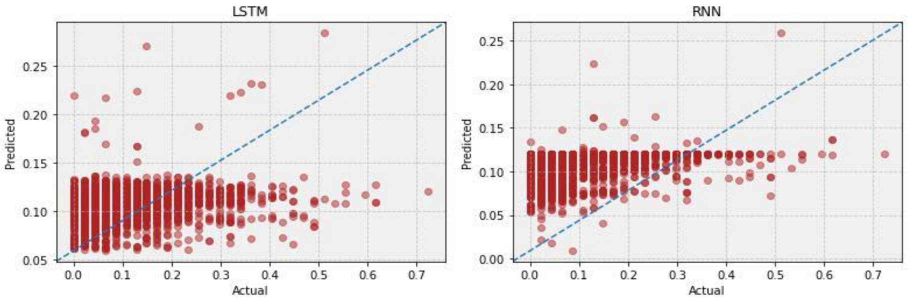

a. LSTM model *b. RNN model*

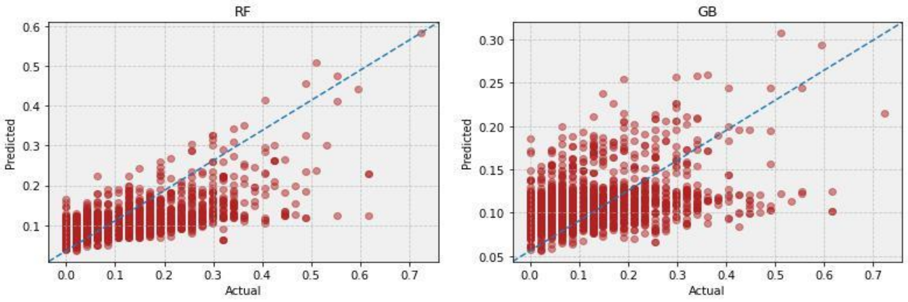

c. RF model *d. GB model*

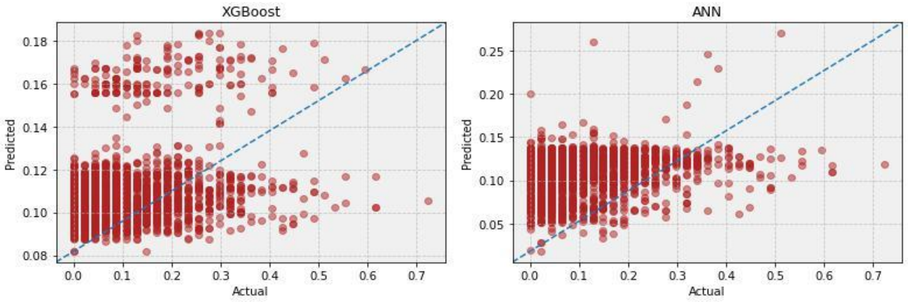

e. XGBoost model *f. ANN model*

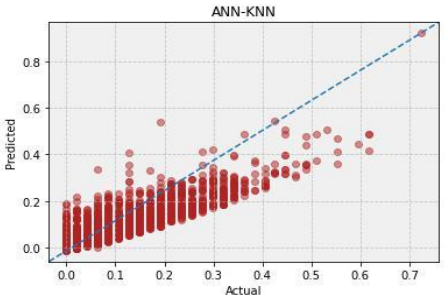

g. ANN-KNN model

Figure 10. *Distributions of actual values and model predictions*

When examining the scatter plots presented in Figure 10, it can be observed that the LSTM, RNN, XGBoost, and ANN models exhibit points that are distant and widely distributed from the y=x line. Therefore, it is concluded that the predictions of these models do not align with the actual values and show low performance, as seen in the results obtained from Table 3 and Figures 6-7-8-9. On the other hand, in the RF and GB models, the points are closer to and more concentrated around the y=x line, indicating relatively better performance compared to the other four models. The best distribution among the models is achieved with the ANN-KNN model, where the points are close to the y=x line and have a smooth distribution.

Conclusion

Due to the major threat posed by earthquake disasters worldwide, continuous studies related to earthquakes are conducted; however, high success in predicting when and where future major earthquakes will occur has not yet been achieved. Nevertheless, in some countries where earthquakes frequently occur and cause significant destruction, earthquake prediction models are actively utilized [36] In this study, a two-phase earthquake analysis was carried out using the main earthquakes that occurred in Türkiye between 2000-2023 data collected from the Kandilli Observatory and Earthquake Research Institute; aiming to contribute to the literature with the analysis results. In the first phase, the dataset was divided into 7 sub-datasets based on the geographical regions of Türkiye using location information, and the table for each region was analyzed based on monthly total earthquake counts and average magnitudes; the depth-magnitude relationship of earthquakes was examined. In the second phase of the study, a hybrid learning model integrating LSTM, RNN, RF, GB, XGBoost, 2 hidden-layer ANN, and ANN with KNN algorithms was used to attempt magnitude estimation of potential future earthquakes; the models' prediction performances were compared using different evaluation metrics. The results present a positive outlook on the usability of earthquake prediction models.

Acknowledgements -

Funding/Financial Disclosure The authors have no received any financial support for the research, authorship, or publication of this study.

Ethics Committee Approval and Permissions The work does not require ethics committee approval and any private permission.

Conflict of Interests The authors stated that there are no conflict of interest in this article.

Authors Contribution Authors contributed equally to the study. All authors read and approved the final manuscript.

References

[1] AFAD. (2023, February 12). *Açıklamalı Afet Yönetimi Terimleri Sözlüğü.* https://www.afad.gov.tr/aciklamali-afet-yonetimi-terimleri-sozlugu

[2] EM-DAT. (2023, February 18). *Disaster Classification.* https://www.emdat.be/

[3] Santos, G. D. C. (2021). 2020 tropical cyclones in the Philippines: A review. Tropical *Cyclone Research and Review*, *10*(3), 191-199. https://doi.org/10.1016/j.tcrr.2021.09.003

[4] Winsemius, H. C., Aerts, J. C., Van Beek, L. P., Bierkens, M. F., Bouwman, A., Jongman, B., Kwadijk, J. C., Ligtvoet, W., Lucas, P. L., & Van Vuuren, D. P. (2016). Global drivers of future river flood risk. *Nature Climate Change*, *6*(4), 381-385. https://doi.org/10.1038/nclimate2893

[5] Özşahin, E. (2013, September 25-27). *Türkiye'de yaşanmiş (1970-2012) doğal afetler üzerine bir değerlendirme.* [Conference presentation]. Türkiye Deprem Mühendisliği ve Sismoloji Konferansı, Hatay, Türkiye.

[6] Bilham, R. (2009). The seismic future of cities. *Bulletin of earthquake engineering*, *7*, 839-887. https://doi.org/10.1007/s10518-009-9147-0

[7] Kavianpour, P., Kavianpour, M., Jahani, E., & Ramezani, A. (2023). A CNN-BiLSTM model with attention mechanism for earthquake prediction. *The Journal of Supercomputing*, *79*(17), 19194-19226. https://doi.org/10.1007/s11227-023-05497-5

[8] Jia, J. (2016). *Modern earthquake engineering: Offshore and land-based structures.* Springer.

[9] Çam, H., & Duman, O. (2016). Yapay Sinir Aği Yöntemiyle Deprem Tahmini: Türkiye Bati Anadolu Fay Hatti Uygulamasi. *Gümüshane University Electronic Journal of the Institute of Social Science/Gümüshane Üniversitesi Sosyal Bilimler Enstitüsü Elektronik Dergisi*, *7*(17).

[10] Mallouhy, R., Abou Jaoude, C., Guyeux, C., & Makhoul, A. (2019, December 18-20). *Major earthquake event prediction using various machine learning algorithms* [Conference presentation]. 2019 International Conference on Information and Communication Technologies for Disaster Management (ICT-DM), Paris, France. 10.1109/ICT-DM47966.2019.9032983

[11] Wang, X., Zhong, Z., Yao, Y., Li, Z., Zhou, S., Jiang, C., & Jia, K. (2023). Small Earthquakes Can Help Predict Large Earthquakes: A Machine Learning Perspective. *Applied Sciences*, *13*(11), 6424. https://doi.org/10.3390/app13116424

[12] Demirelli, E., Solak, H. İ., & Tiryakioglu, İ. (2023). Makine öğrenmesi algoritmaları ile deprem katalogları kullanılarak deprem tahmini. *Gümüşhane Üniversitesi Fen Bilimleri Dergisi*, *13*(4), 979-989. https://doi.org/10.17714/gumusfenbil.1268504

[13] Emre, Ö., Duman, T. Y., Özalp, S., Şaroğlu, F., Olgun, Ş., Elmacı, H., & Çan, T. (2018). Active fault database of Turkey. *Bulletin of earthquake engineering*, *16*(8), 3229-3275. https://doi.org/10.1007/s10518-016-0041-2

[14] Karcı, M., & Şahin, İ. (2022). Derin öğrenme yöntemleri kullanılarak deprem tahmini gerçekleştirilmesi. *Artificial Intelligence Studies*, *5*(1), 23-34.

[15] Kandilli. (2023, January 10). *Kandilli Rasathanesi BDTİM Deprem Sorgulama Sistemi.* http://www.koeri.boun.edu.tr/sismo/zeqdb/

[16] AFAD. (2023, February 18). *Genel Bilgiler.* http://www.koeri.boun.edu.tr/sismo/bilgi/sss_tr.htm

[17] USGS. (2023, January 21). *Earthquakes*. https://www.usgs.gov/

[18] Habek, G. C. (2022). *Makine Öğrenmesi Teknikleri ile Kripto Para Duygu Analizi.* (Tez no. 763894) [Yüksek Lisans Tezi, Manisa Celal Bayar Üniversitesi].

[19] Mitchell, T. M. (1997). *Machine learning* (Vol. 1). McGraw-hill New York.

[20] Friedman, J. H. (2001). Greedy function approximation: a gradient boosting machine. *Annals of Statistics*, *29*(5), 1189-1232.

[21] Freund, Y., Schapire, R., & Abe, N. (1999). A short introduction to boosting. *Journal-Japanese Society For Artificial Intelligence*, *14*(5), 771-780.

[22] Chen, T., & Guestrin, C. (2016). Xgboost: A scalable tree boosting system. *Proceedings of the 22nd acm sigkdd international conference on knowledge discovery and data mining,* 785-794. https://doi.org/10.1145/2939672.29397

[23] Bentéjac, C., Csörgő, A., & Martínez-Muñoz, G. (2021). A comparative analysis of gradient boosting algorithms. *Artificial Intelligence Review*, *54*, 1937-1967. https://doi.org/10.1007/s10462-020-09896-5

[24] Breiman, L. (2001). Random forests. *Machine learning*, *45*, 5-32. https://doi.org/10.1023/A:1010933404324

[25] Kurtgoz, Y., Karagoz, M., & Deniz, E. (2017). Biogas engine performance estimation using ANN. *Engineering Science and Technology, an International Journal*, *20*(6), 1563-1570. https://doi.org/10.1016/j.jestch.2017.12.010

[26] Akhter, M. N., Mekhilef, S., Mokhlis, H., Almohaimeed, Z. M., Muhammad, M. A., Khairuddin, A. S. M., Akram, R., & Hussain, M. M. (2022). An hour-ahead PV power forecasting method based on an RNN-LSTM model for three different PV plants. *Energies*, *15*(6), 2243. https://doi.org/10.3390/en15062243

[27] Bengio, Y., Simard, P., & Frasconi, P. (1994). Learning long-term dependencies with gradient descent is difficult. *IEEE Transactions on Neural Networks*, *5*(2), 157-166. https://doi.org/10.1109/72.279181

[28] LeCun, Y., Bengio, Y., & Hinton, G. (2015). Deep learning. *Nature*, *521*(7553), 436-444. https://doi.org/10.1038/nature14539

[29] Akandeh, A., & Salem, F. M. (2019, August 04-07). *Slim lstm networks: Lstm_6 and lstm_c6* [Conference presentation]. 2019 IEEE 62nd International Midwest Symposium on Circuits and Systems (MWSCAS), Dallas, TX, USA. https://doi.org/10.1109/MWSCAS.2019.8884912

[30] Clarke, M. (1974). Pattern classification and scene analysis. *In: Wiley Online Library* https://doi.org/10.2307/2344977

[31] Akbulut, Y., Sengur, A., Guo, Y., & Smarandache, F. (2017). NS-k-NN: Neutrosophic set-based k-nearest neighbors classifier. *Symmetry*, *9*(9), 179. https://doi.org/10.3390/sym9090179

[32] Demir, F. (2021). Siber saldırı tespiti için makine öğrenmesi yöntemlerinin performanslarının incelenmesi. *Balıkesir Üniversitesi Fen Bilimleri Enstitüsü Dergisi*, *23*(2), 782-791. https://doi.org/10.25092/baunfbed.876338

[33] Nguyen, V. V., Pham, B. T., Vu, B. T., Prakash, I., Jha, S., Shahabi, H., Shirzadi, A., Ba, D. N., Kumar, R., & Chatterjee, J. M. (2019). Hybrid machine learning approaches for landslide susceptibility modeling. *Forests*, *10*(2), 157. https://doi.org/10.3390/f10020157

[34] Robeson, S. M., & Willmott, C. J. (2023). Decomposition of the mean absolute error (MAE) into systematic and unsystematic components. *PloS One*, *18*(2), https://doi.org/10.1371/journal.pone.0279774

[35] Demirtaş, R., & Erkmen, C. (2000). Odak mekanizması çözümü. *Deprem ve Jeoloji, TMMOB Jeoloji Mühendisleri Odası Yayınları*, *52*, 91-94.

[36] Chen, J., & Zhu, S. (2020). Spatial and temporal b-value precursors preceding the 2008 Wenchuan, China, earthquake (Mw= 7.9): implications for earthquake prediction. *Geomatics, Natural Hazards and Risk*, *11*(1), 1196-1211. https://doi.org/10.1080/19475705.2020.1784297

Sinopfbd, 2024; 9(2): 287-301 **https://doi.org/10.33484/sinopfbd.1471890**

Sinop Üniversitesi Fen Bilimleri Dergisi
Sinop Uni J Nat Sci

E-ISSN: 2564-7873

https://dergipark.org.tr/tr/pub/sinopfbd

Al-Ni İntermetalik Bileşiklerinin Gama Radyasyonu Zırhlama Parametrelerinin Hesaplanması

Ömer Faruk ÖZDEMİR[1] ve Nergiz YILDIZ YORGUN[1]

How to cite: Özdemir, Ö. F., & Yıldız Yorgun, N. (2024). Al-Ni intermetalik bileşiklerinin gama radyasyonu zırhlama parametrelerinin hesaplanması. *Sinop Üniversitesi Fen Bilimleri Dergisi, 9*(2), 287-301. https://doi.org/10.33484/sinopfbd.1471890

Araştırma Makalesi

Sorumlu Yazar
Ömer Faruk ÖZDEMİR
o.f.ozdemir@gmail.com

Yazarlara ait ORCID
Ö.F.Ö: 0000-0002-2389-1139
N.Y.Y: 0000-0002-2515-1994

Received: 22.04.2024
Accepted: 24.06.2024

Öz

Bu çalışmada yüksek mukavemet, düşük özgül ağırlık, termal stabilite, yüksek termal iletkenlik (76 W/mK) ve oksidasyon/korozyon direnci gibi sahip oldukları fiziksel özelliklerle nükleer uygulamalar için potansiyel barındıran Al-Ni intermetalik bileşiklerinin (Al_3Ni, Al_3Ni_2, Al_4Ni_3, AlNi, Al_3Ni_5 ve $AlNi_3$) radyasyon zırhlama özellikleri incelendi. WinXCom programı ile 1 keV - 10^5 MeV aralığında, PHITS ve GEANT4 programları ile 0.047 – 2.506 MeV aralığındaki foton enerjileri için yapılan hesaplamalarla kütle soğurma katsayıları, lineer soğurma katsayıları, yarı kalınlık değerleri (YKD), onda bir kalınlık değerleri (OKD), ortalama serbest yolları (MFP) ve etkin atom numaraları elde edildi. Seçilen enerji aralığında her üç programla da elde edilen sonuçların iyi bir uyum içerisinde oldukları tespit edildi. İntermetalik bileşiğin yoğunluğunun artmasıyla, kütle soğurma katsayısı ve etkin atom numaraları değerlerinin arttığı, YKD, OKD ve OSY değerlerinin ise azaldığı görüldü. Hesaplanan parametreler incelenerek Al-Ni intermetalik bileşiklerinin literatürde zırhlama malzemesi olarak önerilen diğer malzemelerle karşılaştırıldığında daha düşük zırhlama kapasitesine sahip olsa da radyasyon zırhlama için yeterli düzeyde olduğu ve $AlNi_3$ bileşiğinin diğer bileşiklere oranla gama zırhlama için daha uygun bir aday olduğu tespit edildi.

Anahtar Kelimeler: Radyasyon zırhlama, Al-Ni, İntermetalik bileşik, Geant, Phits

Calculation of Gamma Radiation Shielding Parameters of Al-Ni İntermetallic Compounds

[1]Van Yüzüncü Yıl Üniversitesi, Fen Fakültesi, Fizik Bölümü, Van, Türkiye

Abstract

In this study, the radiation shielding properties of Al-Ni intermetallic compounds (Al_3Ni, Al_3Ni_2, Al_4Ni_3, AlNi, Al_3Ni_5 and $AlNi_3$), which have the potential for nuclear applications due to their physical properties such as high strength, low density, thermal stability, high thermal conductivity (76 W/mK) and oxidation/corrosion resistance, were investigated. Mass absorption coefficients, linear absorption coefficients, half thickness values (HVL), tenths thickness values (TVL), mean free paths (MFP) and effective atomic numbers were obtained by calculations for photon energies in the range of 1 keV -105 MeV with WinXCom program and 0.047 - 2.506 MeV with PHITS and GEANT4 programs. The results obtained with all three programs were in good agreement in the selected energy range. The values of the mass absorption coefficient and effective atomic numbers were observed to increase with increasing density of the intermetallic compound. In contrast, the values of the HVL, TVL and MFP decreased. By examining the calculated parameters, Al-Ni intermetallic compounds were determined to have lower armouring capacity compared with other materials proposed as armouring materials in literature. Still, they are sufficient for radiation shielding and the $AlNi_3$ compound is a more suitable candidate for gamma shielding compared with other compounds.

Keywords: Radiation shielding, Al-Ni, Intermetalic compound, Geant, Phits

Giriş

Disiplinler arası çalışmaların yeni teknolojilerle desteklenmesi, nükleer teknolojilerin de pek çok alanda kullanımını yaygınlaştırmaktadır. Yüksek enerjili fotonların ve nötronların madde ile etkileşiminin tıp, nükleer enerji ve radyoizotop üretimi, gıda güvenliği, endüstriyel tahribatsız muayene, kriminal çalışmalar ve uzay çalışmaları gibi çeşitli alanlarda faydalı uygulamaları bulunur [1-3]. Bu gelişmeler insan kaynaklı radyasyon maruziyetinin birincil kaynağı olan radyonüklidlerin sayısını da artırır. Sonuçta radyasyonun kaçınılmaz olarak sebep olacağı olumsuz biyolojik etkileri minimum düzeyde tutmak için uygun koruyucu malzemelerin kullanılması gerekliliği de artar. Radyasyon maruziyeti, olumsuz sağlık ve çevresel etkiler doğurur. Uygun radyasyon zırhlama özelliklerine sahip malzemeler, deterministik etkilerin ortaya çıkmasını önlemeye, stokastik etkilerin olasılığını yönetilebilir bir düzeye indirmeye ve çevresel hasarı önlemeye yardımcı olduklarından özellikle biyolojik zırhlama için büyük önem taşırlar [4]. Radyasyon üreten ya da radyasyona duyarlı bazı cihazların ve radyoaktif kaynakların güvenli kullanımı için de etkili radyasyon zırhlamasına sahip malzemelerin kullanılması oldukça önemli bir zorunluluktur. Radyasyon zırhlama için kullanılacak malzemeler, radyoaktif izotoplardan yayılan radyasyonun türüne ve enerjisine bağlı olarak çeşitlilik gösterir ve uygun malzemelerin özelliklerini araştırmak için pek çok çalışma yapılmaktadır. Bu amaçla polimer [4, 5], alaşım [6, 7], seramik [8, 9], cam [10, 11] ve beton [12, 13] benzeri pek çok malzemenin radyasyon zırhlama parametreleri incelenmiştir. Zırhlama malzemesi olarak potansiyele sahip intermetalik bileşikler, metal ve seramiklerin ara özelliklerine sahip, yüksek erime sıcaklığı, düşük yoğunluk ve iyi korozyon direnci de dahil olmak üzere pek çok fiziksel ve mekanik özellikleri ile malzeme bilimi alanında kapsamlı araştırmalara konu olan bir metalik malzeme sınıfıdır [14-19]. Sahip oldukları özellikleri ile, yüksek sıcaklıklı gaz türbini, korozyona dayanıklı malzemeler, ısıl işlem armatürleri, manyetik malzemeler ve hidrojen depolama malzemeleri vb. (>1200 ◦C) yüksek sıcaklık mühendisliği uygulamalarında kullanılmasının yanı sıra nükleer güvenlik sistemlerinde, uzay teknolojilerinde ve tıpta kullanım potansiyeli yüksek olan malzemeler olarak nitelendirilirler [19-21]. İntermetalik bileşiklerden Al-Ni bileşikleri, yüksek mukavemet, düşük özgül ağırlık, termal stabilite, yüksek termal iletkenlik (76 W/mK) ve 1400 °C'ye kadar iyi oksidasyon/korozyon direnci gibi özelliklere sahiptir ve faz diyagramlarının ilk yayınlandığı 1908'den beri birçok araştırmacı tarafından deneysel ve teorik olarak incelenmiştir [14, 15, 17, 20-24]. Al-Ni intermetalik bileşikleri yüksek sıcaklıktaki ortamlarda kullanım için Ni bazlı süper alaşımların yerini alabilecek yüksek potansiyelli hafif malzemeler olarak ayrıca nano ısıtıcı – Ni reaktif nanoyapı vb. – nanoteknolojik uygulamaları da içeren endüstriyel kullanım için önemli malzemeler arasında yer alır [16, 17, 25]. Shi ve ark., [24] Al-Ni faz diyagramlarına dayanarak, Al-Ni sistem bileşiğinde, Al_3Ni, Al_3Ni_2, Al_4Ni_3, AlNi, Al_3Ni_5 ve $AlNi_3$ olmak üzere altı intermetalik bileşiğin mevcut olabileceğini bildirmektedir. Bunlardan $AlNi_3$ ve AlNi, süper alaşımların çoğunda güçlendirme aşamasında işlev gören önemli iki alüminittir [20]. Literatürde Al ve Ni bazlı alaşımların, farklı metallerle intermetalik alaşımları ya da farklı kullanım amaçlarına yönelik üretilen çelik tipleri (superalloy) üzerine, çeşitli fiziksel özellikleri ve radyasyon zırhlama parametreleri ile ilgili çok sayıda araştırma mevcuttur [1, 7, 19, 20, 24, 26-29]. Bu çalışmada intermetalik bileşiklerden Al-Ni bileşiklerinin nükleer uygulamalar için sahip olduğu potansiyel göz önüne alınarak, faz diyagramlarına göre bildirilen altı adet intermetalik bileşiğinin (Al_3Ni, Al_3Ni_2, Al_4Ni_3, AlNi, Al_3Ni_5 ve $AlNi_3$) radyasyon zırhlama özellikleri incelendi. Doğrudan hesaplama programı (WinXCom) ve Monte Carlo simülasyon programları (PHITS 3.27, GEANT4) ile tıp ve radyografi uygulamalarında kullanılan radyoizotopların gama yayınlama enerjileri dikkate alınarak belirlenen enerji aralığında elde edilen sonuçlar, Al-Ni bileşiklerinin gama zırhlama yeterliliğini belirlemek için analiz edildi.

Materyal ve Yöntem

Radyasyon zırhlamasına konu olan malzemelerin, kütle soğurma katsayısı (μ_m), etkin atom numarası (Z_{etk}) gibi radyasyon zırhlama parametreleri deneysel verilerle tespit edilebilmekte ya da deterministik yaklaşımla foton tesir kesiti veri tabanlarına dayalı hesaplama yapan programlar (XCOM, EpiXS, Phy-X/PSD vb.) ve daha kompleks geometrilerde istatistiksel çözümler sunan simülasyon programları (MCNP, GEANT4, FLUKA ve PHITS) ile hesaplanabilmektedir. Verilen üç yöntem de kabul edilebilir doğruluk ve hassasiyete sahiptir, ancak kodlar aracılığıyla doğrudan hesaplama ve simülasyonların deney yapmaya kıyasla daha hızlı ve daha ucuz olması birçok malzemenin radyasyon zırhlama parametrelerinin bu iki yaklaşım kullanılarak incelenmesine olanak sağlar [4, 6, 7, 10, 11, 28, 30, 31]. WinXCom, mermi tanecik olarak yalnızca foton seçilmesine olanak sağlayan ancak herhangi bir geometri tanımlamasına gerek olmadan kütle zayıflama katsayılarını ve zırhlama parametrelerini hesaplamak için kullanılan bir programdır [32]. Çoklu iş parçacığı için optimize edilmiş ve karmaşık simülasyonları yüksek hassasiyetle gerçekleştirebilen Monte Carlo Simülasyon programları ise daha karmaşık geometri tanımlarına olanak sağlarken, mermi tanecik seçiminde de esneklik getirirler. Örneğin PHITS, geniş bir enerji aralığında farklı parçacıklar için radyasyon ve malzemeler arasındaki çarpışmaları simüle eden bir programdır. Hafif yüklü parçacıklar için INCL 4.6 (Liége intranükleer kaskad) ve daha ağır parçacık etkileşimleri için JQMD (Jaeri Quantum Molecular Dynamics) modeli gibi çeşitli fizik modellerini ve veri tabanlarını içeren PHITS, foton-madde etkileşimi hesaplamalarında EPDL97 ve EGS (Electron Gamma Shower) kütüphanelerinin kullanımına olanak sağlar [33]. Yüksek enerji fiziği deneylerinde dedektör simülasyonları için yaygın olarak kullanılan ve radyasyondan korunma ve tıbbi fizik dahil olmak üzere çeşitli alanlarda uygulamaları olan GEANT4 simülasyon programı ise farklı enerji aralıkları için QGS (Quark-gluon String) ve FTF (Fritiof string) gibi modeller içerir [34]. Foton-madde etkileşimi için tesir kesiti hesaplamalarında analitik yaklaşım sağlayan standart elektromagnetik modele ek olarak, Livermore modelleri, Penolope modeli gibi farklı modellerin de kullanılmasına olanak sağlar [35]. Bu çalışmada radyasyon zırhlama parametreleri incelenen Al_3Ni, Al_3Ni_2, Al_4Ni_3, AlNi, Al_3Ni_5 ve $AlNi_3$ intermetalik bileşiklerinin literatürden alınan yoğunluk [24] ve % ağırlık değerleri Tablo 1'de verilmektedir.

Tablo 1. *Seçilen intermetalik bileşiklerin kimyasal içerikleri ve yoğunlukları* [24]

Numune	**Bileşimi (% Ağırlık)**		**Yoğunluk (g/cm^3)**
	Al	**Ni**	
Al_3Ni	0.5797	0.4203	4.1
Al_3Ni_2	0.4081	0.5919	4.9
Al_4Ni_3	0.3800	0.6200	5.22
AlNi	0.3149	0.6851	6.04
Al_3Ni_5	0.2162	0.7838	6.73
$AlNi_3$	0.1329	0.8671	7.5

Gama zırhlama özellikleri incelenen bileşikler için kütle soğurma katsayıları (μ_m), lineer soğurma katsayıları (μ), yarı kalınlık değerleri (YKD), onda bir kalınlık değerleri (OKD), ortalama serbest yolları (OSY), etkin atom numaraları (Z_{etk}) WinXCom [32], PHITS 3.27 [33] ve GEANT4 [34] programları ile elde edildi ve literatürde belirtilen çeşitli ampirik denklemler ile (Eşitlik 1-7) hesaplanarak karşılaştırıldı [29, 31, 36]. Phits ve Geant simülasyonları için literatürdeki deneysel çalışmalarda [11] yer alan temel dar ışın geometrisi kullanıldı (Şekil 1) ve istatistiksel hatanın minimum olması amacıyla hesaplamalar 1000000 parçacıkla yapıldı. PHITS hesaplamalarında foton tesir kesitleri için EGS modeli kullanılırken, GEANT4 hesaplamalarında Standart elektromagnetik model tercih edildi. Her iki simülasyon programında da hedefin kalınlık değeri, düşük enerjilerdeki fotonların tamamıyla soğrulmasını önlemek amacıyla 5 mm olarak ayarlandı.

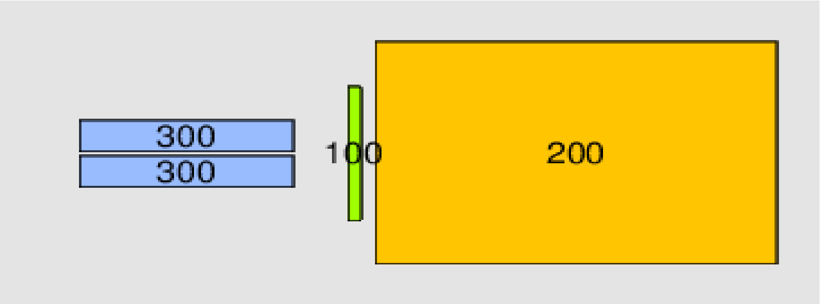

Şekil 1. *Simülasyonda kullanılan geometrinin 2 boyutlu gösterimi.*

Fotonun madde ile etkileşim parametrelerinin en önemlilerinden biri olan ve malzemelerin radyasyondan korunma etkinliğinin tanımlamak için kullanılan kütle soğurma katsayısı (μ_m), Beer-Lambert Yasası ile elde edilir:

$$I = I_0 e^{-\mu t} \tag{1}$$

$$\mu_m = \frac{\mu}{\rho} = \ln(I_0/I)/\rho t \tag{2}$$

Burada I_0 gelen gama ışını yoğunluğu; I ortamdan geçen gama ışını yoğunluğu; μ lineer soğurma katsayısı (cm^{-1}), μ_m kütle soğurma katsayısı (cm^2/g), ρ ortamın yoğunluğu (g/cm^3) ve t ortamın kalınlığıdır (cm). Bir bileşik için kütle soğurma katsayısı, bileşiği oluşturan elementlerin ağırlık oranlarına (w_i) bağlı olarak Eşitlik 3 ile hesaplanır:

$$\mu_m = \sum_i w_i (\mu_m)_i \tag{3}$$

Numunelerin gama ışınını zırhlama etkilerini açıklayan diğer temel teorik parametreler; yarı kalınlık değeri (YKD), gelen radyasyon şiddetinin yarıya azaldığı malzeme kalınlığı, onda-bir kalınlık değeri (OKD), gelen radyasyon şiddetinin onda birine düştüğü malzeme kalınlığı ve ortalama serbest yol (OSY), iki ardışık foton etkileşimi arasındaki ortalama hareket mesafesi olarak tanımlanır. YKD, OKD ve OSY sırasıyla Eşitlik 4-5-6 ile hesaplanabilir.

$$YKD = {}^{ln2}/_{\mu} \tag{4}$$

$$OKD = {}^{ln10}/_{\mu} \tag{5}$$

$$OSY = {}^{1}/_{\mu} \tag{6}$$

Numune, bir karışım veya bileşik olduğunda etkin atom numarası (Z_{etk}) toplam atomik tesir kesiti (σ_a) ile toplam elektronik tesir kesitinin (σ_e) oranı olarak verilir ve aşağıdaki eşitliğe indirgenir [37].

$$Z_{eff} = \frac{\sum_i f_i A_i \left({}^{\mu}/_{\rho}\right)_i}{\sum_j \frac{f_j A_j}{Z_j} \left({}^{\mu}/_{\rho}\right)_j} \tag{7}$$

Burada A : atomik kütle, Z : atom numarası ve f : molar kesirdir.

Bulgular

Yoğunluk ve % ağırlık değerleri Tablo 1'de verilen AlNi intermetalik bileşiklerinin radyasyon zırhlama özelliklerini incelemek için kütle soğurma katsayıları (μ_m), lineer soğurma katsayıları, yarı kalınlık değerleri, onda bir kalınlık değerleri, ortalama serbest yolları, etkin atom numaraları WinXCom, PHITS 3.27 ve GEANT4 programları ve analitik ifadelerle elde edildi. Tablo 1'den, ağırlıkça % oranları değişen Al ve Ni'in oluşturdukları bileşiklerin yoğunluklarının 4.1 ile 7.5 g/cm^3 arasında değiştiği görülür. Yüzde ağırlık ve yoğunluk değişimleri incelendiğinde, artan Ni konsantrasyonu (% ağırlık) ile kütle yoğunluğunun ρ (g/cm^3) yaklaşık olarak doğrusal bir ilişkiyle arttığı söylenebilir [24]. Şekil 2, seçilen intermetalik bileşiklerin 1 keV ile 10^5 MeV aralığındaki enerjilerde, WinXCom ile hesaplanan teorik kütle soğurma katsayı (μ_m) değerlerini göstermektedir. Şekil detaylı olarak incelendiğinde, foton enerjisi arttıkça kütle soğurma katsayısının üstel olarak azaldığı görülür. Bu durum, foton kısmi etkileşim süreçleri temelinde açıklanabilir. Düşük enerji bölgesinde (E <0.04 MeV) fotoelektrik etkinin baskın olduğunu söyleyebiliriz. Bu bölgede, incelenen örnekler için μ_m değeri artan enerjiyle keskin bir şekilde azalmaktadır. Bu durum, fotoelektrik mikroskobik tesir kesitinin gelen foton enerjisi (E) ile ters orantılı olduğu ve örneklerin atom numarası (Z) ile doğru orantılı olduğu ile açıklanabilir. Yine bu bölgede bazı enerji değerlerinde pikler görülmektedir. Bu pikler fotoelektrik etki nedeniyle 1.0081 ve 8.3328 keV'de (Ni'nin L-I ve K soğurma kenarı) ve 1.5596 KeV'de (Al'nin K soğurma kenarı) meydana gelir. 0.04< E <2.6 MeV'de μ_m değerleri yavaş yavaş azalmakta ve bileşiklerin μ_m değerleri arasındaki fark neredeyse sıfıra yaklaşmaktadır. Bu bölge Compton saçılmasının baskın olduğu bölgedir. Bu bölgede mikroskobik tesir kesiti, enerji (E) ile ters orantılı ve soğurucu malzemenin atom numarası (Z) ile doğrusal olarak ilişkili olmasından kaynaklanmaktadır. 2.6 MeV'den sonra μ_m değerleri hafifçe artar ve sonra neredeyde sabit kalır. Bu durum çift oluşum sürecinin ortamın atom numarası Z^2'ye bağımlılığı ile açıklanmaktadır. Araştırılan tüm bileşikler için μ_m değerlerindeki değişiklikler benzer bir model izlemektedir; farklı enerji sınırlarında önce keskin bir azalış daha sonra hafif bir azalış ve en sonunda hafif bir artış şeklindedir. Diğer taraftan, bileşiklerin soğurma yeteneği bileşiklerin yoğunluğu ile güçlü bir şekilde ilişkilidir. Örneğin $AlNi_3$ bileşiğinin yoğunluğu yüksek olduğu için gama fotonlarını daha yüksek soğurma kabiliyetindedir. Her ne kadar bileşiklerdeki μ_m değerleri arasındaki fark küçük olsa da, $AlNi_3$ bileşiğinin μ_m değerleri tüm enerjilerde biraz daha yüksektir. Ayrıca μ_m değerleri, 0.047 ile 2.506 MeV enerji aralığında PHITS 3.27 ve GEANT4 simülasyon kodları kullanılarak hesaplandı. Simülasyon değerlerinin teorik tahminlerle doğrulanması, mevcut sonuçların doğruluğunun ispatlanmasında temel rol oynamaktadır. Bu nedenle PHITS ve GEANT sonuçları WinXCom yazılımı kullanılarak elde edilen teorik değerlerle karşılaştırıldı (Tablo 2). Buna ek olarak Tablo 2'ye WinXCom ile PHITS ve WinXCom ile GEANT arasındaki yüzde sapma (% sapma) değerleri Eşitlik 8 kullanılarak eklendi.

$$\%Sapma = \left| \frac{\left({}^{\mu}/_{\rho}\right)_{\mathrm{T}} - \left({}^{\mu}/_{\rho}\right)_{\mathrm{S}}}{\left({}^{\mu}/_{\rho}\right)_{\mathrm{T}}} \right| X100 \qquad (8)$$

Burada S, simülasyon kodları (PHITS ve GEANT) kullanılarak elde edilen sonuçları, T ise WinXCom yazılımı kullanılarak hesaplanan teorik değerleri ifade etmektedir. En yüksek fark, %10.136 değeriyle 0.099 MeV enerjili fotonda $AlNi_3$ numunesinde gözlendi. Bu nedenle simülasyon sonuçları ile teorik değerler arasında iyi bir uyum olduğu söylenebilir.

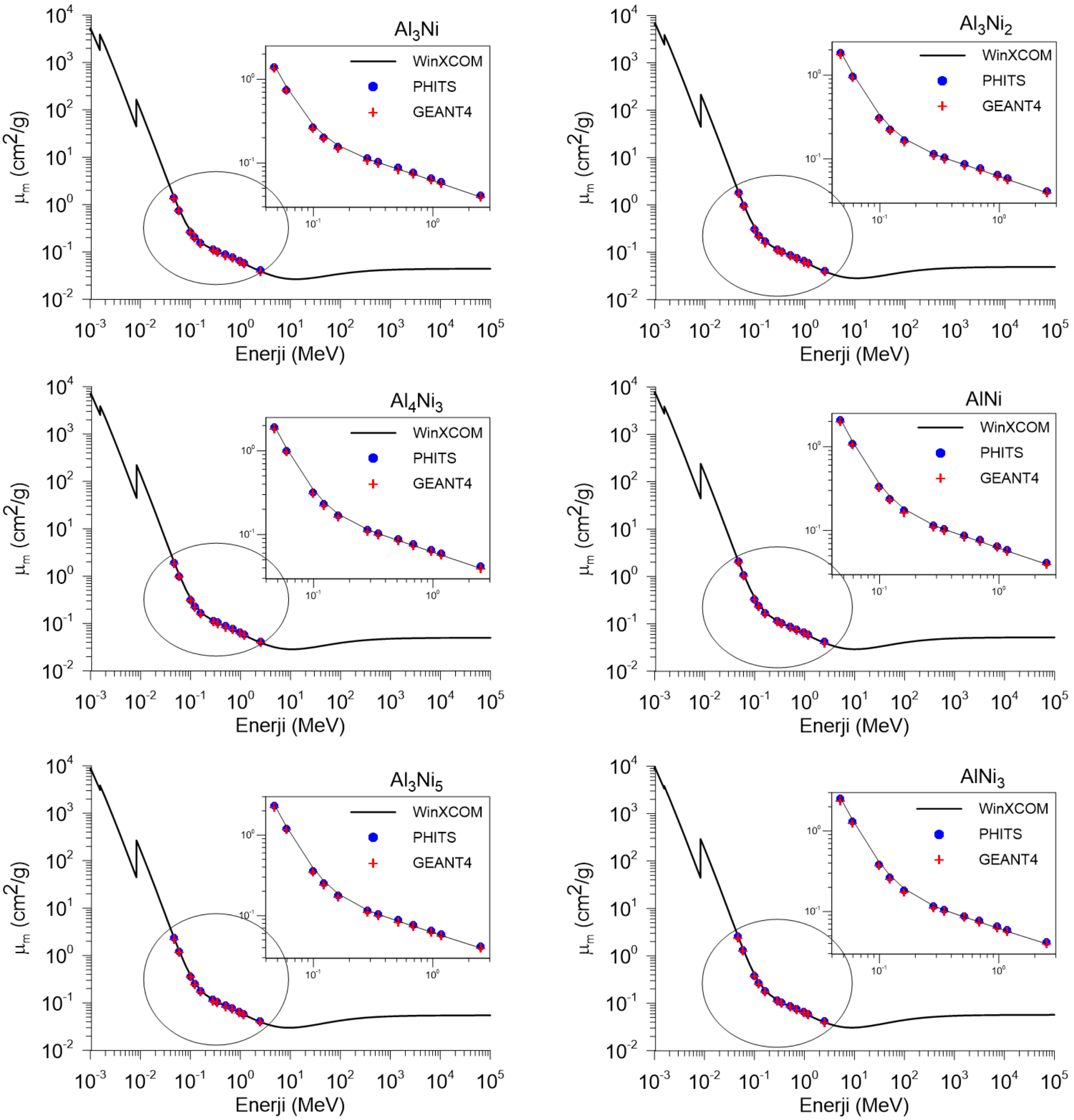

Şekil 2. *Al-Ni intermetalik bileşiklerinin 1 keV ile 10^5 MeV enerji aralığında WinXCom ve seçilen enerjilerde PHITS ve GEANT4 ile hesaplanan kütle soğurma katsayıları*

Tablo 2. *Al-Ni intermetalik bileşiklerinin seçilen enerjilerde WinXCom, PHITS ve GEANT4 ile hesaplanan kütle soğurma katsayıları (cm^2/g)*

Enerji (MeV)	**Al_3Ni**					**Al_3Ni_2**					**Al_4Ni_3**				
	WinXCom	**PHITS**	**GEANT**	**% phits**	**% geant**	**WinXCom**	**PHITS**	**GEANT**	**% phits**	**% geant**	**WinXCom**	**PHITS**	**GEANT**	**% phits**	**% geant**
0.047	1.472	1.389	1.360	5.627	7.618	1.905	1.831	1.767	3.856	7.236	1.976	1.905	1.834	3.588	7.192
0.060	0.811	0.742	0.740	8.471	8.732	1.027	0.960	0.943	6.523	8.216	1.063	0.997	0.975	6.227	8.254
0.099	0.290	0.265	0.262	8.758	9.544	0.338	0.309	0.301	8.742	11.075	0.346	0.316	0.312	8.665	9.832
0.122	0.216	0.202	0.196	6.237	8.939	0.242	0.226	0.219	6.738	9.427	0.246	0.229	0.222	6.771	9.587
0.161	0.162	0.157	0.150	3.500	7.404	0.174	0.167	0.160	4.274	8.066	0.176	0.168	0.161	4.404	8.297
0.284	0.112	0.113	0.108	-0.975	3.681	0.114	0.115	0.110	-0.297	3.813	0.115	0.115	0.110	-0.061	4.367
0.347	0.101	0.103	0.099	-1.882	2.540	0.103	0.104	0.099	-1.508	3.558	0.103	0.104	0.100	-1.304	3.083
0.511	0.085	0.088	0.084	-3.351	0.910	0.085	0.088	0.084	-2.975	1.257	0.085	0.088	0.084	-3.012	1.166
0.689	0.074	0.077	0.074	-3.802	0.118	0.074	0.077	0.074	-3.590	0.201	0.074	0.077	0.074	-3.555	0.301
0.964	0.063	0.065	0.063	-4.227	-0.231	0.063	0.065	0.063	-4.171	-0.023	0.063	0.065	0.063	-4.002	-0.126
1.173	0.057	0.059	0.057	-4.316	-0.281	0.057	0.059	0.057	-4.321	0.261	0.057	0.059	0.057	-4.321	-0.222
2.506	0.039	0.041	0.039	-4.835	0.348	0.039	0.041	0.039	-4.497	0.068	0.039	0.041	0.039342	-4.654	0.308

Enerji (MeV)	**AlNi**					**Al_3Ni_5**					**$AlNi_3$**				
	WinXCom	**PHITS**	**GEANT**	**% phits**	**% geant**	**WinXCom**	**PHITS**	**GEANT**	**% phits**	**% geant**	**WinXCom**	**PHITS**	**GEANT**	**% phits**	**% geant**
0.047	2.140	2.075	1.994	3.039	6.815	2.389	2.330	2.223	2.466	6.978	2.599	2.547	2.384	2.031	8.286
0.060	1.145	1.081	1.052	5.624	8.122	1.270	1.206	1.170	4.983	7.842	1.375	1.313	1.263	4.501	8.102
0.099	0.365	0.334	0.329	8.546	9.917	0.393	0.359	0.353	8.461	10.091	0.416	0.382	0.374	8.320	10.136
0.122	0.256	0.238	0.231	6.892	9.744	0.271	0.252	0.244	7.096	9.938	0.284	0.263	0.255	7.254	10.114
0.161	0.180	0.172	0.165	4.640	8.577	0.187	0.178	0.171	5.067	8.595	0.193	0.182	0.175	5.364	9.027
0.284	0.116	0.116	0.110	0.074	4.573	0.117	0.116	0.111	0.413	5.033	0.118	0.117	0.112	0.574	4.863
0.347	0.103	0.105	0.100	-1.125	3.094	0.104	0.105	0.101	-0.901	2.943	0.105	0.105	0.101	-0.693	3.845
0.511	0.085	0.088	0.084	-2.826	1.278	0.086	0.088	0.084	-2.544	1.782	0.086	0.088	0.085	-2.542	1.184
0.689	0.074	0.077	0.074	-3.475	0.312	0.074	0.077	0.074	-3.354	0.294	0.074	0.077	0.074	-3.251	0.552
0.964	0.063	0.065	0.063	-3.981	-0.281	0.063	0.065	0.063	-3.948	0.037	0.063	0.065	0.063	-3.762	-0.485
1.173	0.057	0.059	0.057	-4.147	-0.250	0.057	0.059	0.057	-4.149	-0.096	0.057	0.059	0.057	-3.975	-0.082
2.506	0.040	0.041	0.040	-4.430	-0.046	0.040	0.042	0.040	-4.597	0.191	0.040	0.042	0.040	-4.565	0.196

Ele alınan intermetalik bileşiklerin Lineer Soğurma Katsayıları (μ), ilgili malzemenin kütle soğurma katsayıları ile yoğunluklarının çarpımıyla elde edilerek, foton enerjisine bağlı değişimi Şekil 3'te verildi. Şekilden μ'nün enerji ile değişim grafiğinin, μ/ρ ile benzer bir eğilime sahip olduğu görülmektedir.

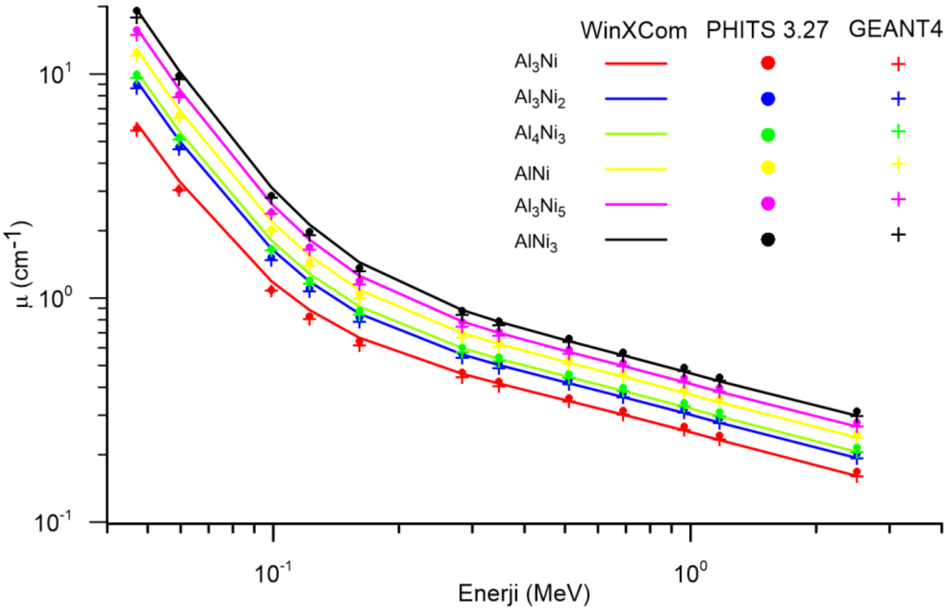

Şekil 3. *Al-Ni intermetalik bileşiklerinin seçilen enerjilerde WinXCom, PHITS ve GEANT4 ile hesaplanan lineer soğurma katsayıları.*

YKD, OKD ve OSY lineer soğurma katsayısı kullanılarak belirlenebilen önemli gama radyasyonu zırhlama parametreleridir. Bu parametreler ile lineer soğurma katsayıları arasında ters orantı olduğundan bu parametrelerin küçük değerleri malzemenin daha iyi bir zırhlama malzemesi olduğunu göstermektedir. Çalışma konusu bileşiklerin OSY, OKD ve YKD değerlerinin foton enerjisiyle değişimi Şekil 4, 5 ve 6'da verilmektedir. Şekillerden de anlaşılacağı üzere, gelen foton enerjisi arttıkça YKD, OKD ve OSY değerleri de artmaktadır. Yoğunluk, bileşiklerin YKD, OKD ve OSY değerlerini önemli ölçüde etkiler; böylece yoğunluğun artmasıyla YKD, OKD ve OSY azalır ve soğurma etkisi artar. Örneğin, bileşikler içinde en düşük yoğunluğa sahip olan Al_3Ni (4.1 g/cm^3)'in 0.047 MeV deki YKD değeri 0.1149 cm iken en yüksek yoğunluğa sahip $AlNi_3$ (7.5 g/cm^3) bileşiğinin bu enerjideki değeri 0.03555 cm olarak hesaplanmıştır. Benzer eğilimler OKD ve OSY'de gözlemlenmektedir. Bu yüzden $AlNi_3$ bileşiği, gama zırhlama uygulamaları için umut verici bir aday olarak düşünülebilir. Etkin atom numarası (Z_{etk}), kompozit malzemelerin foton penetrasyonunu anlamak için sıklıkla kullanılan başka bir parametredir. Şekil 7, enerjinin bir fonksiyonu olarak bileşikler için Z_{etk}'in grafiksel bir temsilini göstermektedir. Genel olarak Z_{etk} değerlerinin fotonun enerjisine ve bileşiklerin yapılarına güçlü bir şekilde bağlı olduğu görülmektedir. Şekil 7 incelendiğinde bileşiklerin teorik Z_{etk} değerlerinin $AlNi_3>Al_3Ni_3>AlNi>Al_4Ni_3>Al_3Ni_2>Al_3Ni$ şeklinde büyükten küçüğe doğru sıralandığı açıkça görülmektedir.

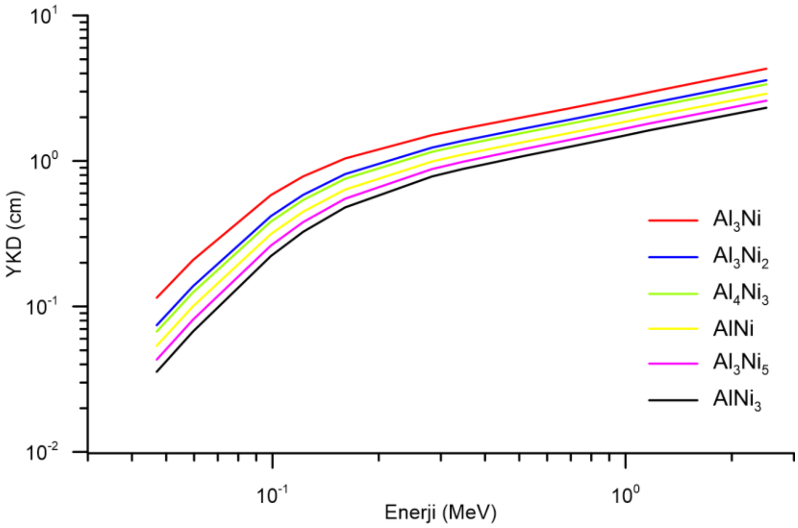

Şekil 4. *Al-Ni intermetalik bileşiklerinin seçilen enerjilerde yarı kalınlık değerleri.*

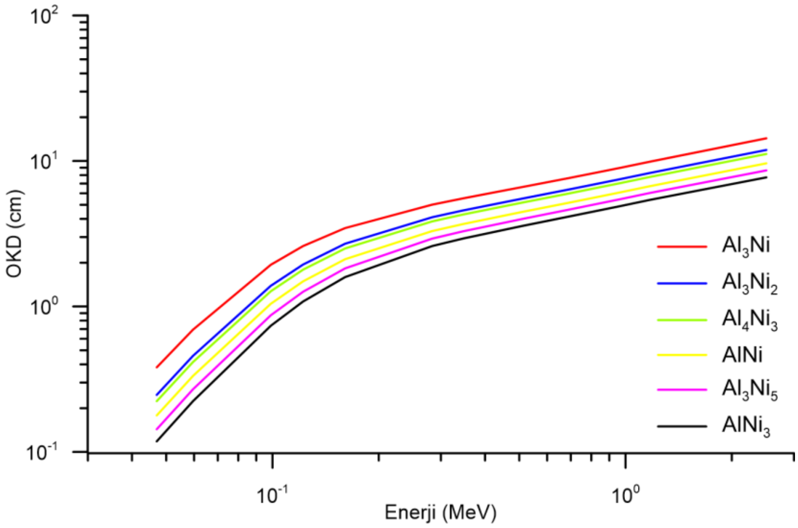

Şekil 5. *Al-Ni intermetalik bileşiklerinin seçilen enerjilerde onda kalınlık değerleri.*

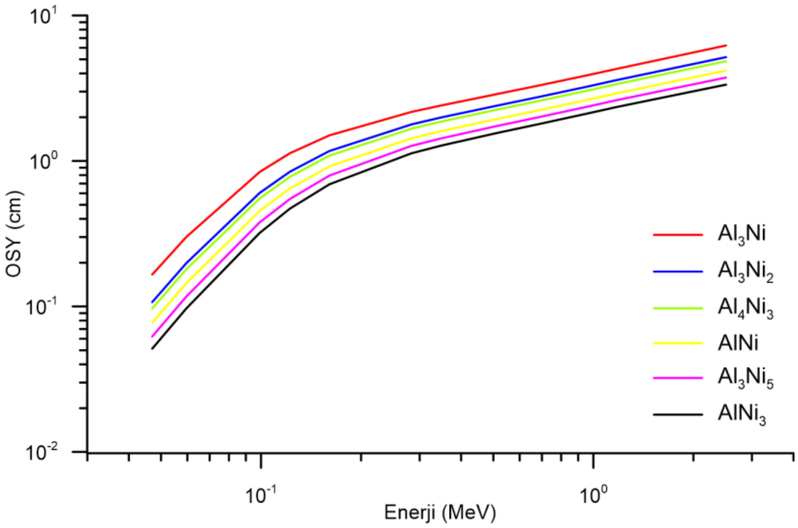

Şekil 6. *Al-Ni intermetalik bileşiklerinin seçilen enerjilerde ortalama serbest yol değerleri.*

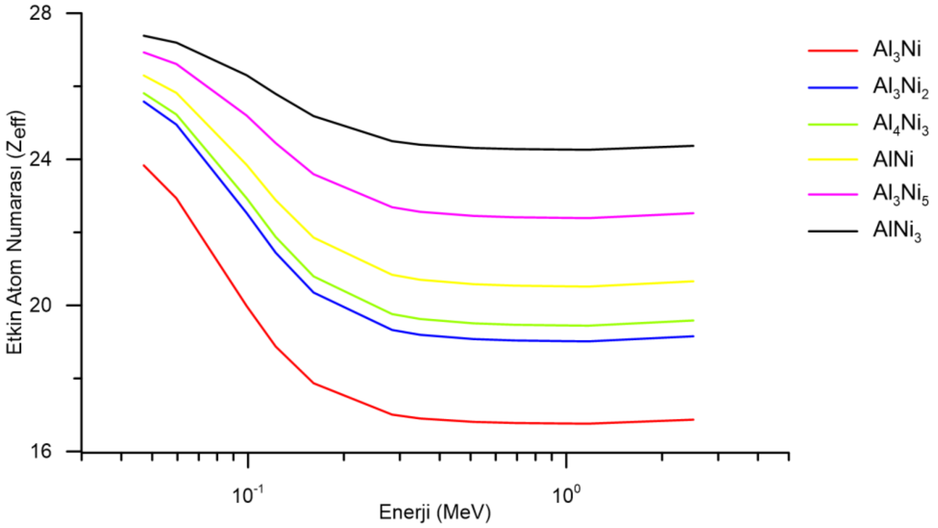

Şekil 7. Al-Ni intermetalik bileşiklerinin seçilen enerjilerde Z_{etk} değerleri.

Tartışma ve Sonuç

Bu çalışmada Al-Ni bileşiklerinin (Al_3Ni, Al_3Ni_2, Al_4Ni_3, AlNi, Al_3Ni_5 ve $AlNi_3$) gama radyasyon zırhlama özellikleri araştırıldı. Her bileşik için kütle soğurma katsayıları PHITS ve GEANT kodu ve XCOM programı kullanılarak, tıp ve radyografi uygulamalarında kullanılan radyoizotopların gama yayınlama enerjileri dikkate alınarak 0.047 – 2.506 MeV enerji aralığında belirlendi. Bu yöntemlerle elde edilen sonuçların iyi bir uyum içerisinde olduğu görüldü. Sonuçlar, intermetalik bileşiğin yoğunluğunun artmasıyla, $\mu_m$ve Z_{etk} değerlerinin arttığını, YKD, OKD ve OSY değerlerinin ise azaldığını göstermiştir. Radyasyondan korunmak için bu parametrelerin hesaplanan verilerinin dikkate alınması ve ayrıca istenen uygulamaya göre uygun bileşiğin seçimi yapılabilir. Hesaplanan parametrelere göre yoğunluğu büyük olan nikelin, bileşikteki yüzde katkısı artıkça intermetalik bileşiğin radyasyon zırhlama kapasitesinin de arttığı görüldü. Bu sonuca dayalı olarak, $AlNi_3$ bileşiğinin diğer bileşiklere oranla gama zırhlama için daha uygun bir aday olduğu tespit edildi. Al-Ni intermetalik bileşikleri, literatürde zırhlama malzemesi olarak önerilen diğer malzemelerle karşılaştırıldığında daha düşük zırhlama kapasitesine sahip olsalar da, gama zırhlama ihtiyacı duyulan alanlarda kullanım için yeterli düzeydedir. Ayrıca Al-Ni bileşiklerinin sahip oldukları fiziksel özellikler de (yüksek mukavemet, düşük özgül ağırlık, termal stabilite vb.) göz önünde bulundurularak bileşiklerin hastanelerde, radyasyon yayan ekipman bulunan odalarda, radyoaktif atık ürünlerin depolanmasında ve nükleer santrallerde gama radyasyonu zırh malzemesi olarak kullanılabileceği öngörülebilir.

Teşekkür -

Fon/Finansman bilgileri Bu çalışma için herhangi bir kurum ve/veya kuruluştan destek alınmamıştır.

Etik Kurul Onayı ve İzinler Çalışma, etik kurul izni veya herhangi bir özel izin gerektirmemektedir.

Çıkar çatışmaları/Çatışan çıkarlar Yazarlar arasında herhangi bir çıkar çatışması yoktur.

Yazarların Katkısı Yazarlar çalışmaya eşit oranda katkı sağlamıştır. Yazarlar makalenin son halini okumuş ve onaylamıştır.

Kaynaklar

[1] Li, T., Wang, D., Zhang, S., & Wang, J. (2023). Corrosion behavior of high entropy alloys and their application in the nuclear industry—An overview. *Metals, 13*(2)*,* 363. https://doi.org/10.3390/met13020363

[2] Simon, A., Barradas, N. P., Jeynes, C., & Romolo, F. S. (2023). Addressing forensic science challenges with nuclear analytical techniques – A review. *Forensic Science International*, *358* 111767. https://doi.org/10.1016/J.FORSCIINT.2023.111767

[3] Daneshvar, H., Milan, K. G., Sadr, A., Sedighy, S. H., Malekie, S., & Mosayebi, A. (2021). Multilayer radiation shield for satellite electronic components protection. *Scientific Reports, 11*(1), 20657. https://doi.org/10.1038/s41598-021-99739-2

[4] Jecong, J. F. M., Hila, F. C., Balderas, C. V., & Guillermo, N. R. D. (2022). Effect of the new photoatomic data library EPDL2017 to mass attenuation coefficient calculation of materials used in the nuclear medicine facilities using EpiXS software. *Nuclear Engineering and Technology*, *54*(9), 3440–3447. https://doi.org/10.1016/J.NET.2022.03.030

[5] Kaçal, M. R., Akman, F., & Sayyed, M. I. (2019). Evaluation of gamma-ray and neutron attenuation properties of some polymers. *Nuclear Engineering and Technology*, *51*(3), 818–824. https://doi.org/10.1016/J.NET.2018.11.011

[6] Yilmaz, M., Erkoyuncu, İ., Gürel Özdemir, H., Demirkol, İ., Kaçal, M. R., & Akman, F. (2023). Bizmut tabanlı bazı alaşımların radyasyon zırhlama kapasitelerinin incelenmesi. *Yüzüncü Yıl Üniversitesi Fen Bilimleri Enstitüsü Dergisi*, *28*(1), 92–105. https://doi.org/10.53433/YYUFBED.1140507

[7] Aygün, Z., & Aygün, M. (2022). Evaluation of radiation shielding potentials of Ni-based alloys, Inconel-617 and Incoloy-800HT, candidates for high temperature applications especially for nuclear reactors, by EpiXS and Phy-X/PSD codes. *Journal of Polytechnic*, *26*(2), 795-801. https://doi.org/10.2339/politeknik.1004657

[8] Ekinci, N., Alsaif, N. A. M., Aygün, B., Sarıtaş, S., Kalecik, S., & Rammah, Y. S. (2023). Assessment of structural, physical properties as well as radiation safety competence of lithium borate glass-ceramics: Experimental and theoretical evaluation. *Physica Scripta*, *98*(4), 045004. https://doi.org/10.1088/1402-4896/ACBEEF

[9] Kavaz, E., El-Agawany, F. I., Tekin, H. O., Perişanoğlu, U., & Rammah, Y. S. (2020). Nuclear radiation shielding using barium borosilicate glass ceramics. *Journal of Physics and Chemistry of Solids*, *142*, 109437. https://doi.org/10.1016/J.JPCS.2020.109437

[10] Kavaz, E., Tekin, H. O., Yorgun, N. Y., Özdemir, F., & Sayyed, M. I. (2019). Structural and nuclear radiation shielding properties of bauxite ore doped lithium borate glasses: Experimental and Monte Carlo study. *Radiation Physics and Chemistry, 162,* 187–193. https://doi.org/10.1016/j.radphyschem.2019.05.019

[11] Yildiz Yorgun, N., Kavaz, E., Tekin, H. O., Sayyed, M. I., & Özdemir, F. (2019). Borax effect on gamma and neutron shielding features of lithium borate glasses: An experimental and Monte Carlo studies. *Materials Research Express*, *6*(11). https://doi.org/10.1088/2053-1591/ab4fcc

[12] Aygün, B., Şakar, E., Agar, O., Sayyed, M. I., Karabulut, A., & Singh, V. P. (2021). Development of new heavy concretes containing chrome-ore for nuclear radiation shielding applications. *Progress in Nuclear Energy*, *133*, 103645. https://doi.org/10.1016/J.PNUCENE.2021.103645

[13] Kilicoglu, O., More, C. V., Kara, U., & Davraz, M. (2023). Investigation of the effect of cement type on nuclear shield performance of heavy concrete. *Radiation Physics and Chemistry*, *209*, 110954. https://doi.org/10.1016/J.RADPHYSCHEM.2023.110954

[14] Stoloff, N. S., Liu, C. T., & Deevi, S. C. (2000). Emerging applications of intermetallics. *Intermetallics*, *8*(9–11), 1313–1320. https://doi.org/10.1016/S0966-9795(00)00077-7

[15] Liu, C. T. (1995). Recent advances in ordered intermetallics. *Materials Chemistry and Physics*, *42*(2), 77–86. https://doi.org/10.1016/0254-0584(95)01546-9

[16] Jogdand, H., Gulsoy, G., Ando, T., Chen, J., Doumanidis, C. C., Gu, Z., Rebholz, C., & Wong, P.. (2008). Fabrication and characterization of nanoscale heating sources (“Nanoheaters”) for nanomanufacturing. *TechConnect Briefs*, *1*, 280–283.

[17] Kaplin, C., Ivanov, R., Paliwal, M., Jung, I. H., & Brochu, M. (2014). The effect of nanostructure on the oxidation of NiAl. *Intermetallics*, *54*, 209–217. https://doi.org/10.1016/J.INTERMET.2014.06.013

[18] Awotunde, M. A., Ayodele, O. O., Adegbenjo, A. O., Okoro, A. M., Shongwe, M. B., & Olubambi, P. A. (2019). NiAl intermetallic composites—a review of processing methods, reinforcements and mechanical properties. *International Journal of Advanced Manufacturing Technology*, *104*(5–8), 1733–1747. https://doi.org/10.1007/S00170-019-03984-9/FIGURES/13

[19] Zhilin, S. G., Predein, V. V., & Komarov, O. N. (2023). Industrial use of high-strength intermetallic compounds based on aluminides and prospects for extending scope of their application. *Metallurgist*, *66*(9–10), 1114–1126. https://doi.org/10.1007/S11015-023-01424-4/METRICS

[20] Sampath, S., Ravi, V. P., & Sundararajan, S. (2023). An overview on synthesis, processing and applications of nickel aluminides: from fundamentals to current prospects. *Crystals*, *13*(3), 435. https://doi.org/10.3390/cryst13030435

[21] Ward-Close, C. M., Minor, R., & Doorbar, P. J. (1996). Intermetallic-matrix composites—a review. *Intermetallics*, *4*(3), 217–229. https://doi.org/10.1016/0966-9795(95)00037-2

[22] Sikka, V. K., Deevi, S. C., Viswanathan, S., Swindeman, R. W., & Santella, M. L. (2000). Advances in processing of Ni3Al-based intermetallics and applications. *Intermetallics*, *8*(9–11), 1329–1337. https://doi.org/10.1016/S0966-9795(00)00078-9

[23] Dey, G. K. (2003). Physical metallurgy of nickel aluminides. *Sadhana - Academy Proceedings in Engineering Sciences*, *28*(1–2), 247–262. https://doi.org/10.1007/BF02717135/METRICS

[24] Shi, D., Wen, B., Melnik, R., Yao, S., & Li, T. (2009). First-principles studies of Al-Ni intermetallic compounds. *Journal of Solid State Chemistry*, *182*(10), 2664–2669. https://doi.org/10.1016/j.jssc.2009.07.026

[25] Bochenek, K., & Basista, M. (2015). Advances in processing of NiAl intermetallic alloys and composites for high temperature aerospace applications. *Progress in Aerospace Sciences*, *79*, 136–146. https://doi.org/10.1016/J.PAEROSCI.2015.09.003

[26] Alzahrani, J. S., Alrowaili, Z. A., Saleh, H. H., Hammoud, A., Alomairy, S., Sriwunkum, C., & Al-Buriahi, M. S. (2021). Synthesis, physical and nuclear shielding properties of novel Pb–Al alloys. *Progress in Nuclear Energy*, *142*, 103992. https://doi.org/10.1016/J.PNUCENE.2021.103992

[27] Sayyed, M. I., Mohammed, F. Q., Mahmoud, K. A., Lacomme, E., Kaky, K. M., Khandaker, M. U., & Faruque, M. R. I. (2020). Evaluation of radiation shielding features of Co and Ni-based superalloys using MCNP-5 code: potential use in nuclear safety. *Applied Sciences*, *10*(21), 7680. https://doi.org/10.3390/APP10217680

[28] Almuqrin, A. H., Jecong, J. F. M., Hila, F. C., Balderas, C. V., & Sayyed, M. I. (2021). Radiation shielding properties of selected alloys using EPICS2017 data library. *Progress in Nuclear Energy*, *137*, 103748. https://doi.org/10.1016/j.pnucene.2021.103748

[29] Yıldırım, S., Tugrul, A. B., Buyuk, B., & Demir, E. (2016). Gamma attenuation properties of some aluminum alloys. *Acta Physica Polonica A*, *129*(4), 813–815. https://doi.org/10.12693/APhysPolA.129.813

[30] El-Mesady, I. A., Hussein, A. E., Semary, M. M., & Othman, S. M. (2023). Investigation of the mechanical properties, shielding parameters and flux distribution in borate - Based glass system using PHITS code; a simulation study. *Optical Materials*, *138*, 113699. https://doi.org/10.1016/j.optmat.2023.113699

[31] Alzahrani, J. S., Alothman, M. A., Eke, C., Al-Ghamdi, H., Aloraini, D. A., & Al-Buriahi, M. S. (2021). Simulating the radiation shielding properties of TeO2–Na2O–TiO glass system using PHITS Monte Carlo code. *Computational Materials Science*, *196*, 110566. https://doi.org/10.1016/J.COMMATSCI.2021.110566

[32] Gerward, L., Guilbert, N., Jensen, K. B., & Levring, H. (2004). WinXCom—a program for calculating X-ray attenuation coefficients. *Radiation Physics and Chemistry*, *71*(3–4), 653–654. https://doi.org/10.1016/J.RADPHYSCHEM.2004.04.040

[33] Sato, T., Iwamoto, Y., Hashimoto, S., Ogawa, T., Furuta, T., Abe, S. I., Kai, T., Matsuya, Y., Matsuda, N., Hirata, Y., Sekikawa, T., Yao, L., Tsai, P., Ratliff, H. N., Iwase, H., Sakaki, Y., Sugihara, K., Shigyo, N., Sihver, L., & Niita, K. (2024). Recent improvements of the particle and heavy ion transport code system – PHITS version 3.33. *Journal of Nuclear Science and Technology*, *61*(1), 127–135. https://doi.org/10.1080/00223131.2023.2275736

[34] Agostinelli, S., Allison, J., Amako, K., Apostolakis, J., Araujo, H., Arce, P., Asai, M., Axen, D., Banerjee, S., Barrand, G., Behner, F., Bellagamba, L., Boudreau, J., Broglia, L., Brunengo, A., Burkhardt, H., Chauvie, S., Chuma, J., Chytracek, R., . . . Zschiesche, D. (2003). Geant4—a simulation toolkit. *Nuclear Instruments and Methods in Physics Research Section A:* Accelerators *Spectrometers Detectors and Associated Equipment*, *506*(3), 250–303. https://doi.org/10.1016/s0168-9002(03)01368-8

[35] Cirrone, G. A. P., Cuttone, G., Di Rosa, F., Pandola, L., Romano, F., & Zhang, Q. (2010). Validation of the Geant4 electromagnetic photon cross-sections for elements and compounds. *Nuclear Instruments and Methods in Physics Research A*, *618*, 315-322. https://doi.org/10.1016/j.nima.2010.02.112

[36] Kuttukaran, S. S., Ambika, M. R., Malathi, C., & Nagaiah, N. (2023). DMSO-Bismuth polymer composite as gamma radiation shield – A computational study. *Materials Today: Proceedings*, *89*, 75–83. https://doi.org/10.1016/J.MATPR.2023.05.398

[37] Manohara, S. R., Hanagodimath, S. M., Thind, K. S., & Gerward, L. (2008). On the effective atomic number and electron density: A comprehensive set of formulas for all types of materials and energies above 1 keV. *Nuclear Instruments and Methods in Physics Research Section B: Beam Interactions with Materials and Atoms*, *266*(18), 3906–3912. https://doi.org/10.1016/J.NIMB.2008.06.034

Sinopfbd, 2024; 9(2): 302-310 **https://doi.org/10.33484/sinopfbd.1460633**

Sinop Üniversitesi Fen Bilimleri Dergisi
Sinop Uni J Nat Sci

E-ISSN: 2564-7873

https://dergipark.org.tr/tr/pub/sinopfbd

Denizli İli Biber Üretim Alanlarında Virüs Hastalıklarının Belirlenmesi

Handan ÇULAL KILIÇ[1] ve Fatma DENİZ[1]

How to cite: Çulal Kılıç, H., & Deniz, F. (2024). Denizli ili biber üretim alanlarında virüs hastalıklarının belirlenmesi. *Sinop Üniversitesi Fen Bilimleri Dergisi,* *9*(2), 302-310. https://doi.org/10.33484/sinopfbd.1460633

Araştırma Makalesi

Sorumlu Yazar
Handan ÇULAL KILIÇ
handankilic@isparta.edu.tr

Yazarlara ait ORCID
H.Ç.K: 0000-0003-4020-9442
F.D: 0009-0009-6493-7963

Received: 28.04.2024
Accepted: 26.06.2024

Öz

2021 ve 2022 yılları vejetasyon dönemlerinde Denizli ili biber üretim alanlarında arazi çalışmaları gerçekleştirilmiştir. Virüs ve virüs benzeri simptomlar gösteren toplam 115 bitki örneği toplanmıştır. Örnekler, DAS-ELISA (Double Antibody Sandwich Enzyme Linked Immunosorbent Assay) serolojik yöntemine göre testlenmiştir. Serolojik test yöntemlerinin uygulanmasında Biber örneklerinin testlenmesinde *Tomato spotted wilt virus* (TSWV), *Cucumber mosaic virus* (CMV), *Tobacco mosaic virus* (TMV) ve *Pepper mild mottle virus* (PMMoV)'e spesifik tanı kitleri kullanılmıştır. Test sonuçları, biber örneklerinin %6.9'u TSWV, %3.4'ü CMV, %2.6'sı PMMoV ve %1.7 'inin TMV ile tek bir etmen tarafından enfekte olduğunu göstermiştir. Ayrıca, %0.86 oranında TMV+TSWV, CMV+TSWV, PMMoV+TMV, PMMoV+CMV ve PMMoV+TMV+CMV olmak üzere ikili ve üçlü karışık enfeksiyonlar saptanmıştır. Hem vektör böcek hem de üretim materyali tohumlar ile taşınan bu etmenlerin yaygınlığının azaltılmasında, vektör popülasyonunun kontrol altına alınması ve sertifikalı üretim materyalinin kullanılması önerilmektedir.

Anahtar Kelimeler: Biber, virüs, teşhis, DAS-ELISA

Detection of Virus Disease in Pepper Production Areas in Denizli Province

[1]Isparta Uygulamalı Bilimler Üniversitesi,
Ziraat Fakültesi,
Bitki Koruma Bölümü
Isparta, Turkey

Abstract

Survey studies were carried out in the pepper production areas in Denizli province during the vegetation periods of 2021-2022. A total of 115 plant samples showing virus and virus-like symptoms were collected. The samples were tested according to DAS-ELISA (Double Antibody Sandwich Enzyme Linked Immunosorbent Assay) serological method. Commercial diagnostic kits specific to *Tomato spotted wilt virus* (TSWV), *Cucumber mosaic virus* (CMV), *Tobacco mosaic virus* (TMV) and *Pepper mild mottle virus* (PMMoV) were used in the serological test methods. The test results showed that 6.9% of the pepper samples were infected with TSWV, 3.4% with CMV, 2.6% with PMMoV and 1.7% with TMV by a single infection. In addition, double and triple mixed infections, TMV+TSWV, CMV+TSWV, PMMoV+TMV, PMMoV+CMV and PMMoV+TMV+CMV were detected at a rate of 0.86 %. To reduce the prevalence of these factors carried by both insects and seeds of production material, it is recommended to control the vector population and use certified production materials.

Keywords: Pepper, virus, detection, DAS-ELISA

Giriş

Biber (*Capsicum annuum* L.), Solanaceae familyasının *Capsicum* cinsine ait bir kültür bitkisidir. İklim isteği yönünden ılık ve sıcak iklim sebzesidir [1]. Dünyada tarımı yapılan kültür bitkileri arasında biber tarımı önemli bir yere sahiptir. İnsanların vazgeçilmez bitkisel besinleri olan sebzelerden biri olan ve dünyada yaygın olarak tüketilen biber, çeşitli vitaminleri, mineral ve antioksidant maddeleri içermektedir. Biber taze, konserve, kurutulmuş, toz ya da pul biber şeklinde, salça, turşu, sos olarak tüketilmesinin yanı sıra tarımsal sanayide, ilaç, boya vb. gibi farklı sektörlerde de kullanılmaktadır [2]. Ilıman iklim kuşağında yer alan Türkiye'nin iklim ve toprak özellikleri, çeşitli sebzelere olduğu gibi biber üretimine de son derece uygundur. Dünya'daki toplam biber üretimine ülkeler bazında baktığımızda FAO'nun 2023 yılı istatistiklerine göre; Çin 16.650.855 ton ile ilk sırada yer alırken, 3.018.775 ton ile Türkiye 2. sırada yer almaktadır [3]. Ülkemizde biber üretiminin yoğun olarak yapıldığı iller Antalya, Bursa, Samsun ve Manisa'dır. Ege Bölgesi'nin doğusunda bulunan Denizli, ülkemiz tarımında önemli bir yeri olan illerimizden birisidir. İlde 2023 yılı itibarıyla toplam 16.548 dekar alanda biber üretimi gerçekleştirilmiş ve 42.233 ton biber elde edilmiştir. Yörede, sivri, dolmalık ve salçalık ve çarliston olmak üzere dört tip biber üretilmektedir. Üretilen biberlerin 28.503 tonunu salçalık biber, 3468 tonunu dolmalık biber, 10.231 tonunu sivri biber ve 31 tonunu çarliston biber oluşturmaktadır [4]. Diğer kültür bitkilerinde olduğu gibi biber bitkisi de birçok hastalıktan etkilenmektedir. Biberi etkileyen çok sayıda fungal, bakteriyel ve virüs gibi fitopatojen verim ve kalite kaybına neden olmaktadır. Biber üretim alanlarında görülen hastalıklar arasında viral enfeksiyonların giderek arttığı bir gerçektir. Virüs ile bulaşık tohum ve enfekteli fide kullanımının yanı sıra yıl içerisinde de mekanik olarak ya da virüliferöz vektörlerle taşınarak yayılmaktadır. Bitkisel üretim alanlarında viral hastalıklara karşı etkili antiviral ürünlerin bulunmaması, bu hastalıkların oluşturduğu tehditin önemini giderek artıran kritik bir sınırlayıcı faktör olarak öne çıkmaktadır. Doğrudan kimyasal mücadele olmaması, virüslerden kaynaklanan hastalıkları önlemede koruyucu tedbirlere yönelmeyi zorunlu kılmaktadır. Virüs hastalıklarının kontrolünde erken tanı ve teşhis, virüs kaynağının ortadan kaldırılması, alet ve ekipmanların dezenfeksiyonu, temiz üretim materyali kullanımı ve etkili vektör ve yabancı ot mücadelesi temel koruyucu önlemlerdir [5, 6]. Biberde hastalık oluşturan ve üretimini sınırlayan pek çok virüs bulunmaktadır. Edwardson ve Christie [7], bu kültür bitkisini doğal olarak tarla şartlarında 55 civarında virüsün enfekte ettiğini bildirmişlerdir. Virüs hastalıkları nedeniyle biberlerde meydana gelen yıllık zarar oranının % 42- % 80 dolayında olduğu tahmin edilmektedir. Bu virüslerin bir kısmı vektörler tarafından, bir kısmı ise tohumla bazıları ise mekanik olarak özsuyu teması ile taşınmaktadır. Virüslerin taşınmasında etkili vektörler arasında afitler, thripsler, yaprak pireleri, beyaz sineklerdir [8]. Hıyar mozaik virüsü (*Cucumber mosaic virus,* CMV), patates Y virüsü (*Potato virus Y*, PVY), ve tütün mozaik virüsü (*Tobacco mosaic virus*, TMV)'nün biber üretilen alanlarda görülen en zararlı virüsler olduğu bildirilmiştir [9]. Ülkemizin farklı bölgelerinde yapılan çalışmalar biber üretim alanlarında çeşitli virüs enfeksiyonlarının bulunduğunu ortaya koymuştur [5, 6, 10 - 24]. Denizli'de

2005 yılında yapılan farklı bir çalışmada; biber, patlıcan ve marul örneklerinde AMV, TSWV ve CMV virüsleri tespit edilmiştir [17]. Bölgede son yıllarda yapılan sürveyler sırasında virüs benzeri belirtilerin gözlemlenmesi ve üreticilerden gelen şikayetlerin artması sebebiyle bu çalışma oluşturulmuştur. Bu amaçla Denizli ili biber üretim alanlarında TSWV, TMV, CMV ve PMMoV bakımından durumunun ortaya konması için tanılama çalışmalarında serolojik yöntemlerden DAS-ELISA yöntemi kullanılmıştır.

Materyal ve Yöntem

Sürvey Çalışmaları

Arazi çalışmaları Denizli ili ve ilçelerinde 2021-2022 yıllarında biber üretilen alanlarında gerçekleştirilmiştir. Bu kapsamda Güney, Kale ve Sarayköy ilçelerinden örneklemeler yapılmıştır. Virüs simptomu sergileyen bitkilerden yaprak örnekleri toplanmıştır. Uygun koşullarda Bitki Koruma Bölümü'ne getirilen örnekler, Viroloji Laboratuvarı'nda çalışmalara kadar -20 °C'de saklanmıştır.

DAS-ELISA Yöntemi

Virüsün teşhisinde bitkilere DAS-ELISA yöntemi uygulanmıştır. Örneklerin serolojik testlenmesinde TMV, CMV, PMMoV ve TSWV'e spesifik ELISA kitleri kullanılmıştır. Kitler Bioreba (İsviçre) firmasından temin edilmiştir. Testleme çalışmaları firmanın önerdiği şekilde yapılmıştır. Öncelikle ELISA tabaklarının her bir çukurcuğuna virüslere özgü antikor ile hazırlanmış tampon çözelti ile kaplanmış ve 37 °C'de 4 saat bekletilmiştir. Yıkamayı takiben ekstraksiyon tampon çözeltisinde örnekler ezilerek her bir çukura 200'er µl konulmuş ve +4 °C'de tüm gece bekletilmiştir. Konjugat buffer ve konjugatlar sulandırılarak her bir çukura ilave edilmiş ve 37 °C'de tekrar bekletilmiştir. Son aşama olarak substrat tamponu ile hazırlanan substrattan her bir çukura 200 µl konularak oda sıcaklığında bekletilerek renk değişimi gözlenmiştir. Sonuçlar 405 nm dalga boyunda okunmuştur. Kontrol bitkisinin absorbans değerlerine göre kontrol değerinin en az iki katı okuma değeri veren örnekler pozitif olarak kabul edilmiştir [25].

Bulgular ve Tartışma

Denizli ili ve ilçelerindeki biber üretim alanlarında sürveyler yapılmış ve virüs simptomu sergileyen 115 bitki örneği toplanmıştır. Örneklerde; yapraklarda mozaik, deformasyon, yapraklarda küçülme simptomu, kloroz, nekroz, damar açılması, bitki boyunda kısalma, meyvelerde renk değişimi, meyvede deformasyon gibi belirtiler gözlemlenmiştir (Şekil 1, 2, 3).

Şekil 1. *Biber meyvesinde halkalı leke ve kırışıklık simptomu*

Şekil 2. *Biber bitkisinin yapraklarında küçülme ve kıvrılma simptomu*

Ayrıca bazı örneklerde fitoplazma benzeri belirtilere rastlanmıştır (Şekil 2). Biberde enfeksiyon yapan virüslerin bu belirtilere neden olduğu farklı çalışmalarda belirtilmiştir [5, 14, 23]. Gerçekleştirilen arazi çalışmalarında, toplanan yaprak örnekleri TMV, CMV, PMMoV ve TSWV bakımından DAS-ELISA yöntemi ile testlenmiştir. DAS-ELISA testi sonuçlarına göre; testlenen 115 biber yaprak örneğinden 22 adetinin bir veya birden fazla virüsle enfekteli olduğu bulunmuştur. Buna göre; örnek alınan yerlere göre enfekteli örnek sayısına baktığımız Kale ilçesinde toplanan örneklerin 11'nin, Sarayköy'de 6'sının ve Güney ilçesinde ise 5'inin bir veya daha fazla virüsle enfekteli olduğu tespit edilmiştir.

Şekil 3. *Biber bitkisinin yapraklarında deformasyon, mozaik simptomu*

ELISA testlerinin sonucunda örneklerin; % 6.9 (8 örnek) unun TSWV ve % 3.4 (4 örnek) ünün de CMV, % 2.6 (3 örnek) sının PMMoV, % 1.7 (2 örnek) inin TMV ile enfekteli olduğu belirlenmiştir**.**

Tablo 1. *Örnek alınan yerler, alınan örnek sayısı ve virüslerin tek ve karışık olarak bulunma durumları*

Örnek Alınan Yer	Güney	Kale	Sarayköy	Toplam
Alınan Örnek Sayısı	32	29	54	115
TSWV	0	5	3	8
CMV	3	1	0	4
TMV	1	0	1	2
PMMoV	1	1	1	3
TMV+TSWV	0	1	0	1
CMV+TSWV	0	1	0	1
PMMoV+TMV	0	1	0	1
PMMoV+CMV	0	0	1	1
PMMoV+CMV+TMV	0	1	0	1

Ayrıca testlenen örneklerde; % 0.86 (1 örnek) oranında TMV+TSWV, CMV+TSWV, PMMoV+TMV, PMMoV+CMV ve PMMoV+TMV+CMV enfeksiyonları belirlenmiştir. İkili enfeksiyonlardan; TMV+TSWV (1 örnek), CMV+TSWV (1 örnek) ve PMMoV+TMV (1 örnek) enfeksiyonları sadece Kale ilçesinde tespit edilirken; PMMoV+CMV (1 örnek) enfeksiyonu ise sadece Sarayköy ilçesinde tespit edilmiştir. PMMoV+TMV+CMV üçlü enfeksiyonu da yine Sarayköy ilçesinde belirlenmiştir. Güney ilçesinde alınan örneklerde ise sadece tekli enfeksiyonlar belirlenmiştir. Benzer şekilde Özdemir ve Erilmez [17], Denizli ili biber, patlıcan ve marul üretim alanlarında yürüttükleri çalışmada, biber örneklerinin % 81.13'ünü TSWV, % 1.89'unu CMV ve % 11.32'sini TSWV, CMV ve AMV ile karışık enfekteli bulmuşlardır. Çalışmada en yaygın etmenin TSWV olduğunu bildirmişlerdir. Arlı Sökmen ve ark. [14] 1998 ve 1999 yıllarında biberde 313 örneği ELISA ile test etmişler ve en yaygın virüsleri sırasıyla PVY, TMV, ToMV, AMV, TSWV ve CMV olarak belirlemişlerdir. Keleş Öztürk ve Baloğlu

[21] Mersin, Adana, Hatay, Osmaniye ve Kahramanmaraş illerinde biber virüslerinin tespit edildiği çalışmada, CMV % 33.68 oran ile en yaygın virüs olarak belirlenmiştir. Antalya'da yapılan bir çalışmada TSWV enfeksiyonu % 35.8 olarak belirlenirken, CMV % 7.3 olarak tespit edilmiştir [26]. Antalya'nın Kumluca ilçesinde yapılan farklı bir çalışmada da biberlerde TSWV enfeksiyon oranı % 96.49 olarak ortaya konulmuştur [5]. Akdura ve Çulal-Kılıç [6] Hakkari'de yaptıkları çalışmada 90 adet biber örneğinin 12'sinde TSWV enfeksiyonunu tespit etmişlerdir. Deligöz ve ark. [23] tek ve karışık TSWV enfeksiyonunu en çok Manisa'da belirlemişlerdir. Çulal-Kılıç [26] Burdur ve Denizli illeri biberlerinde yaptıkları çalışmada, ToMV'nün varlığını DAS-ELISA ve IC-RT-PCR yöntemi ile ortaya koymuşlar ve 209 örneğin 30'unun ToMV ile enfekteli olduğunu bildirmişlerdir. Ülkemizde PMMoV'nün varlığı ilk olarak Güldür ve ark. [13] tarafından tespit edilmiş daha sonra; Güldür ve Çağlar [27], 2006 yılında Şanlıurfa'da biber seralarında PMMoV'nü tanılamışlardır. 2008 yılında Antalya'daki biberlerde şiddetli sistemik simptomlar gösteren biber yapraklarının DAS-ELISA testleri sonucunda bitkilerin PMMoV ile enfekteli olduğu tespit edilmiştir [18]. Adana, Mersin, Antalya, Kahramanmaraş ve Şanlıurfa illerinde 2009–2010 yıllarında yapılan surveyler süresince yerel çeşitlerden 3000 adet biber örneği toplanmıştır. Örnekler ELISA testi ile PMMoV için testlenmiştir. Testler sonucunda Adana ilinden alınan 10, Kahramanmaraş'tan 10, Antalya'dan 2, Mersin'den 3, Şanlıurfa'dan 2 olmak üzere toplam 27 örneğin PMMoV ile bulaşık olduğu belirlenmiştir [28]. Çulal-Kılıç ve ark. [29] 2015 yılında Burdur ilinde yaptıkları çalışmada 124 biber örneğinin serolojik olarak testlenmesi sonucunda 8 örneği CMV, 8 örneğin PMMoV ile enfekteli olduğunu 4 örneğin ise her iki virüs ile enfekteli olduğunu ortaya koymuşlardır. Deligöz ve ark. [23] biber örneklerinde % 0.5 oranında PMMoV enfeksiyonu belirlemişlerdir. Ayrıca % 0.5 oranında TSWV+PMMoV ve % 0.3 PMMoV+ CMV ikili enfeksiyonları tespit edilmiştir. TSWV+ PMMoV+CMV üçlü enfeksiyon oranı ise; % 0.2'dir. Bu çalışma ile Denizli ili biberlerinde TMV, CMV, PMMoV ve TSWV'nin varlığı DAS-ELISA ile belirlenmiştir. Denizli ilindeki biberlerde TMV ve PMMoV'nün varlığı ilk kez ortaya konulmuştur.

Sonuçlar

Yapılan bu çalışmada TSWV'nin diğer virüslere göre en yüksek enfeksiyon oranı (8 örnek) oluşturduğu belirlenmiştir. Biber üretiminde önemli verim kayıplarına yol açan CMV, TMV, TSWV ve PMMoV gibi virüsler vektör böceklerle (yaprak biti ve thrips gibi) ve tohumla etkili bir şekilde taşınmaktadırlar [30]. Bundan dolayı etkin bir savaşım yöntemi bulunmayan virüslerin yayılmasında rol oynayan vektörlerle mücadele edilmesi, dayanıklı çeşitlerin ıslahı ve temiz üretim materyalinin kullanılması ve enfekteli bitkilerin yok edilmesi gibi işlemlerin bölgede yaygınlaştırılması virüs hastalıkları ile mücadelede etkili olacaktır.

Teşekkür **-**

Fon/Finansman Bilgileri Bu çalışma için herhangi bir kurum ve/veya kuruluştan destek alınmamıştır.

Etik Kurul Onayı ve İzinler Çalışma, etik kurul izni veya herhangi bir özel izin gerektirmemektedir.

Çıkar Çatışmaları/Çatışan Çıkarlar Yazarlar arasında herhangi bir çıkar çatışması yoktur.

Yazarların Katkısı 1. yazar %60 oranında, 2. yazar %40 oranında katkı sağlamıştır.

Kaynaklar

[1] Yalçın, D. (2008). Kırmızı pul biber üretiminde kritik kontrol noktaları ve tehlike analizleri. *Kahramanmaraş Sütçü İmam Üniversitesi, Fen ve Mühendislik Dergisi, 11,* 129-137.

[2] Duman, A. D., Zorlugenç, B. & Evliya, B. (2002). Kahramanmaraş kırmızı biberinin önemi ve sorunları. *Kahramanmaraş Sütçü İmam Üniversitesi, Fen ve Mühendislik Dergisi, 5*(1), 111-117.

[3] FAO (2023, Mart). *The World Lettuce Economy.* http://www.fao.org/faostat/en/#data).

[4] TUIK (2023, Mart). *Bitkisel üretim istatistikleri.* http://www.tuik.gov.tr/bitkiselapp/bitkisel.zul.

[5] Yeşil, S. & Gömlekli, Ö. (2021). Determination of prevalence and reservoir weed species of tomato spotted wilt tospovirus-TSWV on peppers grown in greenhouses in Kumluca district of Antalya, Turkey. *Turkish Journal of Agriculture -Food Science and Technology, 9,* 2565-2570, https://doi.org/10.24925/turjaf.v9isp.2565-2570.4933

[6] Akdura, N. & Çulal-Kılıç, H. (2022). Hakkari ili domates ve biber üretim alanlarında yonca mozaik virüsü ve domates lekeli solgunluk virüsü'nün belirlenmesi. *Süleyman Demirel Üniversitesi, Fen Bilimleri Enstitüsü Dergisi, 26*(3), 435-440.

[7] Edwardson, J. R., & Christie R. G. (1997). *Viruses infecting peppers and other solanaceous crops.* University of Florida Agricultural Experimental Station, Florida.

[8] Çandar, A. & Gümüş, M. (2012). Bitki virüslerinin vektörlerle taşınmasına moleküler yaklaşımlar. *Türkiye Entomoloji Bülteni, 2*(3), 207-222.

[9] Palloix, A., Abak, K., Gognalons, P., Daubeze, A. M., Guldur, M., Memouchi, G. & Gebre-Selaissie, K. (1994, September 18-24). *Virus Diseases Infecting Pepper Crops in Turkey* [Conference presentation]. Proceedings of 9th Congress of the Mediterranean Phytopathological Union, Kusadası, Aydın, Turkey

[10] Yılmaz, M. A. & Davis, R. F. (1984). Purification and particle morphology of TMV, CMV and ZYMV isolated from various cultivated crops grown along the coast of Turkey. *Journal of Turkish Phytopathology 13,* 29-38.

[11] Erkan, S. (1986). Potato virus Y on pepper in Turkey. *Phytopathologia Mediterranean, 26,* 149-150.

[12] Çiçek, Y. & Yorgancı, Ü. (1991). Studies on the incidence of Tobacco Mosaic Virus on certified seed of tomato, pepper and eggplant in Aegean Region. *The Journal of Turkish Phytopathology, 20*(2-3), 57-65.

[13] Güldür, M. E., Ozaslan, M., Baloglu, S. & Yılmaz, M. A. (1994, September 18-24). *Pepper mild mottle Virus in Pepper in Turkey* [Conference presentation]. Proceedings of 9th Congress of the Mediterranean Phytopathological Union, Kusadası, Aydın, Turkey

[14] Arlı-Sökmen, M., Mennan, H., Sevik, M. A. & Ecevit, O. (2005). Occurrence of viruses in field-grown pepper crops and some of their reservoir weed hosts in Samsun, Turkey. *Phytoparasitica, 33*(4), 347-358. https://doi.org/10.1007/BF02981301

[15] Buzkan, N., Demir, M., Öztekin, V., Mart, C., Çağlar, B. K. & Yılmaz M. A. (2006). Evaluation of the status of capsicum viruses in the main growing regions of Turkey. *European and Mediterranean Plant Protection Organization Bulletin, 36*(1), 15-19.

[16] Özaslan, M., Baç, B., Aytekin, T. & Sıgırcı, Z. (2006). Identification of pepper viruses by das-elisa assays in Gaziantep-Turkey. *Plant Pathology Journal*, *5*(1), 11-14. https://doi.org/10.3923/ppj.2006.11.14

[17] Özdemir, S. & Erilmez, S. (2007, Ağustos, 27-29). *Denizli Ilinde Yetiştirilen Biber, Patlıcan ve Marul Üretim Alanlarında Bazı Viral Etmenlerin Saptanması* [Conference presentation]. Türkiye II. Bitki Koruma Kongresi, Isparta, Türkiye

[18] Sevik, M. A. (2011). Occurrence of pepper mild mottle virus in greenhousegrown pepper (*Capsicum annuum* L.) in the West Mediterranean region of Turkey. *African Journal of Biotechnology, 10*(25), 4976-4979.

[19] Buzkan, N., Arpacı, B. B., Simon, V., Fakhfakh, H. & Moury, B. (2013). High prevalence of poleroviruses in field-grown pepper in Turkey and Tunisia. *Archives Virology*, *158*(4), 881-885. https://doi.org/10.1007/s00705-012-1553-y

[20] Çulal-Kılıç, H., Yardimci N., Bal A., Güneş A. & Deniz F. (2017). Sensitive detection of tomato spotted wilt virus from pepper plants by DAS-ELISA, RT-PCR and IC-RT-PCR. *Romanian Biotechnological Letters, 22,* 12934-12939.

[21] Keleş Öztürk, P. & Baloğlu, S., (2019). Doğu Akdeniz Bölgesi'nde açık alanda yetiştirilen biberlerde bazı virüslerin serolojik ve moleküler tanısı. *Alatarım, 18*(1), 1-11.

[22] Fidan, H., Sarikaya, P., Yildiz, K., Topkaya, B., Erkis, G. & Calis, O. (2021). Robust molecular detection of the new tomato brown rugose fruit virus in infected tomato and pepper plants from Turkey. *Journal of Integrative Agriculture, 20*(8), 2170-2179. https://doi.org/10.1016/S2095-3119(20)63335-4.

[23] Deligöz, İ., Baltacı, A., Çelik, N., Özdemir, S., Uzunoğulları, N. & Kutluk Yılmaz, N. D. (2023). Türkiye'de biberde enfeksiyon oluşturan virüslerin belirlenmesi. *Anadolu Tarım Bilimleri Dergisi, 38*(1), 117-130.

[24] Güller, A., Usta, M., & Randa-Zelyüt, F. (2023). Genetic diversity and population structure of tomato brown rugose fruit virus (ToBRFV) variants from Antalya province, Turkey. *Notulae Botanicae Horti Agrobotanici Cluj-Napoca*, *51*(3), 13356.

[25] Can, S. & Baloğlu, S. (2020). Akdeniz Bölgesi'nde örtü altı biber üretim alanlarinda hıyar mozaik virüsü (cucumber mosaic virus, CMV) 'nün saptanması ve karakterizasyonu. *Çukurova Üniversitesi, Fen ve Mühendislik Bilimleri Dergisi, 39-3.*

[26] Güneş, N. & Gümüş, M. (2019). Detection and characterization of tomato spotted wilt virus and cucumber mosaic virus on pepper growing areas in Antalya. *Journal of Agricultural Sciences, 25*(3), 259-271. https://doi.org/10.15832/ankutbd.499144

[27] Çulal-Kılıç, H. (2019). Biological, serological and molecular detection of tomato mosaic virus infecting pepper plants from Turkey. *Applied Ecology and Environmental Research*, *17,* 6338-6347.

[28] Güldür, M.E. & Çaglar, B. K. (2006). Outbreaks of Pepper mild mottle virus in greenhouses in Sanlıurfa, Turkey. *Journalof Plant Pathology, 88*(3), 337–340.

[29] Çağlar, B. K., Fidan, H. & Elbeaino, T. (2013). Detection and molecular characterization of pepper mild mottle virus from Turkey. *Journal of Phytopathology, 161*(6), 434-438. https://doi.org/10.1111/jph.12068.

[30] Çulal–Kılıç, H., Yardımcı, N., Serdar, T. & Konu, A. (2015). Cucumber mosaic virus and pepper mild mottle virus in pepper growing areas in Burdur Province Turkey. *International Journal of Scientific and Technological Research, 1*(1), 50-60.

[31] Moury, B. & Verdin, E. (2012). Viruses of pepper crops in the Mediterranean Basin: A Remarkable stasis. In G. Loebenstein, H. Lecoq, (Ed). *Advances in Virus Research. Academic Press,* (pp. 127-162). https://doi.org/ 10.1016/B978-0-12-394314-9.00004-X.

Sinopfbd, 2024; 9(2): 311-330 **https://doi.org/10.33484/sinopfbd.1450774**

Sinop Üniversitesi Fen Bilimleri Dergisi
Sinop Uni J Nat Sci

E-ISSN: 2564-7873

https://dergipark.org.tr/tr/pub/sinopfbd

Assessment of the Spatial and Temporal Variation of Mesozooplankton in the Southern Black Sea, Türkiye

Funda ÜSTÜN[1] Levent BAT[1] Fatma BAYRAM PARTAL[2]
Hakan ATABAY[2] Sabri MUTLU[2] Leyla Gamze TOLUN[2] Orçin UYGUN[1]
Didem ÖZDEMİR MİS[3]

How to cite: Üstün, F., Bat, L., Bayram Partal, F., Atabay, H., Mutlu, S., Tolun, L.G., Uygun, O & Özdemir Mis, D. (2024). Assessment of the spatial and temporal variation of mesozooplankton in the Southern Black Sea, Türkiye. *Sinop Üniversitesi Fen Bilimleri Dergisi, 9*(2), 311-330. https://doi.org/10.33484/sinopfbd.1450774

Research Article

Corresponding Author
Funda ÜSTÜN
fustun@sinop.edu.tr

ORCID of the Authors
F.Ü: 0000-0002-7435-8414
L.B: 0000-0002-2289-6691
F.B.P: 0000-0002-5661-1439
H.A: 0000-0003-2066-2899
S.M: 0000-0001-9222-3102
L.G.T: 0000-0003-3532-3582
O.U: 0000-0001-7778-5211
D.Ö.M: 0000-0002-9962-6577

Received: 11.03.2024
Accepted: 17.07.2024

Abstract

This study investigated the taxonomic composition, abundance, and biomass values of mesozooplankton in the marine area in front of two important rivers (Sakarya River and Yeşilırmak River) and the largest port located on the Black Sea coast in Türkiye (Samsun Port) in July 2019 and January 2020. The average mesozooplankton abundance and biomass were 4187.3 ind. m^{-3} and 89.7 mg m^{-3} in Sakarya River, 3638.5 ind. m^{-3} and 78.2 mg m^{-3} in Samsun Port, and 3327.6 ind.m^{-3} and 77.6 mg m^{-3} in Yeşilırmak River, respectively. In July 2019, the highest abundance value of mesozooplankton (8581 ind. m^{-3}) was recorded at SAK08 station off Sakarya River due to the copepod *Acartia clausi* (3279 ind. m^{-3}). In July 2019, the highest biomass value of mesozooplankton (209.34 mg m^{-3}) was found at YSL07 station off Yeşilırmak River with the contribution of the copepod *Centropages ponticus* (77.90 mg m^{-3}). In January 2020, the highest abundance and biomass values of mesozooplankton (4035 ind. m^{-3} and 66.45 mg m^{-3}) were detected at SLI05 station off Samsun Port due to copepod *Acartia clausi*. A difference in mesozooplankton species composition between the two sampling periods was identified. While Cladocera species and copepod *Acartia tonsa* were exclusive at the sampling stations in July 2019, copepod *Calanus euxinus*, *Pseudocalanus elongatus* and *Oithona similis* were observed at the sampling stations in January 2020. Also, in January 2020, the presence of freshwater Cladocera species was detected off Sakarya River. The changes in biodiversity were determined to depend on temperature changes and riverine input.

Keywords: Species composition, abundance, biomass, Sakarya River, Samsun Port, Yeşilırmak River

Güney Karadeniz'in Mesozooplanktonun Mekansal ve Zamansal Değişiminin Değerlendirilmesi

[1]Sinop University, Faculty of Fisheries, Department of Marine Biology, Sinop, Türkiye

Öz

Mevcut çalışmada, Temmuz 2019 ve Ocak 2020'de Türkiye'nin Karadeniz kıyılarında yer alan iki önemli nehir (Sakarya Nehri ve Yeşilırmak Nehri) ile Karadeniz'in en büyük limanı olan Samsun Limanı önündeki denizel alandaki mesozooplanktonun taksonomik kompozisyonu, bolluk ve biyokütle değerleri incelenmiştir. Ortalama mesozooplankton bolluğu ve biyokütlesi sırasıyla Sakarya Nehri'nde 4187.3 birey m^{-3} ve 89.7 mg m^{-3}, Samsun Limanı'nda 3638.5 birey m^{-3} ve

[2]TUBITAK Marmara Research Center, Climate Change and Sustainability Vice Presidency, Marine Research and Technologies Research Group, Kocaeli, Türkiye

[3]Ege University, Faculty of Fisheries, Department of Marine and Inland Waters Sciences and Technology, İzmir, Türkiye

78.2 mg m^{-3} ve Yeşilırmak Nehri'nde 3327.6 birey m^{-3} ve 77.6 mg m^{-3} olarak hesaplanmıştır. Temmuz 2019'da mezozooplanktonun en yüksek bolluk değeri, Sakarya Nehri açıklarındaki SAK08 istasyonunda kopepod *Acartia clausi*'nin yüksek katkısı (3279 birey m^{-3}) nedeniyle kaydedilmiştir. Temmuz 2019'da mezozooplanktonun en yüksek biyokütle değeri ise Yeşilırmak Nehri açıklarındaki YSL07 istasyonunda, kopepod *Centropages ponticus*'un yüksek katkısıyla (77.90 mg m^{-3}) belirlenmiştir. Ocak 2020'de mesozooplanktonun en yüksek bolluk ve biyokütle değerleri (4035 birey m^{-3} ve 66.45 mg m^{-3}) Samsun Limanı açıklarındaki SLI05 istasyonunda kopepod *Acartia clausi*'nin yüksek katkısı ile tespit edilmiştir. Mesozooplankton tür kompozisyonunda iki örnekleme dönemi arasında farklılık saptanmıştır. Cladocera türleri ve copepod *Acartia tonsa* Temmuz 2019'da örnekleme istasyonlarında tespit edilmişken, *Calanus euxinus*, *Pseudocalanus elongatus* ve *Oithona similis* Ocak 2020'de örnekleme istasyonlarında gözlemlenmiştir. Ayrıca Ocak 2020'de Sakarya Nehri açıklarında tatlısu Cladocera türlerinin varlığı saptanmıştır. Biyoçeşitlilikteki değişikliklerin sıcaklık değişimlerine ve nehir girdisine bağlı olduğu belirlenmiştir.

Anahtar Kelimeler: Tür kompozisyonu, bolluk, biyokütle, Sakarya Nehri, Samsun Limanı, Yeşilırmak Nehri

Introduction

Carried by water currents or slowly floating vertically in the water column, zooplankton is a key group between primary producers and secondary consumers [1]. Zooplankton studies have focused on mesozooplankton (0.2–20 mm) due to its significant role in the marine ecosystem and its contribution to Carbon cycling. Being the main component as a primary consumer in the marine food pyramid, mesozooplankton is the main predator of microplankton and the prey of fish larvae and pelagic fish. Thus, it is an important element in the marine ecosystem playing a role in marine productivity and biogeochemical cycles [2]. Exposed to various environmental conditions, mesozooplankton demonstrates significant seasonal and spatial variations, both in terms of species composition and quantitative data of individual species and their distribution [3, 4]. Temperature [5, 6], anthropogenic impact [7, 8] and water current [9] are among the significant environmental factors that have an impact on the distribution, diversity and quantity of mesozooplanktonic organisms in the Black Sea coastal pelagic ecosystem. Coastal areas under the influence of natural and anthropogenic activities are highly susceptive to environment variability [10]. Responding rapidly to environmental changes due to their short life cycles [11], mesozooplankton is one of the major indicators of environmental changes and pressures in coastal waters [12, 13]. The main objective of the present study is to determine the structure of the coastal mesozooplankton community located off marine areas in front of Sakarya River, Samsun Port, and Yeşilırmak River. The data obtained can be used as background for quantitative assessments in the future.

Materials and Methods

Study Regions

Sakarya River is the third longest river in Türkiye (821 km) and the largest river in the Northwestern Anatolia. It originates from Afyonkarahisar province in the Central Western Anatolia and flows into the Black Sea in the Karasu district of Sakarya province (Figure 1). The average water quantity discharged into the Black Sea from the Sakarya River is 193 m^3 s^{-1}. Yeşilırmak River which is approximately 519 km long originates from Sivas province in Central Anatolia and flows into the Black Sea in Çarşamba district of Samsun province. It is the second-longest river in the Black Sea Region of Türkiye. It has an average annual flow rate of 151 m^3 s^{-1}. Both rivers are utilized for municipal water needs of settlements and industrial establishments for agricultural irrigation and wastewater discharge. They supply potable and irrigation water to the region via the dams built on them [14, 15]. Samsun Port is the largest port on the Black Sea coast of Türkiye which has a wide, international-level hinterland. The delta of Kızılırmak is located to the west and the delta of Yeşilırmak is located to the east of Samsun Port which is situated in a geographically and geomorphologically significant location [16].

Sampling and Laboratory Studies

The study was performed on 6–13 July 2019 (summer season) and 10–18 January 2020 (winter season) at a total of 13 stations in marine areas in front of Sakarya River, Samsun Port, and Yeşilırmak River in Türkiye (southern Black Sea) (Figure 1). Salinity and temperature of the sea surface were measured using SeaBird SBE25Plus CTD+DO (SBE4 conductivity, SBE3 temperature, and depth; plus, SBE43 dissolved Oxygen) and SBE 32 Carousel Water Sampler (8-liter bottles), which was installed on the R/V TUBITAK MARMARA research vessel. Dissolved Oxygen concentration (mg L^{-1}) was measured using the Iodometric Winkler test method [17]. The Chlorophyll-*a* concentrations (µg L^{-1}) were measured by the acetone extraction method in the Spectrophotometer [18]. The mesozooplankton samples were collected using a UNESCO WP2 net (200 µm mesh size, 57 cm mouth diameter) cast from R/V TÜBİTAK Marmara during daytime with a single vertical haul. Following the vertical haul, the net was rinsed gently and the contents of the cod ends of the plankton net were transferred into a plastic bottle and fixed in borax-buffered formaldehyde (seawater solution to a final concentration of 4%) for identification and enumeration of mesozooplankton individuals. In the laboratory, the samples were concentrated to 50 ml or 75 ml, depending on the sample density. Two sub-samples were taken from a Stempel pipette (1 ml) in a homogenized sample. The identification and counting of the mesozooplankton individuals were conducted using a zooplankton counting apparatus (Bogorov Rass Chamber) under a stereomicroscope (Novex RZ 65500). For species that did not appear during subsampling and for rare and large organisms (such as Chaetognatha and Decapoda larvae), the whole sample was investigated [19]. The results were averaged and extrapolated to the whole sample.

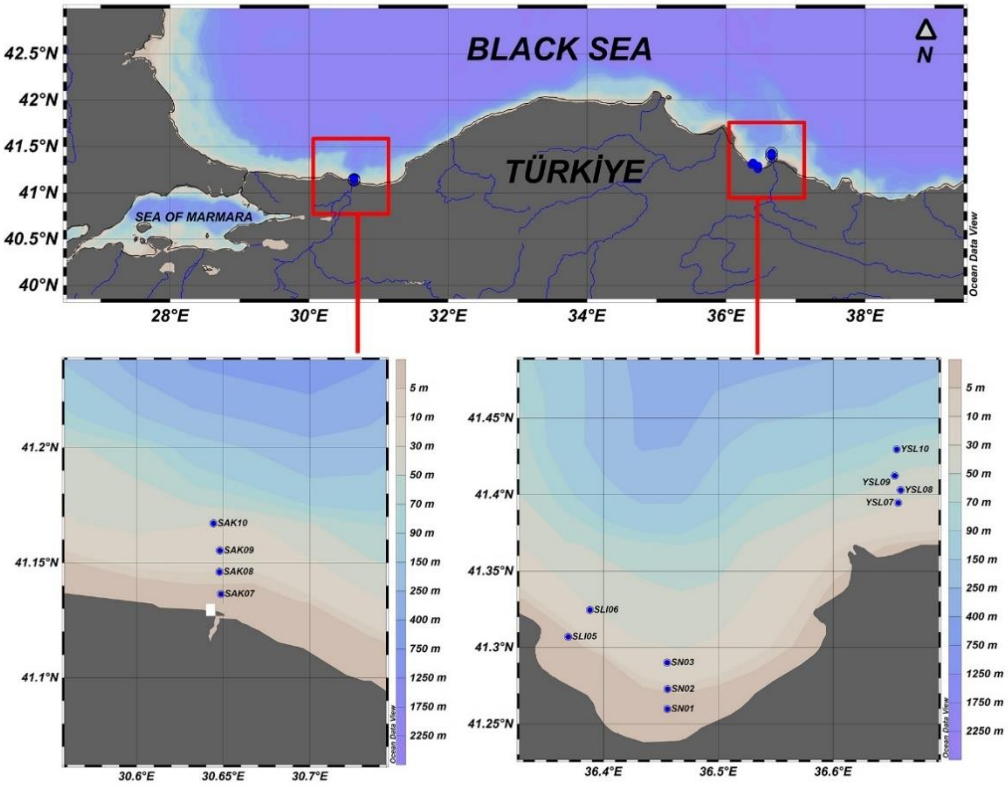

Figure 1. *Location of sampling stations*

According to Petipa [20] and Niermann et al. [21], the biomass transformations were based on the wet individual weights. The mesozooplankton abundance and biomass results were given as individuals per cubic meter (ind.) m^{-3} and mg per cubic meter (mg m^{-3}). All taxa were identified taxonomically to the species level except for the Meroplankton larvae. Mesozooplankton species identification was made mainly after Bradford-Grieve et al. [22] and Conway et al. [23] and the taxonomic nomenclature according to the World Register of Marine Species (WoRMS).

Statistical Analysis

The Spearman rank correlation was applied to assess correlations of the abundance of mesozooplankton species/taxa with environmental parameters, and the abundance of *Noctiluca scintillans* (SPSS 21 IBMCrop., Armonk, NY, USA). Shannon–Weaver diversity index (H′) was applied to the species abundance data to explain the mesozooplankton quantitative data regarding the community assemblage. Abundance data were square root transformed to reduce the dominance of heavily abundant species/groups based on the Bray–Curtis rank similarity matrix. Group average hierarchical cluster analysis (CLUSTER) was applied to test similarities in mesozooplankton assemblage among stations

(SAK07, SAK08, YSL07, SN01 etc.). One-way analysis of similarity (ANOSIM) was applied on mesozooplankton species/taxa abundance to test whether there was a significant difference between the regions (Sakarya River, Samsun Port, Yeşilırmak River). The similarity percentage (SIMPER) procedure was used to reveal mesozooplankton species/taxa responsible for average similarities within regions (Sakarya River, Samsun Port, Yeşilırmak River) and average dissimilarity between the pair combination of regions, and to determine the contribution rates. CLUSTER, ANOSIM, SIMPER and Shannon-Weaver diversity index were conducted using PRIMER 5.0 software.

Results

Environmental Parameters

The surface seawater temperature values of the sampling stations ranged from 25.35 °C to 26.52 °C in July 2019 (average: 25.95 °C) and from 10.81 °C to 11.78 °C in January 2020 (average: 11.17 °C). The surface seawater salinity values fluctuated from 15.84 to 18.11 psu in July 2019 (average: 17.56 psu), and 15.73 to 18.34 psu in January 2020 (average: 17.52 psu). The surface seawater concentrations of dissolved Oxygen (DO) values were between 7.08 and 11.65 mg L^{-1} in July 2019 (average: 7.99 mg L^{-1}) and between 8.69 and 9.83 mg L^{-1} in January 2020 (average: 9.32 mg L^{-1}). The minimum and maximum concentrations of surface seawater Chlorophyll-*a* varied between 0.08 µg L^{-1} and 18.31 µg L^{-1} in July 2019 (average: 2.14 µg L^{-1}) and between 0.68 µg L^{-1} and 2.34 µg L^{-1} in January 2020 (average: 1.24 µg L^{-1}) (Figure 2).

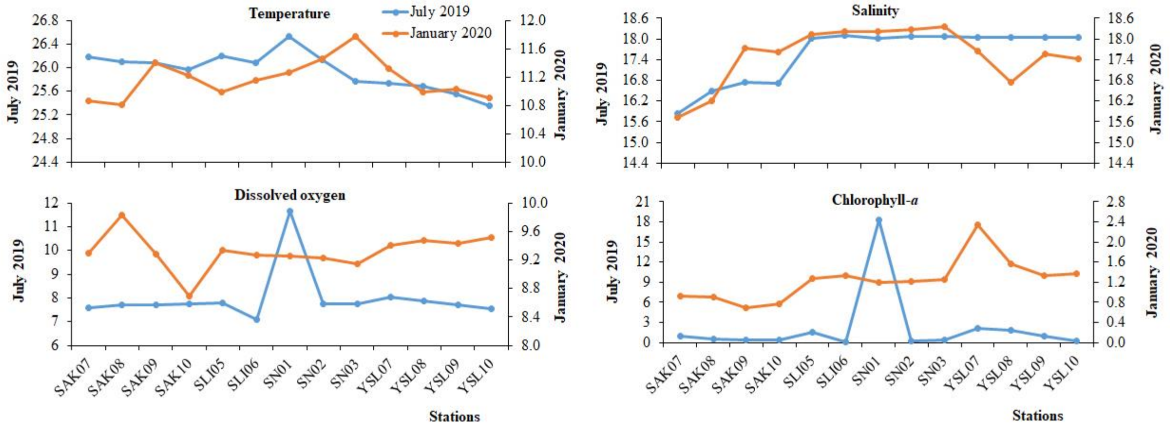

Figure 2. *The seawater temperature (°C), salinity (psu), dissolved Oxygen (mg L^{-1}) and Chlorophyll-a (µg L^{-1}) concentration at a depth of 1 m at sampling stations*

Taxonomic Composition, Abundance and Biomass of Mesozooplankton Species/taxa

The average mesozooplankton abundance and biomass values were higher in July 2019 than in January 2020 in three regions (Table 1). The mesozooplankton abundance and biomass values varied between 4838–8581 ind. m^{-3} and 102–179 mg m^{-3} in Sakarya River, 3652–7020 ind. m^{-3}, and 72–198 mg m^{-3} in Samsun Port and 3363–8001 ind. m^{-3} and 78–209 mg m^{-3} in Yeşilırmak River in July 2019. In January

2020, these values varied between 1875–2642 ind. m^{-3} and 32–59 mg m^{-3} in Sakarya River, 1156–4036 ind. m^{-3}, and 15–66 mg m^{-3} in Samsun Port and 729–2016 ind. m^{-3} and 8–28 mg m^{-3} in Yeşilırmak River (Figure 3).

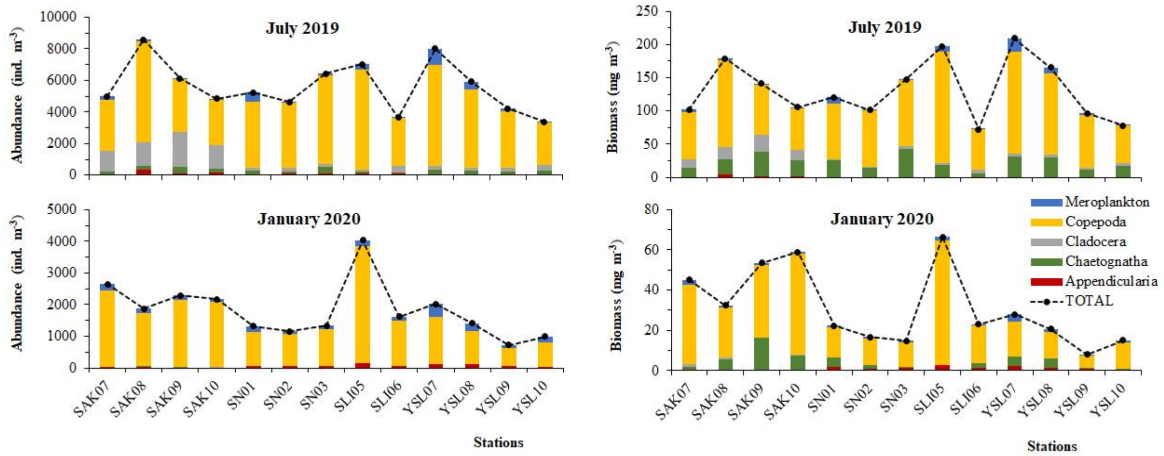

Figure 3. *Abundance (ind. m^{-3}) and biomass (mg m^{-3}) values of mesozooplankton groups at sampling stations*

Oikopleura dioica (Appendicularia) and *Parasagitta setosa* (Chaetognatha) were detected at all stations during the study period. The abundance and biomass of *O. dioica* in July 2019 were 3.3–349 ind. m^{-3} and 0.05–4.3 mg m^{-3} in Sakarya River, 16.3–122 ind. m^{-3} and 0.05–0.71 mg m^{-3} in Samsun Port, 3–47 ind. m^{-3} and 0.01–0.52 mg m^{-3} in Yeşilırmak River (Figure 3). The abundance and biomass of the same species in January 2020 were 6.5–37 ind. m^{-3} and 0.09–0.3 mg m^{-3} in Sakarya River, 49–138 ind. m^{-3} and 0.7–2.7 mg m^{-3} in Samsun Port, 23–105 ind. m^{-3} and 0.3–2.5 mg m^{-3} in Yeşilırmak River (Figure 3). In July 2019, the minimum and maximum abundance of *Parasagitta setosa* were in the range of 217–419 ind. m^{-3} in Sakarya River, 91–372 ind. m^{-3} in Samsun Port and 165–325 ind. m^{-3} in Yeşilırmak River. The minimum and maximum biomass of the species in summer were in the range of 14.4–37 mg m^{-3} in Sakarya River, 5.8–43 mg m^{-3} in Samsun Port and 11–32 mg m^{-3} in Yeşilırmak River (Figure 3). In January 2020, the minimum and maximum abundance of *P. setosa* ranged between 5 and 9.5 ind. m^{-3} in Sakarya River, 0.8 and 4.3 ind. m^{-3} in Samsun Port, and 1.6 and 5.2 ind. m^{-3} in Yeşilırmak River. The minimum and maximum biomass of the species in winter ranged between 1.5 and 16.4 mg m^{-3} in Sakarya River, 0.2 and 4.7 mg m^{-3} in Samsun Port and 0.4 and 4.7 mg m^{-3} in Yeşilırmak River (Figure 3).

Copepoda was the predominant group, with the highest abundance and biomass values among the mesozooplankton in the sampling period. The abundance and biomass of Copepoda (adult+copepodit+nauplii) were 2882–6394 ind. m^{-3} and 64–130 mg m^{-3} in Sakarya River, 3055–6312 ind. m^{-3} and 61–168 mg m^{-3} in Samsun Port, 2680–6399 ind. m^{-3} and 56–153 mg m^{-3} in Yeşilırmak River in July 2019 (Figure 3).

Table 1. *The average abundance (ind. m^{-3}) and biomass (mg m^{-3}) of mesozooplankton species/taxa in front of Sakarya River, Samsun Port and Yeşilırmak River*

	Average Abundance (ind.m^{-3})						**Average Biomass (mg m^{-3})**					
	Sakarya River		**Samsun Port**		**Yeşilırmak River**		**Sakarya River**		**Samsun Port**		**Yeşilırmak River**	
Species	**July 19**	**Jan. 20**	**July 19**	**Jan. 20**	**July 19**	**Jan. 20**	**July 19**	**Jan. 20**	**July 19**	**Jan. 20**	**July 19**	**Jan. 20**
Oikopleura dioica	158.5	17.2	82.2	71.75	26.3	71.85	1.8	0.18	0.5	1.56	0.23	1.26
Evadne spinifera	10.5				1.7		0.04		0		0.007	
Penilia avirostris	451.8		83.1		118.1		12.7		2.33		3.31	
Pleopis polyphemoides	126.9	8.1	9.7		13.1		1.14	0.07	0.09		0.12	
Pseudevadne tergestina	1010		126.4		133.5		4.04		0.51		0.53	
Bosmina longirostris		2.9						0.40				
Ceriodaphnia reticulata		0.3						0.05				
Chydorus sphaericus		0.2						0.02				
Daphnia cucullata		0.2						0.02				
Daphnia magna		0.8						0.11				
Pleuroxus aduncus		0.2						0.02				
Parasagitta setosa	283.4	7.3	202.6	2.04	242.4	2.63	24.8	7.6	21.2	1.97	22.3	2.55
Acartia clausi	1760.7	682.7	1787.3	630.03	1456	308.47	44.3	15.1	43.8	12.7	36.04	5.46
Acartia tonsa	797.9		279.2		241.2		16.4		6.5		5.01	
Acartia sp.	953.2		1512.5		1069.2		10.7		18.2		12.5	
Calanus euxinus		42.2	0.2	12.88		4.65		11.2	0.01	1.19		1.57
Centropages ponticus	342.4	0.9	1041.9		1638.7		13	0.04	30.7	0.006	49.02	
Oithona davisae	3.9	3.9	2.1	2.94	0.4	7.8	0.01	0.01	0.005	0.2	0.001	0.02
Oithona similis		80.9		44.81		82.66		0.4		8.38		0.36

Table 1 continued…

	Average Abundance (ind.m^{-3})						**Average Biomass (mg m^{-3})**					
	Sakarya River		**Samsun Port**		**Yeşilırmak River**		**Sakarya River**		**Samsun Port**		**Yeşilırmak River**	
Species	**July 19**	**Jan. 20**	**July 19**	**Jan. 20**	**July 19**	**Jan. 20**	**July 19**	**Jan. 20**	**July 19**	**Jan. 20**	**July 19**	**Jan. 20**
Paracalanus parvus	94.2	1075.7	18.8	885.01	2.1	458.07	1	9.24	0.2	1.59	0.02	4.16
Pseudocalanus elongatus		57.6		40.36		32.87		1.64		0.07		0.7
Pontella mediterranea					0.8						0.16	0.09
Copepod nauplii	2.8	123.5	12.8	65.79	2.1	87.87	0.003	0.12	0.013	12.7	0.002	0.02
Actinotroch larvae		0.03										
Ascidian larvae		0.3										
Bivalve larvae	14.5	113.8	17.7	116.18	37.4	187.19	0.07	0.57	0.09	0.6	0.19	0.94
Branchiostoma	0.1											
Cirriped larvae	72	10.1	151.3	18.10	252.5	40.84	1.61	0.19	2.43	0.32	4.01	0.67
Cyphanout larvae	2.3				1.4		0.003				0.002	
Decapod larvae	5.9	0.1	15.2	0.21	41.9			0.004		0.01		
Gastropod larvae	6.7	0.4	10.5		31.3	0.98	0.36	0.005	0.94		2.6	0.01
Polychaete larvae	3.7	15.4	7.7	1.24	25.1	1.27	0.07	0.58	0.11	0.05	0.34	0.05
Fish egg	22	0.3	14.6		18.5		0.14		0.29		0.95	
Fish larvae	6.2	0.1	9.9		14.4							
Noctiluca scintillans	111.6	321.9	2.5	267.05	2.8	209.76	9.67	28.3	0.22	23.5	0.24	18.5

Copepoda was represented by seven species, from which Acartiidae (*Acartia clausi* and *Acartia tonsa*) and *Centropages ponticus* revealed the highest abundances in the sampling sites in July 2019. The maximum abundance and biomass values of *A. clausi* were 3279 ind. m^{-3} and 81 mg m^{-3} at station SAK08; and the corresponding values were 1396 ind. m^{-3} and 32.5 mg m^{-3} for *A. tonsa* at station SLI05, 2772 ind. m^{-3} and 34 mg m^{-3} for *Acartia* sp. at station SN03 and 2750 ind. m^{-3} and 78 mg m^{-3} for *C. ponticus* at station YSL07 in July 2019. *Calanus euxinus* was only observed in the Samsun Port (1.1 ind. m^{-3} and 0.05 mg m^{-3} in SN03). *Pontella mediterranea* was only recorded in the Yeşilırmak River (3.3 ind. m^{-3} and 0.65 mg m^{-3} in YSL07) in summer. *Oithona similis* and *Pseudocalanus elongatus* were absent at all the sampling stations in summer (Figure 4A). In January 2020, the minimum and maximum abundances of Copepoda were in the range of 1676–2419 ind. m^{-3} in Sakarya River, 1011–3703 ind. m^{-3} in Samsun Port and 573–1500 ind. m^{-3} in Yeşilırmak River. The minimum and maximum biomass values of Copepoda were in the range of 25–50 mg m^{-3} in Sakarya River, 12–62 mg m^{-3} in Samsun Port and 6–17 mg m^{-3} in Yeşilırmak River in winter (Figure 3). Among the seven copepod species identified in the sampling regions in winter, *A. clausi* and *Paracalanus parvus* were dominant in terms of abundance, and *C. euxinus* was dominant in terms of biomass. The highest abundance and biomass values of *A. clausi* (2224 ind. m^{-3} and 44.3 mg m^{-3}) and *P. parvus* (1283 ind. m^{-3} and 13 mg m^{-3}) were recorded at station SLI05. The peak values of *C. euxinus* (58 ind. m^{-3} and 26 mg m^{-3}) were found at station SAK10. *C. ponticus* was exclusively observed in Sakarya River (3.7 ind.m^{-3} and 0.2 mg m^{-3} in SAK08) in winter, and *A. tonsa, Acartia* sp. and *P. mediterranea* were absent in all the sampling stations in January 2020 (Figure 4A). Abundance and biomass values of Cladocera varied between 1267–2198 ind. m^{-3} and 12.3–26 mg m^{-3} in Sakarya River, 115–384 ind. m^{-3} and 1.6–4.6 mg m^{-3} in Samsun Port and 173–375 ind. m^{-3} and 3.4–4.2 mg m^{-3} in Yeşilırmak River in July 2019 (Figure 3). *Penilia avirostris* and *Pseudoevadne tergestina* were dominant among the identified four cladocerans in July 2019. Maximum abundance and biomass values of *P. avirostris* were 688 ind. m^{-3} and 19.3 mg m^{-3} at station SAK09. The highest abundance and biomass values of *P. tergestina* were 1406 ind. m^{-3} and 6 mg m^{-3} at station SAK09 (Figure 4B). The marine cladocerans were only represented by *Pleopis polyphemoides* in January 2020. This species was exclusively found at stations of the Sakarya River. Freshwater cladocerans were also identified in the Sakarya River (SAK07 and SAK08) in both seasons (Table 1).

The abundance and biomass values of meroplankton varied between 80–236 ind. m^{-3} and 1–4 mg m^{-3} in Sakarya River, 20.5–605 ind. m^{-3} and 0.07–9.5 mg m^{-3} in Samsun Port, 51–1045 ind. m^{-3} and 0.6–20 mg m^{-3} in Yeşilırmak River in July 2019, respectively (Figure 3). In January 2020, the abundance and biomass values of meroplankton varied between 83–187 ind. m^{-3} and 0.8–2.3 mg m^{-3} in Sakarya River, 93–193 ind. m^{-3} and 0.6–1.9 mg m^{-3} in Samsun Port, 101–409 ind. m^{-3} and 0.5–3.5 mg m^{-3} in Yeşilırmak River, respectively (Figure 3).

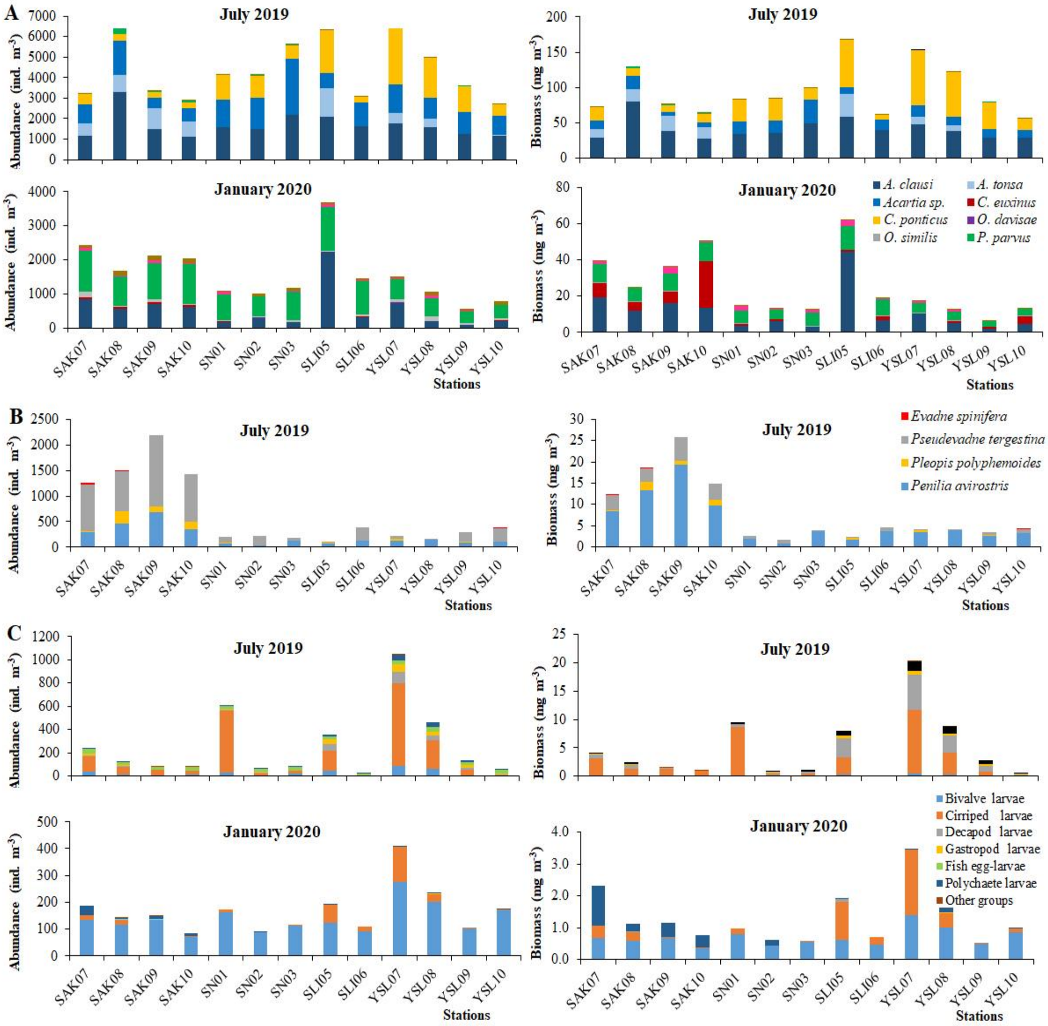

Figure 4. *Abundance (ind. m^{-3}) and biomass (mg m^{-3}) values of (**A**) Copepoda species, (**B**) Cladoceran species and (**C**) Meroplanktonic groups (Other groups: Actinotroch larvae, Ascidian larvae, Branchiostoma, Cyphonaut larvae) at sampling stations*

Among the 11 meroplanktonic groups recorded in the study, cirriped larvae were dominant in July 2019 and bivalve veligers were dominant in January 2020. Maximum abundance and biomass values of cirriped larvae were 714 ind. m^{-3} and 11.3 mg m^{-3} in July 2019 at station YSL07. The highest abundance and biomass values of bivalve veligers were 276 ind. m^{-3} and 1.4 mg m^{-3} in January 2020 at station YSL07 (Figure 4C). The abundance and biomass values of *Noctiluca scintillans* were lower in July 2019. It was absent in the Samsun Port samples from stations SN01, SN03 and SLI06 and Yeşilırmak River region samples (except station YSL07). *N. scintillans* showed maximum abundance and biomass values of 401 ind. m^{-3} and 35 mg m^{-3} at station SAK08 in July 2019. The abundance and biomass of *N. scintillans* were 91–583 ind. m^{-3} and 8–51 mg m^{-3} in Sakarya River, 46–784 ind. m^{-3} and 4–69 mg m^{-3} in Samsun Port, 91–395 ind. m^{-3} and 8–35 mg m^{-3} in Yeşilırmak River in January 2020 (Figure 5A).

Mesozooplankton Community Structure and Relationships with Environmental Parameters

Shannon diversity index values were between 2.8–3.09 in Sakarya River, 2.10–2.51 in Samsun Port and 2.36–2.69 in Yeşilırmak River in July 2019. Shannon diversity index varied from 1.89 to 2.25 in Sakarya River, 1.73 to 2.13 in Samsun Port and 2.33 to 2.74 in Yeşilırmak River in January 2020. Shannon diversity index values determined in July 2019 are higher than those in January 2020 (except for station YSL08 in Yeşilırmak River). Lower Shannon diversity index values (ranging from 1.73 to 1.93) were detected in January 2020 (stations SLI05, SAK10, SN03 and SLI06) due to the numerical dominance of copepods *Paracalanus parvus* and *Acartia clausi* (Figure 5B).

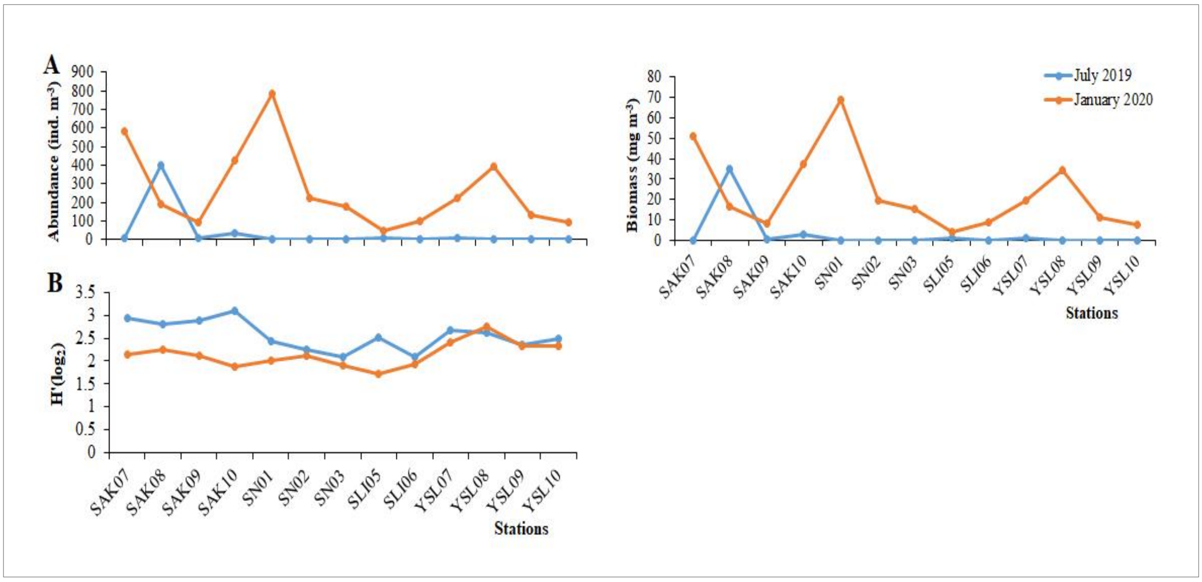

Figure 5. *(**A**) Abundance (ind. m^{-3}) and biomass (mg m^{-3}) values of Noctiluca scintillans at sampling stations. (**B**) The Shannon diversity index (H'(log$_2$)) for mesozooplankton abundance for each month and sampling stations (absent N. scintillans)*

The cluster analysis classified stations into two groups at the 69% similarity level. The first cluster is composed of Sakarya River stations and the second one covered Samsun Port and Yeşilırmak River stations in July 2019 (Figure 6). The ANOSIM test revealed statistically significant differences in the abundances of mesozooplankton assemblages, and between different sampling regions (global R = 0.495, p = 0.003). While there was a statistically significant difference between Sakarya River and Samsun Port (global R = 0.788, p = 0.016) and Sakarya River and Yeşilırmak River group (global R = 0.771, p = 0.029), no difference was determined between Samsun Port and Yeşilırmak River group (global R = –0.056, p = 0.532) in July 2019. The SIMPER analysis showed that the intra-group average similarity value was at 82.61% in Sakarya River, 75.69% in Samsun Port and 78.36% in Yeşilırmak River in July 2019. The community of Sakarya River was characterized by a high abundance of the copepod *A. clausi*, and the cladoceran *P. tergestina*. Samsun Port and Yeşilırmak River were dominated by *A. clausi*, *Acartia* sp., and *C. ponticus*. The average dissimilarity percentages between the sampling regions were low in July 2019 according to the results of SIMPER analysis (Sakarya River and Samsun Port = 31.62%; Sakarya River and Yeşilırmak River = 29.94%; Samsun Port and Yeşilırmak River = 23.03%). The differences in mesozooplankton assemblages among regions were due largely to *A. tonsa*, *P. polyphemoides*, *P. tergestina* and *C. ponticus* based on the SIMPER analysis (Table 2).

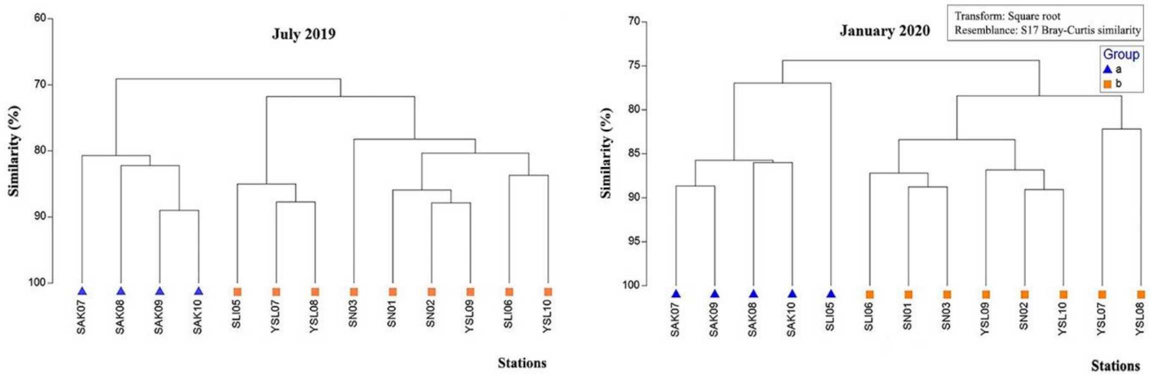

Figure 6. *The cluster dendrogram showing relationships between stations, based on mesozooplankton abundance in July 2019 and January 2020*

According to the results of ANOSIM, the groups were selected at the 74% similarity level in the CLUSTER analysis (Figure 6), and the global R value was 0.466 (p = 0.002) in January 2020. While a statistically significant difference was evident between Sakarya River and Samsun Port (global R = 0.538, p = 0.024) and Sakarya River and Yeşilırmak River group (global R = 0.792, p = 0.029), no significant difference was found between Samsun Port and Yeşilırmak River group (global R = 0.125, p = 0.19) in January 2020. The SIMPER analysis showed that the intra-group average similarity value was at 86.27% in Sakarya River, 81.20% in Samsun Port and 79.35% in Yeşilırmak River in January 2020. The taxa with the highest contributions to the similarity at the Sakarya River, Samsun Port and Yeşilırmak River were *P. parvus*, *A. clausi* and bivalve veligers (Table 2). Similarity percentages showed an average dissimilarity of 22.38% between Sakarya River and Samsun Port, 27.34% between Sakarya and Yeşilırmak Rivers and 21.03% between Samsun Port and Yeşilırmak River. The SIMPER analysis showed that the taxa responsible for the dissimilarity between the sampling regions were *A. clausi* and *P. parvus* (Table 2). Total mesozooplankton abundance and biomass were positively correlated with temperature however negatively correlated with dissolved oxygen and the abundance of *N. scintillans* ($p < 0.01$). No correlations were found between the abundance and biomass of total mesozooplankton and salinity and Chlorophyll-*a*. The dominant species of summer samples—*A. clausi*, *A. tonsa*, *C. ponticus*, *P. avirostris*, *P. tergestina* and Cirripedia larvae—were positively correlated with temperature ($p < 0.01$), but negatively correlated with dissolved oxygen (except cirriped larva) ($p < 0.01$). The dominant taxa of winter—*P. parvus*, *C. euxinus* and bivalve veligers—were negatively correlated with temperature ($p < 0.01$), but positively correlated with dissolved Oxygen ($p < 0.01$; Table 3).

Table 2. *The percent contribution (%) of the mesozooplankton species to in–region similarity (red) or between–region dissimilarity (blue) from SIMPER analysis in July 2019 and January 2020*

July 2019

	Sakarya River		**Samsun Port**		**Yeşilırmak River**	
	Species	**Contribution %**	**Species**	**Contribution %**	**Species**	**Contribution %**
Sakarya River	*A. clausi*	16.94				
	P. tergestina	14.35				
Samsun Port	*A. tonsa*	17.70	*A. clausi*	26.96		
	P. polyphemoides	15.03	*Acartia* sp.	22.01		
			C. ponticus	15.82		
Yeşilırmak River	*P. tergestina*	15.13	*A. tonsa*	15.16	*A. clausi*	21.71
	C. ponticus	14.53	*C. ponticus*	14.57	*Acartia* sp.	18.77
					C. ponticus	18.59

January 2020

	Sakarya River		**Samsun Port**		**Yeşilırmak River**	
	Species	**Contribution %**	**Species**	**Contribution %**	**Species**	**Contribution %**
Sakarya River	*P. parvus*	29.33				
	A. clausi	23.15				
Samsun Port	*A. clausi*	25.55	*P. parvus*	33.25		
			A. clausi	17.50		
			Bivalvia	12.32		
Yeşilırmak River	*P. parvus*	19.73	*A. clausi*	23.67	*P. parvus*	26.40
	A. clausi	18.51	*P.parvus*	20.18	*A. clausi*	15.76
					Bivalvia	15.64

Table 3. *The relationship between the abundance of mesozooplankton species/taxa, and the environmental parameters*

	Temperature	**Salinity**	**Dissolved Oxygen**	**Chlorophyll-*a***	***N. scintillans***
Mesozooplankton abundance	.842**	ns	-.587**	ns	-.544**
Mesozooplankton biomass	.822**	ns	-.601**	ns	-.570**
Total abundance of Copepoda	.802**	ns	-.566**	ns	-.570**
A. clausi	.768**	ns	-.508**	ns	-.569**
A.tonsa	.550**	ns	-.589**	ns	ns
Acartia sp.	.849**	ns	-.591**	ns	-.697**
C. euxinus	-.725**	ns	.654**	ns	.647**
C. ponticus	.752**	ns	-.609**	ns	-.735**
O. davisae	ns	ns	ns	ns	ns
O. similis	-.796**	ns	.705**	ns	.719**
P. parvus	-.682**	ns	.588**	ns	.758**
P. elongatus	-.798**	ns	.662**	ns	.751**
Copepod nauplii	-.719**	ns	.734**	ns	.581**
O. dioica	ns	ns	ns	ns	ns
P. setosa	.712**	ns	-.477*	ns	-.601**
Total abundance of Cladocera	.717**	ns	-.747**	-.511**	-.556**
P. avirostris	.806**	ns	-.649**	ns	-.628**
P. polyphemoides	.475*	-.443*	-.552**	ns	ns
P. tergestina	.790**	ns	-.778**	-.439*	-.650**
Meroplankton	ns	ns	ns	.557**	ns
Bivalve veligers	-.738**	ns	.783**	.545**	.684**
Cirriped larvae	.523**	ns	ns	ns	ns
Decapod larvae	.764**	ns	-.643**	ns	-.681**
Gastropod veligers	.480*	ns	-.632**	ns	-.442*
Polychaete larvae	ns	ns	ns	ns	ns
Fish egg	.830**	ns	-.680**	ns	-.703**
Fish larvae	.717**	ns	-.558**	ns	-.747**

** Correlation is significant at the 0.01 level (2-tailed).
* Correlation is significant at the 0.05 level (2-tailed).
ns = not significant

Discussion

The present study revealed the qualitative and quantitative structure of mesozooplankton in three different regions of the Southern Black Sea during two different seasons (summer and winter). Coastal marine ecosystems, like our study area, are dynamic environments influenced by meteorological events and variations in riverine and terrestrial inputs. These factors influence the quantities of inorganic nutrients and phytoplankton in the marine environment and also affect many other physicochemical properties of the marine environment [24, 25]. The sudden variations in these dynamic environments can influence the quantity, diversity, availability and seasonal cycle of mesozooplanktonic organisms living there [26]. Freshwater cladoceran species were recorded in January 2020 probably due to the positioning of the sampling station on the river plume over marine waters by the Sakarya River (Table 1). The absence of such a freshwater plankton at the Yeşilırmak River mouth is related to the location of the sampling stations out of the freshwater plume (or to a freshwater input feasible from the second river). The very high Chlorophyll-*a* concentration in July 2019 at SN01 station off the coast of Samsun Port is referable to the high eutrophication as a result of the anthropic activities (metal industry) in this region [24, 27]. Temporal and spatial variations in the qualitative and quantitative structure of marine mesozooplankton are the result of the combination of various biotic and abiotic environmental factors, including temperature, salinity, dissolved oxygen and nutrient concentrations [28]. Copepoda is the dominant component of mesozooplankton in the Black Sea coastal marine pelagic ecosystem, accounting for 62–76% of mesozooplankton abundance [29, 30]. Other studies conducted in different coastal regions of the Black Sea showed parallel findings. *A. clausi*, *P. parvus* and *O. davisae* are eurytherm copepods which are seen in all seasons in the Black Sea where they reproduce throughout the year. Detected in high quantities in plankton samples during the summer and autumn seasons, *C. ponticus* and *A. tonsa* are coastal and temperate species of the Black Sea. Defined as cold water species in the Black Sea, *C. euxinus*, *P. elongatus* and *O. similis* become concentrated in hypoxic waters in deep layers. They occur in significant abundance in surface waters exclusively during the cold season [31-35]. The seasonality of the copepod species in this study is in line with other studies of the Black Sea coast of Turkey [29, 32, 33]. Temperature is a major determinant of the presence and abundance of Cladocera in marine coastal areas [30, 36] and has an impact on seasonality and abundance by influencing their reproductive strategies and development [37]. The temporal distributions of Cladocera in the Black Sea demonstrate a significant seasonality. Temperate water cladocerans *P. avirostris*, *P. tergestina* and *E. spinifera* [38, 39] are present in the plankton of the Black Sea during summer and in early autumn [40]. The presence of *P. polyphemoides* in the Black Sea was observed almost all year round, and they were detected in high quantities during the winter-spring period [29]. Meroplankton (pelagic larvae of benthic invertebrates) provide a significant contribution to the mesozooplankton abundance and biomass in coastal waters of the Black Sea. The biodiversity and abundance of meroplankton are significant indicators to comprehend benthic communities in coastal marine waters and to understand the influences of environmental parameters on benthic communities. Larvae of Bivalvia, Gastropoda, Polychaeta and Cirripedia are the dominant meroplankton groups in the Black Sea [12, 41]. Cirripedia and Bivalvia were found in high concentrations in summer samples and in winter samples, respectively, as is also observed along the Romanian coastal waters [30]. *Noctiluca scintillans* is an omnivorous [42, 43] and opportunistic [44] dinoflagellate species that has wide range of diets (bacteria, phytoplankton, zooplankton egg and nauplii). *N. scintillans* can influence mesozooplankton abundance directly by feeding on zooplankton eggs and nauplii and indirectly by competing with mesozooplankton through food competition [45, 46]. Therefore, the Black Sea pelagic community plays a significant role [47, 48] and is called a non-fodder zooplankton component [30]. In this study, a negative correlation was found between the abundance values of *N. scintillans* and the total mesozooplankton abundance and biomass values, and the abundance values of *A. clausi*, *C. ponticus*, *P. avirostris*, *P. tergestina* and fish eggs and larvae. A positive correlation was found between the abundance value of *N. scintillans* and the abundance values of *P. parvus*, copepod nauplii and bivalve larvae. Apart from the continuous, although oscillating abundance and the presence of “perennial species”, we have to pay attention to the seasonally out-bursting ones which could produce biomass accumulation and cause consequent degradation and final eutrophication. Excluding some species evidently coming from freshwater resources (thus unable to survive in marine environments), for the interpretation of differences in presence and abundance, we have to consider that some other species (such as *A. tonsa*) are typical inhabitants of more confined environments, and their presence could be due to just a derivation from confined situations (e.g. ports) of extreme abundances. Finally, coastal species commonly show the possibility to rest during adverse seasons and to dominate plankton during favourable seasons (as all the Cladocera, and *A. tonsa* and *C. ponticus* among Copepoda) [49]

Conclusion

This study is a part of the research carried out within the scope of the ANEMONE project (Assessing the vulnerability of the Black Sea marine ecosystem to human pressures) funded by the European Union to determine the effects of riverine and human influences on the ecosystem along the Turkish coast of the Black Sea. The present study's findings provide data on the mesozooplankton structure in a marine environment located off two major rivers (Sakarya River and Yeşilırmak River) which discharge into the Black Sea, and Samsun Port. In this study, 30 marine and 6 freshwater mesozooplankton species/taxa and *N. scintillans* were identified. Copepoda revealed a high species diversity in all the research areas and Cladocera also showed a high diversification. Copepoda made significant contributions to the mesozooplankton community followed by Cladocera and the meroplanktonic components. These studies need to be planned as long-term studies to examine the influence of environmental factors on mesozooplankton community structure and to observe the regional differences in similar areas under riverine and human influence. In this context, present work is considered to constitute a basis for future studies.

Acknowledgements We thank to the ANEMONE (Assessing the vulnerability of the Black Sea marine ecosystem to human pressures) Project (funded by the European Union under the ENI CBC Black Sea Basin Programme 2014-2020, project number BSB319).

Funding/Financial Disclosure This study was supported by the ANEMONE (Assessing the vulnerability of the Black Sea marine ecosystem to human pressures) Project (funded by the European Union under the ENI CBC Black Sea Basin Programme 2014-2020, project number BSB319).

Ethics Committee Approval and Permissions The study does not require ethics committee permission or any special permission.

Conflict of Interests All authors declare no conflict of interest that could affect the current study.

Authors Contribution Authors contributed equally to the study. All authors read and approved the final manuscript.

References

[1] Theodorou, I., Zervoudaki, S., Varkitzi, I., & Tsirtsis, G. (2023). Assessing good environmental status through mesozooplankton biodiversity: a step forward. *Journal of Plankton Research*, *45*(1), 52–64. https://doi.org/10.1093/plankt/fbac067

[2] Steinberg, D. K., & Landry, M. R. (2017). Zooplankton and the ocean carbon cycle. *The Annual Review of Marine Science*, *9*, 413–444. https://doi.org/10.1146/annurev-marine-010814-015924

[3] Kovalev, A. V., Skryabin, V. A., Zagorodnyaya, Yu. A., Niermann, U., Bingel, F., Kıdeyş, A. E., Niermann, U., & Uysal, Z. (1999). The Black Sea zooplankton: composition, spatial/temporal distribution and history of investigations. *Turkish Journal of Zoology*, *23*(2), 195–209.

[4] Dzierzbicka-Głowacka, L., Kalarus, M., & Żmijewska, M. I. (2013). Interannual variability in the population dynamics of the main mesozooplankton species in the Gulf of Gdańsk (southern Baltic Sea): Seasonal and spatial distribution. *Oceanologia*, *55*(2), 409–434. https://doi.org/10.5697/oc.55-2.409

[5] Piontkovski, S. A., Fonda-Umani, S., Stefanova, K., Kamburska, L., Olazabal, A. De. (2011). An impact of atmospheric anomalies on zooplankton communities in the Northern Adriatic and Black Seas. *International Journal of Oceans and Oceanography*, *5*(1), 53–71.

[6] Gubanova, A., Goubanova, K., Krivenko, O., Stefanova, K., Garbazey, O., Belokopytov, V., Liashko, T., & Stefanova, E. (2022). Response of the Black Sea zooplankton to the marine heatwave 2010: Case of the Sevastopol Bay. *Journal of Marine Science and Engineering*, *10*(12), 1933. https://doi.org/10.3390/jmse10121933

[7] Kovalev, A. V., Niermann, U., Melnikov, V. V., Belokopytov, V., Uysal, Z., Kıdeyş, A. E., Ünsal, M., & Altukhov, D. (1998). Long-term changes in the Black Sea zooplankton: the role of natural and antropogenic factors. In. L, Ivanov, T. Oguz (Ed), *NATO TU-Black Sea Assessment Workshop: NATO TU-Black Sea Project, Symposium on Scientific Results*, (pp. 221–234).

[8] Selifonova, J. (2000). Seasonal and long-term dynamics of the zooplankton community in Novorossiysk Bay of the Black Sea exposed to anthropogenic impact. *Acta Zoologica Bulgarica*, *52*(3), 63–74.

[9] Arashkevich, E. G., Timonin, A. G., Zatsepin, A. G., Kremenetskiy, V. V., & Drits, A. V. (2005). Effect of the rim current regime on the zooplankton distribution in the “shelf-slope-deep sea” system in the Black Sea. *Oceanology*, *45*(Suppl. 1), 149–160.

[10] Rabalais, N. N., Turner, R. E., Díaz, R. J., & Justić, D. (2009). Global change and eutrophication of coastal waters. *ICES Journal of Marine Science*, *66*(7), 1528–1537. https://doi.org/10.1093/icesjms/fsp047

[11] Bedford, J., Ostle, C., Johns, D. G., Atkinson, A., Best, M., Bresnan, E., Machairopoulou, M., Graves, C. A., Devlin, M., Milligan, A., Piotis, S., Mellor, A., Tett, P., & McQuatters-Gollop, A. (2020). Lifeform indicators reveal large-scale shifts in plankton across the North-West European shelf. *Global Change Biology, 26*(6), 3482–3497. https://doi.org/10.1111/gcb.15066

[12] Stefanova, K. (2015). Long-term shifts of the zooplankton community in the western Black Sea (Cape Galata Transect, Bulgarian Coast). *Journal of Research in Environmental and Earth Science, 2*(6), 01–10.

[13] Besiktepe, S., Kucuksezgin, F., Besiktepe, S. T., Eronat, C., Gonul, T., Terbıyık Kurt, T., Sayın, E., & Gubanova, A. (2023). Variations in copepod composition and diversity in relation to eutrophication and hydrology in İzmir Bay, Aegean Sea. *Marine Pollution Bulletin*, *197*, 115745. https://doi.org/10.1016/j.marpolbul.2023.115745.

[14] Isik, S., Dogan, E., Kalin, L., Sasal, M., & Agiralioglu, N. (2008). Effects of anthropogenic activities on the Lower Sakarya River. *Catena, 75*(2), 172–181. https://doi.org/10.1016/j.catena.2008.06.001

[15] Şimşek, A., Türkten, H., & Bakan, G. (2022). Evaluation of water quality of the middle Black Sea region, Kızılırmak and Yeşilırmak Rivers using water quality index and statistical analysis. *The Black Sea Journal of Sciences*, *12*(2), 645–662. https://doi.org/10.31466/kfbd.1100682 (in Turkish).

[16] Yılmaz, A. (2006). The port of Samsun. *Türk Coğrafya Dergisi*, *45*, 85–100. (in Turkish).

[17] Hansen, H. P. (1999). Determination of oxygen. In K. Grasshoff, K. Kremling, M. Ehrhard (Ed). *The methods of seawater analysis*, (pp. 75–89). 3rd ed. Wiley: VCH Verlag, https://doi.org/10.1002/9783527613984.ch4

[18] Parsons, T. R., Maita, Y., & Lalli, C. M. (Ed.) (1984). *A manual of chemical and biological methods for seawater analysis*. Oxford (UK): Pergamon Press.

[19] Postel, L., Fock, H., & Hagen, W. (2000). Collecting zooplankton. In R. Harris, P. Wiebe, H.R. Skjoldal, M. Huntley (Ed). *ICES Zooplankton methodology manual*, (pp. 53–81). London (UK): Academic Press.

[20] Petipa, T. S. (1957). On average weight of the main zooplankton forms in the Black Sea. *Proceedings of Sevastopol Biological Station*, *9*, 39–57. (in Russian).

[21] Niermann, U., Kideys, A. E., Besiktep,e S., Nicolae, B., Goubanova, A., Khoroshilov, V., Mikaelyan, A., Moncheva, S., Mutlu, E., Nezlin, N., Petruanu, A., Senichkina, L., Shiganova, T. (1995). An assessment of recent Phyto and Zooplankton investigations in the Black Sea and planning for future. Report on the meeting of Marine Biologists in Erdemli, Turkey, 20 February-3 March 1995. TU-Black Sea Project, NATO Science for Stability Program. M.E.T.U., Institute of Marine Sciences, Erdemli, İçel, Turkey; p. 100.

[22] Bradford-Grieve, J. M., Markhaseva, E. L., Rocha, C. E. F., & Abiahy, B. (1999). Copepoda. In D. Boltovskoy, (Ed), *South Atlantic Zooplankton*, (pp. 869–1098). Leiden: Backhuys Publishers.

[23] Conway, D. V. P., White, R. G., Hugues-Dit-Ciles, J., Gallienne, C. P., & Robins, D. B. (Ed.) (2003). *Guide to the coastal and surface zooplankton of the south-western Indian Ocean*. Plymouth: United Kingdom.

[24] Lazăr, L., Boicenco, L., Denga, Y., Tolun, L., & Kurt, G (Ed) (2021a). *Anthropogenic pressures and impacts on the Black Sea coastal ecosystem*. CD Press: Bucharest, Romania.

[25] Lazăr, L., Boicenco, L., Moncheva, S., Denga, Y., & Atabay, H. et al. (Ed.) (2021b). *Impact of the rivers on the Black Sea Ecosystem*. CD Press: Bucharest, Romania.

[26] Calbet, A., Garrido, S., Saiz, E., Alcaraz, M., & Duarte, C. M. (2001). Annual zooplankton succession in coastal NW Mediterranean waters: the importance of the smaller size fractions. *Journal of Plankton Research*, *23*(3), 319–331. https://doi.org/10.1093/plankt/23.3.319

[27] Tan, İ., Atabay, H., Mutlu, S., Tolun, L. G., Polat Beken, S. Ç. (2023). A comparison of the surface water quality in distinct areas of the southern Black Sea coast under various pressures. *Research Square*, 1–12. https://doi.org/10.21203/rs.3.rs-3100718/v1

[28] Rekik, A., Guermazi, W., Kmiha-Megdiche, S., Sellami, I., Pagano, M., Ayadi, H., & Elloumi, J. (2023). Spatial variation of summer microphytoplankton and zooplankton communities related to environmental parameters in the coastal area of Djerba Island (Tunisia, Eastern Mediterranean). *Mediterranean Marine Science*, *24*(1), 156–172. https://doi.org/10.12681/mms.30650

[29] Üstün, F., Bat, L., & Mutlu, E. (2018). Seasonal variation and taxonomic composition of mesozooplankton in the Southern Black Sea (off Sinop) between 2005 and 2009. *Turkish Journal of Zoology*, *42*(5), 541–556. http://dx.doi.org/10.3906/zoo-1801-13

[30] Bişinicu, E., Lazăr, L., & Timofte, F. (2023a). Dynamics of zooplankton along the Romanian Black Sea coastline: Temporal variation, community structure, and environmental drivers. *Diversity*, *15*(9), 1024. https://doi.org/10.3390/d15091024

[31] Besiktepe, S. (2001). Diel vertical distribution, and herbivory of copepods in the south-western part of the Black Sea. *Journal of Marine Systems*, *28*(3–4), 281–301. https://doi.org/10.1016/S0924-7963(01)00029-X

[32] Yıldız, İ., & Feyzioğlu, A. M. (2014). Biological diversity and seasonal variation of mesozooplankton in the southeastern Black Sea coastal ecosystem. *Turkish Journal of Zoology*, *38*(2), 179–190. https://doi.org/10.3906/zoo-1304-32

[33] Üstün, F. (2019). Seasonal cycle of zooplankton abundance and biomass in Hamsilos Bay, Sinop, southern Black Sea, Turkey. *Journal of Natural History*, *53*(7–8), 365–389. https://doi.org/10.1080/00222933.2019.1592257

[34] Prusova, I. Yu., & Galagovets, E. A. (2022). Sex ratios of calanoid copepods in the northern Black Sea. *Regional Studies in Marine Science, 55,* 102576. https://doi.org/10.1016/j.rsma.2022.102576

[35] Bişinicu, E., Harcota, G. E., & Lazăr, L. (2023b). Interactions between environmental factors and the mesozooplankton community from the Romanian Black Sea waters. *Turkish Journal of Zoology*, *47*(4), 202–2015. https://doi.org/10.55730/1300-0179.3133

[36] Gülşahin, N., & Tarkan, A. N. (2012). Seasonal changes in distribution and abundance of the cladoceran species in relation to environmental factors in Gökova Bay (Muğla, Aegean Sea, Turkey). *Fresenius Environmental Bulletin*, *21*(7a), 1853–1863.

[37] Bedikoğlu, D., Yilmaz, I. N., & Demirel, N. (2022). Reproductive strategies and population characteristics of key Cladocera species in the Sea of Marmara. *Regional Studies in Marine Science*, *54*, 102450. https://doi.org/10.1016/j.rsma.2022.102450

[38] Marazzo, A., & Valentin, J. L. (2000). A report on the marine cladoceran *Evadne spinifera* Müller (Crustacea, Branchiopoda) in Guanabara Bay, Rio de Janeiro, Brazil. *Revista brasileira de Zoologia*, *17*(4), 1101–1102.

[39] Marazzo, A., & Valentin, J. L. (2001). Spatial and temporal variations of *Penilia avirostris* and *Evadne tergestina* (Crustacea, Branchiopoda) in a Tropical Bay, Brazil. *Hydrobiologia*, *445*(1–3), 133–139. https://doi.org/10.1023/A:1017592323388

[40] Lebedeva, L. P., Lukasheva, T. A., Anokhina, L. L., & Chasovnikov, V. K. (2015). Interannual variability in the zooplankton community in Golubaya Bay (Northeastern part of the Black Sea) in 2002–2012. *Oceanolog*y, *55*(3), 355–363. https://doi.org/10.1134/S0001437015030091

[41] Vereshchaka, A. L., Anokhina, L. L., Lukasheva, T. A., & Lunina, A. A. (2019). Long-term studies reveal major environmental factors driving zooplankton dynamics and periodicities in the Black Sea coastal zooplankton. *PeerJ*, *7*, e7588. https://doi.org/10.7717/peerj.7588

[42] Kirchner, M., Sahling, G., Uhlig, G., Gunkel, W., & Klings, K. W. (1996). Does the red tide-forming dinoflagellate *Noctiluca scintillans* feed on bacteria? *Sarsia*, *81*(1), 45–55. https://doi.org/10.1080/00364827.1996.10413610

[43] Mikaelyan, A. S., Malej, A., Shiganova, T. A., Turk, V., Sivkovitch, A. E., Musaeva, E. I., Kogovsek, T., & Lukasheva, T. A. (2014). Populations of the red tide forming dinoflagellate *Noctiluca scintillans* (Macartney): A comparison between the Black Sea and the northern Adriatic Sea. *Harmful Algae*, *33*, 29–40. http://dx.doi.org/10.1016/j.hal.2014.01.004

[44] Oguz, T., & Velikova, V. (2010). Abrupt transition of the northwestern Black Sea shelf ecosystem from a eutrophic to an alternative pristine state. *Marine Ecology Progress Series*, *405*, 231–242. https://doi.org/10.3354/meps08538

[45] Nikishina, A. B., Drits, A. V., Vasilyeva, Yu. V., Timonin, A. G., Solovyev, K. A., Ratkova, T. N., & Sergeeva, V. M. (2011). Role of the *Noctiluca scintillans* population in the trophic dynamics of the Black Sea plankton over the spring period. *Oceanology*, *51*(6), 1029–1039. https://doi.org/10.1134/S0001437011060129

[46] Aytan, Ü., & Şentürk, Y. (2018) Dynamics of *Noctiluca scintillans* (Macartney) Kofoid & Swezy and its contribution to mesozooplankton in the southeastern Black Sea. *Aquatic Sciences and Engineering*, *33*(3), 84–89. https://doi.org/10.26650/ASE201814

[47] Oguz, T., Malanotte-Rizzoli, P., & Ducklow, H. W. (2001). Simulations of phytoplankon seasonal cycle with multi-level and multi-layer physical-ecosystem models: the Black Sea example. *Ecological Modelling*, *144*(2–3), 295–314. https://doi.org/10.1016/S0304-3800(01)00378-7

[48] Kopuz, U., Feyzioglu, A. M., & Valente, A. (2014). An unusual red-tide event of *Noctiluca scintillans* (Macartney) in the southeastern Black Sea. *Turkish Journal of Fisheries and Aquatic Sciences*, *14*(1), 261–268. http://doi.org/10.4194/1303-2712-v14_1_28 (in Turkish)

[49] Belmonte, G., & Rubino, F. (2019). Resting cysts from coastal marine plankton. *Oceanography and Marine Biology, 57,* 1 – 88.

Sinopfbd, 2024; 9(2): 331-350 **https://doi.org/10.33484/sinopfbd.1436134**

Sinop Üniversitesi Fen Bilimleri Dergisi
Sinop Uni J Nat Sci

E-ISSN: 2564-7873

https://dergipark.org.tr/tr/pub/sinopfbd

Farklı Eğim Açılı Levhalarla Sınırlandırılmış Çarpan Slot ve Dairesel Jetlerde Taşınımla Isı Transferi Etkilerinin Karşılaştırılması

Haluk KELEŞ[1] ve Yücel ÖZMEN[2]

How to cite: Keleş, H., & Özmen, Y. (2024). Farklı eğim açılı levhalarla sınırlandırılmış çarpan slot ve dairesel jetlerde taşınımla ısı transferi etkilerinin karşılaştırılması. *Sinop Üniversitesi Fen Bilimleri Dergisi, 9*(2), 331-350. https://doi.org/10.33484/sinopfbd.1436134

Araştırma Makalesi

Sorumlu Yazar
Haluk KELEŞ
hkeles@artvin.edu.tr

Yazarlara ait ORCID
H.K: 0000-0002-6562-8902
Y.Ö: 0000-0003-1127-1060

Received: 13.02.2024
Accepted: 18.07.2024

Öz

Bu çalışmada, farklı eğim açılı levhalarla sınırlandırılmış çarpan slot ve dairesel türbülanslı hava jetlerinde, hedef çarpma levhası yüzeyleri boyunca ısı transfer karakteristikleri etkileri deneysel olarak incelenmiştir. Sınırlayıcı levha eğim açısının θ = 0°, 15°, 30° ve 45°, levhalar arası açıklık oranı H/W(D) = 0.5, 1, 3, 6 ve Reynolds sayısının 20000 ile 30000 değerleri için hedef çarpma levhası boyunca termal kamera ile yüzey sıcaklık ölçümleri yapılmıştır. Ölçümlenen sıcaklık değerlerinden hesaplanan Nusselt dağılımları, sınırlayıcı levha eğim açısı, Reynolds sayısı (Re) ve levhalar arası açıklık oranı parametrelerine göre incelenip değişimler değerlendirilmiştir. Hem slot hem de dairesel jetlerde, levhalar arası açıklık oranının H/W(D)≤1 ve sınırlayıcı levha eğim açısının θ≤15° olduğu durumlarda, çarpma levhası üzerindeki Nusselt sayısı dağılımlarında ikincil pikler oluşmaktadır. Levhalar arası açıklık oranı arttıkça, ikincil piklerin etkisi azalmakta ve konumları levha uçlarına doğru kaymaktadır. Artan sınırlandırıcı levha eğim açısı ile birlikte, slot jetlerde ikincil pikler hızla kaybolurken, dairesel jetlerde bu durumun daha yavaş olduğu gözlenmiştir.

Anahtar Kelimeler: Dairesel jet, eğimli sınırlandırıcı levha, ikincil artışlar, Nusselt dağılımları, Slot jet

Comparison of Convective Heat Transfer Effects in Impinging Slot and Circular Jets Confined by Plates With Different Inclination Angles

[1]Artvin Çoruh Üniversitesi, Elektrik-Elektronik Mühendisliği Bölümü, Artvin, Türkiye

[2]Karadeniz Teknik Üniversitesi, Makina Mühendisliği Bölümü, Trabzon, Türkiye

Abstract

In this study, the effects of heat transfer characteristics along the target impingement plate surfaces in impinging slot and circular turbulent air jets confined by plates with different inclination angles are experimentally investigated. Surface temperature measurements were conducted with a thermal imaging camera on the target impingement plate for inclination angles of confinement plate θ = 0°, 15°, 30° and 45°, rate of plate-to-plate spacing H/W(D) = 0.5, 1, 3, 6 and Reynolds numbers (Re) 20000 and 30000. The Nusselt distributions calculated from the measured temperature values are analyzed and the changes are evaluated according to the confining plate inclination angle, Reynolds number and rate of plate-to-plate spacing parameters. For both slot and circular jets, secondary top points become visible in the Nusselt number distributions on the impingement plate when the rate of plate-to-plate spacing is H/W(D)≤1 and the inclination angle of confinement plate is θ≤15°. As the interval among the plates increases, the influence of the secondary top points decreases and their positions shift towards the plate ends. As the angle of inclination of the confining plate increases, the secondary top points disappear rapidly for slot jets, but more slowly for circular jets.

Keywords: Circular jet, Inclined confined plate, Nusselt distributions, Secondary top points, Slot jet

Giriş

Uçaklarda buzlanmanın engellenmesi, cam ve metallerin temperlenmesi, kâğıt ve kumaş ürünlerinin kurutulması, gaz türbin kanatlarının soğutulmasının yanı sıra elektronik devre elemanların soğutulması gibi çeşitli uygulamalarda jet akışlarına başvurulmaktadır. Çoklukla ısı transferini arttırmak için kullanılan jet akışları, türbülans modellerinin gelişimine de katkı sağlamaktadır. Çarpan jet akışlarında ısı transferinde, akışkan türü, miktarı ve sıcaklığı, akışın çıktığı lülenin geometrisi ve çapı, lüle-levha arası açıklık oranı, jet çıkışındaki akış hızı ve türbülans şiddeti, çevre ortam ve çarpma levhası sıcaklıkları, jetin sınırlandırılma durumu, çarpma levhasının geometrik şekli ve jet sayısı gibi birçok parametre etkili olmaktadır. Çarpan jetlerde, sınırlandırılmamış ve sınırlandırılmış jet uygulamaları, soğutma amaçlı olarak yaygın kullanılmaktadır. Akış alanında sınırlayıcı levhanın varlığı, lüle-levha arası açıklığın küçük değerlerinde karmaşık akış yapılarını oluşturmakta, lüle-levha arası açıklığın büyük değerlerinde ise çarpma levhası yüzeyince ortaya çıkan duvar jetinin yayılımını geciktirmektedir [1]. Çarpma yüzeyindeki ısı transferinde iyileşme sağlamak amacıyla, sınırlayıcı levha/levhalar eğimli olarak da uygulanabilmektedir. Çarpan jet akışları konusunda literatürde, akış yapısını ve ısı transferi karakteristiklerini belirlenmesi amacıyla oldukça fazla sayıda deneysel ve sayısal çalışma bulunmaktadır. Slot jetlere yönelik çalışmalar, dairesel jetlere göre daha az sayıdadır. Gardon ve Akfirat [2] çarpan slot jet akışını deneysel olarak inceledikleri çalışmalarında, slot lüle çıkışındaki akışın türbülans şiddeti ve derecesinin ısı transferi üzerindeki etkisinin açıklığın 6'dan büyük olduğu durumlarda nispeten küçük olduğunu ve ısı transferindeki ikincil artışların jet duvarı boyunca gelişen sınır tabakadaki akışın laminerden türbülansa geçişinden etkilendiğini ifade etmişlerdir. Livingood ve Hrycak [3] gerçekleştirdikleri çalışma sonucunda potansiyel öz bölgesinin, dairesel jetler için lüle çıkışından itibaren lüle çapının 7 katına ve slot jetler için slot genişliğinin 7.7 katına kadar uzandığını ifade etmişlerdir. Senter ve Solliec [4] hareketli düz bir yüzeye çarpan sınırlandırılmış türbülanslı slot hava jetini, parçacık görüntüleme ile hız ölçümü (PIV) yöntemi kullanılarak incelemişlerdir. Lüle-levha arası açıklık oranının $H/W \leq 0.5$ olduğu durumlarda (H-sınırlayıcı levha ile çarpma levhası arasındaki mesafe, W-slot lüle genişliği), hız dağılımlarının Reynolds sayısından çok az etkilendiğini belirtmişlerdir. Konik levhayla sınırlandırılmış çarpan laminer slot su jeti akışını deneysel ve sayısal olarak inceleyen Cavadas ve ark. [5] konik levha üzerinde jet çıkışı civarında akışın ayrıldığını, ters akış bölgelerinin oluştuğu ve genişliğinin artan Reynolds sayısı ile doğru orantılı olarak arttığını belirtmişlerdir. Açılı levhalar kullanarak slot jeti sınırlayan Özmen ve Kınay [6], düz bir yüzeye çarptırdığı slot jetin, Reynolds sayısı, sınırlayıcı levha eğim açısı ve çarpma levhası açıklığının çarpma levhası üzerindeki basınç katsayısı ve Nusselt sayısı dağılımlarına etkisini incelemiştir. Basınç katsayısı dağılımlarında gözlenen ikincil piklerin, artan sınırlandırıcı levha eğim açısı ile daha büyük r/D (r-çarpan jet merkez ekseninden olan radyal mesafe, D-dairesel jet lülesi çapı) konumlarına kaydığını ve levhalar arası açıklığın 1'den küçük değerlerde çarpma levhası uçlarına doğru Nusselt sayılarında artış olduğunu belirtmiştir. Çarpan slot jetlerle ilgili gerçekleştirdikleri sayısal bir çalışmada Kunugi ve Kawamura [7], çarpma yüzeyi üzerindeki ısı transfer karakteristiklerini incelemişlerdir. Farklı slot genişlikleri, lüle-levha arası açıklık oranları ve Reynolds sayıları için sınırlandırma etkisini inceledikleri çalışmada, sınırlandırılmış ve sınırlandırılmamış çarpan jet durumlarına ait sıcaklık dağılımlarının benzer olduğunu belirtmişlerdir. Chiriac [8] tarafından yapılan bir diğer sayısal çalışmada, slot jetlerde sınırlandırıcının potansiyel öz uzunluğunu arttırdığı ve türbülans seviyesini ve durma noktasındaki ısı transferi performansını azalttığı ifade edilmiştir. Yousefi-Lafouraki ve ark. [9], hem çarpma levhasının hem de sınırlayıcı levhanın eğimli olduğu çalışmalarında, akış ve ısı transferi etkilerini sayısal olarak modelleyip incelemişlerdir. Düşük eğim açılarında gerçekleştirilen çalışmada, eğim açısının artmasıyla ortalama Nusselt sayısının arttığını göstermiştir. Çarpan dairesel jetler konusunda literatürde oldukça fazla sayıda çalışma bulunmaktadır. Bu çalışmaların önemli bir kısmı ise ısı transferi üzerine odaklanmıştır. Schrader [10] tarafından dairesel jetlerle ilgili gerçekleştirilen bir çalışmada, çarpma bölgesinin jet lülesi çapının %20 fazlasına dek genişlediğini bildirilmiştir. Sınırlandırılmamış akış koşullarında, önceden ısıtılan bir yüzeye çarpan dairesel sıcak hava jetlerindeki taşınım ile ısı transferini yaptıkları deneysel bir çalışmada inceleyen Goldstein ve ark. [11], ısı transfer katsayısının çevre ortam ile hava jetinin sıcaklık farkından bağımsız olduğunu, ancak çarpma levhası ile hava jeti arasındaki sıcaklık farkının bu katsayı üzerinde etkili olduğunu belirtmişlerdir. Baughn ve Shimizu'nun [12] yürüttüğü bir deneyde, artan lüle ve levha arasındaki mesafeyle birlikte çarpma levhasındaki yerel ısı transfer katsayısının azaldığı belirlenmiştir. Popiel ve Trass [13], dairesel bir lüleden çıkan çarpan jet akışında, akış alanını duman yöntemiyle görüntülemişlerdir. Halka şeklinde ortaya çıkan girdapların küçük lüle-levha arası açıklık oranlarında duvar jeti bölgesi boyunca yoğunlaştığını ifade etmişlerdir. Çarpan dairesel jetlerde, Mohanty ve Tawfek [14], çarpma levhası yüzeyi boyunca ısı transfer katsayısının durma bölgesinde maksimum pik değeri aldığını, sonrasında levha yüzeyi boyunca radyal doğrultuda üstel bir şekilde azaldığını belirtmişlerdir. Benzer bir çalışma olan Huang ve El-Genk'in [15] çalışmasında, ortalama Nusselt sayısının $Re^{0.76}$ ile doğru orantılı olduğu belirtilmektedir. Küçük Lüle-levha arası açıklık oranı ($H/D<1$) değerlerinde, Lytle ve Webb [16], termal kamera kullanarak çarpma levhası üzerindeki sıcaklık dağılımlarını elde ettikleri çalışmalarında, çarpma bölgesi dışında ısı transferi karakteristik dağılımlarında ikincil artışların meydana geldiğini ifade etmişlerdir. Isı transfer katsayılarında meydana gelen bu ikincil artışları, çarpma yüzeyi boyunca gelişen duvar jetinde akışın laminerden türbülansa geçişi ile ilişkili olduğunu açıklamışlardır. Sınırlandırılmış çarpan dairesel jet akışı içinde, Colucci ve Viskanta [17], açıklık oranının 0.25 - 6 aralığındaki değerleri için termokromik sıvı kristal kullanarak, çarpma levhası boyunca yerel ısı transferi karakteristiklerini gözlemlemişlerdir. Isı transferi karakteristik ve performansının sınırlandırılmış jet koşulları altında, Reynolds sayısı ve lüle-levha arası açıklığın sınırlandırılmamış jette olduğundan daha fazla etkilendiğini ifade etmişlerdir. Sınırlandırılmış çarpan jet akışlarında Baydar [18] ile Baydar ve Özmen [19], 500 ila 50000 aralığındaki Reynolds sayıları için yaptıkları çalışmalarda, 2700'den büyük Reynolds sayısı değerleri ve 2'den küçük lüle ile çarpma levhası arası açıklık oranları için levha yüzeyinde ortam altı (subatmosferik) basınç bölgelerinin oluştuğunu gözlemlemişlerdir. Sınırlandırılmamış akış durumunda, önceden ısıtılmış bir levhaya çarpan dairesel jet üzerine bir çalışma yapan Özmen ve Baydar [20], akış yapısı ve ısı transferi performans ve karakteristiklerinin belirlenmesi amacıyla deneyler gerçekleştirmişlerdir. Çarpma yüzeyi boyunca Nusselt sayısındaki zirvelerin türbülans şiddetindeki piklerle uyum gösterdiğini ifade etmişlerdir. Çarpan laminer jet akışını sınırlandırılmamış durumun yanı sıra sınırlandırılmış durum için de hem sayısal hem de deneysel olarak inceleyen Miranda ve Campos [21], Reynolds sayısı aynı iken, sınırlandırılmış jetlerde akış alanlarındaki ters akış bölgelerinin daha uzun olduğunu ifade etmişlerdir. Behnia ve ark. [22], yaptıkları sayısal çalışmada, sınırlandırılmış ve sınırlandırılmamış jet akışı durumlarını incelemişler ve sınırlandırmanın genel olarak çarpma yüzeyindeki ortalama ısı transferini azalttığını ifade etmişlerdir. Sınırlandırıcının ısı transferi performansındaki pozitif etkisinin lüle-levha arası açıklığın 0.25'ten daha küçük değerlerinde ortaya çıktığını belirtmişlerdir. Çarpan jetlerde, Herrero ve Buchlin [23], lüle geometrik şeklinin yerel ısı transferi dağılımı üzerinde etkisini deneysel olarak incelemişler ve çeşitli lüle geometrik eklentilerinin yerel ısı transferi dağılımını nasıl etkilediğini açıklamışlardır. Lee ve ark. [24], laminer çarpan slot jet akışını deneysel ve sayısal olarak incelemiş ve Reynolds sayısının, lüle ile hedef levha arasındaki aralığın ve yerel Nusselt sayısının akış alanı üzerindeki etkilerini araştırmışlardır. Cavadas ve ark. [25], konik bir plaka ile sınırlandırılmış laminer slot su jeti akışını deneysel ve sayısal olarak incelemiş ve akışın konik plaka üzerinde jet çıkışına yakın ayrıldığını ve ters akış bölgelerinin uzunluğunun Reynolds sayısı ile arttığını belirtmişlerdir. Al Mubarek ve ark. [26] tarafından yürütülen deneysel çalışmada, çarpan jet akışına maruz kalan eğimli bir yüzey üzerindeki ısı transferi etkileri incelenmiştir. Reynolds sayısı arttıkça ortalama yerel Nusselt sayısının da arttığı ifade edilip aralarında doğrudan bir ilişki olduğu vurgulanmıştır. Yousefi-Lafouraki ve ark. [27] hem çarpan hem de sınırlayan plakaların eğimli olduğu çarpan yarıklı jet akışında akış ve ısı transferi etkilerini sayısal olarak incelemiş ve ortalama Nusselt sayısının artan eğim açısı ile arttığını göstermişlerdir. Bhagwat ve Sridharan [28] eğimli bir yüzeye çarpan jet akışındaki ısı transferi etkilerini sayısal olarak incelemişler ve Nusselt dağılımının, özellikle çarpma plakasının düşük eğim açılarında, lüle ve levha arasındaki aralıktan önemli ölçüde etkilendiğini ortaya koymuşlardır. Li ve ark. [29], düz bir yüzeye belli bir açıyla çarpan çoklu jetlerin neden olduğu ısı transferi etkilerini deneysel ve sayısal olarak incelemişler ve Reynolds sayısının, lüleler arasındaki mesafenin ve lüle-hedef levha aralığının çarpma yüzeyindeki ısı transferi üzerinde önemli etkileri olduğunu vurgulamışlardır. Di Venuta ve ark. [30], dikdörtgen profilli bir lüleden çıkan türbülanslı slot jet akışında, hedef duvar yüzeyindeki Nusselt sayısı dağılımlarını LES türbülans modeliyle incelemişler ve literatürdeki deneysel çalışma sonuçlarıyla diğer türbülans modellerine kıyasla daha iyi bir uyum bulmuşlardır. Joshi ve Sahu [31], farklı geometrik çıkıntılara sahip iç bükey bir yüzeye çarpan jet akışında ısı transferi karakteristiklerini sayısal olarak incelemişler ve çıkıntı varlığının ısı transferi oranında iyileşme sağladığını belirtmişlerdir. Talapati ve Katti [32], sentetik hava jeti sıcaklığının çarpan sentetik hava jetinin yerel ısı transferi dağılımı üzerindeki etkisini pürüzsüz düz bir yüzey üzerinde deneysel olarak incelenmişler ve ısı transferi dağılımının özellikle düşük orifis-jet mesafesinde sentetik hava jeti sıcaklığından güçlü bir şekilde etkilendiği ifade etmişlerdir. Javidan ve Moghadam [33], çarpan jet dizisi ile fotovoltaik bir modülün soğutmasında nanoakışkan kullanımının etkisini deneysel olarak incelemişler ve nanoakışkana sahip çok delikli nozulların kullanılması durumunda fotovoltaik modülün daha düzgün sıcaklık dağılımına sahip olduğunu belirtmişlerdir. Literatürde gerçekleştirilen çalışmalardan farklı olarak bu çalışmada, çarpma levhası yüzeylerindeki ısı transferi karakteristiklerinin farklı eğim açılı levhalar ile sınırlandırılan çarpan türbülanslı slot ve dairesel hava jetleri üzerinde deneysel olarak incelenmesine yoğunlaşmaktadır. Reynolds sayısının, levhalar arası mesafenin ve sınırlandırıcı levha eğim açısının çarpma levhası yüzeyi boyunca Nusselt dağılımlarına olan etkisinin belirlenmesi, bu çalışmanın ana amacıdır ve bu amaç doğrultusunda çarpma levhası üzerindeki sıcaklık dağılımları termal kamera ile ölçülerek incelenmiştir. Ayrıca, çalışma, slot ve dairesel jet durumlarının karşılaştırmalı analizi ve sınırlandırıcı levhaların eğim açısının etkisinin belirlenmesi açısından özgün bir yaklaşım sunmaktadır.

Materyal ve Metot

Çalışma kapsamında, θ = 0°, 15°, 30° ve 45° açıya (θ – Sınırlandırıcı levhanın normal düzlemi ile yaptığı açı) sahip eğimli levhalar kullanılarak sınırlandırılan çarpan slot jet ve çarpan dairesel jet akış düzeneklerinde, levhalar arası mesafenin (H/W(D)) 0.5, 1, 3 ve 6 olduğu ve iki farklı Reynolds sayısı (20000 ve 30000) için önceden ısıtılmış çarpma levhasının arka yüzeyi boyunca merkez eksen doğrultusunca termal kamera ile yüzey sıcaklıkları ölçülmüştür. Çarpan slot jet akışı için, çarpma levhası boyunca ısı transferi karakteristiğini incelemek amacıyla oluşturulan, θ = 0°, 15°, 30° ve 45° eğim açılarına sahip levhalar ile sınırlandırılan düşey eksenli akış düzenekleri, Plint and Partners Limited üretimi seri numarası TE.88/3961 olan bir hava üfleyici sistem modifiye edilerek kullanılmıştır. Hava üfleyici cihaz fanı; 0.45 kW güce ve dakikada 2800 devir dönüş hızına sahip bir elektrik motoruyla tahrik edilmektedir. Şekil 1a'da gösterilen deney düzeneğinde, fanla desteklenen hava huzme cihazına çekilir ve ardından genleşme odası ve ızgara aşamalarını geçerek, düşey doğrultuda yerleştirilen akış düzeneklerine iletilmektedir. Debi ayar valfi yardımıyla lüle çıkışında istenilen hız değerleri elde edilebilmektedir.

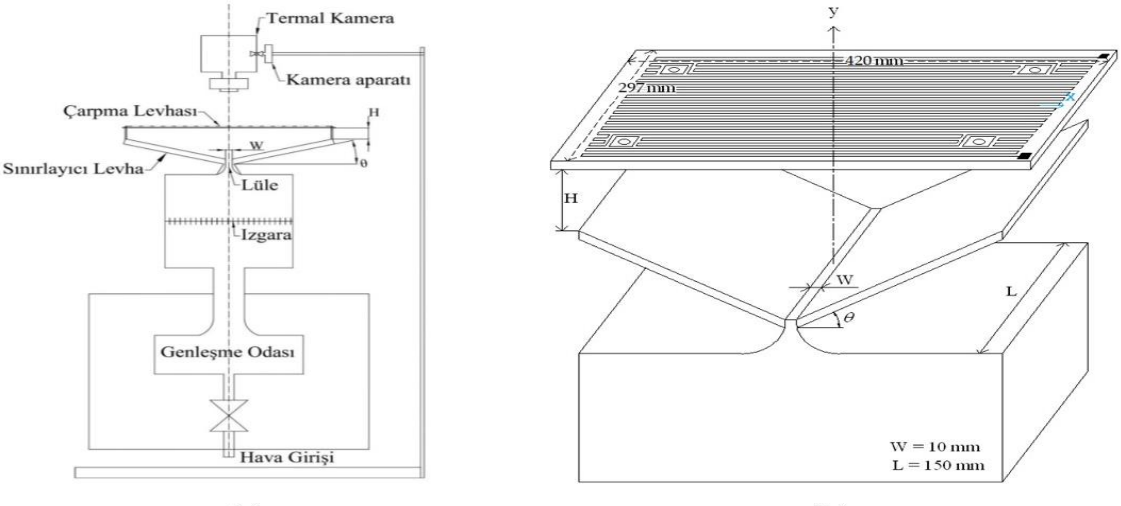

(a) (b)

Şekil 1. *Eğimli levhalarla sınırlandırılmış düşey eksenli çarpan slot jet deney düzeneğinin şematik görüntüsü. (a) genel görünüm; (b) ayrıntılı izometrik görünüm*

Lüleden çıkan hava jeti, üzerinde sıcaklık ölçümlerinin gerçekleştirildiği epoksi malzemeden imal edilmiş ve elektriksel olarak ısıtılmış çarpma levhasına çarpmaktadır. Epoksi levhanın arka yüzeyi üzerinde sıcaklık ölçümleri, termal kamera ile yüzeye dik bir doğrultuda gerçekleştirilmektedir. θ, sınırlayıcı levha eğim açısını, H, levhalar arası açıklığı ve W, slot genişliğini göstermektedir. Çalışma kapsamında oluşturulan ve Şekil 1b'de örnek görüntüsü verilen akış düzeneklerinde, genişliği (W) ve uzunluğu (L) sırasıyla 10 mm ve 150 mm olan tekli slot lüleler kullanılmıştır. Slot lüle için eşdeğer hidrolik çap (D_h) ise 18.75 mm'dir. θ = 0°, 15°, 30° ve 45° eğim açılarına sahip levhalar lüle çıkışlarına enlemesine yerleştirilerek akış alanları sınırlandırılmıştır. Hava jetleri lülelerden çıkarak, sınırlandırıcı levha uçlarından H değeri kadar uzak mesafede konumlandırılan ve lüle eksenine 90° açı ile bakan doğrultuda yerleştirilen elektriksel olarak ısıtılmış düz levhalara çarpmaktadır. Reynolds sayısının her iki değeri (20000 ve 30000) için, lüle çıkış hızları, lüle çıkışında konumsal harekete izin veren sabit tutacak üzerine yerleştirilen Pitot tüpü yardımıyla sırasıyla 16.53 m/s ve 24.8 m/s olarak ölçümlenmiştir. Epoksi malzemeden üretilen çarpma levhası 1.5 mm kalınlığa, 297mm genişlik ve 420 mm uzunluk ebadında yüzey alanına sahiptir. Üniform sıcaklık dağılımını çarpma levhasında sağlamak maksadıyla, PCB (Printed Circuit Board **-** Baskılı Devre Kartı) yöntemi ile 1 mm genişliğinde ve 40 µm kalınlığında bakır şeritlerle elektriksel bir devre oluşturulmuştur. PCB çarpma levhasının arka yüzeyi mat siyah renktedir. Düşey eksenli jet düzeneğinde, hedef levha (PCB çarpma levhası) boyunca, ayarlanabilir bir varyak ile 75 Volt gerilim ve 2.02 Amper alternatif akım kullanılarak sabit ısı akısı 1375 W/m^2 değerinde oluşturulmuştur. Yatay eksenli çarpan dairesel jet deney düzeneği, hedef çarpma levhası üzerindeki ısı transferinin incelenmesi amacıyla tasarlanmıştır. Şekil 2a'da şematik olarak gösterilen deney düzeninde, fan tarafından emilen ortam hava, yatay bir bağlantı borusu aracılığıyla genleşme odasına yönlendirilir. Genleşme odasının çıkışına yerleştirilen dairesel jetten çıkan hava, Joule etkisi ile önceden ısıtılan hedef çarpma levhasına çarptırılmaktadır.

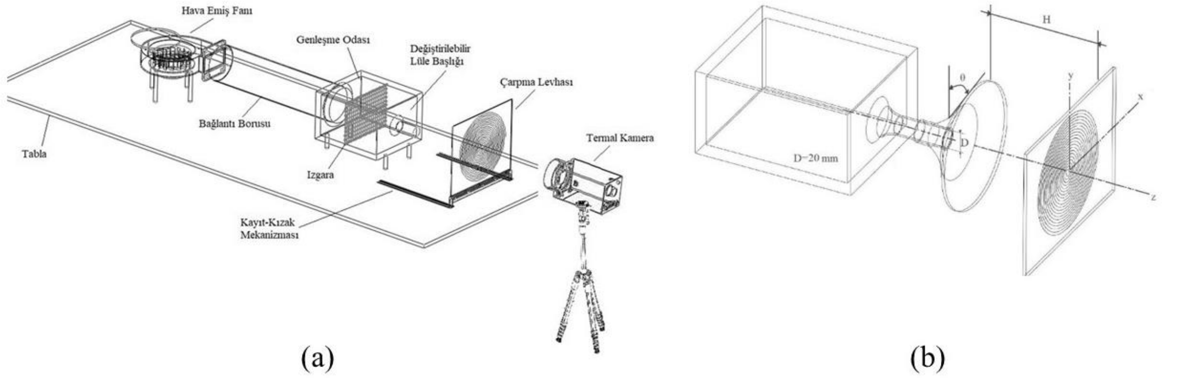

Şekil 2. *Yatay eksenli çarpan dairesel jet deney düzeneğinin şematik görüntüsü. (a) genel görünüm; (b) lüle ve çarpma levhası ayrıntılı görünüm*

Düşey konumda bulunan ısıtıcılı çarpma levhası, kayıt-kızak mekanizması ile yatay doğrultuda hareket kabiliyetine kazanmıştır. Bu mekanizma ile lüle ve levha arası mesafe istenilen değerde ayarlanabilmektedir. Fan girişindeki kapak açıklığı ile farklı akış debileri ayarlanabilmektedir. Yüzey sıcaklık dağılımlarının ölçümü, PCB levhanın arka tarafında, levha yüzeyine dik doğrultuda konumlandırılmış bir tripod üzerine kurulu termal kamera ile gerçekleştirilmiştir. Yatay eksenli çarpan dairesel jet deney düzeneğinde, lüle çıkışına yerleştirilen farklı θ eğim açılarına sahip sınırlayıcı levhalarla oluşturulan sınırlandırılmış dairesel jet akış düzeneklerinin örnek şematik görüntüsü Şekil 2b'de verilmiştir. Dairesel lülenin çapı (D) 20 mm, lüle uzunluğu ise 80 mm olarak gerçekleşmiştir. Hava jeti, lüleden çıktıktan sonra, belirli bir H değeri kadar açıklıkta konumlandırılan ve jet eksenine dik bir doğrultuda bulunan Joule etkisi ile önceden ısıtılan levhalara çarpar. Reynolds sayısı 20000 ve 30000 değerleri için, konumsal harekete izin veren sabit tutacak üzerine yerleştirilen Pitot tüpü yardımı ile lüle çıkışındaki akış hızlarının 15.10 m/s ve 22.65 m/s olduğu saptanmıştır. Kalınlığı 1.5 mm olan hedef çarpma levhasının dairesel ısıtıcı yüzeyinde, tekdüze sıcaklık dağılımının sağlanması maksadıyla baskılı devre kartı (PCB) tekniği ile 1 mm genişliğinde ve 40 μm kalınlığında bakır şeritlerle dairesel bir elektrik devresi oluşturulmuştur. 300x400mm2 dikdörtgen yüzey alanına sahip levhada, dairesel jet akışı ile uyumluluk dikkate alınarak 180mm'lik çapta dairesel form ısıtıcı yüzeyi oluşturulmuştur. Bu ısıtıcılı çarpma levhasının arka yüzeyi mat siyah renge sprey boya ile boyanmıştır. Epoksi levhanın emisivitesi 0.95 dir. Yatay eksenli jet düzeneğindeki hedef PCB çarpma levhası üzerine ayarlanabilir varyak kullanılarak 20.3 volt ve 2.01 amper elektrik akımı uygulanmış ve 1603.5 W/m^2 düzeyinde sabit ısı akısı oluşturulmuştur.

Hem çarpan slot jeti hem de çarpan dairesel jet durumlarında, hedef levhaya çarpan ortam hava sıcaklığındaki jetin, levhadan gerçekleşen ısı transferi, önceden ısıtılan levhanın arka yüzeyine dik doğrultuda konumlandırılmış olan termal kamera ile sıcaklık dağılımı ölçümleri şeklinde yapılarak incelenmiştir. -40°C ila +500 °C aralığında ölçüm yapabilen, 0.08 °C sıcaklık hassasiyetine ve QVGA (Quarter Video Graphics Array - Çeyrek Video Grafik Dizisi) yani 320x240 piksel çözünürlüğe sahip FLIR A20 marka termal kamera ile yüzey sıcaklık ölçümleri gerçekleştirilmiştir. Sıcaklık değerleri, ThermaCAM yazılımı kullanılarak kayıt altına alınmıştır (Şekil 3). Çarpma levhasının her iki yüzeyine yerleştirilen T tipi termokupllar ile termal kamera ile ölçülen sıcaklık değerlerinin doğrulaması yapılmıştır. Termoelemanla ölçülen levhanın gerçek sıcaklığı ve bilgisayarda okunan levha sıcaklığı arasındaki karşılaştırmayla, termal kameranın kalibrasyon eğrisi çıkarılmış, ölçüm sonuçları doğrulanmıştır. Bu yöntem ile çarpma yüzeyindeki sıcaklığın arka yüzeyle eşit olduğu kabulü yapılmıştır. Çarpma yüzeyine yerleştirilen termokupl tarafından ölçülen sıcaklık değeri, aynı nokta için termal kamera tarafından ölçülen sıcaklık değeri ile karşılaştırılarak yüzeyin emisivite değeri (ε) 0.98 olarak belirlenmiştir. Çarpma levhası yüzeyindeki sıcaklık değerleri, yerel sıcaklıkların zaman içinde değişmediği ve akışın sürekli bir duruma ulaştığı süre boyunca kaydedilmiştir.

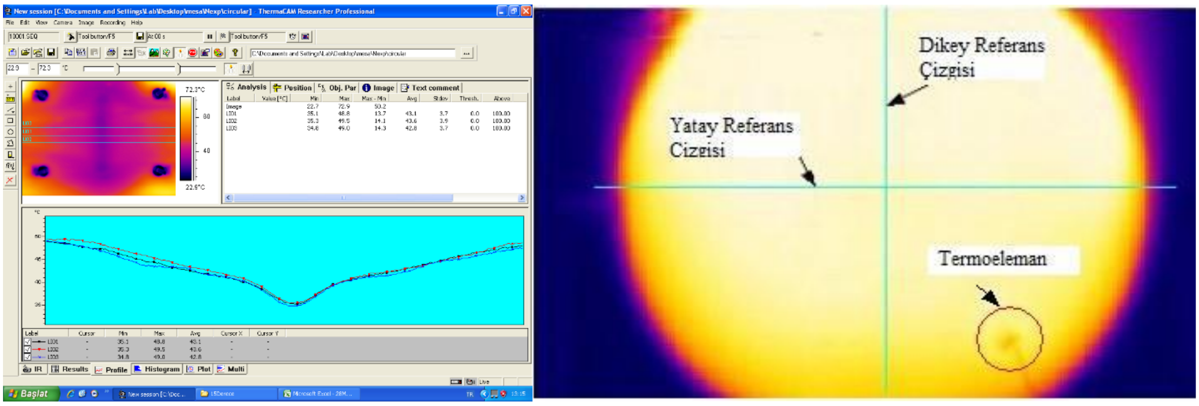

Şekil 3. *Sıcaklık ölçümüne ilişkin görüntüler*

Isı Transferi Parametreleri ve Matematiksel Formülasyon

U_o, dairesel veya slot hava jeti çıkış hızını ifade etmekte olup, bununla ilişkilendirilen Reynolds sayısı aşağıdaki denklemlerle hesaplanmıştır.

$$U_0 = \sqrt{2\Delta P/\rho} \tag{1}$$

$$Re = \frac{\rho U_0 D(W)}{\mu} \tag{2}$$

Denklemlerde, basınç farkı ΔP, akışkan yoğunluğu ρ, dinamik viskozite μ ile gösterilmekte olup, lüle çapı D, slot genişliği ise W ile ifade edilmiştir. Isı transferi etkileri, çarpan jet akışlarında çarpma levhaları üzerindeki ısı taşınım katsayısı (h) ve boyutsuz Nusselt sayısı (Nu) denklemleri ile araştırılır.

$$h = Q_{taşınım}/A_w(T_w - T_j) \tag{3}$$

$$Nu = \frac{hD(W)}{k} \tag{4}$$

Burada taşınım ile ısı akısı $Q_{taşınım}$, levhanın ısıtıcı yüzey alanı A_w, lehvanın jete maruz kalan tarafındaki yüzey sıcaklığı T_w, ve jet çıkış sıcaklığı ise T_j ile ifade edilmektedir. Nusselt denkleminde, havanın ısıl iletim katsayısı k ile tanımlanmıştır. Düz bir yüzeye çarpan jet akışında ısı transferi üzerine etkili olan büyüklükler Şekil 4'te şematik bir şekilde tasvir edilmiştir.

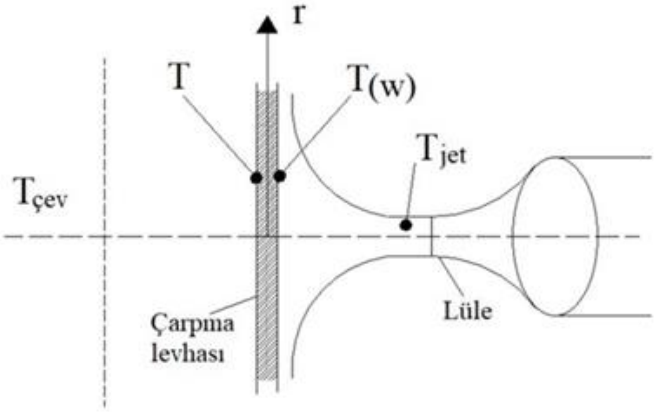

Şekil 4. *Jetlerde ısı transferi hesaplamalarında dikkate alınan tanımlamalar*

Termal kamera yardımıyla ölçümlenen yüzey sıcaklığı T ile gösterilmiş olup, çevre ortam sıcaklığı $T_{çev}$, levha yüzeyinin jete maruz kalan tarafındaki sıcaklığı ise $T_{(w)}$ ile gösterilmiştir. Deneylerin gerçekleştirildiği laboratuvar ortamının sıcaklığı bir termometre ile 295 K olarak tespit edilmiştir.

Joule etkisi ile üretilen toplam ısı akısı q''_{toplam}'dan ısı kayıplarının çıkarılması ile $q_{taşınım}$ hesaplanmıştır. Enerji dengesi ile çarpma levhası yüzeyinden olan ısı transferi,

$$q''_{taşınım} = q''_{toplam} - q''_{iletim} - q''_{ışınım} - q''_{doğaltaşınım} \tag{5}$$

ifadesi ile hesaplanabilmektedir. İfadeye göre, burada q''_{toplam}, toplam ısı akısı miktarını, q''_{iletim}, $q''_{ışınım}$ ve $q''_{doğaltaşınım}$ ise sırasıyla çarpma yüzeyinden iletimle, ışınımla ve doğal taşınım ile kaybedilen ısıyı temsil eder. Epoksi levhaya uygulanan toplam güç, ayarlı varyak tarafından sağlanan gerilim ve levha direnci değerleri kullanılarak hesaplanır ve aşağıdaki denklemle ifade edilir.

$$Q_{toplam} = IV = V^2/R \tag{6}$$

Isıl kayıplar, levhanın jet tarafından etkilenmeyen yüzeyi boyunca ışınım, iletim ve doğal taşınım etkilerine bağlıdır. Çarpma levhası üzerindeki radyal yönde iletimle oluşan ısı transferi, radyal yönde mesafenin fazla olması ve sıcaklık gradyanının az olması sebebiyle dikkate alınmamıştır. Levhanın jete maruz kalan tarafındaki ışınım kayıpları ise bakırın düşük emisivite değeri sebebiyle ihmal edilmiştir. Çarpma levhasının arka yüzeyi ile çevre ortamı arasındaki sıcaklık farkından kaynaklanan ışınım yoluyla ısı transferi, aşağıda verilen Stefan-Boltzmann denklemi [34] kullanılarak hesabı gerçekleştirilmiştir.

$$q_{ışınım} = \varepsilon A_s \sigma (T_w^4 - T_{çev}^4) \tag{7}$$

Çarpma levhasının emisivite değeri ε ile gösterilmektedir. Stefan-Boltzmann sabiti ise $\sigma=5.67\text{x}10^{-8}$ $[W/(m^2K^4)]$ değerindedir. Burada A_s çarpma levhasındaki ısıtılan yüzeyin alanını temsil etmektedir. Yatay konumlandırılan çarpma levhası üzerinden doğal taşınım yoluyla oluşan ısı kaybı, Lloyd ve

Moran [35] tarafından üretilen empirik bağıntı ile aşağıda verildiği gibi hesaplanmıştır. Bu bağıntıda Ra, Rayleigh sayısını ifade etmektedir.

$$Nu_L=0.15Ra^{1/3} \qquad 10^7 \leq Ra \leq 10^{11} \qquad (8)$$

Slot jet akışında laboratuvar ortam şartları için Prandtl sayısı (Pr) 0,7 olarak belirlenmiş olup yatay konumlandırılmış çarpma levhası için Ra=2.04x10^8 olarak hesaplanmıştır. Düşey olarak konumlandırılmış çarpma levhası üzerinden doğal taşınım yoluyla gerçekleşen ısı kaybı, Churcill ve Chu [36] tarafından sunulan aşağıdaki empirik bağıntı kullanılarak hesaplanmıştır.

$$\overline{Nu}_L = 0.68 + \frac{0.670 \cdot Ra^{1/4}}{\left[1+\left(\left(\frac{0.492}{Pr}\right)^{9/16}\right)^{4/9}\right]} \qquad Ra \leq 10^9 \qquad (9)$$

Dairesel jet akışında laboratuvar ortam şartları için Prandtl sayısı (Pr) 0,7 olarak belirlenmiş olup düşey konumlandırılmış çarpma levhası için Ra=1.6x10^7 olarak hesaplanmıştır. Bu denklemlerde, Rayleigh sayısını Ra ve Prandtl sayısı ise Pr ile ifade edilmiştir. Verilen bu denklemleri kullanarak, slot jet düzeneğinde gerçekleşen ısı kayıplarından doğal taşınım ve ışıma kayıpları, toplam ısı miktarının sırasıyla %5'i ve %7'si olarak, dairesel jet düzeneğinde gerçekleşen kayıplar ise doğal taşınım için toplam ısı miktarının %3’ü, ışıma kayıpları için ise %4’ü olarak hesaplanmıştır. Slot jet akışında, toplam kayıplar, toplam ısı akısının %12’si, dairesel jet akışında ise %7’si değerinde olmaktadır.

Belirsizlik Analizi

Ölçümler, Kline ve McClintock [37] tarafından tavsiye edilen denklem ve hesaplama yöntemi kullanılarak belirsizlik analizine tabi tutulmuştur. İncelenen Reynolds sayısı için hesaplanan belirsizlik oranı ± %2.61 iken, Nusselt sayısı için ± %2.87 seviyesindedir.

Bulgular ve Tartışma

Bu çalışmada, farklı eğim açılı levhalar ile sınırlandırılmış türbülanslı slot ve dairesel hava jetlerinde çarpma yüzeyleri üzerindeki ısı transferi etkileri deneysel olarak araştırılmıştır. Çarpma levhası boyunca sıcaklık değerleri, önceden ısıtılan levhanın yüzeyinin arka yüzeyi boyunca levha yüzeyine dik konumlandırılmış bir termal kamera yardımı ile ölçülerek kaydedilmiştir. Sıcaklık dağılımları ise çarpma levhasının merkez ekseni doğrultusunca çizilen bir hat üzerinde elde edilmiştir. Bu sıcaklık dağılımları kullanılarak, Reynolds sayısı, levhalar arası açıklık oranı, sınırlandırıcı levha eğim açısı ve lüle tipinin çarpma levhası üzerindeki Nusselt dağılımlarına etkisi incelenmiştir. Çarpma levhası üzerindeki sıcaklık dağılımları, çarpan slot jet ve çarpan dairesel jet deney düzeneklerinde Reynolds sayısının her iki değeri (20000 ve 30000), sınırlandırıcı levha eğim açısı değerlerinin $\theta = 0°, 15°, 30°$ ve 45° olduğu durumlar ve sınırlandırıcı levha ile hedef çarpma levhası arasındaki açıklık oranı değerlerinin $H/D(W) = 0.5, 1, 3$ ve 6 olduğu durumlar için gerçekleştirilmiştir.

θ = 0° Eğimli Levhalar ile Sınırlandırılmış Jet

Sınırlandırıcı levha eğim açısı θ=0° için, Reynolds sayısının 20000 ve 30000 değerlerinde slot ve dairesel jet akış sistemlerinde çarpma levhası merkez ekseni doğrultusunca elde edilmiş olan Nusselt dağılımları levhalar arası açıklık oranı değerleri H/W(D)=0.5, 1, 3 ve 6 olduğu durumlar için Şekil 5'te verilmiştir.

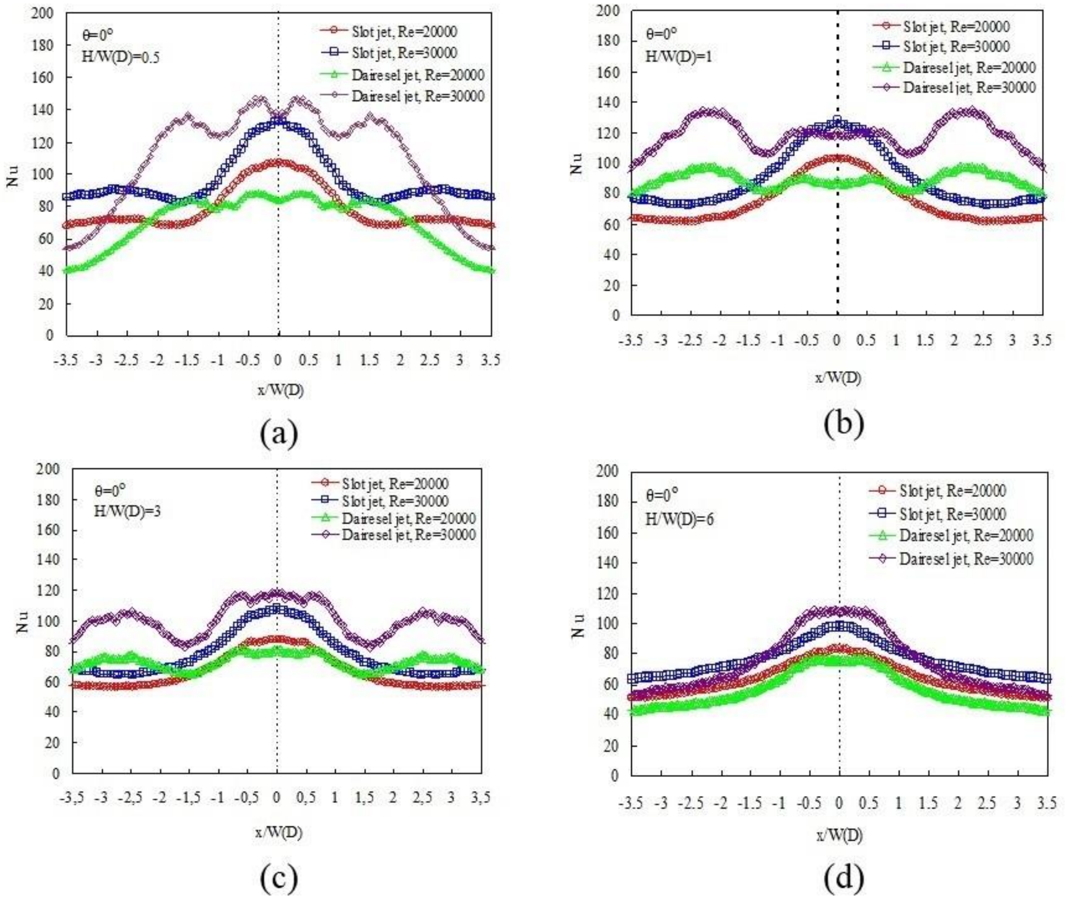

(a) (b)

(c) (d)

Şekil 5. θ=0° için çarpma levhası boyunca Nusselt dağılımları. (a) H/W(D)=0.5, (b) H/W(D)=1, (c) H/W(D)=3, (d) H/W(D)=6

H/W(D)=0.5 değeri için, iki farklı Reynolds sayısında slot ve dairesel jetlere ait çarpma levhalarının üzerinde orta eksen boyunca Nusselt dağılımlarının verildiği Şekil 5a'da, artan Reynolds sayısı ile birlikte Nusselt değerlerinin çarpma levhası üzeri boyunca artış sergilediği anlaşılmaktadır. Çarpma levhaları üzerinde lüle ekseni doğrultusundaki durma noktalarında yerel Nusselt sayıları maksimum değer almaktadır. Çarpma levhaları üzerindeki Nusselt dağılımlarında ortaya çıkan ikincil pikler slot jetlerde durma noktasından x/W≈±2.5 **(**Slot jetlerde boyutsuz x-eksenindeki mesafe) kadar ileri konumunda oluşurken, dairesel jetlerde x/D≈±1.5 (Dairesel jetlerde boyutsuz radyal eksendeki mesafe) konumunda oluşmaktadır. İkincil pikler, artan Reynolds sayısı ile daha belirgin hale gelmektedir. H/W(D)=1 ve H/W(D)=3 açıklık oranları için, slot ve dairesel jetlere ait çarpma levhalarının üzerinde farklı Reynolds sayısı durumları için Nusselt dağılım sonuçları Şekil 5b ve 5c'de görülmektedir. Her iki açıklık oranına ait Nusselt dağılımları da Şekil 4a'da H/W(D)=0.5 iken elde edilen dağılımlarla benzerlik göstermektedir. Bu açıklık oranlarında, Nusselt dağılımlarındaki ikincil pikler, slot jetlerde etkisi azalmış şekilde durma noktasından itibaren x/W≈±3.5 konumunda, dairesel jetlerde ise x/D≈±2.5 konumunda gerçekleşmektedir. Şekil 5d'de verilen Nusselt dağılımlarından, çarpma levhaları üzerinde düşük açıklık oranlarında oluşan ikincil piklerin H/W(D)=6 açıklık oranında kaybolduğu ve slot ve dairesel jetlere ait profillerin birbirlerine yaklaştığı görülmektedir. Slot ve dairesel jetlere ait çarpma levhaları üzerinde, farklı levhalar arası açıklık oranları ve farklı Reynolds sayıları için elde edilen Nusselt dağılımlarından, her iki Reynolds sayısı için de artan levhalar arası açıklık oranı ile Nusselt sayısının azaldığı anlaşılmaktadır. Re=30000 değerinde, çarpma levhaları üzerindeki Nusselt değerleri dairesel jette slot jete göre daha yüksek olmaktadır. Hem durma noktasındaki hem de ikincil piklerin oluştuğu konumlardaki Nusselt değerleri, artan Reynolds sayısı ile artmaktadır. Artan açıklık oranı ile ikincil pikler etkisini kaybederken, slot ve dairesel jetlerin Nusselt dağılım profilleri de birbirlerine yaklaşmaktadır.

θ = 15° Eğimli Levhalar ile Sınırlandırılmış Jet

Sınırlandırıcı levha eğim açısı θ=15° için, Reynolds sayısının 20000 ve 30000 değerlerinde slot ve dairesel jet akış sistemlerinde çarpma levhası merkez ekseni üzeri boyunca elde edilen Nusselt dağılımları levhalar arası açıklık oranı değerleri H/W(D)=0.5, 1, 3 ve 6 olduğu durumlar için Şekil 6'da verilmiştir. Şekil 6a'da, H/W(D)=0.5 değeri için, iki farklı Reynolds sayısında slot ve dairesel jetlere ait çarpma levhalarının üzerinde orta eksen boyunca Nusselt dağılımları görülmektedir. Artan Reynolds sayısı ile birlikte, çarpma levhası yüzeyi boyunca Nusselt değerlerinin de artış sergilediği görülmektedir. Hem slot jette hem de dairesel jette her iki Reynolds sayısı için de yerel Nusselt sayılarının durma noktasında maksimum değer aldığı anlaşılmaktadır.

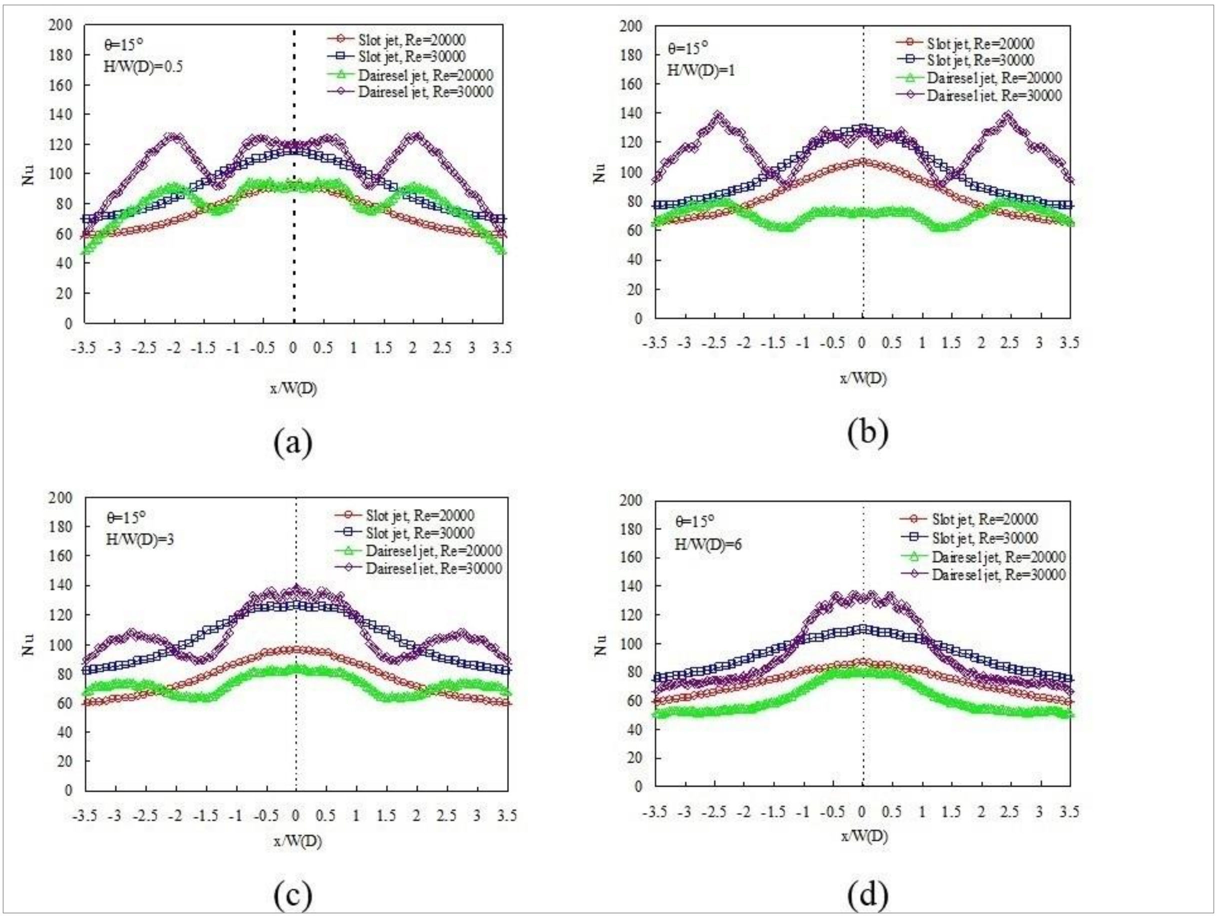

Şekil 6. *θ=15° için çarpma levhası üzerinde Nusselt dağılımları. (a) H/W(D)=0.5, (b) H/W(D)=1, (c) H/W(D)=3, (d) H/W(D)=6*

Dairesel jete ait Nusselt dağılımlarında, durma noktasından itibaren x/D≈±0.5 ve 2 konumlarında ikincil pikler oluşmaktadır. İkincil pikler artan Reynolds sayısı ile daha belirgin olmaktadır. Slot jete ait Nusselt dağılımları ise yayvan bir değişim göstermekte ve herhangi bir ikincil pik oluşmamaktadır. H/W(D)=1 ve H/W(D)=3 açıklık oranları için, slot ve dairesel jetlere ait çarpma levhalarının üzerinde farklı Reynolds sayısı değerlerinde elde edilen Nusselt dağılımları Şekil 6b ve 6c'de verilmektedir. Her iki açıklığa ait Nusselt dağılımları da Şekil 5a'da H/W(D)=0.5 iken elde edilen dağılımlarla benzerlik göstermektedir. H/D=1 açıklık oranında, dairesel jete ait Nusselt dağılımlarındaki ikincil piklerin daha keskin hale geldiği ve konumlarının x/D≈±0.5 ve 2.5 değerlerine kaydığı görülmektedir. H/D=3 açıklık oranında ise dairesel jete ait Nusselt dağılımlarındaki ikincil piklerin etkisi hafiflemektedir. H/D=6 açıklık oranına ait Nusselt dağılımlarının verildiği Şekil 6d'de, dairesel jete ait Nusselt sayılarındaki ikincil piklerin kaybolduğu görülmektedir. Slot ve dairesel jetlere ait çarpma levhaları üzerinde, farklı Reynolds sayıları ve farklı levhalar arası açıklık oranları için elde edilmiş Nusselt dağılımlarından, her iki Reynolds sayısı değeri için de levhalar arası açıklık oranı arttıkça Nusselt sayısı değerlerinin azalış gösterdiği anlaşılmaktadır. Dairsel jete ait çarpma levhası üzerindeki Nusselt dağılımlarında, düşük levhalar arası açıklık oranlarında (H/D<3) ortaya çıkan ikincil pikler, artan levhalar arası açıklık oranı ile birlikte etkisini kaybetmektedir. Dairesel jete ait Nusselt dağılımlarında görülen ikincil piklerin konumu sınırlayıcı levhaların eğimli olması nedeniyle durma noktasından uzaklaşmaktadır.

θ = 30° Eğimli Levhalar ile Sınırlandırılmış Jet

Sınırlandırıcı levha eğim açısı θ=30° için, Reynolds sayısının 20000 ve 30000 değerlerinde slot ve dairesel jet akış sistemlerinde çarpma levhası merkez ekseni doğrultusunca elde edilmiş Nusselt dağılımları levhalar arası açıklık oranı değerinin H/W(D)=0.5, 1, 3 ve 6 olduğu durumlar için Şekil 7'de verilmiştir. H/W(D)=0.5 değeri için, iki farklı Reynolds sayısında slot ve dairesel jetlere ait çarpma levhalarının üzerinde orta eksen boyunca Nusselt dağılımlarının verildiği Şekil 7a'da, artan Reynolds sayısı ile birlikte çarpma levhası yüzeyi boyunca Nusselt değerlerinde artışlar oluştuğu görülmüştür. Çarpma levhaları üzerinde lüle ekseni doğrultusundaki durma noktalarında yerel Nusselt sayıları maksimum değer almaktadır. Dairesel jete ait Nusselt dağılımlarında, durma noktasından itibaren x/D≈±1 ve 2.5 konumlarında ikincil pikler oluşmaktadır. İkincil pikler artan Reynolds sayısı ile daha belirgin olmaktadır. Slot jete ait Nusselt dağılımları ise yayvan bir değişim göstermekte ve herhangi bir ikincil pik oluşmamaktadır. H/W(D)=1 açıklık oranı için, slot ve dairesel jetlere ait çarpma levhalarının üzerinde farklı Reynolds sayılarında elde edilen Nusselt dağılımları Şekil 7b'de verilmektedir. H/D=1 açıklık oranında, dairesel jete ait Nusselt dağılımlarındaki ikincil piklerin konumları x/D≈±1 ve 3 değerlerine kaymaktadır. H/D=3 açıklık oranında ise dairesel jete ait Nusselt dağılımlarındaki ikincil piklerin etkisi hafiflemektedir (Şekil 7c). H/D=6 açıklığına ait Nusselt dağılımlarının verildiği Şekil 7d'de, hem slot hem de dairesel jette, Nusselt sayılarındaki ikincil piklerin kaybolduğu görülmektedir.

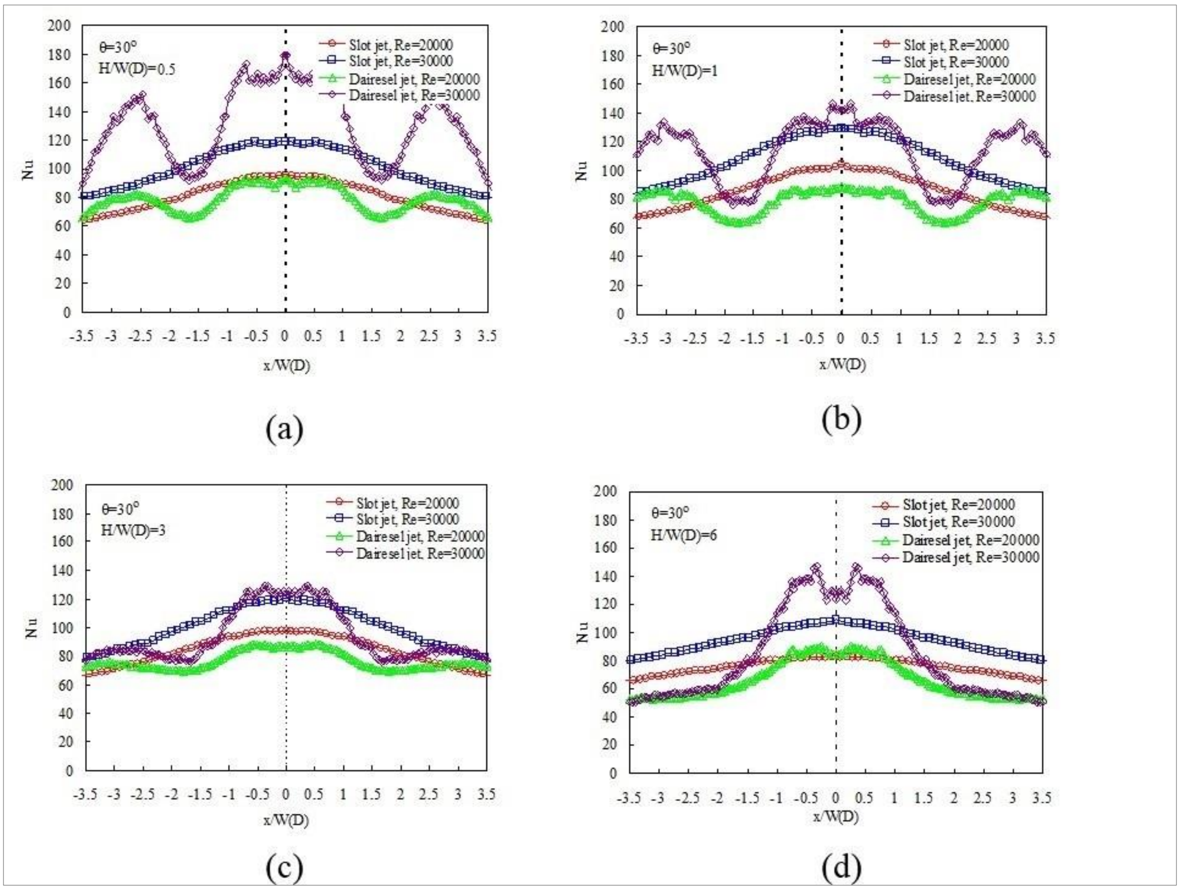

Şekil 7. *θ=30° için çarpma levhası üzerinde Nusselt dağılımları (a) H/W(D)=0.5 (b) H/W(D)=1 (c) H/W(D)=3 (d) H/W(D)=6*

θ = 45° Eğimli Levhalar ile Sınırlandırılmış Jet

Sınırlandırıcı levha eğim açısı θ=45° için, Reynolds sayısının 20000 ve 30000 değerlerinde slot ve dairesel jet akış sistemlerinde çarpma levhası merkez ekseni doğrultusunca elde edilmiş olan Nusselt dağılımları levhalar arası açıklık oranı değerinin H/W(D)=0.5, 1, 3 ve 6 olduğu durumlar için Şekil 8'de verilmiştir. H/W(D)=0.5 değeri için, iki farklı Reynolds sayısında slot ve dairesel jetlere ait çarpma levhalarının üzerinde orta eksen boyunca Nusselt dağılımlarının verildiği Şekil 8a'da, artan Reynolds sayısı ile birlikte çarpma levhası yüzeyi boyunca Nusselt değerlerinde artışlar oluştuğu görülmüştür. Çarpma levhaları üzerinde lüle ekseni doğrultusundaki durma noktalarında yerel Nusselt sayıları maksimum değer almaktadır. Dairesel jete ait Nusselt dağılımlarında, durma noktasından x/D≈±2.5 kadar ileride ikincil pikler oluşmaktadır. Bu ikincil pik ve artışlar artan Reynolds sayısı ile daha belirgin olmaktadır. Slot jete ait Nusselt dağılımları ise yayvan bir değişim göstermekte ve herhangi bir ikincil pik oluşmamaktadır.

H/W(D)=1 açıklık oranı için, slot ve dairesel jetlere ait çarpma levhalarının üzerinde farklı Reynolds sayılarında elde edilen Nusselt dağılımları Şekil 8b'de verilmektedir. H/D=1 açıklık oranında, dairesel jete ait Nusselt dağılımlarında yine x/D≈±2.5 konumunda ikincil pikler oluşmaktadır. H/W(D)=3 ve

H/W(D)=6 açıklık oranlarında, slot ve dairesel jetlere ait Nusselt dağılımlarında herhangi bir ikincil pik oluşmamaktadır (Şekil 8c ve 8d).

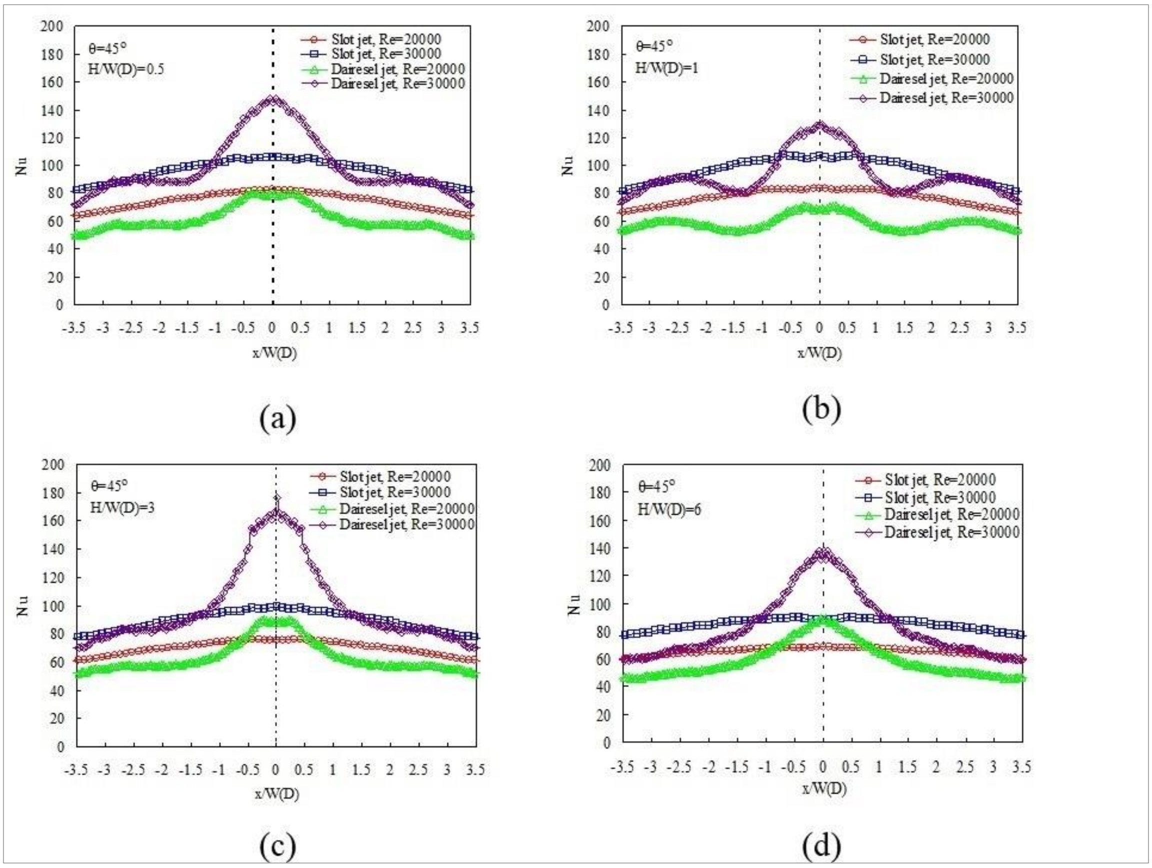

(a) (b) (c) (d)

Şekil 8. *θ=45° için çarpma levhası üzerinde Nusselt dağılımları, (a) H/W(D)=0.5, (b) H/W(D)=1, c) H/W(D)=3, (d) H/W(D)=6*

Çarpan slot jet akışında, sınırlayıcı levha eğim açısının, Reynolds sayısının ve sınırlayıcı levha-çarpma levhası arası açıklığın farklı değerleri için çarpma levhası yüzeyi boyunca ölçümlenen sıcaklık değerleri ve dağılımları beraber değerlendirildiğinde, sınırlayıcı levha eğim açısının (θ=0°) ve levhalar arası açıklık oranı değerinin (H/W=0.5 ve 1) küçük olduğu durumlarda çarpma levhası üzerindeki Nusselt dağılımlarında ikincil piklerin ortaya çıktığı, sınırlandırıcı levha eğim açısı (θ=15°, 30° ve 45°) değerlerinin büyük olduğu durumlarda ise levhalar-arası açıklığın hiçbir değerinde ikincil piklerin oluşmadığı görülmüştür. Çarpan dairesel jet akışında, sınırlayıcı levha eğim açısının, Reynolds sayısının ve sınırlayıcı levha-çarpma levhası arası açıklığın farklı değerleri için çarpma levhası yüzeyi boyunca ölçümü gerçekleştirilen sıcaklık değerleri ve dağılımları beraber değerlendirildiğinde, sınırlayıcı levha eğim açısının (θ=0° ve 15°) ve levhalar arası açıklık oranı değerinin (H/D=0.5 ve 1) küçük olduğu durumlarda çarpma levhası üzerindeki Nusselt dağılımlarında ikincil piklerin daha belirgin olduğu, sınırlayıcı levha eğim açısının (θ=30° ve 45°) ve levhalar arası açıklık oranının (H/D=3 ve 6) büyük değerlerinde ikicil piklerin etkisinin azaldığı görülmektedir. Çarpma levhaları üzerindeki Nusselt dağılımlarında ortaya çıkan ikincil piklerin dairesel jette daha belirgin ve yaygın olduğu ve konumlarının sınırlayıcı levha eğim açısından etkilendiği görülmüştür.

Sonuçlar

Deneysel olarak gerçekleştirilen bu çalışmada, çarpan slot ve dairesel jet akış alanlarındaki hedef çarpma levhası yüzeyleri boyunca ısı transferi etkilerini incelemiştir. Sıcaklık değerleri ve dağılımları bir termal kamera ile görüntüleme yapılarak ölçümlenmiştir. Elde edilen sıcaklık dağılımları, çarpma levhasının merkez ekseni boyunca incelenmiştir. Bu sıcaklık dağılımları üzerinden, Reynolds sayısı, levhalar arası açıklık oranı ve sınırlandırıcı levha eğim açısı parametrelerinin çarpma levhasındaki Nusselt dağılımları üzerine etkisi araştırılmış ve sonuçlar karşılaştırılmıştır. Çalışmadan aşağıdaki sonuçlara ulaşılmıştır:

1. Sınırlandırılmış çarpan slot ve dairesel jet akışlarında, çarpma levhası üzeri boyunca Nusselt değerleri artan Reynolds sayısı ile birlikte artmakta, artan levhalar arası açıklık oranı ile azalmaktadır. Levhalar arası açıklığın $H/W(D) \leq 1$ ve sınırlayıcı levha eğim açısının $\theta \leq 15°$ olduğu durumlarda, çarpma levhası üzerindeki Nusselt sayısı dağılımlarında ikincil pikler oluşmaktadır. Levhalar arası açıklık oranı arttıkça, ikincil piklerin etkisi azalmakta ve konumları levha uçlarına doğru ilerlemektedir.
2. Sınırlandırılmış çarpan slot jet akışında, çarpma levhası yüzeyindeki Nusselt dağılımları, artan sınırlandırıcı levha eğim açısı ve artan levhalar arası açıklık oranıyla olumsuz etkilenmektedir.
3. Artan sınırlandırıcı levha eğim açısı ile birlikte, slot jetlerde ikincil pikler hızla kaybolurken, dairesel jetlerde bu durumun daha yavaş olmaktadır.

Mevcut çalışma esas olarak çarpan slot ve dairesel jetlerde ısı transferi performansının sınırlayıcı levha durumuna göre karşılaştırılıp değerlendirilmesi üzerine odaklanmıştır. Çalışmadan elde edilen sonuçlarda boyutsuz radyal ve eksenel mesafeler boyunca ortaya çıkan ikincil artışların, hedef çarpma levhası yüzeyinden daha fazla ısının daha homojen bir şekilde süpürülmesine olanak sağladığı görülmektedir. Özellikle elektronik devre elemanlarının soğutulmasında yüzeyin daha homojen bir şekilde soğutulması, söz konusu elemanların ömürleri ve performansları için oldukça kritiktir. Çarpan jetlerde eğimli sınırlandırıcı levha kullanımının, elektronik devre elemanlarında yüzey boyunca ortaya çıkan sıcaklık değişimlerinin neden olduğu stresin azaltılmasına katkıda bulunabileceği düşünülmektedir.

Teşekkür Bu çalışma K.T.Ü. Makina Mühendisliği Bölümü Hidrolik ve Akışkanlar Mekaniği Laboratuvarında gerçekleştirilmiştir. Sağladıkları çalışma alanı ve verdikleri ekipman desteği için teşekkür ederiz.

Fon/Finansman Bilgileri Bu çalışma için herhangi bir kurum ve/veya kuruluştan destek alınmamıştır.

Etik Kurul Onayı ve İzinler Çalışma, etik kurul izni veya herhangi bir özel izin gerektirmemektedir.

Çıkar Çatışmaları/Çatışan Çıkarlar Yazarlar arasında herhangi bir çıkar çatışması yoktur

Yazarların Katkısı Haluk KELEŞ makaleye %50 oranında katkıda bulunmuş, deneyleri gerçekleştirmiş, analiz etmiş ve grafikleri hazırlamıştır. Yücel ÖZMEN makaleye %50 oranında katkıda bulunmuş, grafikleri yorumlamış ve makaleyi yazmıştır

Kaynaklar

[1] Danek, C. J. (1995). *Heat transfer under impinging jets at very close jet-to-target spacings*. [Doktora Tezi, Stanford Üniversitesi, Ann Arbor, ABD].

[2] Gardon, R., & Akfirat, J. C. (1965). The role of turbulence in determining the heat-transfer characteristics of impinging jets. *International Journal of Heat and Mass Transfer, 8*(10), 1261-1272. https://doi.org/10.1016/0017-9310(65)90054-2

[3] Livingood, J. N. B., Hrycak, P., & Hrycak, P. (1973), Impingement heat transfer from turbulent air jets to flat plates: a literature survey. NASA Technical Memorandum, Ohio, ABD. https://ntrs.nasa.gov/api/citations/19730016200/downloads/19730016200.pdf

[4] Senter, J., & Solliec, C. (2007). Flow field analysis of a turbulent slot air jet impinging on a moving flat surface. *International Journal of Heat and Fluid Flow, 28*(4), 708-719. https://doi.org/10.1016/j.ijheatfluidflow.2006.08.002

[5] Cavadas, A. S., Pinho, F.T., & Campos, J. B. L. M. (2012). Laminar flow field in a viscous liquid impinging jet confined by inclined plane walls. *International Journal of Thermal Sciences, 59,* 95-110. https://doi.org/10.1016/j.ijthermalsci.2012.04.004

[6] Özmen, Y., & Kınay, H. (2023). Investigation of flow and heat transfer characteristics of impinging slot jets confined with inclined plates. *Heat Mass Transfer, 59,* 509–534. https://doi.org/10.1007/s00231-022-03279-y

[7] Kunugi, T., & Kawamura, H. (1987, Ekim). *Application of a Two-Equation Turbulence Model to Heat Transfer and Fluid Flow of an Impinging Round Jet.* 2nd International Symposium on Transport Phenomena in Turbulent Flows, Tokyo, Japonya.

[8] Chiriac, V. A., & Ortega, A. (2002). A numerical study of the unsteady flow and heat transfer in a transitional confined slot jet impinging on an isothermal surface. *International Journal of Heat and Mass Transfer, 45*(6), 1237-1248. https://doi.org/10.1016/S0017-9310(01)00224-1

[9] Yousefi-Lafouraki, B., Ramiar, A., & Ranjbar, A. A. (2014). Laminar forced convection of a confined slot impinging jet in a converging channel. *International Journal of Thermal Sciences, 77,* 130-138. https://doi.org/10.1016/j.ijthermalsci.2013.10.014

[10] Schrader, H. (1961). *Trocknung feuchter Oberflächen mittels Warmluftstrahlen*, VDI-Verl. Düsseldorf.

[11] Goldstein, R. J., Sobolik, K. A., & Seol, W. S. (1990). Effect of entrainment on the heat transfer to a heated circular air jet ımpinging on a flat surface. *ASME Journal of Heat Transfer*, *112*(3), 608-611. https://doi.org/10.1115/1.2910430

[12] Baughn, J. W., & Shimizu, S. (1989). Heat transfer measurements from a surface with uniform heat flux and an impinging jet. *Journal of Heat Transfer, 111*(4), 1096-1098. https://doi.org/10.1115/1.3250776

[13] Popiel, C. O., & Trass, O. (1991). Visualization of a free and impinging round jet. *Experimental Thermal and Fluid Science, 4*(3), 253-264. https://doi.org/10.1016/0894-1777(91)90043-Q

[14] Mohanty, A. K., & Tawfek, A. A. (1993). Heat transfer due to a round jet impinging normal to a flat surface. *International Journal of Heat and Mass Transfer, 36*(6), 1639-1647. https://doi.org/10.1016/S0017-9310(05)80073-0

[15] Huang, L., & El-Genk, M. S. (1994). Heat transfer of an impinging jet on a flat surface. *International Journal of Heat and Mass Transfer, 37*(13), 1915-1923. https://doi.org/10.1016/0017-9310(94)90331-X

[16] Lytle, D., & Webb, B. W. (1994). Air jet impingement heat transfer at low nozzle-plate spacings. *International Journal of Heat and Mass Transfer, 37*(12), 1687-1697. https://doi.org/10.1016/0017-9310(94)90059-0

[17] Colucci, D. W., & Viskanta, R. (1996). Effect of nozzle geometry on local convective heat transfer to a confined impinging air jet. *Experimental Thermal and Fluid Science, 13*(1), 71-80. https://doi.org/10.1016/0894-1777(96)00015-5

[18] Baydar, E. (1999). Confined impinging air jet at low reynolds numbers. *Experimental Thermal and Fluid Science, 19*(1), 27-33. https://doi.org/10.1016/S0894-1777(98)10044-4

[19] Baydar, E., & Özmen, Y. (2005). An experimental and numerical investigation on a confined impinging air jet at high reynolds numbers. *Applied Thermal Engineering, 25*(2-3), 409-421. https://doi.org/10.1016/j.applthermaleng.2004.05.016

[20] Özmen, Y., & Baydar, E. (2008). Flow structure and heat transfer characteristics of an unconfined impinging air jet at high jet reynolds numbers. *Heat and Mass Transfer, 44*(11), 2008, 1315-1322. https://doi.org/10.1007/s00231-008-0378-4

[21] Miranda, J. M., & Campos, J. B. L. M. (1999). Impinging jets confined by a conical wall: Laminar flow predictions. *AIChE Journal, 45*, 2273-2285. https://doi.org/10.1002/aic.690451103

[22] Behnia, M., Parneix, S., Shabany, Y., & Durbin, P. A. (1999). Numerical study of turbulent heat transfer in confined and unconfined impinging jets. *International Journal of Heat Fluid Flow, 20*, 1-9. https://doi.org/10.1016/S0142-727X(98)10040-1

[23] Herrero, R., & Buchlin, J. M. (2010, Temmuz 24-29). *Effect of nozzle shape on local heat transfer distribution in impinging jets*. 10th International Conference on Quantitative InfraRed Thermography, Quebec, Kanada. https://doi.org/10.21611/qirt.2010.054

[24] Lee, D. H., Bae, J. R., Park, H. J., Lee, J. S. & Ligrani, P. (2011). Confined, milliscale unsteady laminar impinging slot jets and surface nusselts numbers. *International Journal of Heat and Mass Transfer, 54*:2408–24. https://doi.org/10.1016/j.ijheatmasstransfer.2011.02.021

[25] Cavadas, A. S., Pinho, F. T. & Campos, J. B. L. M. (2012). Laminar flow field in a viscous liquid impinging jet confined by inclined plane walls. *International Journal of Thermal Sciences, 59*, 95-110. https://doi.org/10.1016/j.ijthermalsci.2012.04.004

[26] Al Mubarak, A. A., Shaahid, S. M. & Al-Hadhrami, L. M. (2013). Heat transfer in a channel with inclined target surface cooled by single array of centered impinging jets. *Thermal Science, 17*, 1195-1206. https://doi.org/10.2298/TSCI110630010A

[27] Yousefi-Lafouraki, B., Ramiar, A., & Ranjbar, A. A. (2014). Laminar forced convection of a confined slot impinging jet in a converging channel. *International Journal of Thermal Sciences, 77*, 130-138, 2014. https://doi.org/10.1016/j.ijthermalsci.2013.10.014

[28] Bhagwat, A., & Sridharan, A. (2017). Numerical simulation of oblique air jet impingement on a heated flat plate. *Journal of Thermal Science and Engineering Application.,* 1–10. https://doi.org/10.1115/1.4034913

[29] Li, Y., Li, B., Qi, F., & Cheung, S. C. P. (2018). Flow and heat transfer of parallel multiple jets obliquely impinging on a flat surface. *Applied Thermal Engineering, 10,* 2174–2185. https://doi.org/10.1016/j.applthermaleng.2018.01.064

[30] Di Venuta, I., Boghi, A., Petracci, I. & Gori, F. (2023). Heat transfer on a flat wall due to a rectangular turbulent jet. *International Communications in Heat and Mass Transfer, 144,* https://doi.org/10.1016/j.icheatmasstransfer.2023.106769

[31] Joshi, J. & Sahu, S. K. (2023). Effect of single and multiple protrusions on thermal performance of slot jet impingement with curved surface. *Applied Thermal Engineering, 230.* https://doi.org/10.1016/j.applthermaleng.2023.120757

[32] Talapati, R. J. & Katti, V. V. (2022). Influence of synthetic air jet temperature on local heat transfer characteristics of synthetic air jet impingement. *International Communications in Heat and Mass Transfer, 130,* 105796. https://doi.org/10.1016/j.icheatmasstransfer.2021.105796

[33] Javidan, M. & Moghadam, A. J. (2022). Effective cooling of a photovoltatic module using jet-impingement array and nanofluid coolant. *International Communications in Heat and Mass Transfer, 137.* https://doi.org/10.1016/j.icheatmasstransfer.2022.106310

[34] Bergman, T. L., Lavine, A. S., Incropera, F. P., & Dewitt, D. P. (2011). *Introduction to Heat Transfer.* Wiley, Sixth Edition. New Jersey, ABD.

[35] Lloyd, J. R., & Moran, W. R. (1974). Natural convection adjacent to horizontal surface of various planforms. *Journal of Heat Transfer, 96,* 443-447. https://doi.org/10.1115/1.3450224

[36] Churchill, S. W., & Chu, H. H. S. (1975). Correlating equations for laminar and turbulent free convection from a vertical plate. *International Journal of Heat and Mass Transfer, 18,* 1323-1329. https://doi.org/10.1016/0017-9310(75)90243-4

[37] Kline, S., & Mcclintock, F. (1953). Describing uncertainties in single-sample experiments. *Mechanical Engineering, 75,* 3-8.

Sinopfbd, 2024; 9(2): 351-368 **https://doi.org/10.33484/sinopfbd.1484733**

Sinop Üniversitesi Fen Bilimleri Dergisi
Sinop Uni J Nat Sci

E-ISSN: 2564-7873

https://dergipark.org.tr/tr/pub/sinopfbd

Standart Klima Sistemini Yeniden Dizayn Ederek Otomobil Koltuklarının Soğutulması

Ali ATEŞ

How to cite: Ateş, A., (2024). Standart klima sistemini yeniden dizayn ederek otomobil koltuklarının soğutulması. *Sinop Üniversitesi Fen Bilimleri Dergisi,* 9(2), 351-368. https://doi.org/10.33484/sinopfbd.1484733

Araştırma Makalesi

Sorumlu Yazar
Ali ATEŞ
aates@sinop.edu.tr

Yazarlara ait ORCID
A.A: 0000-0002-5506-8200

Received: 15.05.2024
Accepted: 18.07.2024

Öz

Güvenli bir yolculuk için araç güvenlik sistemleri kadar insan vücudunun ısıl konforu da dikkate alınmalıdır. Seyahat esnasında yolcuların yanı sıra özellikle sürücünün araç kullanırken kendini rahat hissetmesi güvenlik açısından son derece önemlidir. Bu çalışmada insan vücudunun ısıl konforu dikkate alınarak konvansiyonel bir araç kliması üzerinde bazı değişiklikler yapılmıştır. Bu sayede daha etkili bir iklimlendirme ile daha konforlu bir sürüş gerçekleştirilebileceği hesaplanmıştır. Bunun için bir otomobilin sürücü koltuğu yeniden dizayn edilerek deneysel çalışmalar yapılmıştır. Çalışmalar sonunda soğutma proseslerinde en iyi sonuçlar ortalama devirler için elde edilmiştir. Elde edilen bulgular grafik çıktılarla desteklenmiş ve yorumlanmıştır.

Anahtar Kelimeler: Otomobillerde ısıl konfor, klima destekli otomobil koltuğu, otomobil koltuğunun soğutulması.

Cooling Car Seats by Redesigning the Standard Air Conditioning System

[1]Sinop Üniversitesi, Mühendislik ve Mimarlık Fakültesi, Makine Mühendisliği Bölümü, Sinop, Türkiye

Abstract

For a safe journey, not only vehicle safety systems but also the thermal comfort of the human body should be considered. In addition to the passengers during the journey, it is extremely important for the driver to feel comfortable while driving. In this study, some modifications have been made to a conventional vehicle air conditioner by considering the thermal comfort of the human body. It has been calculated that a more comfortable driving experience can be achieved with a more effective air conditioning system. For this purpose, experimental studies were carried out by redesigning the driver's seat of a car. As a result of the studies, the best results in cooling processes were obtained for average revolutions. The obtained findings have been supported and interpreted with graphic outputs.

Keywords: Thermal comfort in automobiles, air-assisted car seat, cooling car seat.

Giriş

Otomobillerde ısıl konfor, kişisel konfordan çok sürüş güvenliği açısından önem arz etmektedir. Yolculuk süresi arttıkça sürüş konforu ve sürüş güvenliği daha önemli bir hal alır. Özellikle sıcak yaz günlerinde terlemeye neden olan ortam sıcaklığını ve vücut sıcaklığını düşürmek için klima ile soğutmaya daha çok başvurulur. Otomobil kabininin ısıtılması ya da soğutulması belli bir zaman alır. Bu zaman zarfında lokal soğutma yapılarak insan vücudu doğrudan etkilenebilir. Önden insan vücuduna doğru yüksek bir hızda üfürülen soğuk havanın sağlık açısından olumsuz etkileri olabilmektedir. Yaz aylarının sıcak günlerinde camları kapalı olarak park halinde duran bir otomobile binen bir kişi terli ise üflenen soğuk hava sağlık yönünden olumsuz etkiler meydana getirebilir. Eğer otomobil koltuğu klima sistemi ile ayrıca soğutuluyorsa baldırlar ve bel kısmı da gövdenin ön kısmı ile aynı anda soğuyacağından bir ısıl denge oluşacaktır. Ayrıca her ne kadar giysilerin bir direnci olsa da koltuktan soğutma prosesinde temas yoluyla bir ısı transferi gerçekleşmektedir. Konvansiyonel otomobil klimalarında insan vücudunun ısıl konforunu etkileyen parametreler dikkate alınarak otomobil koltuğu doğrudan soğutulursa daha etkili ve daha ekonomik bir ısıl konfor sağlanmış olacak ve klima sisteminin soğutma yükü azalacaktır. Bode ve ark. [1] elektrikli arabaların elektrik sarfiyatını azaltmak için insan vücudunun ısıl konforunu dikkate alan bir sistem geliştirmişlerdir. Bu sistemde, insan vücudunun hassas noktaları dikkate alınarak eşit olmayan bir enerji dağılımı yapılmıştır. Bu sayede enerji kullanımı yarıya düşmesine rağmen standart araç koltuğunun konforunun yakalanabileceğini, buna karşılık araç menzilinde %1.2 - %1.5 arasında bir artış sağlanabileceğini göstermişlerdir. Kipp ve ark. [2] çalışmalarında koltuğun yan taraflarından hava kanalları açarak kabin içi iklimlendirme ve insan vücudunun ısıl konforu için etkili bir yöntem geliştirmeye çalışmışlardır. Elde edilen sonuçlara göre bu değişikliğin soğutma için iyi sonuçlar verdiği ancak ısıtma için beklenen sonuçların alınamadığını vurgulamışlardır. Dehne ve ark. [3] çalışmalarında otomobil kabininin uçaklardakine benzer bir şekilde havalandırılması ve iklimlendirilmesi için bir sistem önermişlerdir. Bu sisteme göre otomobilin döşeme ve tavanından delik ya da kanallar açılarak kabin içi iklimlendirilmeye çalışılmıştır. Bunun için dört adet termal manken kullanmışlardır. Babalık ve Cengiz [4], dört denek ve iki farklı ortamda, dört ayrı klimalı otomobil sürücü koltuğu ile yaptıkları deneylerde ısıl konfor etkilerini objektif ölçümler ve sübjektif sorgulamalarla karşılaştırmalı olarak değerlendirmişlerdir. Babalık ve Cengiz [5] farklı bir çalışmada; dört denek ve iki ayrı ortam sıcaklığı için dört ayrı klima otomobil sürücü koltuğu ile yaptıkları konfor deneyinde sekiz ayrı noktada deri sıcaklığını, iki ayrı noktada vücut nemini ölçmüşler ve konfor değerlendirmesinde nemin deri sıcaklığına göre daha doğru bir ölçek olduğu sonucuna varmışlardır. Esen ve Hoşöz [6] çalışmalarında R12 ve R134a soğutucu akışkanları ile iklimlendirilen otomobil klimasında farklı kompresör devirleri ve ısı yükleri için karşılaştırmalı bir performans analizi yapmışlardır. Sonuç olarak aynı soğutma yükünde R134a'nın R12'ye oranla daha düşük soğutucu akışkan kütle debisi ile çalıştığını tespit etmişlerdir. Kılıç ve Akyol [7] otomobillerin ısıtma işlemi sürecinde farklı hava yönlendiricileri seçiminde sürekli değişen ve kabin içinde düzensiz bir dağılım gösteren ısıl konfor parametrelerinin değişimini deneysel olarak test etmişlerdir. Yiğit ve Atmaca [8], insan vücudu üzerinde ısı ve kütle transferi, denetim mekanizmaları ve çevre şartlarının modellerinin analitik ve sayısal çözümleri üzerinde çalışmışlardır. Solmaz ve Özgören [9] güneş enerjisi (PV) destekli çalışan taşıt klima sisteminin dinamik performansını deneysel olarak araştıran bir çalışma yapmışlardır.

Çalışmada Türkiyenin güneş enerjisi yönünden zengin olan beş ayrı ili için klima sisteminin termodinamik bir analizi yapılmıştır. Ünal ve ark. [10] otobüslerde kullanılan buhar sıkıştırmalı soğutma sistemlerinin ejektörlü hale getirilmesi ile oluşturulan yeni bir sistemde, soğutma etkinliğinin kütlesel debi oranı ile değişimini teorik olarak incelemişlerdir. Bu çalışmada konvansiyonel bir otomobil kliması üzerinde konstrüktif bazı değişiklikler yapılarak sürücü koltuğu klima sistemi ile soğutulmuştur. Koltuğun oturak ve sırt kısımlarına özel olarak yerleştirilen boru demetlerinin bir evaparatör görevi yapması sağlanmıştır. Çeşitli kompresör devirleri için deneysel çalışmalar yapılmıştır. Elde edilen bulgular grafik çıktılarla desteklenmiş ve yorumlanmıştır.

İnsan Vücudunun Isıl Konforu ve Otomobillerde Isıl Konfor

Isıl konfor, kişinin ısıl yönden kendini rahat hissetme duygusu olarak tanımlanabilir. Otomobillerde ısıl konfor, kişisel konfordan çok sürüş güvenliği açısından önemlidir. Yolculuk süresi arttıkça sürüş konforu ve sürüş güvenliği daha önemli bir hal alır. Sürücü ve yolcuları terletmeyecek kadar soğutulabilen bir koltuk iyi bir ısıl konfor sağlayacaktır. Fanger [11] tarafından geliştirilen sürekli rejim modelleri, vücudun ısıl dengede olduğunu ve enerji depolamasının ihmal edilebileceğini kabul eder. Bu modelde vücut içi ve deri tek bir bölme olarak ele alınır. Bu nedenle titreme ve kan akışı ile ısıl denetim göz önüne alınmaz ve sıcaklık zamana göre sabit kabul edilir. Buna göre sürekli rejimde üretilen ısıl enerji, ısı kaybına eşit olur ve enerji dengesi:

$$M - W = Q_{sk} + Q_{res} = (C + R + E_{sk}) + (C_{res} + E_{res}) \qquad (1)$$

bağıntısı ile verilir.

Bu bağıntıda; M metabolik ısı enerjisi üretimini, W yapılan mekanik işi, Q_{res} solunum yoluyla olan toplam ısı kaybını, Q_{sk} deriden olan toplam ısı kaybını, C_{res} solunumla olan taşınım ısı kaybını, E_{res} solunumla buharlaşma kaybını, $C + R$ deriden olan duyulur ısı kaybını ve E_{sk} deriden toplam buharlaşma kaybını ifade ederler.

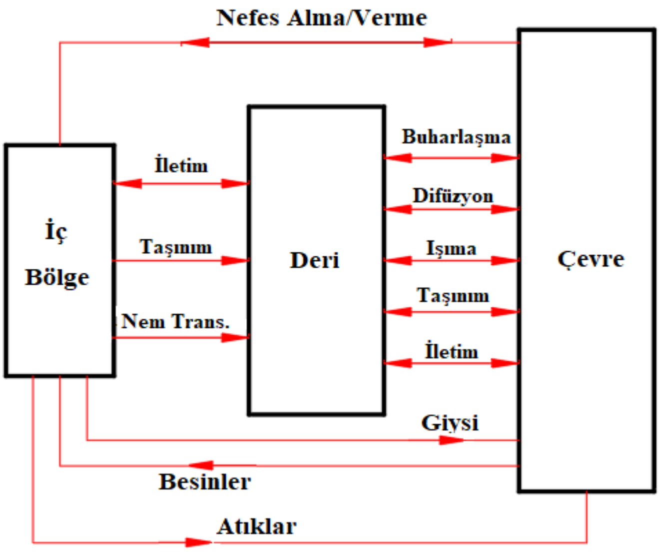

Şekil 1. *İnsan vücudu ile çevre arasındaki ısıl ilişki* [8]

Giyinik bir vücuttan, taşınım C ve ışınım R ile olan ısı kayıpları, bir ısı geçiş katsayısı ve giyinik vücudun ortalama dış sıcaklığı $\mathbf{t_{cl}}$ ile çevre sıcaklığı arasındaki farkın çarpımı olarak;

$$C = f_{cl}\, h(t_{cl} - t_0) \tag{2}$$

$$R = f_{cl} - h_r\, (t_{cl} - t_r) \tag{3}$$

şeklinde yazılabilir [12]

Burada, h_c taşınım katsayısı, h_r doğrusal ışınımla ısı transferi katsayısıdır. f_{cl} ise giysi alan çarpanıdır.

$$(C+R) = f_{cl}\, h\, (\, t_{cl} - t_0) \tag{4}$$

olarak yazılabilir. Burada,

$$t_0 = (\, h_r\, t^*\, r + h_c\, t_0\,) \text{ ve } h = h_r + h_c \tag{5}$$

şeklindedir.

Deriden buharlaşma yoluyla ısı kaybı Esk için şu bağıntı yazılabilir [13].

$$E_{sk} = w\, (p_{sk,s} - p_a) / [R_{e,cl} + 1\, (\, f_{cl}\ \ h_e\,)] \tag{6}$$

Bu bağıntıda; w deri ıslaklığı (boyutsuz), p_a çevre havanın su buharı basıncı, $p_{sk,s}$ deri üzerinde su buharı basıncı, $R_{e,cl}$ giysi tabakasının buharlaşma ile ısı geçiş direnci, h_e buharlaşma ile ısı transferi katsayısını temsil etmektedirler. Solunum sırasında, vücuda giren havaya taşınım ve buharlaşma yoluyla duyulur ve gizli ısı geçişi olur. Solunumla ilişkili duyulur ve gizli ısı kayıpları şöyle ifade edilebilirler; [13].

$$C_{res} = \dot{m}_{res}\, c_{p,a}\, (\, t_{ex} - t_a\,) / A_D \tag{7}$$

$$E_{res} = \dot{m}_{res}\, h_{fg}\, (W_{ex} - W_a)\, A_D \tag{8}$$

Bu denklemlerde; $\dot{m}_{res}$ solunan hava debisi, W_{ex} vücuttan dışarı atılan havanın özgül nemi, t_{ex} dışarı atılan havanın sıcaklığı, W_a solunan (çevre) havanın özgül nemi, $C_{p,a}$ çevre havanın özgül ısısıdır. Bu denklemlerde A_D m^2 cinsinden çıplak vücut yüzey alanıdır ve hesaplama için DuBois tarafından şu bağıntı teklif edilmiştir:

$$A_D = 0{,}202\, m^{0{,}425}\, l^{0{,}725} \tag{9}$$

Bu bağıntıda m vücut kütlesi, l ise boydur. Isı dengesi tüm denklemlerde birim DuBois yüzey alanına göre ifade edilmiştir. Normal bir insan için DuBois alanı A_D = 1.8 m^2 değerindedir. Bir DuBois alanı için metabolik hızı ifade eden birim ***met*** olup dinlenme halindeki bir insanın (oturur, sakin durumda) metabolik hızı olarak tanımlanmıştır. 1 ***met*** = 58.2 W/m^2 = 50 kcal/m^{2}h dir. Ortalama sağlıklı bir erkeğin maksimum enerji kapasitesi 20 yaşında M_{act} = 12 met olup, 70 yaşında 7 met değerine düşer. Araba kullanan bir kişinin ortalama metabolik ısı üretimi 60-115 W/m^2 olarak alınabilir. Bu da 1-2 *met*'e karşılık gelmektedir. İnsan vücudunun ürettiği ısı önemlidir ancak asıl önemli olan bir otomobilin ısıl kazancıdır. Çünkü konfor için ısı fazlası klima yoluyla dışarı atılmalıdır. Bir otomobilin normal şartlarda ısı kazançları şu şekilde özetlenebilir [14]:

- Transmisyonla oluşan ısı kazancı,
- Cam ve opak yüzeylerden ışınımla olan ısı kazancı,
- İnsanlardan kaynaklanan ısı kazancı,
- Araç içinde çalışan cihazlardan kaynaklanan ısı kazancı,
- Havalandırmadan kaynaklanan ısı kazancı

Isıl konfor hesaplamalarında bu ısıl kazançlar dikkate alınmalı ve gerektiği hallerde her biri için tek tek hesaplamalar yapılmalıdır.

Deneysel Çalışma

Bu deneysel çalışmada Renault Toros SW marka bir araç kullanılmıştır. Araç üzerine standart bir otomobil kliması monte edilmiş ve otomobil sürücü koltuğu özel olarak modifiye edilmiştir. Koltuğun oturak ve sırt kısımlarına sürücüyü rahatsız etmeyecek şekilde ince borulardan oluşan soğutucu serpantinler yerleştirilmiştir. Otomobil klima sisteminden ayrılan bir boru ile bu serpantinlere soğutucu akışkan üflenmek suretiyle koltuk soğutulmuştur. Soğutucu serpantinlere bir kollektör aracılığı ile soğutkan (refrigerator) verilmekte ve toplayıcı başka bir kollektörden soğutkan çıkışı olmaktadır. Koltukta ayarlanabilen ısıtma-soğutma fonksiyonu bulunmamaktadır. Kademeler ancak kompresör devri ile yapılabilmektedir. Şekil 2 ve Şekil 3'de deney ünitesinin bağlantı şeması ile deney düzeneğinin şematik görüntüsü verilmiştir. Koltuk sırt ve oturak kısımlarında 5'er adet ısıl çift aracılığı ile ölçülen sıcaklık değerlerinin ortalaması alınarak sırt ve oturak kısımların sıcaklıkları tespit edilmiştir. Ayrıca koltuğa giriş ve çıkış sıcaklıkları, otomobil kliması evaparatörüne giriş ve çıkış sıcaklıkları, kompresör giriş ve çıkış sıcaklıları gibi pek çok noktadan sıcaklık değerleri ölçülmüştür. Ortam sıcaklığını ölçen ısıl çift ile beraber toplam 22 noktada sıcaklık değerleri ölçülmüştür. Ayrıca kompresör giriş ve çıkış basınçları ile kompresör devirleri ayrı ayrı ölçülerek kaydedilmiştir.

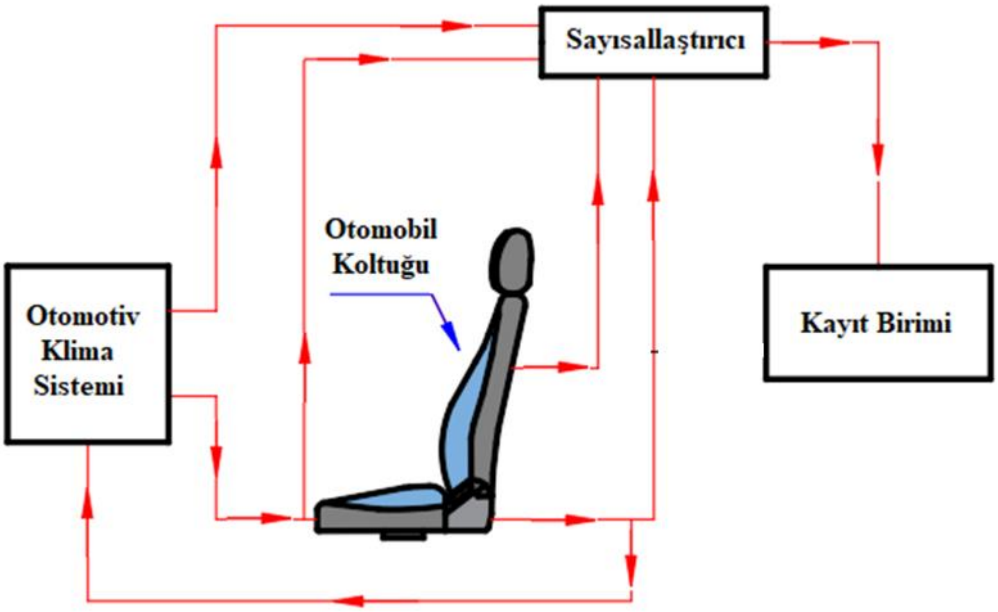

Şekil 2. Otomobil koltuğu kliması için deney ünitesi bağlantı şeması

Daha hassas ölçümler için kompresör, araç motoru yerine invertör aracılığı ile devirleri değiştirilebilen bir doğru akım elektrik motoru ile tahrik edilmiştir. Deneylerde canlı mankenler kullanılmıştır. Mankenlerin özellikle bel ve baldır sıcaklıkları ölçülerek ısıl konfor yönünden rahatlık hissi duyup duymadıkları araştırılmıştır.

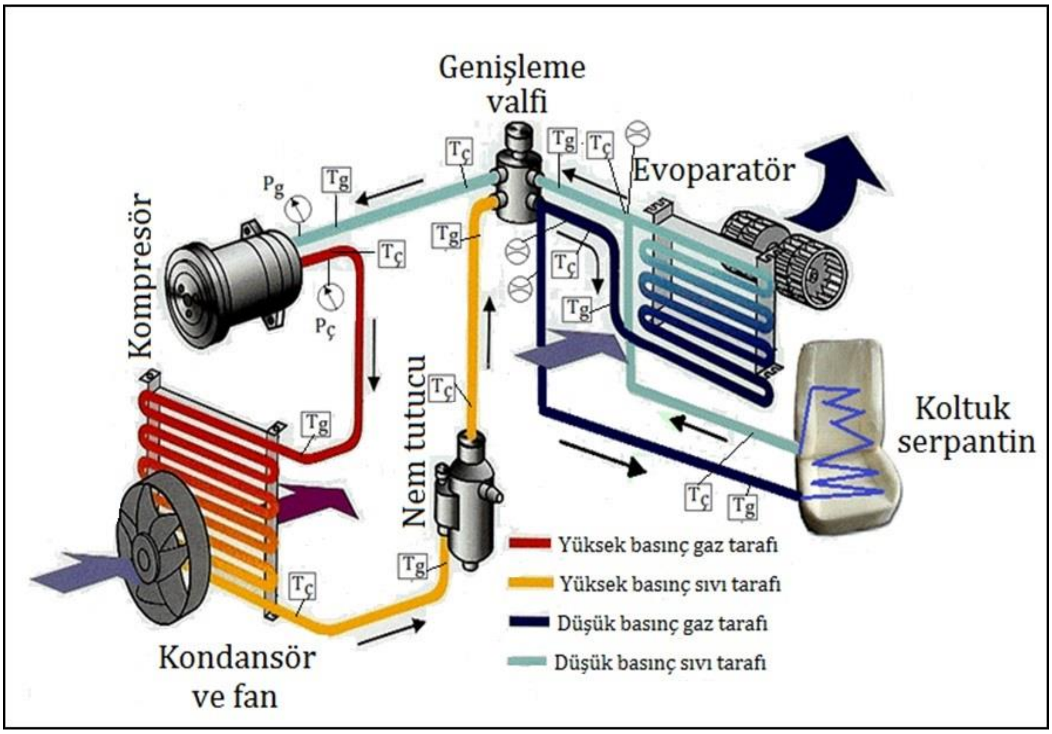

Şekil 3. *Deney düzeneğinin şematik gösterimi*

Deneyin Yapılışı

Her bir deneye başlamadan önce bazı ön hazırlıklar yapılmıştır. Her şeyden önce klima sistemindeki borularda gaz kaçağı olup olmadığı sık sık kontrol edildi. Her deneyden önce data logger'a bağlı ısıl çiftler için doğru ölçüm yapıp yapmadıkları kontrol edildi. Data logger beş saniyede bir ölçüm yapacak şekilde ayarlandı. Data logger ölçümlerin kayıt edileceği bilgisayara bağlandı. Sistem ilk beş dakika rölantide çalıştırıldı. Her bir devir adımındaki deneyler için ölçümler alınmadan önce sistemin sürekli rejime girmesi için on dakika beklendi. Her bir devir adımında on beş dakika süreyle veri alındı. Bu on beş dakikanın ilk beşinci dakikasından itibaren beş dakika boyunca koltuğa bir kişi oturtularak deneyler tekrarlandı. Koltuğa oturtulan kişiye ısıl yönden rahat olup olmadığına dair sorular soruldu. Her bir deney adımında elektrik motorunun volt ve amper değerleri ölçülerek kaydedildi. Ayrıca her bir deney adımında kompresör giriş ve çıkış basınçları ölçülerek kaydedildi. Deneyler 500 dev/dak dan 1600 dev/dak ya kadar 100 dev/dak lık adımlarla tekrarlandı. Şekil 4 ve Şekil 5'de deney setinin resmi gösterilmiş ve resim üzerinde ana elemanlar işaretlenmiştir. Bu deneyde soğutulan ortam koltuk olduğundan, evaparatör koltuk olacaktır. Kompresörden geçen akışkanın basıncı artarak kondansöre gelir. Gaz fazındaki akışkan kondensörde yoğunlaşarak ve ısısını dışarıya vererek sıvı fazına geçer. Sıvı fazdaki akışkan genleşme valfinden geçerek basıncı ve sıcaklığı düşer. Evaparatöre gelen sıvı akışkan koltuğu soğutur ve dışarıdan ısı alır. Çevrim bu şekilde sürekli tekrar eder.

Şekil 4. *Deney düzeneğinin önden görünüşü ve kontrol paneli* **a.** *Fan,* ***b.*** *İnvertör,* ***c.*** *Elektrik açma kapama şartelleri,* ***d.*** *Ortam sıcaklığını ölçen termometre,* ***e.*** *Kompresör giriş ve çıkış basınçlarını ölçen manometre,* ***f.*** *Koltuk soğutmayı devreye sokan sivitç*

Şekil 5. *Deney düzeneğinin arkadan görünüşü* ***a.*** *Elektrik motoru,* ***b.*** *Kompresör,* ***c.*** *Kurutucu,* ***d.*** *Kondansör*

Deney setinin soğutma çevrimi şeması Şekil 6'da verilmiştir.

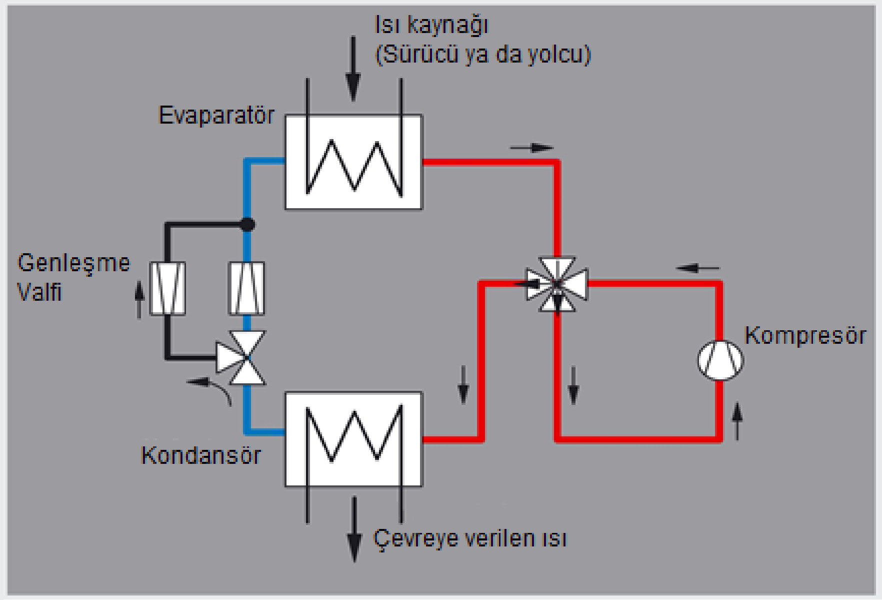

Şekil 6. *Deney sisteminin soğutma çevrimi şeması*

Hesaplamalar

Üç fazlı bir DC motor için birim zamandaki iş ifadesi şöyledir;

$$\dot{W}_{komp.} = V \cdot I \cdot Cos\phi \cdot \sqrt{3} \cdot \eta_{el.} \qquad (10)$$

Bu denklemde $cos\emptyset$=0.82 olarak motor etiketi üzerinden okunmuştur. Yine motor katoloğundan motor verimi $\eta el.$=0.85 olarak alınmıştır.

Ayrıca;

$$\dot{W}_{komp.} = \dot{m}\left(h_2 - h_1\right) \qquad (11)$$

$$\dot{Q}_L = \dot{m}\left(h_1 - h_3\right) = \dot{m}\left(h_1 - h_4\right) \qquad (12)$$

$$STK = \frac{Q_L}{\dot{W}_{komp.}} \qquad (13)$$

yazılabilir. Elde edilen sonuçlar Tablo 1’de gösterilmiştir.

Tablo 1. *Soğutma prosesinde tüm devirler için hesaplanan değerler*

Devir (rpm)	ṁ (g/s)	W (Watt)	V (Volt)	I (Amper)	Q_L (Watt)	STK
500	15.39	585	169	2.86	2031	4.47
600	16.17	603	199	2.51	2150	4.56
700	16.69	667	227	2.42	2136	4.20
800	17.27	673	255	2.19	2193	4.26
900	18.16	708	282	2.11	2324	4.28
1000	18.10	724	306	1.97	2298	4.17
1100	18.44	774	341	1.89	2323	4.00
1200	18.63	782	371	1.76	2347	4.00
1300	18.79	795	397	1.66	2386	3.99
1400	18.92	794	409	1.61	2421	4.05
1500	18.39	775	413	1.56	2354	4.03
1600	18.05	741	415	1.48	2310	4.10

Belirsizlik analizi

Deneysel çalışmalarda elde edilen sonuçların güvenilir olduğunu göstermesi bakımından bir hata analizinin yapılması gerekir. Çeşitli hata analizi yöntemleri içerisinde en çok kullanılanı belirsizlik analizidir. Belirsizlik analizinde hesaplanması gereken büyüklük *R* ve buna bağlı bağımsız değişkenler de $x_1, x_2, \ldots x_n$ olsun. Matematiksel olarak $R=R(x_1, x_2, \ldots x_n)$ şeklinde gösterilebilir. Her bir bağımsız değişkene ait hatalar $w_1, w_2, \ldots w_n$ olsun. *R* bağımlı değişkeninin hata oranı da w_R olsun. Buna göre;

$$w_R = \left[\left(\frac{\partial R}{\partial x_1} w_1\right)^2 + \left(\frac{\partial R}{\partial x_2} w_2\right)^2 + \cdots + \left(\frac{\partial R}{\partial x_n} w_n\right)^2\right]^{1/2} \tag{14}$$

bağıntısı yazılabilir.

Yukarıda yazılan bağıntıların ilgili değişkenlere göre kısmi türevleri şöyle olur;

$$\dot{W}_{komp.} = \dot{m}\left(h_2 - h_1\right) \tag{15}$$

$$\frac{\partial \dot{W}_{komp}}{\partial \dot{m}} = h_2 - h_1 \tag{16}$$

$$\frac{\partial \dot{W}_{komp}}{\partial h_2} = \dot{m} \tag{17}$$

$$\frac{\partial \dot{W}_{komp}}{\partial h_1} = -\dot{m} \tag{18}$$

$$\dot{Q}_L = \dot{m}\left(h_1 - h_3\right) = \dot{m}\left(h_1 - h_4\right) \tag{19}$$

$$\frac{\partial \dot{Q}_L}{\partial \dot{m}} = \left(h_1 - h_3\right) \tag{20}$$

$$\frac{\partial \dot{Q}_L}{\partial h_1} = \dot{m} \tag{21}$$

$$\frac{\partial \dot{Q}_L}{\partial h_3} = -\dot{m} \tag{22}$$

$$STK = \frac{\dot{Q}_L}{\dot{W}_{komp.}} \tag{23}$$

$$\frac{\partial STK}{\partial Q_L} = \frac{1}{\dot{W}_{komp.}} \tag{24}$$

$$\frac{\partial STK}{\partial \dot{W}_{komp.}} = -\frac{\dot{Q}_L}{\left(\dot{W}_{komp.}\right)^2} \tag{25}$$

$$\dot{\omega}_{\dot{W}_{komp.}} = \left[\left(\frac{\partial \dot{W}_{komp.}}{\partial \dot{m}}\,\omega_{\dot{m}}\right)^2 + \left(\frac{\partial \dot{W}_{komp.}}{\partial h_2}\,\omega_{h_2}\right)^2 + \left(\frac{\partial \dot{W}_{komp.}}{\partial h_1}\,\omega_{h_1}\right)^2\right]^{1/2} \tag{26}$$

$$\dot{\omega}_{\dot{Q}_L} = \left[\left(\frac{\partial \dot{Q}_L}{\partial \dot{m}}\,\omega_{\dot{m}}\right)^2 + \left(\frac{\partial \dot{Q}_L}{\partial h_1}\,\omega_{h_1}\right)^2 + \left(\frac{\partial \dot{Q}_L}{\partial h_3}\,\omega_{h_3}\right)^2\right]^{1/2} \tag{27}$$

$$\dot{\omega}_{STK} = \left[\left(\frac{\partial STK}{\partial \dot{Q}_L}\,\omega_{Q_L}\right)^2 + \left(\frac{\partial STK}{\partial \dot{W}_{komp.}}\,\omega_{kom.}\right)^2\right]^{1/2} \tag{28}$$

Yukarıda belirlenen bağıntılara göre hesaplanan belirsizlik analizi çıktıları her bir devir için Tablo 2’de topluca verilmiştir.

Tablo 2. *Belirsizlik analizi yöntemine göre hesaplanan hata analizi sonuçları*

Devir (rpm)	$\omega_{Wkomp.}$ (% hata)	ω_{QL} (%hata)	ω_{STK} (% hata)
500	3.812	1.524	0.391
600	3.734	1.543	0.359
700	3.813	1.530	0.389
800	3.732	1.529	0.375
900	3.651	1.515	0.355
1000	3.578	1.527	0.345
1100	3.503	1.523	0.335
1200	3.573	1.518	0.343
1300	3.574	1.517	0.343
1400	3.432	1.527	0.309
1500	3.368	1.528	0.300
1600	3.433	1.529	0.309

Bulgular ve Tartışma

Bu çalışmada, sürücünün ısıl konforu için otomobil sürücü koltuğunun soğutma deneyleri 500 dev/dak dan 1600 dev/dak' ya kadar her 100 dev/dak'lık kompresör devri artışları için ayrı ayrı yapılmış ve her deney standart olarak 15 dakika sürmüştür. Bu süre zarfında her 5 saniyede bir ölçümler data logger aracılığı ile kaydedilmiştir. Elde edilen verilerle çeşitli grafikler hazırlanmış ve yorumlanmıştır. Tüm deneylerde ortam sıcaklığı ortalama 22 °C olarak ölçülmüştür.

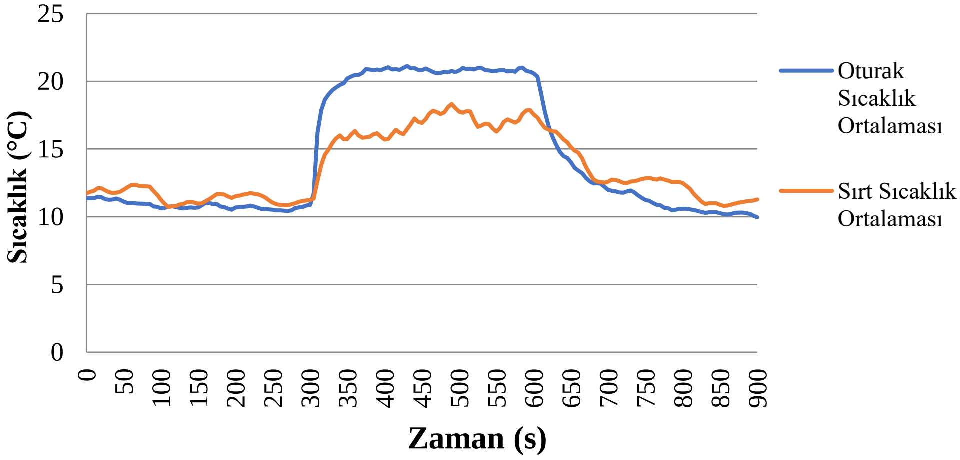

Şekil 8. *500 dev/dak için soğutma prosesi sıcaklık-zaman grafiği*

Şekil 8'de verilen 500 dev/dak için sıcaklık-zaman grafiğinde sıcaklıkların 12 °C ile 22 °C arasında değiştiği görülmektedir. Bu aralık ısıl konfor açısından oldukça düşük bir değerdir. Sıcaklığın belli bir değerin altına düştüğü durumlarda termostatik bir kesici ile prosesin durdurulması gerekir. Ancak bizim deney düzeneğimizde çeşitli nedenlerle bu gerçekleştirilememiştir. Grafikten de anlaşılacağı üzere 300 saniye ile 600 saniye arasındaki aralıkta yani canlı mankenin koltuğa oturduğu zaman aralığında insan vücudundan gerçekleşen ısı transferinden dolayı sıcaklık değerleri yükselmektedir. Sıcaklıktaki yükselme sırt kısmına göre oturak kısmında daha fazla gözlenmektedir. Bu da insanın uyluklarından daha etkili bir iletimle ısı transferi gerçekleştiğinin göstergesidir. Çünkü uyluklar sırt kısmına göre daha mükemmel şekilde koltuğa yapışmaktadır. 600 dev/dak için verilen Şekil 9'daki grafikte evaparatör (sürücü koltuğu) sıcaklık değerlerinin 500 dev/dak'ya göre biraz daha düştüğü gözlenmektedir. 300 saniyeye kadar olan kısım ile 600 saniyeden sonraki kısımlarda koltuğun oturak kısmı sıcaklık değerlerinin sırt kısmı sıcaklık değerlerine göre daha düşük olduğu görülmektedir. Bu da oturak kısmında daha etkili bir ısı transferinin gerçekleştiğinin göstergesidir. 300 saniye ile 600 saniye arasında oturak kısmı sıcaklık değerinin sırt kısmı sıcaklık değerinden daha yüksek olduğunun sebebi yukarıda izah edilmiştir.

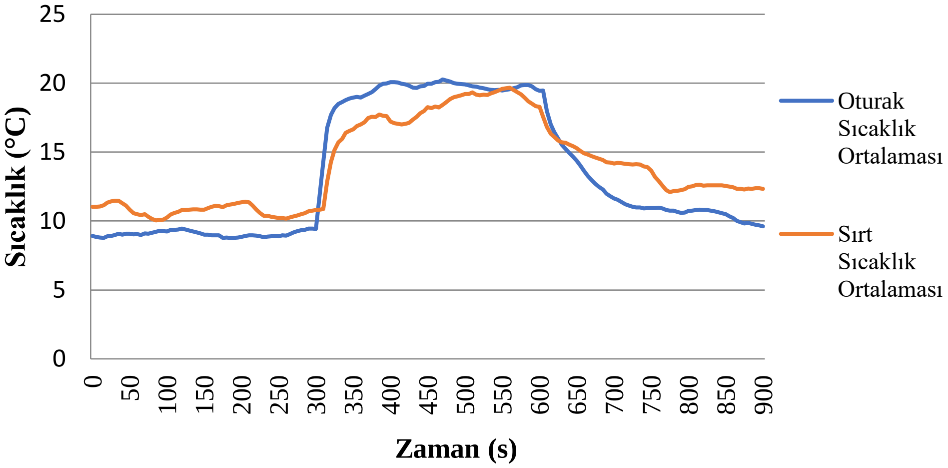

Şekil 9. *600 dev/dak için soğutma prosesi sıcaklık-zaman grafiği*

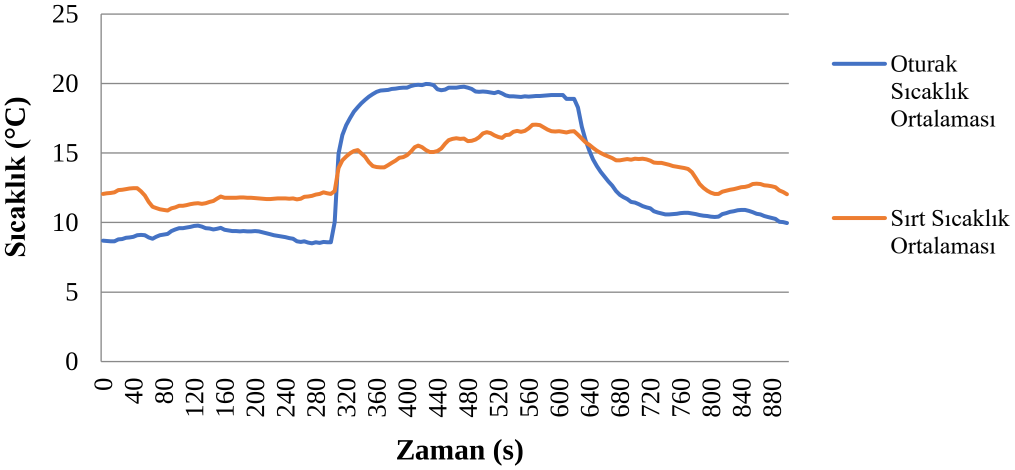

Şekil 10. *700 dev/dak için soğutma prosesi sıcaklık-zaman grafiği*

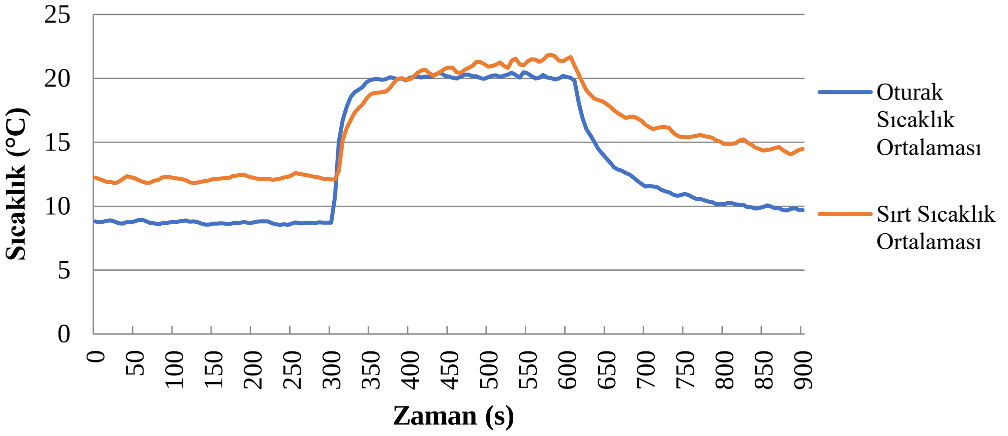

Şekil 11. *800 dev/dak için soğutma prosesi Sıcaklık-Zaman grafiği*

600 dev/dak ile 800 dev/dak arasındaki üç grafik (Şekil 9 – Şekil 11) birbirlerine benzerlik göstermektedirler. Her üç grafikte de başlangıçta oturak kısmı sıcaklığı 9 ºC civarında iken sırt kısmı sıcaklığı 11 ºC civarındadır. 300 saniye ile 600 saniye arasında doğal olarak her iki sıcaklık değeri de yükselmekte ancak oturak kısmı sıcaklığı sırt kısmı sıcaklığından daha yüksek olmaktadır. Yukarıda da izah edildiği gibi bunun sebebi baldırlardan olan iletimle ısı transferinin bel ya da sırt kısmına göre daha etkili olmasıdır.

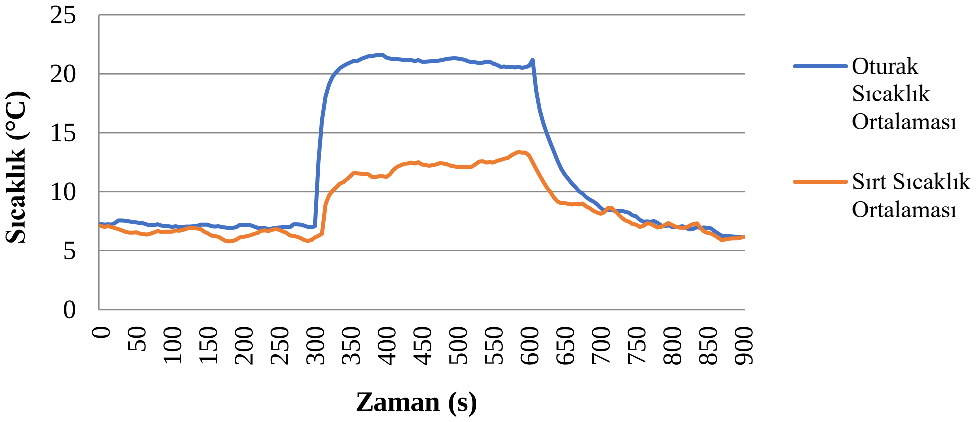

Şekil 12. *900 dev/dak için soğutma prosesi sıcaklık-zaman grafiği*

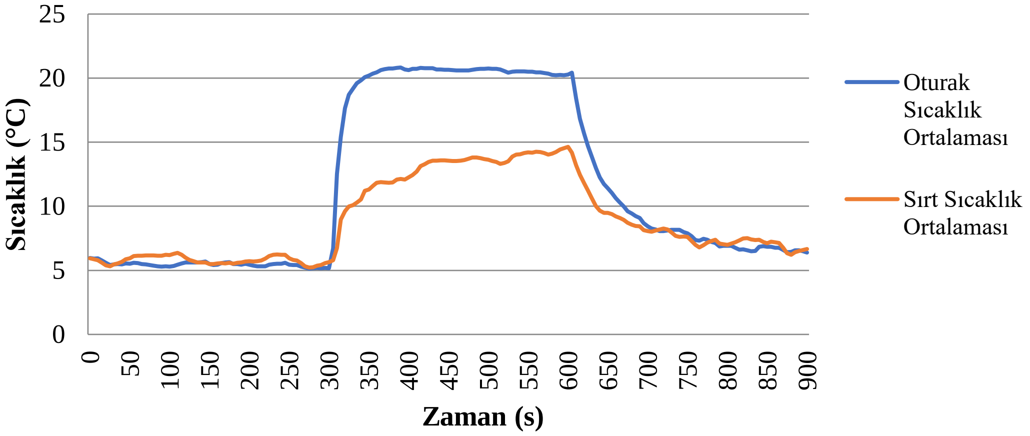

Şekil 13. *1000 dev/dak için soğutma prosesi sıcaklık-zaman grafiği*

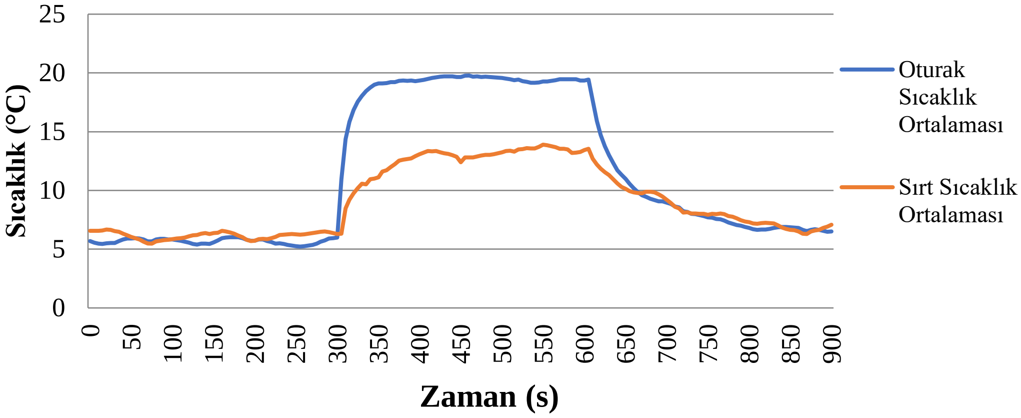

Şekil 14. 1100 dev/dak için soğutma prosesi sıcaklık-zaman grafiği

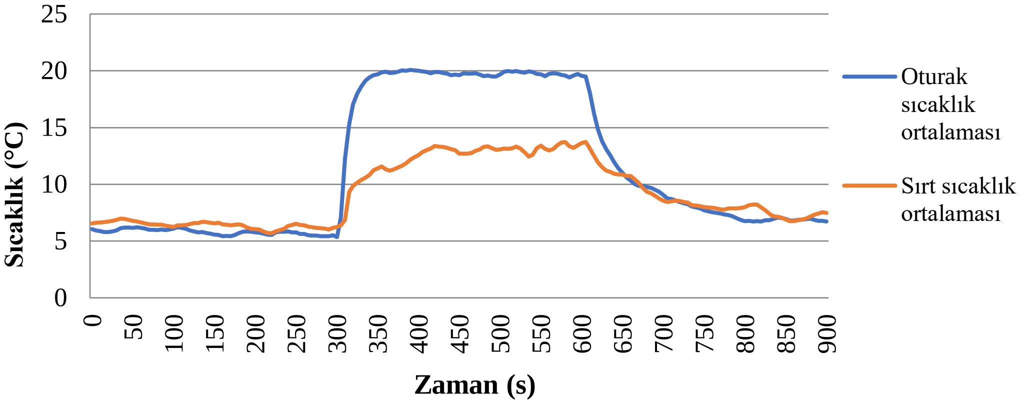

Şekil 15. 1200 dev/dak için soğutma prosesi sıcaklık-zaman grafiği

900 dev/dak ile 1200 dev/dak arasındaki dört grafik de (Şekil 12 - Şekil 15) aynı şekilde birbirlerine benzerlik göstermektedirler. Bu grafiklerde başlangıçta oturak ve sırt kısmı sıcaklıkları 6-7 °C civarında ve birbirlerine çok yakın değerdedirler. Aynı şekilde 600 saniyeden sonra sıcaklık değerleri tekrar 6-7 °C civarına inmektedir. Her dört grafikte de 300-600 saniye arasında sırt kısmı sıcaklığı 13-15 °C civarlarında iken oturak kısmı sıcaklıkları 20-22 °C civarlarında seyretmektedir.

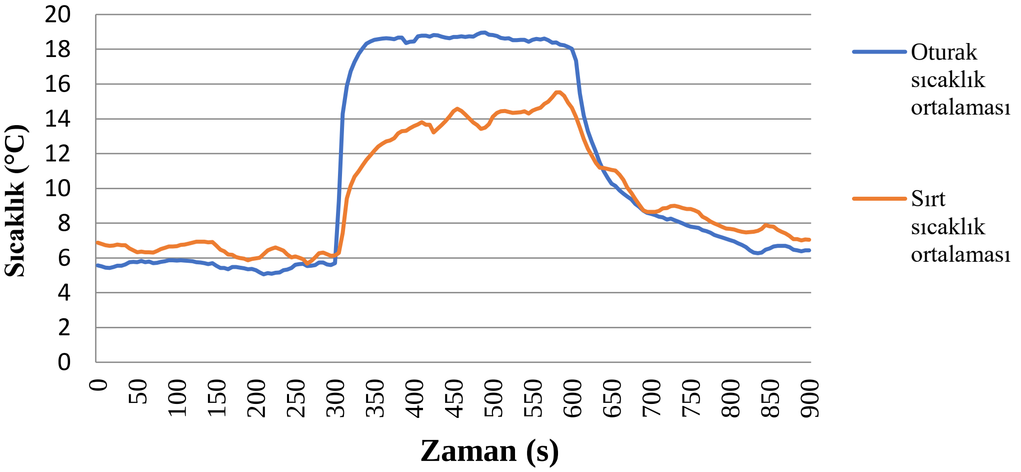

Şekil 16. 1300 dev/dak için soğutma prosesi sıcaklık-zaman grafiği

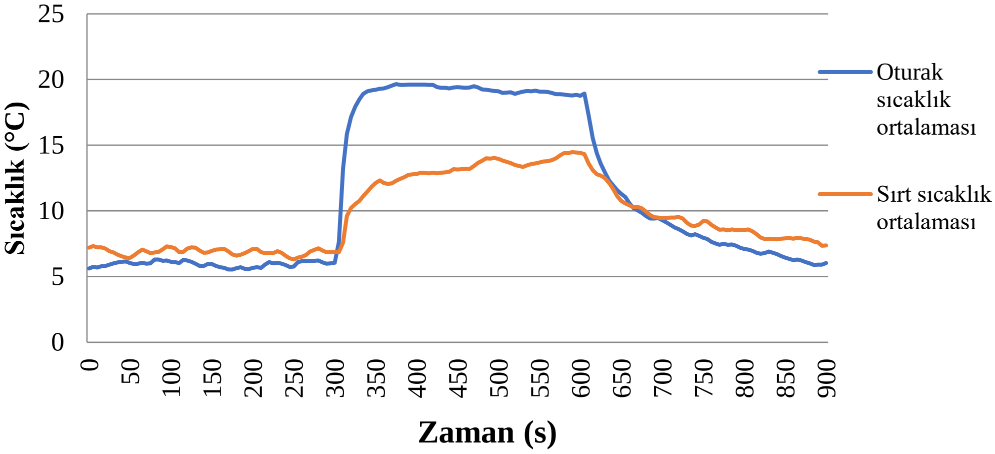

***Şekil 17**. 1400 dev/dak için soğutma prosesi sıcaklık-zaman grafiği*

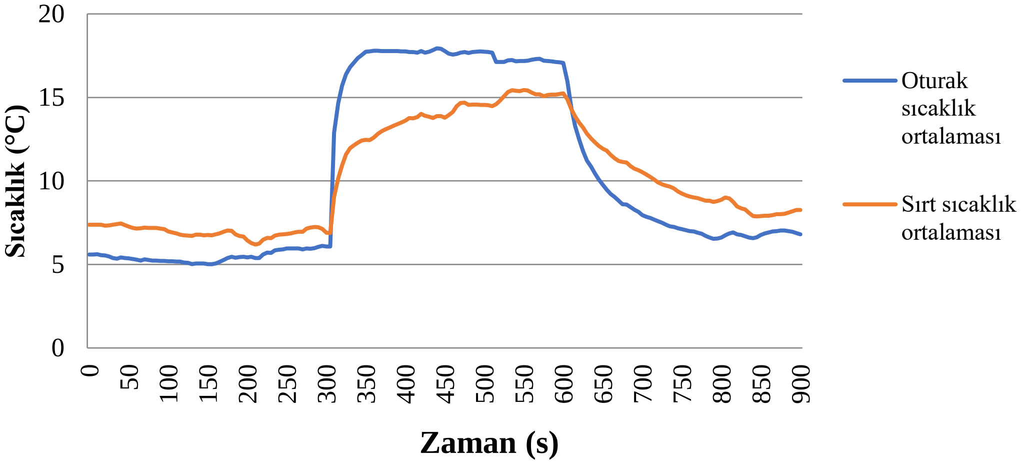

***Şekil 18.** 1500 dev/dak için soğutma prosesi sıcaklık-zaman grafiği*

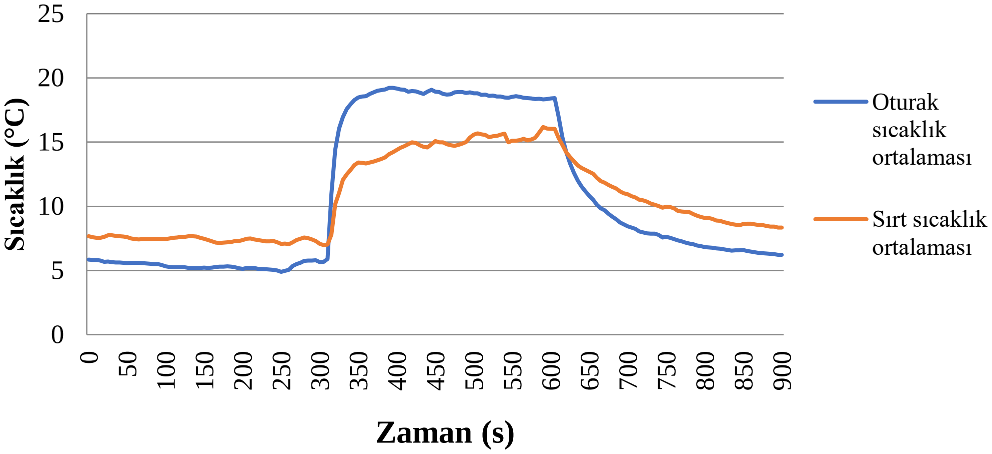

***Şekil 19.** 1600 dev/dak için soğutma prosesi sıcaklık-zaman grafiği*

1300 dev/dak ile 1600 dev/dak arasındaki grafiklerde (Şekil 16 - Şekil 19) 300 saniyeye kadar olan kısımda oturak sıcaklıkları 5-6 ºC civarında iken sırt kısmı sıcaklıkları 6-8 ºC arasında seyretmektedir. 600 saniyeden sonra ise her iki kısmın sıcaklık değerlerinde başlangıca göre 1-2 ºC lik bir artış olduğu gözlenmektedir. 300-600 saniyeler arasında ise sırt kısmı sıcaklığı ortalama olarak 15 °C civarında seyrederken oturak kısmı ortalama sıcaklığı biraz daha düşerek 18 °C civarına inmektedir. Buradan da devir sayısı arttıkça soğutma etkisinin daha çok arttığı sonucu çıkarılabilir. Koltuk kısmındaki oturak ve sırt kısmına ait evaporatörlerde sıcaklık değerlerinin bu denli düşmesi makul değildir. Bunun sebebi debisi daha yüksek soğutucu akışkanın daha kısa mesafeli serpantin borularını kat etmeleri ile izah edilebilir. Bu durumda soğutucu akışkan daha fazla buharlaşmaya fırsat bulamadan evaporatörü terk etmektedir. Ancak koltuk kısmına sevk edilen soğutucu akışkan debisinin düşürülmesiyle bu durum telafi edilebilir. Bizim deney düzeneğimizde ayar mekanizması olmadığı için bu yapılamamıştır. Diğer yandan 1400 dev/dak'dan sonra soğutucu akışkan debisinde kısmi bir azalma gözlenmektedir. Bunun sebebi yukarıda izah edildiği üzere kompresörün yüksek devrinden dolayı emme ve basma zamanlarının üst üste binmesi olarak yorumlanabilir. Her devir için ölçülen maksimum ve minimum oturak/sırt sıcaklık değerleri Tablo 3'de verilmiştir. Tablo 3.'de görüldüğü gibi oturak bölgesinde 900 dev/dk da en yüksek, 1600 dev/dk da en düşük sıcaklık ölçülmüştür. Sırt bölgesinde ise en yüksek sıcaklık 800 dev/dak için elde edilirken en düşük sıcaklık 1000 dev/dak 'da elde edilmiştir.

Tablo 3. *Her devir için ölçülen maksimum/minimum sıcaklıklar*

	OTURAK		SIRT	
Devir Sayısı (dev/dk)	Ölçülen Maksimum Sıcaklık (°C)	Ölçülen Minimum Sıcaklık(°C)	Ölçülen Maksimum Sıcaklık (°C)	Ölçülen Minimum Sıcaklık(°C)
500	21.13	9.96	18.33	10.72
600	20.27	8.77	19.67	10.05
700	19.974	8.506	17.044	10.868
800	20.486	8.544	**21.84**	11.794
900	**21.59**	6.14	13.37	5.786
1000	20.828	5.136	14.636	***5.22***
1100	19.776	5.224	13.896	5.484
1200	20.076	5.354	13.734	5.688
1300	18.964	5.056	15.526	5.674
1400	19.656	5.538	14.476	6.308
1500	17.942	5.014	15.446	6.188
1600	19.22	***4.892***	16.174	6.976

Sonuçlar

Soğutma prosesi grafiklerinde görüldüğü gibi koltuğa oturan kişi koltuğa kendi ısısını vermektedir. Bu beklenen bir şeydir. Sağlıklı bir insan vücudunun sıcaklığı 35-37 °C arasında olduğundan oturma süresince gerçekleşen ısı transferi nedeniyle koltuğun sıcaklığı bir miktar artmaktadır. Verimi arttırmak için farklı özelliklerde soğutucu akışkan kullanılması düşünülebilir. Ancak bazı gazların tehlikeli yönleri ya da yan etkileri olabileceği de göz ardı edilmemelidir. Deney ölçümlerinde, koltuğun oturak bölümünde en yüksek sıcaklık 900 dev/dk da ölçülürken en düşük oturak sıcaklığı 1600 dev/dak da ölçülmüştür. Koltuğun sırt bölümünde en yüksek sıcaklık değeri 800 dev/dak da ölçülmüş, en düşük sıcaklık değeri ise 1000 dev/dak da ölçülmüştür. Sıcaklığın çok fazla düşük olması ısıl konfor yönünden tercih edilmez. Çünkü insan vücudunun ısıl konforu belli bir sıcaklığın altında konforsuzluğa dönüşür. Ancak soğutucu akışkan debisi ayarlanarak bu problem ortadan kaldırılabilir. Bu çalışmada termostatik bir sıcaklık kontrol sistemi kullanılmadığından koltuk evaporatör kısmı sıcaklığı çok düşmüştür. Ancak bu durum, oturma süresi 5 dakika olan canlı mankeni ısıl konfor açısından aşırı etkilememiştir. Genel bir değerlendirme yapılacak olursa otomobil sürücü koltuğunun standart otomobil kliması ile soğutulmasının tatmin edici sonuçlar verdiği deneysel verilerden anlaşılmaktadır. Buna göre otomobil koltukları standart klima sistemiyle verimli ve ekonomik olarak soğutulabilir. Bu çalışma, deney düzeneği geliştirilerek daha ileri bir düzeye taşınabilir. Özellikle kütlesel debi ve basınç düşüşü ölçümlerinde çok daha hassas cihazlar kullanılmalıdır. Ayrıca değişik soğutkanlar kullanılmak suretiyle değişik ve ilginç sonuçlar elde edilebilir. Örneğin hem soğutmanın hem de ısıtmanın etkili olabileceği yüksek ısı tutumu olan soğutucu akışkanlar denenebilir.

Teşekkür **-**

Fon/Finansman Bilgileri Bu çalışma Selçuk Üniversitesi Bilimsel Araştırma Projelerini Destekleme Fonu (BAP) tarafından desteklenmiştir. (Proje No.: 11401028)

Etik Kurul Onayı ve İzinler Çalışma, etik kurul izni veya herhangi bir özel izin gerektirmemektedir.

Çıkar Çatışmaları/Çatışan Çıkarlar **-**

Yazarların Katkısı Yazar makalenin son halini okumuş ve onaylamıştır.

Kaynaklar

[1] Bode, F., Burnete, N. V., Fechete Tutunaru, L., & Nastase, I. (2023). Improving electric vehicle range and thermal comfort through an innovative seat heating system. *Sustainability, 15,*(6) 5534. https://doi.org/10.3390/su15065534

[2] Kipp, M., Rolle, A., & Bengler, K. (2021). An Innovative Seat Ventilation Concept: Does the Seat Provide Overall Thermal Comfort in Autonomous Vehicles? *In: Black, N.L., Neumann, W.P., Noy, I. (eds) Proceedings of the 21st Congress of the International Ergonomics Association (IEA 2021), Lecture Notes in Networks and Systems, 221,* 701-709, Springer, Cham. https://doi.org/10.1007/978-3-030-74608-7_85

[3] Dehne, T., & Westhoff, A. (2020). Efficient Cooling of a Generic Car Cabin by Novel Ventilation Systems. *In: Dillmann, A., Heller, G., Krämer, E., Wagner, C., Tropea, C., Jakirlić, S. (eds) New Results in Numerical and Experimental Fluid Mechanics XII. DGLR 2018. Notes on Numerical Fluid Mechanics and Multidisciplinary Design, 142,* 416-426, Springer, Cham. https://doi.org/10.1007/978-3-030-25253-3_40

[4] Babalık, F. C., & Cengiz, T. G. (2009). Klimalı otomobil sürücü koltuğunda termal konfor üzerine deneysel bir çalışma. *Mühendis ve Makine, 45,* 539.

[5] Babalık, F. C., & Cengiz, T. G. (2005, 26-28 Aralık). *Klimalı koltuklarda koltuk sürücü temas noktalarındaki ölçümlerle konfor araştırması*. 11. Ulusal Ergonomi Kongresi İTU, İstanbul, www.11uek.org.

[6] Esen, D. Ö., & Hoşöz, M. (2006). R12 ve R134a Soğutucu akışkanları kullanan otomobil iklimlendirme sisteminin deneysel performans analizi. *Gazi Üniversitesi Mühendislik Fakültesi Dergisi, 21*(4), 703-709.

[7] Kılıç, M., & Akyol, Ş. M. (2009). Otomobil kabinlerinin ısıtılmasında farklı hava yönlendiricileri kullanılmasının ısıl konfora etkisi. *Journal of Thermal Science and Technology, 29*(1), 25-36.

[8] Yiğit, A., & Atmaca, İ. (2008, 12-14 Mayıs). *Isıl konfor PMV İndeksinin deneysel değişiminin incelenmesi ve ampirik sonuçlarla karşılaştırılması*. TTMD VIII. Uluslararası Yapıda Tesisat Teknolojisi Sempozyumu, CD kayıt. http://ttmd.org.tr/

[9] Solmaz, Ö. (2013). *Investigation of dynamic performance of a vehicle air-conditioning system driven by solar energy (PV)*. [Doktora tezi, Selçuk Üniversitesi].

[10] Ünal, Ş., Yımaz, T., Cihan., E., & Büyükalaca, O. (2013). Enjektörlü klima sisteminde soğutma etkinliğinin kütlesel debi oranı ile değişimi. *Çukurova Üniversitesi Mühendislik Mimarlık Fakültesi Dergisi, 28*(1), 61-76.

[11] Fanger, P. O. (1970). *Thermal Comfort, Analysis and Applications in Environmental Engineering,* Danish Technical Press, Copenhagen.

[12] *ASHRAE handbook – Fundamentals, Chapter 8, (1989).* Atlanta: American Society of Heating Refrigeration and Air-Conditioning.

[13] *ASHRAE handbook – Fundamentals, Chapter 8, (1993).* Atlanta: American Society of Heating, Refrigeration and Air-conditioning Engineers.

[14] Solmaz, O., Ozgoren, M., & Aksoy M. H. (2014). Hourly cooling load prediction of a vehicle in the southern regionof Turkey by Artificial Neural Network. *Energy Conversion and Management, 82,* 177-187 https://doi.org/10.1016/j.enconman.2014.03.017

[15] Öngel, K., & Mergen, H. (2009) Isil konfor parametrelerinin insan vücudundaki etkilerine yönelik literatür taramasi. *Medical Journal of Suleyman Demirel University, 16*(1), 21-25.

Sinopfbd, 2024; 9(2): 369-387 **https://doi.org/10.33484/sinopfbd.1458580**

Sinop Üniversitesi Fen Bilimleri Dergisi
Sinop Uni J Nat Sci

E-ISSN: 2564-7873

https://dergipark.org.tr/tr/pub/sinopfbd

Classification of Heart Diseases with Ensemble Learning Algorithms

Kenan ERDEM[1] **Elham Tahsin YASİN**[2] **Müslüme Beyza YILDIZ**[3] **and Murat KÖKLÜ**[3]

How to cite: Erdem, K., Yasin, E. T., Yıldız, M. B., & Köklü, M. (2024). Classification of heart diseases with ensemble learning algorithms. *Sinop Üniversitesi Fen Bilimleri Dergisi, 9*(2), 369-387. https://doi.org/10.33484/sinopfbd.145880

Research Article

Corresponding Author
Murat KÖKLÜ
mkoklu@selcuk.edu.tr

ORCID of the Authors
K.E: 0000-0001-6002-5873
E.T.Y: 0000-0003-3246-6000
M.B.Y: 0009-0002-0231-687X
M.K: 0000-0002-2737-2360

Received: 25.03.2024
Accepted: 05.08.2024

Abstract

The heart is one of the vital organs of the human body. Preserving heart health is a crucial factor that affects our overall well-being. Heart diseases are considered a prominent health issue of our time and are recognized as one of the leading causes of death worldwide. This underscores the importance of the heart once again. Understanding this critical health issue better, developing early diagnosis techniques, and creating effective treatment plans require continuous research and effort. In this study, performance measurements of three different machine learning algorithms were obtained using a dataset with 18 features from 319795 records of individuals with and without heart disease. The research results indicate that ensemble methods (AdaBoost, Stacking, and Gradient Boosting) can be successfully applied in the diagnosis of heart disease. The classification accuracies of these algorithms are as follows: 88.80% for AdaBoost, 91.50% for Stacking, and 91.60% for Gradient Boosting. Results from this study indicate that successful methods can be used to diagnose heart disease.

Keywords: Heart disease, Artificial Intelligence Techniques, Diagnosis and Classification, Ensemble, Gradient Boosting

Kalp Hastalıklarının Topluluk Öğrenme Algoritmaları ile Sınıflandırılması

[1]Selcuk University, Faculty of Medicine, Department of Cardiology, Konya, Türkiye

[2]Selcuk University, Graduate School of Natural and Applied Sciences, Department of Computer Engineering, Konya, Türkiye

[3]Selcuk University, Faculty of Technology, Department of Computer Engineering, Konya, Türkiye

Öz

Kalp, insan vücudunun hayati organlarından biridir. Kalp sağlığının korunması genel refahımızı etkileyen çok önemli bir faktördür. Kalp hastalıkları çağımızın en önemli sağlık sorunlarından biri olarak kabul edilmekte ve dünya çapında önde gelen ölüm nedenlerinden biri olarak kabul edilmektedir. Bu da kalbin önemini bir kez daha vurgulamaktadır. Bu kritik sağlık sorununu daha iyi anlamak, erken teşhis teknikleri geliştirmek ve etkili tedavi planları oluşturmak sürekli araştırma ve çaba gerektirmektedir. Bu çalışmada, kalp hastalığı olan ve olmayan bireylere ait 319795 kayıttan elde edilen 18 özellikli bir veri kümesi kullanılarak üç farklı makine öğrenimi algoritmasının performans ölçümleri elde edilmiştir. Araştırma sonuçları, topluluk yöntemlerinin (AdaBoost, Stacking ve Gradient Boosting) kalp hastalığı teşhisinde başarıyla uygulanabileceğini göstermektedir. Bu algoritmaların sınıflandırma doğrulukları aşağıdaki gibidir: AdaBoost için %88.80, Stacking için %91.50 ve Gradient Boosting için %91.60. Bu sonuçlar, kalp hastalığının teşhisinde kullanılabilecek başarılı yöntemlerin varlığını vurgulamaktadır.

Anahtar Kelimeler: Kalp Hastalığı, Yapay Zeka Teknikleri, Teşhis ve Sınıflandırma, Ensemble, Gradient Boosting

Introduction

In modern societies, heart disease has become a significant health concern. Recognized as one of the leading causes of death worldwide, heart disease plays a central role in medical research. Continuous efforts have been made to gain a deeper understanding of the causes and effects of these diseases and to develop effective diagnostic and treatment methods [1]. Following a better understanding of this crucial health problem, new technologies such as machine learning are gaining importance for their potential contributions in this field [2]. Moreover, the ability of machine learning algorithms to quickly and reliably analyze large amounts of data facilitates the diagnostic process for individuals with and without heart disease [3, 4].

In their study, Mohan et al. [5] achieved an accuracy level of 88.7% in the detection of heart disease using the Hybrid Random Forest with a Linear Model (HRFLM) model. They did not impose restrictions on feature selection and used all features. The heart disease data were collected from the UCI Machine Learning Repository, comprising 297 patient records in the dataset with 13 features. In cases where an individual does not have heart disease, the value is set to 0. For patients with heart disease, values range from 1 to 4, representing the severity of the disease, with scaling indicating seriousness (4 being the highest) [5].

Repaka et al. [6] employed the Naive Bayes Bayesian algorithm in the design and implementation of Smart Heart Disease Prediction (SHDP). They utilized the UCI dataset, allocating 80% of the dataset for training and the remaining 20% for testing. With the Naive Bayes Bayesian algorithm, they achieved an accuracy of 89.77% [6].

Anitha & Sridevi [7] utilized the UCI dataset. When comparing the KNN, Naive Bayes, and SVM algorithms, they found that the Naive Bayes algorithm detected heart disease with an accuracy of 86.6% [7].

Shah et al. [8] aimed to conceptualize the probability of developing heart disease in patients. They used the dataset available from the Cleveland database in the UCI repository for patients heart disease. The dataset contained 303 samples and 76 features, however they considered only 14 features for testing. They utilized the WEKA tool for preprocessing the dataset in ARFF format (attribute-relation file format). The K-Nearest Neighbors, Naive Bayes, and Random Forest algorithms showed the best results in this model, achieving accuracies of 78.94%, 88.15%, and 84.21%, respectively [8].

Motarwar et al. [9] utilized the Cleveland dataset in their research. They trained the model using 80% of the data (242 samples) and predicted the remaining 20% (61 samples). To predict the probability of developing heart disease, they employed machine learning algorithms, such as Random Forest, Naive

Bayes, Support Vector Machine, Hoeffding Decision Tree, and Logistic Model Tree. Random Forest achieved the highest accuracy with an initial accuracy of 88.52% [9].

Junaid and Kumar [10] employed a hybrid algorithm in their study, combining Naive Bayes, Support Vector Machine (SVM), and Artificial Neural Network (ANN) algorithms. The accuracy, precision, and recall values they obtained were 88.54%, 82.11%, and 91.47%, respectively [10].

Sharma and Parmar [11] utilized the UCI dataset in their study for the detection of heart disease. They evaluated algorithms such as KNN, SVM, Naive Bayes, and Random Forest. Deep Neural Networks (DNN) using Talos optimization outperformed other optimizations, providing a higher accuracy of 90.76% [11].

Anbuselvan [12] utilized the UCI machine learning dataset for their project. In supervised learning models, Logistic Regression, and the ensemble technique XGBoost, Random Forest achieved better results with an accuracy of 86.89% compared to other methods such as Naive Bayes, Support Vector Machine, K-Nearest Neighbors, and Decision Tree algorithms [12].

Kavitha et al. [3] proposed a new machine learning approach to predict heart disease in their project. They used the Cleveland heart disease dataset, which contained 303 samples and approximately 14 features. Seventy percent of the dataset was used for training, and the remaining 30% was used for testing. The hybrid model, consisting of a combination of Random Forest and Decision Tree, demonstrated an accuracy level of 88.7% [3].

Rani et al. [13] in their research on predicting heart disease, employed Support Vector Machine, Naive Bayes, Logistic Regression, Random Forest, and Adaboost classifiers. The Random Forest classifier yielded the most accurate results with an accuracy rate of 86.6%. They used the Cleveland heart disease dataset from the UCI (University of California, Irvine) machine learning repository [13].

Jindal et al. [14] developed a cardiovascular disease detection model in their study using three machine learning classification models (Logistic Regression, Random Forest, and KNN). They utilized the UCI repository for their dataset, which includes 304 patients from different age groups and 13 medical features. The model which was applied using the KNN and Logistic Regression, achieved an average accuracy of 85%. Among these algorithms, KNN was the most effective, reaching an accuracy of 88.52% [14].

Goel [15] collected a dataset consisting of 13 features and 383 individual values. Among the algorithms, Logistic Regression, KNN, Naïve Bayes, Decision Tree, and Random Forest, SVM achieved the highest accuracy rate of 86% [15].

Boukhatem et al. [16] utilized four classification methods, namely Multilayer Perceptron (MLP), Support Vector Machine (SVM), Random Forest (RF), and Naïve Bayes (NB), for cardiovascular disease detection in their study. The SVM model exhibited the best performance with an accuracy of 91.67%. They used the Heart Disease UCI dataset from Kaggle for cardiovascular disease detection [16].

Sugendran and Sujatha [17] used an Enhanced Genetic Algorithm (EGA) based Fuzzy Weight update Support Vector Machine (FWSVM) algorithm in their research to predict the early stages of heart disease. They employed the Cleveland heart disease dataset from the open-source UCI repository to validate their proposed model. The dataset contains 303 samples and 76 features. The EGA-FWSVM classifier, utilizing fuzzy weighted evaluation, achieved an accuracy of 91.68% [17].

Erdem et al. [18] emphasized the significance of early diagnosis and identification of risk factors in combating heart disease, a leading cause of global mortality. Recognizing the challenges in traditional diagnosis methods, the study explores the efficacy of seven machine learning algorithms on a dataset with 4238 records and 16 patient characteristics. Naive Bayes, Decision Trees, Random Forests, Support Vector Machines (SVM), Artificial Neural Networks (ANNs), K Nearest Neighbors, and Logistic Regressions achieve accuracies of 78.9%, 79.9%, 83.9%, 70.9%, 83.7%, 83.4%, and 85.5%, respectively [18].

The literature in this section delves deeply into the topic of heart disease by various aspects, risk factors, and potential treatments. Additionally, it focuses on the application of artificial intelligence techniques, such as machine learning for the classification and detection of heart diseases. Throughout this section, numerous studies have been conducted to illuminate advancements and findings in the field of cardiology. The data presented in Table 1 encompasses previous research related to heart diseases.

Different machine learning algorithms have been suggested for the classification of heart diseases. The results obtained in the research using ensemble methods in the effective diagnosis of heart disease, paving the way for more accurate and efficient diagnostic tools in healthcare.

Table 1. *Summary of previously published studies on heart diseases*

Dataset	**Methods**	**Accuracy**	**References**
297	Hybrid Random Forest with Linear Model (HRFLM)	88.70%	[5]
-	Naive Bayes	89.70%	[6]
76 features and 14 attributes	Naive Bayes	86.6%	[7]
303 samples and 76 features	Naive Bayes	88.15%	[8]
303	Random Forest	88.52%	[9]
76 features and 14 attributes	Hybrid Naïve Bayes, Support Vector Machine, and Artificial Neural Network	88.54%	[10]
303 samples and 14 features	Using Talos optimization for Deep Neural Network	90.76%	[11]
303 samples and 14 features	Random Forest	86.89%	[12]
303 samples and 14 features	Hybrid Random Forest and Decision Tree	88.70%	[3]
303 samples and 76 features	Random Forest	86.60%	[13]
13 medical features and 304 patients	K-Nearest Neighbor	88.52%	[14]
13 features and 383 individual values	Support Vector Machine	86%	[15]

Table 1 continued…

Dataset	Methods	Accuracy	References
303 samples and 13 features	Support Vector Machine	91.67%	[16]
303 samples and 76 features	EGA-FWSVM	91.68%	[17]
4238 records and 16 patient characteristics	NB, DT, RF, SVM, ANNs, KNN, LR.	78.90%, 79.90%, 83.90%, 70.90%, 83.70%, 83.40%, 85.50%	[18]

Materials and Methods

The scope of the article involves the use of a single dataset for the detection of heart disease. For this purpose, AdaBoost, Stacking, and Gradient Boosting algorithms were employed. The steps followed to complete the research are illustrated in Figure 1, and the study was conducted successfully.

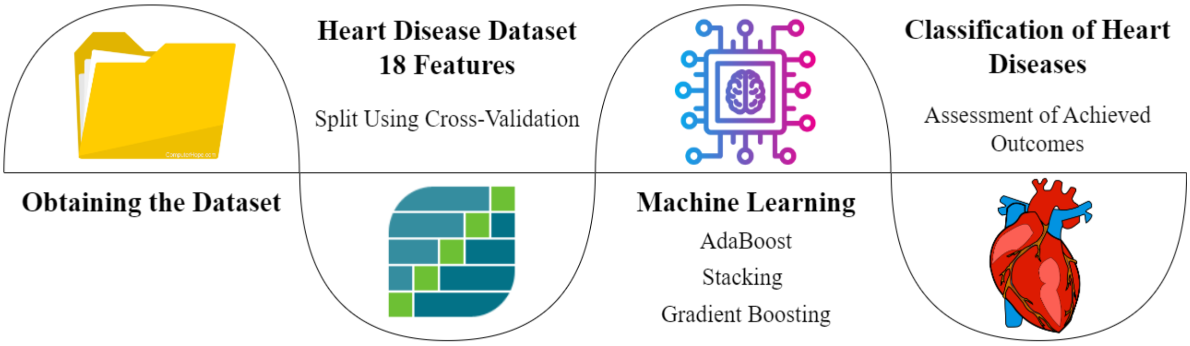

Figure 1. *Flow diagram depicting the evaluation of classification performances for heart disease detection*

Dataset

The dataset used for diagnosing heart disease is the (Heart Disease) dataset, obtained from the Kaggle data sharing site. Originally published by Abu Bakar Siddique Mahi [19], this dataset encompasses 18 different patient features [20-23]. In total, there are 319795 records were included in the dataset. The values and value ranges of the features in this dataset are presented in Figure 2 [24]. The data were split into training and testing sets using the cross-validation technique. Dividing the dataset into 10 and using 1 part as test and the rest as train. Then changing the test in the second fold and leaving the rest as train data. Table 2 provides an overview of the patient characteristics in the heart disease dataset.

Table 2. *Patient characteristics in the heart disease dataset*

Patient Characteristics					
1	Heart Disease	7	Mental Health Status	13	Physical Activity
2	BMI (Body Mass Index)	8	Walking Difficulty	14	General Health Status
3	Smoking	9	Gender	15	Sleep Duration
4	Alcohol Consumption	10	Age Category	16	Asthma
5	Stroke	11	Race	17	Kidney Disease
6	Physical Health Status	12	Diabetes Status	18	Skin Cancer

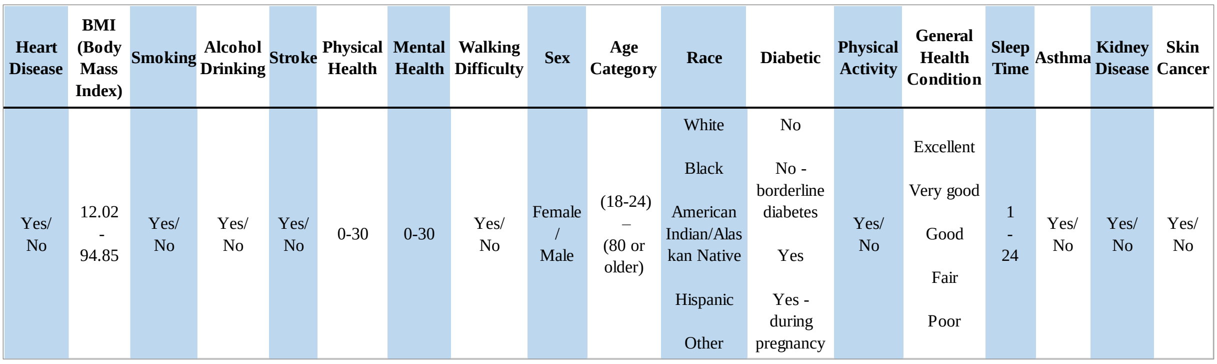

Heart Disease	**BMI (Body Mass Index)**	**Smoking**	**Alcohol Drinking**	**Stroke**	**Physical Health**	**Mental Health**	**Walking Difficulty**	**Sex**	**Age Category**	**Race**	**Diabetic**	**Physical Activity**	**General Health Condition**	**Sleep Time**	**Asthma**	**Kidney Disease**	**Skin Cancer**
Yes/ No	12.02 - 94.85	Yes/ No	Yes/ No	Yes/ No	0-30	0-30	Yes/ No	Female / Male	(18-24) – (80 or older)	White Black American Indian/Alaskan Native Hispanic Other	No No - borderline diabetes Yes Yes - during pregnancy	Yes/ No	Excellent Very good Good Fair Poor	1 - 24	Yes/ No	Yes/ No	Yes/ No

Figure 2*. Values and value ranges of the features in the dataset*

Cross Validation

Cross-validation is an important evaluation method that better assesses how a machine learning model will generalize to real-world data and measures the model's performance more reliably. Another objective of the model is to detect issues such as overfitting. The most common cross-validation technique is known as "k-fold cross-validation" [25]. In this method, the dataset is divided into k subsets. Then, the model is trained and tested k times. For each training-test pair, performance metrics of the model are recorded. Ultimately, a performance value is obtained based on the number of iterations. K-fold cross-validation may incur additional costs, particularly in large datasets, as it requires k rounds of model training and testing [26]. Although extra time is recuired to ensure a more accurate performance assessment of the model, this is disadvantage [27]. The diagram of the cross-validation method is presented in Figure 3.

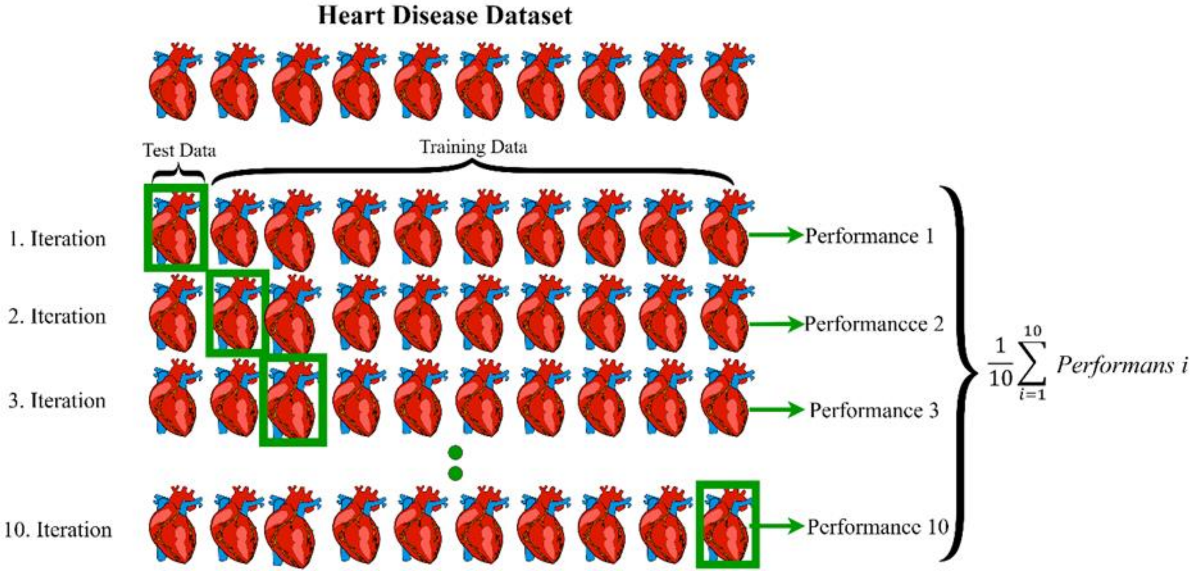

Figure 3. *Diagram of the cross-validation method*

Performance Metric and Confusion Matrix

The confusion matrix is a metric table used to evaluate the performance of classification algorithms in machine learning and statistical modeling. In classification problems, it can be considered of as a summary table that shows instances of data that a model classifies correctly or incorrectly. For a binary classification problem, the confusion matrix attempting to distinguish between two classes includes four different terms: True Positives, True Negatives, False Positives, and False Negatives [28, 29]. These terms, and their explanations, are included in Table 3.

Table 3. *Confusion matrix with explanations*

		Actual Class	
		Positive	***Negative***
Predicted Class	***Positive***	**TP** True Positives (TP) represents the number of data points that the model correctly predicted as positive.	**FP** False Positives (FP) represents the number of data points that the model incorrectly predicted as positive when they actually should be negative.
	Negative	**FN** False Negatives (FN) represents the number of data points that the model incorrectly predicted as negative when they actually should be positive.	**TN** True Negatives (TN) represents the number of data points that the model correctly predicted as negative.

A performance metric is a criterion or measure used to assess and evaluate the success level of a model or system. These metrics help us understand the strengths and weaknesses of a model by determining various features such as accuracy, precision, recall, F1 score, among others [30]. Confusion matrix is used to calculate various measurements when evaluating the performance of a model [28, 31].

Accuracy is a good choice when there is a balanced distribution among classes in the dataset, and the sizes of the classes are similar. It shows the ratio of correctly predicted data points to all data points [32].

$$(TN + TP)/(TN + FP + TP + FN) \tag{5}$$

Precision is a good choice when the class distribution is imbalanced or when the cost of false positives is high. It shows the ratio of correctly predicted positive data points to the total predicted positive data points.

$$TP/(TP + FP) \tag{6}$$

Recall, also known as Sensitivity, is important when the cost of false negatives (FN) is high or when the class of primary interest is rare and crucial. It shows the ratio of correctly predicted positive data points to the total actual positive data points.

$$TP/(TP + FN) \tag{7}$$

F1 Score is important when there is imbalance among classes or when the cost of false positives and false negatives is comparable. It is a metric that combines precision and recall.

$$2 * (Precision * Recall)/(Precision + Recall) \tag{8}$$

Ensemble Learning Techniques in Machine Learning

Throughout this research endeavor, we leveraged the capabilities of AdaBoosting, Stacking, and Gradient Boosting techniques to refine our analytical framework. This section provides a nuanced exposition of each method, elucidating their distinct applications and contributions to the overarching methodology implemented in our study.

Ensemble methods provide notable benefits compared with individual machine learning techniques, principally because they can merge many models to attain superior performance and generalization. These techniques frequently produce greater accuracy than individual models by mitigating the risk of overfitting and enhancing resilience. Ensemble approaches can decrease the variability of predictions by taking the averaging of numerous models. This is especially advantageous for minimizing the influence of outliers and noise in the data. Ensemble approaches have a tendency to exhibit superior generalization capabilities when applied to unknown data, leading to more dependable and consistent predictions. Moreover, these techniques are adaptable and varied, able to integrate several models such as decision trees, neural networks, and logistic regression, so utilizing the advantages of each to enhance overall performance. Boosting and bagging are techniques that are especially developed to address the problem of overfitting. Boosting aims to repair the errors made by weak learners, while bagging decreases overfitting by averaging the predictions of many models trained on distinct subsets of the data. When comparing the three main ensemble approaches - boosting, stacking, and bagging - it becomes apparent that each method has its own distinctive attributes and advantages. Boosting is a technique that applies weak learners to the data in a sequential manner, where each learner corrects the errors made by the previous one. This method provides exceptional precision and the capability to manage intricate data patterns, demonstrating excellent performance even on datasets with uneven distributions. Nevertheless, the process of boosting might be susceptible to overfitting if not adequately regularized and requires significant computer resources. Some examples of algorithms are AdaBoost, Gradient Boosting, and XGBoost. Stacking is a technique that entails training several base learners and then using a meta-learner to merge their predictions. This approach provides significant adaptability by integrating various models, frequently resulting in enhanced performance by capitalizing on the advantages of distinct models. Nevertheless, the implementation and fine-tuning of stacking are more intricate, resulting in a greater computational burden since many models need to be trained. Bagging is a technique that entails training numerous models separately on various subsets of the data, which are generated using bootstrapping. The predictions of these models are then averaged. This method effectively decreases variance and overfitting, is straightforward to execute, and may be parallelized. Nevertheless, its performance is diminished when applied to datasets with significant bias and it can be computationally burdensome when dealing with really big datasets. Some examples of algorithms are Random Forest and Bagged Decision Trees.

AdaBoost

In the initial stage, a weak learner model is created when data samples have equal weights. It is evaluated on the data samples, and as misclassified examples' weights increase, the weights of correctly classified examples decrease. Then, subsequent models are created by focusing on the previous errors. The predictions of all models are combined predominantly with weights [33]. The combination of these steps results in a strong model. AdaBoost can achieve higher accuracy in classification problems by combining low-performing models [34]. The diagram of a two-class AdaBoost classifier designed to distinguish individuals with and without heart disease is shown in Figure 4.

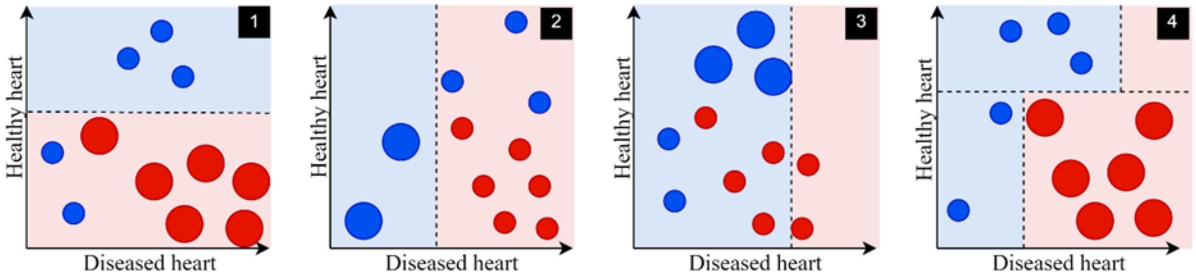

***Figure 4**. Two-Class AdaBoost diagram*

Stacking

Stacking is a machine learning algorithm that is used as an ensemble learning technique. Ensemble learning aims to improve predictions or classifications by combining the results of multiple learning algorithms. Stacking is a new framework in ensemble learning that uses meta-learners to combine the results generated by each base learner [35, 36]. Base learners are referred to as first-level learners, and combiners are called meta-learners or second-level learners. Stacking first trains the first-level learner using the initial training dataset. Then, the output of the first-level learner is used as the input feature for the meta-learner. Finally, a new dataset is created by using the relevant original labels as new labels to train the meta-learner. If the learners at the first level use the same type of learning algorithm, theyit are called homogeneous ensembles; otherwise, they are called heterogeneous ensembles [37-40]. The diagram of an example Stacking classifier is shown in Figure 5. Stacking is a method used in machine learning that creates a meta-model by combining numerous basic models. The Stacking widget incorporates an Aggregate input that is used to merge the input models. The models used for the heart disease dataset were AdaBoost and Gradient Boosting.

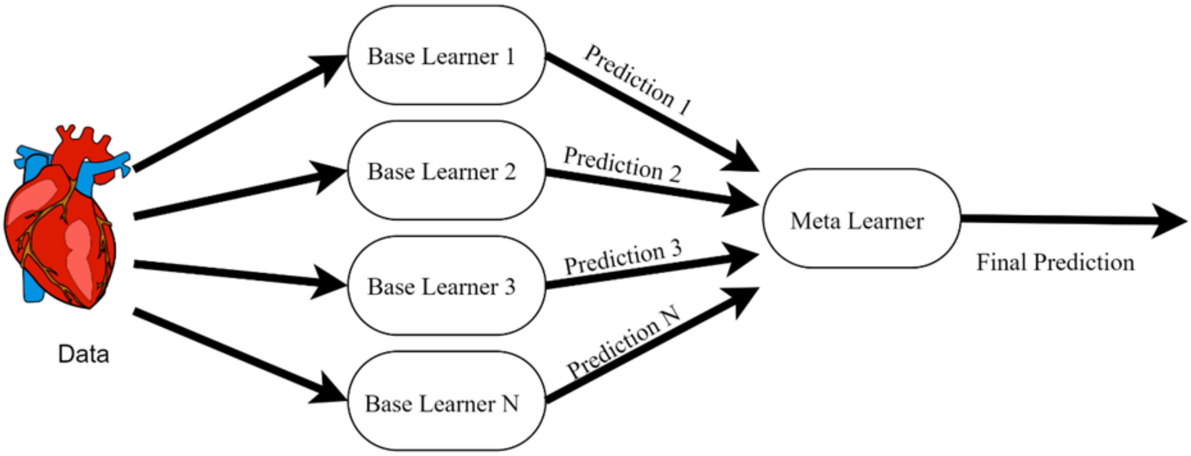

Figure 5. *Stacking diagram*

Gradient Boosting

Gradient Boosting is a widely used ensemble learning method in the field of machine learning. This technique builds weak learner models sequentially, allowing each subsequent model to focus on the errors of the previous ones. As a result, a new model is created, leading to the development of a strong predictive model. Gradient Boosting is particularly effective in regression and classification problems, providing high performance [41]. The diagram of the gradient boosting algorithm is shown in Figure 6.

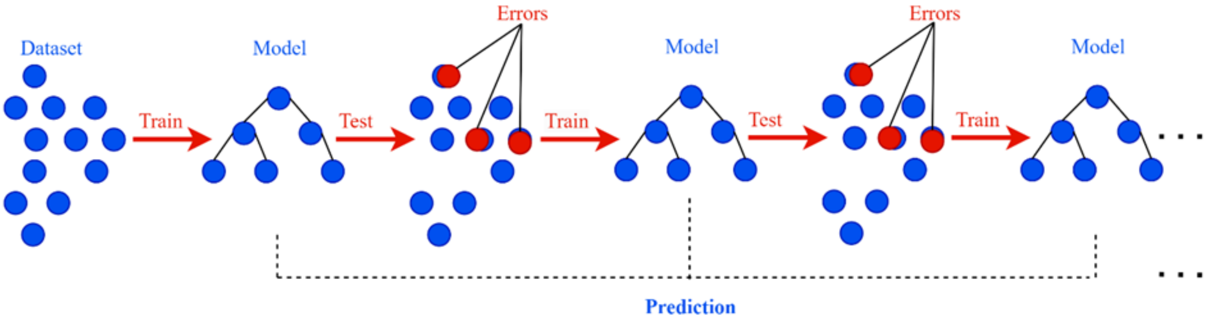

***Figure 6**. Diagram of the Gradient Boosting algorithm*

The AdaBoost method was used in our investigation with predefined parameter settings. The decision tree was chosen as the base estimator, and a total of 50 estimators were used in the boosting procedure. The learning rate for AdaBoost was adjusted to 1.00000, which increased the importance of the contribution of each weak learner. In addition, the classification boosting approach utilized the SAMME.R algorithm, whereas for regression tasks, the loss function used was linear. A specific set of parameters was employed to efficiently train the models using gradient boosting. In this instance, the ensemble employed a total of 100 trees, while maintaining a moderate learning rate of 0.100. In order to manage the growth of trees in the group, a particular parameter was used to restrict the number of levels in each tree to a maximum of 3. The parameter configurations were meticulously selected to strike a balance between the complexity of the model and its predictive accuracy across different tasks in our investigation.

Experimental Results

The classification results using AdaBoost, Stacking, and Gradient Boosting methods are presented in this section. In the dataset used in the study, there are a total of 319795 records. The hardware specifications used to run these algorithms are shown in Table 4.

***Table 4.** Specifications of the hardware used in the study*

HARDWARE UNIT	FEATURES
CPU	Intel® Core i7™ 12700 K 3.61 GHz
RAM	64 GB
Graphics Card	NVIDIA GeForce RTX 3080 Ti
Operating System	Windows 11

In the study, confusion matrices were used to evaluate the performance of classification algorithms. A separate confusion matrix was created for each classification algorithm [42-44], and performance analyses were conducted using the TP (True Positive), TN (True Negative), FP (False Positive), and FN (False Negative) values in these matrices. During the training of the algorithms, cross-validation was employed to achieve a more accurate classification result. In this method, the k value was set to 10. The average classification accuracies of the AdaBoost, Stacking, and Gradient Boosting methods applied in the study are summarized in Table 5.

Table 5. *Performance metric results for the applied methods*

	AdaBoost	Stacking	Gradient Boosting
Accuracy	88.80%	91.50%	91.60%
Precision	87.0%	89.0%	89.0%
Recall	88.80%	91.5%	91.6%
F1-Score	87.80%	89.3%	89.0%

With the AdaBoost algorithm, the classification of heart disease achieved an accuracy rate of 88.80% in 273.46 seconds of training time and 5.02 seconds of testing time. The Stacking algorithm achieved an accuracy of 91.50% with 2777.97 seconds of training time and 6.20 seconds of testing time. The most impressive result was obtained with the Gradient Boosting algorithm, which classified heart disease with an accuracy rate of 91.60%, 291.04 seconds of training time, and 1.15 seconds of testing time. A comparison of the performance times (training time and testing time) of the algorithms is better visualized in Figure 7 and Figure 8.

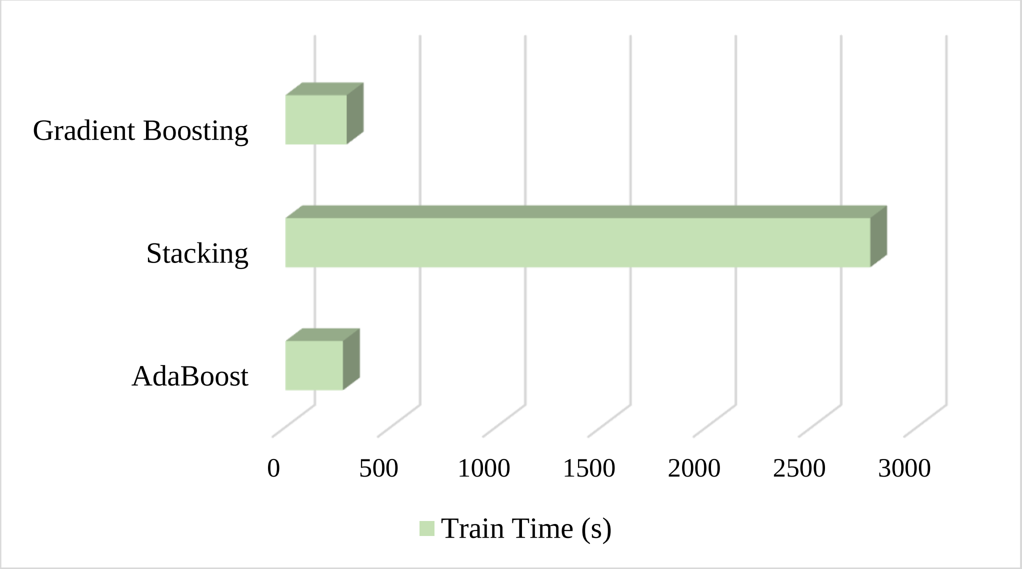

Figure 7. *Training time graph for all machine learning algorithms*

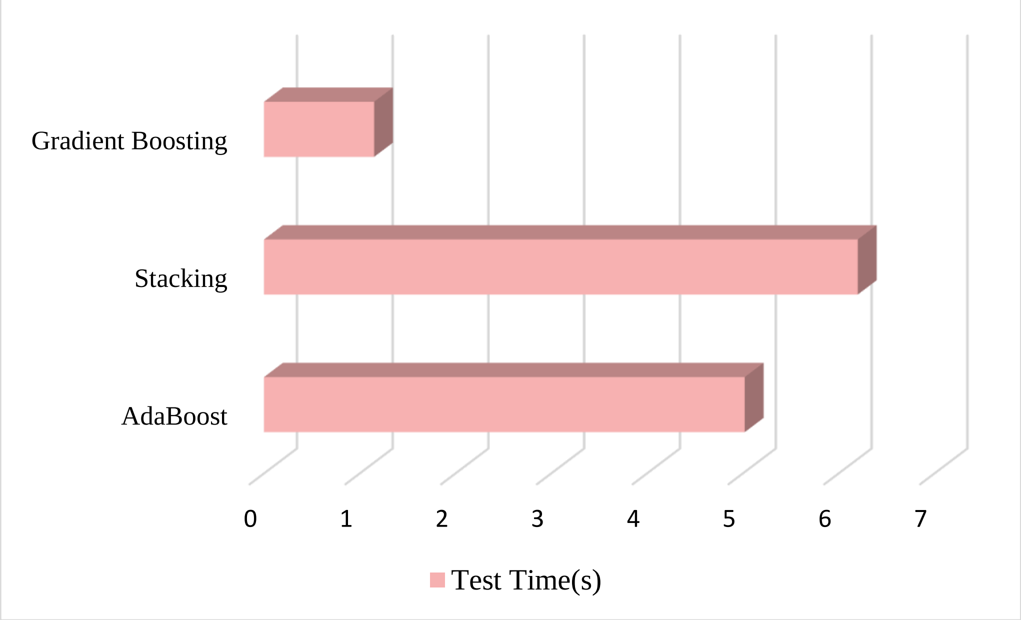

Figure 8. *Testing time graph for all machine learning algorithms*

Figure 9 includes the confusion matrix for machine learning algorithms. Without any feature extraction, AdaBoost achieved an accuracy of 88.80%, Stacking 91.50%, and Gradient Boosting 91.60%. Based on the confusion matrix in Figure 9, when classifying the diagnosis of heart disease, it correctly classified 290331 records as a healthy heart and predicted them as a healthy heart while using Gradient Boosting. At the same time, using Gradient Boosting, it correctly identified 2594 images as a diseased heart. The Gradient Boosting model misclassified 2091 images from healthy heart images and 24779 images from diseased heart images, as shown in Figure 9.

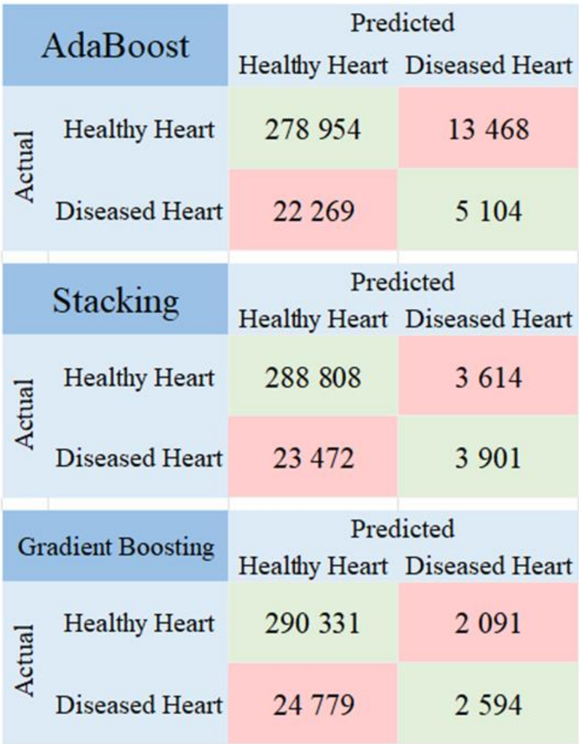

AdaBoost		Predicted	
		Healthy Heart	Diseased Heart
Actual	Healthy Heart	278 954	13 468
	Diseased Heart	22 269	5 104

Stacking		Predicted	
		Healthy Heart	Diseased Heart
Actual	Healthy Heart	288 808	3 614
	Diseased Heart	23 472	3 901

Gradient Boosting		Predicted	
		Healthy Heart	Diseased Heart
Actual	Healthy Heart	290 331	2 091
	Diseased Heart	24 779	2 594

Figure 9*. Confusion matrix for AdaBoost, Stacking, and Gradient Boosting algorithms*

Despite not finding any articles for comparison on the same dataset, we discovered Kaggle code executions using the same dataset. The dataset's link, as provided on Kaggle, was included in the data availability section. Notably, the machine learning results obtained in our study are higher than those reported on Kaggle.

Receiver Operating Characteristic (ROC) curve is used to evaluate the performance of classification models by plotting the True Positive Rate (TPR) against the False Positive Rate (FPR) at various threshold settings, with the area under the ROC curve (AUC) serving as a measure of the model's ability to distinguish between classes. AdaBoost combines multiple weak learners to create a strong classifier, with each subsequent model attempting to correct the errors of the previous models. Gradient Boosting operates similarly to AdaBoost but builds models sequentially, training each new model to correct the errors made by its predecessors. Stacking involves training multiple models, such as AdaBoost and Gradient Boosting, and then combining their predictions using another model to improve overall performance. The ROC curve is shown in Figure 10.

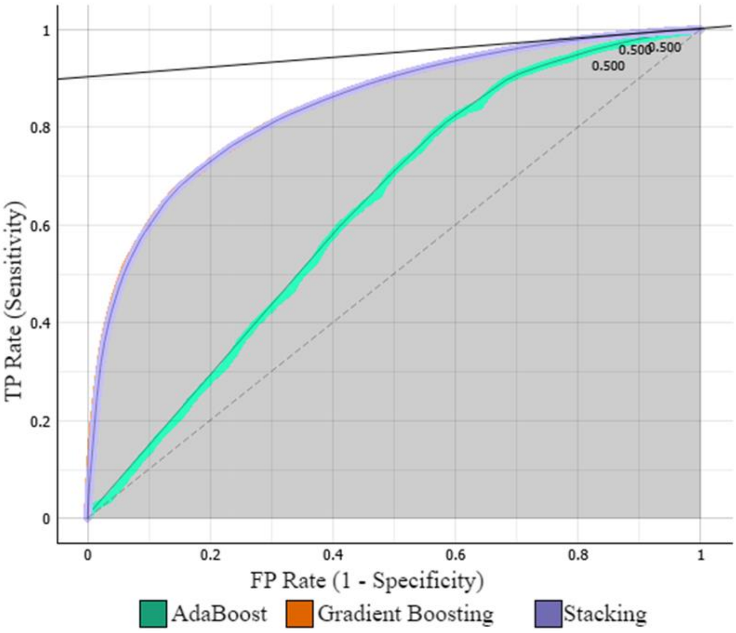

Figure 10. *ROC curve for AdaBoost, Stacking, and Gradient Boosting algorithms*

The ROC results focus on identifying the 'No' class, indicating individuals without heart disease. Both false positive and false negative prediction errors have an associated cost of 500. With a target probability threshold of 91.0%, models predicting a 91.0% chance or higher of an individual not having heart disease classify them as 'No.' A higher Area Under the Curve (AUC) value suggests a better-performing model. Comparing AUC values for AdaBoost, Gradient Boosting, and the stacking ensemble helps identify which model best distinguishes between individuals with and without heart disease. Since false positive and false negative costs are equal, balancing sensitivity (True Positive Rate) and specificity (1 - False Positive Rate) is essential. The 91.0% threshold reflects a conservative approach to avoid false negatives.

Conclusion

The present study assessed the efficacy of three ensemble machine learning algorithms—AdaBoost, Stacking, and Gradient Boosting—by analyzing a dataset consisting of 319795 records with 18 variables pertaining to heart disease. The efficacy of these algorithms was evaluated by doing statistical analysis on the confusion matrices obtained from their classification outcomes.

Of the algorithms assessed, Gradient Boosting proved to be the most effective, attaining an accuracy rate of 91.6%. It had a training time of 291.04 seconds and a testing time of 1.15 seconds. The performance of the algorithm highlights its ability process extensive datasets and a multitude of attributes efficiently. The Stacking approach achieved a high accuracy rate of 91.5%, but it necessitated a somewhat longer training duration. Although AdaBoost achieved an accuracy of 88.8%, it outperformed the other two algorithms.

The study emphasizes the potential of ensemble approaches in the early detection of cardiac disease. The exceptional efficacy of Gradient Boosting, specifically, indicates its appropriateness for medical applications of this nature. Subsequent investigations may delve into the incorporation of supplementary data mining methodologies and the creation of more intricate models to augment the predicted precision for diagnosing heart disease.

In its entirety, the research highlights the effectiveness of ensemble machine learning algorithms in identifying heart illness, particularly Gradient Boosting, which stands out for its quick and precise performance. This study establishes the foundation for future research endeavors focused on enhancing early detection and treatment approaches using sophisticated machine learning methods.

Data Availability

The dataset can be accessed using the links provided:

https://www.kaggle.com/datasets/abubakarsiddiquemahi/heart-disease-dataset

https://www.kaggle.com/code/sumitkumarprasad/heart-disease-prediction-with-gradio-deployment

Acknowledgement We would like to thank the Scientific Research Coordinator of Selcuk University for their support with the project titled “Diagnosis and Classification of Heart Disease with Artificial Intelligence Techniques” numbered 23401163

Funding/Financial Disclosure The authors declare that they have no financial interests or relationships pertaining to the publication of this article

Ethics Committee Approval and Permissions The study does not require ethics committee approval or any special permission.

Conflicts of Interest The authors declared no conflict of interest.

Authors Contribution All authors read and approved the final manuscript.

References

[1] Erdem, K., & Duman, A. (2023). Pulmonary artery pressures and right ventricular dimensions of post-COVID-19 patients without previous significant cardiovascular pathology. *Heart & Lung*, *57*, 75-79. https://doi.org/10.1016/j.hrtlng.2022.08.023

[2] Erdem, K., Kobat, M. A., Bilen, M. N., Balik, Y., Alkan, S., Cavlak, F., Poyraz, A. K., Barua, P. D., Tuncer, I., & Dogan, S. (2023). Hybrid-Patch-Alex: A new patch division and deep feature extraction-based image classification model to detect COVID-19, heart failure, and other lung conditions using medical images. *International Journal of Imaging Systems and Technology*, *33*(4), 1144-1159. https://doi.org/10.1002/ima.22914

[3] Kavitha, M., Gnaneswar, G., Dinesh, R., Sai, Y. R., & Suraj, R. S. (2021). Heart disease prediction using hybrid machine learning model. 2021 6th international conference on inventive computation technologies (ICICT). Coimbatore, India, 1329-1333. https://doi.org/10.1109/ICICT50816.2021.9358597.

[4] Buber, M., Fadime, S., Bulut, I., & Kursun, R. (2015). Cloud computing environments which can be used in health education. *International Journal of Intelligent Systems and Applications in Engineering*, *3*(4), 124-126. https://doi.org/10.18201/ijisae.92756

[5] Mohan, S., Thirumalai, C., & Srivastava, G. (2019). Effective heart disease prediction using hybrid machine learning techniques. *IEEE Access*, *7*, 81542-81554. https://doi.org/10.1109/ACCESS.2019.2923707

[6] Repaka, A. N., Ravikanti, S. D., & Franklin, R. G. (2019). Design and implementing heart disease prediction using naives Bayesian. 2019 3rd International conference on trends in electronics and informatics (ICOEI). Tirunelveli, India, 292-297, https://doi.org/10.1109/ICOEI.2019.8862604

[7] Anitha, S., & Sridevi, N. (2019). Heart disease prediction using data mining techniques. *Journal of Analysis and Computation*, *7*(2), 48-55.

[8] Shah, D., Patel, S., & Bharti, S. K. (2020). Heart disease prediction using machine learning techniques. *SN Computer Science*, *1*, 1-6. https://doi.org/10.1007/s42979-020-00365-y

[9] Motarwar, P., Duraphe, A., Suganya, G., & Premalatha, M. (2020). Cognitive approach for heart disease prediction using machine learning. 2020 international conference on emerging trends in information technology and engineering (ic-ETITE). Vellore, India, 1-5, https://doi.org/10.1109/ic-ETITE47903.2020.242

[10] Junaid, M. J. A., & Kumar, R. (2020). Data science and its application in heart disease prediction. 2020 International Conference on Intelligent Engineering and Management (ICIEM). London, UK, 396-400, https://doi.org/10.1109/ICIEM48762.2020.9160056

[11] Sharma, S., & Parmar, M. (2020). Heart diseases prediction using deep learning neural network model. *International Journal of Innovative Technology and Exploring Engineering (IJITEE)*, *9*(3), 2244-2248. https://doi.org/10.35940/ijitee.C9009.019320.

[12] Anbuselvan, P. (2020). Heart disease prediction using machine learning techniques. *International Journal of Engineering Research & Technolog*, *9*(11), 515-518.

[13] Rani, P., Kumar, R., Ahmed, N. M. S., & Jain, A. (2021). A decision support system for heart disease prediction based upon machine learning. *Journal of Reliable Intelligent Environments*, *7*(3), 263-275. https://doi.org/10.1007/s40860-021-00133-6

[14] Jindal, H., Agrawal, S., Khera, R., Jain, R., & Nagrath, P. (2021). Heart disease prediction using machine learning algorithms. *IOP Conference Series: Materials Science and Engineering*, *1022*(1), 01-10. https://doi.org/ 10.1088/1757-899X/1022/1/012072

[15] Goel, R. (2021). Heart disease prediction using various algorithms of machine learning. Proceedings of the International Conference on Innovative Computing & Communication (ICICC). Delhi, India, https://dx.doi.org/10.2139/ssrn.3884968

[16] Boukhatem, C., Youssef, H. Y., & Nassif, A. B. (2022). Heart disease prediction using machine learning. 2022 Advances in Science and Engineering Technology International Conferences (ASET). Dubai, United Arab Emirates, 1-6, https://doi.org/10.1109/ASET53988.2022.9734880

[17] Sugendran, G., & Sujatha, S. (2023). Earlier identification of heart disease using enhanced genetic algorithm and fuzzy weight based support vector machine algorithm. *Measurement: Sensors*, 100814. https://doi.org/10.1016/j.measen.2023.100814.

[18] Erdem, K., Yildiz, M. B., Yasin, E. T., & Koklu, M. (2023). A Detailed Analysis of Detecting Heart Diseases Using Artificial Intelligence Methods. *Intelligent Methods in Engineering Sciences*, *2*(4), 115-124. https://doi.org/10.58190/imiens.2023.4

[19] Mahi, A. B. S. (2023). Heart disease dataset (Version 1) [Dataset]. Kaggle. https://www.kaggle.com/datasets/abubakarsiddiquemahi/heart-disease-dataset, Community Data License Agreement – Sharing, Version 1.0

[20] Ozkan, I. A., & Koklu, M. (2017). Skin lesion classification using machine learning algorithms. *International Journal of Intelligent Systems and Applications in Engineering*, *5*(4), 285-289.

[21] Ozkan, I. A., Koklu, M., & Sert, I. U. (2018). Diagnosis of urinary tract infection based on artificial intelligence methods. *Computer Methods and Programs in Biomedicine*, *166*, 51-59. https://doi.org/10.1016/j.cmpb.2018.10.007

[22] Koklu, M., & Unal, Y. (2013). Analysis of a population of diabetic patients databases with classifiers. *International Journal of Biomedical and Biological Engineering*, *7*(8), 481-483.

[23] Tunc, A., Tasdemir, S., Koklu, M., & Cinar, A. C. (2022). Age group and gender classification using convolutional neural networks with a fuzzy logic-based filter method for noise reduction. *Journal of Intelligent & Fuzzy Systems*, *42*(1), 491-501. https://doi.org/10.3233/JIFS-219206.

[24] Prasad S. k. (2022). Heart disease prediction with gradio deployment (Version 1) [Dataset]. Kaggle. https://www.kaggle.com/code/sumitkumarprasad/heart-disease-prediction-with-gradio-deployment/notebook

[25] Butuner, R., Cinar, I., Taspinar, Y. S., Kursun, R., Calp, M. H., & Koklu, M. (2023). Classification of deep image features of lentil varieties with machine learning techniques. *European Food Research and Technology*, *249*, 1303–1316. https://doi.org/10.1007/s00217-023-04214-z

[26] Taspinar, Y. S., Koklu, M., & Altin, M. (2021). Fire Detection in Images Using Framework Based on Image Processing, Motion Detection and Convolutional Neural Network. *International Journal of Intelligent Systems and Applications in Engineering*, *9*(4), 171-177. https://doi.org/10.18201/ijisae.2021473636

[27] Yasin, E. T., & Koklu, M. (2023, April 28-30). Classification of Organic and Recyclable Waste based on Feature Extraction and Machine Learning Algorithms. International Conference on Intelligent Systems and New Applications (ICISNA'23). Liverpool, United Kingdom. 59-65.

[28] Yasin, E. T., Ozkan, I. A., & Koklu, M. (2023). Detection of fish freshness using artificial intelligence methods. *European Food Research and Technology, 249,* 1979-1990. https://doi.org/10.1007/s00217-023-04271-4

[29] Koklu, M., & Sabanci, K. (2015). The classification of eye state by using kNN and MLP classification models according to the EEG signals. *International Journal of Intelligent Systems and Applications in Engineering*, *3*(4), 127-130.

[30] Cinar, I., & Koklu, M. (2021). Determination of effective and specific physical features of rice varieties by computer vision in exterior quality inspection. *Selcuk Journal of Agriculture and Food Sciences, 35*(3), 229-243.

[31] Al Bataineh, A., & Manacek, S. (2022). MLP-PSO hybrid algorithm for heart disease prediction. *Journal of Personalized Medicine*, *12*(8), 1208. https://doi.org/10.3390/jpm12081208

[32] Cinar, I., Taspinar, Y. S., Kursun, R., & Koklu, M. (2022). Identification of Corneal Ulcers with Pre-Trained AlexNet Based on Transfer Learning. 2022 11th Mediterranean Conference on Embedded Computing (MECO). Budva, Montenegro, 1-4. https://doi.org/10.1109/MECO55406.2022.9797218

[33] Tutuncu, K., Cinar, I., Kursun, R., & Koklu, M. (2022). Edible and poisonous mushrooms classification by machine learning algorithms. 2022 11th Mediterranean Conference on Embedded Computing (MECO), Budva, Montenegro, 1-4. https://doi.org/10.1109/MECO55406.2022.9797212

[34] Mahesh, T., Dhilip Kumar, V., Vinoth Kumar, V., Asghar, J., Geman, O., Arulkumaran, G., & Arun, N. (2022). AdaBoost ensemble methods using K-fold cross validation for survivability with the early detection of heart disease. *Computational intelligence and neuroscience*, 2022, Article ID 9005278, https://doi.org/10.1155/2022/9005278.

[35] Cui, S., Yin, Y., Wang, D., Li, Z., & Wang, Y. (2021). A stacking-based ensemble learning method for earthquake casualty prediction. *Applied Soft Computing, 101,* 107038. https://doi.org/10.1016/j.asoc.2020.107038

[36] Taspinar, Y. S., Cinar, I., & Koklu, M. (2022). Classification by a stacking model using CNN features for COVID-19 infection diagnosis. *Journal of X-ray Science and Technology, 30*(1), 73-88.

[37] Chiu, C.-C., Wu, C.-M., Chien, T.-N., Kao, L.-J., Li, C., & Jiang, H.-L. (2022). Applying an improved stacking ensemble model to predict the mortality of ICU patients with heart failure. *Journal of Clinical Medicine*, *11*(21), 6460. https://doi.org/10.3390/jcm11216460

[38] Papouskova, M., & Hajek, P. (2019). Two-stage consumer credit risk modelling using heterogeneous ensemble learning. *Decision Support Systems*, *118,* 33-45. https://doi.org/10.1016/j.dss.2019.01.002.

[39] Jiang, M., Liu, J., Zhang, L., & Liu, C. (2020). An improved Stacking framework for stock index prediction by leveraging tree-based ensemble models and deep learning algorithms. *Physica A: Statistical Mechanics and its Applications*, *541*, 122272. https://doi.org/10.1016/j.physa.2019.122272

[40] Dong, Y., Zhang, H., Wang, C., & Zhou, X. (2021). Wind power forecasting based on stacking ensemble model, decomposition and intelligent optimization algorithm. *Neurocomputing*, *462*, 169-184. https://doi.org/10.1016/j.neucom.2021.07.084

[41] Bentéjac, C., Csörgő, A., & Martínez-Muñoz, G. (2021). A comparative analysis of gradient boosting algorithms. *Artificial Intelligence Review, 54*, 1937-1967. https://doi.org/10.1007/s10462-020-09896-5

[42] Koklu, M., Kahramanli, H., & Allahverdi, N. (2014). A new accurate and efficient approach to extract classification rules. *Journal of the Faculty of Engineering and Architecture of Gazi University, 29*(3), 477-486.

[43] Koklu, M., Kahramanli, H., & Allahverdi, N. (2012). A new approach to classification rule extraction problem by the real value coding. *International Journal of Innovative Computing, Information and Control, 8*(9), 6303-6315

[44] Koklu, M., Kahramanli, H., & Allahverdi, N. (2015. May 27-29). Applications of rule based classification techniques for thoracic surgery. Managing Intellectual Capital and Innovation for Sustainable and Inclusive Society: Managing Intellectual Capital and Innovation; Proceedings of the MakeLearn and TIIM Joint International Conference 2. Bari, Italy. 1991-1998.

Sinopfbd, 2024; 9(2): 388-420 **https://doi.org/10.33484/sinopfbd.1470329**

Sinop Üniversitesi Fen Bilimleri Dergisi
Sinop Uni J Nat Sci

E-ISSN: 2564-7873

https://dergipark.org.tr/tr/pub/sinopfbd

An Example of Classification Using a Neural Network Trained by the Zebra Optimization Algorithm

Emine BAŞ[1] and Şaban BAŞ[2]

How to cite: Baş, E., & Baş, Ş. (2024). An example of classification using a neural network trained by the zebra optimization algorithm. *Sinop Üniversitesi Fen Bilimleri Dergisi, 9*(2), 388-420. https://doi.org/10.33484/sinopfbd.1470329

Research Article

Corresponding Author
Emine BAŞ
ebas@ktun.edu.tr

ORCID of the Authors
E.B: 0000-0003-4322-6010
Ş.B: 0000-0002-4142-6580

Received: 18.04.2024
Accepted: 07.08.2024

Abstract

Artificial intelligence techniques are a broad field of research with training, computation and prediction capabilities. Among these techniques, artificial neural networks (ANNs) are widely used as a predictive model. Learning algorithms in ANN classifiers have great importance on the success of ANN. The ANN model generally uses gradient-based learning models. However, due to the disadvantages of gradient-based learning models in local search, they have begun to be replaced by heuristic-based algorithms in recent years. Heuristic algorithms have attracted the attention of many researchers in recent years due to their success in problem solving. In this study, the Zebra Optimization Algorithm (ZOA), which has been proposed recently to train ANN networks, was examined. The main purpose of this study is to train the neural network using ZOA and increase the sensitivity of the perceptron neural network. In this study, a new ANN network integrated with ZOA is proposed. In this study, a detailed parameter analysis was carried out to show the effect of the population size and maximum generation number parameter settings, which form the basis for ZOA, on the ANN network. Then, a parameter analysis was carried out for the number of layers, number of neurons and epoch values, which are important for ANN networks. Such an ideal ANN network has been identified. This ideal ANN model was run on seven different data sets and was successful in predicting accurate data. In addition, three different heuristic algorithms (Gazelle Optimization Algorithm (GOA), Prairie Dogs Optimization (PDO), and Osprey Optimization Algorithm (OOA)) selected from the literature were integrated on the same ANN model and compared with the results of ANN integrated with ZOA operated under similar conditions. The results reveal that the proposed algorithm leads to greater convergence with the neural network coefficient compared to other algorithms. In addition, the proposed method caused the prediction error in the neural network to decrease.

Keywords: ANN, zebra, layer, neuron, network, prediction

Zebra Optimizasyon Algoritması Tarafından Eğitilmiş Bir Sinir Ağının Kullanıldığı Sınıflandırma Örneği

Öz

Yapay zeka teknikleri eğitim, hesaplama ve tahmin yeteneklerine sahip geniş bir araştırma alanıdır. Bu teknikler arasında yapay sinir ağları (YSA) tahmin modeli olarak yaygın olarak kullanılmaktadır. YSA

[1]Konya Technical University, Faculty of Engineering and Nature Sciences, Department of Software Engineering, Konya, Türkiye

[2]Selcuk University, Beyşehir Ali Akkanat Vocational School, Konya, Türkiye

sınıflandırıcılarındaki öğrenme algoritmaları YSA'nın başarısı üzerinde büyük önem taşımaktadır. YSA modeli genellikle gradyan tabanlı öğrenme modellerini kullanır. Ancak yerel aramada gradyan tabanlı öğrenme modellerinin dezavantajları nedeniyle son yıllarda yerini sezgisel tabanlı algoritmalar almaya başlamıştır. Sezgisel algoritmalar problem çözmedeki başarılarından dolayı son yıllarda birçok araştırmacının dikkatini çekmiştir. Bu çalışmada YSA ağlarının eğitimi için son dönemde önerilen Zebra Optimizasyon Algoritması (ZOA) incelenmiştir. Bu çalışmanın temel amacı sinir ağını ZOA kullanarak eğitmek ve algılayıcı sinir ağının duyarlılığını arttırmaktır. Bu çalışmada ZOA ile entegre yeni bir YSA ağı önerilmektedir. Bu çalışmada ZOA'ya temel oluşturan popülasyon büyüklüğü ve maksimum nesil sayısı parametre ayarlarının YSA ağı üzerindeki etkisini göstermek amacıyla detaylı bir parametre analizi yapılmıştır. Daha sonra YSA ağları için önemli olan katman sayısı, nöron sayısı ve çağ değerleri için parametre analizi yapılmıştır. Böyle ideal bir YSA ağı belirlendi. Bu ideal YSA modeli yedi farklı veri seti üzerinde çalıştırılmış ve doğru verileri tahmin etmede başarılı olmuştur. Ayrıca literatürden seçilen üç farklı sezgisel algoritma (Ceylan Optimizasyon Algoritması (GOA), Çayır Köpekleri Optimizasyonu (PDO), and Balıkkartalı Optimizasyon Algoritması (OOA)) aynı YSA modeli üzerine entegre edilmiş ve benzer koşullar altında çalışan ZOA ile entegre edilmiş YSA'nın sonuçları ile karşılaştırılmıştır. Sonuçlar, önerilen algoritmanın diğer algoritmalara göre sinir ağı katsayısı ile daha fazla yakınsamaya yol açtığını ortaya koymaktadır. Ayrıca önerilen yöntem sinir ağındaki tahmin hatasının azalmasına neden olmuştur.

Anahtar Kelimeler: ANN, zebra, katman, nöron, ağ, tahmin

Introduction

Artificial Neural Networks (ANNs), proposed in 1943, are one of the most widely used artificial intelligence approaches in the literature [1]. ANN was inspired by the biological nervous system. ANNs have been used in various problem solutions in recent years (classification, regression, pattern recognition, forecasting and time series problems, etc.) [2-5]. ANNs are a frequently used classifier in the field of data mining. ANNs can be used for supervised and unsupervised learning. Training of ANNs is one of the most important tasks. It has a complex structure. Classification error is minimized by updating the weights during the ANN training process. This means ANNs can recognize patterns and respond to their behavior accordingly [6-8]. There are two types of supervised trainers: deterministic trainers and stochastic trainers. Gradient descent and backpropagation-based methods are well-known deterministic trainers [9]. Learning algorithms used in ANN network training are generally gradient-based learning algorithms. These algorithms have several negative aspects. These algorithms depend on local minima and primary weights. Additionally, it may not show the same performance on all datasets [10, 11]. Therefore, despite their simplicity and fast convergence rates, they are not reliable in practical applications trainers [12]. Stochastic algorithms, on the other hand, start the learning process with stochastic solutions and improve them. Randomness is the most important feature of stochastic trainers. The most important advantage of stochastic trainers is the avoidance of high local minima. However, their most important disadvantage is that they work slower than deterministic algorithms. When the literature is examined, it shows that stochastic trainers are more preferred due to their ability to avoid local minima. Stochastic trainers are divided into two main categories: single solution and multiple solutions. It has been proven in many studies that multi-solution stochastic trainers avoid local optimum traps better than single-solution stochastic trainers [13-19]. Local pitfalls can be avoided by using meta-heuristic algorithms in ANN training. By using heuristic algorithms in ANN training, acceptable solutions are provided in a reasonable time to solve complex problems. Heuristic algorithms are less likely to get stuck in local minima than gradient-based search algorithms. Heuristic algorithms can be used in almost all types of ANNs [11]. The slow convergence and learning ability deficiencies of ANN have been overcome with heuristic algorithms. Determining the weights and bias values of ANN with heuristic algorithms improved the learning process of ANN [20]. Various heuristic algorithms have been used for ANN training in the literature. Some of these are Chimp Optimization Algorithm (COA) [12], Invasive Weed Optimization (IWO) [21], Particle Swarm Optimization (PSO) [22, 23], Firefy algorithms (FA) [22], Genetic Algorithms (GA) [23], Arithmetic Optimization Algorithm (AOA) [24], etc. Khishe and Mosavi [12] developed an ANN trained with Chimpanzee Optimization Algorithm (ChOA) for classification of underwater acoustic dataset Movassagh et al. [21] designed an ANN training model with IWO and demonstrated its success on heart, cancer, and iris datasets in a 5 and 10 layer network structure. Dang et al. [22] developed an ANN model optimized with particle swarm optimization and firefy algorithm to predict the scour depths around circular piers in the equilibrium phase. Jamali et al. [23] proposed an Artificial Neural Network (ANN) model based on PSO-GA optimization algorithm to predict a Solar Space Heating System (SSHS) performance. Khatir et al. [24] proposed IANN-AOA and IANN-BCMO developed with Arithmetic Optimization Algorithm and Composite Motion Optimization (BCMO) and solved the problem of damage measurement. They compared both methods. For damage measurement, IANN-AOA provided more accurate results than IANN-BCMO. The proposed algorithm is compared with Ion Motion Algorithm (IMA), Gray Wolf Optimization (GWO) and a hybrid algorithm. The results prove that the newly proposed algorithm performs better than other benchmark algorithms in most cases. The results obtained were compared with an ANN network trained by the Levenberg-Marquardt (LM) algorithm, which is widely adopted in the literature. It can be seen that the prediction results obtained from the proposed models are better compared to the values obtained from the single ANN model trained by LM. To demonstrate the success of the PSO-GA-ANN model, the results are compared to High Exploration Particle Swarm Optimization (HEPSO) and Team Game Algorithm (TGA). According to the results, the highest R2 and RMSE belong to PSO-GA-ANN. Gurgenc et al. [25] trained the MLP network with the adaptive opposition slime mold algorithm and estimated the reservoir temperature of geothermal resources. The results were compared with MLP-ANNs and basic artificial neural networks trained with the whale optimization algorithm and the antlion algorithm under equal conditions. The results prove that AOSMA-MLP outperforms the baseline MLP and other metaheuristic-based MLPs. Altay and Altay [26] also developed the Gray Wolf Optimizer (GWO) and hybridized the developed new GWO and MLP. As a result, the IMP-GWO-MLP algorithm was proposed and its success was tested on various datasets. The obtained results were proposed in the literature and compared with the commonly used GWO, particle swarm optimization, whale optimization algorithm, antlion algorithm and genetic algorithm-based MLP methods. Experimental results show that the proposed method is superior to other current methods in the literature. Altay et al. [27] hybridized Gray Wolf Optimizer with MLP (GWO-MLP) and used naïve Bayes classifier, K-nearest neighbor, linear discrimination analysis, binary decision tree and support vector machine approaches to predict the reservoir temperature using hydrogeochemical data of different. They used it in geothermal areas in Anatolia [27]. Altay and Gurgenc [28] estimated wear losses using the proposed hybrid golden jackal optimizer-multilayer perceptron (GJO-MLP) method. The performance of GJO-MLP was compared with whale optimization-MLP (WOA-MLP), genetic algorithm-MLP (GA-MLP) and antlion optimization-MLP (ALO-MLP) methods. Cinar [29] trained a feed forward MLP (FF MLP) networks using the Tree Seed Algorithm. Particle swarm optimization, gray wolf optimizer, genetic algorithm, ant colony optimization, evolution strategy, population-based incremental learning, artificial bee colony, biogeography-based optimization were compared with TSA. The results confirmed the superiority of TSA. In this study, the newly proposed Zebra Optimization Algorithm (ZOA) was used in ANN training [30]. The reason why the ZOA algorithm was preferred in this study is because it has been newly proposed in recent years. Herustic algorithms continue to be proposed in recent years. The success of the newly proposed heuristic algorithms is higher than the old algorithms. Due to the success of ZOA in the tests performed in the original paper, it was preferred as the heuristic algorithm for MLP-ANN training in this study. Additionally, when the literature was examined, ZOA had never been used as a training algorithm in MLP-ANN before. The motivation for this study begins at this point. Learning algorithms are of great importance in ANN-based classifier models. In this study, an ANN training model with ZOA is proposed. The local and global search capabilities offered by ZOA have been transferred to the ANN training and learning model. Thus, ANN classification was performed faster. First of all, a detailed parameter analysis was carried out to determine the best parameter values. ANN training was carried out with the ZOA learning model on the zoo dataset for ten different population sizes (10, 20, 30, 40, 50, 60, 70, 80, 90, and 100) and the most appropriate population size was determined as 100. Then, the effect of four different maximum iteration values (20, 50, 75, and 100) on ANN classification is shown. Six different ANN network structures were determined and the effects of ZOA on the ANN learning model were examined. The effect of four different epoch values (500, 1000, 5000, and 10000) on the ANN learning model of ZOA is detailed in this study. In this study, the effect of ZOA on the ANN learning model was demonstrated on six different datasets (somerville happiness survey 2015, iris, breast cancer wisconsin, wine, ecoli, and fertility), apart from the zoo dataset, on the ANN network model determined using the most appropriate parameter values. In addition, the effect of Gazelle Optimization Algorithm (GOA) [31], Prairie Dogs Optimization (PDO) [32], and Osprey Optimization Algorithm (OOA) [33] heuristic algorithms on the ANN learning model is shown and compared with ZOA. The results showed that ZOA can be used as an training model. In this study, the success of ZOA in an ANN training model was demonstrated for the first time. In this respect, this study shows originality. The rest of this work follows: In Section 2, the structure of ZOA, ANN training model, and dataset definitions are explained. In Section 3, parameter analyzes of ZOA determined for ANN training and comparisons of ZOA with different heuristic algorithms are presented. In the last section, the results are explained.

Related Works

Heuristic algorithms are frequently used in the literature in training Multi-Layer Perceptron Artificial Neural Networks (MLP-ANN*)*. Some of these are presented in Table 1.

Table 1. *A comprehensive review of related work on MLP-ANN*

References	Using Heuristic Algorithms	Models of ANN	Recommended Method
[12]	Chimpanzee Optimization Algorithm (COA)	Multilayer perceptron (MLP)	MLP-ChOA
[21]	Invasive Weed Optimization (IWO)	Multilayer perceptron (MLP)	MLP-IWO
[22]	Particle Swarm Optimization (PSO) and Firefy Algorithm (FA)	Multilayer perceptron (MLP)	MLP-PSO MLP-FA
[23]	Particle Swarm Optimization (PSO) and Genetic Algorithm (GA)	Multilayer perceptron (MLP)	PSO-GA-ANN
[24]	Arithmetic Optimization Algorithm (AOA) and Composite Motion Optimization (BCMO)	Multilayer perceptron (MLP)	IANN-AOA IANN-BCMO
[25]	Adaptive Opposition Slime Mold Algorithm (AOSMA)	Multilayer perceptron (MLP)	AOSMA-MLP
[26, 27]	Gray Wolf Optimizer (GWO)	Multilayer perceptron (MLP)	IMP-GWO-MLP
[28]	Golden Jackal Optimizer	Multilayer perceptron (MLP)	GJO-MLP
[29]	Tree Seed Algorithm (TSA)	Multilayer perceptron (MLP)	TSA-MLP

The Main Contribution of the Study

- ZOA is used for training the feed forward (FF) MLP ANN for the first time.
- ZOA is compared and outperformed on 7 different datasets with 3 metaheuristic algorithms (GOA, PDO, and OOA).
- ZOA finds eligible weights and biases of FF MLP ANN.
- In terms of average classification rates, ZOA ranked second in 7 different datasets, except Zoo.

- A detailed analysis was made with ZOA for the effects of population sizes and maximum iteration on classification success.
- A detailed analysis was conducted with ZOA for the effects of 6 different MLP-ANN network structures on classification success.
- A detailed analysis was carried out with ZOA for the effects of 4 different epoch values on the classification success of MLP-ANN.

Zebra Optimization Algorithm (ZOA)

Zebras are animals from the horse breed and generally live in eastern and southern Africa. The body feathers of these animals are black and white striped. Their most charismatic features come from this fur structure. Zebras are social living creatures. They exhibit two types of characteristic behaviors in social life. These are: food search and defense behaviors against predators. A zebra leads the zebras in their search for food. Lead zebras are responsible for guiding other zebras in the herd towards food sources. Zebras exhibit two behaviors to escape predators. The first of these is to escape with a zigzag movement pattern. The second is to come together and try to confuse or scare the predator [30]. Zebra Optimization Algorithm (ZOA) was created inspired by the behavior of zebras in social life.

Mathematical model of ZOA:

Initialization: The zebra population in ZOA is defined mathematically as candidate solutions searching the search space. Zebras are initially placed randomly in the search space, that is, on the plain where the food sources are located. The position of each zebra is a matrix of decision variables. The number of decision variables varies depending on the problem size. When the population matrix is first created in ZOA, it is randomly generated according to Equation 1 [30].

$$X = \begin{bmatrix} X_1 \\ \vdots \\ X_i \\ \vdots \\ X_{pop} \end{bmatrix}_{pop \times dim} = \begin{bmatrix} x_{1,1} & \cdots & x_{1,j} & \cdots & x_{1,dim} \\ \vdots & \ddots & \vdots & ⋰ & \vdots \\ x_{1,i} & \cdots & x_{i,j} & \cdots & x_{i,dim} \\ \vdots & ⋰ & \vdots & \ddots & \vdots \\ x_{pop,i} & \cdots & x_{pop,j} & \cdots & x_{pop,dim} \end{bmatrix}_{pop \times dim} \tag{1}$$

where X is zebra population, X_i is the i^{th} zebra, $x_{i,j}$ is position for the j^{th} dimension of the i^{th} zebra, pop is the population size of the zebra, and dim is the dimension of the problem. Each zebra individual represents one candidate solution. By using the size values of each zebra individual, the function values of the target zebras are calculated. Values from the objective function of the zebra population are stored in a matrix. This matrix structure is shown in Equation 2 [30].

$$Fitness = \begin{bmatrix} Fit_1 \\ \vdots \\ Fit_i \\ \vdots \\ Fit_{pop} \end{bmatrix}_{pop \times 1} = \begin{bmatrix} Fit(X_1) \\ \vdots \\ Fit(X_i) \\ \vdots \\ Fit(X_{pop}) \end{bmatrix}_{pop \times 1} \tag{2}$$

where $Fitness$ is the matris of the objective function values.

The values obtained with the objective function are compared with the individuals in the population and the leader zebra in the best position is determined. Depending on the type of problem, the zebra with the lowest fitness value or the zebra with the highest fitness value is determined as the best leader zebra. In each iteration, the positions of the zebras and their fitness values in their new positions are updated. Two types of behavior of zebras are used when determining new positions of the zebra population [30].

These behaviors are: (a) searching for food and (b) defending against predators.

(a) Foraging Behavior: Zebras spend most of their time eating food. Generally, their food sources are grasses and sedges. One of the zebras is defined as the plains zebra and this zebra leads the population. In ZOA, the best member of the population is considered the lead zebra and leads the other population members towards its position in the search area. Mathematical modeling of this stage is shown in Equations 3 and 4 [30].

$$x_{i,j}^{new1} = x_{i,j} + rand.(Zebra_j^{Best} - I.x_{i,j}) \tag{3}$$

$$X_i = \begin{cases} X_i^{new1}, & Fit_i^{new1} < Fit_i; \\ X_i, & else, \end{cases} \tag{4}$$

where X_i^{new1} is the new position of the *i^th^* zebra based on foraging behavior, $x_{i,j}^{new1}$ is the *j^th^* dimension position of the *i^th^* new zebra, Fit_i^{new1} is the fitness value of the *i^th^* new zebra, $Zebra_j^{Best}$ is the pioneer zebra, $rand$ is a random number in interval [0, 1], and I = round (1 + rand) [30].

(b) Defense Strategies Against Predators:

At this stage, the defense strategies of zebras against their enemies were modeled mathematically in order to update their positions in the search space of the zebra population. Zebras' defense strategies vary depending on the type of their enemies. They escape against their main enemies, the lions, in a zigzag pattern and with a random side-turning movement. They act in a confusing and frightening manner towards other enemies. These two defensive strategies are assumed to be similarly likely. In Equation 5, the defense strategy of zebras against lions is modeled in M1, and the defense strategy of zebras against other predators is modeled in M2. The position of the zebras is updated in Equation 6 [30].

$$x_{i,j}^{new2} = \begin{cases} M1: x_{i,j} + R.(2.rand - 1).\left(1 - \frac{Iter}{Iter_{max}}\right).x_{i,j}\,, & S \leq 0.5; \\ M2: x_{i,j} + rand.\left(Zebra^{Attack} - I.x_{i,j}\right), & else, \end{cases} \tag{5}$$

$$X_i = \begin{cases} X_i^{new2}, & Fit_i^{new2} < Fit_i; \\ X_i, & else, \end{cases} \tag{6}$$

where X_i^{new2} is the new position of the i^{th} zebra based on defense strategies behavior, $x_{i,j}^{new2}$ is the j^{th} dimension position of the i^{th} new zebra, Fit_i^{new2} is the fitness value of the i^{th} new zebra, $Zebra_j^{Attack}$ is the attack zebra, $rand$ is a random number in interval [0, 1], and I = round (1 + rand), $Iter$ is current iteration number, $Iter_{max}$ is maximum iteration number, R is a constant value (R=0.01). S is the probability of choosing one of the defense strategies for randomly generated zebras in the range [0, 1]. Figure 1 shows the flowchart of the ZOA [30].

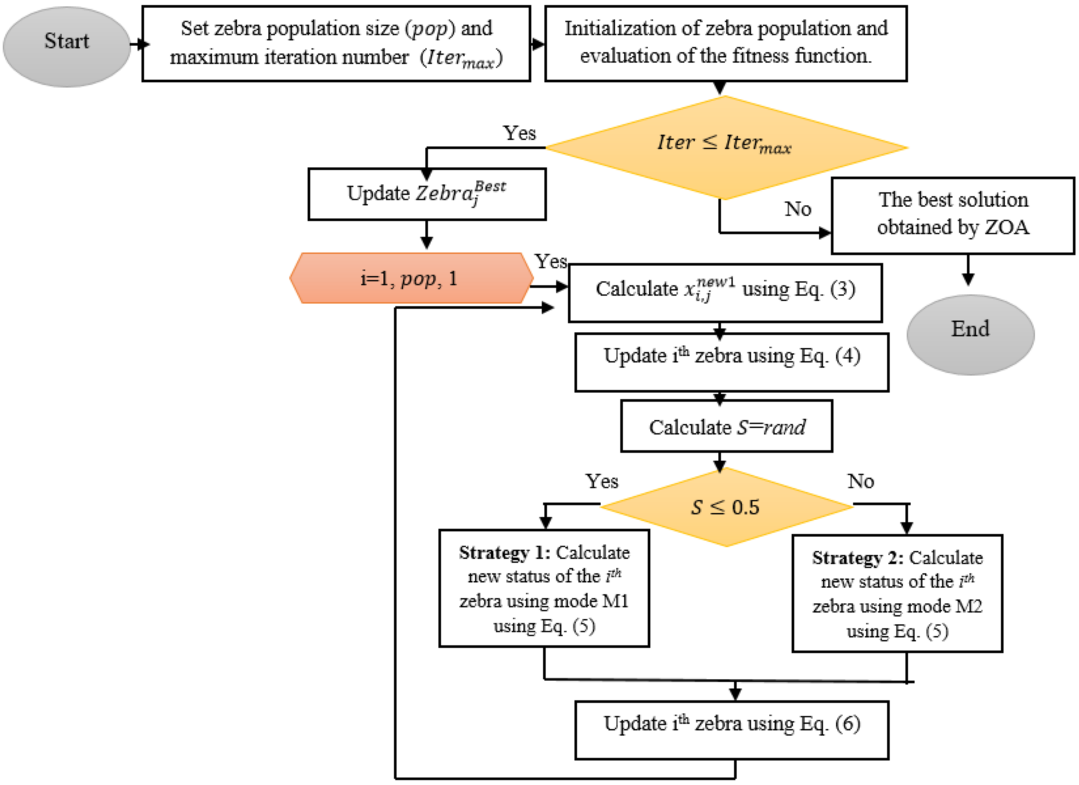

Figure 1. *The flowchart of the ZOA [30]*

Artificial Neural Network (ANN)

Artificial neural network (ANN) is a classification technique inspired by the human brain cell structure (neuron). Generally, ANNs consist of three layers. These are: input layer, hidden layers and output layer. An ANN structure can consist of a single hidden layer or it can consist of many hidden layers. The purpose of an ANN is to find the optimum weight values and make the most appropriate classification in the least possible iterations. There are many types of ANNs in the literature. Some of them are feedforward networks (FNNs) [34], Kohonen self-organizing networks [35], radial basis function (RBF) networks [36], recurrent neural networks [37], convolutional neural networks [38], spiking neural networks [39], etc. Multilayer perceptron (MLP), a special type of feed-forward networks (FNNs), is one of the most widely used models in the literature [34, 40]. In this study, an MLP-ANN structure was analyzed by training it with a metaheuristic algorithm selected from the literature. It is often seen that heuristic algorithms are used as training algorithms in MLP structures.

Multi-Layer Perceptron Artificial Neural Networks (MLP-ANN): Similar to ANNs, MLP works by matching a set of input values to a corresponding set of output values. This mapping is accomplished through a transformation process designed to derive the output. An MLP consists of three layers: the input layer contains n input values; The size of the hidden layer located between the input and output layers varies depending on the type of problem; and there is the output layer, which combines the results of the MLP network [25, 41]. The input layer hosts *n* neurons, the output layer includes *k* neurons, and the hidden layer comprises *m* neurons. Each neuron in the hidden layer performs two critical operations: summation and activation. The sum obtained is subsequently passed through an activation function, as depicted in Equation 7. Here $w_{i,j}$ is the connection weight between the hidden neuron j and the input neuron i. b_j is the bias value. y_j is the output value of neuron j, and *f* is the sigmoid function. Figure 2 shows a single hidden layer MLP network.

$$Sum_j = \sum_{i=1}^{n} w_{i,j} * in_i + b_j \tag{7}$$

$$y_j = f(Sum_j) \tag{8}$$

$$f(Sum_j) = \frac{1}{1+e^{-Sum_j}} \tag{9}$$

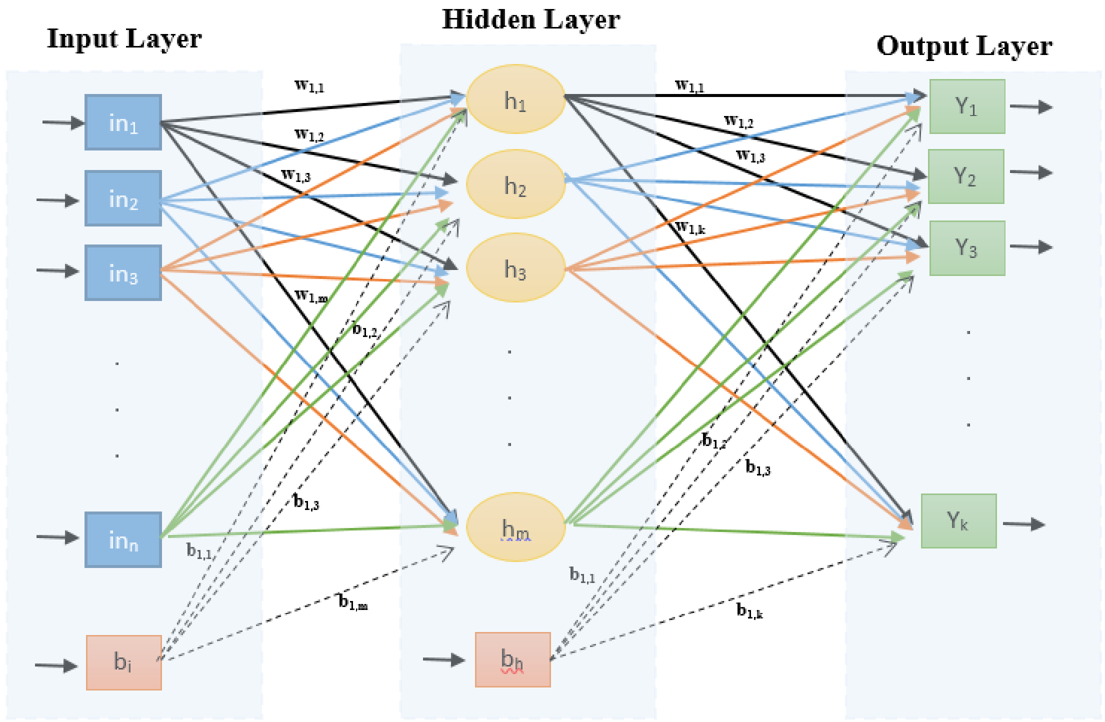

Figure 2. *The single hidden layer MLP network [25]*

Training An ANN and Dataset Definition

In this subsection, the updates of ZOA that can be classified with Multi Layered Perceptron ANN (MLP ANN) are explained. To train the ANN network, weights and bias values, which are ANN components, were placed on the dimensions of each population in the ZOA structure [12, 42]. The dimension value of zebra population individuals was calculated using Equation 10. The problem dimension was calculated using the number of inputs in the ANN (number of features in the datasets) (m) and the number of neurons in the hidden layers (n) (Equation 11). The ANN network was created by recombining the ANN values (weights and biases) in each dimension value from the zebra population. Classification was made using the created network. Mean Square Error (MSE) was used to evaluate the classification rate. MSE has also been used to evaluate ZOA individuals as a fitness function. MSE calculation is shown in Equation 12 [12, 42]. In this study, the datasets shown in Table 2 obtained from the UCI library were used (https://archive.ics.uci.edu/) [43]. 80% of the datasets used in classification were set as training and 20% as test dataset.

$$Length\ of\ problem\ dimension = (m \times n) + (2 \times n) + 1 \tag{10}$$

$$Zebra_i = \ [weight_1\ weight_2\ weight_3 \ldots bias_1\ bias_2\ bias_3 \ldots] \tag{11}$$

$$Minimization \qquad Fitness\ Function = MSE = \frac{1}{k}\sum_{i=1}^{k}(X_{real} - X_{model})^2 \tag{12}$$

where X_{real} is desired values and X_{model} is evaluated values. k is the number of instances in the training dataset [12, 42].

Table 2. *Dataset descriptions*

ID	Dataset	Number of features	Number of instances	Number of classes	Missing values	Type
1	Zoo	17	101	7	No	Life
2	Somerville Happiness Survey 2015	7	143	2	No	Health and Medicine
3	Iris	5	150	3	No	Biology
4	Breast Cancer Wisconsin	31	569	2	No	Health and Medicine
5	Wine	14	178	3	No	Physics and Chemistry
6	Ecoli	8	336	8	No	Biology
7	Fertility	10	100	2	No	Health and Medicine

Results and Discussion

In this subsection, classification was made by training an ANN with the ZOA algorithm. All applications were carried out with a machine with the features used in Table 2. The success of ZOA's parameter settings in ANN training is analyzed in detail in this subsection. Analysis of parameter settings was performed on the zoo dataset.

Table 3. *PC specifications*

Name	**Detailed settings**
Hardware	
CPU	Core i5
Frequency	1.19 GHz
RAM	12 GB
Software	
Operating system	Windows 10 (64-bit)
Language	MATLAB R2014A

Parameter Analyzes

a- The Analyses of the Population Size: The success of ten different population values on ZOA was analyzed for ANN. The parameter settings used in the population analysis are shown in Table 4. The results are shown in Table 5. The best results are marked in bold. According to the results, the population size is directly proportional to the success of ZOA in ANN training. The most successful population size relative to the average is 100, 80 and 90, respectively. The least successful population values are 10, 20 and 30 respectively. According to the best value, the best population size is 60. According to the standard deviation, the best population size is 90. According to the time value, the fastest working population size is 10. Figure 3 shows the convergence chart of the population size analysis for ZOA on ANN. Figure 4 shows the boxplot of the population size analysis for ZOA on ANN. Figure 5 shows the graphics of the results from ANN trained with ZOA on zoo train data (for pop=100) and Figure 6 shows the graphics of the results from ANN trained with ZOA on zoo test data (for pop=100). In the graphs, it can be seen that as the population size increases, ZOA's success in ANN training increases. At the same time, for the value of 100, which is the most successful population amount, the actual values in both the training and test data sets in the zoo data set and the training and test results of the ANN trained with ZOA were compared graphically. In this study, the population size was selected as 20 in classifying other datasets with ANN. In Figure 3, the x axes value shows the MSE value and the y axes value shows the iteration number. According to Figure 3, the fastest convergences were obtained at pop=90 and pop=100 values. The slowest convergent value was pop=10. In Figure 4, the x axes value shows the MSE value and the y axes value shows the population sizes. According to Figure 4, the average values vary in almost all population values. In this case, as the population size changes, the similarities between the results also differ. In Figure 5, the x axes value shows the training data set class values, and the y axes value shows the number of training data set samples. Figure 5 shows the error amounts between the actual training dataset values and the predicted training datasets. According to Figure 5, there is not much difference between the predicted target value and the actual target values for the training data set. Close values have been estimated. In Figure 6, the x axes value shows the test data set class values, and the y axes value shows the number of test data set samples. Figure 6 shows the error amounts between the actual test dataset values and the predicted test datasets. According to Figure 6, there is not much difference between the predicted target value and the actual target values for the test data set.

Table 4. *Parameter settings*

Parameters	**Values**
Population size (pop)	10, 20, 30, 40, 50, 60, 70, 80, 90, 100
The maximum number of iterations ($Iter_{max}$)	20
Dimension	16
R value	0.1
The number of run	20
Training data rate	80% (81 instance for zoo dataset)
Test data rate	20% (20 instance for zoo dataset)
Search space boundary	[-1,1]
Hidden Layer number	1
Neuron number	5
Epochs (for ANN)	500
Transfer function (for ANN)	Tansig

Table 5. *The results of ZOA for population size analysis on zoo dataset*

MSE	**pop =10**	**pop =20**	**pop =30**	**pop =40**	**pop =50**	**pop =60**	**pop =70**	**pop =80**	**pop =90**	**pop =100**
Best	0.3472	0.4256	0.1805	0.3788	0.3042	**0.1652**	0.2770	0.1806	0.1675	0.1919
Worst	3.3380	2.7869	2.1350	1.7901	1.3299	1.0884	0.8718	0.6493	0.6810	0.7707
Median	1.5175	0.9517	0.5818	0.5720	0.6019	0.4783	0.5049	0.3849	0.3875	0.3565
Mean	1.7167	1.0625	0.7272	0.6809	0.6367	0.5228	0.5027	0.3894	0.3915	**0.3782**
SD	0.8521	0.5393	0.4969	0.3344	0.2702	0.2319	0.1609	0.1356	**0.1262**	0.1354
Time	**7.3397**	13.9212	20.7881	36.1899	36.7285	43.6268	54.3813	60.8385	69.7256	85.3010
Rank (According Mean)	10	9	8	7	6	5	4	2	3	**1**

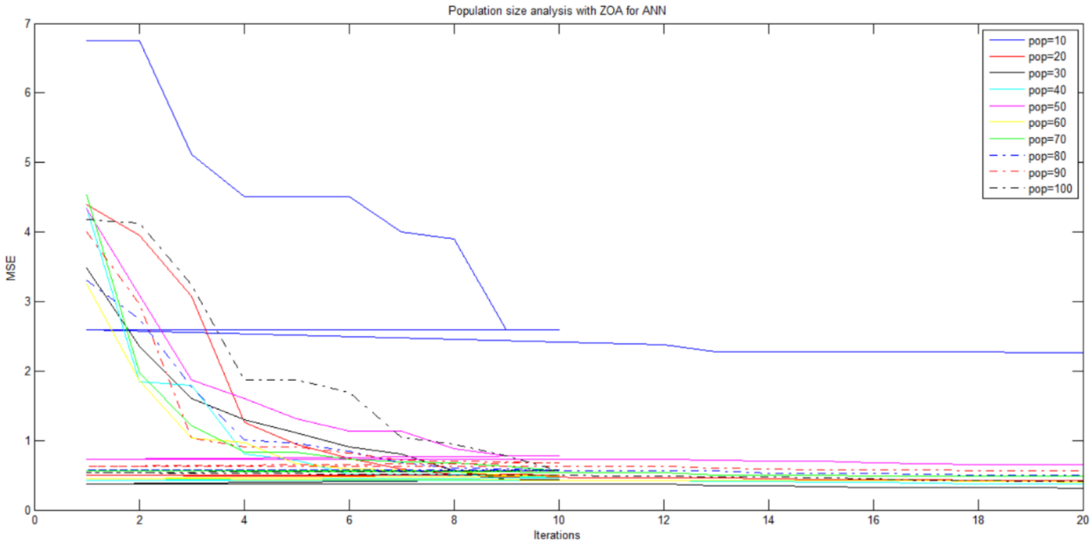

Figure 3. *The convergence chart of the population size analysis for ZOA on ANN*

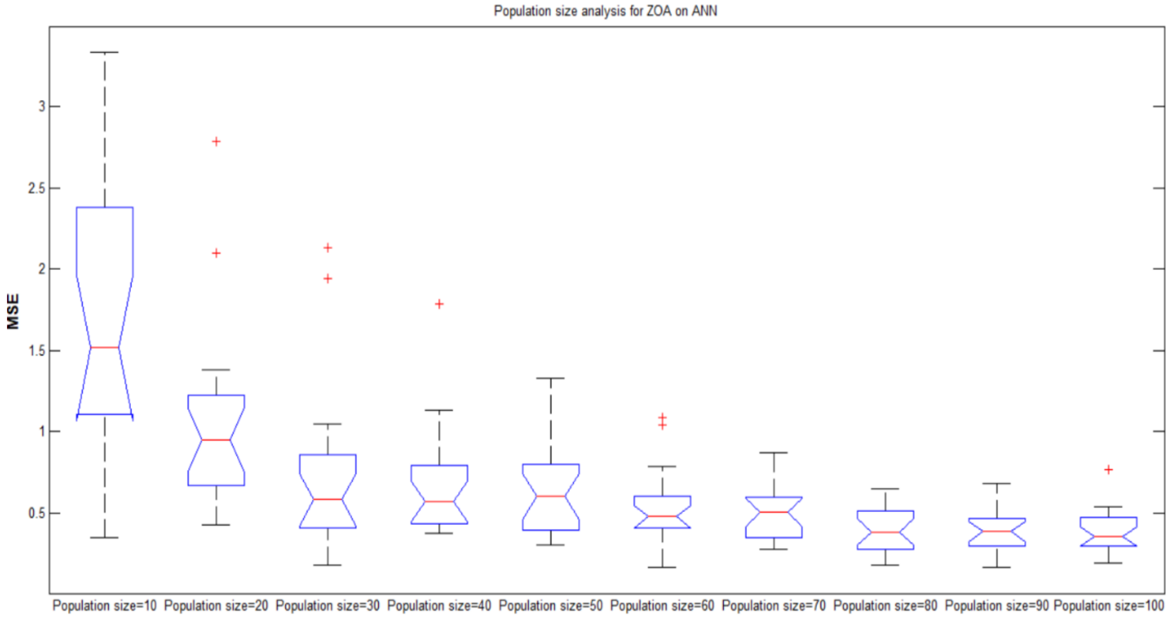

Figure 4. *The boxplot of the population size analysis for ZOA on ANN*

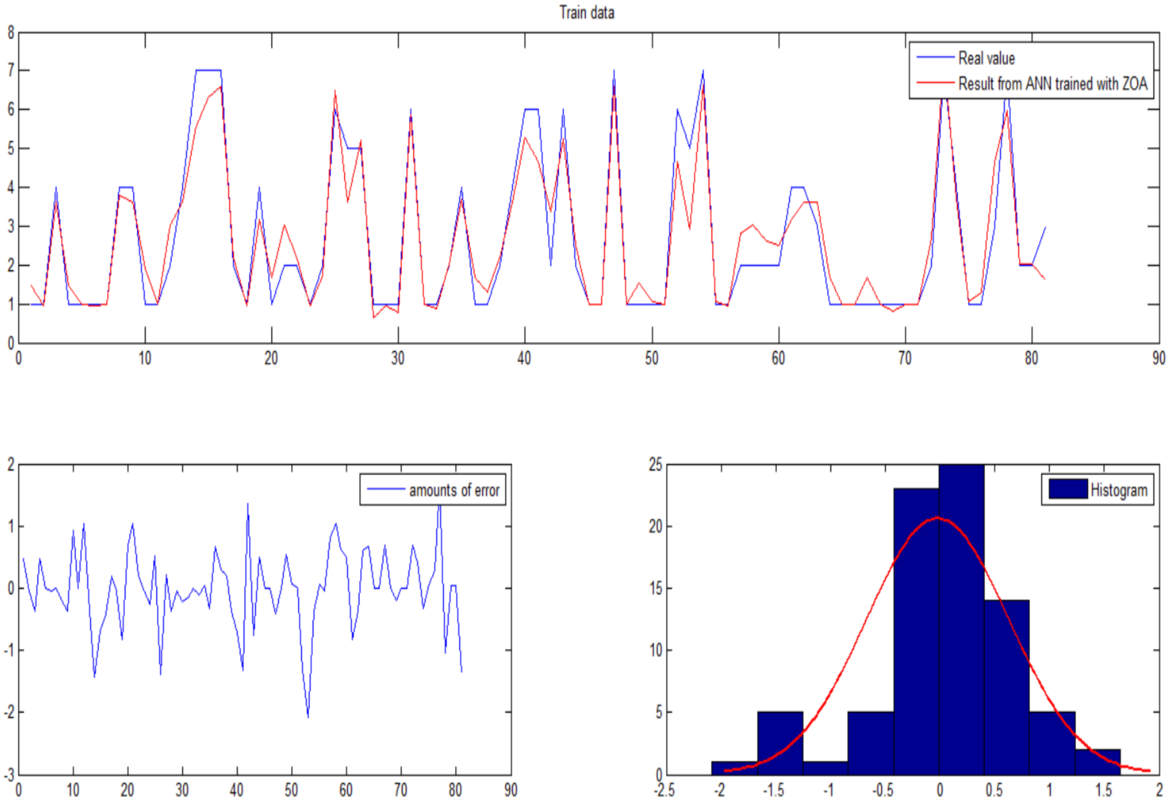

Figure 5. *The graphics of the results from ANN* trained *with ZOA on zoo train data (for pop=100).*

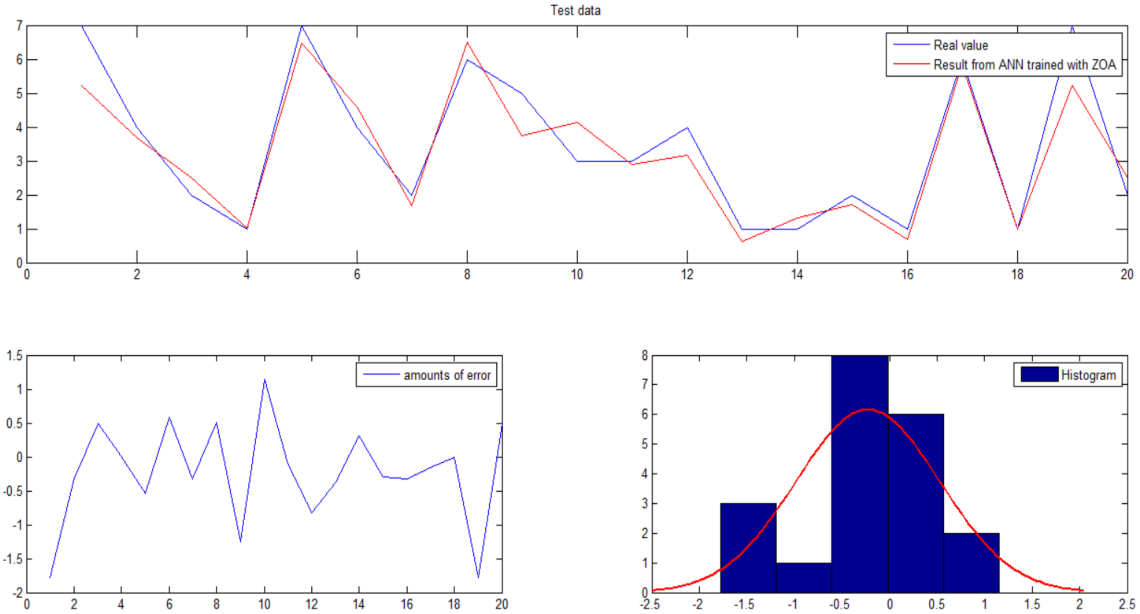

Figure 6. *The graphics of the results from ANN* trained *with ZOA on zoo test data (for pop=100)*

b- The Analyses of the Maximum Iteration: The success of four different maximum number of iterations on ZOA was analyzed for ANN. The parameter settings used in the maximum number of iterations are shown in Table 6. The results are shown in Table 7. The best results are marked in bold. According to the results, the maximum number of iterations is directly proportional to the success of ZOA in ANN training. The most successful maximum number of iterations relative to the average is 100 and 75, respectively. The least successful maximum number of iterations are 20 and 50, respectively. According to the best value, the best maximum number of iteration is 75. According to the standard deviation, the best maximum number of iteration is 75. According to the time value, the fastest working maximum number of iteration is 20. Figure 7 shows the convergence chart of the maximum number of iteration analysis for ZOA on ANN. Figure 8 shows the boxplot of the maximum number of iteration analysis for ZOA on ANN. Figure 9 shows the graphics of the results from ANN trained with ZOA on zoo train data (for $Iter_{max}$=100) and Figure 10 shows the graphics of the results from ANN trained with ZOA on zoo test data (for $Iter_{max}$=100). In the graphs, it can be seen that as the maximum number of iteration increases, ZOA's success in ANN training increases. At the same time, for the value of 100, which is the most successful number of the maximum iteration, the actual values in both the training and test data sets in the zoo data set and the training and test results of the ANN trained with ZOA were compared graphically. In this study, the maximum number of iteration was selected as 50 in classifying other datasets with ANN. In Figure 7, the x axes value shows the MSE value and the y axes value shows the iteration number. According to Figure 7, the fastest convergences were obtained at maximum iteration=75 and maximum iteration=100 values. The slowest convergent value was maximum iteration=20. In Figure 8, the x axes value shows the MSE value and the y axes value shows the number of the maximum iteration. According to Figure 8, the average values vary in almost all numbers of the maximum iterations. In this case, as the number of the maximum iterations changes, the similarities between the results also differ. In Figure 9, the x axes value shows the training data set class values, and the y axes value shows the number of training data set samples. Figure 9 shows the error amounts between the actual training dataset values and the predicted training datasets. According to Figure 9, there is not much difference between the predicted target value and the actual target values for the training data set. Close values have been estimated. In Figure 10, the x axes value shows the test data set class values, and the y axes value shows the number of test data set samples. Figure 10 shows the error amounts between the actual test dataset values and the predicted test datasets. According to Figure 10, there is not much difference between the predicted target value and the actual target values for the test data set.

Table 6. *Parameter settings*

Parameters	**Values**
Population size (pop)	20
The maximum number of iterations ($Iter_{max}$)	20, 50, 75, 100
Dimension	16
R value	0.1
The number of run	20
Training data rate	80% (81 instance for zoo dataset)
Test data rate	20% (20 instance for zoo dataset)
Search space boundary	[-1,1]
Hidden Layer number	1
Neuron number	5
Epochs (for ANN)	500
Transfer function (for ANN)	Tansig

Table 7. *The results of ZOA for population size analysis on zoo dataset*

MSE	$Iter_{max}$**=20**	$Iter_{max}$**=50**	$Iter_{max}$**=75**	$Iter_{max}$**=100**
Best	0.4256	0.2503	**0.1516**	0.1572
Worst	2.7869	0.9374	0.8963	0.9777
Median	0.9517	0.5579	0.3111	0.3998
Mean	1.0625	0.5568	0.3630	**0.4440**
SD	0.5393	0.1955	**0.1756**	0.1898
Time	**13.9212**	36.3699	55.5139	77.3042
Rank (According Mean)	4	3	2	**1**

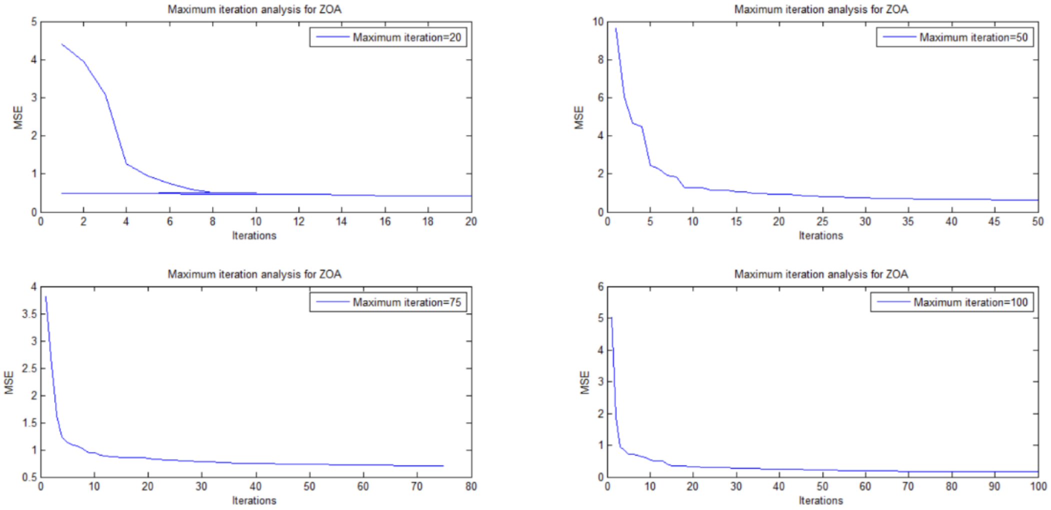

Figure 7. *The convergence chart of the maximum iteration analysis for ZOA on ANN.*

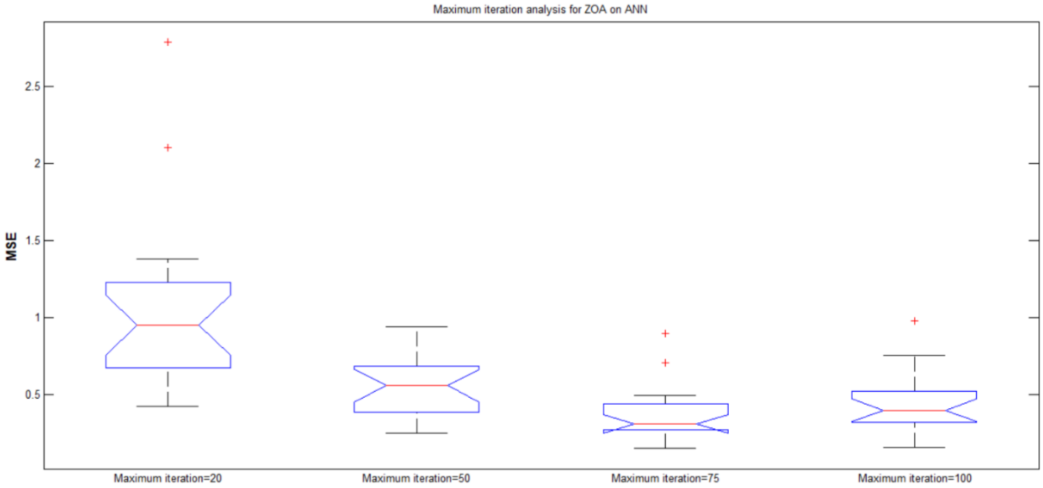

Figure 8. *The boxplot of the the maximum iteration analysis for ZOA on ANN.*

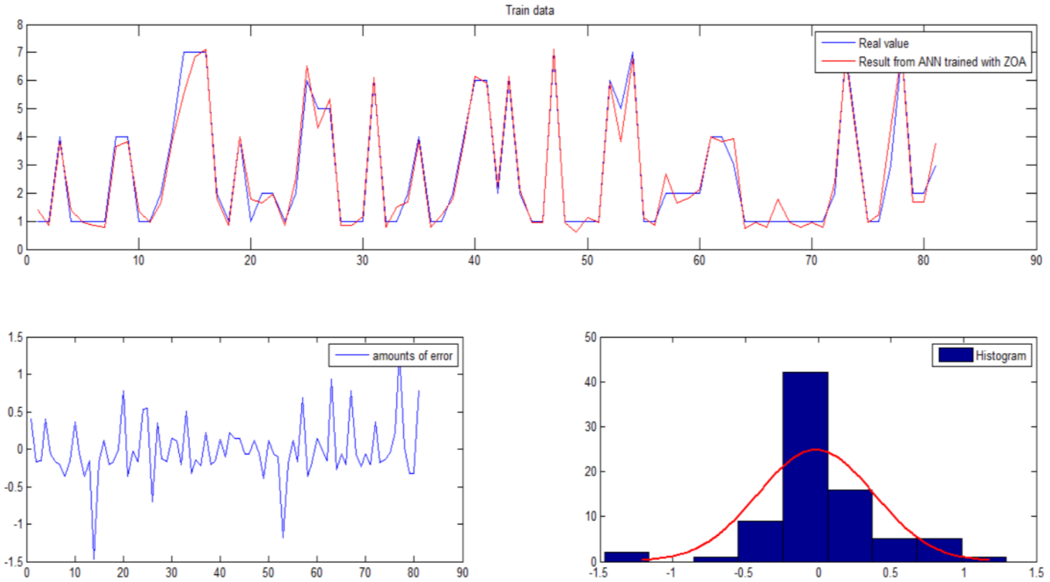

Figure 9. *The graphics of the results from ANN trained with ZOA on zoo train data (for* $Iter_{max}$*=100)*

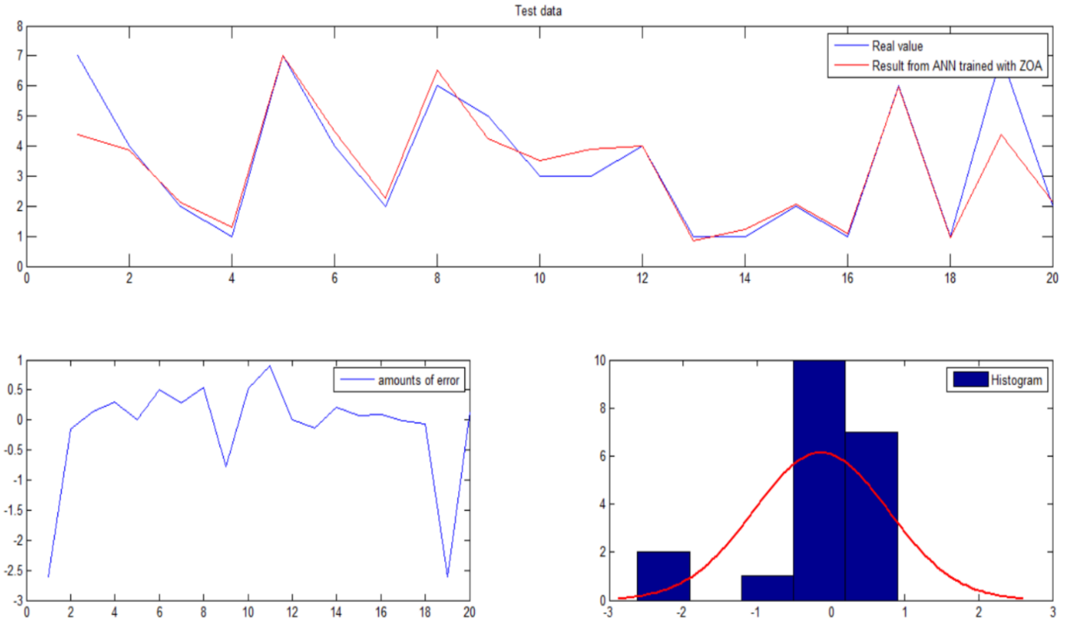

Figure 10. The graphics of the results from ANN trained with ZOA on zoo test data (for $Iter_{max}$=100)

c- The Analyses of the Layer and Neuron Number: The success of three different layer number and six different neuron number on ZOA was analyzed for ANN. The parameter settings used in the number of the layer and neuron are shown in Table 8. The results are shown in Table 9. The best results are marked in bold. According to average values, the most successful network design is a two-layer network design with five and ten neurons each (Network4 = {5,10}). Figure 11 shows the convergence chart of the different ANN networks analysis for ZOA.

***Table 8.** Parameter settings*

Parameters	Values
Population size (pop)	20
The maximum number of iterations ($Iter_{max}$)	50
Dimension	16
R value	0.1
The number of run	20
Training data rate	80% (81 instance for zoo dataset)
Test data rate	20% (20 instance for zoo dataset)
Search space boundary	[-1,1]
Hidden Layer number	{1, 2, 3}
Neuron number	{5},{10},{5, 5},{5, 10},{5, 5, 5}, {10, 10, 10}
Epochs (for ANN)	500
Transfer function (for ANN)	Tansig, purelin

Table 9. *The results of ZOA for layer and neuron number analysis on zoo dataset*

MSE	Network1={5}	Network2={10}	Network3={5,5}	Network4={5,10}	Network5={5, 5, 5}	Network6={10, 10, 10}
Best	0.2503	0.2596	0.1826	**0.1595**	0.2419	0.2285
Worst	0.9374	0.9411	1.6367	0.8175	1.7184	1.0251
Median	0.5579	0.3776	0.6605	0.3692	0.8875	0.3316
Mean	0.5568	0.4198	0.6827	**0.4168**	0.8804	0.4331
SD	0.1955	**0.1597**	0.3655	0.1789	0.3617	0.2034
Time	36.3699	25.7894	27.7151	**24.6374**	47.5577	46.2427
Rank (According Mean)	4	2	5	**1**	6	3

Figure 12 shows the boxplot of the different ANN networks analysis for ZOA. Figure 13 shows the graphics of the results from ANN trained with ZOA on zoo train data (for Network6={=10 10 10}) and Figure 14 shows the graphics of the results from ANN trained with ZOA on zoo test data (for Network6={=10 10 10}). In this study, the number of layers and neurons was selected as Network4 = {5,10} in the classification of other data sets with ANN. In Figure 11, the x axes value shows the MSE value and the y axes value shows the iteration number. According to Figure 11, the fastest convergences were obtained at Network4 and Network3. The slowest convergent value was Network5. In Figure 12, the x axes value shows the MSE value and the y axes value shows the number of the network. According to Figure 12, the average values vary in almost all networks (except Network2 and Network4). In this case, as the networks changes, the similarities between the results also differ. In Figure 13, the x axes value shows the training data set class values, and the y axes value shows the number of training data set samples. Figure 13 shows the error amounts between the actual training dataset values and the predicted training datasets. According to Figure 13, there is not much difference between the predicted target value and the actual target values for the training data set. Close values have been estimated. In Figure 14, the x axes value shows the test data set class values, and the y axes value shows the number of test data set samples. Figure 14 shows the error amounts between the actual test dataset values and the predicted test datasets. According to Figure 14, there is much difference between the predicted target value and the actual target values for the test data set.

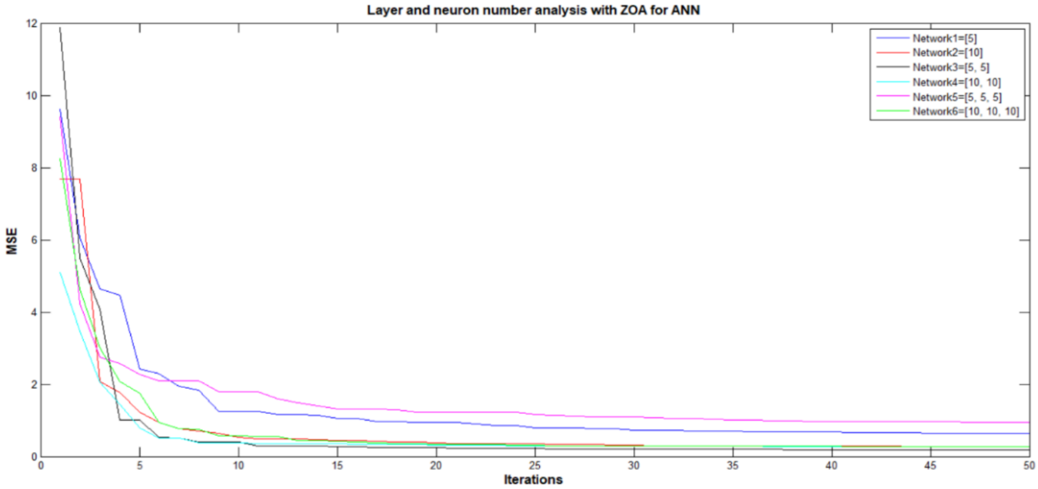

Figure 11. *The convergence chart of the layer and neuron number analysis for ZOA on ANN*

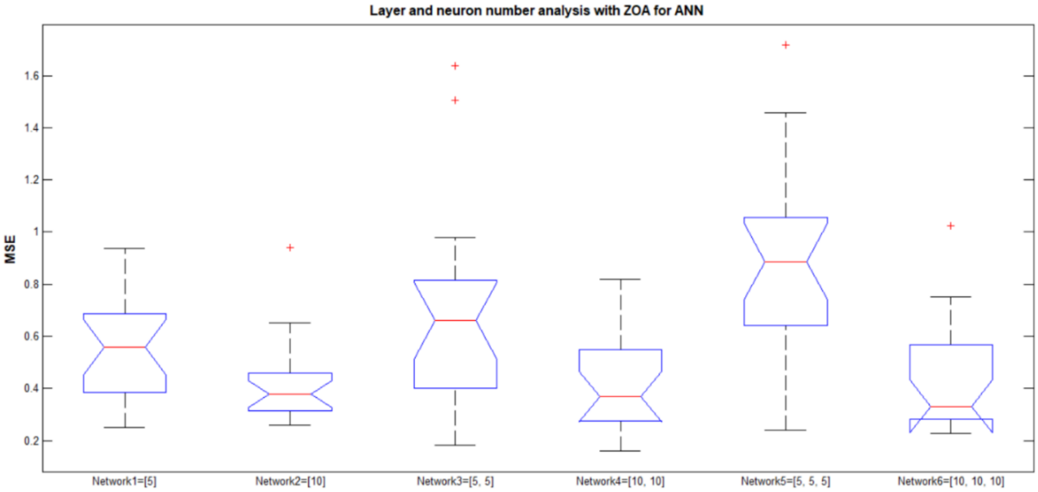

Figure 12. *The boxplot of the the layer and neuron number analysis for ZOA on ANN.*

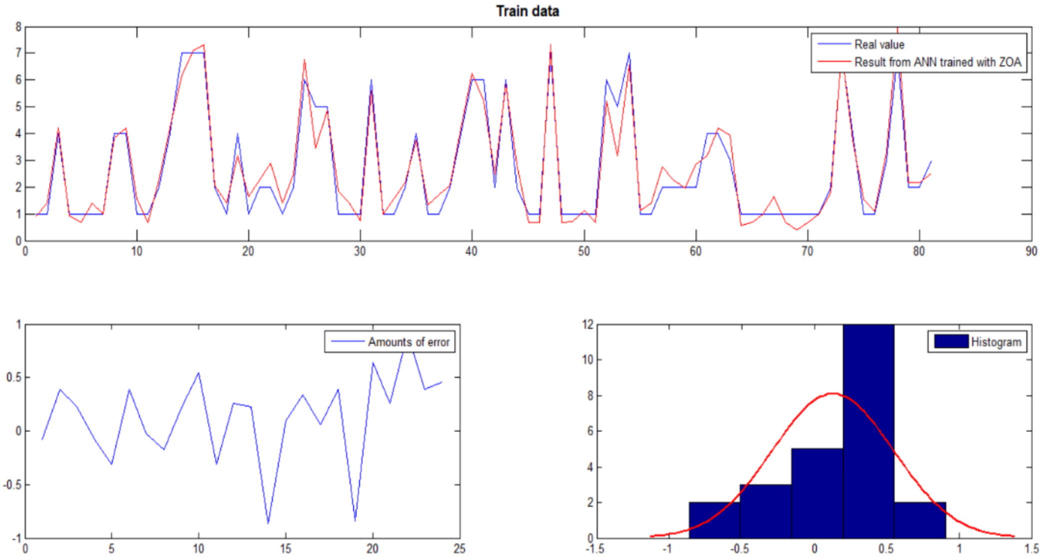

Figure 13. *The graphics of the results from ANN* trained *with ZOA on zoo train data (for Network6={10, 10, 10}).*

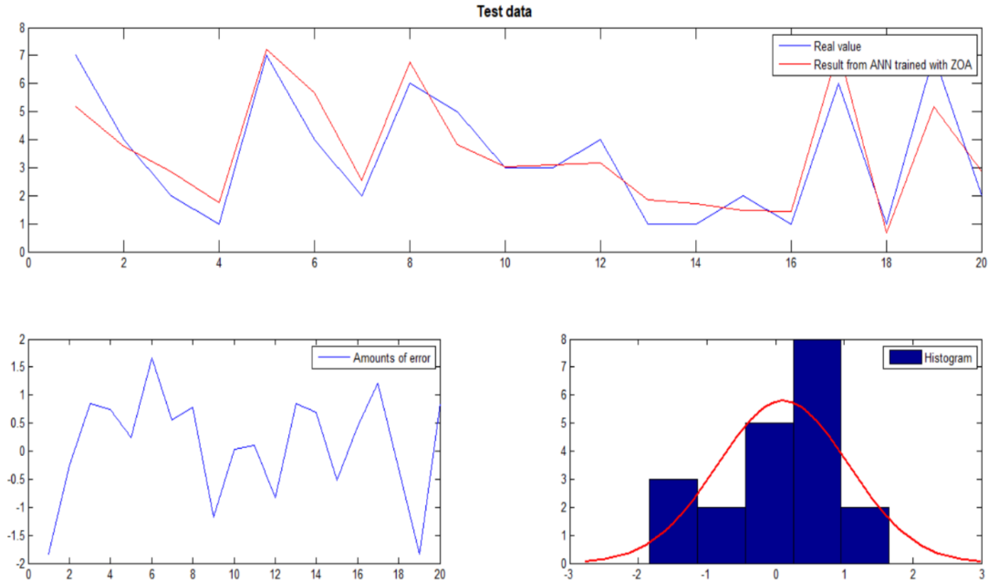

Figure 14. *The graphics of the results from ANN* trained *with ZOA on zoo test data (for Network6={10, 10, 10}).*

d- The Analyses of the Number of Epoch for ANN: The success of four different epochs values on ZOA was analyzed for ANN. The parameter settings used in the epochs values (500, 1000, 5000, and 10000) are shown in Table 10. The results are shown in Table 11.

Table 10. *Parameter settings*

Parameters	Values
Population size (pop)	20
The maximum number of iterations ($Iter_{max}$)	50
Dimension	16
R value	0.1
The number of run	20
Training data rate	80% (81 instance for zoo dataset)
Test data rate	20% (20 instance for zoo dataset)
Search space boundary	[-1,1]
Hidden Layer number	2
Neuron number	{5, 10}
Epochs (for ANN)	500, 1000, 5000, 10000
Transfer function (for ANN)	Tansig, purelin

Table 11. *The results of ZOA for number of epochs analysis on zoo dataset*

MSE	**Epochs=500**	**Epochs=1000**	**Epochs=5000**	**Epochs=10000**
Best	0.1595	0.1843	0.2835	0.2054
Worst	0.8175	1.0438	0.8614	1.0442
Median	0.3692	0.4306	0.5215	0.5908
Mean	0.4168	0.4796	0.5464	0.5692
SD	0.1789	0.2362	0.1719	0.2324
Time	24.6374	41.8842	33.4862	25.1088
Rank (According Mean)	**1**	2	2	3

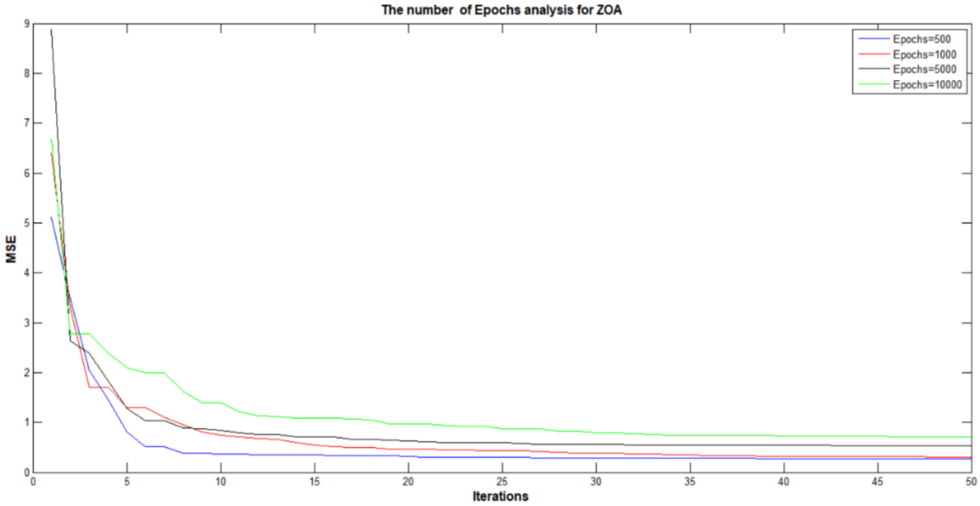

Figure 15. *The convergence chart of the number of epochs analysis for ZOA on ANN.*

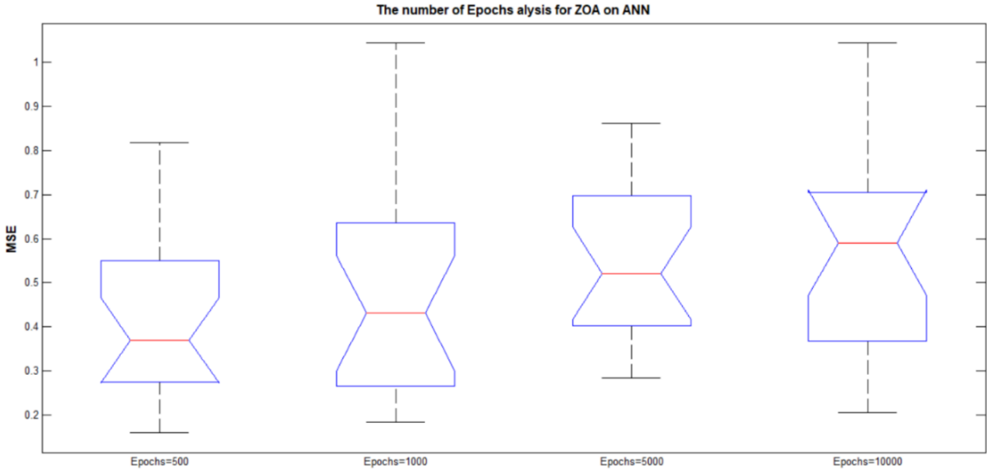

Figure 16. *The boxplot of the number of epochs analysis for ZOA on ANN*

The best results are marked in bold. According to average values, the most successful epoch value is 500. Figure 15 shows the convergence chart of the different epoch values analysis for ZOA. Figure 16 shows the boxplot of the different epoch values analysis for ZOA. Figure 17 shows the graphics of the results from ANN trained with ZOA on zoo train data (for Epoch value=1000) and Figure 18 shows the graphics of the results from ANN trained with ZOA on zoo test data (for Epoch value=1000). In this study, the epoch value was selected as 500 in the classification of other data sets with ANN. In Figure 15, the x-axis value shows the MSE value and the y-axis value shows the number of iterations. According to Figure 15, the fastest convergence was achieved at Epochs=500 and Epochs=1000. The slowest convergent value was Epochs=10000. In this case, the ANN network faced overfitting at high epoch values. In Figure 16, the x-axis value shows the MSE value and the y-axis value shows the number of epochs. According to Figure 16, the average values differ in almost all epochs. In this case, as the number of epoch change, the similarities between the results also differ. In Figure 17, the x-axis value shows the training data set class values, and the y-axis value shows the number of training data set samples. Figure 17 shows the error amounts between the actual training data set values and the predicted training data sets. According to Figure 17, there is not much difference between the predicted target value and the actual target values for the training data set. Close values have been estimated. In Figure 18, the x-axis value shows the test data set class values, and the y-axis value shows the number of test data set samples. Figure 18 shows the error amounts between the actual test data set values and the predicted test data sets. According to Figure 18, there is not a lot of difference between the predicted target value and the actual target values for the test data set.

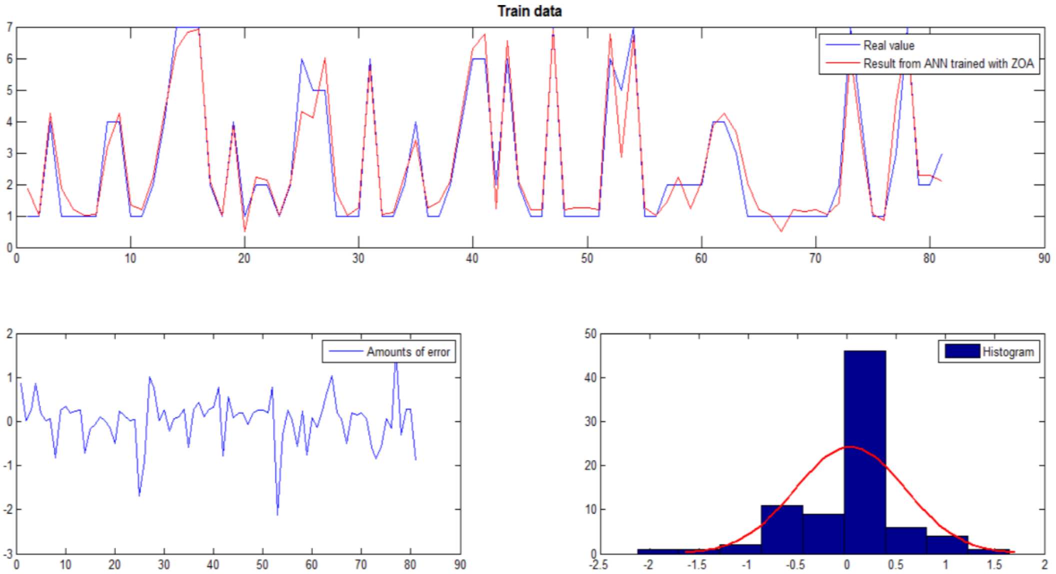

Figure 17. *The graphics of the results from ANN* trained *with ZOA on zoo train data (for Epochs=1000).*

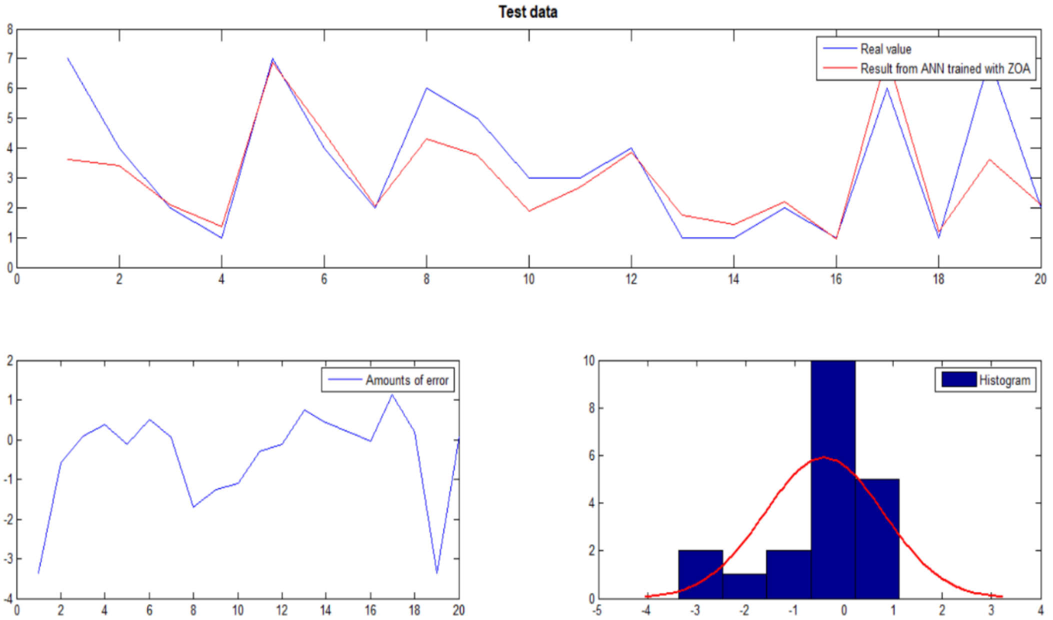

Figure 18. *The graphics of the results from ANN* trained *with ZOA on zoo test data (for Epochs=1000).*

Evaluation of the Success of the ZOA Algorithm and Other Algorithms on Different Data Sets: In this subsection, ZOA is compared with three different heuristic algorithms that have been proposed in recent years and selected from the literature. These heuristic algorithms are Gazelle Optimization Algorithm (GOA) [31], Prairie Dogs Optimization (PDO) [32], and Osprey Optimization Algorithm (OOA) [33]. GOA was created inspired by the behavior of gazelles. PDO was inspired by the social lifestyle of Prairie dogs. OOA was proposed inspired by the lifestyle of osprey creatures. The parameter settings used in the population analysis are shown in Table 12. The results are shown in Table 13.

Table 12. *Parameter settings*

Parameters	**Values**
Population size (pop)	20
The maximum number of iterations ($Iter_{max}$)	50
Dimension	16
R value for ZOA	0.1
The number of run	20
Training data rate	80%
Test data rate	20%
Search space boundary	[-1,1]
Hidden Layer number	2
Neuron number	{5, 10}
Epochs (for ANN)	500
Transfer function (for ANN)	Tansig, purelin
Fixed parameters for PDO	rho=0.005; epsPD=0.1
Fixed parameters for GOA	PSRs=0.34; S=0.88;

The best results are marked in bold. A detailed comparison analysis was performed on seven different datasets (zoo, somerville happiness survey 2015, iris, breast cancer wisconsin, wine, ecoli, and fertility). The details of these datasets are shown in Table 1. Total mean, standard deviation (SD), and time results are shown in Figure 19, Figure 20, and Figure 21, respectively. Figure 22 and Figure 23 show the convergence and box plots of the comparison algorithms on ANN training. Figure 24, Figure 25, and Figure 26 compare the results from the ANN trained and tested with ZOA, GOA, PDO and OOA on the zoo, wine, and iris datasets, respectively, with their real values. When Table 13 is examined, according to the average results, GOA algorithm is ranked first and ZOA algorithm is ranked second in almost every dataset. According to the total average results, ZOA, GOA, PDO and OOA are listed respectively. According to the total average results, the best heuristic algorithm that trained the ANN network was ZOA, and the worst heuristic algorithm was OOA. Figure 19 proves this situation. The best total standard deviation results belong to GOA, while the worst total standard deviation results belong to OOA. Figure 20 proves this situation. According to Figure 21, the fastest running heuristic algorithm was PDO, while the slowest running heuristic algorithm was OOA. The best working speeds of heuristic algorithms on ANN are listed as PDO, GOA, ZOA and OOA, respectively. Figure 22 shows the convergence of the comparison algorithms on each data set while training the ANN. In general, OOA converged slowly to optimum results, while ZOA converged faster. It can be seen that the ANN training success of ZOA on the iris data set is not very good. In Figure 23, the success of the comparison algorithms in ANN training on three different data sets is shown as box plots. On the Zoo data set, the results of ZOA, GOA and PDO algorithms, except OOA, are close to each other. There is consistency among the results obtained. The GOA algorithm obtained the most consistent results on the Iris data set. It is also seen that ZOA, PDO and OOA algorithms do not achieve very good results. The most successful ANN training on the Wine dataset belongs to ZOA and GOA. In this case, the box plots are close to each other and it can be said that the results are consistent. The heuristic algorithms that performed the least successful ANN training on the Wine dataset were PDO and OOA. In Figure 24, the predictions made by the comparison algorithms during ANN training and testing on the zoo dataset are compared with the real prediction values. According to the results, the best predictive heuristics were ZOA and GOA, while PDO and OOA were ranked lower. In Figure 25, the predictions made by the comparison algorithms during ANN training and testing on the wine dataset are compared with the real prediction values. A similar situation shown by the algorithms in Figure 24 can also be seen in Figure 26. In Figure 26, the predictions made by the comparison algorithms during ANN training and testing on the iris dataset are compared with the real prediction values. It is seen that a better ANN training is performed on the iris dataset with PDO and GOA heuristic algorithms.

Table 13. *The comparison results of ZOA and other algorithms on different data sets*

Datasets	MSE	ZOA	GOA	PDO	OOA
Zoo	***Best***	**0.1595**	0.5798	0.7316	4.2066
	Worst	0.8175	1.5346	2.9024	25.5013
	Median	0.3692	0.9183	1.7671	11.0427
	Mean	**0.4168**	0.9257	1.7519	12.5194
	SD	**0.1789**	0.2847	0.5680	6.7819
	Time	24.6374	24.4081	**18.1180**	36.6146
Rank		1	2	3	4
Somerville Happiness Survey 2015	***Best***	**0.1795**	0.1824	0.2054	0.1947
	Worst	0.2207	0.2028	0.2355	0.2279
	Median	0.2030	0.1951	0.2147	0.2081
	Mean	0.2011	**0.1941**	0.2164	0.2090
	SD	0.0110	**0.0050**	0.0081	0.0070
	Time	32.3040	25.6380	**17.2326**	38.0155
Rank		2	1	4	3
Iris	***Best***	0.0435	0.0392	**0.0344**	0.0379
	Worst	0.1573	0.0498	0.1005	0.1215
	Median	0.0684	0.0420	0.0539	0.0855
	Mean	0.0784	**0.0425**	0.0625	0.0847
	SD	0.0318	**0.0029**	0.0206	0.0243
	Time	60.3356	24.9541	**14.5459**	40.1815
Rank		3	1	2	4

Table 13 continued…

Breast Cancer Wisconsin	***Best***	0.0480	0.0467	**0.0376**	0.0680
	Worst	0.0931	0.0878	0.1030	0.2274
	Median	0.0583	0.0580	0.0644	0.1276
	Mean	0.0645	**0.0601**	0.0688	0.1411
	SD	0.0130	**0.0107**	0.0200	0.0437
	Time	31.8206	31.4186	**21.6767**	44.8578
Rank		2	1	3	4
Wine	***Best***	**0.0728**	0.0750	0.0775	0.1071
	Worst	0.1476	0.1198	0.2783	0.3567
	Median	0.1038	0.0997	0.1454	0.1909
	Mean	0.1065	**0.0988**	0.1577	0.1907
	SD	0.0219	**0.0136**	0.0528	0.0613
	Time	38.8456	27.5143	**20.0673**	40.0668
Rank		2	**1**	3	4
Ecoli	***Best***	0.8076	0.8019	0.8735	1.1652
	Worst	1.5705	1.0730	1.4427	2.3248
	Median	1.0107	0.9376	0.9918	1.4828
	Mean	1.0462	**0.9343**	1.0792	1.5353
	SD	0.1802	**0.0652**	0.1878	0.2944
	Time	28.8783	24.5822	**14.7665**	122.8615
Rank		2	**1**	3	4
Fertility	***Best***	**0.0872**	0.0934	0.1064	0.1028
	Worst	0.1090	0.1049	0.1232	0.1117
	Median	0.1006	0.1002	0.1103	0.1076
	Mean	0.1001	**0.0996**	0.1125	0.1073
	SD	0.0051	0.0034	0.0047	**0.0022**
	Time	38.9971	24.3091	**22.4168**	26.3487
Rank		2	**1**	4	3
Total mean		2.0136	2.3551	3.449	14.7875
Rank		**1**	2	3	4

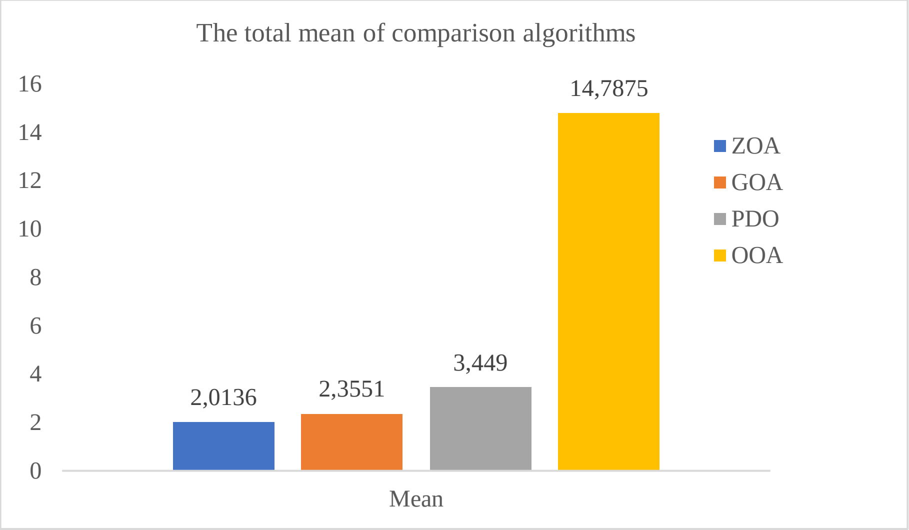

Figure 19. *The graphic of total mean of ZOA and comparison algorithms*

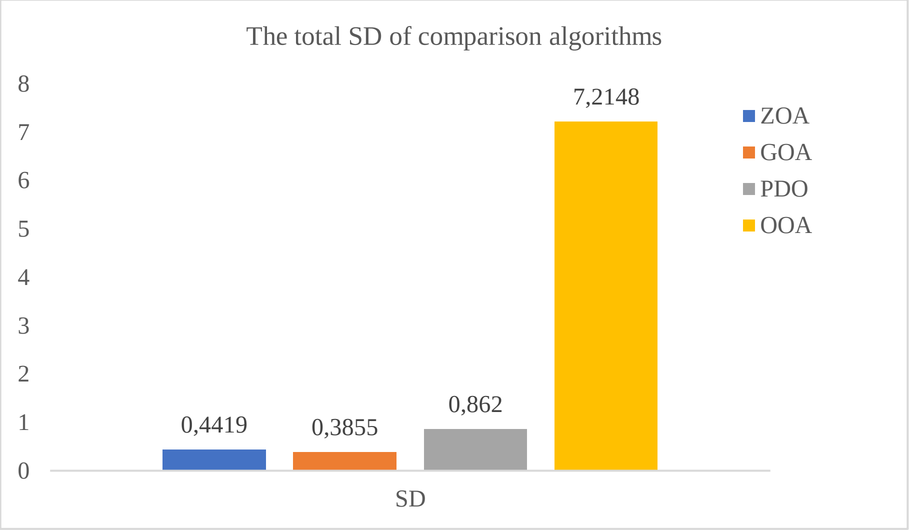

Figure 20. *The graphic of total SD of ZOA and comparison algorithms*

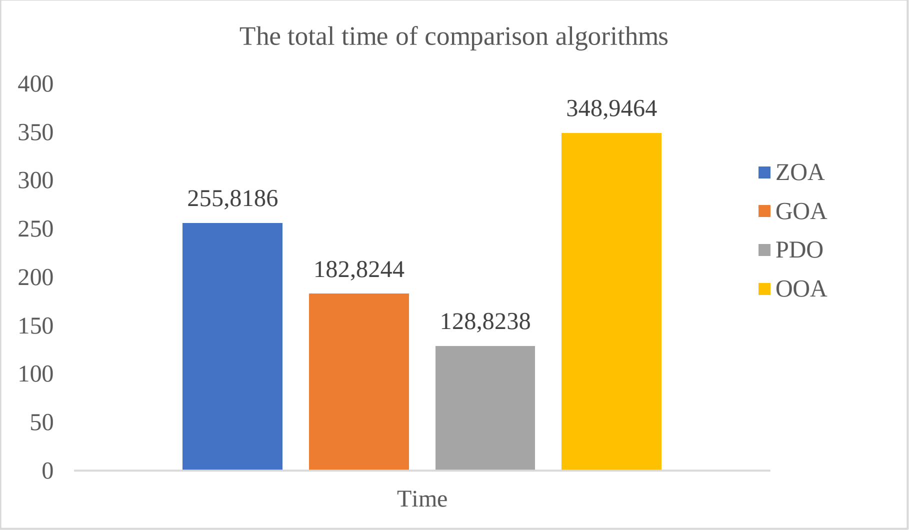

Figure 21. *The graphic of total time of ZOA and comparison algorithms*

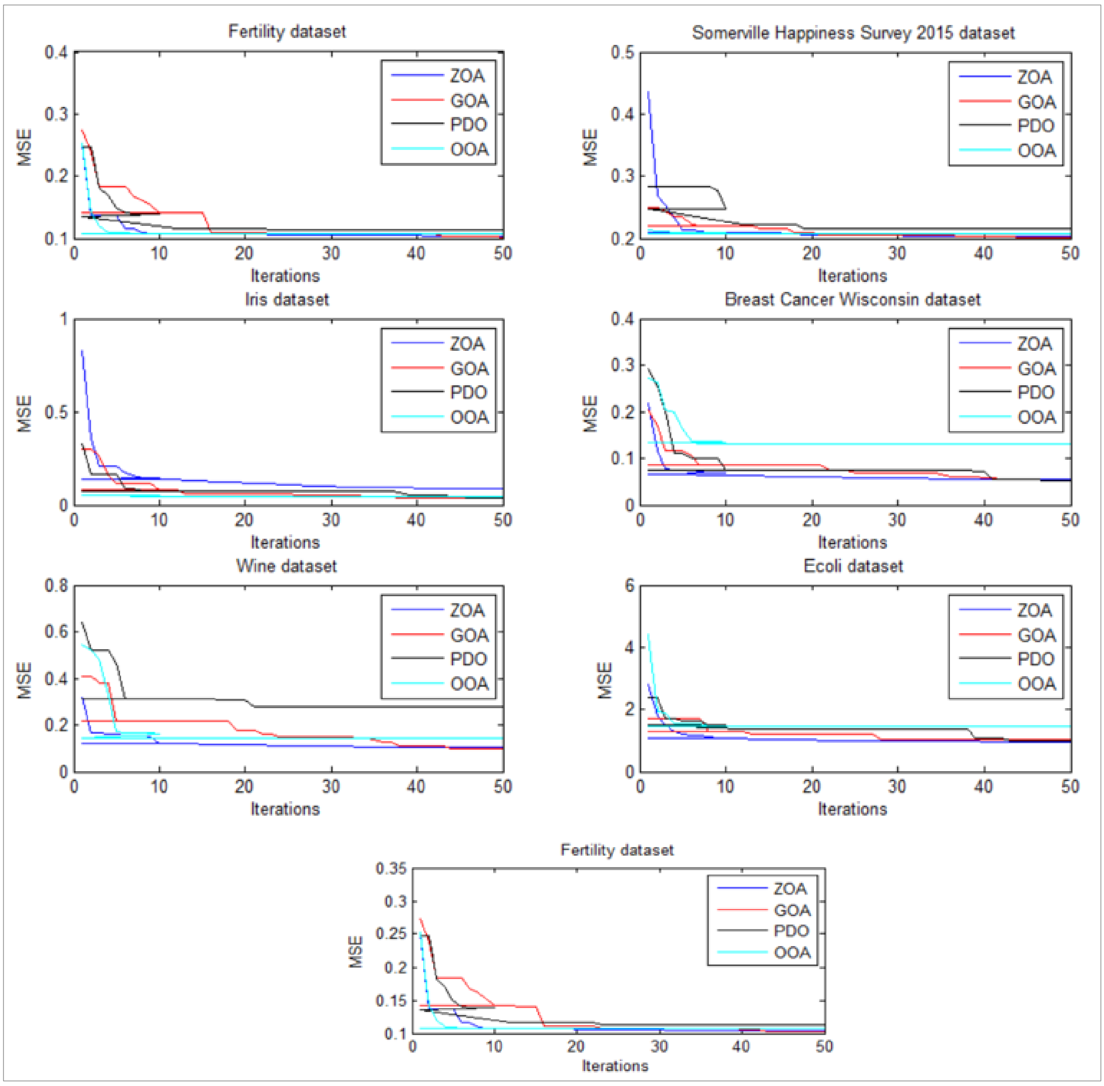

Figure 22. The convergence chart of ZOA and comparison algorithms on ANN

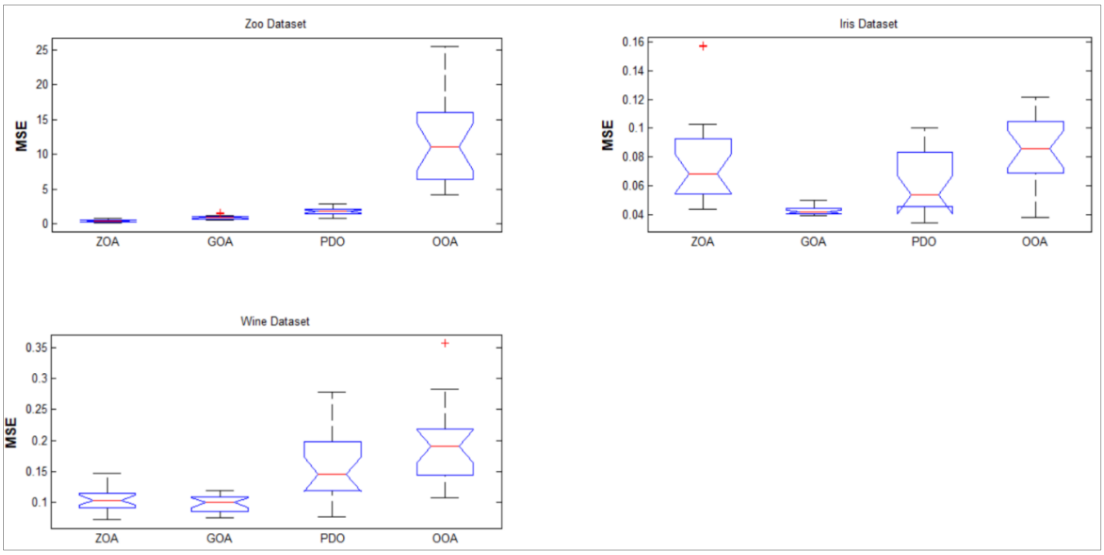

Figure 23. The boxplot chart of ZOA and comparison algorithms on Zoo, Iris, and Wine datasets

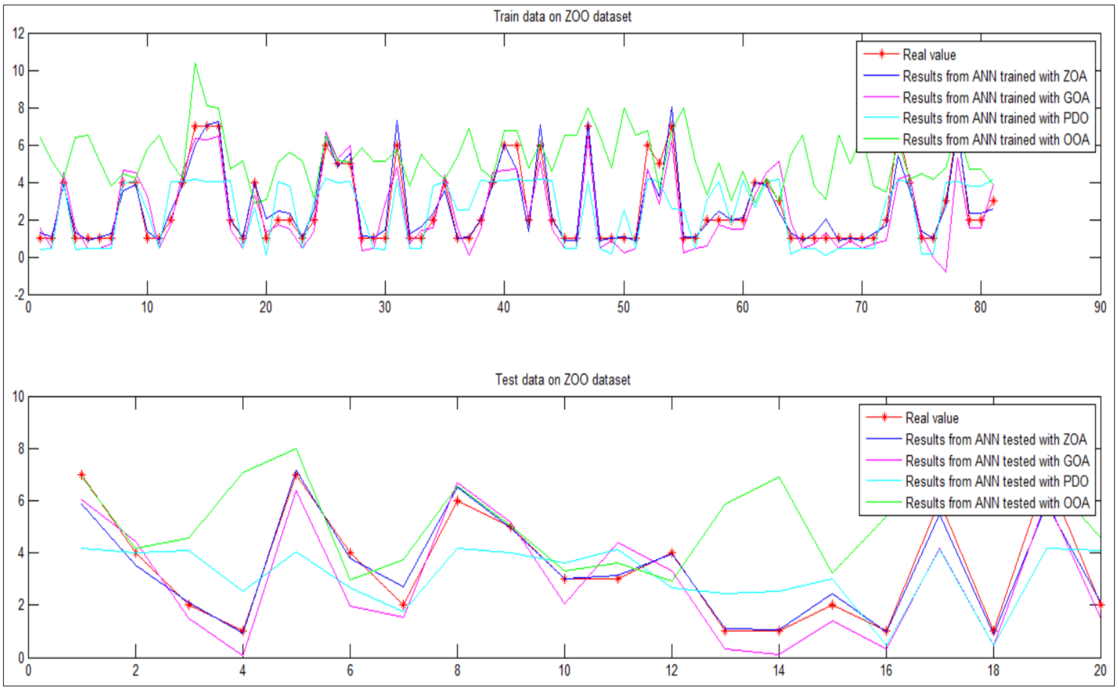

Figure 24. *The graphics of the results from ANN* trained *and tested with ZOA, GOA, PDO, OOA on zoo dataset*

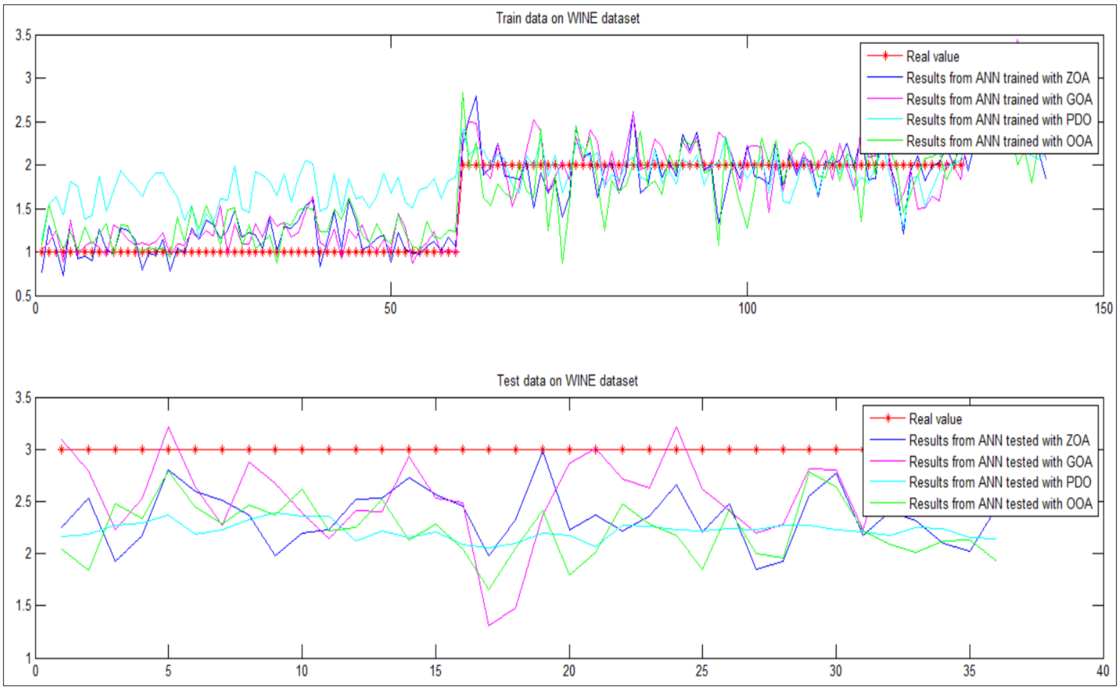

Figure 25. *The graphics of the results from ANN* trained *and tested with ZOA, GOA, PDO, OOA on wine dataset*

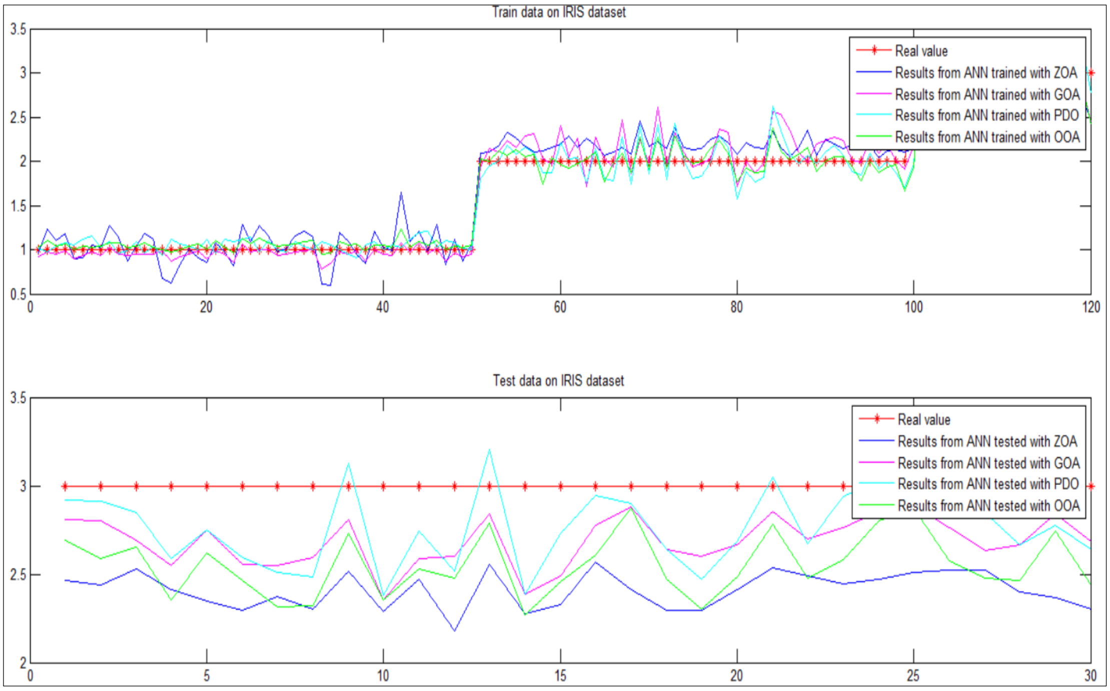

Figure 26. *The graphics of the results from ANN* trained *and tested with ZOA, GOA, PDO, OOA on iris dataset*

Conclusions

In this study, an Artificial Neural Network (ANN) model with predictive ability was designed on seven different data sets obtained from the UCI data set. In this designed ANN model, weight values were determined by the Zebra Optimization Algorithm (ZOA), a heuristic algorithm. Due to the success of heuristic algorithms in estimating weight values, classical gradient-based algorithms were abandoned in this study and replaced by heuristic-based algorithms. First, a detailed parameter analysis was carried out for parameter settings that are important for ZOA and ANN. Thus, the effects of population size and maximum number of iterations on ANN training are shown. Additionally, the effects of neuron, layer, and epoch values on the success of ANN are explained in detail. As a result, a suitable ANN network was designed with a ZOA with the most appropriate parameter values. Predictions were made on seven different data sets with this ANN model with ZOA. The results obtained were compared with the ANN model created with three different state-of-the-art heuristic algorithms (Gazelle Optimization Algorithm (GOA), Prairie Dogs Optimization (PDO), and Osprey Optimization Algorithm (OOA)) with similar network structures selected from the literature. The results show that the ANN model trained with ZOA is more successful in predicting layer weights. While faster convergence was achieved, the amount of error in predicting the classes of the data decreased. The predictive analytics performed by the proposed model can also improve ANN performance with proper convergence. While the ANN model integrated and trained with ZOA can find better coefficients, other algorithms used in this paper except GOA cannot obtain suitable outputs. ZOA's capabilities in local and global search are also reflected in the training of the ANN network. In the future, we plan to further increase the success of estimating ANN weights by improving ZOA's local and global search capabilities with the help of chaotic maps.

Acknowledgements The Zebra Optimization Algorithm (ZOA) code used in this study is available on MATLAB Central File Exchange: Zebra Optimization Algorithm (ZOA). Furthermore, the datasets for instances referenced in this study can be accessed at https://archive.ics.uci.edu/datasets. We would like to express our gratitude to these sources for providing valuable data for our research.

Funding/Financial Disclosure The author (s) has not received any financial support for the research. authorship or publication of this study.

Ethics Committee Approval and Permissions The study does not require ethics committee permission or any special permission.

Conflict of Interests No conflict of interest or common interest has been declared by the authors.

Authors Contribution The authors contributed equally to the study. The authors read and approved the final manuscript.

References

[1] McCulloch, W. S., & Pitts, W. (1943). A logical calculus of the ideas immanent in nervous activity. *The Bulletin of Mathematical Biophysics, 5*(4), 115-133. https://doi.org/10.1007/BF02478259

[2] Feng, Z. K., & Niu, W. J. (2021). Hybrid artificial neural network and cooperation search algorithm for nonlinear river flow time series forecasting in humid and semi-humid regions. *Knowledge-Based Systems*, *211*, 106580. https://doi.org/10.1016/j.knosys.2020.106580

[3] Fuqua, D., & Razzaghi, T. (2020). A cost-sensitive convolution neural network learning for control chart pattern recognition. *Expert Systems with Applications*, *150*, 113275. https://doi.org/10.1016/j.eswa.2020.113275

[4] Chatterjee, S., Sarkar, S., Hore, S. Dey, N., Ashour, A. S., & Balas, V. E. (2017). Particle swarm optimization trained neural network for structural failure prediction of multistoried RC buildings. *Neural Computing and Applications*, *28*, 2005-2016. https://doi.org/10.1007/s00521-016-2190-2

[5] Ulas, M., Altay, O., Gurgenc, T., & Ozel, C. (2020). A new approach for prediction of the wear loss of PTA surface coatings using artificial neural network and basic, kernel-based, and weighted extreme learning machine. *Friction*, *8*, 1102-1116. https://doi.org/ 10.1007/s40544-017-0340-0

[6] Vosniakos, G. C., & Benardos, P. G. (2007). Optimizing feedforward artifcial neural network architecture. *Engineering Applications of Artificial İntelligence, 20*(3), 365-382. https://doi.org/10.1016/j.engappai.2006.06.005

[7] Mosavi, M. R., Khishe, M., & Ghamgosar, A. (2016). Classification of sonar data set using neural network trained by gray wolf optimization. *Neural Network World*, *26*(4), 393-415. https://doi.org/ 10.14311/NNW.2016.26.023

[8] Mosavi, M. R., Khishe, M., Parvizi, G. R., Naseri, M. J., & Ayat, M. (2019). Training multi-layer perceptron utilizing adaptive best-mass gravitational search algorithm to classify sonar dataset. *Archives of Acoustics*, *44*(1), 137-51. https://doi.org/10.24425/aoa.2019.126360

[9] Mosavi, M. R., & Khishe, M. (2017). Training a feed-forward neural network using particle swarm optimizer with autonomous groups for sonar target classification. J. Circuits. *Journal of Circuits, Systems and Computers, 26*(11), 1-20. https://doi.org/10.1142/S0218126617501857

[10] Yaghini, M., Khoshraftar, M. M., & Fallahi, M. (2011). *HIOPGA: a new hybrid metaheuristic algorithm to train feedforward neural networks for prediction* [Conference presentation]. In Proceedings of the International Conference on Data Science (ICDATA). The Steering Committee of The World Congress in Computer Science, Computer Engineering and Applied Computing (WorldComp). Las Vegas, NV, USA. http://world-comp.org

[11] Kiranyaz, S., Ince, T., Yildirim, A., & Gabbouj, M. (2009). Evolutionary artifcial neural networks by multi-dimensional particle swarm optimization. *Neural Networks*, *22*(10), 1448-1462. https://doi.org/10.1016/j.neunet.2009.05.013

[12] Khishe, M., & Mosavi, M. R. (2020). Classification of underwater acoustical dataset using neural network trained by Chimp Optimization Algorithm. *Applied Acoustics*, *157*, 107005. https://doi.org/10.1016/j.apacoust.2019.107005

[13] Afrakhteh, S., Mosavi, M., Khishe, M., & Ayatollahi, A. (2020). Accurate classification of EEG signals using neural networks trained by hybrid population-physic-based algorithm. *International Journal of Automation and Computing*, *17*, 108-122. https://doi.org/10.1007/s11633-018-1158-3

[14] Khishe, M., Mosavi, M. R., & Kaveh, M. (2017). Improved migration models of biogeography based optimization for sonar data set classification using neural network. *Applied Acoustics, 118,* 15-29. https://doi.org/10.1016/j.apacoust.2016.11.012

[15] Khishe, M., Mosavi, M. R., & Moridi, A. (2018). Chaotic fractal walk trainer for sonar data set classification using multi-layer perceptron neural network and its hardware implementation. *Applied Acoustics*, *137*, 121-39. https://doi.org/10.1016/j.apacoust.2018.03.012

[16] Ravakhah, S., Khishe, M., Aghababaee, M., & Hashemzadeh, E. (2017). Sonar false alarm rate suppression using classification methods based on interior search algorithm. *International Journal of Computer Science and Network Security, 17*(7), 58-65.

[17] Mosavi, M. R., Khishe, M., & Akbarisani, M. (2017). Neural network trained by biogeographybased optimizer with chaos for sonar data set classification. *Wireless Personal Communications, 95*(4), 4623-4642. https://doi.org/10.1007/s11277-017-4110-x

[18] Kaveh, M., Khishe, M., & Mosavi, M. R. (2019). Design and implementation of a neighborhood search biogeography-based optimization trainer for classifying sonar dataset using multi-layer perceptron neural network. *Analog Integrated Circuits Signal Process*, *100*, 405-428. https://doi.org/10.1007/s10470-018-1366-3

[19] Mosavi, M. R., Khishe, M., Hatam Khani, Y., & Shabani, M. (2017). Training radial basis function neural network using stochastic fractal search algorithm to classify sonar dataset. *Iranian Journal of Electrical & Electronic Engineering, 13*(1), 100-111.

[20] Dangare, C. S., & Apte, S. S. (2012). Improved study of heart disease prediction system using data mining classifcation techniques. *International Journal of Computer Applications, 47*(10), 44-48.

[21] Movassagh, A. A., Alzubi, J. A., Gheisari, M., Rahimi, M., Mohan, S., Abbasi, A. A., & Nabipour, N. (2023). Artificial neural networks training algorithm integrating invasive weed optimization with differential evolutionary model. *Journal of Ambient Intelligence and Humanized Computing*, *14*, 6017-6025. https://doi.org/10.1007/s12652-020-02623-6

[22] Dang, N. M., Tran Anh, D., & Dang, T. D. (2021). ANN optimized by PSO and Firefly algorithms for predicting scour depths around bridge piers. *Engineering with Computers*, *37*, 293-303. https://doi.org/10.1007/s00366-019-00824-y

[23] Jamali, B., Rasekh, M., Jamadi, F., Gandomkar, R., & Makiabadi, F. (2019). Using PSO-GA algorithm for training artificial neural network to forecast solar space heating system parameters. *Applied Thermal Engineering*, *147*, 647-660. https://doi.org/10.1016/j.applthermaleng.2018.10.070

[24] Khatir, S., Tiachacht, S., Le Thanh, C., Ghandourah, E., Mirjalili, S., & Wahab, M. A. (2021). An improved Artificial Neural Network using Arithmetic Optimization Algorithm for damage assessment in FGM composite plates. *Composite Structures*, *273*, 114287. https://doi.org/10.1016/j.compstruct.2021.114287

[25] Gurgenc, E, Altay, O, & Altay, E. V. (2024). AOSMA-MLP: A novel method for hybrid metaheuristics artificial neural networks and a new approach for prediction of geothermal reservoir temperature. *Applied Sciences*, *14*(8), 3534. https://doi.org/10.3390/app14083534

[26] Altay, O., & Altay, E. V. (2023). A novel hybrid multilayer perceptron neural network with improved grey wolf optimizer. *Neural Computing and Applications*, *35*, 529–556. https://doi.org/10.1007/s00521-022-07775-4

[27] Altay, E. V., Gurgenc, E., Altay, O., & Dikici, A. (2022). Hybrid artificial neural network based on a metaheuristic optimization algorithm for the prediction of reservoir temperature using hydrogeochemical data of different geothermal areas in Anatolia (Turkey). *Geothermics*, *104*, 102476. https://doi.org/10.1016/j.geothermics.2022.102476

[28] Altay, O., & Gurgenc, T. (2024). GJO-MLP: a novel method for hybrid metaheuristics multi-layer perceptron and a new approach for prediction of wear loss of AZ91D magnesium alloy worn at dry, oil, and H-BN nanoadditive oil. *Surface Review and Letters (SRL)*, *31*, 06, 1-16. https://doi.org/10.1142/S0218625X24500483

[29] Cinar, A. C. (2020). Training feed-forward multi-layer perceptron artificial neural networks with a tree-seed algorithm. *Arabian Journal for Science and Engineering*, *45*, 10915–10938. https://doi.org/10.1007/s13369-020- 04872-1

[30] Trojovská, E., Dehghani, M., & Trojovský, P. (2022). Zebra optimization algorithm: A new bio-inspired optimization algorithm for solving optimization algorithm. *IEEE Access*, *10*, 49445-49473. https://doi.org/10.1109/ACCESS.2022.3172789

[31] Agushaka, J. O., Ezugwu, A. E. & Abualigah, L. (2023). Gazelle optimization algorithm: a novel nature-inspired metaheuristic optimizer. *Neural Computing and Applications*, *35*, 4099–4131. https://doi.org/10.1007/s00521-022-07854-6

[32] Ezugwu, A. E., Agushaka, J. O., Abualigah, L., Mirjalili, S., & Gandomi, A. H. (2022). Prairie dog optimization algorithm. *Neural Computing and Applications*, *34*, 20017–20065. https://doi.org/10.1007/s00521-022-07530-9

[33] Dehghani, M., & Trojovský, P. (2023). Osprey optimization algorithm: A new bio-inspired metaheuristic algorithm for solving engineering optimization problems. *Frontiers in Mechanical Engineering*, *8*, 1126450. https://doi.org/10.3389/fmech.2022.1126450

[34] Yang, J., & Ma, J. (2019). Feed-forward neural network training using sparse representation. *Expert Systems with Applications*, *116*, 255–264. https://doi.org/10.1016/j.eswa.2018.08.038

[35] Siemon, H. P., & Ultsch, A. (1990, July 9–13). *Kohonen networks on transputers: implementation and animation* [Conference presentation]. In: International Neural Network Conference (INNC), Springer, Dordrecht. https://doi.org/10.1007/978-94-009-0643-3_31

[36] Orr, M. (1996). Introduction to radial basis function networks. Technical Report, center for cognitive science. The University of Edinburgh.

[37] Kousik, N., Natarajan, Y., Raja, R. A., Kallam, S., Patan, R., Gandomi, A. H. (2021). Improved salient object detection using hybrid convolution recurrent neural network. *Expert Systems with Applications, 166*, 114064. https://doi.org/10.1016/j.eswa.2020.114064

[38] Winoto, A. S., Kristianus, M., & Premachandra, C. (2020). Small and slim deep convolutional neural network for mobile device. *IEEE Access*, *8*, 125210-125222. https://doi.org/10.1109/ACCESS. 2020.3005161

[39] Ghosh-Dastidar, S., & Adeli, H. (2009). Spiking neural networks. *International journal of neural systems*, *19*, 295-308. https://doi.org/10.1142/ S0129065709002002

[40] Fekri-Ershad, S. (2020). Bark texture classification using improved local ternary patterns and multilayer neural network. *Expert Systems with Applications*, *158*, 113509. https://doi.org/10.1016/j.eswa.2020.113509

[41] Ren, H., Ma, Z., Lin, W., Wang, S., & Li, W. (2019). Optimal design and size of a desiccant cooling system with onsite energy generation and thermal storage using a multilayer perceptron neural network and a genetic algorithm. *Energy Conversion and Management*, *180*, 598-608. https://doi.org/10.1016/j.enconman.2018.11.020

[42] Aljarah, I., Faris, H., & Mirjalili, S. (2018). Optimizing connection weights in neural networks using the whale optimization algorithm. *Soft Computing*, *22*(1), 1-15. https://doi.org/10.1007/s00500-016-2442-1

[43] Bache, K., & Lichman, M. (2024, December 5). UCI Machine learning repository. http:// archive.ics.uci.edu/ml.

Sinopfbd, 2024; 9(2): 421-430 **https://doi.org/10.33484/sinopfbd.1425952**

Sinop Üniversitesi Fen Bilimleri Dergisi
Sinop Uni J Nat Sci

E-ISSN: 2564-7873

https://dergipark.org.tr/tr/pub/sinopfbd

The Effect of Larval Density on Pupation Rate and Time to Emergence from Pupation in *Tenebrio molitor* Linnaeus, 1758 (Coleoptera: Tenebrionidae) Reared on Two Different Feeds

Yeşim KOÇ

How to cite: Koç, Y., (2024). The effect of larval density on pupation rate and time to emergence from pupation in *Tenebrio molitor* Linnaeus, 1758 (Coleoptera: Tenebrionidae) reared on two different feeds. *Sinop Üniversitesi Fen Bilimleri Dergisi, 9*(2), 421-430. https://doi.org/10.33484/sinopfbd.1425952

Research Article

Corresponding Author
Yeşim KOÇ
ykoc@sinop.edu.tr

ORCID of the Authors
Y.K: 0000-0001-7125-2561

Received: 04.02.2024
Accepted: 12.08.2024

Abstract

In our research, the yellow mealworm, *Tenebrio molitor* L. was used. The effects of two different foods on the pupation rate and time to emergence from pupation of *T. molitor* at different larval densities were investigated. The experiments were carried out under continuous dark laboratory conditions with a temperature of 27±2°C and a relative humidity of 60%±5%. Two different nutrient and four larval density groups were used in the study. The first nutrient composition consisted of dry yeast and wheat germ (150 gr in total, 1/2) The second nutrient composition consisted of whole wheat flour and corn flour (150 gr in total, 1/1). Insects were bred primarily on the tested nutrient media. Experimental sets were prepared at four different larval densities for both foods. The number of larvae in plastic containers was adjusted to 20, 60, 200 and 600. To ensure equality, all larvae were selected from small larvae. (between 50 mg-120 mg). In our study, pupation rates were high, especially in groups consisting of 20 and 60 larvae. The percentage of pupation decreased at 200 larval densities and sharply decreased at 600 larval densities in both diets. Especially the negative effects of the density are more obvious in the second food. The effects on intensity were more pronounced, especially in pupation of larvae, not in terms of pup time. As a result, it would be advantageous for the larvae density not to be above 200 in terms of getting more yield and increasing the reproduction rate from *T. molitor*, which is demanded in large numbers as live feed. In conclusion, for the production of *T. molitor*, which is commonly used as live feed, it is preferable to have a larval density below 200 in order to get a higher yield and better reproduction rates.

Keywords: *Tenebrio molitor*, larval density, pupation rate, time to emergence from pupation

İki Farklı Besinde Larval Yoğunluğun, *Tenebrio molitor* Linnaeus, 1758 (Coleoptera: Tenebrionidae) un Pupalaşma Oranı ve Pupadan Çıkış Süresine Etkisi

Sinop University, Faculty of Education, Department of Mathematics and Science Education, Sinop, Türkiye

Öz

Araştırmamızda un kurdu *Tenebrio molitor* L. kullanılmıştır. İki farklı besinin, farklı larval yoğunluğunda *T. molitor*' un pupalaşma oranı ve pupadan çıkış süresine etkisi araştırılmıştır. Denemeler, sıcaklığı 27±2°C ve nisbi nemi %60±5 olan devamlı karanlık laboratuvar koşullarında yapılmıştır. Araştırmada iki farklı besin tipi kullanılmıştır. 1. besin; buğday rüşeymi ve kuru mayadan oluşurken, 2. besin; tam buğday unu ve mısır unun (eşit miktarda) dan oluşmuştur. Öncelikle denenen besin ortamlarında böcekler yetiştirilmiştir. Her iki besin için de dört farklı larva yoğunluğunda deney seti hazırlanmıştır. Plastik kaplarda larva sayısı, 20, 60, 200 ve 600 olacak şekilde ayarlanmıştır. Biyolojik testlerde 50 mg-120 mg arası küçük larvalar tercih edilmiştir. Pupalaşma yüzdesi her iki besinde de 200 larva yoğunluğunda azalmış, 600 larva yoğunluğunda ise keskin bir düşüş olmuştur. Özellikle yoğunluğun ortaya çıkardığı negatif etkilerin 2. besinde daha bariz ortaya çıktığı tespit edilmiştir. Pup süreleri bakımından değil, özelikle larvaların pupalaşmasında yoğunluktaki etkiler daha bariz olmuştur. Sonuç olarak, canlı yem olarak çok fazla sayıda talep gören *T. molitör* den daha fazla verim almak, üreme hızını arttırmak bakımından larva yoğunluğunun özellikle 200 ün üzerinde olmaması avanvajlı olacaktır

Anahtar Kelimeler: *Tenebrio molitor,* larval yoğunluk, pupalaşma oranı, pupadan çıkış süresi

Introduction

The yellow mealworm, *Tenebrio molitor* Linnaeus, 1758 is a pest of stored products. It is also a natural feed for poultry and fish due to its high nutritional content. The ability of its larvae to break down polystyrene and plastic parts, being a natural feed source and being recommended for human nutrition has increased the interest in this insect in recent years. [1-5]. Research efforts to reduce the cost of producing *T. molitor* are focused on determining the ideal rearing conditions and diet [6-15]. On the other hand, larval density, in particular, can significantly affect production efficiency. Previous studies have found that in many tenebrionid species, pupation is delayed or inhibited by crowding, including *T. molitor* [16]. Weaver and McFarlane, [17] reported that larval crowding negatively affects growth in *T. molitor* and found that growth rates decreased with increasing larval densities. A different study reported that larval crowding is well-tolerated by *T. molitor* [18]. Larval crowding reduced pupation in *Tribolium castaneum* (Herbst, 1797) (Coleoptera: Tenebrionidae) [19]. In *Gnatocerus cornutus* (Fabricaus, 1798) (Coleoptera: Tenebrionidae), increased larval density delayed development and increased mortality and cannibalism [20]. Similarly, in *Alphitobius diaperinus* Panzer, 1797 (Coleoptera: Tenebrionidae), high larval densities were associated with prolonged development times and decreased pupal weight [21]. Further research is needed to determine the optimal larval density in the mass production of *T. molitor*. The growing importance of this species, particularly for use as animal feed, requires a more in-depth understanding of the effect of different rearing conditions and larval density on production. Therefore, it is important to determine the optimal cut-off point for larval density.

Material and Methods

Material

In this study, *Tenebrio molitor*, one of the most common stored grain pests in Türkiye, was used. The larvae used for biological tests were obtained from the stock culture at the Science Research Laboratory of Sinop University Faculty of Education.

Method

This study researches the effect of larval density on pupation rate and time to emergence from pupation in *Tenebrio molitor* (Coleoptera: Tenebrionidae) reared on two different feeds. The trials were conducted under laboratory conditions in continuous dark (CD) with a temperature of 27±2°C and relative humidity of 60%±5. Two different nutrient and four larval density groups were used in the study. The first nutrient composition consisted of dry yeast and wheat germ (150 gr in total, 1/2). The second nutrient composition consisted of whole wheat flour and corn flour (150 gr in total, 1/1). The studies first started by rearing the beetle with this nutrient. The beetles were reared in medium size wide plastic containers (30×20×5 cm). Wood dust was added to nutrients to ease movement and the nutrients were renewed every 10 days. The larvae in the old nutrients were sieved and transferred to the new nutrient. Small pieces (2 for each, 4×4×6 cm) were cut from egg boxes which provide convenience for adults to mate and which is also preferred to lay eggs and they were placed in containers. While the plastic containers were covered to prevent other living beings from being transmitted, small holes were opened on the top side to enable the insects to breathe. Potato was used for humidity (3×3 cm). Potatoes were given wrapped in aluminium foil to prevent from contacting with the nutrients which otherwise may lead to the decaying of the potatoes and moistening of the nutrients as well. Potatoes were changed every 3 days for the litter not to get mouldy. Litter for nutrients was adjusted as 4-5 cm high.

Biological Tests

The research was started with the beetle reared for two generations in the nutrient composition studied. Each nutrient composition was prepared in the abovementioned amounts. For each nutrient composition and different larval density groups (20, 60, 200, and 600 larvae), four sample groups were formed with the beetle taken from the population at different times. Experimental sets were prepared at four different larval densities for both foods. The number of larvae in plastic containers was adjusted to 20, 60, 200 and 600. To ensure equality, all larvae were selected from small larvae. (between 50 mg-120 mg). As the pups formed in the vessels, they were taken into separate containers. The number of pupating larvae and dead larvae were recorded. The dishes were checked every day and the pups were taken the day they were first formed and then placed in petri dishes (9 cm x1.5 cm). Petri dishes were observed daily and the time from pups to adults was recorded. The time to emerge from the pupa was determined by calculating the time at each adult emergence. Three repetitions were performed for each intensity on each food and the results were averaged.

Statistical Analysis

In the study, pupation percentages and time to emergence from pupation (in days) were presented as descriptive statistics and compared based on different larval density groups (20, 60, 200, and 600 larvae). The ANOVA test was used for statistical comparison. The groups that were significantly different in the

ANOVA test were compared with the Tukey test. All statistical hypothesis tests were performed using the R-Project software. The margin of error was determined as 5% in hypothesis testing.

Results

Table 1 presents the descriptive statistics for pupation rates (%) based on larval density groups.

Table 1. *Descriptive statistics for pupation rates for Feed 1 and Feed 2.*

Feed	**Group**	**$\bar{X}$**	**SD**	**Min**	**Max**
Feed 1	20 larvae	92.2	1.4	90.7	93.3
	60 larvae	95.9	1.2	94.5	96.6
	200 larvae	83.0	1.5	81.8	84.7
	600 larvae	61.4	3.0	58.8	64.6
Feed 2	20 larvae	83.9	4.4	80.5	88.8
	60 larvae	91.9	1.3	90.8	93.4
	200 larvae	71.4	2.4	68.9	73.6
	600 larvae	51.0	3.1	48.9	54.5

$\bar{X}$: Mean, SD: Standard deviation, Min: Minimum, Max: Maximum

Table 2. *Descriptive statistics for time to emergence (days) for Feed 1 and Feed 2.*

Feed	**Group**	**$\bar{X}$**	**SD**	**Min**	**Max**
Feed 1	20 larvae	6.6	1.2	5.0	9.0
	60 larvae	6.7	1.3	5.0	9.0
	200 larvae	6.9	1.2	5.0	9.0
	600 larvae	7.2	1.0	6.0	9.0
Feed 2	20 larvae	6.9	1.1	5.0	9.0
	60 larvae	6.7	1.0	5.0	9.0
	200 larvae	6.7	1.2	5.0	9.0
	600 larvae	7.5	1.0	6.0	9.0

$\bar{X}$: Mean, SD: Standard deviation, Min: Minimum, Max: Maximum

Table 2 presents the descriptive statistics for time to emergence (days) based on larval density groups.

Table 3. *ANOVA test results where pupation percentages for Feed 1 is the dependent variable*

	DF	**SS**	**MS**	**F**	***P***
Group	3	2152.6	717.5	202.100	**<0.001**
Error	8	28.4	3.6		

DF: Degree of freedom, SS: Sum of squares, MS: Mean sum of squares

Table 3 presents the ANOVA test results for pupation percentages considering different larval density groups (20, 60, 200, 600 larvae) for Feed 1. According to the ANOVA table, pupation percentages for Feed 1 were significantly different between larval density groups (F=202.100, *P*<0.05). Tukey test, a multiple comparison test, was applied to larval density groups that were significantly different.

Table 4. *Pupation percentages of T. molitor for groups of different larval densities with Feed 1*

	MD	**95% CI**		***P***
		Lower limit	**Upper limit**	
20 larvae-200 larvae	9.2	4.2	14.1	**0.002**
600 larvae-200 larvae	-21.6	-26.6	-16.7	**<0.001**
60 larvae-200 larvae	12.9	7.9	17.8	**<0.001**
600 larvae-20 larvae	-30.8	-35.7	-25.9	**<0.001**
60 larvae-20 larvae	3.7	-1.2	8.6	0.153
60 larvae-600 larvae	34.5	29.6	39.4	**<0.001**

MD: Mean difference, CI: Confidence interval of mean difference

For larval density groups that were found to be significantly different (see Table 3), a Tukey test was performed to determine the group from which the difference originated and the results are presented in Table 4. According to the post hoc analysis, with Feed 1, the group with a larval density of 60 had a significantly higher pupation percentage compared with the groups of 200 and 600 larvae. Moreover, with Feed 1, the group with the larval density of 600 had a significantly lower pupation percentage compared with the groups of 20 and 200 larvae. On the other hand, with Feed 1, the group with a larval density of 20 had a significantly higher pupation percentage compared with the group of 200 larvae.

Table 5. *ANOVA test results where pupation percentages for Feed 2 is the dependent variable*

	DF	**SS**	**MS**	**F**	***P***
Group	3	2859.9	953.3	106.600	**<0.001**
Error	8	71.5	8.9		

DF: Degree of freedom, SS: Sum of squares, MS: Mean sum of squares

Table 5 presents the ANOVA test results for pupation percentages based on different larval density groups (20, 60, 200, 600 larvae) for Feed 2. According to the ANOVA table, pupation percentages for Feed 2 were significantly different between larval density groups (F=106.600, *P*<0.05). Tukey test, a multiple comparison test, was determined to be appropriate to compare larval density groups that were significantly different.

Table 6. *Pupation percentages of T. molitor for groups of different larval densities with Feed 2*

	MD	**95% CI**		***P***
		Lower limit	**Upper limit**	
20 larvae-200 larvae	12.4	4.6	20.3	**0.004**
600 larvae-200 larvae	-20.4	-28.3	-12.6	**<0.001**
60 larvae-200 larvae	20.5	12.7	28.3	**<0.001**
600 larvae-20 larvae	-32.9	-40.7	-25.0	**<0.001**
60 larvae-20 larvae	8.1	0.2	15.9	**0.043**
60 larvae-600 larvae	40.9	33.1	48.8	**<0.001**

MD: Mean difference, CI: Confidence interval of mean difference

For larval density groups that were found to be significantly different (see Table 5), a Tukey test was performed to determine the group from which the difference originated and the results are presented in Table 6. According to the post hoc analysis, with Feed 2, the group with the larval density of 600 had a significantly lower pupation percentage compared with the groups of 200, 20, and 60 larvae. Moreover, with Feed 2, the group with the larval density of 60 had a significantly higher pupation percentage compared to groups with 20 and 200 larvae. On the other hand, with Feed 2, the group with the larval density of 20 had a significantly higher pupation percentage compared to the group with 200 larvae.

Table 7. *ANOVA test results where time to emergence (days) for Feed 1 is the dependent variable*

	DF	**SS**	**MS**	**F**	***P***
Group	3	5.5	1.8	1.328	0.269
Error	116	161.1	1.4		

DF: Degree of freedom, SS: Sum of squares, MS: Mean sum of squares

Table 7 presents the ANOVA test results for time to emergence (days) based on different larval density groups (20, 60, 200, 600 larvae) for Feed 1. According to the ANOVA table, time to emergence from pupation (days) with Feed 1 was not statistically different between groups of larval densities (F=1.328, *P*>0.05).

Table 8. *ANOVA test results where time to emergence (days) for Feed 2 is the dependent variable*

	DF	**SS**	**MS**	**F**	***P***
Group	3	15.0	5.0	4.192	**0.007**
Error	116	138.7	1.2		

DF: Degree of freedom, SS: Sum of squares, MS: Mean sum of squares

Table 8 presents the ANOVA test results for time to emergence (days) according to larval density groups (20, 60, 200, 600 larvae) for Feed 2. According to the ANOVA table, time to emergence from pupation (days) for Feed 2 was significantly different considering larval densities (F=4.192, *P*>0.05). Tukey test, a multiple comparison test, was found to be appropriate to compare larval density groups that were significantly different.

Table 9. *Time to emergence from pupation for T. molitor between groups of larval densities with Feed 2*

	MD	**95% CI**		***P***
		Lower limit	**Upper limit**	
20 larvae-200 larvae	0.3	-0.5	1.0	0.781
600 larvae-200 larvae	0.9	0.1	1.6	**0.014**
60 larvae-200 larvae	-0.0	-0.7	0.7	1.000
600 larvae-20 larvae	0.6	-0.1	1.3	0.151
60 larvae-20 larvae	-0.3	-1.0	0.5	0.781
60 larvae-600 larvae	-0.9	-1.6	-0.1	**0.014**

MD: Mean difference, CI: Confidence interval of mean difference

For larval density groups that were found to be significantly different (see Table 8), a Tukey test was performed to determine the group from which the difference originated and the results are presented in Table 9. According to the post hoc analysis, with Feed 2, the time to emergence (in days) was significantly longer for the group with the larval density of 600 compared to groups with 200 and 60 larvae.

Discussion

Several studies on *T. molitor* Linnaeus, 1758 report negative effects with high larval density, in parallel with our results. Producers often resort to cold exposure to increase production yield in this species; on the other hand, it will be favorable to determine the exact effect of larval density on the reproduction of *T. molitor*. According to Tschinkel and Willson [16] the negative impact of larval crowding in certain tenebrionids is due to physical contact between larvae, or in other words, mechanical stimulation. Although *T. molitor* is comparatively insensitive to mechanical disturbances, pupation was significantly delayed by tactile stimulation (disturbing with chains) and vibration at low larval densities. Weaver and McFarlane [17] hypothesized that in the setting of high larval density, the reduced growth in *T. molitor* was due to reduced feeding opportunities caused by intraspecific competition. The same authors reared one-day-old larvae of *Tenebrio molitor* at 30±1°C at 55%±5% RH at densities of 1, 2, 5, 10, and 20 larvae per 455 mL rearing jar. After one month, larvae reared at a density of 20 were significantly larger compared to those reared at a density of two individuals, which were the smallest. Harada and Spence, [22] investigated the effects of rearing density on the duration of nymphal development in two wing-dimorphic water strider species, namely *Gerris buenoi* Kirkaldy and *Gerris pingreensis* Drake and Hottes (Hemiptera: Gerridae). Accordingly, they noted that under higher larval density, the average nymphal period was significantly reduced by approximately 4-5 days for both species. However, they did not find larval density to be significantly associated with per cent survival in either species. Silva et al. [23] conducted a study to develop a mass production method for *Euschistus heros* (Fabricius, 1798) (Hemiptera: Pentatomidae) in laboratory. Nymphs were reared at egg densities of 100, 200, 300, and 400 per petri dish (diameter 9 cm), and adults at densities of 50, 100, 150, and 200 couples per rearing dish (900 mL). The highest survival rate was recorded in the group with an egg density of 100 (89%). They reported that a density of 100 couples per rearing cage was the best density to improve the quality of the progeny. Ito [24] reported that in *O. strigicollis* and *O. laevigatus*, when the initial nymphal density was 100–400, the average rate of individuals reaching the adult stage was 74–87% while noting that the studied species had a high breeding capacity. In another study on *T. molitor*, reproductive output per female decreased with increasing adult density. In this study, progeny per unit area peaked at a density of 14 adults/dm and then sharply declined. Larval growth was also adversely affected by larval density in *Tenebrio molitor* Linn, possibly due to reduced feeding opportunities as a result of increased competition [25]. In our study, the decreased pupation rates recorded with high larval densities may be due to nutritional deficiency associated with competition. This decrease was particularly prominent in groups with a larval density of up to 600. Pupation rates were higher at relatively lower densities. This is consistent with the study which concluded that *T. molitor* well adapts to high larval densities and can boost immunity in crowded conditions to prevent infection [26]. However, in our study, particularly at a density of 600 larvae, the pupation rate was 61.4% with Feed 1 and 51% with Feed 2 (Table 1). The higher pupation rate achieved with Feed 1 may be because of the compatibility of its composition to the biological requirements of the species. Pupation began to decrease particularly after a density of 60 larvae, and this decrease was even more prominent after passing a larval density of 200. Overall, with Feed 1, time to emergence was not prominently associated with larval density, that is results were similar for all larval density groups. With Feed 2, time to emergence was significantly longer in the group with a larval density of 600 (Table, 2).

Conclusions

In our study, pupation rates were higher especially in groups with densities of 20 and 60 larvae. The negative impact of crowding was particularly prominent with Feed 2. This may be because Feed 1 was more compatible with the biological requirements of the studied species. The effects of crowding were even more prominent on pupation rates compared to time to emergence from pupation. In conclusion, for the production of *T. molitor*, which is commonly used as a live feed, it is preferable to have a larval density below 200 to get a higher yield and better reproduction rates.

Acknowledgements -

Funding/Financial Disclosure The author has no received any financial support for the research, authorship, or publication of this study.

Ethics Committee Approval and Permissions The study does not require ethics committee permission or any special permission.

Conflict of Interests -

Authors Contribution The author read and approved the final manuscript.

References

[1] Finke, M. D. (2015). Complete nutrient content of four species of commercially available feeder insects fed enhanced diets during growth. *Zoo Biology, 34,* 554-564. https://doi.org/10.1002/zoo.21246

[2] Ravzanaadii, N., Kim, S., Choi, W. H., Hong, S., Kim, N. J. (2012). Nutritional Value of mealworm, *Tenebrio molitor* as food source. *International Journal of Industrial Entomology, 25*(1),93-98. https://doi.org/10.7852/ijie.2012.25.1.093

[3] Hong, J., Han, T., Kim, Y. Y. (2020). Mealworm (*Tenebrio molitor* larvae) as an alternative protein source for monogastric animal: A review. *Animals. 10*(11), 2068. https://doi.org/10.3390/ani10112068

[4] Tekeli, A. (2014). Hayvan beslemede alternatif protein kaynağı olarak böceklerin kullanımı. *Türk Tarım ve Doğa Bilimleri Dergisi 1*(4), 531-538.

[5] Van Huis, A. V., Itterbeeck, J. V., Klunder, H., Mertens, E., Halloran, A., Muir, G. & Vantomme, P. (2013). Edible insects: Future prospects for food and feed security. FAO Forestry Paper, Wageningen, 171.

[6] Morales-Ramos, J. A., Rojas, M. G., Shapiro-Ilan, D. I. & Tedders, W. L. (2010). Developmental plasticity in *Tenebrio molitor* (Coleoptera: Tenebrionidae): Analysis of instar variation in number and development time under different diets. *Journal of Entomological Science. 45*, 75-90. https://doi.org//10.18474/0749-8004-45.2.75

[7] Morales-Ramos, J. A., Rojas, M. G., Shapiro-Ilan, D. I., Tedders, W. L. & Tedders, A. W. L. (2011). Self-selection of two diet components by *Tenebrio molitor* (Coleoptera: Tenebrionidae) larvae and its impact on fitness. *Environmantal. Entomology, 40*, 1285-94. https://doi.org//10.1603/EN10239

[8] Morales-Ramos, J. A., Rojas, M. G., Shapiro-llan, D. I. & Tedders, W. L. (2013). Use of nutrient self-selection as a diet refining tool in *Tenebrio molitor* (Coleoptera: Tenebrionidae). *Journal of Entomological Science*, *48*(3),206-221. https://doi.org//10.18474/0749-8004-48.3.206

[9] Morales-Ramos, J. A., Rojas, M. G., Shelby, K. S. & Coudron, T. A. (2016). Nutritional value of pupae versus larvae of *Tenebrio molitor* (Coleoptera: Tenebrionidae) as food for rearing Podisus maculiventris (Heteroptera: Pentatomidae). *Journal of Economic Entomology, 109*(2), 564-571. https://doi.org/10.1093/jee/tov338

[10] Oonincx, D. G. A. B., Van Broekhoven, S., Van Huis, A. & Van Loon, J. J. A. (2015). Feed conversion, survival and development, and composition of four insect species on diets composed of food by-products. *PLoS One, 10*, e0144601

[11] Rho, M. S., Lee, K. P. (2016). Balanced intake of protein and carbohydrate maximizes lifetime reproductive success in the mealworm beetle, *Tenebrio molitor* (Coleoptera: Tenebrionidae*). Journal of Insect Physiology, 91-92*, 93-99. https://doi.org//10.1016/j.jinsphys.2016.07.002

[12] Ribeiro, N., Abelho, M. & Costa, R. A. (2018). review of the scientifc literature for optimal conditions for mass rearing *Tenebrio molitor* (Coleoptera: Tenebrionidae). *Journal of Entomological Science, 53*, 434-454. https://doi.org/10.18474/JES17-67.1

[13] Rojas, M. G., Morales-Ramos, J. A. & Riddick, E. W. (2016). Use of *Tenebrio molitor* (Coleoptera: Tenebrionidae) powder to enhance artifcial diet formulations for *Coleomegilla maculata* (Coleoptera: Coccinellidae). *Biological Control, 100*, 70-78. https://doi.org/10.1016/j.biocontrol.2016.05.018

[14] Rumbos, C. I., Adamaki-Sotiraki, C., Gourgouta, M., Karapanagiotidis, I. T., Asimaki, A., Mente, E., & Athanassiou, C. G. (2021). Strain matters: Strain effect on the larval growth and performance of the yellow mealworm, *Tenebrio molitor* L. *Journal of Insects Food Feed, 7*(8), 1195-1205. https://doi.org/10.3920/JIFF2021.0035

[15] Adamkova, A., Mlcek, J., Adamek, M., Borkovcova, M., Bednarova, M., Hlobilova, V. Knížková, I., & Juríková, T. (2020). *Tenebrio molitor* (Coleoptera: Tenebrionidae)-optimization of rearing

conditions to obtain desired nutritional values. *Journal Insect Science, 20*(5), 24; 1-10. https://doi.org/10.1093/jisesa/ieaa100

[16] Tschinkel, W. R. & C. D. Willson. (1971). Inhibition of pupation due to crowding in some tenebrionid beetles. *Journal of Experimantal Zoology, 176,* 137-146.

[17] Weaver, D. K. & J. E. McFarlane. (1990). The effect of larval density on growth and development of *Tenebrio molitor*. *Journal of Insect Physiology, 36,* 531-536. https://doi.org/10.1016/0022-1910(90)90105-O

[18] Zaelor, J. & S. Kitthawee. (2018). Growth response to population density in larval stage of darkling beetles (Coleoptera; Tenebrionidae) *Tenebrio molitor* and *Zophobas atratus*. *Agriculture and Natural Resources, 52,* 603-606. https://doi.org/10.1016/j.anres.2018.11.004

[19] Via, S. (1999). Cannibalism facilitates the use of a novel environment in the flour beetle, Tribolium castaneum. *Heredity*, *82*(3), 267-275.

[20] Savvidou, N., & C. H. Bell. (1994). The effect of larval density, photoperiod and food change on development of *Gnatocerus cornutus* (F.) (Coleoptera: Tenebrionidae). *Journal of Stored Products Research, 30,* 17-21. https://doi.org/10.1016/0022-474X(94)90268-2

[21] Parween, S. & Begum, M. (2001). Effect of larval density on the development of the lesser mealworm, *Alphitobius diaperinus* Panzer (Coleoptera: Tenebrionidae). *International Pest Control ,43*, 205-207.

[22] Harada, T. & Spence, J. R. (2000). Nymphal density and life histories of two water striders (Hemiptera: Gerridae). *The Canadian Entomologist, 132*(03), 353-363.

[23] Sılva, C. C., Laumann, R. A., Blassıolı, M. C., Pareja, M. & Borges, M. (2008). *Euschistus heros* mass rearing technique for the multiplication of *Telenomus podisi. Pesquisa Agropecuaria Brasileira*, *43*(5) 575-580. https://doi.org/10.1590/S0100-204X2008000500004

[24] Ito, K. (2007). A simple mass-rearing method for predaceous *Orius* bugs in the laboratory. *Applied Entomology and Zoology, 42*(4), 573-577. https://doi.org/10.1303/aez.2007.573

[25] Morales-Ramos, J. A., & Rojas, M. G. (2015). Effect of larval density on food utilization efficiency of *Tenebrio molitor* (Coleoptera: Tenebrionidae). *Journal of Economic Entomology*, *108*(5), 2259-2267. https://doi.org/10.1093/jee/tov208

[26] Barnes, A. I., & Siva-Jothy, M. T. (2000). Density–dependent prophylaxis in the mealworm beetle Tenebrio molitor L. (Coleoptera: Tenebrionidae): cuticular melanization is an indicator of investment in immunity. *Proceedings of the Royal Society of London. Series B: Biological Sciences*, *267*(1439), 177-182. https://doi.org/10.1098/rspb.2000.0984

Sinopfbd, 2024; 9(2): 431-448 **https://doi.org/10.33484/sinopfbd.1449027**

Sinop Üniversitesi Fen Bilimleri Dergisi
Sinop Uni J Nat Sci

E-ISSN: 2564-7873

https://dergipark.org.tr/tr/pub/sinopfbd

A Preliminary Study on the Meat Yield, Nutritional Composition, Lipid Quality Indices, and Mineral and Heavy Metal Contents of Annular Seabream (*Diplodus annularis* Linnaeus, 1758) Caught in the Black Sea

Bengünur ÇORAPCI

How to cite: Corapci, B. (2024). A preliminary study on the meat yield, nutritional composition, lipid quality indices, and mineral and heavy metal contents of annular seabream (*Diplodus annularis* Linnaeus, 1758) caught in the Black Sea *Sinop Üniversitesi Fen Bilimleri Dergisi,* *9*(2), 431-448. https://doi.org/10.33484/sinopfbd.1449027

Research Article

Corresponding Author
Bengünur ÇORAPCI
bengucorapci@hotmail.com

ORCID of the Authors
B.C: 0000-0002-1005-5406

Received: 08.03.2024
Accepted: 13.08.2024

Abstract

In this study, the meat yield, nutritional composition (protein, fat, moisture, ash, carbohydrate), amino acid content, fatty acid composition, and mineral and heavy metal contents of annular seabream (*Diplodus annularis)* were investigated. Additionally, the lipid quality indices (LQI) of annular sea bream were examined. The meat yield of annular seabream was found to be 29.69%. Protein, fat, moisture, ash and carbohydrate values were 17.78 g/100g, 2.28 g/100g, 76.96 g/100g, 1.80 g/100g and 1.19 g/100g, respectively. The total amount of essential amino acids and non-essential amino acids were determined as 147.45 mg/g and 462.74 mg/g, respectively. Polyunsaturated fatty acids (PUFAs) were the predominant fatty acids (37.74%), followed by saturated fatty acids (SFAs) (34.85%) and monounsaturated fatty acids (MUFAs) (27.36%). Atherogenicity Index (AI), Thrombogenicity Index (TI) and Polyene Index (PI) from LQIs were calculated as 0.47, 0.35 and 0.91, respectively. The H/H (Hypocholesterolemic/hypercholesterolemic) ratio of annular seabream was 2.83 and FLQ (Fish Lipid Quality) was 14.48. The first three of the most abundant minerals in annular sea bream were potassium (K), phosphorus (P) and sodium (Na). The heavy metals Hg, Pb and Cd were found within the allowed limit values. As a result, the annular seabream meat was found to have low fat values and high protein content, and to contain essential amino acids, polyunsaturated fatty acids and important minerals. The current study is the first research conducted on the nutritional composition of annular sea bream in the Black Sea.

Keywords: Annular seabream, meat yield, nutritional composition, amino acid, fatty acids, lipid quality indices, mineral composition, heavy metals

Karadeniz’de Avlanan Isparoz Balığı (*Diplodus annularis* Linnaeus, 1758)’nın Et Verimi, Besin Kompozisyonu, Lipid Kalite Indeksleri, Mineral ve Ağır Metal İçerikleri Üzerine Bir Ön Çalışma

Department of Fishing and Seafood Processing Technology, Sinop University, Faculty of Fisheries, Sinop, Türkiye

Öz

Bu çalışmada isparozun et verimi, besin kompozisyonu (protein, yağ, nem, kül, karbonhidrat), aminoasit içeriği, yağ asitleri kompozisyonu, mineral içeriği ve ağır metal içerikleri araştırılmıştır. Ayrıca isparoz balığının yağ kalite indeksleri incelenmiştir. Isparoz balığının et verimi %29.69 olarak bulunmuştur. Protein, yağ, nem, kül ve karbonhidrat değerleri sırasıyla, 17.78 g/100g, 2.28 g/100g, 76.96 g/100g, 1.80 g/100g ve 1.19 g/100g olarak tespit edilmiştir. Toplam esansiyel aminoasit miktarı 147.45 mg/g, toplam esansiyel olmayan aminoasit miktarı ise 462.74 mg/g olarak belirlenmiştir. Çoklu doymamış yağ asitleri (PUFAs) (37.74%) baskın yağ asitleri olup, onu doymuş yağ asitleri (SFAs) (34.85%) ve tekli doymamış yağ asitleri (MUFAs) (27.36%) takip etmiştir. Yağ kalite indekslerinden aterojenite indeksi (AI), trombojenite indeksi (TI) ve polien indeksi (PI) sırasıyla 0.47, 0.35 0.91 olarak tespit edilmiştir. İsparoz balığının H/H oranı 2.83 ve FLQ ise 14.48 olarak bulunmuştur. İsparoz balığında en fazla bulunan minerallerden ilk üçü potasyum (K), fosfor (P)ve sodyum (Na) olarak ölçülmüştür. Ağır metallerden Hg, Pb ve Cd izin verilen limit değerler içerisinde bulunmuştur. Sonuç olarak bu çalışmada isparoz balığı etinin, düşük yağ ve yüksek protein içeriğine sahip olduğu, esansiyel aminoasitleri, çoklu doymamış yağ asitlerini ve önemli mineralleri bünyesinde bulundurduğu tespit edilmiştir. Mevcut çalışma Karadeniz'de isparoz balığının besinsel kompozisyonuna yönelik olarak gerçekleştirilen ilk araştırma özelliğini taşımaktadır.

Anahtar Kelimeler: Isparoz, et verimi, besin kompozisyonu, aminoasit, yağ asitleri, yağ kalite indeksleri, mineral kompozisyonu, ağır metaller

Introduction

Fish is considered a nutritionally valuable part of the human diet and its consumption twice a week is recommended, generally due to the content of polyunsaturated fatty acids (PUFA) in fish meat [1]. Moreover, it is an important source of high-quality protein, valuable oils, vitamins and minerals [2]. The findings reveal that fish is a valuable source of essential amino acids and polyunsaturated fatty acids that play important physiological functions in the maintenance and development of fetuses, neonates, and infant brains [3]. For all these reasons, fish is a nutrient which human need beginning from the mother's womb till adulthood and throughout their lives. It is also an indispensable part of healthy and balanced nutrition. The annular seabream (*Diplodus annularis* Linnaeus, 1758) is a species of fish from the family Sparidae. It is locally known as 'ısparoz', 'ispari' or 'isparoz' in Türkiye. Its colours may be silver grey or yellow green depending on where it lives and what it eats. It is adapted to seagrasses in terms of appearance and colour. Its abdominal parts are generally white. The black band on the tail stalk is its most distinctive feature. Their bodies are covered with large scales. It is a demersal fish species. They survive in seagrass (*Posidonia*) beds on sandy bottoms and rarely on rocky bottoms. It is caught using trawl nets, bottom gillnets and fishing lines [4, 5]. In some regions, this species may prefer places where fish farms are located, to feed on fishmeal distributed from cages to the environment [6]. It is found in the Eastern Atlantic from southwestern France to southwestern Spain and Portugal, including the Canary Islands, throughout the Mediterranean, and in the Black Sea and the Sea of Azov [7]. The annular seabream can survive between depths of 0-90 meters. It feeds on worms, crustaceans, molluscs, echinoderms and hydrozoans. Although this is a hermaphrodite species, both sexes are seen in a population. Some individuals are protandric. Although the maturity length varies between 8-19.6 cm, the maximum growth length has been reported as 28 cm [7]. Despite the fact that the breeding time depends on water temperature, the periods were reported as June-August in the Black Sea, April-August in the Marmara Sea and the Mediterranean, and March-August in the Aegean Sea.

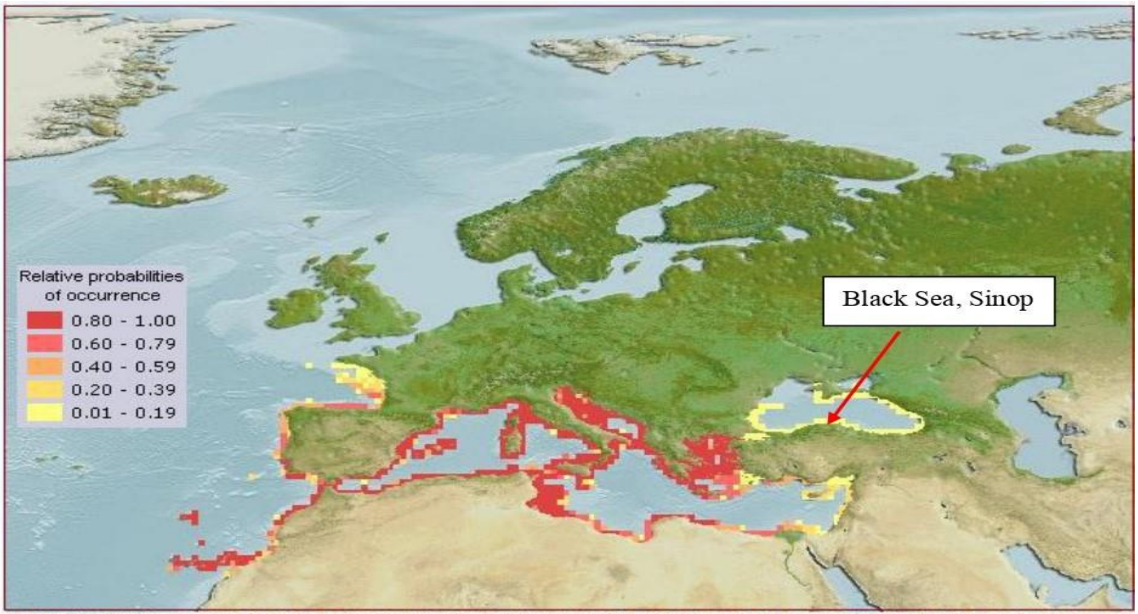

Note: Distribution range colours indicate degree of suitability of habitat which can be interpreted as probabilities of occurrence.

Figure 1. *Distribution of annular seabream (Diplodus annularis) in marine areas and the sampling area [7]*

Recommended consumption months of annular seabream are January, February, October, November and December for the Marmara Sea and the Mediterranean; January, February, March, April, October, November and December for the Black Sea; and January, October, November and December for the Aegean Sea [8]. The production quantity of annular sea bream over the past decade (2013-2022) has been reported as 106.6, 58.7, 75, 84.2, 86.6, 45.9, 54.1, 54, 55, 38.2 tonnes/per year, respectively [9]. When the available data is considered, it can be said that the production amount of annular seabream can be suggested to generally decrease over time. The population density of annular seabream in the Black Sea is lower than those at the Aegean and the Mediterranean coasts of Türkiye and in the European and African coasts of the Eastern Atlantic. The quite low production amount is probably due to the low population density on the Turkish coast, as well as the fact that hunting as a target species is not a much-preferred approach [6]. Many studies have been carried out on the age, growth, feeding habits and nets used in hunting the annular sea bream [10 – 14]. In addition, the species has been the subject of various studies in recent years to evaluate marine pollution and ecological risks [15, 16]. Studies on the chemical composition of annular sea bream are quite limited [17, 18]. Information on the fatty acid content of annular seabream can be obtained through literature [19 – 21]. Annular seabream is not an economically valuable fish. It is not caught as a target species. However, it is a by-catch, which can be sold by fishermen at certain periods in some provinces of the Black Sea, especially in Sinop. Research on the nutritional composition of this fish is quite limited. Moreover, no studies on the nutritional composition of annular sea bream caught in the Black Sea have been encountered in literature. The current study will serve as a pioneering work and is important in terms of its contribution to literature as well as its informative content to consumers. This study aims to examine the meat yield, nutritional composition, amino acids, fatty acids, lipid quality indices, and the mineral and heavy metal contents of annular seabream caught in the Black Sea. It is thought that the data obtained will provide significant contributions to future studies on the subject.

Materials and Methods

Material

In the present study, 2 kg (n=10) of annular seabream (*Diplodus annularis*) with average lengths of 19.04±0.24 cm and average weights of 136.30±6.02 g were used as raw material. To create homogeneous samples, larger fish were selected based on their sexual maturity. The fish were purchased from a local fisherman in Sinop, (Türkiye) in May 2023. The fish were covered with ice chips in styrofoam boxes and brought to the laboratory in 20 minutes.

Methods

Determination of Meat Yield (%)

The head, fins, internal organs, skin and bones of the fish were cut and weighed separately to calculate the meat yield of the fish. Following removal of the head, fins, skin, bones and all internal organs, the meat weight of the fish was assessed. The ratio of edible meat weight to total body weight was calculated as meat yield. The obtained values were used in the formula below and the results were evaluated.

Meat yield (%) = [edible meat weight (g)/whole weight(g)]x100 [22]

Nutritional Composition Analyses

Nutritional Composition

Crude protein and crude fat contents of the samples were determined according to the methods of AOAC [23] and Bligh and Dyer [24], respectively. Determination of % moisture content was carried out according to Ludorf and Meyer [25]. Crude ash contents were analyzed according to the methods used by AOAC [26]. Energy value was calculated following Falch et al. [27]. All measurements were carried out in triplicate.

Amino Acids

Homogenized fish meat (0.5 g) was weighed and burned with 20 ml HCl at 110°C for 18-24 hours [28]. 20 ml of pure water was added to the sample and it was dried in an evaporator at 70°C. The volume was completed to 50 ml in a volumetric flask with pure water. Amino acids were separated by Zorbax Eclipse AAA, UFLC using a 4.6 X 150 mm, 3.5 µm column. The flow rate was set to 1 mL/min and the column temperature was set to 40 °C. All samples were analyzed in duplicate and the results were given in mg/g.

Fatty Acids

Fatty acid compositions of samples were detected by Gas Chromatography/Mass Spectrometry (GC/MS, Thermo Scientific ISQ LT) equipped with an autosampler. The capillary column used was Trace Gold TG-WaxMS (60 m) with an inner diameter of 0.25 µm and a thickness of 0.25 µm. The temperature was held initially at 100°C for 3 min and then increased to 240°C at a rate of 4°C/min, with an initial hold of 6 min. The carrier gas used was helium (1 ml/min) and the split ratio was 1:20. Front inlet temperature was set to 240°C, MS transfer line temp and ion source temperatures were 250°C and 240°C, respectively. The mass spectrometer was operated in the electron impact ionization mode (70 eV). A FAME mix (Supelco, 37 comp., Bellefonte, PA, USA) was used to provide standards for comparison [29].

Lipid Quality Indices (LQI)

Atherogenic Index (AI), Thrombogenicity Index (TI), Polyene Index (PI), Hypocholesterolemic/hypercholesterolaemic Index (HH) and Fish Lipid Quality (FLQ) were calculated by using following equations described by Ulbricht and Southgate [30], Lubis and Buckle [31], Santos-Silva et al. [32] and Abrami et al. [33].

$$AI = \frac{\mathrm{C12+(4XC14)+C16}}{\mathrm{\Sigma n6+\Sigma n3+\Sigma MUFA}} \quad (1)$$

$$TI = \frac{\mathrm{C14+C16+C18}}{\mathrm{(0.5X\Sigma MUFA)+(0.5X\Sigma n-6)+(3x\Sigma n-3)+(n-3)/(n-6)}}. \quad (2)$$

$$PI = \frac{\mathrm{(C20{:}5+C22{:}6)}}{\mathrm{C16}}. \quad (3)$$

$$HH = \frac{(C18{:}1n{-}9 + C18{:}2n{-}6 + C18{:}3n{-}3 + C20{:}4n{-}6 + C20{:}5n{-}3 + C22{:}5n{-}3 + C22{:}6n{-}3)}{\mathrm{(C14{:}0 + C16{:}0)}}. \quad (4)$$

$$FLQ = \frac{\mathrm{(EPA\%+DHA\%)}}{\mathrm{Total\ fatty\ acids\%}} x100. \quad (5)$$

Determination of Minerals and Heavy Metals

According to the method described by Milestone [34] the acid (7 ml of HNO_3 65%, 1 ml H_2O_2 30%: Merck, Darmstadt, Germany) digestion of the sample in a closed vessel device is provided using a temperature control microwave (Ethos D, Milestone Inc. Sorisole, Italy) for the determination of metals by spectroscopic methods. Analyses of 28 elements (Macro, trace elements and heavy metals: Na, Mg, K, P, Ca, Si, Fe, Zn, Al, Rb, Sr, Cr, Ti, Be, Se, Cu, Mn, Li, Mo, Ni, Sb, Cs, Ba, Gd, As, Hg, Pb, Cd) were carried out using inductively coupled plasma mass spectrometry using dynamic reaction cell technology (Agilent Technologies / 7700X ICP-MS Systems). Results are expressed in milligrams of element per kilogram of fish meat. All samples were analyzed in triplicate.

Public Health Risk Analysis

Metal Pollution Index (MPI)

The following formula was used to find the MPI value;

$$MPI = (C1XC1X \dots\dots .XCn)\frac{1}{n} \quad (6)$$

Cn = metal concentration in the sample (mg·kg-1)
n = number of samples [35]

Estimated Daily Intake (EDI), Estimated Weekly Intake (EWI)

The weekly seafood consumption amount used in calculating the EDI and EWI values was calculated using the average per capita seafood consumption amount in Türkiye in 2022. This value is approximately 0.140 kg·week-1 (7.3 kg/52 weeks annually) [36].
The USEPA [37] equation (7) below was used to calculate the EDI value:

$$EDI = \frac{MxW}{BW} \quad (7)$$

where:
M = metal concentration in the sample (mg·kg-1)
W =daily amount of seafood consumption (kg)
BW = body weight (kg)
The relation between the EWI and EDI is presented in the equation (8).

$$EWI = EDIx7 \quad (8)$$

In the study, the average weight of an adult was taken as 70 kg (18 years old) and
32 kg for children (10 years old) [38].

Results and Discussion

Meat Yield (%)

The length, weight and meat yield of annular seabream are shown in Table 1. The average length and average weight of annular seabream were found as 19.04 cm and 136.30 g, respectively. Kasapoglu and Duzgunes [39] reported minimum and maximum length and weight values of annular sea bream in the Black Sea as 6.4-7.8 cm and 2.79-8.21 g. In another study conducted in the Black Sea, these values were given as 13.3-23 cm and 50.3-235.8 g [6]. In a study comparing the length and weight values of annular seabream for Turkish waters, the minimum/maximum length was reported as 12-23.2 cm and the weight as 28.69-180 g [13]. Samsun et al. [40] reported that the minimum and maximum length-weight values of annular seabream in the central Black Sea (Sinop) were 12.5-23.4 cm and 39.9-249.3 g, respectively.

Table 1. *The length, weight and meat yield of annular seabream (Diplodus annularis)*

	Min	**Avg**	**Max**
Fish Total Lenght (cm)	17.8	19.04±0.24	20
Fish Total Weight (g)	107.64	136.30±6.02	174.57
Fillet weight (g)	31.24	40.47±1.85	54.56
Meat yield (%)	27.33	29.69±0.58	33.38

Values are shown as mean ± standard error (n=10)

The average meat yield of annular seabream was found as 29.69%. To select homogeneous samples, larger fish were picked based on their sexual maturities. Lenght-weight ratios and meat yield % may vary depending on various factors. Age of the fish, catch region, maturity, nutritional status, water temperature, etc. are some of these factors.

Nutritional Composition

Protein, fat, moisture, ash and carbohydrate contents of annular seabream were found as 17.78%, 2.28%, 76.96%, 1.80% and 1.19%, respectively (Figure 2). The energy value of the annular seabream was calculated as 96.35 kcal/100g.

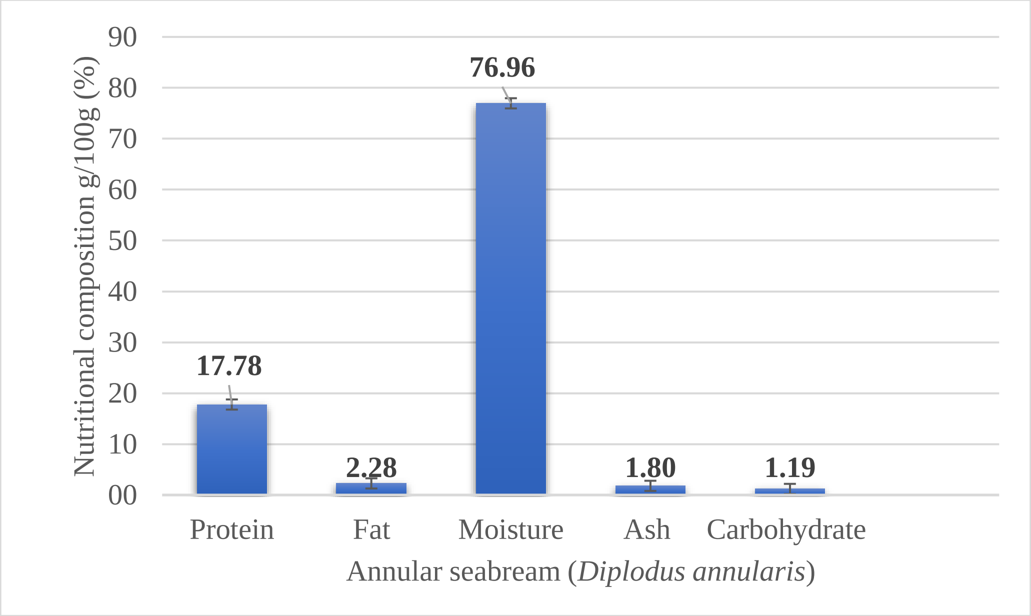

Figure 2. *Nutritional composition of the annular seabream (Diplodus annularis) (g 100g/wet weight (ww))*

No study has been found in literature investigating the nutritional composition of annular seabream inhabiting the Black Sea. Moreover, Smichi et al. [41] pointed out that there is no published data on the nutritional quality and composition of annular seabream, although it has a wide distribution in the Mediterranean. However, Ketata-Khitouni et al. [17] examined the protein, fat, moisture and ash amounts of samples taken from different body parts of the male and female annular sea breams, separately. In another study, the chemical composition of sea bream was investigated seasonally. When compared with the sampling conducted by the researchers in May, the moisture and protein % values of the data obtained were found to be close to our study, while the fat and ash values were higher than those found in our study [18]. Smichi et al. [41] calculated the protein, fat and moisture values of annular seabream on dry weight. Accordingly, the % moisture value of annular sea bream was reported as 18.67% based on dry matter. Ozogul et al. [21] reported the fat value of annular sea bream as 2.52%. In another study, Passi [19] reported this value as 2.32%. It can be said that these fat values are quite close to the values found in our study.

Amino Acids

The amino acid composition of annular seabream is shown in Table 2. Seafood is one of the most aromatic foods. It has a particularly delicious and different aroma compared to other foods, especially because it contains a high proportion of glutamic acid [42]. The first three amino acids most abundant in annular seabream were glutamic acid, aspartic acid and alanine, respectively. However, the least abundant ones were cystine, tyrosine and histidine, respectively. While the total amount of essential amino acid was 147.45 mg/g, the total amount of non-essential amino acid was measured as 462.74 mg/g. The ratio of essential/non-essential amino acids (E/NE) was observed to be 0.32 in the annular seabream. The amount of total sweet amino acids was found to be higher than the total bitter amino acids.

Table 2. *Amino acid composition of annular seabream (Diplodus annularis)*

Amino acids (mg/g / ww)	**Annular seabream (*Diplodus annularis*)**
Alanine	56.39±2.33
Leucine*	18.24±1.57
Aspartic acid	100.57±1.94
Arginine	13.96±1.20
Cystine	1.48±0.14
Glutamine	15.16±1.07
Glutamic acid	225.40±25.93
Histidine*	8.07±1.30
Isoleucine*	18.12±1.87
Lysine*	15.10±1.33
Methionine	9.41±2.21
Phenylalanine*	8.83±0.23
Proline	23.27±2.11
Serine	33.42±0.65
Threonine	43.32±2.34
Tyrosine	7.05±0.22
Valine*	12.42±0.42
Total amino acids	**610.19±39.92**
Total essential amino acids (E)*	**147.45±3.65**
Total non-essential amino acids (NE)	**462.74±32.02**
E/NE	**0.32±0.00**
Sweet amino acids	**315.22±27.52**
Bitter amino acids	**55.35±5.73**

All samples were analyzed in duplicate. Values are shown as mean ± standard error

No study has been found in literature investigating the amino acid composition of annular seabream (*Diplodus annularis*). However, in recent years, protein hydrolyzate studies have been carried out on this species [43, 44]. Kouroupakis et al. [45] studied the amino acid composition of the species *Diplodus* *sargus*. When the data obtained in the aforementioned study were compared with the present study, it was observed that glutamic acid was the highest amino acid in both studies. Similarly, total essential amino acids were lower than total non-essential amino acids in both studies.

Fatty Acids

The fatty acid composition of annular seabream is shown in Table 3. The ΣSFA amount was found to be 34.85%. While the highest amount of saturated fatty acid was found as palmitic acid (15.86%), the lowest amount of saturated fatty acid was tridecanoic acid (0.02%). The amount of ΣMUFA was 27.36%. Oleic acid was the highest monounsaturated fatty acid with 19.42%, whereas erucic acid was the lowest with 0.11%. The amount of ΣPUFA was measured as 37.74%. The highest amounts of polyunsaturated fatty acids were detected as linoleic acid (8.78%) and docosahexaenoic acid (8.76%), respectively. These fatty acid values were found to be close to each other. However, the lowest amount of polyunsaturated fatty acid was docosadienoic acid with a value of 0.16%. The amounts of ω3 and ω6 were 19.00% and 17.36%, respectively. Accordingly, the ω3/ω6 ratio was calculated as 1.09%. Ketata-Khitouni et al. [18] examined the seasonal fatty acid profile of annular sea bream. The total amount of SFA, MUFA and PUFA in spring was reported as 42.43%, 35.32% and 22.24% in males, and 41.28%, 37.17% and 21.54% in females, respectively. In another study, the ΣSFA, ΣMUFA and ΣPUFA contents were reported as 28.73%, 54.66 %and 16.6%, respectively [41]. PUFA values in our study were found to be higher than those found in both of these aforementioned studies. However, SFA and MUFA values are different from each other. Another research was carried out on fish caught off the coasts of Tunisia. There are many factors (such as catch location, catch time, nutritional status, age, and gender) that affect the nutritional composition of fish in general. Passi et al. [19] and Bouhlel et al. [20] reported that the amounts of palmitic acid, oleic acid and docosahexanoic acid in annular seabream were higher than the other fatty acids detected. These results are similar to our study.

Lipid Quality Indices (LQI)

Lipid Quality Indices (LQI) of annular seabream are shown in Table 4. In the simplest terms, the Atherogenicity Index (AI) shows the relationship between total major saturated fatty acids and total major unsaturated fatty acids. A low AI value is desirable to prevent micro and macro coronary diseases. The Thrombogenicity Index (TI) indicates a tendency to form clots in blood vessels. It is defined as the relationship between pro-thrombogenetic (saturated) and anti-thrombogenetic fatty acids (MUFAs, PUFAs – n6 and PUFAs – n3) [30]. It has been reported that AI and TI values should be lower than 1 to prevent heart diseases [30, 46]. The AI and TI values obtained in our study were within the recommended values.

Table 3. *Fatty acid composition of annular seabream (Diplodus annularis) (g 100g/wet weight(ww))*

Fatty acid (%)		Annular seabream
C12:0	Lauric acid	0.12±0.00
C13:0	Tridecanoic acid	0.02±0.00
C14:0	Myristic acid	3.44±0.06
C15:0	Penta decanoic acid	0.91±0.04
C16.0	Palmitic acid	15.86±0.24
C17:0	Heptadecanoic acid	1.33±0.00
C18:0	Stearic acid	8.65±0.11
C20:0	Arachidic acid	0.84±0.02
C21:0	Heneicosanoic acid	0.04±0.01
C22:0	Behenic acid	0.57±0.03
C23:0	Tricosanoic acid	0.24±0.00
C24:0	Lignocerik acid	2.85±0.07
ΣSFA		**34.85±0.32**
C14:1	Myristoleic acid	0.40±0.01
C15:1 cis-10	Pentadecenoic acid	0.22±0.00
C16.1	Palimiteloic acid	1.57±0.04
C17:1 cis-10	Heptadecanoic acid	0.87±0.01
C18:1n9c	Oleic acid	19.42±0.02
C18:1n9t	Elaidic acid	1.96±0.09
C20:1 cis-11	Eicosenoic acid	1.88±0.01
C22:1n9	Erucic acid	0.11±0.01
C24:1	Nervonic acid	0.95±0.07
ΣMUFA		**27.36±0.07**
C18:2n6t	Linoleadic acid	0.56±0.04
C18:2n6c	Linoleic acid	8.78±0.03
C18:3n3	a-Linolenic acid	2.99±0.03
C18:3n6	g-Linolenic acid	0.33±0.01
C20:2 cis 11,14	Eicosadienoic acid	1.23±0.02
C20:3n3 cis 11,14,17	Eicosatrienoic acid	1.54±0.01
C22:2 cis 13,16	Docosadienoic acid	0.16±0.01
C20:5n3 cis 5,8,11,14,17	Eicosapentanoic acid	5.71±0.02
C22:6n3 cis-4,10,13,16,19	Docosahexanoic acid	8.76±0.15
C20:4n6	Arachidonic acid	6.46±0.10
C20:3n6 cis-_8_11_14	Eicosatrienoic acid	1.23±0.02
ΣPUFA		**37.74±0.36**
ω3		**19.00±0.22**
ω6		**17.36±0.13**
Unidentified		**0.06±0.03**
ω3/ω6		**1.09±0.00**

All samples were analyzed in triplicate. Values are shown as mean ± standard error

Table 4. *Lipid Quality Indices (LQI) of annular seabream (Diplodus annularis)*

Indices	Annular seabream	References
AI (Atherogenicity Index)	0.47±0.00	Ulbricht and Southgate [30]
TI (Thrombogenicity Index)	0.35±0.00	Ulbricht and Southgate [30]
PI (Polyene Index)	0.91±0.02	Lubis and Buckle [31]
H/H (Hypocholesterolemic/hypercholesterolemic ratio)	2.83±0.05	Santos-Silva et al. [32]
FLQ (Fish Lipid Quality)	14.48±0.17	Abrami et al. [33]

Values are shown as mean ± standard error

The Polyene Index (PI) was used as a measure of PUFA damage [31]. In our study, the PI value was calculated as 0.91. An increase in the amount of cholesterol in the blood is called hypercholesterolemia, and a decrease in it is called hypocholesterolemia [47]. In the current study, the Hypocholesterolemic/Hypercholesterolemic (H/H) ratio was 2.83. This ratio should be high in terms of healthy nutrition. Based on the total lipids, fish lipid quality (FLQ) demonstrates the percentage of the main HUFA-n3 (EPA and DHA) in total fatty acids of the muscle. The higher the value of this index, the higher the quality of the dietary lipid source [33]. In the current study, the FLQ value of annular seabream was found as 14.48.

Minerals and Heavy Metals

Mineral and heavy metal contents of annular seabream are shown in Table 5 and Table 6. The mineral content of muscle foods such as seafood is relatively variable and depends on several factors. Some of these factors can be considered as nutrition, species, breed, sex, age at slaughter, muscle types, physiological status, production system, processing methods and method of analysing the mineral content of the meat samples [48 – 50]. In the present study, the concentrations of K, P, Na, Ca and Mg minerals in the annular sea bream were in the order of K>P> Na>Ca>Mg. The potassium (K) and phosphorus (P) content of the annular seabream were 6228.02 mg/kg and 3726.48 mg/kg, respectively. The rarest minerals in the annular seabream were Cs, Mo, Gd, Ni and Sb, respectively. Ketata-Khitouni et al. [18] reported that annular sea bream was rich in potassium (K) and calcium (Ca) in all seasons. In another study, Smichi et al. [41] reported the main minerals in annular seabream as sodium (Na), calcium (Ca) and magnesium (Mg). However, in the present study, P was found to be one of the most abundant main elements, along with K, Na, Ca and Mg. In the current study, Fe, Zn, Cu and Ni values were measured as 8.59 mg/kg, 7.89 mg/kg, 0.30 mg/kg and 0.02 mg/kg, respectively. These values were reported as 12.20 mg/kg, 135.77 mg/kg, 0.11 mg/kg and 0.66 mg/kg in another work [51]. It was observed that the findings of both studies were different from each other. Bat [52] reported the Fe, Zn and Cu values of annular sea bream in the Black Sea as 19.3 mg/kg, 10.2 mg/kg and 0.17 mg/kg, respectively. Accordingly, while the Fe and Zn values in our study were lower than the values of Bat [52], the Cu value was found to be higher.

Table 5. *Mineral contents of annular seabream (Diplodus annularis)* (mg kg^{-1}, ww)

Mineral elements	Annular seabream (mg kg-1, ww)
Na	900.88±0.59
Mg	454.82±2.20
K	6228.02±10.03
P	3726.48±20.05
Ca	584.83±0.15
Mn	0.22±0.00
Se	0.50±0.00
Si	10.21±0.16
Fe	8.59±0.04
Zn	7.89±0.08
Al	4.09±0.03
Rb	1.13±0.00
Sr	1.95±0.01
Cr	0.83±0.00
As	0.71±0.01
Ti	0.59±0.02
Be	0.57±0.00
Cu	0.30±0.00
Li	0.05±0.00
Ba	0.08±0.00
Gd	0.02±0.00
Ni	0.02±0.00
Sb	0.02±0.00
Cs	0.01±0.00
Mo	0.01±0.00
Hg	0.15±0.00
Pb	0.02±0.00
Cd	0.01±0.00

All samples were analyzed in triplicate,
Values are shown as mean ± standard error, ww. wet weight

In a study conducted with the Black Sea annular seabream, Cd, Hg and Pb values were reported as 0.01 mg/kg, 0.02 mg/kg and 0.12 mg/kg, respectively [52]. Cd values of the current study were similar to those given by Bat [52]. However, in the current study, Hg values were found to be higher, while Pb values were lower. Ben Salem and Ayadi [51] reported Pb and Cd values in annular sea bream as 0.17 mg/kg and 0.76 mg/kg, respectively. The same researchers reported the Hg value as 0.20 mg/kg [53]. The European Commission has set maximum levels for heavy metals in fish muscle. The legal limits for Hg, Pb, and Cd are 500, 300, and 50 µg/kg w.w., respectively [54]. The values of Hg, Pb, and Cd in the muscles of fish in the current study were below the maximum limits set by Commission Regulation (EC) [54].

Public Health Risk Analysis

Metal Pollution Index (MPI)

The MPI value of the annular seabream was calculated as 0.23. Gencer and Kocatepe [55] reported that high heavy metal contamination in the samples increased the MPI value. Haseeb-ur-Rehman et al. [56]

reported in a study that the MPI values of various seafood products varied between 0.62 and 2.78. Compared to these values, the metal pollution of annular seabream can be considered as quite low.

Estimated Daily Intake (EDI), Estimated Weekly Intake (EWI)

The EDIs and EWIs of metals through the consumption of annular seabream muscles are shown in Table 6. EWI values of Cd, Hg and Pb were compared with the Provisional Tolerable Weekly Intake (PTWI) to assess public health risks. The PTWI values were assumed to be 0.007 mg for Cd, 0.004 mg for Hg [38] and 0.025 mg for Pb [57].

Table 6. *EDIs and EWIs of metals via consumptions of annular seabream muscles*

Elements	PTWI*	PTWI**	EDI	EWI
Cd	0.007	0.49	2.86E-06	2.00E-05
Pb	0.025	1.75	5.71E-06	4.00E-05
Hg	0.004	0.28	4.29E-05	3.00E-04

* Internationally recommended PTWI safe levels for the studied metals.
Provisional tolerable weekly intake in mg/week/kg body weight [38]
**PTWI for a 70 kg adult (mg/week/kg body weight)
EDI Estimated Daily Intake (mg/day body weight)
EWI Estimated Weekly Intake (mg/week body weight)

The Estimated Weekly Intake (EWI) values for metals are based on an adult's weekly consumption. Annular seabream's EDI and EWI values were found to be below the recommended standard reference values.

Conclusion

In the current study, meat yield, nutritional composition, amino acids, fatty acids, lipid quality indices, and mineral and heavy metal contents of annular seabream caught in the Black Sea were investigated. Accordingly, annular seabream was observed to have high protein and low fat content. The most abundant amino acids in annular sea bream meat were found as glutamic acid, aspartic acid and alanine. In addition, polyunsaturated fatty acids (PUFAs) were the predominant fatty acids. AI and TI values were found to be less than 1. One can say that annular seabream is rich in potassium, phosphorus and sodium minerals. Additionally, the amounts of Hg, Pb and Cd were found to be within the permitted limits for consumption. As a result, annular seabream *(Diplodus annularis)* can be an alternative species that can be consumed in healthy diets since it contains high protein, low fat, rich essential amino acids, high quality fatty acids and important minerals. However, considering the annually declining stocks, future studies should focus on the reasons for the low population density of this valuable fish.

Acknowledgement -

Funding/Financial Disclosure The author has no received any financial support for the research, authorship, or publication of this study.

Ethics Committee Approval and Permissions The study does not require ethics committee approval or any special permission.

Conflicts of Interest The authors declare no conflict of interest.

Authors Contribution The author read and approved the final manuscript.

References

[1] Khalili Tilami, S., & Sampels, S. (2018). Nutritional value of fish: Lipids, proteins, vitamins, and minerals. *Reviews in Fisheries Science & Aquaculture, 26*(2), 243–253. https://doi.org/10.1080/23308249.2017.1399104

[2] Food and Agriculture Organization (2020). *The State of World Fisheries and Aquaculture. Sustainability in Action.* Rome. https://doi.org/10.4060/ca9229en

[3] Maulu, S., Nawanzi, K., Abdel-Tawwab, M., & Khalil, H. S. (2021). Fish nutritional value as an approach to children's nutrition. *Frontiers in Nutrition, 8.* 780844. https://doi.org/10.3389/fnut.2021.780844

[4] Isparoz balığı, (*Diplodus annularis*). Balıknet. 07.02.2024. https://baliknetcom.wordpress.com/2021/04/21/isparoz-baligi-diplodus-annularis/

[5] Isparoz- *Diplodus annularis* (Linnaeus, 1758). Su Ürünleri Merkez Araştırma Enstitüsü. 07.02.2024. https://www.surkoopekutuphane.org/baliklari-taniyalim/)

[6] Erat, S. (2019). *Güneydoğu Karadeniz kıyılarında ısparoz balığı (Diplodus annularis (Linnaeus, 1758)'nın bazı populasyon parametreleri.* (Tez no. 655634) [Yüksek Lisans Tezi, Ordu Üniversitesi].

[7] Fishbase. (*Diplodus annularis* (Linnaeus, 1758). Annular seabream. 07.02.2024. https://www.fishbase.se/summary/diplodus-annularis)

[8] Deniz balıkları. İspari. 09.02.2024. https://tarim.ibb.istanbul/tarim-ve-su-urunleri-mudurlugu/deniz-baliklari.html.

[9] Türkiye İstatistik Kurumu (2024). *Su Ürünleri İstatistikleri.* https://data.tuik.gov.tr/Kategori/GetKategori?p=tarim-111&dil=1

[10] Ozekinci, U. (2005). Determination of the selectivity of monofilament gillnets used for catching the annular sea bream (*Diplodus annularis* L., 1758) by length-girth relationships in İzmir Bay (Aegean Sea). *Turkish Journal of Veterinary & Animal Sciences, 29,* 375-380.

[11] Ayaz, A., Altınagac, U., Ozekinci, U., Cengiz, Ö., & Oztekin, A. (2010). Effects of hanging ratio on gill net selectivity for annular sea bream (*Diplodus annularis*) in the Northern Aegean Sea, Turkey. *Journal of Animal and Veterinary Advances, 9*(7):1137-1142.

[12] Chaouch, H., Ben Abdallah-Ben Hadj Hamida, O., Ghorbel, M., & Jarboui, O. (2014). Feeding habits of the annular seabream, *Diplodus annularis* (Linnaeus, 1758) (Pisces: Sparidae), in the Gulf of Gabes (Central Mediterranean). *Cahiers de Biologie Marine, 55,* 13-19.

[13] Cengiz, O., Kızılkaya, B., & Parug, S. S. (2019). Türkiye suları için isparoz balığı'nın (*Diplodus annularis* Linnaeus, 1758) büyüme özellikleri. *Kahramanmaraş Sütçü İmam Üniversitesi Tarım ve Doğa Dergisi*, *22*(5): 817-822. https://doi.org/10.18016/ksutarimdoga.vi.525929

[14] Ayyıldız, H., & Altın, A. (2020). Gökçeada sığ sularında bulunan isparoz, diplodus annularis larva ve juvenillerinin günlük yaş ve büyüme özellikleri. *Yüzüncü Yıl Üniversitesi Tarım Bilimleri Dergisi, 30* (1): 57-67. https://doi.org/10.29133/yyutbd.652859

[15] Gonul, L. T., Kucuksezgin, F., & Pazi, İ. (2018). Levels, distribution, and ecological risk of organochlorines in red mullet (*Mullus barbatus*) and annular sea bream (*Diplodus annularis*) from the Gulf of Izmir, Eastern Aegean, in 2009–2012. *Environmental Science and Pollution Research, 25*. 25162-25174. https://doi.org/10.1007/s11356-018-2528-7

[16] Gharred, T., Mannai, R., Belgacem, M., & Jebali, J. (2020). Incidence of morphometry variation, growth alteration, and reproduction performance of the annular sea bream (*Diplodus annularis*) as effective tools to assess marine contamination: how useful is a multi-biotimarkers approach? *Environmental Science and Pollution Research, 27,* 4075-4088. https://doi.org/10.1007/s11356-019-07014-9

[17] Ketata-Khitouni, I., Abdelmouleh, A., Bouain, A., & Boudhrioua Mihoubi, N. (2010). Variations of the chemical composition of five coastal catch fish species of the Gulf of Gabès (Tunisia). *Cybium, 34*(2), 175-183.

[18] Ketata Khitouni, I., Boudhrioua Mihoubi, N., Bouain, A., & Ben Rebah, F. (2014). Seasonal variation of the chemical composition, fatty acid profiles and mineral elements of *Diplodus annularis* (Linnaeus, 1758) caught in the Tunisian Coastal Water. *Journal of Food and Nutrition Research, 2*(6), 306-311.

[19] Passi, S., Cataudella, S., Di Marco, P., De Simone, F., & Rastrelli, L. (2002). Fatty acid composition and antioxidant levels in muscle tissue of different mediterranean marine species of fish and shellfish. *Journal of Agricultural Food Chemistry, 50,* 7314-7322.

[20] Bouhlel, I., Mnari, A., Chraief, I., Hammami, M., El Cafsi, M., & Chaouch, A. (2009). Fatty acids in muscles, liver and gonads in *Diplodus annularis* from the Tunisian coasts. *Cahiers de Biologie Marine, 50,* 223-229.

[21] Ozogul, Y., Ozogul, F., Cicek, E., Polat, A., & Kuley, E. (2009). Fat content and fatty acid compositions of 34 marine water fish species from the Mediterranean Sea. *International Journal of Food Sciences and Nutrition, 60*(6), 464-475.

[22] Bosworth, B. G., Wolters, W. R. Silva, J. L., Chamul, R. S., & Park, S. (2004). Comparison of production, meat yield, and meat quality traits of NWAC103 line channel catfish, norris line channel catfish, and female channel catfish x male blue catfish F1 hybrids. *North American Journal of Aquaculture, 66,* 177-183. https://doi.org/10.1577/A03-032.1

[23] Association of Official Analytical Chemists (1961). *Officials Methods of Analysis*. Washington. D.C. https://academic.oup.com/jaoac/issue/44/1

[24] Bligh, E. G., & Dyer, W. J. (1959). A rapid method of total lipid extraction and purification. *Canadian Journal of Biochemistry Physiology, 37*(8), 911-917. https://doi.org/10.1139/o59-099

[25] Ludorff, W., Meyer, V. (1973). Fishe und fisherzeuge. Z. Auflage. Verlag Paul Parey. In, Berlin und Hamburg: 209-210.

[26] Association of Official Analytical Chemists (1984). *Officials Methods of Analysis*. Washington. D.C. http://lib3.dss.go.th/fulltext/scan_ebook/aoac_1984_v67_n2.pdf

[27] Falch, E., Overrien, I., Solberg, C., & Slizyte, R. (2010). Composition and Calories. In: Nollet, L. M. L. - Toldrá, F. (Eds): *Seafood and Seafood Product Analysis*. (pp 257-288). CRC Press.

[28] Blackburn, S. (1968). *Amino Acid Determination: Methods and Techniques*. M. Dekker.

[29] International Union of Pure and Applied Chemistry (1987). *Preparation of Fatty Acid Methyl Ester, in Standard Methods for Analysis of Oils, Fats and Derivatives.* (IUPAC Standard No. 2.301). https://old.iupac.org/publications/books/ISBN0632033371_compress.pdf

[30] Ulbritcth, T. L. V., & Southgate, D. A. T. (1991). Coronary heart disease: seven dietary factors. *Lancet, 338,* 985-992.

[31] Lubis, Z., & Buckle, K. A. (1990). Rancidity and lipid oxidation of dried-salted sardines. *International Journal of Food Science and Technology, 25,* 295-303.

[32] Santos-Silva, J., Bessa, R., & Santos-Silva, F. (2002). Effect of genotype, feding system and slaughter weighton the quality of light lambs: II. Fattyacid composition of meat. *Livestock Production Science, 77*(2-3), 187-194. https://doi.org/10.1016/S0301-6226(02)00059-3

[33] Abrami, G., Natiello, F., Bronzi, P., McKenzie, D., Bolis, L., & Agradi, E. (1992). A comparison of highly unsaturated fatty acid levels in wild and farmed eels (*Anguilla anguilla*). *Comparative Biochemistry and Physiology, 101,* 79-81. https://doi.org/10.1016/0305-0491(92)90161-j

[34] Milestone (2018). Milestone SK-10 High Pressure Rotor Application notes. http://subitam.sinop.edu.tr/fileman/Uploads/Subitam/Mikrodalga.pdf.

[35] Usero, J., Gonzalez-Regalado, E., Gracia, I. (1997). Trace metals in the bivalve molluscs *Ruditapes decussatus* and *Ruditapes philippinarum* from the Atlantic Coast of Southern Spain. *Environment International, 23*(3), 291-298. https://doi.org/10.1016/S0160-4120(97)00030-5

[36] Tarımsal Ekonomi ve Politika Geliştirme Enstitüsü (2023). *Ürün Raporu. Su Ürünleri*. Yayın No: 373.

[37] United States Environment Protection Agency, (2000). *Guidance for Assessing Chemical Contaminant Data for Use in Fish Advisories Risk Assessment and Fish Consumption Limits* https://www.epa.gov/sites/production/files/2015-06/documents/volume2.pdf

[38] World Health Organization (2000). *Evaluation of certain food additives and contaminants. Report of the Fifty-Third of the Joint FAO/ WHO Expert Committee on Food Additives.* Technical Report Series, https://www.who.int/publications/i/item/9241208961

[39] Kasapoglu, N. & Duzgunes, E. (2014). Length-weight relationships of marine species caught by five gears from the Black Sea. *Mediterranean Marine Science, 15*(1), 95-100. https://doi.org/10.12681/mms.463

[40] Samsun, O., Akyol, O., Ceyhan, T., & Erdem, Y. (2017). Length-weight relationships for 11 fish species from the Central Black Sea, Turkey. *Ege Journal of Fisheries and Aquatic Sciences, 34*(4), 455-458. https://doi.org/10.12714/egejfas.2017.34.4.13

[41] Smichi, N., Kharrat, N., Achouri, N., Gargouri, Y., Miled, N., & Fendri, A. (2016). Physicochemical characterization and nutritional quality of fish by-products: In vitro oils digestibility and synthesis of flavour esters. *Journal of Food Processing & Technology, 7,*(7). 1000602. https://doi.org/10.4172/2157-7110.1000602

[42] Corapci, B. (2021). Quality of black scorpionfish (*Scorpaena porcus*, Linnaeus 1758) meat cooked in different cooking materials. *The Journal of Food, 46*(6), 1415-1424. https://doi.org/10.15237/gida.GD21115

[43] Hamed, F., Elgaoud, I., Eljoudi, S., Deracinois, B., Flahaut, C., Nedjar, N., Barkia, A. (2024). Diplodus protein hydrolysates: Antioxidant and antibacterial properties and identification of biopeptides. *Waste and Biomass Valorization, 15,* 4309-4323.

[44] Hamed, F., Elgaoud, I., Deracinois, B., Flahaut, C., Nedjar, N., Barkia, A. (2022). Production of hydrolysates and peptides from a new protein source: *Diplodus annularis*. *Food Bioscience, 50,* Part B, 102129.

[45] Kouroupakis, E., Grigorakıs, K., Vardalı, S., Ilıa, V., Batjakas, I., Kotzamanıs, Y. (2019). Evaluation of the fillet quality of wild-caught white sea bream (*Diplodus sargus* L.) and brown meagre (*Sciaena umbra* L.) captured from the Aegean Sea. *Mediterranean Marine Science, 20*(2), 373-379. http://dx.doi.org/10.12681/mms.18878

[46] Bouriga, N., Bahri, W. R., Mili, S., Massoudi, S., Quignard, J. P., & Trabelsi, M. (2022). Variations in nutritional quality and fatty acids composition of sardine (*Sardina pilchardus*) during canning process in grape seed and olive oils. *Journal of Food Science and Technology, 59*(12), 4844-4852. https://doi.org/10.1007/s13197-022-05572-4

[47] Lipid metabolizması bozuklukları. 13 Ağustos 2022. file:///C:/Users/PC/Downloads/Ecz.%20Eczac%C4%B1l%C4%B1%C4%9F%C4%B1%20Kurulu%202 Lipid%20metabolizmas%C4%B1%20bozukluklar%C4%B1n%C4%B1n%20biyokimyasal%20temeli%20(2).pdf

[48] Domaradzki, P., Florek, M., Staszowska, A., & Litwińczuk, Z. (2016). Evaluation of the mineral concentration in beef from polish native cattle. *Biological Trace Element Research, 171*(2), 328-332. https://doi.org/10.1007/s12011-015-0549-3

[49] Tomović, V. M., Jokanović, M. R., Švarc-Gajić, J. V., Vasiljević, I. M., Šojić, B. V., Škaljac, S. B., Pihler, I. I., Simin, V. B., Krajinovic, M. M., & Zujovic, M. M. (2016). Physical characteristics and proximate and mineral composition of Saanen goat male kids meat from Vojvodina (Northern Serbia) as influenced by muscle. *Small Ruminant Research, 145,* 44-52. https://doi.org/10.1016/j.smallrumres.2016.10.019

[50] Falowo, A. B. (2021). A Comprehensive review of nutritional benefits of minerals in meat and meat products. *Science Letters, 9*(2), 55-64. https://doi.org/10.47262/SL/9.2.132021010

[51] Ben Salem, Z., & Ayadi, H. (2016). Heavy metal accumulation in *Diplodus annularis*, *Liza aurata*, and *Solea vulgaris* relevant to their concentration in water and sediment from the southwestern Mediterranean (coast of Sfax). *Environmental Science and Pollution Research, 23,* 13895-13906. https://doi.org/10.1007/s11356-016-6531-6

[52] Bat, L. (2019, September 4-6). Metals levels in edible fish species of the Black Sea: Evaluation of potential health risks to consumers. [Conference presentation]. 4th International Science Symposium, Kiev-Ukraine. https://www.firatakademi.com/symposiums.asp?lang=2&symposiumID=5

[53] Ben Salem, Z., & Ayadi, H. (2017). Assessment of trace metals contamination in *Diplodus annularis* (Linnaeus, 1758) from the south coast of Sfax, Tunisia. *Euro-Mediterranean Journal for Environmental Integration, 2*,13. https://doi.org/10.1007/s41207-017-0023-z

[54] European Commission. (2006). *Commission Regulation (EC) No 1881/2006 of 19 December 2006 setting maximum levels for certain contaminants in foodstuffs.* https://eur-lex.europa.eu/LexUriServ/LexUriServ.do?uri=OJ:L:2006:364:0005:0024:EN:PDF

[55] Gencer, D. C., Kocatepe, D. (2024). Mineral content of some crustaceans and molluscs in Turkiye and risk assessments for public health. *Scientific Study & Research Chemistry & Chemical Engineering, Biotechnology, Food Industry, 25*(1), 19-34.

[56] Haseeb-ur-Rehman, M., Munshi, A. B., Atique, U., Kalsoom, S. (2023). Metal pollution and potential human health risk assessment in major seafood items (fish, crustaceans, and cephalopods), *Marine Pollution Bulletin, 188,* 114581. https://doi.org/10.1016/j.marpolbul.2023.114581

[57] Food and Agriculture Organization / World Health Organization. (2011). *Report of The Fifth Session of The Codex Committee on Contaminants in Foods. (Codex Circular Letter CL 2011/6-CF)* https://www.fao.org/fao-who-codexalimentarius/committees/committee/en/?committee=CCCF

Sinopfbd, 2024; 9(2): 449-466 **https://doi.org/10.33484/sinopfbd.1456956**

Sinop Üniversitesi Fen Bilimleri Dergisi
Sinop Uni J Nat Sci

E-ISSN: 2564-7873

https://dergipark.org.tr/tr/pub/sinopfbd

Sosyal Medya Etkileşimlerinde Depresyonu Tanımlamak için Derin Öğrenme Tekniklerinin Kullanılması

Ordak Ibrahim NOORULDEEN[1] ve Serkan SAVAŞ

How to cite: Nooruldeen, O. I., & Savaş, S. (2024). Sosyal medya etkileşimlerinde depresyonu tanımlamak için derin öğrenme tekniklerinin kullanılması. *Sinop Üniversitesi Fen Bilimleri Dergisi, 9*(2), 449-466. https://doi.org/10.33484/sinopfbd.1456956

Araştırma Makalesi

Sorumlu Yazar
Ordak Ibrahim Nooruldeen
ordakibrahim@gmail.com

Yazarlara ait ORCID
O.I.N: 0009-0004-9477-1187
S.S: 0000-0003-3440-6271

Received: 22.03.2024
Accepted: 30.08.2024

Öz

Depresyon, en yaygın zihinsel sorunlardan biridir ve intiharların önemli bir nedenidir. Sosyal medya platformlarının kullanımının artması, kullanıcıların günlük dilini kullanarak ifade ettikleri cümleler üzerinden depresyonun erken teşhisine olanak sağlamıştır. Sosyal medya platformlarının bireylerin günlük hayatlarında merkezi bir rol oynamaya devam etmesiyle, bu platformları ruh sağlığı analizi için kullanma konusunda artan bir ilgi bulunmaktadır. Bu çalışmada, Twitter (günümüzde X) üzerinden depresyon sınıflandırması yapılmıştır. Bu çalışmanın amacı Twitter'dan alınan tweetler arasında depresif özellik taşıyan tweetleri tespit etmektir. Çalışmada, Çift Yönlü Uzun Kısa Süreli Bellek (Bi-LSTM) mimarisi kullanarak depresyon tahmini için yenilikçi bir model sunulmuştur. Bu model, tweetlerdeki dil özelliklerini kullanarak depresyonun daha doğru tespiti için uygun temizleme ve ön işleme tekniklerinden faydalanmaktadır. Çalışma için, Twitter API yoluyla elde edilen özel bir veri seti oluşturulmuş ve analizler bu veri seti üzerinde gerçekleştirilmiştir. Önerilen Bi-LSTM modeli, %97.22'lik bir doğruluk oranı elde ederek dikkate değer bir etkinlik göstermiştir. Elde edilen sonuçlar, Twitter kullanıcılarının duygularındaki depresyonla ilgili örüntüleri ayırt etmek için derin öğrenme tekniklerinin kullanılabilirliği ve etkinliğini göstermiştir. Bu araştırma, ruh sağlığı izlemede ileri düzey tahmin analitikleri için bir temel oluşturmakta ve depresyon tespit modellerinin doğruluğunu ve verimliliğini artırmada Bi-LSTM'in potansiyelini vurgulamaktadır.

Anahtar Kelimeler: Sosyal Medya, Depresyon Sınıflandırması, Twitter, Derin Öğrenme, Bi-LSTM

Using Deep Learning Techniques to Identify Depression in Social Media Interactions

[1]Çankırı Karatekin Üniversitesi, Fen Bilimleri Enstitüsü, Elektronik ve Bilgisayar Mühendisliği Anabilim Dalı, Çankırı, Türkiye.

Abstract

Depression is one of the most common mental problems and an important cause of suicide. The increased use of social media platforms has enabled early diagnosis of depression through the sentences expressed by users using everyday language. As social media platforms continue to play a central role in individuals' daily lives, there is a growing interest in using these platforms for mental health analysis. In this study, Twitter (nowadays X) was used to categorize depression. The aim of this study is to identify tweets with depressive characteristics among tweets retrieved from Twitter. We present an innovative model for depression prediction using a Bi-directional Long Short-Term Memory (Bi-LSTM) architecture. This model utilizes appropriate cleaning and preprocessing techniques for more accurate detection of depression using language features in tweets.

[2]Kırıkkale Üniversitesi,
Mühendislik ve Doğa Bilimleri
Fakültesi, Bilgisayar
Mühendisliği Bölümü,
Kırıkkale, Türkiye.

For the study, a special dataset obtained through Twitter API was created and analyses were performed on this dataset. The proposed Bi-LSTM model has shown remarkable effectiveness, achieving an accuracy rate of 97.22%. The results obtained demonstrated the feasibility and effectiveness of deep learning techniques for recognizing depression-related patterns in the emotions of Twitter users. This research provides a foundation for advanced predictive analytics in mental health monitoring and highlights the potential of Bi-LSTM in improving the accuracy and efficiency of depression detection models.

Keywords: Social Media, Depression Classification, Twitter, Deep Learning, Bi-LSTM

Giriş

Depresyon, küresel bir psikiyatrik bozukluk olarak, dünyanın sağlık problemlerinin önemli bir kısmını oluşturmakta ve nüfusun %4.4'ünü etkilemektedir [1]. Bu durum kişisel, ailesel ve toplumsal refahı derinden etkileyerek zor çocukluklar, istismar, bağımlılık ve toplumsal baskılar gibi çeşitli faktörlerle ortaya çıkabilir [2]. Bilinen tedavilere rağmen, ruh sağlığı sorunlarının şiddeti, özellikle depresyon hem bireyler hem de toplum için ciddi zorluklar yaratmaktadır [3, 4]. Özellikle ergenler için engelliliğe, kendine zarar vermeye ve hatta intihara yol açma potansiyeli göz önüne alındığında depresyonun ciddiyetini anlamak acil bir konu haline gelmektedir [5]. Günümüz dünyasında sosyal medya, görüşlerin ifade edilmesi ve duyguların paylaşılması için hayati öneme sahiptir. Twitter ve Facebook gibi büyük platformlar kullanıcıların duyguları üzerine değerli veriler sunmaktadır [4]. Bireylerde depresyon tespiti zor kalmakta, araştırmacıları erken tespit için sosyal medyanın potansiyelini keşfetmeye teşvik etmektedir [6]. Küresel nüfusun %57'den fazlası sosyal medya kullandığı için bu platformlar benzersiz bir fırsat sunmaktadır. Online tarama araçları, geleneksel yöntemleri geride bırakarak ruh sağlığı değerlendirmeleri için önemli hale gelmiştir [7, 8]. Özellikle Twitter'ın günlük büyük tweet hacmi düşünüldüğünde ruh sağlığı araştırmalarında etkili modellerin eğitimi için bu platform daha da değerli hale gelmektedir [9, 10]. Platformlar tarafından sunulan Uygulama Programlama Arayüzü (Aplication Programming Interface - API), düzenli ifadeler kullanarak sosyal medya platformlarından veri almayı kolaylaştırır [11 - 13]. Doğal Dil İşleme (Natural Language Processing - NLP) ve Duygu Analizi (Sentiment Analysisi - SA), metinlerdeki duygusal yönleri değerlendirerek, sosyal medya içeriği aracılığıyla depresyon seviyelerine dair iç görüler sağlar [14, 15]. Dil kalıplarından yararlanarak Yapay Zeka (YZ) ve NLP tabanlı teknikler, sosyal medya kullanıcıları arasında depresyonun erken tespitinde araştırmacılara yardımcı olur [16]. Böylece makine öğrenimi ve derin öğrenme modelleri, özellikle depresyon olmak üzere ruh sağlığı bozuklukları hakkında değerli iç görüler ortaya çıkarma imkânı sunmaktadır. Bu çalışmada, ruh sağlığı bozukluklarıyla ilişkili çeşitli anahtar kelimeler kullanarak Twitter'dan tweetler alınmıştır. Çalışmanın amacı potansiyel olarak ruh sağlığı sorunları yaşayan veya depresyon deneyimleyen kullanıcıları tespit etmektir. Bu bağlamda sosyal medyadan empirik olarak desteklenen psikolojik iç görüleri gözlemleme mümkün olmaktadır. Bu çalışma sosyal medya üzerinden depresyon tespitine yönelik bir temel oluşturmaktadır. Gelecek çalışmalarla birlikte ruh sağlığı bozuklukları alanında duyguların ve hislerin daha kesin bir şekilde tanımlanmasına yol açabilir. Bu çalışmanın yapısı şöyle oluşturulmuştur. İkinci bölümde konu ile ilgili alan çalışmaları özetlenmiştir. Üçüncü bölümde çalışmada kullanılan materyal açıklanmış ve uygulanan metodoloji anlatılmıştır. Dördüncü bölümde çalışmadan elde edilen bulgular sunulmuş ve tartışılmıştır. Beşinci bölümde ise çalışma sonuçlandırılmıştır.

İlgili Çalışmalar

Sosyal medya metin verilerinin sınıflandırılması için çeşitli makine öğrenimi algoritmaları ve istatistiksel teknikler kullanılmaktadır. Geleneksel çalışmalar, depresyon ile sosyal medya kullanımı arasında bir ilişki olduğunu göstermektedir [17]. Bu amaçla literatürde farklı çalışmalar gerçekleştirilmiştir. Costello ve ark. [17], internet platformlarında kullanılan dil temelinde psikolojik özelliklerin çevrimiçi davranışlarda haritalanabileceğini belirtmişlerdir. Eichstaedt ve ark. [18], Facebook durum güncellemelerinde makine öğrenimi uygulayarak %69'luk bir depresyon tahmini elde etmişlerdir. Ahmad ve ark. [19] ise sosyal medyada %93 doğruluk oranıyla depresyonu tanımlamak için derin öğrenme kullanmışlardır. Bir başka çalışmada Priva ve ark. [20] tarafından beş makine öğrenimi algoritması kullanılmış ve Naif Bayes (Naive Bayes - NB) algoritmasının en yüksek doğruluğa sahip olduğu belirtilmiştir. Mori ve Haruno [21] tarafından Twitter verilerinde dört farklı makine öğrenimi algoritmasıyla 24 kişisel veriye ait 239 özellik analiz edilmiştir. Çalışmada dört tür sosyal ağ hizmeti bilgisine ait 23 alt ölçeğin toplu olarak tahmin edebileceği belirtilmiştir [21]. Tao ve ark. [22] tarafından gerçekleştirilen çalışmada depresif içerik tahminine odaklanılarak %90 F1 puanı elde edilmiştir. Bu çalışmalar, sosyal medya aracılığıyla depresyonu karakterize etmede çeşitli makine öğrenimi yaklaşımlarının başarılı sonuçlar üretebileceğini göstermektedir [22]. Guntuku ve arkadaşlarının [23] yaklaşık 400 milyon tweet toplayarak yalnızlıkla ilgili terimler üzerine gerçekleştirdiği çalışmada yalnızlık seviyeleri tahmin edilmiştir. Makine öğrenimi sınıflandırıcıları ve NLP tekniklerini kullanarak Rastgele Orman (Random Forest - RF) modeliyle 0.86'lık bir AUC (Area Under the Curve) elde etmişlerdir [23]. Smys ve Raj [24], bir Twitter veri seti kullanarak hastalık riskini erken teşhis yoluyla azaltmayı hedeflemişlerdir. Araştırmacılar çeşitli makine öğrenimi algoritmalarını kullanmış ve bireysel sınıflandırıcılardan daha üstün performans gösteren, duyguları tanıma ve tahmin doğruluğunda daha yüksek başarı elde eden hibrit bir yaklaşım önermişlerdir [24]. Hiraga [25] ise araştırmasında, Japon bloglarında ruhsal bozuklukları sınıflandırmak için geleneksel makine öğrenimi algoritmalarını kullanarak NB ile %95'lik en yüksek doğruluk oranını elde etmiştir. Wu ve ark. [26], Weibo kullanıcılarında tükenmişlik hissini tahmin etmek için makine öğrenimi algoritmalarını kullanmışlardır. Araştırmacılar yüksek geri çağırma, hassasiyet ve F1 puanı ile Aşırı Gradyan Artırma (eXtreme Gradient Boosting - XGBoost) modelinin tükenmişlik hislerini tespit etmedeki başarısını vurgulamışlardır [26]. Bir başka çalışmada sosyal medya metinlerinden doğum sonrası depresyonu tahmin etmek için makine öğrenimi teknikleri uygulanmıştır [14]. Çalışmada, Çok Katmanlı Algılayıcı (Multilayer Perceptron -

MLP) algoritmasının depresif içeriği tanımlamada ve doğum sonrası depresyon içeriğini yüksek doğrulukla tahmin etmede Destek Vektör Makinesi (Support Vector Machine - SVM) ve Lojistik Regresyon'dan (Logistic Regression - LR) daha üstün performans gösterdiği belirtilmiştir [14]. Orabi ve ark. [27], Twitter kullanıcılarında zihinsel hastalık belirtilerini tespit etmek için derin sinir ağları kullanmışlardır. Çalışmada dört sinir ağı modeli değerlendirilmiş ve Evrişimli Sinir Ağı (Convolutional Neural Network - CNN) ile maksimum %87,957'lik en yüksek doğruluğa ulaşılmıştır. CNN tabanlı modellerin Yinelemeli Sinir Ağları (Recurrent Neural Network – RNN) tabanlı modellere göre daha iyi performans gösterdiği görülmüştür [27]. Farklı bir platform olarak Reddit kullanıcılarında erken depresyon tespiti için Shah ve ark. [28], derin öğrenme tabanlı kelime yerleştirme tekniklerini kullanmış ve Word2VecEmbed ile Meta özelliklerin kombinasyonuyla depresyon tespitinde üstün performans elde etmişlerdir [28]. Shen ve ark. [29] tarafından gerçekleştirilen çalışmada Twitter'da depresif kullanıcıları tespit etmek için çok modlu sözlük öğrenme yöntemi önerilmiş ve minimum tanım uzunluğu ilkesiyle %85'lik en yüksek F1 puanına ulaşılmıştır. De Choudhury ve ark. [30], sosyal medyada depresyon tespiti için SVM algoritmasıyla, etiketlenmiş eğitim verilerinden ayırt edici özellikler kullanarak %70 sınıflandırma doğruluğu elde etmişlerdir. Sosyal ağlarda kullanıcı tarafından üretilen içerik analizi yoluyla ruh sağlığı seviyelerini ayırt etme potansiyelini inceleyen bir çalışmada Aldarwish ve Ahmad [31], NB yöntemi kullanarak %92'lik bir doğruluk oranı elde etmişlerdir. Guntuku ve ark. [32] tarafından gerçekleştirilen çalışmada sosyal medya aracılığıyla depresyonun tahmin edilmesi için çeşitli yöntemler karşılaştırılmış ve standart verilerin sosyal medya verileriyle entegre edilmesinin gerekliliği vurgulanmıştır. Çalışmada 0.70 ile 0.91 arasında değişen AUC değerleri, sosyal medyanın geleneksel yöntemlere kıyasla ruhsal hastalıkları tahmin etme potansiyelini göstermiştir [32]. Ahmad ve ark. [33] tarafından gerçekleştirilen çalışmada Twitter'dan elde edilen veri seti kullanılarak çevrimiçi kullanıcıların depresyon belirtileri gösterip göstermediğini belirlemek için makine öğrenmesi ve derin öğrenme modelleri kullanılmıştır. Çift Yönlü Uzun Kısa Süreli Bellek (Bidirectional Long Short-Term Memory - Bi-LSTM) modeli, %93.5 doğruluk oranıyla diğer modellerden daha iyi bir performans sergilemiştir [33]. Syms ve Raj [24], zihinsel sağlık sorunları ve intihar risklerinden korunmaya yönelik erken tahmin sistemi geliştirmek için bir hibrit yöntem önermişlerdir. Shah ve arkadaşlarının [28] gerçekleştirdiği çalışmada, kullanıcıların metin gönderilerini analiz ederek depresyonu tespit edebilen bir model önerilmiştir. Bu model, eğitim verileri kullanılarak derin öğrenme algoritmalarıyla eğitilmiş ve performansı, Reddit'in CLEF eRisk 2017'de yayınlanan 'Depresyonun Erken Tespiti' adlı pilot çalışmasının test verileriyle değerlendirilmiştir. Çalışmada Bi-LSTM modeli, çeşitli kelime gömme teknikleri ve meta veri özellikleri kullanarak başarılı sonuçlar elde etmiştir [28]. Figuerêdo ve ark. [34] tarafından gerçekleştirilen çalışmada depresyonun erken tespitine yönelik CNN tabanlı bir yöntem önerilmiştir. Önerilen yöntemin potansiyel olarak depresyon belirtileri gösteren kullanıcıları tespit edebildiği ve birçok temel metrik açısından diğer yöntemlere eşit veya daha iyi performans gösterdiği belirtilmiştir [36]. Marriwala ve ark. [35] tarafından depresyon tespiti için, hastanın yanıtlarının metinsel ve işitsel özelliklerini birleştiren hibrit bir model önerilmiştir. Depresyonlu hastaların davranışsal özelliklerini incelemek için DAIC-WoZ veri tabanı kullanılmıştır. Önerilen yöntem üç bileşenden oluşmaktadır. İlk bileşen yalnızca metin özellikleriyle eğitilen bir metinsel CNN modelidir. İkinci bileşen yalnızca ses özellikleriyle eğitilen bir işitsel CNN modelidir. Üçüncü bileşen ise ses ve metinsel özelliklerin bir kombinasyonundan oluşan hibrit modeldir. Bu modellerde LSTM algoritmaları kullanılmıştır. Önerilen çalışmada, Bi-LSTM modeli olarak adlandırılan geliştirilmiş bir LSTM versiyonu da kullanılmıştır. Bi-LSTM'nin %88 doğruluk oranı ile diğer modellere göre daha iyi öğrenme performansı sergilediği gözlenmiştir [36].

Materyal ve Metodoloji

Bu araştırmada, tweetlerin depresyonu işaret edip etmediğini belirlemek için Twitter kullanıcı yorumlarından veri toplama ve analiz etme konusunda kapsamlı bir yöntem kullanılmıştır. Twitter'dan veri toplama ve depresyon belirtisi gösteren bireylerin tweetlerini diğerlerinden ayırarak iki ayrı dosyada yerleştirme işlemi gerçekleştirilmiştir. Sonrasında elde edilen bu veriler analiz edilerek çalışmada oluşturulan modelin performansı değerlendirilmiştir. Çalışmanın blok diyagramı Şekil 1'de gösterilmiştir.

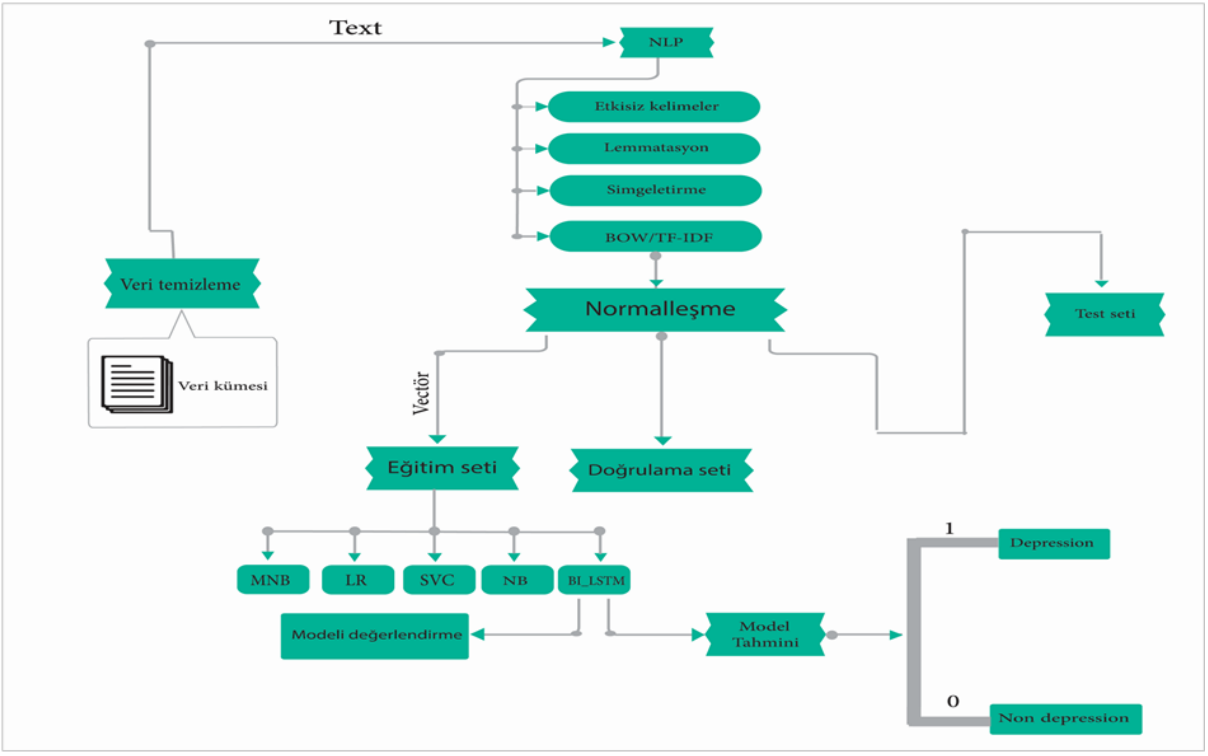

Şekil 1. *Veriler üzerinde ön işleme ve özellik çıkarımı adımları*

Veri Seti

Bu çalışmada kullanıcılardan veri toplamak için Twitter'ın API kullanılmıştır. API, geliştiricilerin manuel işlemlere gerek kalmadan büyük miktarda kamuya açık veriyle programatik olarak etkileşimde bulunmalarını sağlar. API erişimi, bir geliştirici hesabı oluşturarak araştırma çalışmasını detaylandırma ve geliştirici anlaşması ile sağlanmıştır. Sonuç olarak, API 'anahtarı' ve 'erişim belirteci' kullanımı için yetki alınmıştır. Veri alımını kolaylaştırmak için bir Python kütüphanesi olan Tweepy kullanılmıştır. Şekil 2, veri setini edinmek için kullanılan metodolojiyi göstermektedir.

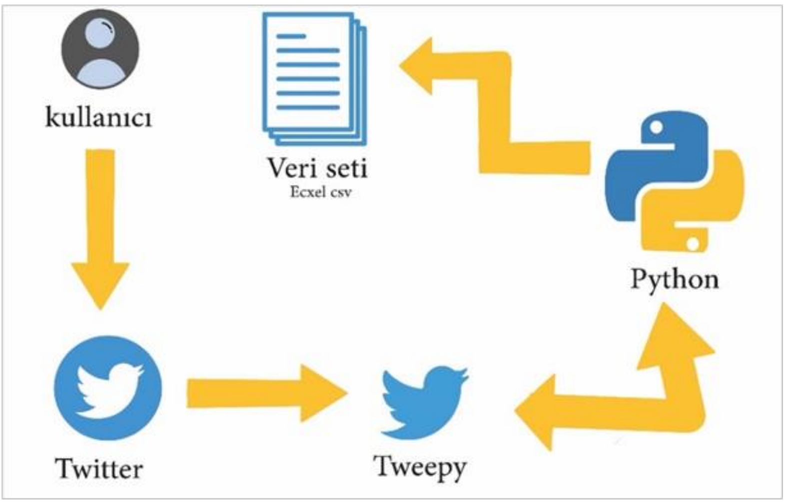

Şekil 2*. Veri setini edinmek için kullanılan metodoloji*

Çalışmada gerçekleştirilen analiz hem tweetlerdeki sözcük seçimlerine hem de ifade edilen depresif belirtilerin türlerine dayanmaktadır. Twitter API yardımıyla toplamda 100,033 veri çekilmiştir. Bu veriler içerisinden %60 oranında eğitim verisi, %20 oranında doğrulama verisi ve %20 oranında ise test verisi rastgele seçilerek alt kümeler oluşturulmuştur. Bu tweetlerde ifade edilen duygular iki sınıfa ayrılmıştır. İlk sınıf 'depresyon', 'kötü', 'kendimi kötü hissediyorum', 'gergin', 'intihar', 'şizofren', 'yorgun', 'stres', 'anksiyete', 'çaresiz' ve 'kriz' gibi terimleri içermektedir. İkinci sınıf ise 'mutlu', 'iyi', 'memnun', 'neşeli', 'daha iyi', 'umut', 'güzel' ve 'heyecanlı' gibi pozitif duyguları kapsamaktadır. Veriler daha sonra analiz için Excel CSV formatına dönüştürülmüştür. Analiz için tweet veri seti gruplara ayrılmıştır. Her grup; 'No', 'Tarih', 'tweet_id', 'Metin', 'KullanıcıAdı', 'Ad', 'Konum', 'takipçi_sayısı', 'Dil' ve 'Etiket' sütunlarını içermektedir. Son adım, bu tweetleri filtreleyerek depresif belirtilerle en alakalı olanları belirlemektir.

Ön İşleme

Veri madenciliği sürecinde veri ön işleme, ham metin verilerini temizleme ve ardından yapılacak işlemler veya analizler için verileri hazırlama için kritik bir adımdır. Bu süreç, tokenizasyon, etkisiz kelimeleri (stop words) kaldırma, kök bulma (stemming) ve kökten türetme (lemmatization) gibi birkaç önemli adımı içermektedir. Bu adımlar, metin verilerinin boyutunu azaltmaya ve NLP görevlerinde doğruluğu artırmaya yardımcı olmaktadır. Metin verileri doğası gereği yapılandırılmamış olup sıklıkla yazım hataları, dilbilgisi hataları ve standart olmayan biçimlendirme gibi gürültü içerir. Bu gürültüler de verilerin işlenmesini zorlaştırır. Bu çalışmadaki ön işleme aşamaları verideki gürültüyü hafifletmeyi ve böylece veri analizini kolaylaştırmayı hedeflemektedir. Kullanılan veri ön işleme yöntemleri arasında tweetleri temizleme, dengesizlikleri giderme, retweetleri eleme ve analiz için kullanıcı tarafından üretilen içerik ve kullanıcı profil verilerinin kullanılabilirliğini sağlama yer almaktadır. Özellikle kullanıcı tanımlayıcıları (örn. @kullanıcıadı), etiketler, bağlantılar, harf olmayan karakterler, semboller, sayılar, boş dizgiler, NaN değerleri içeren satırlar ve çift girişler gibi fazlalık unsurların kaldırılması hedeflenmiştir. Tweet içindeki bağlantılar, tahmin amaçları için alakasız oldukları ve hesaplama karmaşıklığını artırdıkları için hariç tutulmuştur. Ayrıca, analizi çarpıtmamak için tweetlerden tarihler, saatler, sayılar ve etiketler kaldırılmıştır. Emojiler, fazla boşluklar ve etkisiz kelimeler de çıkarılmıştır. Doğal dil aracı (Natural Language Toolkit - NLTK) paketi, metinlerden etkisiz kelimeleri çıkarmada önemli bir rol oynamıştır. Porter Stemmer gibi teknikler kullanılarak kelime köklerine indirgemek ve ekleri çıkarmak amacıyla kök bulma işlemi gerçekleştirilmiştir. Şekil 3, ön işlemenin ardından temizlenmiş depresyon tweetlerini göstermektedir.

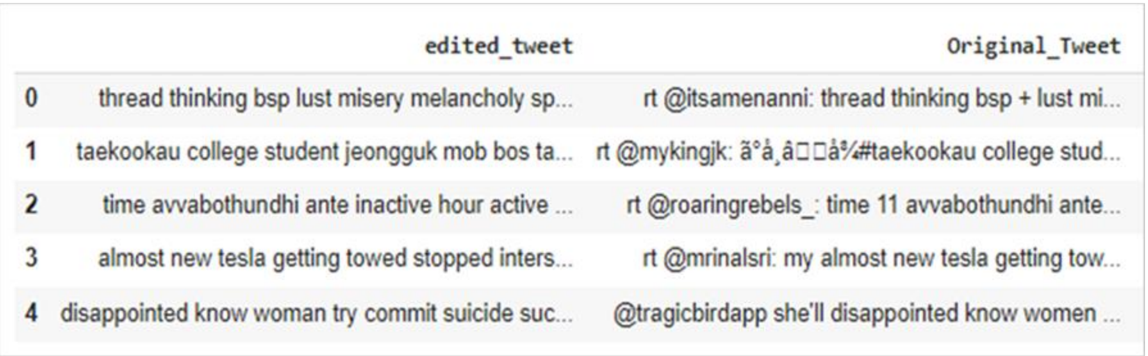

	edited_tweet	Original_Tweet
0	thread thinking bsp lust misery melancholy sp...	rt @itsamenanni: thread thinking bsp + lust mi...
1	taekookau college student jeongguk mob bos ta...	rt @mykingjk: ã°å¸â□□å¾#taekookau college stud...
2	time avvabothundhi ante inactive hour active ...	rt @roaringrebels_: time 11 avvabothundhi ante...
3	almost new tesla getting towed stopped inters...	rt @mrinalsri: my almost new tesla getting tow...
4	disappointed know woman try commit suicide suc...	@tragicbirdapp she'll disappointed know women ...

Şekil 3. *Ön işlemenin ardından temizlenmiş depresyon tweetlerini göstermektedir*

Makine öğrenimi algoritmaları ilk başta metin verilerini anlamsal olarak yorumlama yeteneğinden doğal olarak yoksundur. Bu açığı kapatmak için kelimeleri sayısal değerlere eşlemek gereklidir. Bu işlem özellik çıkarma yoluyla gerçekleştirilir. Bu sayısal eşleme metinlerin anlamlarını etkili bir şekilde kapsüllemeyi amaçlar. Bu bağlamda metin verilerini sayısal özelliklere dönüştüren iki yaygın teknik araştırılmıştır. Bunlar, kelime torbası modelinden türeyen CountVectorizer ve Terim Frekansı-Ters Belge Frekansı (Term Frequency-Inverse Document Frequency - TF-IDF) yöntemleridir. CountVectorizer, metin analizinde kullanılan bir yöntemdir ve bir metin belgeleri koleksiyonunu kelime (token) sayılarının bir matrisine dönüştürür. Temelde metni bireysel kelimelere ayırır ve her bir belgedeki oluşum sayılarını sayar. Bu işlem metin verilerini makine öğrenimi algoritmalarının yorumlayabileceği sayısal bir formata dönüştürür. Ayrıca veri işlemede veri normalleştirme tekniği kullanılmıştır. Normalizasyon, bir veri kümesindeki değerleri, değerlerin aralığındaki farkları bozmadan veya bilgi kaybetmeden ortak bir ölçeğe ayarlamak için kullanılan bir tekniktir. Veri setindeki her bir satır, metnin kelimelere ayrılmasıyla belirteçleştirilmiştir (tokenizasyon). Bu işlem NLP yöntemleri için ön işlemenin temel adımıdır. Şekil 4'te veri setindeki metinleri kelimelere ayırma işlemi gösterilmektedir.

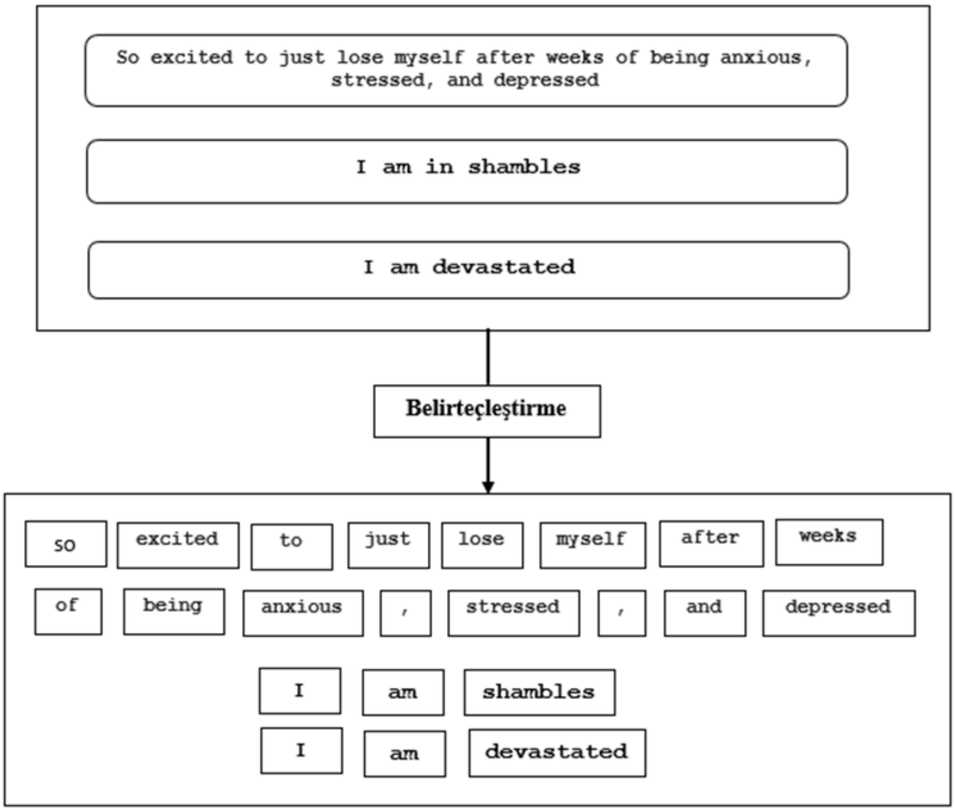

Şekil 4. *Veri setindeki metinleri kelimelere ayırma işlemi*

Kelime bulutu, bu çalışmada tweetlerden elde edilen ve ön işlemeden geçirilen depresyon içeren ve depresyon içermeyen veri setlerini temsil etmektedir. Şekil 5'te, ön işleme sonrası oluşturulan kelime bulutu görülmektedir.

Şekil 5. *Depresyon içeren ve içermeyen kelime bulutları*

Kullanılan Modeller

Çalışmada analiz işlemlerini gerçekleştirmek makine öğrenimi modellerinden faydalanılmıştır. NB, Lojistik Regresyon (LR), Çok Terimli Naive Bayes (MultinomialNB), Destek Vektör Sınıflandırıcısı (Support Vector Classifier - SVC) ve Bi-LSTM gibi modeller performansları açısından karşılaştırılmıştır.

a) Bi-LSTM Modeli

Bi-LSTM özellikle NLP görevlerinde kullanılan temel LSTM modelinin gelişmiş bir varyantıdır. Veriyi tek bir yönde (ileri veya geri) işleyen standart LSTM algoritmasının aksine Bi-LSTM, veriyi eş zamanlı olarak her iki yönde de işler. Bu çift yönlü işleme modelin veri dizisinin hem geçmiş (geri) hem de gelecek (ileri) durumlarından bilgi toplamasına olanak tanır. Bi-LSTM algoritmasının temel avantajı geleneksel LSTM algoritmasına göre bağlamı daha iyi anlayabilmesidir. Algoritma, tek yönlü bir yaklaşımla kaçırılacak olan verilerdeki desenleri ve bağımlılıkları etkili bir şekilde öğrenebilir. Potansiyel bir dezavantajı ise hesaplama karmaşıklığıdır. İki yönden veri işlemek daha fazla hesaplama kaynağı ve zaman gerektirir, bu da modeli standart LSTM algoritmasına kıyasla daha kaynak yoğun hale getirir. Tasarımı özellikle sıralı girdi verilerinden öğrenmek ve hem ileri hem de geri yönde bağımlılıkları yakalamak için özelleştirilmiştir. Önerilen Bi-LSTM modelinin mimarisi, depresyon belirtisi içeren ve içermeyen tweetlerin sınıflandırılması amacıyla tasarlanmıştır. Bu mimarinin temel bileşeni, giriş metnini bir dizi belirteç indeksine dönüştüren metin vektörleştirme katmanıdır. Müteakip aşamada, bu belirteçler, her kelimeye eğitilebilir bir vektör atayan gömme katmanına iletilir. Yeterli eğitim süreci sonrasında bu vektörler, semantik açıdan benzer kelimelerin benzer vektörel temsillere sahip olmasını sağlayacak şekilde optimize edilir. Elde edilen veriler, ardından bu dizileri işleyen ve nihai olarak tek bir logit değerine indirgeyerek sınıflandırma çıktısı üreten Çift Yönlü LSTM katmanlarına aktarılır. Depresyon sınıflandırması bağlamında, her bir tweet "normal" veya "depresif" olmak üzere ikili bir sınıflandırmaya tabi tutulmuştur. Bu amaçla geliştirilen Bi-LSTM modeli, Çizelge 1'de detaylandırılan parametreler kullanılarak uygulanmıştır.

Tablo 1. *Bi-LSTM modelinin parametre ayarları*

Model Parametresi	Değer
Num hidden units	97
İnput size	1
Num classes	2
Loss	Categorical_crossentropy
Optimizer	Adam
metrics	Accuracy
Epoches	17
Validation split	0.2
Verbose	1

b) Naive Bayes Modeli

Bayes teoremi, NB algoritması yoluyla doğal dil işlemede de kullanılan matematiksel bir çerçeve olup bir dilin "kurallarına" ve "türlerine" dayanan bir sınıflandırma teorisidir. Bayes teoreminin formülü Denklem (1)'de gösterilmiştir.

$$P(A \mid B) = \frac{P(B|A) \cdot P(A)}{P(B)} \tag{1}$$

c) Lojistik Regresyon Modeli

LR, iki tür veriyi analiz etmek için kullanılan istatistiksel bir yöntemdir. Verileri analiz etmek için belirli bir etiketli veri kategorisi kullanır. Ayrıca karar alma süreçlerinde çeşitli kaynaklardan gelen verileri analiz etme ve şirketlerde en iyi eylem planını tahmin etmek gibi durumlarda da kullanılır. LR, birden fazla veri türünü analiz etmenin karmaşıklıklarını ele almak için önemli bir araçtır [36].

d) Destek Vektör Sınıflandırıcı Modeli

SVC, SVM algoritmasının bir varyantı olarak çeşitli sınıflandırma görevleri için kullanılan bir makine öğrenimi algoritmasıdır. Büyük ve karmaşık veri kümelerinden öğrenmek için son derece etkilidir. Bu algoritma veri setlerinden veri analizi yapmak, verileri daha anlamlı bir formata dönüştürmek ve en son bilgilere dayalı yeni veri üretmek gibi birçok uygulamada kullanılabilir [37].

e) Çok Terimli Naive Bayes Modeli

MultinomialNB, çeşitli veri türleri arasındaki benzerlikleri ve farklılıkları belirleme ve analiz etmeye odaklanan bir NB algoritmasıdır. Bir makine öğrenimi yaklaşımı olarak MultinomialNB çok yönlüdür ve metin, e-postalar, SMS ve daha fazlası gibi geniş bir veri yelpazesine uygulanabilir. Bayes teoremini kullanarak en yaygın veri türlerini ve aralarındaki ilişkileri belirler.

Değerlendirme Metrikleri

Çeşitli ölçümler kullanılarak kapsamlı bir değerlendirme yapılmadan bir makine öğrenimi modelini yeni verilere uygulamak sorunlara ve yanlış tahminlere yol açabilir [38]. Modellerin tahmin performansını iyileştirmek için doğruluk, kesinlik, hatırlama ve F1 puanı gibi metrikler önemlidir. Karışıklık matrisi yoluyla elde edilen doğru pozitif, yanlış pozitif, doğru negatif ve yanlış negatif sonuçları, modellerin performansı ile ilgili öngörüler sağlar. Değerlendirme için kullanılan metrikler, Denklemler (2), (3), (4) ve (5)'te verilmiştir.

$$\text{Doğruluk} = \frac{TP+TN}{TP+FP+FN+TN} \tag{2}$$

$$\text{Kesinlik} = \frac{TP}{TP+FP} \tag{3}$$

$$\text{Hatırlama} = \frac{TP}{TP+FN} \tag{4}$$

$$F1 \text{ puanı} = 2 \times \frac{\text{Kesinlik} \times \text{Haturlama}}{\text{Kesinlik} + \text{Hatırlama}} \tag{5}$$

Denklemlerde doğru pozitif için TP, yanlış pozitif için FP, doğru negatif için TN ve yanlış negatif içinse FN kısaltmaları kullanılmıştır.

Bulgular ve Tartışma

Bu bölümde her modelin performansı ve sonuçları ilgili değerlendirmeler gerçekleştirilmiştir. Şekil 6'da modellerin karışıklık matrisi sonuçları gösterilmiştir.

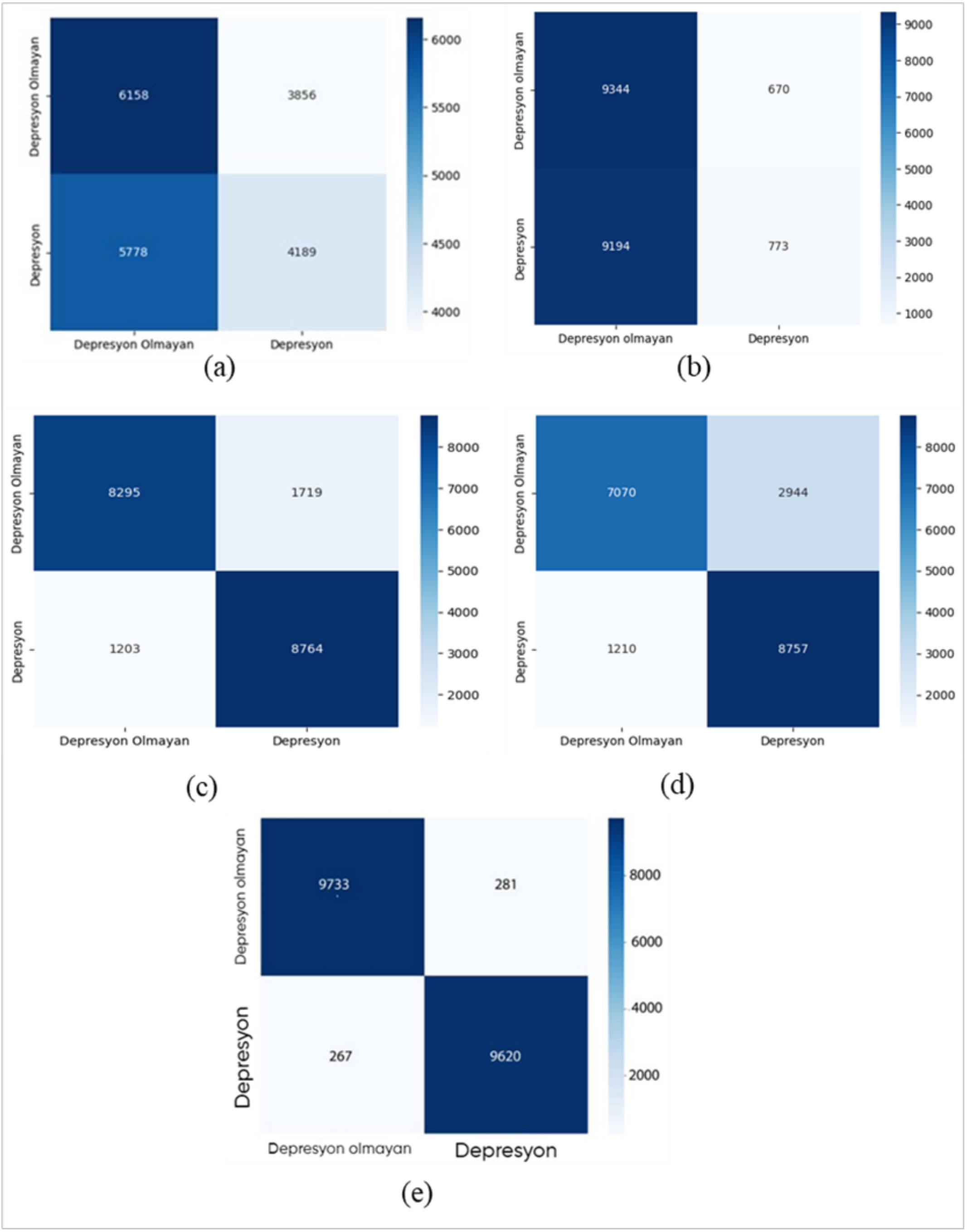

Şekil 6. *Modellerin karışıklık matrisleri (a) MultinomialNB, (b) NB, (c) LR, (d) SVC (e) Bi-LSTM*

Çalışmada kullanılan modeller içerisinde en başarılı model olarak karışıklık matrisinde ön plana çıkan (doğru pozitif sayısı 9620 ve doğru negatif sayısı 9733) Bi-LSTM modeline ait doğruluk ve kayıp grafikleri Şekil 7'de gösterilmiştir.

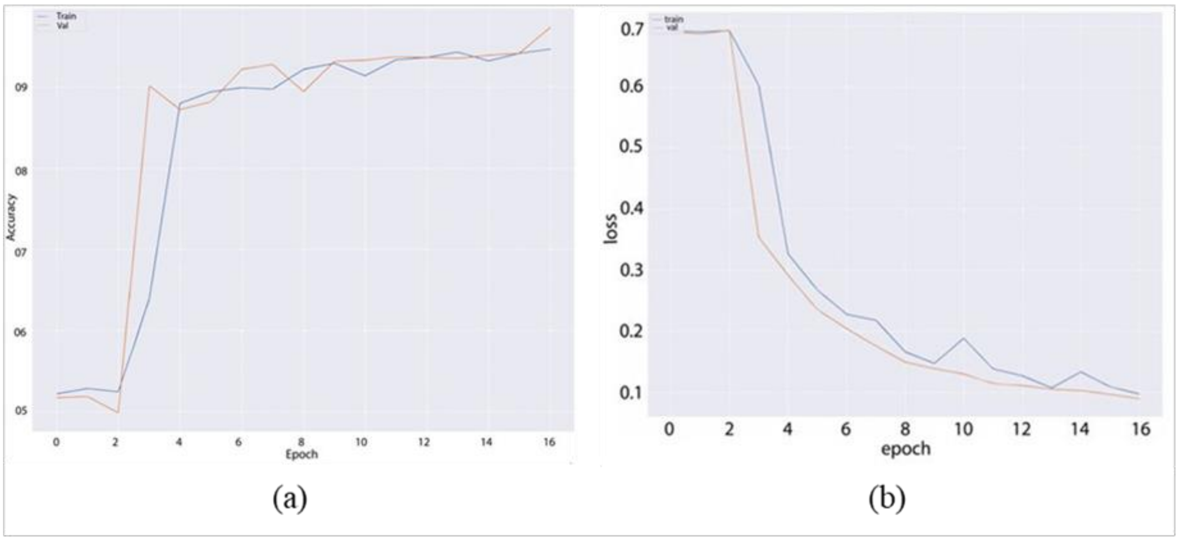

(a) (b)

Şekil 7. *Bi-LSTM modelinin doğruluk ve kayıp grafikleri*

Bir sınıflandırıcının değeri ne kadar yüksekse, pozitif ve negatif kategoriler arasında ayırma yeteneği o kadar güçlüdür. Şekil 8'de Bi-LSTM modeline ait Alıcı İşletim Karakteristiği (Receiver Operating Characteristic - ROC) eğrisinin AUC değeri gösterilmiştir. Sonuç olarak önerilen Bi-LSTM modelinin veri kümesinin pozitif sınıfını etkili bir şekilde sınıflandırdığı sonucuna varılabilir.

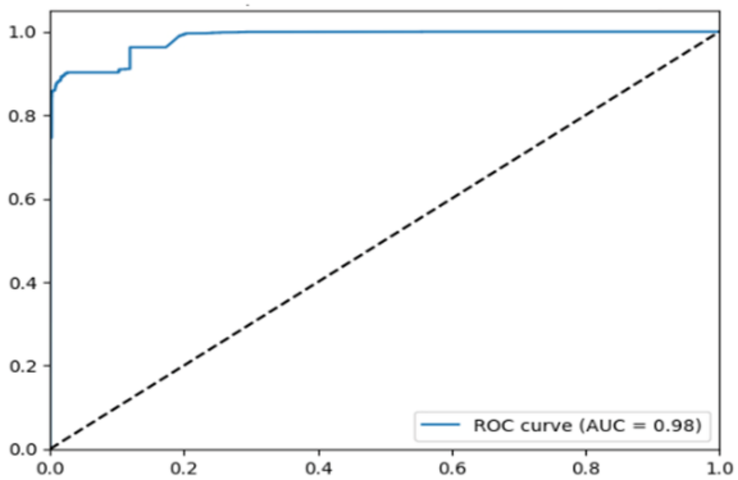

Şekil 8. *ROC grafiği*

Metin sınıflandırmasında genellikle metin verilerinden elde edilen sayısal özellikler için minimum-maksimum normalizasyon tercih edilir. Bu teknik, özellikleri (örneğin kelime sayıları veya TF-IDF değerleri) belirli bir aralıkta (genellikle [0, 1]) standartlaştırarak, model eğitimi verimliliğini ve performansını artırabilir. Modelin normalizasyon olmadan eğitilmesi ise özelliklerin farklı ölçeklerde ve dağılımlarda olmasına bağlı zorluklarla karşılaşılmasına neden olabilir. Ayrıca modelin yeni veriye etkili şekilde genelleme yapma yeteneğini olumsuz etkileyebilir. Tablo 2, metin sınıflandırmasında min-max normalleştirme ve normalleştirme olmadan model eğitimi konusunda iki farklı yaklaşımı temsil etmektedir.

Tablo 2. *Bi-LSTM modellerinin karşılaştırması*

Model	Doğruluk	Kesinlık	Hatırlama	F1 Puanı
Normalizayon ile eğitilen Bi-LSTM modeli	%97.22	%98	%97	%97
Normalizasyon olmadan eğitilen Bi-LSTM modeli	%91	%97	%84	%90

Çalışmadaki Bi-LSTM modeli, yüksek doğruluk oranlarıyla (pozitif 9620 ve negatif 9733) dikkat çekerek tweetlerde depresyonu tanımlamada oldukça etkili olmuştur. Öte yandan NB modeli, depresif olmayan birçok tweeti doğru bir şekilde tanımlamasına rağmen, depresif tweetlerde önemli sayıda yanlış sınıflandırma gerçekleştirmiştir. Bu, bağlamsal duyarlılık eksikliğine veya daha yaygın sınıflara karşı bir önyargıya işaret etmektedir. LR modeli, depresif tweetler için makul sayıda doğru pozitiflerle daha dengeli bir yaklaşım sergilese de yüksek yanlış sınıflandırma oranları göstermiştir. Bu, depresif ve depresif olmayan tweetler arasında orta düzeyde bir ayrım yeteneğine işaret etmektedir. SVC modeli, depresif tweetleri yüksek sayıda doğru pozitiflerle tanımlamada iyi bir performans gösterirken, her iki sınıf için de önemli yanlış sınıflandırma sorunları göstermiştir. Bu, NB modeline benzer şekilde tweetlerde kullanılan nüanslı dili kavramada zorluk çektiğine işaret etmektedir. Bu nedenle, metin içindeki bağlamı anlama yeteneği ve üstün doğruluğu ile Bi-LSTM modeli bu uygulama için en uygun seçim olarak öne çıkmaktadır. Buna karşılık, NB, LR ve SVC modelleri, belirli açılardan yararlı olmalarına rağmen, özellikle sosyal medya içeriğinden depresyon tespit etme gibi uygulamalarda dilin inceliklerinin kritik olduğu doğal dil işleme ve duygu analizi alanındaki karmaşıklıklarla başa çıkmada sınırlılıklar göstermektedir. Tablo 3'te beş modelin doğruluk, kesinlik, hatırlama ve F1 puanları karşılaştırılmıştır. Bu karşılaştırmaya göre Bi-LSTM modeli, Twitter veri setini 'depresif' ve 'depresif olmayan kategorilere sınıflandırmada diğer yaklaşımlardan daha başarılı performans göstermektedir.

Tablo 3. *Önerilen modeller arasındaki sonuçların karşılaştırılması*

Model	Doğruluk	Kesinlik	Hatırlama	F1 Puanı
Bi-LSTM	%97.22	%98	%97	%97
NB	%51	%50	%92	%65
LR	%85	%88	%83	%85
SVC	%79	%86	%71	%77
MultinomialNB	%52	%52	%61	%56

Bi-LSTM modeli, tüm metriklerde üstün performans sergileyerek %97.22 doğruluk, %98 kesinlik, %97 hatırlama ve %97 F1 puanı ile öne çıkmaktadır. Bu, ilgili durumları doğru bir şekilde tanımlamada yüksek güvenilirliğini ve kesinlik ile hatırlama arasında dengeli bir tutum sergilediğini göstermektedir. Diğer yandan, NB modeli, %51 doğruluk ve %50 kesinlik ile performansı düşükken, %92 ile üstün bir hatırlama göstermektedir. Bu, %65'lik F1 puanı ile yüksek hatırlama ve düşük kesinlik arasındaki tutarsızlığı göstermektedir. LR modeli, %85 doğruluk, %88 kesinlik, %83 hatırlama ve %85 F1 puanı ile orta derecede bir performans göstermektedir. Model, kesinlik ve F1 puanı konusunda dengeli bir yetenek sergilemektedir. SVC, %79 doğruluk, %86 kesinlik, %71 hatırlama ve %77 F1 puanı ile düşük bir performans sergilemiştir. Benzer şekilde MultinomialNB modeli %52 doğruluk, %52 kesinlik, %61 hatırlama ve %56 F1 puanı ile nispeten daha düşük performans sergilemiştir. Bu sonuçlar, Bi-LSTM'nin yüksek doğruluk ve kesinlik ile hatırlama arasında dengeli bir yaklaşım gerektiren görevler için en uygun model olduğunu göstermektedir. Diğer modellerin, özellikle NB'nin, yüksek geri çağırma öncelikli senaryolarda, artan yanlış pozitiflerin potansiyeli göz önünde bulundurularak daha uygun olabileceğini göstermektedir. Pratik uygulamalardaki model seçimi, bu nedenle eldeki görevin özel gereksinimlerine bağlı olacaktır. Çalışma yöntemi, sosyal medyada zihinsel sağlık sorunları olan kullanıcıları belirlemede etkili bir araç olma potansiyeline sahiptir ve araştırmada yeni bir dönemin habercisi olabilir. Ayrıca, ruhsal bozuklukları tanımak için özelleştirilmiş NLP yöntemleri kullanılması, kullanıcıların gönderilerine dayanarak potansiyel ruh sağlığı sorunlarını tespit etmeyi kolaylaştırabilir. Bu yaklaşım, kolayca erişilebilir sosyal medya verilerinden yararlanmaktadır. Bu tür analizler için kullanıcıların hesaplarına erişmeden önce onaylarının alınması gerektiğini belirtmek önemlidir. Onay alındıktan sonra bu doğrulanmış modeller, çevrimiçi platformlardaki kullanıcıların gönderilerine dayanarak çeşitli zihinsel bozuklukların olasılığını ortaya çıkarabilir. Sonuç olarak bu çalışma, sosyal medyada zihinsel hastalıkları tespit etmenin gelecekte önemli bir araştırma alanı olabileceğini öne sürmektedir.

Sonuç

Bu çalışmada derin sinir ağı modeli olan Bi-LSTM kullanılarak Twitter gönderilerinden depresyonlu tweetleri tespit etmeye yönelik bir model önerilmiştir. Önerilen Bi-LSTM modeli, metin verilerindeki sıralı bağımlılıkları etkili bir şekilde yakalayabilir ve kullanabilir. Bu özellik, kelimelerin veya ifadelerin sırasının metnin anlamını, duygusunu veya sınıflandırmasını önemli ölçüde etkilediği görevler için son derece önemlidir. Bi-LSTM, bilgileri hem ileri hem de geri yönde aynı anda işleyerek metin içindeki bağlamı ve nüansları daha iyi anlayabilir. Bi-LSTM'deki çift yönlülük, modelin tahmin yaparken hem önceki hem de sonraki kelimeleri dikkate alabilmesine olanak tanır. Bu yetenek, bir cümle içindeki duygu değişimlerini anlamak veya sosyal medya gönderilerindeki depresyonun inceliklerini belirlemek gibi cümle bağlamının kritik bir rol oynadığı görevler için değerlidir. Son olarak çalışmada tweetler normal veya depresif olarak sınıflandırılmıştır. Farklı makine öğrenimi modelleriyle yapılan deneylerde modellerin performansları Twitter API aracığıyla elde edilen veri seti üzerinde değerlendirilmiştir. Önerilen model depresyon tespitinde iyi performans göstermiştir. Bi-LSTM modelinin F1 puanı (%97), hatırlama (%91), doğruluk (%97.22) ve kesinlik (%98) metriklerinde diğer yaklaşımlara göre daha iyi sonuçlar verdiği gözlenmiştir. Bu araştırmanın temel bulgusu, makine öğrenimi modellerinin Twitter kullanıcılarında depresif belirtileri tespit etme ve anlamada önemli bir etkiye sahip olduğudur. Bu içgörü kritiktir çünkü makine öğrenimi ve Bi-LSTM gibi tekniklerin, teorik araştırmaların yanı sıra pratik uygulamalarda da özellikle depresyonla başa çıkan bireylerin yaşam kalitesini artırmada potansiyeli olduğunu vurgulamaktadır. Çalışmanın sonuçları önemlidir ve ruh sağlığı izleme ve müdahalesinde ileri analitiklerin kullanımı için umut verici bir gelecek sunmaktadır. Bu çalışma aynı zamanda profesyonellerin depresyonlu kişileri analiz etmek için ilk verilere ulaşmalarına yardımcı olabilir. Gelecekte, bir kullanıcının sosyal ağının ve etkileşimlerinin onun depresif durumunu nasıl etkileyebileceği dikkate alınarak bu çalışma genişletilebilir ve faktörlerin etkisini ölçmenin daha güvenilir bir yolunun bulunması sağlanabilir.

Teşekkür "Araştırma süreci boyunca değerli katkıları, önerileri ve desteği için Dr. Öğr. Üyesi Serkan SAVAŞ'a teşekkür ederim."

Fon/Finansman Bilgileri Bu çalışma için herhangi bir kurum ve/veya kuruluştan destek alınmamıştır.

Etik Kurul Onayı ve İzinler Çalışma, etik kurul izni veya herhangi bir özel izin gerektirmemektedir.

Çıkar çatışmaları/Çatışan Çıkarlar Yazarlar arasında herhangi bir çıkar çatışması yoktur

Yazarların Katkısı Yazarların Katkısı 1. yazar %60 oranında, 2. yazar %40 oranında katkı sağlamıştır

Kaynaklar

[1] Uddin, M. Z., Dysthe, K. K., Følstad, A., & Brandtzaeg, P. B. (2022). Deep learning for prediction of depressive symptoms in a large textual dataset. *Neural Computing and Applications*, *34*(1), 721–744. https://doi.org/10.1007/s00521-021-06426-4

[2] Oquendo, M. A., Ellis, S. P., Greenwald, S., Malone, K. M., Weissman, M. M., & Mann, J. J. (2001). Ethnic and sex differences in suicide rates relative to major depression in the United States. *American Journal of Psychiatry*, *158*(10), 1652–1658. https://doi.org/10.1176/appi.ajp.158.10.1652

[3] Zafar, A., & Chitnis, S. (2020). Survey of depression detection using social networking sites via data mining. *IEEE Xplore*, 88-93. https://doi.org/10.1109/Confluence47617.2020.9058189

[4] Martínez-Castaño, R., Pichel, J. C., & Losada, D. E. (2020). A big data platform for real time analysis of signs of depression in social media. *International Journal of Environmental Research and Public Health*, *17*(13), 4752. https://doi.org/10.3390/ijerph17134752

[5] Patel, V., Ramasundarahettige, C., Vijayakumar, L., Thakur, J., Gajalakshmi, V., Gururaj, G., Suraweera, W., & Jha, P. (2012). Suicide mortality in India: A nationally representative survey. *The Lancet*, *379*(9834), 2343–2351. https://doi.org/10.1016/S0140-6736(12)60606-0

[6] Lin, C., Hu, P., Su, H., Li, S., Mei, J., Zhou, J., & Leung, H. (2020, June 8-11). *Sensemood: depression detection on social media [Conference Presentation]*. International Conference on Multimedia Retrieval, Dublin Ireland. https://doi.org/10.1145/3372278.3391932

[7] Conway, M. & O'Connor, D. (2016). Social media, big data, and mental health: Current advances and ethical implications. *Current Opinion in Psychology*, *9*, 77–82. https://doi.org/10.1016/j.copsyc.2016.01.004

[8] Ebert, D. D., Harrer, M., Apolinário-Hagen, J., & Baumeister, H. (2019). Digital Interventions for Mental Disorders: Key Features, Efficacy, and Potential for Artificial Intelligence Applications. In: Kim, Y. K. (ed), *Frontiers in Psychiatry*, (pp. 583–627). Springer.

[9] Javed, A. R., Sarwar, M. U., Beg, M. O., Asim, M., Baker, T., & Tawfik, H. (2020). A collaborative healthcare framework for shared healthcare plan with ambient intelligence. *Human-Centric Computing and Information Sciences, 10,* 1-21. https://doi.org/10.1186/s13673-020-00245-7

[10] Kale, S. S. (2015). *Tracking mental disorders across Twitter users* [Doctoral Dissertation, University of Georgia].

[11] Coppersmith, G., Dredze, M., & Harman, C. (2014). Quantifying Mental Health Signals in Twitter. In *Resnik, P., Resnik, R., and Mitchell, M.(eds), Workshop on Computational Linguistics and Clinical Psychology: From Linguistic Signal to Clinical Reality,* (pp. 51-60). Association for Computational Linguistics.

[12] Losada, D. E., & Crestani, F. (2016). A test collection for research on depression and language use. *Experimental IR Meets Multilinguality, Multimodality, and Interaction*, 28-39. https://doi.org/10.1007/978-3-319-44564-9_3

[13] Ríssola, E. A., Aliannejadi, M., & Crestani, F. (2020, April 14–17). Beyond Modelling: Understanding Mental Disorders in Online Social Media. In J. M. Jose., Yilmaz, E., Magalhães, J., Castells, P., Ferro, N., Silva, M.J., Martins, F. (Eds.), *Advances in Information Retrieval: 42nd European Conference on IR Research, ECIR,* (pp. 296-310). Springer International Publishing. https://doi.org/10.1007/978-3-030-45439-5_20

[14] Fatima, I., Abbasi, B. U. D., Khan, S., Al-Saeed, M., Ahmad, H. F., & Mumtaz, R. (2019). Prediction of postpartum depression using machine learning techniques from social media text. *Expert Systems*, *36*(4), e12409. https://doi.org/10.1111/exsy.12409

[15] Suman, S. K., Shalu, H., Agrawal, L. A., Agrawal, A., & Kadiwala, J. (2020). A novel sentiment analysis engine for preliminary depression status estimation on social media. *arXiv*:2011.14280. https://doi.org/10.1111/exsy.12409

[16] Zehra, W., Javed, A. R., Jalil, Z., Khan, H. U., & Gadekallu, T. R. (2021). Cross corpus multi-lingual speech emotion recognition using ensemble learning. *Complex & Intelligent Systems*, *7*(4), 1-10. https://doi.org/10.1525/collabra.18731

[17] Costello, C., Srivastava, S., Rejaie, R., & Zalewski, M. (2021). Predicting mental health from followed accounts on Twitter. *Collabra: Psychology*, *7*(1), 18731. https://doi.org/10.1525/collabra.18731

[18] Eichstaedt, J. C., Smith, R. J., Merchant, R. M., Ungar, L. H., Crutchley, P., Preoţiuc-Pietro, D., & Schwartz, H. (2018). Facebook language predicts depression in medical records. *National Academy of Sciences*, *115*(44), 11203-11208. https://doi.org/10.1073/pnas.1802331115

[19] Ahmad, H., Asghar, M. Z., Alotaibi, F. M., & Hameed, I. A. (2020). Applying deep learning technique for depression classification in social media text. *Journal of Medical Imaging and Health Informatics*, *10*(10), 2446- 2451. https://doi.org/10.1166/jmihi.2020.3169

[20] Priya, A., Garg, S., & Tigga, N. P. (2020). Predicting anxiety, depression and stress in modern life using machine learning algorithms. *Procedia Computer Science, 167,* 1258-1267. https://doi.org/10.1016/j.procs.2020.03.442

[21] Mori, K., & Haruno, M. (2021). Differential ability of network and natural language information on social media to predict interpersonal and mental health traits. *Journal of Personality*, *89*(2), 228-243. https://doi.org/10.1111/jopy.12578

[22] Tao, X., Zhou, X., Zhang, J., & Yong, J. (2016, December 12-15). *Sentiment analysis for depression detection on social networks* [Conference presentation]. *12th International Conference, ADMA Australia.* https://doi.org/10.1007/978-3-319-49586-6_59

[23] Guntuku, S. C., Schneider, R., Pelullo, A., Young, J., Wong, V., Ungar, L., & Merchant, R. (2019). Studying expressions of loneliness in individuals using twitter: an observational study. *BMJ Open*, *9*(11). https://doi.org/10.1136/bmjopen-2019-030355

[24] Smys, D. S., & Raj, D. J. S. (2021). Analysis of deep learning techniques for early detection of depression on social media network-a comparative study. *Journal of Trends in Computer Science and Smart Technology*, *3*(1), 24-39. https://doi.org/10.36548/jtcsst.2021.1.003

[25] Hiraga, M. (2017). Predicting depression for japanese blog text. *Proceedings of the 55th Annual Meeting of the Association for Computational Linguistics- Student Research Workshop,* 107–113 https://doi.org/10.18653/v1/P17-3018 P

[26] Wu, J., Ma, J., Wang, Y., & Wang, J. (2021). Understanding and predicting the burst of burnout via social media. *Proceedings of the ACM on Human-Computer Interaction*, *4*(CSCW3), 1-27. https://doi.org/10.1145/3434174

[27] Orabi, A. H., Buddhitha, P., Orabi, M. H., & Inkpen, D. (2018). Deep learning for depression detection of twitter users. *Proceedings of the Fifth Workshop on Computational Linguistics and Clinical Psychology: From Keyboard to Clinic*, 88-97. https://doi.org/10.18653/v1/W18-0609

[28] Shah, F. M., Ahmed, F., Joy, S. K. S., Ahmed, S., Sadek, S., Shil, R., & Kabir, M. H. (2020). Early depression detection from social network using deep learning techniques, *IEEE Region 10 Symposium (TENSYMP)*, 823-826. https://doi.org/10.1109/TENSYMP50017.2020.9231008

[29] Shen, G., Jia, J., Nie, L., Feng, F., Zhang, C., Hu, T., & Zhu, W. (2017). Depression detection via harvesting social media: A multimodal dictionary learning solution. *Proceedings of the Twenty-Sixth International Joint Conference on Artificial Intelligence (IJCAI-17),* 3838-3844. https://doi.org/10.24963/ijcai.2017/536

[30] De Choudhury, M., Gamon, M., Counts, S., & Horvitz, E. (2013). Predicting depression via social media. *Proceedings of the International AAAI Conference on Web and Social Media*, *7*(1), 128-137. https://doi.org/10.1609/icwsm.v7i1.14432

[31] Aldarwish, M. M., & Ahmad, H. F. (2017). Predicting depression levels using social media posts. *2017 IEEE 13th International Symposium on Autonomous Decentralized System (ISADS)*. 277-280. https://doi.org/10.1109/ISADS.2017.41

[32] Guntuku, S. C., Yaden, D. B., Kern, M. L., Ungar, L. H., & Eichstaedt, J. C. (2017). Detecting depression and mental illness on social media: an integrative review. *Current Opinion in Behavioral Sciences*, *18*, 43-49. https://doi.org/10.1016/j.cobeha.2017.07.005

[33] Ahmad, H., Asghar, M. Z., Alotaibi, F. M., & Hameed, I. A. (2020). Applying deep learning technique for depression classification in social media text. *Journal of Medical Imaging and Health Informatics*, *10*(10), 2446-2451. https://doi.org/10.1166/jmihi.2020.3169

[34] Figuerêdo, José Solenir L., Ana Lúcia L. M. Maia, & Rodrigo Tripodi Calumby. (2022). Early depression detection in social media based on deep learning and underlying emotions. *Online Social Networks and Media*, *31*, 100225. https://doi.org/10.1016/j.osnem.2022.100225

[35] Marriwala, Nikhil, & Deepti Chaudhary. (2023). A hybrid model for depression detection using deep learning. *Measurement: Sensors, 25,* 100587. https://doi.org/10.1016/j.measen.2022.100587

[36] Yapıcı, M. M. (2022). Lojistik Regresyon Modeli. In Savaş, S. & Buyrukoğlu, S., (Eds). *Teori ve Uygulamada Makine Öğrenmesi (*pp 37-67). Ankara: Nobel Akademik Yayıncılık Eğitim Danışmanlık TİC. LTD. ŞTİ.

[37] Karakış, R. (2022). Destek Vektör Makinesi In Savaş, S. & Buyrukoğlu, S., (Eds). *Teori ve Uygulamada Makine Öğrenmesi* (pp 93-118). *Ankara: Nobel Akademik Yayıncılık Eğitim Danışmanlık TİC. LTD. ŞTİ.*

[38] Schwartz, H. A., Eichstaedt, J., Kern, M., Park, G., Sap, M., Stillwell, D., & Ungar, L. (2014). Towards assessing changes in degree of depression through facebook. In *Resnik, P., Resnik, R., and Mitchell, M.(eds), Proceedings of the workshop on computational linguistics and clinical psychology: from linguistic signal to clinical reality.* (pp 118–125) Association for Computational Linguistics. https://doi.org/10.3115/v1/W14-3214

Sinopfbd, 2024; 9(2): 467-482 **https://doi.org/10.33484/sinopfbd.1445026**

Sinop Üniversitesi Fen Bilimleri Dergisi
Sinop Uni J Nat Sci

E-ISSN: 2564-7873

https://dergipark.org.tr/tr/pub/sinopfbd

2-Aminopiridin Türevleri ile 4-Kloro-5-sülfamoilbenzoik Asit Tuzlarının Sentezi, Karakterizasyonu ve Antimikrobiyal Özelliklerinin İncelenmesi

Halil İLKİMEN[1] Cengiz YENİKAYA[1] ve Aysel GÜLBANDILAR[2]

How to cite: İlkimen., H., Yenikaya, C., & Gülbandılar, A. (2024). 2-Aminopiridin türevleri ile 4-kloro-5-sülfamoilbenzoik asit tuzlarının sentezi, karakterizasyonu ve antimikrobiyal özelliklerinin incelenmesi. *Sinop Üniversitesi Fen Bilimleri Dergisi, 9*(2), 467-482. https://doi.org/10.33484/sinopfbd.1445026

Araştırma Makalesi

Sorumlu Yazar
Halil İLKİMEN
halil.ilkimen@dpu.edu.tr

Yazarlara ait ORCID
H.İ: 0000-0003-1747-159X
C.Y: 0000-0002-5867-9146
A.G: 0000-0001-9075-9923

Received: 01.03.2024
Accepted: 02.11.2024

Öz

Bu çalışmada, 4-kloro-5-sülfamoilbenzoik asit (HClsba) ile 2-aminopiridin (2ap), 2-amino-3-pikolin (2a3p), 2-amino-5-pikolin (2a5p) ve 2-amino-6-pikolin'in (2a6p) proton transfer tuzları (**1-4**) sentezlenmiştir. Sentezlenen bileşiklerin yapıları, ^{1}H *NMR*, IR, elementel analiz ve UV ile açıklanmıştır. Çalışmada kullanılan ve sentezlenen tüm maddelerin *Candida albicans* (ATCC 14053) mayasına ve *Enterococcus faecalis* (*ATCC 29212*), *Staphylococcus aureus* (NRRL-B 767), *Bacillus subtilis*, *Listeria monocytogenes* (*ATCC 7644)* (Gram pozitif), *Pseudomonas aeruginosa* (*ATCC 27853)* ve *Escherichia coli* (ATCC 25922) (Gram negatif) bakterilerine karşı antimikrobiyal aktiviteleri incelenmiştir. Antimikrobiyal aktiviteleri Flukonazol, Levofloksasin, Vankomisin ve Sefepim ile kıyaslanmıştır. Bileşiklerde en iyi aktivite değerleri *S. aureus* bakterisinde tüm bileşikler (HClsba hariç), *E. coli* bakterisinde HClsba ve 2ap, *P. aeruginosa* bakterisinde tüm bileşikler (2a6mp ve **3** hariç), *L. monocytogenes* bakterisinde HClsba, 2a3mp, **1**, **3** ve **4**, *E. faecalis* bakterisinde tüm bileşikler (**3** hariç), *B. subtilis* bakterisinde 2a5mp ve *C. albicans* mayasında tüm bileşikler (**3** hariç) gözlenmiştir.

Anahtar Kelimeler: 4-Kloro-5-Sülfamoilbenzoik asit, 2-Aminopiridin, 2-Aminopikolin, proton transfer tuzu, antimikrobiyal aktivite

Synthesis, Characterization and Investigation of Antimicrobial Properties of Salts of 2-Aminopyridine Derivatives and 4-Chloro-5-Sulfamoylbenzoic Acid

[1]Kütahya Dumlupınar Üniversitesi Fen-Edebiyat Fakültesi, Kimya Bölümü, 43100 Kütahya, Türkiye

[2]Gıda Mühendisliği Bölümü, Ziraat Mühendisliği Fakültesi, Eskisehir Osmangazi Üniversitesi, 26000 Eskisehir, Türkiye

Abstract

In this study, proton transfer salts (**1-4**) of 4-chloro-5-sulfamoylbenzoic acid (HClsba) with 2-aminopyridine (2ap), 2-amino-3-picoline (2a3p), 2-amino-5-picoline (2a5p) and 2-amino-6-picoline (2a6p) were synthesized. The structures of the synthesized compounds were elucidated by ^{1}H NMR, IR, elemental analysis, and UV. The antimicrobial activities of all substances used and synthesized in the study are examined against the yeast *Candida albicans* (ATCC 14053), and the bacteria *Enterococcus faecalis* (*ATCC 29212*), *Staphylococcus aureus* (NRRL-B 767), *Bacillus subtilis*, *Listeria monocytogenes* (*ATCC 7644)* (Gram positive), *Pseudomonas aeruginosa* (ATCC 27853) and *Escherichia coli* (ATCC 25922) (Gram negative). Their antimicrobial activities were compared with Fluconazole, Levofloxacin, Vancomycin and Cefepime. The best activity values of the compounds are all compounds (except HClsba) for *S. aureus* bacteria, HClsba and 2ap for *E. coli* bacteria, all compounds (except 2a6mp and **3**) for *P. aeruginosa* bacteria, HClsba, 2a3mp, **1**, **3** and **4** for *L. monocytogenes* bacteria, all compounds (except **3**) for E. *faecalis* bacteria, 2a5mp for *B. subtilis* bacteria, and all compounds (except **3**) were observed for *C. albicans* yeast.

Keywords: 4-Chloro-5-Sulfamoylbenzoic acid, 2-Aminopyridine, 2-Aminopicoline, proton transfer salt, antimicrobial activity

Giriş

Proton transfer reaksiyonları, bir protonun molekül içi veya moleküller arası olarak bir bağlanma bölgesinden diğerine aktarıldığı çok sayıda kimyasal işlem arasında benzersizdir. Bunlar yalnızca herhangi bir yardımcı elektron olmadan bir çekirdeğin taşınmasını içerir. Özellikle, bu tür reaksiyonlar, bağ elektronlarında ciddi bir düzensizlik olmaksızın ve bağ yapmayan elektronlar arasındaki itme kuvvetlerini devreye sokmadan meydana gelebilir [1]. Proton transferi, birçok kimyasal ve biyokimyasal reaksiyonda önemli bir rol oynayan en temel süreçlerden biridir [2, 3]. Son zamanlarda, proton transferi ile ilgili araştırmalar esas olarak kristal mühendisliği [4, 5], katalitik reaksiyonlar [6, 7], organik ferroelektrikler [8, 9], enerjik malzemeler [10-12], doğrusal olmayan optik malzemeler [13, 14], hidrojen depolama [15-18] ve ilaç endüstrisi [19, 20] gibi diğer ilgili alanlara odaklanmıştır. Proton transferi ayrıca birçok biyokimyasal süreçte önemli bir adım olarak bilinir [21-25]. Proton transfer tuzlarının sentezinde genellikle aromatik/alifatik karboksilik asitler ve aromatik/alifatik bazlar kullanılmaktadır. Bu bileşikler genellikle suda çözünebilen bileşiklerdir [26]. Sentezlenen tuzların asidik bileşeni olan 4-kloro-5-sülfamoilbenzoik asitin (HClsba) antibakteriyel [27] ve antihipertansif [28], bazik bileşeni olan 2-aminopiridin türevleri, antifungal, antiviral, antiinflamatuar, antihistaminik, antibakteriyel, antiparazitik, antikonvülsan, antialzheimer, antidiyabetik ve analjezik gibi aktivitelere sahiptir [29]. Grubumuz suda çözülebilecek 3-sülfamoilbenzoik asit türevleri ile 2-aminopiridin türevlerinden oluşan proton transfer tuzu, tuzların metal komplekslerinin sentezi ve biyolojik aktivite özelliklerini incelemektedir [30-41]. Bu çalışmada, 4-kloro-5-sülfamoilbenzoik asit (HClsba) ile 2-aminopiridin (2ap), 2-amino-3-pikolin (2a3p), 2-amino-5-pikolin (2a5p) ve 2-amino-6-pikolin'in (2a6p) proton transfer tuzları (**1-4**) sentezlenmiştir. Sentezlenen bileşiklerin yapıları, elementel analiz, ^{1}H *NMR*, IR ve UV ile açıklanmıştır. Tüm maddelerin *Candida albicans* (ATCC 14053) mayasına, *Enterococcus faecalis* (*ATCC 29212*), *Staphylococcus aureus* (NRRL-B 767), *Bacillus subtilis, Listeria monocytogenes* (*ATCC 7644)* (Gram pozitif), *Pseudomonas aeruginosa* (*ATCC 27853)* ve *Escherichia coli* (ATCC 25922) (Gram negatif) bakterilerine karşı antimikrobiyal aktiviteleri incelenmiştir.

Materyal ve Metot

Kimyasal maddeler Merck firmasından alınmıştır. Elementel analiz için Elementar Vario III EL, FT-IR için BRUKER OPTICS VERTEX 70; ^{1}H NMR için 500 MHz UltraShield NMR Spektrometrisi ve UV–Vis analizi için SHIMADZU UV-2550 cihazları kullanılmıştır.

Yöntem

Proton Transfer Tuzlarının Sentezi

5 mmol HClsba (1,1782 g) ve 5 mmol 2-aminopiridin türevi {**1** için 0.4706 2ap, **2** için 0.5407 g 2a3p, **3** için 0.5407 g 2a5p ve **4** için 0.5407 g 2a6p} bileşikleri balonda 100 mL saf etanolde çözüldü. Oda koşullarında karıştırılan çözeltide oluşan beyaz renkli proton transfer tuzları (**1-4**) süzüldü ve kurutuldu (Şekil 1).

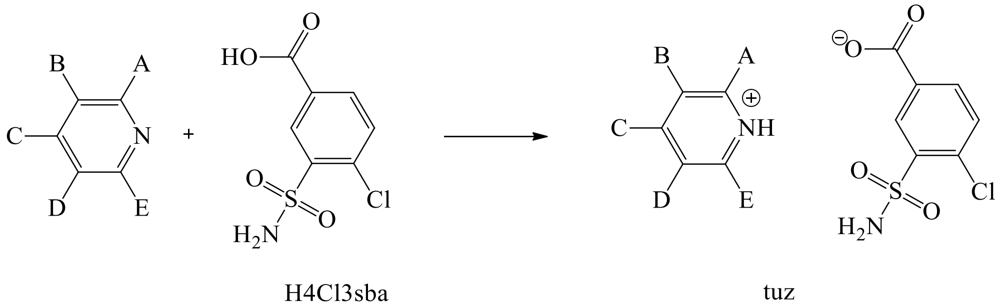

A = NH_2, B = H, C = H, D = H, E = H (**1**)
A = NH_2, B = CH_3, C = H, D = H, E = H (**2**)
A = NH_2, B = H, C = H, D = CH_3, E = H (**3**)
A = NH_2, B = H, C = H, D = H, E = CH_3 (**4**)

Şekil 1. 1-4 *Tuzlarının sentezi*

Antimikrobiyal Aktivite Çalışmaları

Bileşiklerin mikroorganizmaların gelişimini inhibe eden en düşük konsantrasyon değerinin (MİK) belirlenmesinde mikro-tüp seyreltme tekniği uygulandı. Bu amaçla mikrodilüsyon yönteminde U şeklinde 96 kuyucuklu mikro plakalar kullanıldı. Mueller Hinton Agar ortamı tek ve çift kuvvet olarak hazırlandı. Kullanılan, sentezlenen ve referans bileşiklerin 4 mg örneği 2 mL DMSO içerisinde çözüldü. Kullanılan bakteri ve mantar türleri tek kuvvetli MHB besiyerinde gece boyunca inkübe edildi ve taze kültürleri hazırlandı. Kültürlerin süspansiyonları hazırlandı ve hücre yoğunlukları 0.5 Mc Farland tüp bulanıklığına (1.0.10^8 (kob)/mL) ayarlandı [37, 40, 41].

Bulgular ve Tartışma

NMR Spektrumu Sonuçları

Sentezlenen **1-4** proton transfer tuzları d_6-DMSO ve D_2O ilaveli d_6-DMSO ortamında alınan ^{1}H-NMR spektrumları sırasıyla Şekiller 2-5'de ve kimyasal kayma değerleri Tablo 1'de verilmiştir.

1 Tuzunun ^{1}H-NMR sonuçları

1 Tuzunun 7.30 ve 8.10 ppm'de gözlenen 1H'lık dublet pikler (H^5, $^3J_{H5-H4}$ = 7.281 Hz ve H^8, $^4J_{H8-H4}$ = 2.036 Hz) ile 7.92 ppm'de gözlenen 1H'lık dublet-dublet pik (H^4, $^3J_{H4-H5}$ = 8.218 Hz, $^4J_{H4-H8}$ = 2.031 Hz), ve 7.77 ppm'de gözlenen 2H'lık (H^{10}) singlet pikler yapıda bulunan Clsba grubunun protonlarından kaynaklanmaktadır. 6.48 ppm'de gözlenen 2H'lık (H^{12} ve H^{15}, $^{3}J_{H13\text{-}H14\ veya\ H15\text{-}H14/H16}$ = 7.649 Hz) ve 7.45 ppm'de gözlenen 1H'lık (H^{14}, $^{3}J_{H14\text{-}H15/H16}$ = 4.872 Hz, $^{4}J_{H14\text{-}H16}$ = 1.378 Hz) triplet-dublet pikler ile 7.77 ppm'de gözlenen 1H'lık dublet pik (H^{16}, $^{3}J_{H18\text{-}H17}$ = 4.896 Hz) ve 6.35 ppm 2H'lık (H^{17}) olması gerekirken 1H'lık gözlenen singlet pik yapıda bulunan Hap^{+} grubunun protonlarından kaynaklanmaktadır.

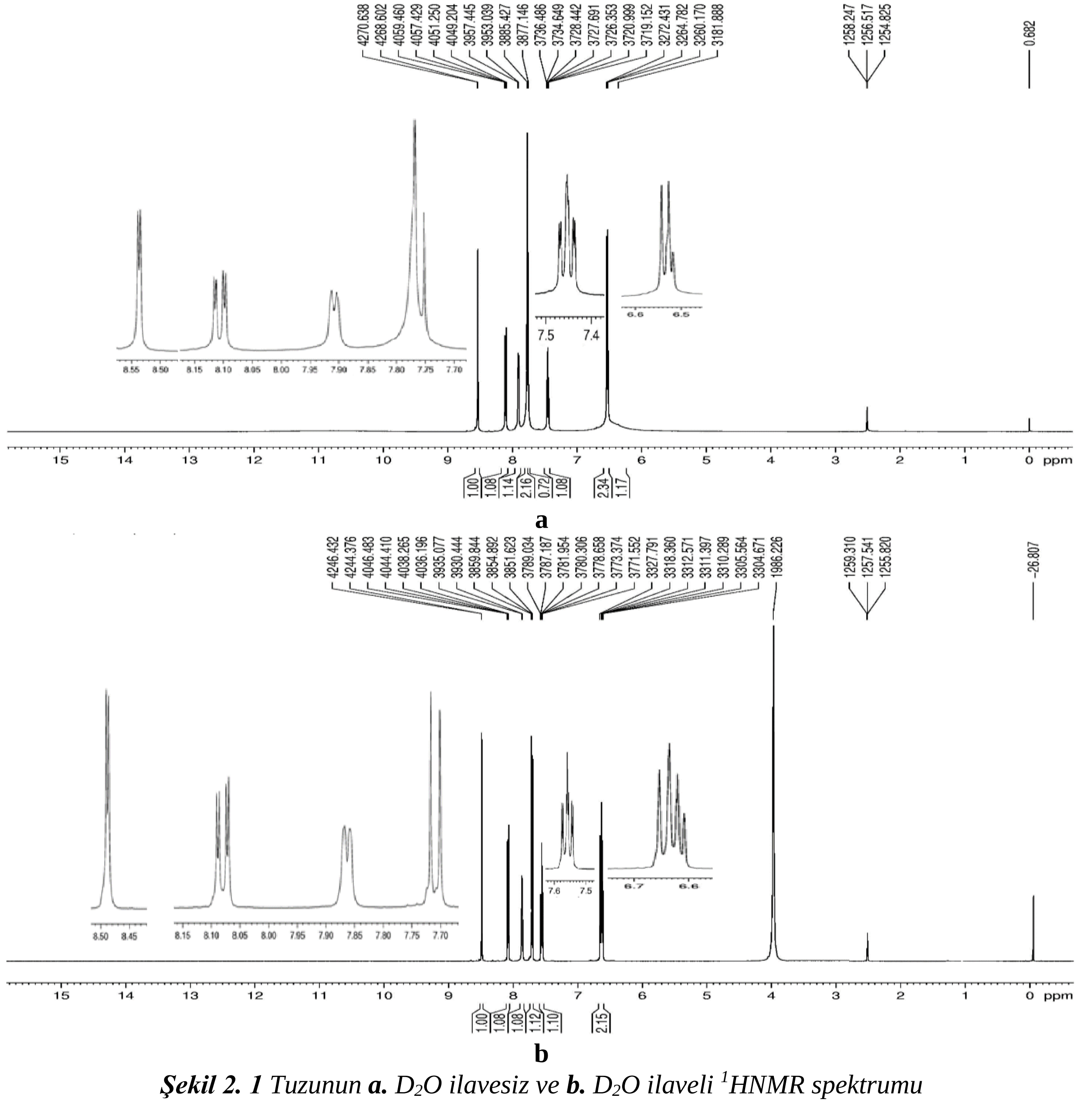

***Şekil 2. 1** Tuzunun **a.** D_2O ilavesiz ve **b.** D_2O ilaveli ^{1}HNMR spektrumu*

2 Tuzunun ^{1}H-NMR Sonuçları

2 Tuzunun yapısında bulunan H^{4} protonu 7.92 ppm'de 1H'lık dublet-dublet olarak ($^{3}J_{H4\text{-}H5}$ = 8.320 Hz, $^{4}J_{H4\text{-}H8}$ = 2.061 Hz); H^{5}, H^{10} ve H^{16} protonları 7.77 ppm'de 4H'lık multiplet olarak ($^{3}J_{H5\text{-}H4\ veya\ H16\text{-}H15}$ = 8.181 Hz, $^{4}J_{H16\text{-}H14}$ = 1.170 Hz); H^{8} ve H^{14} protonları 8.53 ppm ve 7.28 ppm'de dublet olarak ($^{4}J_{H8\text{-}H4}$ = 2.037 Hz ve $^{3}J_{H14\text{-}H15}$ = 7.115 Hz); H^{15} protonu 6.49 ppm'de 1H'lık triplet olarak ($^{3}J_{H15\text{-}H14/H16}$ = 6.121 Hz), H^{17} (2H'lık) ve H^{18} (3H'lık) protonları 5.98 ppm ve 2.05 ppm'de singlet olarak gözlenmiştir.

Tablo 1. 1-4 *Tuzlarının ^{1}H-NMR spektrumunun kimyasal kayma değerleri δ(ppm)*

1		**2**	
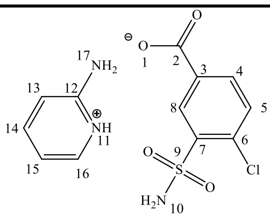		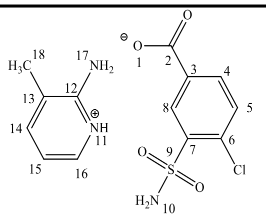	
H^{4}	7.92 (1H, dxd) [$^{3}J_{\text{H4-H5}}$ = 8.218 Hz, $^{4}J_{\text{H4-H8}}$ = 2.031 Hz]	H^{4}	7.92 (1H, dxd) [$^{3}J_{\text{H4-H5}}$ = 8.320 Hz, $^{4}J_{\text{H4-H8}}$ = 2.061 Hz]
H^{5}	7.30 (1H, d) [$^{3}J_{\text{H5-H4}}$ = 7.281 Hz]	H^{5}, H^{10}, H^{16}	7.77 (4H, m) [$^{3}J_{\text{H5-H4 veya H16-H15}}$ = 8.181 Hz, $^{4}J_{\text{H16-H14}}$ = 1.170 Hz]
H^{8}	8.10 (1H, d) [$^{4}J_{\text{H8-H4}}$ = 2.036 Hz]	H^{8}	8.53 (1H, d) [$^{4}J_{\text{H8-H4}}$ = 2.037 Hz]
H^{10}	7.77 (2H, s)	H^{11}	-
H^{11}	-	H^{14}	7.28 (1H, d) [$^{3}J_{\text{H14-H15}}$ = 7.115 Hz]
H^{13}, H^{15}	6.48 (2H, d+t) [$^{3}J_{\text{H13-H14 veya H15-H14/H16}}$ = 7.649 Hz]	H^{15}	6.49 (1H, t) [$^{3}J_{\text{H15-H14/H16}}$ = 6.121 Hz]
H^{14}	7.45 (1H, txd) [$^{3}J_{\text{H14-H15/H16}}$ = 4.872 Hz, $^{4}J_{\text{H14-H16}}$ = 1.378 Hz]	H^{17}	5.98 (2H, s)
H^{16}	7.77 (1H, d) [$^{3}J_{\text{H18-H17}}$ = 4.896 Hz]	H^{18}	2.05 (3H, s)
H^{17}	6.35 (1H, s)		
3		**4**	
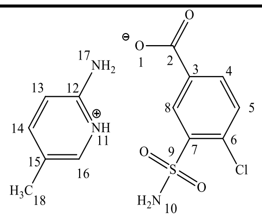		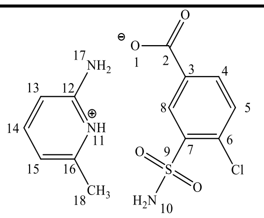	
H^{4}	8.10 (1H, dxd) [$^{3}J_{\text{H4-H5}}$ = 8.215 Hz, $^{4}J_{\text{H4-H8}}$ = 2.108 Hz]	H^{4}	8.11 (1H, dxd) [$^{3}J_{\text{H4-H5}}$ = 8.197 Hz, $^{4}J_{\text{H4-H8}}$ = 1.952 Hz]
H^{5}, H^{10}, H^{16}	7.76 (4H, m) [$^{3}J_{\text{H5-H4 veya H16-H15}}$ = 8.209 Hz, $^{4}J_{\text{H16-H14}}$ = 2.681 Hz]	H^{5}, H^{10}	7.76 (3H, s+d) [$^{3}J_{\text{H5-H4}}$ = 8.219 Hz]
H^{8}	8.10 (1H, d) [$^{4}J_{\text{H8-H4}}$ = 2.044 Hz]	H^{8}	8.10 (1H, d) [$^{4}J_{\text{H8-H4}}$ = 1.956 Hz]
H^{11}	-	H^{11}	-
H^{13}	6.48 (1H, d) [$^{3}J_{\text{H13-H14}}$ = 8.478 Hz]	H^{13}, H^{15}	6.40 (2H, d+d) [$^{3}J_{\text{H13-H14 veya H15-H14}}$ = 7.199 Hz]
H^{14}	7.31 (1H, dxd) [$^{3}J_{\text{H14-H13}}$ = 8.484 Hz, $^{4}J_{\text{H14-H16}}$ = 2.187 Hz]	H^{14}	7.40 (1H, t) [$^{3}J_{\text{H14-H13/H15}}$ = 7.525 Hz]
H^{17}	6.35 (1H, s)	H^{17}	6.80 (1H, s)
H^{18}	2.10 (3H, s)	H^{18}	2.30 (3H, s)

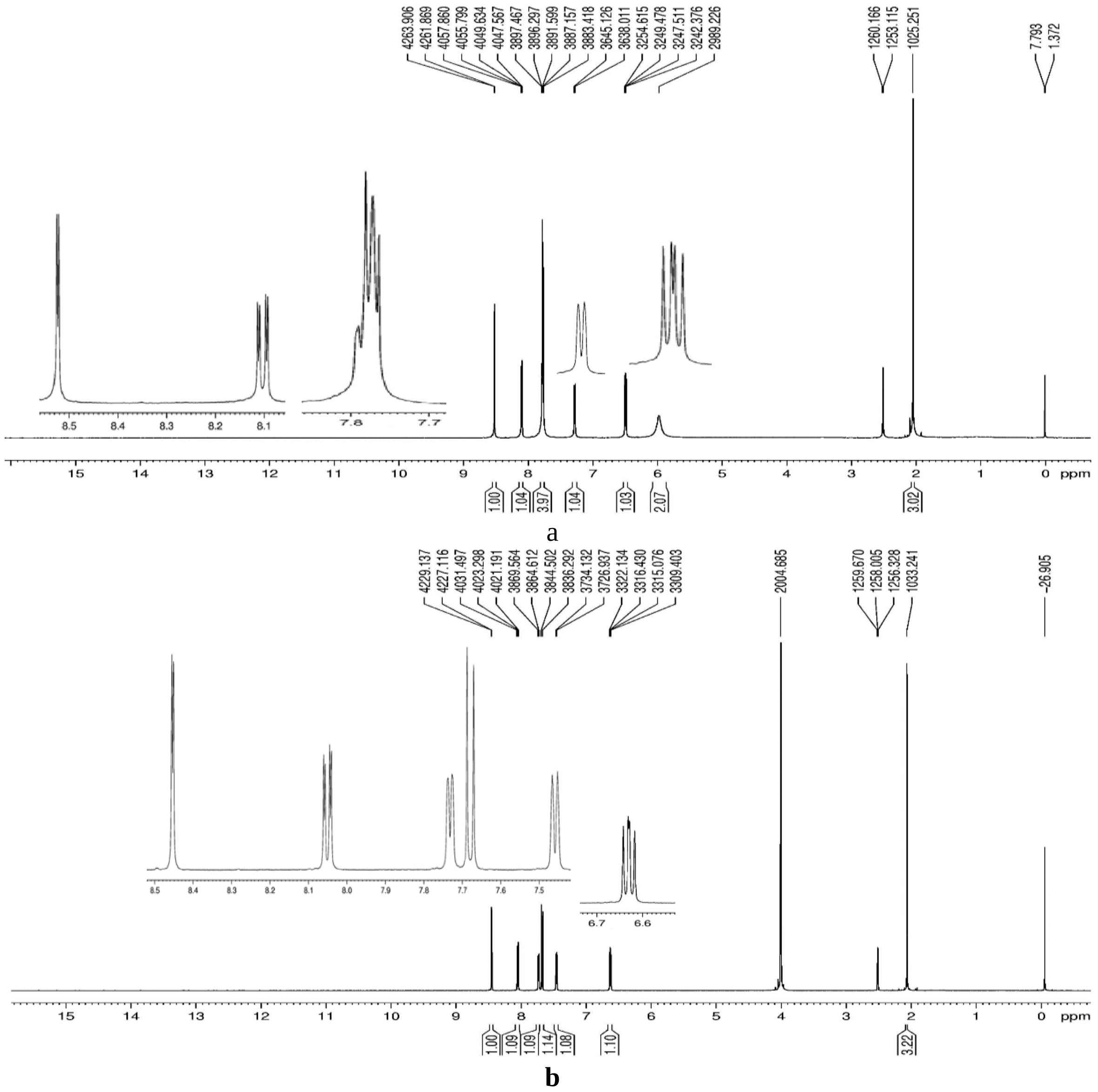

Şekil 3. *2 Tuzunun **a.** D_2O ilavesiz ve **b.** D_2O ilaveli ^{1}HNMR spektrumu*

3 Tuzunun ^{1}H-NMR Sonuçları

3 Tuzunun yapısında bulunan H^4 protonu 8.10 ppm'de 1H'lık dublet-dublet olarak ($^3J_{H4\text{-}H5}$ = 8.215 Hz. $^4J_{H4\text{-}H8}$ = 2.108 Hz); H^5, H^{10} ve H^{16} protonları 7.76 ppm'de 4H'lık multiplet olarak ($^3J_{H5\text{-}H4 \text{ veya } H16\text{-}H15}$ = 8.209 Hz, $^4J_{H16\text{-}H14}$ = 2.681 Hz); H^8 ve H^{13} protonları 8.10 ppm ve 6.48 ppm'de 2H'lık dublet olarak ($^4J_{H8\text{-}H4}$ = 2.044 Hz ve $^3J_{H13\text{-}H14}$ = 8.478 Hz); H^{14} protonu 7.31 ppm'de 1H'lık dublet-dublet olarak ($^3J_{H14\text{-}H13}$ = 8.484 Hz, $^4J_{H14\text{-}H16}$ = 2.187 Hz) ve H^{17} (2H gözlenmesi gerekirken 1H'lık gözlenmiş) ve H^{18} (3H'lık) protonları 6.35 ppm ve 2.10 ppm'de singlet olarak gözlenmiştir.

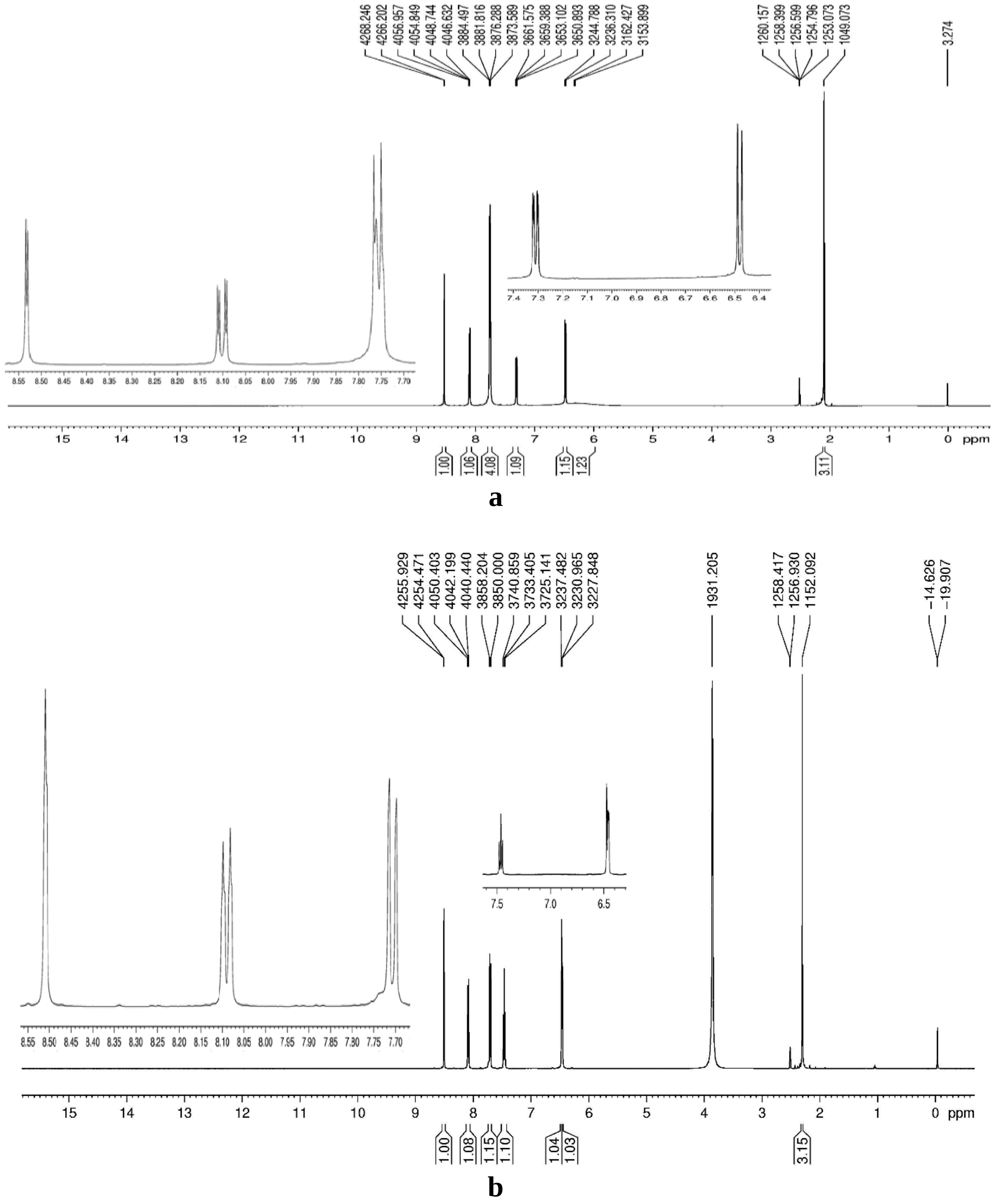

Şekil 4. 3 *Tuzunun* ***a.*** *D_2O ilavesiz ve* ***b.*** *D_2O ilaveli ^{1}HNMR spektrumu*

4 Tuzunun ^{1}H-NMR Sonuçları

4 Tuzunun yapısında bulunan H^4 protonu 8.11 ppm'de 1H'lık dublet-dublet olarak ($^3J_{H4\text{-}H5}$ = 8.197 Hz. $^4J_{H4\text{-}H8}$ = 1.952 Hz); H^5 ve H^{10} protonları 7.76 ppm'de 3H'lık singlet+dublet olarak ($^3J_{H5\text{-}H4}$ = 8.219 Hz); H^8 proton 8.10 ppm'de 1H'lık dublet olarak ($^4J_{H8\text{-}H4}$ = 1.956 Hz); H^{13} ve H^{15} protonları 6.40 ppm'de 2H'lık dublet+dublet olarak ($^4J_{H8\text{-}H4}$ = 2.044 Hz ve $^3J_{H13\text{-}H14}$ = 8.478 Hz); H^{14} protonu 7.40 ppm'de 1H'lık triplet olarak ($^3J_{H14\text{-}H13/H15}$ = 7.525 Hz) ve H^{17} (2H gözlenmesi gerekirken 1H'lık gözlenmiş) ve H^{18} (3H'lık) protonları 6.80 ppm ve 2.30 ppm'de singlet olarak gözlenmiştir.

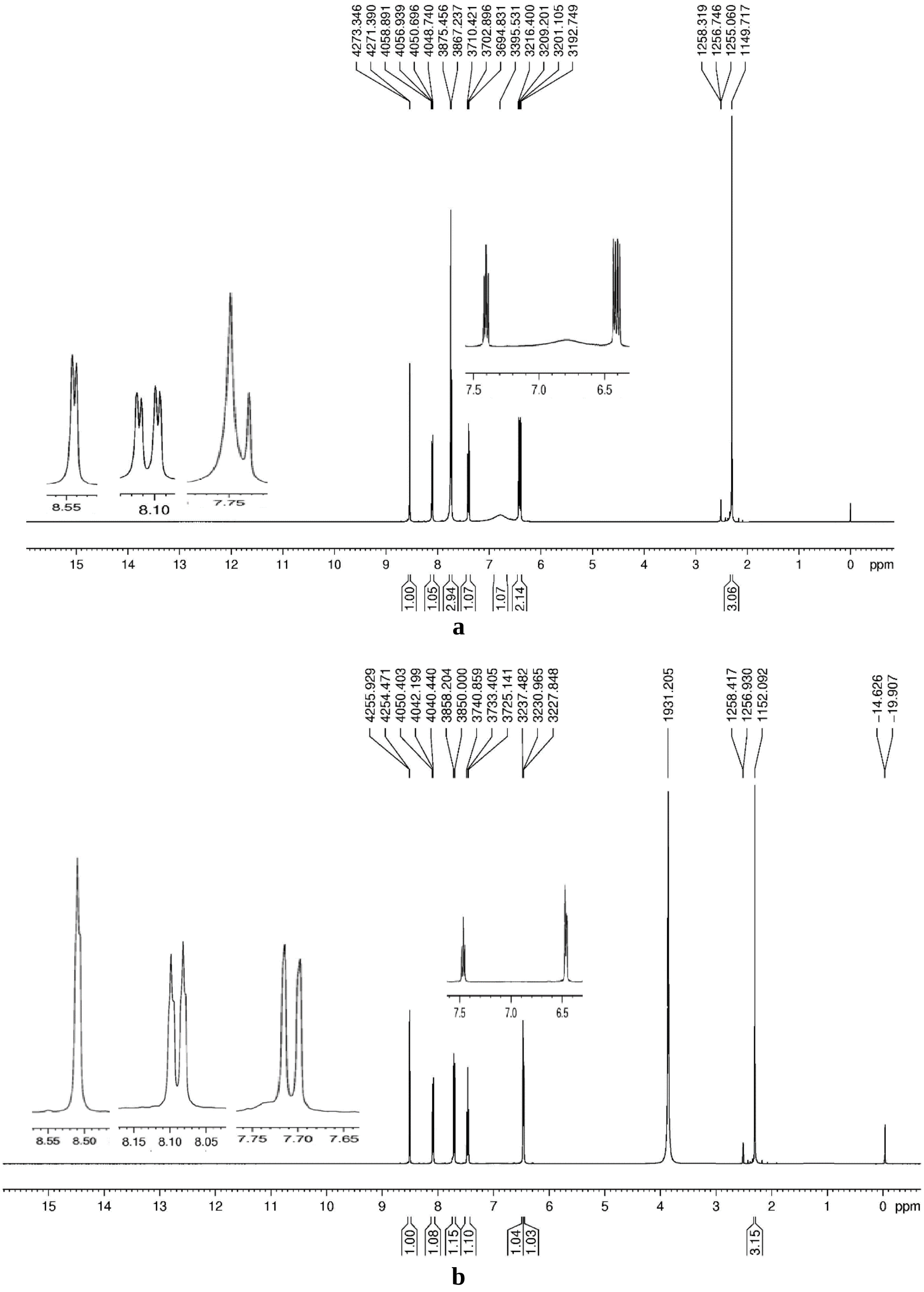

Şekil 5. *4 Tuzunun* ***a.*** *D_2O ilavesiz ve* ***b.*** *D_2O ilaveli ^{1}HNMR spektrumu*

Tuzlarda 13 ppm civarında beklenen HClsba'a ait –COOH hidrojenleri (H^1) spektrumlarda gözlenmemiştir. Bu hidrojenlerin aminopiridinlerdeki N^{11}'e transfer olduğu düşünülmektedir (H^{11}). $H^1 \rightleftharpoons H^{11}$ tersinir tepkimesi nedeniyle spektrumunda gözlenememiştir. Katı tuzların IR spektrumlarında H^{11}'ün varlığı belirlenmiştir (Şekiller 6-9). d_6-DMSO çözeltisine D_2O ilavesinden sonra çekilen ^{1}H-NMR spektrumlarında (Şekiller 2b-5b); H^{10} ve H^{17} hidrojenleri gözlenmemiştir.

Elementel Analiz Sonuçları

1-4 Tuzların önerilen yapılardaki deneysel(teorik) element miktarları Tablo 2'de verilmiştir. Bu sonuçlara göre asit:baz oranları 1:1 olarak görülmektedir.

Tablo 2. *Tuzların elementel analiz sonuçları*

Bileşik	Kapalı formülü	% Deneysel(% Teorik)			
		C	H	N	S
1	$C_{12}H_{12}ClN_3O_4S$	43.70(43.71)	3.70(3.67)	12.85(12.74)	9.75(9.72)
2	$C_{13}H_{14}ClN_3O_4S$	45.50(45.42)	4.00(4.10)	12.25(12.22)	9.35(9.33)
3	$C_{13}H_{14}ClN_3O_4S$	45.45(45.42)	4.05(4.10)	12.20(12.22)	9.34(9.33)
4	$C_{13}H_{14}ClN_3O_4S$	45.40(45.42)	41(4.10)	12.23(12.22)	9.30(9.33)

IR Sonuçları

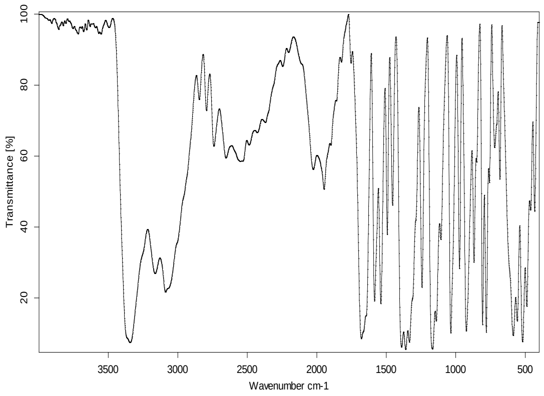

Şekil 6. 1 *Tuzunun IR spektrumu*

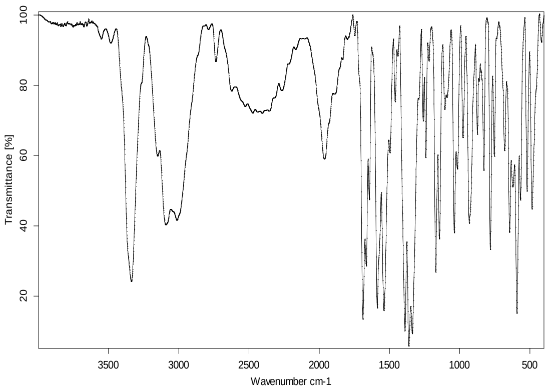

Şekil 7. 2 *Tuzunun IR spektrumu*

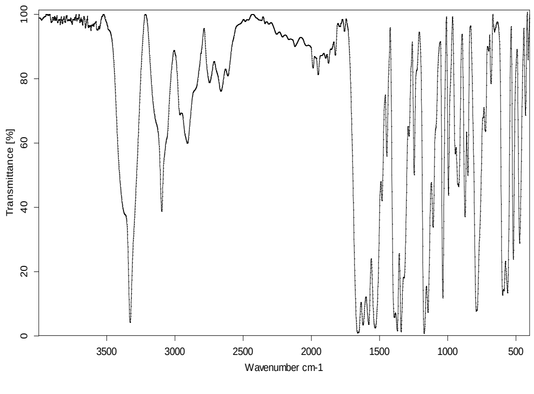

Şekil 8. 3 *Tuzunun IR spektrumu*

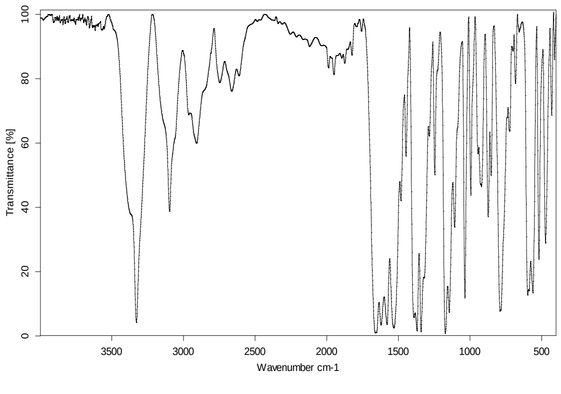

Şekil 9. 4 *Tuzunun IR spektrumu*

1-9 Bileşiklerinin IR değerleri Tablo 3'te, elde edilen tuzların FT-IR spektrumları Şekiller 6-9'da verilmiştir. Spektrumlarda tuzların yapılarını destekleyen bantlar mevcuttur. ν(N-H) gerilmeleri **1** tuzunda 3418, 3357, 3275 ve 3147 cm^{-1}, **2** tuzunda 3438 ve 3336 cm^{-1}, **3** tuzunda 3484, 3337, 3260 ve 3151 cm^{-1} ve **4** tuzunda 3376, 3329 ve 3142 cm^{-1}'de gözlenmiştir. ν(N^{+}-H) titreşim bantları **1** tuzunda

2767 ve 2498 cm^{-1}, **2** tuzunda 2702 ve 2515 cm^{-1}, **3** tuzunda 2736 ve 2528 cm^{-1} ve **4** tuzunda 2747 ve 2485 cm^{-1}'de gözlenmiştir. Bu bantların gözlenmesi tuzlarda bazın protonlandığını göstermektedir (Şekil 1) [42]. Karboksilat ν(C=O) gerilmeleri **1** tuzunda 1669 ve 1490 cm^{-1}, **2** tuzunda 1675 ve 1475 cm^{-1}, **3** tuzunda 1689 ve 1459 cm^{-1} ve **4** tuzunda 1661 ve 1482 cm^{-1}'de gözlenmiştir. **1-4** Tuzlarında, 3080-3098 cm^{-1} aralığında aromatik ν(C-H) gerilmeleri, 2818-3013 cm^{-1} aralığında alifatik ν(C-H) gerilmeleri (**1** tuzu hariç), 1440-143 cm^{-1} aralığında ν(C=N) ve ν(C=C) gerilmeleri, 1088-1392 cm^{-1} aralığında ν(C-O), 1142-1260 cm^{-1} aralığında ν(S=O) gerilmeleri ve 782-798 cm^{-1} aralığında piridin halkasından kaynaklanan pikler gözlenmiştir.

Tablo 3. 1-4 *Tuzlarının IR bantları (cm^{-1})*

	1	**2**	**3**	**4**
ν(NH$_2$)	3418(oş)	3438(oş)	3484(oş)	3376(oş)
	3357(oş)	3336(oş)	3337(oş)	3329(oş)
	3275(oş)		3260(oş)	3142(oş)
	3147(oş)		3151(oş)	
ν(CH)$_{Ar}$	3080(z)	3098(z)	3093(z)	3097(z)
ν(CH)$_{Alf.}$	2964(z)	2989(z)	3013(z)	2952(z)
	2937(z)	2948(z)	2860(z)	2910(z)
	2859(z)	2869(z)	2818(z)	2860(z)
ν(N$^+$H)	2767(z)	2702(z)	2736(z)	2747(z)
	2498(z)	2515(z)	2528(z)	2485(z)
ν(C=O)	1669(ş)	1675(ş)	1689(ş)	1661(ş)
	1490(ş)	1475(ş)	1459(ş)	1482(ş)
ν(C=N)	1618(ş)	1634(ş)	1643(ş)	1622(ş)
ν(C=C)	1582(ş)	1583(ş)	1586(ş)	1580(ş)
	1571(ş)	1538(ş)	1539(ş)	1532(ş)
	1546(ş)	1440(ş)	1496(ş)	1447(ş)
	1470(ş)		1440(ş)	
ν(CO)	1389(ş)	1390(ş)	1389(ş)	1392(ş)
	1284(ş)	1245(ş)	1292(ş)	1284(ş)
	1088(ş)	1149(ş)	1091(ş)	1107(ş)
ν(S=O)	1241(ş)	1212(ş)	1260(ş)	1246(ş)
	1169(ş)	1171(ş)	1170(ş)	1173(ş)
	1142(ş)	1149(ş)	1144(ş)	1145(ş)
ν(py)	798(ş)	786(ş)	782(ş)	791(ş)

*ş; şiddetli, oş; orta şiddetli, z; zayıf

UV-Vis Sonuçları

HClsba, 2ap, 2a3mp, 2a5mp, 2a6mp ve **1-4** tuzlarının DMSO çözücüleri içinde alınan UV-Visible spektrumlarında $\pi \rightarrow \pi^*$ elektronik geçişlerinin dalga boyu ve ε_0 değerleri HClsba için 306 (34750 Lmol^{-1}cm^{-1}) ve 290 nm (27560 Lmol^{-1}cm^{-1}), 2ap için 313 nm (32610 Lmol^{-1}cm^{-1}), 2a3mp için 296 nm (34190 Lmol^{-1}cm^{-1}), 2a5mp için 325 (28780 Lmol^{-1}cm^{-1}) ve 295 nm (29280 Lmol^{-1}cm^{-1}), 2a6mp için 321 (32150 Lmol^{-1}cm^{-1}) ve 308 nm (31940 Lmol^{-1}cm^{-1}), **1** tuzu için 300 (13550 Lmol^{-1}cm^{-1}) ve 289 nm (13060 Lmol^{-1}cm^{-1}), **2** tuzu için 315 (35390 Lmol^{-1}cm^{-1}) ve 290 nm (26970 Lmol^{-1}cm^{-1}), **3** tuzu için 322 (41190 Lmol^{-}

^{1}cm^{-1}) ve 291 nm (28730 Lmol^{-1}cm^{-1}) ve **4** tuzu için 322 (37760 Lmol^{-1}cm^{-1}) ve 291 nm (27670 Lmol^{-1}cm^{-1}) olarak gözlenmiştir.

Antimikrobiyal Aktivite Çalışmaları

Bu çalışmada, başlangıç maddeleri ve **1-4** tuzlarının mikrodilüsyon yöntemi ile antifungal ve antibakteriyel aktivite sonuçlarının MİK değerleri Tablo 4'te verilmiştir.

Tablo 4. *Bileşiklerin antimikrobiyal aktivite değerleri (µg/mL)*

	S. aureus	***E. coli***	***P. aeruginosa***	***L. monocytogenes***	***E. faecalis***	***B. subtilis***	***C. albicans***
Sefepim	62.50	62.50	31.25	31.25	31.25	62.50	-
Vankomisin	31.25	31.25	62.50	125.00	62.50	250.00	-
Levofloksasin	31.25	31.25	31.25	31.25	62.50	62.50	-
Flukonazol	-	-	-	-	-	-	62.50
HClsba	62.50	15.60	62.50	31.25	62.50	62.50	62.50
2ap	62.50	15.60	62.50	62.50	62.50	62.50	62.50
2a3mp	62.50	31.25	62.50	31.25	62.50	62.50	62.50
2a5mp	62.50	62.50	62.50	62.50	62.50	7.80	62.50
2a6mp	62.50	62.50	125.00	62.50	62.50	62.50	62.50
1	62.50	31.25	62.50	31.25	62.50	62.50	62.50
2	62.50	31.25	62.50	62.50	62.50	31.25	62.50
3	62.50	62.50	125.00	31.25	125.00	62.50	125.00
4	125.00	62.50	62.50	31.25	62.50	31.25	62.50

Bileşiklerin *S. aureus* bakterisine karşı aktivitelerinin Vankomisin ve Levoflaksin ile karşılaştırıldığında; tüm bileşiklerin kontrol bileşiklerine göre daha az etkili, Sefepim ile karşılaştırıldığında; **4** hariç bileşikler aynı derecede etkili iken, **4** ise daha az etkili olduğu gözlenmiştir. *E. coli* bakterisine karşı Vankomisin ve Levoflaksin ile kıyaslandığında; HClsba ve 2ap en iyi aktiviteye sahip iken, 2a3mp, **1** ve **2** aynı derecede etkili olduğu, diğer maddelerin ise daha az etkili olduğu gözlenmiştir. Sefepim ile kıyaslandığında ise; HClsba, 2ap, 2a3mp, **1** ve **2** daha iyi etkili olduğu, diğer bileşiklerin aynı derecede etkili olduğu gözlenmiştir. *P. aeruginosa* bakterisine karşı aktivitelerinin Sefepim ve Levoflaksin ile karşılaştırıldığında; tüm bileşikler kontrol bileşiklerine göre daha az etkili, Vankomisin ile karşılaştırıldığında; 2a6mp ve **3** hariç bileşikler aynı derecede etkili iken, 2a6mp ve **3** ise daha az etkili olduğu gözlenmiştir. *L. monocytogens* bakterisine karşı aktivitelerinin Sefepim ve Levoflaksin ile kıyaslandığında; HClsba, 2a3mp, **1**, **3** ve **4** aynı derece aktiviteye sahipken diğer maddeler daha az aktiviteye sahip olduğu gözlenmiştir. Vankomisin ile kıyaslandığında ise; bileşiklerin daha iyi etkiye sahip olduğu gözlenmiştir. *E. faecalis* bakterisine karşı aktivitelerinin Sefepim ile kıyaslandığında; tüm bileşikler daha az etkiye sahiptir. Vankomisin ve Levoflaksin ile kıyaslandığında; **3** hariç diğer bileşikler aynı derecede etkili iken, **3** daha az etkili olduğu gözlenmiştir. *B. subtilis* bakterisine karşı aktivitelerinin Sefepim ve Levoflaksin (62.50 µg/mL) ile kıyaslandığında; 2a5mp, **2** ve **4** daha iyi aktivite gösterirken, diğer bileşikler ise benzer aktivite göstermiştir. Vankomisin ile kıyaslandığında ise tüm bileşikler daha iyi etki göstermiştir.

Candida albicans mayasına karşı aktivitelerinin Fluconazole ile kıyaslandığında; **3** hariç diğer bileşikler aynı derecede etkili iken, **3** daha az etkili olduğu gözlenmiştir.

Sonuçlar

Bu çalışmada, 4-kloro-5-sülfamoilbenzoik asit (Hclsba) ile 2-aminopiridin (2ap), 2-amino-3-pikolin (2a3p), 2-amino-5-pikolin (2a5p) ve 2-amino-6-pikolin'in (2a6p) proton transfer tuzları (**1-4**) sentezlenmiştir. Başlangıç maddeleri ve proton transfer tuzlarının maya (*C. albicans*) ve bakterileri *(S. aureus, B. subtilis, E. faecalis, L. monocytogenes, E. coli* ve *P. aeruginosa)* karşı antibakteriyel ve anti fungal aktiviteleri incelenmiştir. Tuzların spektrum sonuçlarına göre HClsba:ap oranları 1:1 olarak hesaplanmıştır. Tuzların yapılarında bulunan fonksiyonel grupların gerilme ve titreşim bantları IR spektrumlarında mevcuttur. Aktivite çalışmaları sonucunda tüm bileşiklerin maya ve bakterilere karşı aktiviteye sahip olduğu gözlenmiştir. Bileşiklerin en iyi aktivite değerleri *S. aureus* bakterilerinde tüm bileşikler (HClsba hariç), *E. coli* bakterisinde HClsba ve 2ap, *P. aeruginosa* bakterisinde tüm bileşikler (2a6mp ve **3** hariç), *L. monocytogenes* bakterisinde HClsba, 2a3mp, **1**, **3** ve **4**, *E. faecalis* bakterisinde tüm bileşikler (**3** hariç), *B. subtilis* bakterisinde 2a5mp ve *C. albicans* mayasında tüm bileşikler (**3** hariç) gözlenmiştir. Yapı-aktivite ilişkisi incelendiğinde, Tablo 4'te göre metil grubunun piridin azotuna yaklaşması genel olarak *S. aureus* ve *E. coli* için aktivite değerlerini azaltırken, *P. aeruginosa, E. faecalis ve C. albicans* için aktivite değerlerini değiştirmezken, *L. monocytogenes* ve *B. subtilis* için aktivite değerlerini arttırmıştır. Bu sonuçlar literatürde bulunan benzer maddelerin sonuçları ile uyum içerisindedir [31-33, 36, 37, 40, 41].

Teşekkür Katkılarından dolayı Kütahya Dumlupınar Üniversitesi Bilimsel Araştırma Projeleri Komisyonu'na teşekkür ederiz.

Fon/Finansman Bilgileri Bu çalışma, Kütahya Dumlupınar Üniversitesi Bilimsel Araştırma Projeleri Komisyon'unca, 2020/24 numaralı projesinden alınan maddeler kullanarak hazırlanmıştır.

Etik Kurul Onayı ve İzinler Çalışma, etik kurul izni ve herhangi bir özel izin gerektirmemektedir.

Çıkar Çatışmaları/Çatışan Çıkarlar Yazarlar çıkar çatışması olmadığını beyan eder.

Yazarların Katkısı Tüm yazarlar eşit oranında katkı sağlamıştır. Tüm yazarlar makalenin son halini okumuş ve onaylamıştır.

Kaynaklar

[1] Gupta, S. K. S. (2016). Proton transfer reactions in apolar aprotic solvents. *Journal of Physical Organic Chemistry, 29*, 251-264. https://doi.org/10.1002/poc.3524

[2] Armentano, D., De Munno, G., Mastropietro, T. F., Julve, M., & Lloret, F. (2005). Intermolecular proton transfer in solid phase: a rare example of crystal-to-crystal transformation from hydroxo-to oxo-bridged iron (III) molecule-based magnet. *Journal of the American Chemical Society*, *127*(31), 10778-10779. https://doi.org/10.1021/ja051203w

[3] Root, M. J., & MacKinnon, R. (1994). Two identical noninteracting sites in an ion channel revealed by proton transfer. *Science, 265*, 1852-1856. http://www.jstor.org/stable/2884657

[4] O'Malley, C., Erxleben, A., McArdle, P., & Simmie, J. M. (2021). Crystallization of organic salts from the gas phase: when does proton transfer take place? *Crystal Growth & Design*, *21*(1), 23–27. https://doi.org/10.1021/acs.cgd.0c01248

[5] Cruz-Cabeza, A. J., Lusi, M., Wheatcroft, H. P., & Bond, A. D. (2022). The role of solvation in proton transfer reactions: implications for predicting salt/co-crystal formation using the Δp_{Ka} rule. *Faraday Discussions, 235*, 446-466. https://doi.org/10.1039/D1FD00081K

[6] Nichols, D. A., Hargis, J. C., Sanishvili, R., Jaishankar, P., Defrees, K., Smith, E. W., Wang, K. K., Prati, F., Renslo, A. R., Woodcock, H. L. & Chen, Y. (2015). Ligand-ınduced proton transfer and low-barrier hydrogen bond revealed by X-ray crystallography. *Journal of the American Chemical Society*, *137*, 8086-8095. https://doi.org/10.1021/jacs.5b00749

[7] Gerlits, O., Wymore, T., Das, A., Shen, C. H., Parks, J. M., Smith, J. C., Weiss, K. L., Keen, D. A., Blakeley, M. P., Louis, J. M., Langan, P., Weber, I. T., & Kovalevsky, A. (2016). Long-range electrostatics-induced two-proton transfer captured by neutron crystallography in an enzyme catalytic site. *Angewandte Chemie International Edition, 55*, 4924-4927. https://doi.org/10.1002/anie.201509989

[8] Seyedraoufi, S., Sødahl, E. D., Görbitz, C. H., & Berland, K. (2024). Database mining and first-principles assessment of organic proton-transfer ferroelectrics. *Physical Review Materials*, *8*, 054413. https://doi.org/10.1103/PhysRevMaterials.8.054413

[9] Liu, H., Ye, Y., Zhang, X., Yang, T., Wen, W., & Jiang, S. (2022). Ferroelectricity in organic materials: from materials characteristics to de novo design. *Journal of Materials Chemistry C*, *10*, 13676-13689. https://doi.org/10.1039/D2TC01330D

[10] Shimizu, G. K., Taylor, J. M. & Kim, S. (2013). Proton conduction with metal-organic frameworks. *Science*, *341*, 354-355. https://doi.org/10.1126/science.1239872

[11] Yoon, M., Suh, K., Natarajan, S. & Kim, K. (2013). Proton conduction in metal-organic frameworks and related modularly built porous solids. *Angewandte Chemie International Edition*, *52*, 2688-2700. https://doi.org/10.1002/anie.201206410

[12] Bolton, O. & Matzger, A. J. (2011). Improved stability and smart-material functionality realized in an energetic cocrystal. *Angewandte Chemie International Edition*, *50*, 896-8963. https://doi.org/10.1002/anie.201104164

[13] Srividya, J., Sivamadhavi, V., & Anbalagan, G. (2022). Synthesis, molecular structural, optical, thermal and third harmonic nonlinear optical analysis of Piperazine-1,4-diium bis(2-carboxy-6-nitrobenzoate) tetrahydrate single crystal Author links open overlay panel. *Optical Materials*, *129*, 112503. https://doi.org/10.1016/j.optmat.2022.112503

[14] Jayanalina, T., Rajarajan, G., Boopathi, K. & Sreevani, K. (2015). Synthesis, growth, structural, optical and thermal properties of a new organic nonlinear optical crystal: 2-amino 5-chloropyridinium-L-tartarate. *Journal of Crystal Growth, 426*, 9-14. https://doi.org/10.1016/j.jcrysgro.2015.05.014

[15] Lototskyy, M. V., Tolj, I., Davids, M. W., Klochko, Y. V., Parsons, A., Swanepoel, D., Ehlers, R., Louw, G., van der Westhuizen, B., Smith, F., Pollet, B. G., Sita, C. & Linkov, V. (2016). Metal hydride hydrogen storage and supply systems for electric forklift with low-temperature proton

exchange membrane fuel cell power module. *International Journal of Hydrogen Energy*, *41*, 13831-13842. https://doi.org/10.1016/j.ijhydene.2016.01.148

[16] Adamson, A., Guillemin, J. C. & Burk, P. (2015). Proton transfer reactions of hydrazine-boranes. *Journal of Physical Organic Chemistry, 28,* 244-249. https://doi.org/10.1002/poc.3401

[17] Spry, D. B. & Fayer, M. D. (2009). Proton transfer and proton concentrations in protonated Nafion fuel cell membranes. *Journal of Physical Chemistry B*, *113*, 10210-10221. https://doi.org/10.1021/jp9036777

[18] Cochlin, D. (2014). Graphene’s promise for proton transfer in fuel cell membranes. *Fuel Cells Bulletin*, 2014(12), 1-12. https://doi.org/10.1016/S1464-2859(14)70354-2

[19] Bica, K., Shamshina, J., Hough, W. L., MacFarlaned, D. R. & Rogers, R. D. (2010). Liquid forms of pharmaceutical co-crystals: exploring the boundaries of salt formation. *Chemical Communications, 47,* 2267-2269. https://doi.org/10.1039/C0CC04485G

[20] Steed, J. W. (2013). The role of co-crystals in pharmaceutical design. *Trends in Pharmacological Sciences, 34,* 185-193. https://doi.org/10.1016/j.tips.2012.12.003

[21] Chen, K., Hirst, J., Camba, R., Bonagura, C.A., Stout, C. D., Burgess, B. K. & Armstrong, F. A. (2000). Atomically defined mechanism for proton transfer to a buried redox centre in a protein. *Nature, 405*, 814-817. https://doi.org/10.1038/35015610

[22] Chen, K. Y., Chen, K. Y., Cheng, Y. M., Lai, C. H., Hsu, C. C., Ho, M. L., Lee, G. H. & Chou, P. T. (2007). Ortho green fluorescence protein synthetic chromophore; excited-state ıntramolecular proton transfer via a seven-membered-ring hydrogen-bonding system. *Journal of the American Chemical Society, 129,* 4534-4535. https://doi.org/10.1021/ja070880i

[23] Luecke, H., Richter, H. T. & Lanyi, J. K. (1998). Proton transfer pathways in bacteriorhodopsin at 2.3 angstrom resolution. *Science*, *280*, 1934-1937. https://doi.org/10.1126/science.280.5371.1934

[24] Heberle, J., Riesle, J., Thiedemann, G., Oesterhelt, D. & Dencher, N. A. (1994). Proton migration along the membrane surface and retarded surface to bulk transfer. *Nature*, *370*, 379-382. https://doi.org/10.1038/370379a0

[25] Dellago, C. & Hummer, G. (2006). Kinetics and mechanism of proton transport across membrane nanopores. *Physical Review Letters*, 97, 245901. https://doi.org/10.1103/PhysRevLett.97.245901

[26] Aghabozorg, H., Sadrkhanlou, E., Shokrollahi, A., Ghaedi, M. & Shamsipur., M. (2009). Synthesis, characterization, crystal structures, and solution studies of Ni(II), Cu(II) and Zn(II) complexes obtained from pyridine-2,6-dicarboxylic acid and 2,9-dimethyl-1,10-phenanthroline. *Journal of Iranian Chemical Society*, *6*(1), 55-70. https://doi.org/10.1007/BF0324650

[27] Kavitha, C., Narendra, K., Ratnakar, A., Poojith, N., Sampath, C., Banik, S., Suchetan, P. A., Potla, K. M. & Naidu, N. V. (2020). An analysis of structural, spectroscopic signatures, reactivity and anti-bacterial study of synthetized 4- chloro-3-sulfamoylbenzoic acid. *Journal of Molecular Structure*, *1202*, 127176. https://doi.org/10.1016/j.molstruc.2019.127176

[28] Horie, T., Ohno, T. & Kinoshita, K. (1981). Studies on the metabolism of tripamide, a new antihypertensive agent. I. Characterization of metabolites in rats. *Xenobiotica*, *11*(3), 197-206. https://doi.org/10.3109/00498258109045292

[29] Marinescu, M. (2013). 2-Aminopyridine-A classic and trendy pharmacophore. *International Journal of Pharma and Bio Sciences, 8*(2), 338-355. http://dx.doi.org/10.22376/ijpbs.2017.8.2.p338-355

[30] İlkimen, H. & Yenikaya, C. (12-13 Şubat 2021). *2,4-Dikloro-5-Sülfamoilbenzoik Asit İle 2-Aminopiridin Türevlerinin Karışık Ligandlı Cu(II) Komplekslerinin Sentezi ve Karakterizasyonu* [Konferans sunumu]. Hodja Akhmet Yassawi 4th International Conference on Scientific Research, Ankara, Türkiye. https://www.yesevikongresi.org/_files/ugd/614b1f_3c87a06525de4399a9817edf0021c4fc.pdf

[31] İlkimen, H., Yenikaya, C. & Gülbandılar, A. (2023). 2-Metoksi-5-sulfamoyilbenzoik asit ile 2-aminonitropiridin türevlerinin sentezi, karakterizasyonu, antimikrobiyal ve antifungal aktivitelerinin incelenmesi. *3rd International Conference on Innovative Academic Studies, 3*(1), 784-793. https://doi.org/10.59287/icias.1632

[32] İlkimen, H. & Gülbandılar, A. (2023 November 4-5). *2-Amino-6-Substitüepiridin Türevleri ile 2-Metoksi-5-Sulfamoyilbenzoik Asitin Proton Transfer Tuzlarının Sentezi, Karakterizasyonu, Antimikrobiyal ve Antifungal Aktivitelerinin İncelenmesi* [Konferans sunumu]. 2nd International Conference on Contemporary Academic Research, ICCAR 2023, Konya, Türkiye https://drive.google.com/file/d/1k9kgUYg4y3ioVmaARt7caRBCPfP6u2Yp/view

[33] İlkimen, H. & Gülbandılar, A. (2023 November 4-5). *2-Amino-5-Substitüepiridin Türevleri ile 2-Metoksi-5-Sulfamoyilbenzoik Asitin Proton Transfer Tuzlarının Sentezi, Karakterizasyonu, Antimikrobiyal ve Antifungal Aktivitelerinin İncelenmesi* [Konferans sunumu]. 2nd International Conference on Contemporary Academic Research, ICCAR 2023, Konya, Türkiye. https://drive.google.com/file/d/1k9kgUYg4y3ioVmaARt7caRBCPfP6u2Yp/view

[34] İlkimen, H. & Yenikaya, C. (2023 October 19-20). *2,4-Dikloro-5-Sülfamoilbenzoik Asit ile Aminometilpiridin Türevlerinin Cu(II) Komplekslerinin Sentezi ve Karakterizasyonu* [Konferans sunumu]. 2nd International Conference on Recent Academic Studies, ICRAS 2023, Konya, Türkiye https://drive.google.com/file/d/1GXn3oVliFak0Sy6wFrMJ0VcQ-2MDXXRk/view

[35] İlkimen, H., Salün, S. G. & Yenikaya, C. (19-20 Haziran 2021). *2-Metoksi-5-Sülfamoilbenzoik Asitin Metal Komplekslerinin Sentezi ve Karakterizasyonu* [Konferans sunumu]. SOCRATES 1st International Health, Engineering and Applied Sciences Congress, Ankara, Türkiye. https://www.socrateskongresi.org

[36] İlkimen, H., Yenikaya, C. & Gülbandılar, A. (2022 September 23-25). *2-Metoksi-5-Sulfamoyilbenzoik Asit ile 2,3-Diaminopiridin Türevlerinin Proton Transfer Tuzları ve Cu(II) Komplekslerinin Sentezi, Karakterizasyonu, Antimikrobiyal Özelliklerinin İncelenmesi* [Konferans sunumu]. III. Baskent International Conference on Multidisciplinary Studies, Ankara, Türkiye. https://www.izdas.org/_files/ugd/614b1f_ededc0fb2e91434f8f254ec769d3339f.pdf

[37] İlkimen, H., Yenikaya, C. & Gülbandılar, A. (2023). 2-Aminopiridin türevleri ile 2-metoksi-5-sülfamoilbenzoik asit tuzlarının sentezi, karakterizasyonu, antimikrobiyal aktivitelerinin incelenmesi. *Selçuk Üniversitesi Fen Fakültesi Fen Dergisi*, *49*(2), 53-63. https://doi.org/10.35238/sufefd.1315568

[38] İlkimen, H. & Yenikaya, C. (2021). 2,4-Dikloro-5-sülfamoilbenzoik asit ile 2-aminopiridin türevlerinin karışık ligandlı Cu(II) komplekslerinin sentezi ve karakterizasyonu. *Euroasia Journal of Mathematics, Engineering, Natural & Medical Sciences*, *8*(14), 96-103. https://doi.org/10.38065/euroasiaorg.505

[39] İlkimen, H. (2019). Synthesis and characterization of mixed ligand Cu(II) complexes of 2-methoxy-5-sulfamoylbenzoic acid and 2-aminopyridine derivatives. *Macedonian Journal of Chemistry and Chemical Engineering*, *38*(1), 13-17. https://doi.org/10.20450/mjcce.2019.1698

[40] İlkimen, H., Türken, N. & Gülbandılar, A. (2021). Synthesis, characterization, antimicrobial and antifungal activity of studies of two novel aminopyridine-sulfamoylbenzoic acid salts and their Cu(II) complexes. *Journal of the Iranian Chemical Society*, *18*, 1941-1946. https://doi.org/10.1007/s13738-021-02157-4

[41] İlkimen, H. & Gülbandılar, A. (2023). Synthesis, characterization, antimicrobial and antifungal activity studies of four novel 2-aminopyridine and 2,4-dichloro-5-sulfamoylbenzoic acid salts and their Cu(II) complexes. *Kuwait Journal of Science*, *50*(3A), 1-11. https://doi.org/10.48129/kjs.19163

[42] Cook, D. (1961). Vibrational spectra of pyridinium salts. *Canadian Journal of Chemistry*, *39,* 2009-2024. https://doi.org/10.1139/v61-271@cjc-csc.issue01

Sinopfbd, 2024; 9(2): 483-501 **https://doi.org/10.33484/sinopfbd.1522122**

Sinop Üniversitesi Fen Bilimleri Dergisi
Sinop Uni J Nat Sci

E-ISSN: 2564-7873

https://dergipark.org.tr/tr/pub/sinopfbd

Mitochondrial Genetic Diversity and Historical Population Dynamics of the Bank Vole *Clethrionomys glareolus* in Northern Anatolia: Insights from *Cytb* and *COI* Gene Sequences

Fatma Hümeyra TAŞ[1], Gül OLGUN KARACAN[2], Reyhan ÇOLAK[1] and Ercüment ÇOLAK[1]

How to cite: Taş, F. H., Olgun Karacan, G., Çolak, R., & Çolak, E. (2024). Mitochondrial genetic diversity and historical population dynamics of the bank vole *Clethrionomys glareolus* in northern Anatolia: insights from *cytb* and *coi* gene sequences. *Sinop Üniversitesi Fen Bilimleri Dergisi, 9*(2), 483-501. https://doi.org/10.33484/sinopfbd.1522122

Research Article

Corresponding Author
Gül OLGUN KARACAN
glolgn@gmail.com

ORCID of the Authors
F.H.T: 0000-0002-4848-8100
G.O.K: 0000-0002-7160-5766
R.Ç: 0000-0003-1031-4073
E.Ç: 0000-0001-5826-1615

Received: 25.07.2024
Accepted: 09.10.2024

Abstract

This study presents a genetic analysis of *Clethrionomys glareolus* populations across northern Anatolia, utilizing mitochondrial *Cytb* and *COI* gene sequences. Phylogenetic analysis identified two distinct Turkish clades, Clade 1 and Clade 2. Neutrality tests and mismatch distribution analyses indicate a recent population expansion following a genetic bottleneck associated with Pleistocene climatic changes. Interestingly, bank voles from Uludağ in Bursa Province of northwestern Anatolia exhibited a closer phylogenetic relationship with northeastern populations than with other northwestern populations, suggesting complex historical population dynamics, possibly involving a population replacement in northern Anatolia and relic survival in Uludağ. The geographic boundaries between the clades did not align closely with main rivers, suggesting that these geographic features did not act as strong long-term barriers to gene flow among bank vole populations. Our mtDNA study lays the foundation for future research to evaluate these scenarios using phylogeographic patterns of genome-wide diversity for a comprehensive understanding of the complex evolutionary history of bank voles in Türkiye.

Keywords: Bank vole, mitochondrial DNA, Turkish Pleistocene refugia, inland water barriers, Türkiye

Kuzey Anadolu'da Bank Vole (*Clethrionomys glareolus*) Populasyonlarının Mitokondriyal Genetik Çeşitliliği ve Tarihsel Populasyon Dinamikleri: *Cytb* ve *COI* Gen Dizilerinden Elde Edilen Bilgiler

[1]Ankara University, Faculty of Science, Department of Biology, Ankara, Türkiye

[2]Aksaray University, Vocational School of Health Services, Department of Medical Services and Techniques, Aksaray, Türkiye

Öz

Bu çalışma, Kuzey Anadolu'daki *Clethrionomys glareolus* populasyonlarının mitokondriyal *Cytb* ve *COI* gen dizileri kullanılarak yapılan genetik analizlerini sunmaktadır. Filogenetik analizler, iki ayrı Türkiye kladını, Klad 1 ve Klad 2'yi ayırt etmiştir. Nötralite testleri ve uyumsuzluk analizleri, Pleistosen dönemi iklim değişiklikleri ile ilişkili genetik bir darboğazın ardından yakın zamanda bir populasyon genişlemesi olduğunu ortaya koymuştur. Dikkat çekici bir şekilde, Bursa'nın Uludağ bölgesinden alınan kızıl sırtlı orman faresi örnekleri, diğer kuzeybatı populasyonları yerine kuzeydoğu populasyonları ile daha yakın filogenetik ilişkiler sergilemiştir. Bu durum, kuzey Anadolu'da potansiyel bir populasyon değişimi ve Uludağ'da bir kalıntı populasyonun hayatta kalmasını içeren karmaşık tarihsel populasyon dinamiklerine işaret etmektedir. Kladlar arasındaki coğrafi sınırlar, ana nehirlerle doğru orantılı olmayıp, bu coğrafi özelliklerin kızıl sırtlı orman faresi populasyonları arasındaki gen akışına ciddi engeller oluşturmadığını göstermektedir. Bu mitokondriyal DNA çalışması, Türkiye'deki kızıl sırtlı orman farelerinin evrimsel tarihini derinlemesine anlamak amacıyla gelecekte yapılacak araştırmalar için sağlam bir temel oluşturarak, genetik çeşitlilik gösteren filocoğrafik desenlerin kullanılmasını önermektedir.

Anahtar Kelimeler: Kızıl sırtlı orman faresi, mitokondriyal DNA, Türkiye Pleistosen sığınakları, iç su bariyerleri, Türkiye

Introduction

During the Pleistocene glaciations, many European species found refugia in the Mediterranean region of Europe. However, some species also survived in temperate areas in northern Anatolia [1, 2]. The bank vole, *Clethrionomys glareolus* Schreber, 1780 (sometimes also called *Myodes glareolus*; Kryštufek et al. [3]), is a species extensively studied to comprehend the response of the European fauna to Pleistocene climate changes [4-12]. This species is found in temperate and boreal forests across Europe and western Asia, including northern Anatolia [13, 11]. Recent phylogenetic and phylogeographic studies by Deffontaine et al. [4], Filipi et al. [7], Çolak et al. [8], Lu et al. [9], Chiocchio et al. [11] and Kotlik et al. [12] have highlighted the significant role of climatic fluctuations and environmental changes during the Pleistocene period (starting around 1.81 million years ago) in influencing the genetic differentiation of *Clethrionomys glareolus*. Bank voles are distributed along the boreal forests of Anatolia. According to Osborn [14], the bank vole exhibits a fragmented distribution in Anatolia, with noticeable morphological differences observed among specimens in the western and eastern parts of northern Anatolia. Several major geographic features, including the Sakarya River, Kızılırmak River, Melet River, İkizdere stream, and the Izmit Gulf–Lake Sapanca–Sakarya Valley waterway [15], may have contributed to the fragmentation of the geographic range of terrestrial species in Anatolia, potentially leading to phylogeographical breaks. However, the impact of these barriers on the differentiation of *C. glareolus* remains unknown. Çolak et al. [16] identified two distinct groups in the northern Anatolia region based on allozyme data, with the differentiation largely associated with altitudinal differences. Similarly, Beteş et al. [17] revealed the existence of two lineages as western and eastern, in the northern Anatolia through RAPD-PCR analysis. Çolak et al. [8] identified two lineages in Anatolia as northeastern and northwestern, using phylogenetic analysis of the mitochondrial DNA (mtDNA) *Cytb* and D-*loop* regions, which were separated by the Kızılırmak valley. Interestingly, the study showed that specimens from Uludağ region (N=2) in the northwestern Anatolia clustered together with the northeastern Anatolia lineage. Uludağ, a prominent mountain located in the Marmara Region of the northwestern Anatolia, reaches an elevation of 2543 meters and presents a distinct ecological setting that may contribute to genetic differentiation within the species. In a parallel vein, İbiş et al. [18], through their study on *Crocidura leucodon*, suggested the existence of a glacial refuge in the Uludağ-Bursa region for this species. It is noteworthy that *C. glareolus* and *Crocidura leucodon* shares similar characteristics as having a small size and a limited mobility, traits that allow these species to potentially respond rapidly to environmental and climatic factors. Building upon the insights presented in the study by İbiş et al. [18], we aim to investigate whether Uludağ and its surroundings served as a Pleistocene refugium for *C. glareolus*. For the purpose to achieve this, we expanded the sample size in this area incorporating additional gene regions into our analysis, complementing the findings of Çolak et al. [8]. The primary objective of our study is to investigate the genetic differentiation and past population dynamics of bank vole populations in Anatolia. Specifically, we aim to reassess the distinctions of the Uludağ population as a unique genetic entity, utilizing sequences of the *COI* gene region selected for its lower variability relative to the *D-loop* region used in previous studies [8]. By expanding our sample size from Uludağ and its surrounding areas, our aim is to achieve a more comprehensive understanding of the genetic diversity and population structure across the region spanning from Uludağ to northeastern Anatolia, and to explore potential drivers such as geographical barriers and climatic changes during the Pleistocene.

Materials and Method

Sample Collection

We examined a total of 66 cytochrome b (*Cytb*) gene sequences for bank voles collected from 24 different locations across northern Anatolia, covering the species' distribution in Türkiye (Table 1, Figure 1).

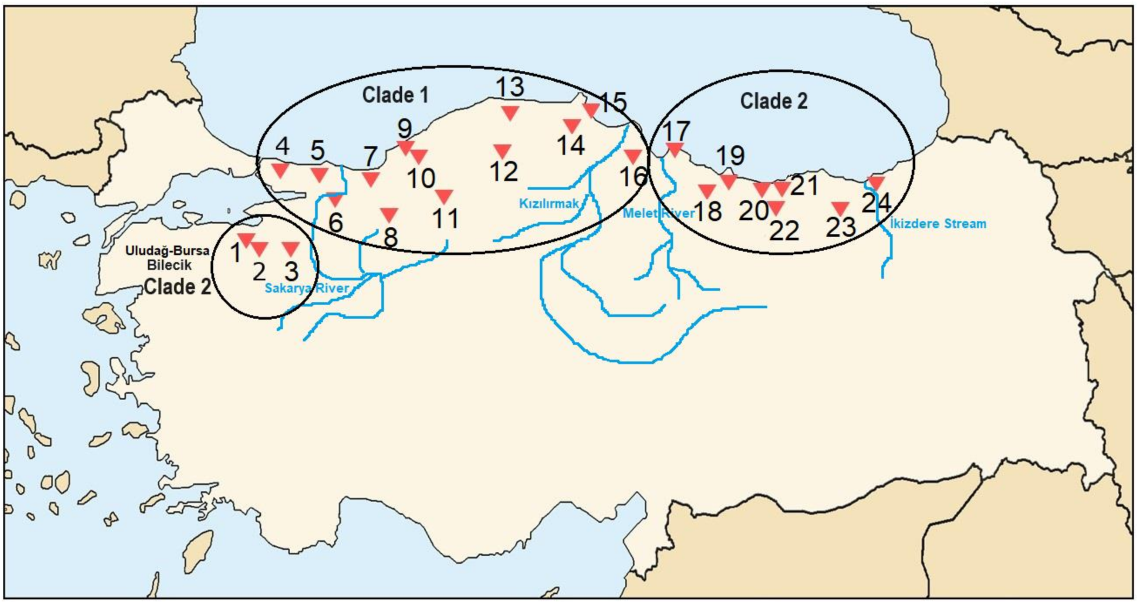

***Figure 1.** Sampling localities of the bank voles from Anatolia (see the map references in Table 1)*

Among these, 34 samples had been previously analyzed for the *Cytb* gene by Çolak et al. [8]. In this study, we extended the *Cytb* analysis by including additional 32 specimens. Furthermore, we conducted the first analysis of the cytochrome c oxidase subunit I (*COI*) gene region using 63 samples in Türkiye. Ethical permits were obtained from the Animal Experiments Local Ethics Committee of Ankara

University (no: 2019-11-108) for the collection of all specimens.In addition to the Turkish samples, specimens from GenBank were included in phylogenetic tree construction and genetic distance calculations (Appendix E). *Clethrionomys centralis* (KY968281 for *Cytb* and KY968255 for *COI*) [17] was used as the outgroup.

Table 1. *Map references, locality name, number of specimens from each locality and GenBank Accession numbers of the bank vole haplotypes from Anatolia*

Map references	**Locality**	**Total number of specimens**	**GenBank Accession Number**	
			Cytb	***COI***
1	Bursa	9	KM508997, KM508998 OM674439	OM674417
2	Uludağ-Bursa	3	KM508997, KM508998, KM508997	OM674417, OM674418
3	Muratdere-Bilecik	3	OM674439	-
4	Şile-İstanbul	4	KM508989, KM508990	OM674420, OM674421
5	Kandıra-Kocaeli	3	KM508989, KM508991, KM508992	OM674417, OM674420
6	Kartepe-Kocaeli	3	KM509000, KM509001, KM509002	OM674420, OM674427
7	Akçakoca-Düzce	3	KM508993, KM508990, KM508994, OM674428	OM674420
8	Abant-Bolu	4	KM508995, KM508995, KM508996	OM674419, OM674420 OM674423
9	Zonguldak	4	KM508999, KM508989	OM674419, OM674420
10	Çaycuma-Zonguldak	1	OM674433	OM674419
11	Kızılcahamam-Ankara	1	KM509003	OM674420
12	Ilgaz-Çankırı	4	OM674435, OM674436 OM674437, OM674438	OM674420
13	Küre-Kastamonu	3	KM509005, KM508996	OM674419, OM674422
14	Bürnük-Sinop	2	KM509006	OM674419, OM674420
15	Göktepe-Sinop	4	KM509007, KM509008 OM674431	OM674419, OM674420 OM674423
16	Çakallı-Samsun	1	KM509009	OM674417
17	Ünye-Ordu	2	KM509011	OM674417
18	Gürgentepe-Ordu	2	KM509010, OM674429	OM674424
19	Ulubey-Ordu	2	KM509010, OM674432	OM674417
20	Bulancak-Giresun	1	KM509012	OM674425
21	Bicik-Giresun	1	KM509012	OM674417
22	Barça village-Giresun	2	KM509013	OM674417, OM674424
23	Sümela-Trabzon	3	KM509014, OM674430	OM674417
24	İkizdere-Rize	1	OM674434	OM674426

Laboratory Methods

Genomic DNA was extracted from muscle and kidney tissues of the samples using Doyle [20]'s Cetyltrimethyl Ammonium Bromide (CTAB) isolation protocol. The *Cytb* gene was amplified using the universal primers L14724 and H15915 [21]. Additionally, a 700 bp fragment of the *COI* gene was amplified using the primers LCO1490 and HCO2198 [22]. Sanger sequencing was performed, and both forward and reverse sequences were obtained for each amplicon. The sequences have been deposited in GenBank under accession numbers OM674417-OM674439 (Table 1). The polymerase chain reaction (PCR) mixture and amplification of the *Cytb* gene region were conducted following the procedures described in Çolak et al. [8]. For the *COI* gene region, the PCR protocol consisted of an initial denaturation step at 96 °C for 1 min, followed by 35 cycles of denaturation at 94 °C for 1 min, annealing at 55 °C for 1 min, extension at 72 °C for 1.5 min, and a final extension step at 72 °C for 10 min.

Phylogenetic Inferences, Genetic Distances and Network Analyses

The sequences were aligned using the ClustalW alignment tool implemented in BioEdit (ver. 7.2.5) [23]. Unique haplotypes were identified using DnaSP (ver.6.12.03) [24]. We reconstructed the phylogenetic relationships among haplotypes separately for each gene region, *Cytb* and *COI*, using both maximum likelihood (ML) and Bayesian inference (BI) approaches. For ML analysis, we employed IQ-TREE (ver. 1.6) [25]. The best-fitting model of sequence evolution for each gene region was determined by applying the Bayesian information criterion (BIC) in MEGAX. The HKY+G models were chosen for the *COI* and *Cytb* regions, respectively. This model is used for the ML and BI reconstructions. The Nearest-Neighbor Interchange (NNI) algorithm was employed as the tree-building method for ML analysis. Bootstrap resampling (BP) was used to generate the ML tree with 1000 replicates, providing a measure of the tree's robustness. For the Bayesian analysis, we utilized MrBayes (version 3.2.7a) [26]. Separate Markov chain Monte Carlo (MCMC) Bayesian analyses were conducted for *COI* and *Cytb* gene regions. In each analysis, we performed 2 million iterations for the *COI* gene region and 5 million iterations for the *Cytb* gene region to ensure robust results. Empirically determined, the initial 25% of each run was discarded as a burn-in. Bayesian posterior probabilities (BPP) were calculated based on the 50% majority rule consensus of trees sampled every 1000 generations. We used a significance level of $P < 0.01$ for Bayesian posterior probabilities to determine the statistical support for clades. The median-joining networks (MJN) were constructed to illustrate the relationships between haplotypes for each gene region using Network (ver. 10.2) [27]. The genetic distance between the groups appearing in the phylogenetic trees was estimated with the Kimura-2 parameter (K2P) using the MEGA X software. To explore the connection between geographical distances and genetic differentiation among *C. glareolus* populations, we conducted a Mantel test using the IBD: Isolation By Distance v1.52 software [28]. For this purpose, pairwise differences (pi) were computed among three groups representing Eastern haplotypes, Western haplotypes, and Uludağ-Bilecik haplotypes. Distance data between populations were determined by measuring the geographical distances between the Sümela (representing Eastern haplotypes), Şile (representing Western haplotypes), Abant, and Uludağ localities using the distances in kilometres obtained through Google Earth. Uludağ locality was chosen due to the clustering of haplotypes with Eastern haplotypes in the phylogenetic tree. This allowed us to assess whether geographical distance has an effect on genetic distance among populations.

Demographic History and Neutrality

Nucleotide diversity (π), haplotype diversity (h), and mismatch distribution analyses were assessed using DnaSP (ver. 6.12.03) [24]. The Arlequin software (ver. 3.5.2.2) [29] was utilized for neutrality analyses, including Tajima's D [30] and Fu's Fs [31] tests, which provide insights into population expansion and bottlenecks.

Mutation Rates

The parameter τ (Tau) estimated by DnaSP was utilized to determine the time since the last population expansion. The time (T) elapsed since the last population expansion for each group, based on the studied gene regions, was calculated using the formula "$T = \tau/2u$” (as described by Honda et al. [32]). Three different mutation rates, 0.11, 0.047, and 0.028 substitutions/site/My [32-34], were used to estimate the expansion times of *C. glareolus* groups in Anatolia during the Pleistocene period. According to Ho et al. [35], using mutation rates for molecular dating is particularly suitable when investigating intraspecific variations and time frames within the last 2 million years.

Results

A total of 716 base pairs (bp) of the *COI* gene were analyzed for 63 specimens, along with 1,110 bp of the *Cytb* gene from 32 new specimens. Additionally, 34 *C. glareolus* samples (KM508990-KM509014) from the study of Çolak et al. [8] were included. In total, the *COI* sequences revealed 11 haplotypes, while the *Cytb* sequences exhibited 35 haplotypes.

Phylogenetic Analysis

Phylogenetic trees constructed from the *COI* and *Cytb* gene regions revealed consistent clustering patterns among bank vole populations in Türkiye, placing them in two distinct clades: Clade 1 and Clade 2. Additional clades were identified for populations from other regions, aligning with previous studies (Figures 2 and 3, Appendix C and D). Clade 1 comprises the majority of specimens from the northwestern Anatolia region, while Clade 2 includes specimens from both the southern Marmara region in northwestern Anatolia (including Uludağ, Bursa and Bilecik; haplotypes 01, 02, and 35) as well as from the northeastern Anatolia region. In the *Cytb* tree (Figure 2), both Clade 1 and 2 are moderately to well supported, with moderate bootstrap support for them being sister clades and thus monophyly of Turkish bank voles. In contrast, in the *COI* tree, the monophyly of Turkish bank voles is well supported (85%), but Clade 2 is not recovered as monophyletic, with some haplotypes placed at the base of the entire Turkish clade (Figure 3). Additionally, the phylogenetic trees constructed using the *Cytb* data (no

Balkan haplotypes were present in *COI* data) support clustering of the Balkan and Anatolian populations in one clade (BS=93% and BI=0.88%), consistent with the previous studies.

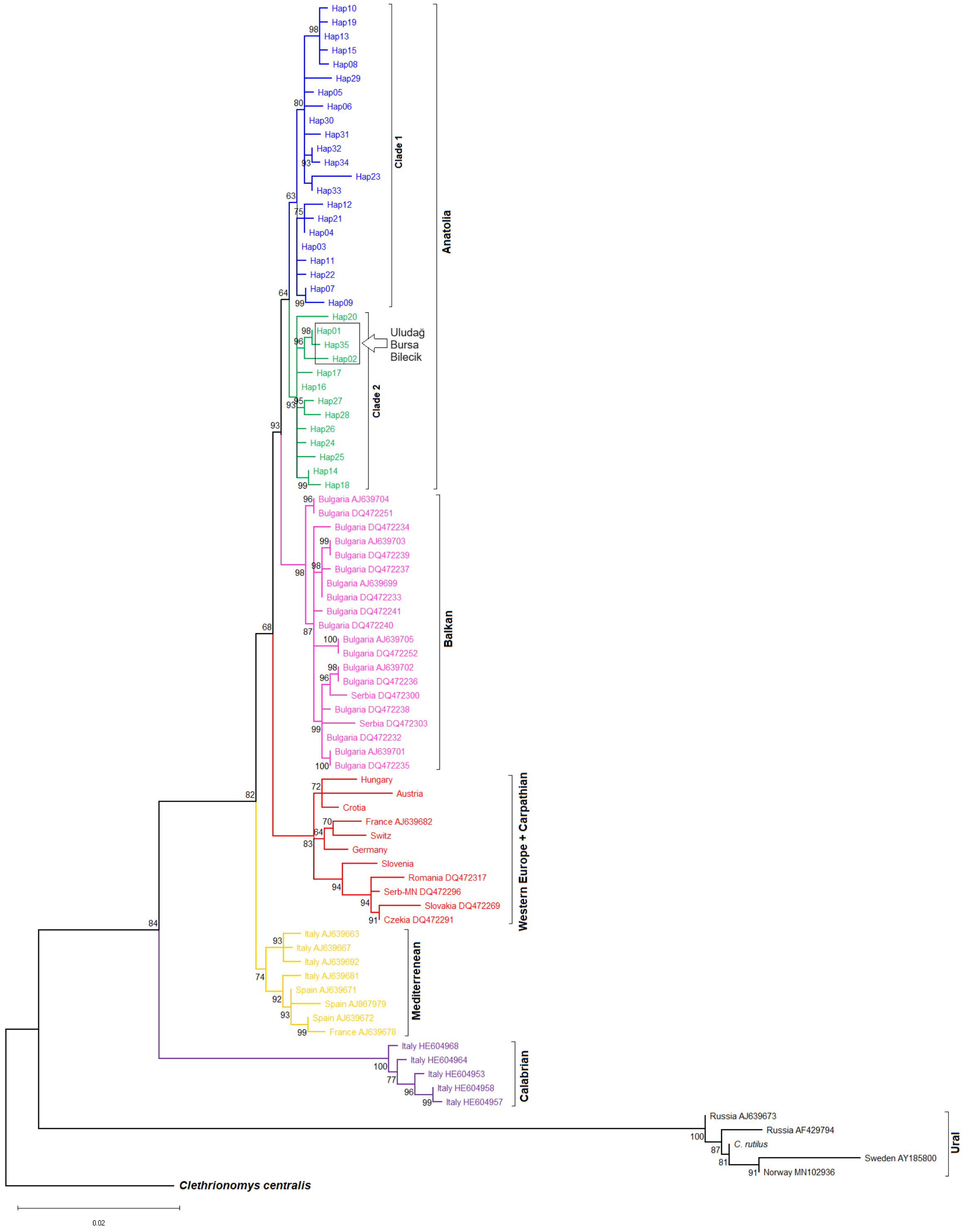

Figure 2. *Maximum likelihood tree obtained for Cytb gene. Clethrionomys centralis is used as an outgroup. Bootstrap supports are showed on each node for each main group*

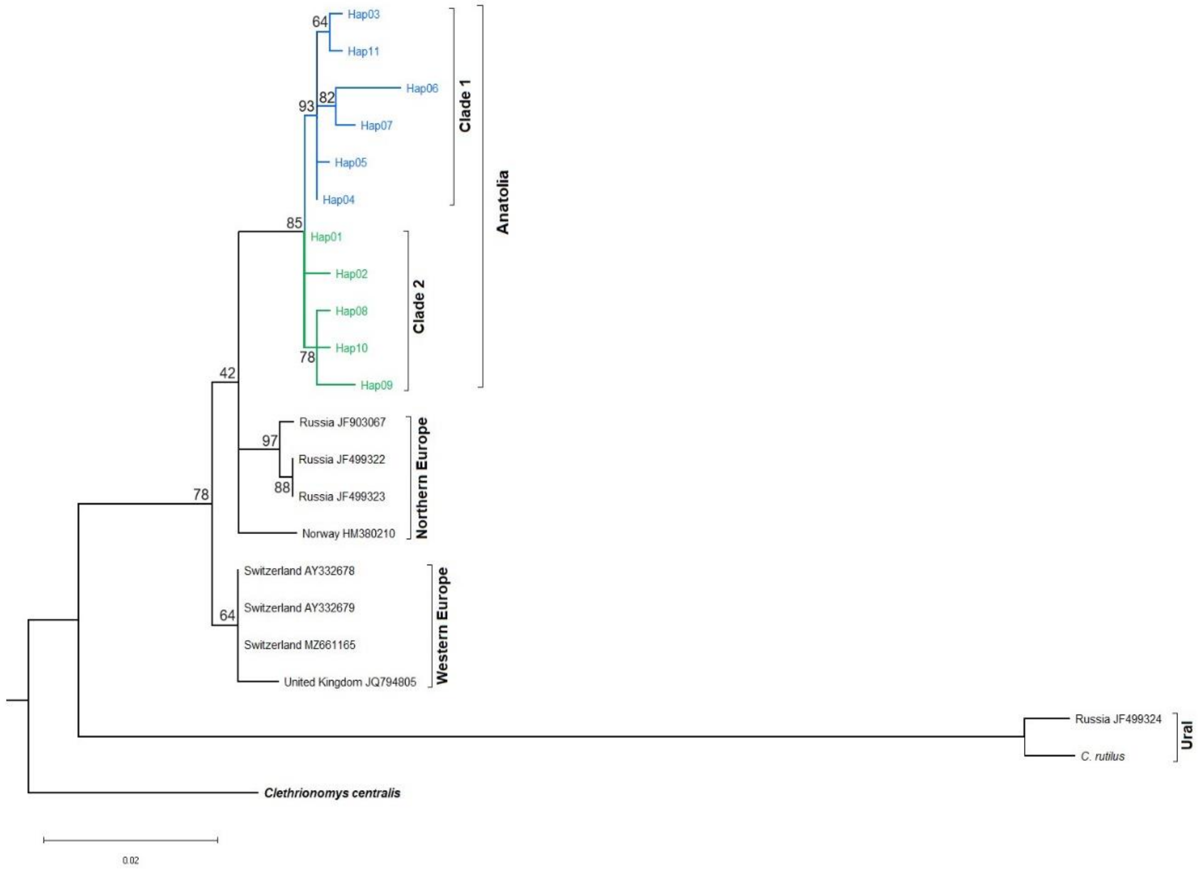

Figure 3. *Maximum likelihood tree obtained for COI gene. Clethrionomys centralis is used as an outgroup. Bootstrap supports are showed on each node for each main group*

In the MJN constructed for *Cytb* and *COI* haplotypes, Turkish haplotypes formed two distinct groups, consistent with the phylogenetic trees, and were separated by two and single mutational steps in the *Cytb* and *COI* MJNs, respectively (Appendix G and F). The *Cytb* groups each exhibited a star-like topology (Appendix G). The group of *Cytb* haplotypes from the Balkans was separated from Clade 1 by three mutational steps (no Balkan haplotypes were present in *COI* MJN), while the European group was differentiated from Clade 2 by six and three mutational steps in the *Cytb* and *COI* networks, respectively.

Genetic Diversity

Haplotype diversity was relatively high for both of the northwestern and northeastern Anatolia samples, while nucleotide diversity was low in both gene regions. In contrast, the Uludağ population showed notably lower haplotype diversity and nucleotide diversity when compared to other populations (Table 2).

Table 2. *Genetic diversity within bank vole populations (N: number of specimens, H: Number of haplotypes, Hd: Haplotype diversity, π: Nucleotide diversity, SD: Standard deviations, NW: northwestern, NE: northeastern)*

Lineage	*Cytb*				*COI*			
	N	H	Hd (±SD)	π (±SD)	N	H	Hd (±SD)	π (±SD)
NW Anatolia	36	22	0.96 (±0.01)	0.003 (±0.0003)	36	22	0.94 (±0.02)	0.003 (±0.0003)
NE Anatolia	15	10	0.92 (±0.05)	0.002 (±0.0005)	15	12	0.96 (±0.04)	0.003 (±0.0005)
Uludag-Bursa	15	3	0.73 (±0.06)	0.002 (±0.0004)	12	2	0.72 (±0.11)	0.002 (±0.0003)

Genetic Distance

The genetic distance within the Turkish clades of *C. glareolus*, as determined by the Kimura 2-parameter (K2P) model, was very low (K2P% = 0.63 for *Cytb* and K2P% = 0.72 for *COI*). However, the K2P value was relatively high between the Turkish and European populations (K2P% = 2.21 for *Cytb* and K2P% = 1.79 for *COI*). Specifically, based on the *Cytb* sequences, 0.98% differentiation was observed between the Balkan and Anatolian populations. (Table 3).

Table 3. *Degree of sequence divergence (in per cent) with Kimura 2-parameter distance for the Cytb and COI between clades (The standard errors (in parenthesis) are based on 10.000 bootstrap replicates of the Kimura 2-parameter)*

Clades	*Cytb*	*COI*
Clade 1/Clade 2	0.63 (0.16)	0.72 (0.21)
Anatolia/Europe	2.21 (0.26)	1.79 (0.46)
Anatolia/Balkan	0.98 (0.23)	-

Mantel Test

The Mantel Test analysis allowed us to assess the correlation between pairwise geographical distances and genetic distances based on the *Cytb* and *COI* gene regions. While the calculated correlation coefficient (r) indicated a negative relationship between geographical and genetic distances, the relationship was not statistically significant (r = -0.2618, *P* <= 0.7140).

Mismatch Distribution and Neutrality Tests

Mismatch distribution analysis and neutrality tests were conducted for both *COI* and *Cytb* sequences, considering the presence of two clusters in the phylogenetic tree (Clade 1 and Clade 2). In the case of *COI*, Fu's test statistic FS exhibited significantly negative values different from zero in both Clade 1 (FS = -16.9, *P* < 0.01) and Clade 2 (FS = -10.2, *P* < 0.01), indicating an excess of recent mutations or rare alleles. However, Tajima's D values for Clade 1 (D = -0.71, *P* = 0.26) and Clade 2 (D = -0.99, *P* = 0.17) were not statistically significant. For *Cytb*, Tajima's D and Fu's test statistic Fs displayed significantly negative values different from zero in Clade 1 (D = -1.81, *P* < 0.05, FS = -15.86, *P* < 0.01). Although Tajima's *D* and Fu's test statistic Fs values were negative for Clade 2, the values were not statistically significant (D = -1.54, *P* = 0.07, FS = -4.57, *P* = 0.99). The mismatch distributions of both Clade 1 and Clade 2 were unimodal, providing support for rapid expansion (Figure. 4).

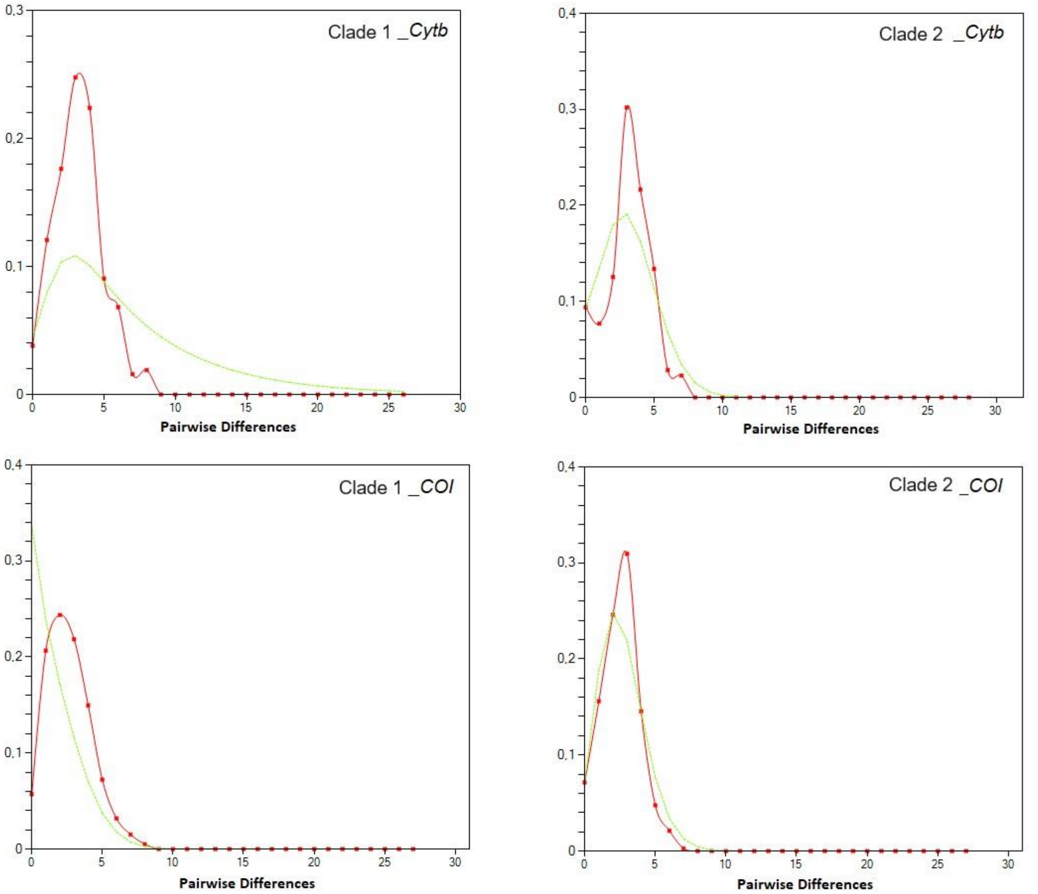

Figure 4. *Observed (red line) and expected (green line) mismatch distributions of the bank vole group for Cytb and COI showing the demographic history in panels.*

Expansion Times

The τ values obtained to estimate the last expansion time of the groups were between 6.126 (Clade 1) and 6.350 (Clade 2) for the *COI* gene region. Based on three different mutation rates (0.11, 0.047, and 0.028 substitutions/site/My), the elapsed time since the last expansion was approximately 40.000, 90.000, and 150.000 years ago, respectively (Table 4). For the *Cytb* gene region, the τ values ranged from 3.237 (Clade 1) to 3.213 (Clade 2), and the estimated expansion times were 13.000, 30.000, and 50.000 years ago (Table 4).

Table 4. *Expansion time estimates inferred from Cytb and COI genes for bank voles from Anatolia with three potential evolutionary rates (* Expansion times of populations were calculated with three different evolutionary rates stated in literature. These evolutionary rates are the rate of mutation in 1 million years, substitutions/site/My. (My, Million years.)*

		Tau (τ)	Expansion times (My)*		
			0.028	0.047	0.11
COI					
	Clade 1	6.126	0.152	0.091	0.038
	Clade 2	6.35	0.158	0.094	0.04
Cytb					
	Clade 1	3.237	0.052	0.03	0.013
	Clade 2	3.213	0.051	0.03	0.013

Discussion

Phylogeny

The bank vole, *Clethrionomys glareolus* has been used as a model organism in many genetic studies to investigate the effects of climatic fluctuations during the Pleistocene period on mammalian species (reviewed by Kotlík et al. [36]). The most comprehensive phylogenetic study to date on the bank vole population in Türkiye was conducted by Çolak et al. [8], using the *Cytb* and *D-loop* gene regions, identifying two haplotype groups in northern Anatolia. They also asserted that despite the distant geographical separation, the Uludag population in southern Marmara showed closer genetic affinity with samples from the northeastern Anatolia rather than the adjacent northwestern Anatolian populations. However, the scarcity of samples from important regions, and the use of the *D-loop* region with its high mutation rate and highly variable nature, may have constrained the study by Çolak et al. [8]. Therefore, this study aimed to reassess the phylogenetic analyses of Anatolian bank vole populations by expanding sampling efforts in the Uludağ region and nearby areas, and comparing results obtained from different additional mtDNA gene. Specifically, the *COI* gene was chosen to explore the long-term connectivity between bank vole populations in Anatolia due to its low mutation rates, contributing to a better understanding of population dynamics and evolutionary processes. The phylogenetic and MJN analyses of the *COI* and *Cytb* datasets consistently support the presence of two main groups within the bank vole population in Anatolia, which aligns with previous studies, including those utilizing RAPD-PCR [17] and *Cytb* [8]. These groups, referred to as Clade 1 and Clade 2, are located in the northwestern Anatolia region (Clade 1) and the southern Marmara region (Uludağ, Bursa and Bilecik) and the northeastern Anatolia region (Clade 2), respectively (Figure 2, 3). The observed lower haplotype and nucleotide diversity in the Uludağ-Bursa-Bilecik population may suggest that this population underwent a stronger bottleneck than other populations (or experienced a stronger selective sweep), potentially during cold periods of the Pleistocene [37]. The clustering of Uludağ-Bursa-Bilecik haplotypes within Clade 2, predominantly found in northeastern Anatolia, is intriguing due to its discontinuous distribution compared to Clade 1, which is widespread throughout central Türkiye (Figure 1). The minimal haplotype differences within Clade 2 and its star-like structure suggest a recent origin from a single ancestor. It is plausible that Clade 2 initially expanded from a glacial refugium, covering much of northern Anatolia, with subsequent replacement of central populations by those from Clade 1. Whether this replacement involved only mtDNA or entire populations cannot be determined from the present data. Similar population replacements, initially identified through mtDNA phylogeography, have been documented in other regions of the bank vole range, such as Britain [38, 39] and Fennoscandia [40]. This evidence suggests that population dynamics in bank voles have been climate-driven, reflecting adaptations of populations from different refugia to varying environmental conditions [41]. An alternative explanation that the Uludağ-Bursa-Bilecik populations share a more recent ancestor with those of Clade 1 and the discordance between phylogeny and geography is due to incomplete lineage sorting, seems less likely. This is indicated by the small differences among Clade 2 haplotypes, suggesting a recent common ancestor between Uludağ-Bursa-Bilecik and northeastern Anatolia. Our results do not support the role of altitude in the observed geographic structure suggested by isoenzyme studies [16] as the high-altitude populations (altitude 1020-1650 m above sea level) in Abant (Hap09-Hap10), Kartepe (Hap 29-Hap30), and Ilgaz (Hap 31-Hap34) were clustered with populations at lower altitudes. These results highlight the complexity of population structure and genetic diversity in bank voles in Anatolia and possible differences between mtDNA and nuclear genetic structure that require further investigation to uncover the underlying factors shaping these patterns. In phylogenetic analyses by Ledevin et al. [42] the specimens from Uludağ (the only bank vole locality from Türkiye included in that study) were clustered with the Balkan lineage. In our study, the samples from Uludağ were grouped together with specimens from the northeastern Anatolia region and the remaining samples from northern Anatolia. Our findings are consistent with Ledevin et al. [42] in that the Anatolian clades form a sister clade to the Balkan clade, highlighting regional genetic affinities within the bank vole populations across these areas.

Genetic Divergence

The genetic distance within the Turkish clades of *C. glareolus*, as determined by the Kimura 2-parameter (K2P) model, was remarkably low (K2P% = 0.63 for *Cytb* and K2P% = 0.72 for *COI*). These values indicate a relatively low genetic divergence among the studied populations. Similar patterns of low genetic divergence have been observed in other rodent species distributed in Anatolia, such as squirrels and hamsters [43-46]. According to Baker and Bradley [47], populations with genetic divergence values below 2% are unlikely to represent different species. While the genetic divergence values suggest the specimens within the Turkish groups of bank vole are closely related, the lack of shared haplotypes between the two clades indicates that ongoing gene flow between these populations is unlikely. However, comparatively higher K2P values were observed between the Turkish and European populations (K2P% = 2.21 for *Cytb* and K2P% = 1.79 for *COI*). Specifically, based on the *Cytb* sequences, a distance of 0.98% was observed between the Balkan and Anatolian populations.

Past Population Demography

The nucleotide and haplotype diversities observed in the Spanish and Italian phylogroups of the bank voles were low, attributed to population fragmentation during glaciations [4]. In contrast, the two groups in Anatolia exhibited high haplotype diversity and low nucleotide diversity in both gene regions, which could indicate a rapid expansion following the Last Glacial Maximum (LGM) [37]. The MJN constructed from *Cytb* haplotypes revealed a star-like topology for each of the two Turkish clades, which may have been a result of such an expansion. Consistent with such a scenario, Tajima's D was found to be significantly negative only for *Cytb* sequences, supporting the evidence of recent demographic expansion in Clade 1. Although Tajima's D was negative in Clade 2 for *Cytb* and in all groups for *COI*, the values were not statistically significant. On the other hand, Fu's F_S was negative in all groups for both *Cytb* and *COI*, but it was statistically insignificant only in Clade 2 for the *Cytb* gene. The differences between Tajima's D and Fu's F_S values can be attributed to the calculation of these two neutrality tests using different parameters. Tajima's D estimates the nucleotide differences in the sequences, while Fu's F_S considers the haplotype diversity in the population [48]. In this study, nucleotide diversity in the bank vole groups was found to be lower than haplotype diversity, leading to differences in the neutrality calculations. Moreover, the number of segregating sites (S: segregating sites) differed between the gene regions. The highest number of segregating sites was observed in the *Cytb* sequences of Clade 1 (S=28), which explains why Tajima's D value was significantly negative only in this group. The significantly negative Fu’s Fs values suggest an excess of rare haplotypes, likely reflecting a recent population expansion following a bottleneck, while the less significant Tajima’s D values indicate that the nucleotide diversity has not fully recovered from past events. This discrepancy underscores the complex demographic history of *C. glareolus*, with the combination of these tests providing a more nuanced understanding of population growth after the Last Glacial Maximum.

Timing of Population Expansion

Based on the population expansion analyses conducted in our study, the bank vole populations in Anatolia exhibit a complex demographic history shaped by the climatic fluctuations during the Pleistocene. The presence of glacial refugia and subsequent population expansions during interglacial periods has been documented in various species [1, 6, 49, 50]. We estimated the expansion time of bank vole groups in Anatolia by analyzing mismatch distribution and using various mutation rates reported in literature. The results consistently indicated rapid population growth towards the end of the Pleistocene, with estimates ranging from approximately 13.000 to 50.000 years ago (MIS1 and MIS3) based on *Cytb* sequences, and from approximately 40.000 to 150.000 years ago (MIS3 and MIS6) based on *COI* sequences. These patterns of expansion likely indicate the dynamic response of bank vole populations in Anatolia to changing climatic conditions over time. The discrepancies between the two gene regions may be attributed to differences in mutation rates. Further studies should consider specific mutation rates for the *COI* gene in expansion time analyses, as previous studies have focused primarily on *Cytb* gene analyses [32-34].

Geographic Barriers

Geographic barriers in northern Anatolia, including the major river systems Sakarya River, Kızılırmak River, Melet stream, İkizdere stream, and Izmit Gulf–Lake Sapanca–Sakarya Valley, have been implicated in shaping the phylogeography of various animal species during the Plio-Pleistocene period [50-55]. However, our phylogenetic analysis and the relatively low support values suggest that these barriers did not play significant roles in separating bank vole populations in Anatolia. The Melet River, specifically examined in relation to dormouse populations [53], did not appear to have acted as a strong barrier affecting the phylogenetic patterns of bank voles. Similarly, the closure of the Izmit Gulf-Lake Sapanca-Sakarya Valley waterway approximately 11.7 thousand years ago [15] did not seem to act as a barrier for the bank vole population in the Sakarya Valley (Localities 4-8 in Figure. 1), as indicated by the clustering of specimens from surrounding locations (Hap03, Hap04 and Hap12 for *Cytb*, Hap03-Hap07 for *COI*). This suggests a potential rapid westward expansion of Clade 1 specimens following the closure of the waterway. In the case of the Kızılırmak River, although considered a potential barrier for gene flow in the region [50, 55], haplotypes from the localities at the west of the river such as Bürnük and Göktepe (Hap13, Hap15, and Hap19 for *Cytb*; Hap04 for *COI*) and those from Çakallı on the east (Hap26 for *Cytb*; Hap01 for Çakallı) were found in different clades in both *Cytb* and *COI* phylogenetic trees. This discrepancy underscores the need for more comprehensive sampling and the use of microsatellite markers to detail the polymorphism between haplotypes on either side of the Kızılırmak River. On the other hand, the absence of bank vole specimens in the eastern part of the İkizdere stream suggests the need for further investigations in this region to determine the relationships of bank voles in this area.

Conclusion

Our examination of mitochondrial DNA variation in bank voles from northern Türkiye has yielded several noteworthy findings. Phylogenetic and network analyses of *Cytb* and *COI* sequences support the existence of two genetically distinct clades in northern Anatolia, which are closely related to the Balkan populations from Europe. These Turkish clades likely occupied major refugia during the Pleistocene glaciations, one in the western part and the other in the eastern part of northern Anatolia. Evidence of recent population expansion and the broadly estimated times of this expansion highlight the impact of climatic fluctuations towards the end of the Pleistocene on bank vole demography in Türkiye. The close relationship between the Uludağ-Bursa-Bilecik haplotypes and those from northeastern Anatolia indicates a recent common ancestor for the populations from these regions. This suggests that the survival of a relic population in the vicinity of Uludağ, probably after a mitochondrial DNA or population replacement in northern Anatolia. Main Turkish rivers except for the Kızılırmak River, do not seem to have acted as strong long-term barriers inhibiting gene flow among bank vole populations. The clustering of haplotypes near the Kızılırmak River in different clades suggests it may influence gene flow, pointing to the need for further detailed analysis with increased sampling. These insights not only deepen our understanding of the evolutionary history of bank voles in this region but also underscore the complex interplay between geographic and climatic factors in shaping genetic diversity and structure. Moving forward, integrating nuclear DNA markers or genome-wide diversity studies would allow for a more comprehensive understanding of both historical and contemporary population dynamics. Such studies could also help to uncover the roles of selective pressures on these populations, particularly in light of current climatic changes.

Acknowledgements This research article incorporates information from the thesis titled "Phylogenetic Analysis of *Myodes glareolus* Schreber, 1780 (Mammalia: Rodentia) Distributed in Turkey," prepared by Fatma Hümeyra TAŞ. The related master's thesis was completed at the Department of Biology, Graduate School of Natural and Applied Sciences, Ankara University, on 02/26/2021.

Funding/Financial Disclosure This study was funded by the Scientific Research Project Office of Ankara University (AUBAP-Project Number: 19L0430009).

Ethics Committee Approval and Permissions Ethical approval for the study was obtained from Ankara University Animal Experiments Local Ethics Committee (2019-11-108), and the research permit was acquired from the General Directorate of Nature Conservation and National Parks of the Ministry of Agriculture and Forestry (21264211-288.04-2175385).

Conflict of Interests No conflict of interest or common interest has been declared by the authors.

Authors Contribution The authors contributed equally to the study. The authors read and approved the final manuscript

References

[1] Hewitt, G. M. (1996). Some genetic consequence of ice ages, and their role in divergence and speciation. *Biological Journal of the Linnean Society, 58*, 247-276. https://doi.org/10.1006/bijl.1996.0035

[2] Hewitt, G. M. (2011). Mediterranean Peninsulas: The Evolution of Hotspots. In: Zachos, F., Habel, J. (eds) Biodiversity Hotspots. Springer, Berlin, Heidelberg.

[3] Kryštufek, B., Tesakov, A. S., Lebedev, V. S., Bannikova, A. A., Abramson, N. I. & Shenbrot, G. (2020). Back to the future: the proper name for red-backed voles is *Clethrionomys tilesius* and not Myodes Pallas. *Mammalia, 84*, 214-217. https://doi.org/10.1515/mammalia-2019-0067

[4] Deffontaine, V., Libois, R., Kotlík, P., Sommer, R., Nieberding, C., Paradis, E., Searle, B. & Michaux, J. R. (2005). Beyond the Mediterranean peninsulas: evidence of central European glacial refugia for a temperate forest mammal species, the bank vole (*Clethrionomys glareolus*). *Molecular Ecology, 14,* 1727-1739. https://doi.org/10.1111/j.1365-294X.2005.02506.x

[5] Deffontaine, V., Ledevin, R., Fontaine, M. C., Quere, J. P., Renaud, S., Libois, R. & Michaux, J. R. (2009). A relict bank vole lineage highlights the biogeographic history of the Pyrenean region in Europe. *Molecular Ecology*, *18,* 2489–502. https://doi.org/10.1111/j.1365-294X.2009.04162.x

[6] Wójcik, J. M., Kawałko, A., Marková, S., Searle, J. B. & Kotlík, P. (2010). Phylogeographic signatures of northward post-glacial colonization from high latitude refugia: a case study of bank voles using museum specimens. *Journal of Zoology, 281,* 249-262. https://doi.org/10.1111/j.1469-7998.2010.00699.x

[7] Filipi, K., Marková, S., Searle, J. B. & Kotlík, P. (2015). Mitogenomic phylogenetics of the bank vole *Clethrionomys glareolus*, a model system for studying end glacial colonization of Europe. *Molecular Phylogenetics and Evolution, 82,* 245-57. https://doi.org/10.1016/j.ympev.2014.10.016

[8] Çolak, R., Karacan, G. O., Kandemir, İ., Çolak, E., Kankılıç, T., Nuri, Y. & Michaux, J. (2016). Genetic variations of Turkish bank vole, *Myodes glareolus* (Mammalia: Rodentia) inferred from mtDNA. *Mitochondrial DNA Part A,* 27*,* 4372-4379. https://doi.org/10.3109/19401736.2015.1089537

[9] Lu, T., Zhu, M., Yi, C., Si, C., Yang, C. & Chen, H. (2017). Complete mitochondrial genome of the gray redbacked vole (*Myodes rufocanus*) and a complete estimate of the phylogenetic relationships in Cricetidae. *Mitochondrial DNA Part A, 28,* 62-64. https://doi.org/10.3109/19401736.2015.1110799

[10] Ledevin, R., Chevret, P., Helvaci, Z., Michaux, J. R. & Renaud, S. (2018). Bank Voles in Southern Eurasia: Vicariance and Adaptation. *Journal of Mammalian Evolution, 25,* 119-129. https://doi.org/10.1007/s10914-016-9368-3

[11] Chiocchio, A., Colangelo, P., Aloise, G., Amori, G., Bertolino, S., Bisconti, R., Castiglia, R. & Canestrelli, D. (2019). Population genetic structure of the bank vole *Clethrionomys glareolus* within its glacial refugium in peninsular Italy. *Journal of Zoological Systematical and Evolutionary Research, 57,* 959-969. https://doi.org/10.1111/jzs.12289

[12] Kotlík, P., Deffontaine, V., Mascheretti, S., Zima, J., Michaux, J. R. & Searle, J. B. (2006). A northern glacial refugium for bank voles (*Clethrionomys glareolus*). *Proceedings of the National Academy of Sciences, 103,* 14860-14864. https://doi.org/10.1073/pnas.0603237103

[13] Amori, G., Contoli, L. & Nappi, A. (2008). Fauna d'Italia, Mammalia II: Erinaceomorpha, soricomorpha, lagomorpha, rodentia. Calderini, Milano.

[14] Osborn, D. J. (1962). Rodents of the subfamily Microtinae from Anatolia. *Journal of Mammalogy, 43,* 515-29. https://doi.org/10.2307/1376914

[15] Elmas, A. (2003). Late Cenozoic tectonics and stratigraphy of northwestern Anatolia: the effects of the North Anatolian Fault to the region. *International Journal of Earth Sciences, 92,* 380-396. https://doi.org/10.1007/s00531-003-0322-2

[16] Çolak, R., Kandemir, I., Karacan, G. O., Kankılıç, T., Çolak, E., Yiğit, N. & Özkurt, Ş. Ö. (2013). Allozyme variation in bank vole, *Clethrionomys glareolus* (Mammalia: Rodentia) in Northern

Anatolia. *Biochemical Systematics and Ecology, 50,* 304-309. https://doi.org/10.1016/j.bse.2013.04.013

[17] Beteş, D., Çolak, R., Karacan, G. O., Kandemir, I., Kankılıç, T. & Çolak, E. (2014). Population genetic variability of *Clethrionomys glareolus* (Schreber, 1780) (Mammalia: Rodentia) distributed in northern Anatolia as revealed by RAPD-PCR analysis. *Acta Zoologica Bulgarica, 66,* 31-7.

[18] İbiş, O., Koepfli, K-P., Özcan, S. & Tez, C. (2023). Whole mitogenomes of Turkish white-toothed shrews, genus *Crocidura* (Eulipotyphla: Soricidae), with new insights into the phylogenetic positions of *Crocidura leucodon* and the *Crocidura suaveolens* group. *Organisms Diversity & Evolution, 23,* 221-241. https://doi.org/10.1007/s13127-022-00579-3

[19] Tang, M. K., Jin, W., Tang, Y., Yan, C. C., Murphy, R. W., Sun, Z. Y., Zhang, X. Y., Zeng, T., Liao, R., Hou, Q. F., Yue, B. S. & Liu, S. Y. (2018). Reassessment of the taxonomic status of *Craseomys* and three controversial species of *Myodes* and *Alticola* (Rodentia: Arvicolinae). *Zootaxa, 4429,* 1-52. https://doi.org/10.11646/zootaxa.4429.1.1

[20] Doyle, J. J. (1990). Isolation of plant DNA from fresh tissue. *Focus, 12,* 13-15. https://doi.org/10.1080/09397140.2022.2058193

[21] Irwin, D. M., Kocher, T. D. & Wilson, A. C. (1991). Evolution of the Cytochrome-B Gene of Mammals. *Journal of Molecular Evolution, 32,* 128-144. https://doi.org/10.1007/BF02515385

[22] Folmer, O., Black, M., Hoeh, W., Lutz, R. & Vrijenhoek, R. (1994). DNA primers for amplification of mitochondrial cytochrome c oxidase subunit I from diverse metazoan invertebrates. *Molecular Marine Biology and Biotechnology, 3,* 294-299.

[23] Hall, T. A. (1999). BioEdit: a user-friendly biological sequence alignment, editor and analysis program for Windows 95/98/ NT. *Nucleic Acids Symposium Series, 41,* 95-98.

[24] Rozas, J., Ferrer-Mata, A., Sánchez-DelBarrio, J. C., Guirao-Rico, S., Librado, P., Ramos-Onsins, S. E. & Sánchez-Gracia, A. (2017). DnaSP 6: DNA sequence polymorphism analysis of large datasets. *Molecular Phylogenetics and Evolution, 34,* 3299-3302. https://doi.org/10.1093/molbev/msx248

[25] Nguyen, L-T., Schmidt, H. A., Haeseler, A. von. & Minh, B. Q. (2017). IQ-TREE: A fast and effective stochastic algorithm for estimating maximum likelihood phylogenies. *Molecular Biology and Evolution, 32,* 268-274. https://doi.org/10.1093/molbev/msu300

[26] Huelsenbeck, J. P. & Ronquist, F. (2001). MrBayes: Bayesian inference of phylogeny. *Bioinformatics, 17,* 754-755. https://doi.org/10.1093/bioinformatics/17.8.754

[27] Bandelt, H. J., Forster, P. & Röhl, A. (1999). Median-joining networks for inferring intraspecific phylogenies. *Molecular Biology and Evolution, 16,* 37-48. https://doi.org/10.1093/oxfordjournals.molbev.a026036

[28] Bohonak, A. J. (2002). IBD (Isolation by Distance): A program for analyses of isolation by distance. *Journal of Heredity, 93,* 153-154. https://doi.org/10.1093/jhered/93.2.153

[29] Excoffier, L. & Lischer, H. E. L. (2010). Arlequin suite ver 3.5: A new series of programs to perform population genetics analyses under Linux and Windows. *Molecular Ecology Resources, 10,* 564-567. https://doi.org/10.1111/j.1755-0998.2010.02847.x

[30] Tajima, F. (1989). The effect of change in population size on DNA polymorphism. *Genetics, 123,* 597-601. https://doi.org/10.1093/genetics/123.3.597

[31] Fu, Y. X. (1997). Statistical tests of neutrality of mutations against population growth, hitchhiking and background selection. *Genetics, 147,* 915-25. https://doi.org/10.1093/genetics/147.2.915

[32] Honda, A., Murakami, S., Harada, M., Tsuchiya, K, Kinoshita, G. & Suzuki, H. (2019). Late Pleistocene climate change and population dynamics of Japanese *Myodes* voles inferred from mitochondrial cytochrome b sequences. *Journal of Mammalogy, 100,* 1156-1168. https://doi.org/10.1093/jmammal/gyz093

[33] Suzuki, Y., Tomozawa, M., Koizumi, Y., Tsuchiya, K. & Suzuki, H. (2015). Estimating the molecular evolutionary rates of mitochondrial genes referring to quaternary ice age events with inferred population expansions and dispersals in Japanese Apodemus. *BMC Evolutionary Biology, 15,* 187. https://doi.org/10.1186/s12862-015-0463-5

[34] Hanazaki, K., Tomozawa, M., Suzuki, Y., Kinoshita, G., Yamamoto, M., Irino, T. & Suzuki, H. (2017). Estimation of evolutionary rates of mitochondrial DNA in two Japanese wood mouse species based on calibrations with quaternary environmental changes. *Zoological Science, 34,* 201-210. https://doi.org/10.2108/zs160169

[35] Ho, S. Y. W., Phillips, M. J., Cooper, A. & Drummond, A. J. (2005). Time dependency of molecular rate estimates and systematic overestimation of recent divergence times. *Molecular Biology and Evolution, 22,* 1561-1568. https://doi.org/10.1093/molbev/msi145

[36] Kotlík, P., Deffontaine, V., Mascheretti, S., Zima, J., Michaux, J. R. & Searle, J. B. (2006). A northern glacial refugium for bank voles (*Clethrionomys glareolus*). *Proceedings of the National Academy of Sciences, 103,* 14860-14864. https://doi.org/10.1073/pnas.0603237103

[37] Avise, J. C. (2000). Phylogeography: The History and Formation of Species. Harvard University Press, Cambridge, Massachussets.

[38] Searle, J. B., Kotlík, P., Rambau, R. V., Marková, S., Herman, J. S., and McDevitt, A. D. (2009). The Celtic fringe of Britain: insights from small mammal phylogeography. *Proceedings of the Royal Society B: Biological Sciences, 276,* 4287-4294. https://doi.org/10.1098/rspb

[39] Kotlík, P., Marková, S., Konczal, M., Babik, W., Searle, J. B. (2018). Genomics of end-Pleistocene population replacement in a small mammal. *Proceedings of the Royal Society B: Biological Science, 285,* 20172624. https://doi.org/10.1098/rspb.2017.2624

[40] Marková, S., Horníková, M., Lanier, H. C., Henttonen, H., Searle, J. B., Weider, L. J. & Kotlík, P. (2020). High genomic diversity in the bank vole at the northern apex of a range expansion: The role of multiple colonizations and end-glacial refugia. *Molecular Ecology, 29,* 1730-1744. https://doi.org/10.1111/mec.15427

[41] Kotlík, P., Marková, S., Vojtek, L., Stratil, A., Šlechta, V., Hyršl, P. & Searle, J. B. (2014). Adaptive phylogeography: functional divergence between haemoglobins derived from different glacial refugia in the bank vole. *Proceedings of the Royal Society B: Biological Science, 281,* 20140021. https://doi.org/10.1098/rspb.2014.0021

[42] Ledevin, R., Chevret, P., Helvaci, Z., Michaux, J.R. & Renaud, S. (2018). Bank Voles in Southern Eurasia: Vicariance and Adaptation. *Journal of Mammalian Evolution,* 25, 119-129. https://doi.org/10.1007/s10914-016-9368-3

[43] İbiş, O., Selçuk, A. Y., Teber, S., Baran, M., Kaya, A., Özcan, S., Kefelioğlu, H. & Tez, C. (2022). Complete mitogenomes of Turkish tree squirrels, *Sciurus anomalus* and *S. vulgaris*, (Sciuridae:

Rodentia: Mammalia) and their phylogenetic status within the tribe Sciurini, *Gene, 841*. https://doi.org/10.1016/j.gene.2022.146773

[44] Demirtaş, S. (2022). Phylogeographic structure of the Persian Squirrel, *Sciurus anomalus* Güldenstädt, 1785 (Mammalia: Rodentia) in the Anatolian Peninsula, based on mitochondrial DNA sequences: implications for metapopulation. *Zoology in the Middle East, 68,* 95-108. https://doi.org/10.1080/09397140.2022.2058193

[45] Kankılıç, T., Şeker, P. S., Erdik, A. C., Kankılıç, T., Selvi, E., Yiğit, N. & Çolak, E. (2018). Determination of genetic variations in the genus *Dryomys* Thomas, 1906 (Rodentia: Gliridae) distributed in Anatolia using NADH dehydrogenase 1 (ND1) gene. *Mitochondrial DNA Part A, 29,* 933-942. https://doi.org/10.1080/24701394.2017.1389915

[46] Neumann, K., Yiğit, N., Fritzsche, P., Çolak, E., Feoktistova, N., Surov, A. & Michaux, J. (2017). Genetic structure of the Turkish hamster (*Mesocricetus brandti*). *Mammalian Biology, 86,* 84-91. https://doi.org/10.1016/j.mambio.2017.06.004

[47] Baker, R. J. & Bradley, R. D. (2006). Speciation in Mammals and the Genetic Species Concept. *Journal of Mammalogy, 87,* 643-662. https://doi.org/10.1644/06-MAMM-F-038R2.1

[48] Ramírez-Soriano, A., Ramos-Onsins, S. E., Rozas, J., Calafell, F. & Navarro, A. (2008). Statistical power analysis of neutrality tests under demographic expansions, contractions and bottlenecks with recombination. *Genetics, 179,* 555-67. https://doi.org/10.1534/genetics.107.083006

[49] Riemsdijk, I. V., Arntzen, J. W., Bogaerts, S., Franzen, M., Litvinchuk, S. N., Olgun, K. & Wielstra, B. (2018). The Near East as a cradle of biodiversity: A phylogeography of banded newts (Genus *Ommatotriton*) reveals extensive inter and intraspecific genetic differentiation. *Molecular Phylogenetics and Evolution, 114,* 73-81. https://doi.org/10.1016/j.ympev.2017.05.028

[50] Wielstra, B., Espregueira Themudo, G., Güclü, Ö., Olgun, K., Poyarkov, N. A. & Arntzen, A. Z. (2010). Cryptic crested newt diversity at the Eurasian transition: the mitochondrial DNA phylogeography of Near Eastern Triturus newts. *Molecular Phylogenetics and Evolution, 56,* 888-896. https://doi.org/10.1016/j.ympev.2010.04.030

[51] Wielstra, B., Baird, A. B. & Arntzen, J. W. (2013). A multimarker phylogeography of crested newts (*Triturus cristatus* superspecies) reveals cryptic species. *Molecular Phylogenetics and Evolution, 67,* 167-175. https://doi.org/10.1016/j.ympev.2013.01.009

[52] Wielstra, B., Burke, T., Butlin, R. K., Avcı, A., Üzüm, N., Bozkurt, E., Olgun, K. & Arntzen, J. W. (2017). A genomic footprint of hybrid zone movement in crested newts. *Evolution Letters, 1*(2), 93-101. https://doi.org/10.1002/evl3.9

[53] Helvacı, Z., Renaud, S., Ledevin, R., Adriaens, D., Michaux, J., Çolak, R., Kankılıç, T., Kandemir, İ., Yiğit, N. & Çolak, E. (2012). Morphometric and genetic structure of the edible dormouse (*Glis glis*): a consequence of forest fragmentation in Anatolia. *Biological Journal of the Linnean Society, 107,* 611-623. https://doi.org/10.1111/j.1095-8312.2012.01952.x

[54] Kaya, S. & Çıplak, B. (2017). Phylogeography and taxonomy of the *Psorodonotus caucasicus* (Orthoptera, Tettigoniidae) group: independent double invasion of the Balkans from the Caucasus. *Systematic Entomology, 42,* 118-133. https://doi.org/10.1111/syen.12197

[55] Karacan, G. O., Çolak, R. & Çolak, E. (2021). The roles of possible geographic barriers and geological events on the phylogeographic structure of the Eastern broad toothed field Mouse (*Apodemus mystacinus*). *Mammalia, 85,* 401-411. https://doi.org/10.1515/mammalia-2020-0017

Sinopfbd, 2024; 9(2): 502-515 **https://doi.org/10.33484/sinopfbd.1444748**

Sinop Üniversitesi Fen Bilimleri Dergisi
Sinop Uni J Nat Sci
E-ISSN: 2564-7873

https://dergipark.org.tr/tr/pub/sinopfbd

On The Non-Newtonian Padovan and Non-Newtonian Perrin Numbers

Orhan DİŞKAYA

How to cite: Dişkaya, O. (2024). On the non-Newtonian Padovan and non-Newtonian Perrin numbers. *Sinop Üniversitesi Fen Bilimleri Dergisi*, *9*(2), 502-515. https://doi.org/10.33484/sinopfbd.1444748

Research Article

Corresponding Author
Orhan DİŞKAYA
orhandiskaya@mersin.edu.tr

ORCID of the Authors
O.D: 0000-0001-5698-7834

Received: 29.02.2024
Accepted: 14.10.2024

Abstract

In this work, we introduce a novel version of Padovan and Perrin numbers which we refer to as non-Newtonian Padovan and non-Newtonian Perrin numbers. Furthermore, we examine about a number of their properties. Additionally, we provide a variety of identities and formulas involving these new kinds, including the Binet-like formulas, the generating functions, the partial sum formulas, and the binomial sum formulas.

Keywords: Non-Newtonian calculus, Padovan numbers, Binet formula, generating functions, binomial sum

Newtonian Olmayan Padovan ve Newtonian Olmayan Perrin Sayıları Hakkında

Mersin University, Faculty of Science, Department of Mathematics, Mersin, Türkiye

Öz

Bu çalışmada Newtonian olmayan Padovan ve Newtonian olmayan Perrin sayıları olarak adlandırdığımız Padovan ve Perrin sayılarının yeni bir versiyonunu tanıtıyoruz. Ayrıca bunların bazı özelliklerini de inceliyoruz. Ek olarak, Binet benzeri formüller, üreteç fonksiyonları, kısmi toplam formülleri ve binom toplam formülleri de dahil olmak üzere bu yeni türleri içeren çeşitli özdeşlikler ve formüller sağlıyoruz.

Anahtar Kelimeler: Newtonian olmayan analiz, Padovan sayıları, Binet formülü, üreteç fonksiyonları, binom toplamı

Introduction

Numerous calculi with various features have been developed since Newton and Leibnitz established modern calculus. As an alternative to Newton and Leibniz's standard calculus, Grossman and Katz created a new family of calculi known as non-Newtonian calculus, and, defined modern forms of integrals and derivatives that converted addition and subtraction operations into multiplication and division operations [1]. In classical calculus, every property finds an analogue in non-Newtonian calculus. Non-Newtonian calculus offers a distinct approach to problems traditionally tackled by calculus. For certain scenarios, such as those involving wage rates (in dollars, euros, etc.), proponents suggest employing bigeometric calculus, a type of non-Newtonian calculus, instead of the conventional Newtonian approach [1–3].

Duyar and Sağır aimed to generalize the traditional Lebesgue measure on real numbers to the context of non-Newtonian real numbers. To achieve this, they introduced the concept of Lebesgue measure for both open and closed sets in the non-Newtonian framework and explored its fundamental properties [4].

Erdoğan and Duyar introduced non-Newtonian improper integrals and investigated their convergence conditions. Additionally, key theorems such as the second mean value theorem and the intermediate value theorem were proved within the non-Newtonian framework to provide convergence tests [5].

Değirmen and Duyar introduced one of these gains by introducing non-Newtonian Fibonacci and non-Newtonian Lucas numbers. Additionally, they provide some formulas and identities such as the Binet formula, d'Ocagne identity, Cassini identity, and Gelin-Cesaro identity, and find the functions that generate these numbers [6].

Yağmur introduced a new type of Pell and Pell-Lucas numbers in terms of non-Newtonian calculus, and studied some significant identities and formulas for classical Pell and Pell-Lucas numbers [7].

In this research endeavor, we commence by providing essential insights into non-Newtonian calculus. Subsequently, we present the definition and certain properties of Padovan numbers, establishing their connection with non-Newtonian calculus. We then delve into an examination of various identities associated with these numbers. An injective function is called a generator, and its codomain is a subset of $\mathbb{R}$, and whose domain is $\mathbb{R}$. There is precisely one arithmetic produced by each generator, and there is exactly one generator that produces each arithmetic. We select the exponential function from $\mathbb{R}$ to the set $\mathbb{R}^+$ as a generator, in other words,

$$\alpha : \mathbb{R} \to \mathbb{R}^+, \quad \lambda \rightarrowtail \alpha(\lambda) = e^{\lambda} = \mu,$$
$$\alpha^{-1} : \mathbb{R}^+ \to \mathbb{R}, \quad \lambda \rightarrowtail \alpha^{-1}(\lambda) = \ln \mu = \lambda.$$

I is referred to as the unit function, whose inverse is oneself, if $I(\lambda) = \lambda$ for all $\lambda \in \mathbb{R}$. The definition of the non-Newtonian real number set $\mathbb{R}(\mathcal{N})$ is as follows:

$$\mathbb{R}(\mathcal{N}) := \{\alpha(\lambda) : \lambda \in \mathbb{R}\}.$$

It is important to recognize that every concept in classical arithmetic has an inherent equivalent in $\alpha-$arithmetic. As an example, the $\alpha-$integers shown to be as follows:

$$..., \alpha(-3), \alpha(-2), \alpha(-1), \alpha(0), \alpha(1), \alpha(2), \alpha(3), \ldots.$$

For every integer m, we set $\dot{m} = \alpha(m)$. Naturally, if $\dot{m}$ is an $\alpha-$positive integer, then

$$\dot{m} = \underbrace{\dot{1}\dot{+}\ldots\dot{+}\dot{1}}_{m \quad \text{terms}}.$$

For a generator α with range $A = \mathbb{R}(\mathcal{N})$, which is a subset of the real numbers, $\alpha-$arithmetic denotes arithmetic operations defined on the domain A as follows: For any generator α and $\lambda, \mu \in \mathbb{R}(\mathcal{N})$,

$$\begin{aligned}
\alpha - addition &\rightarrow \lambda\dot{+}\mu = \alpha\{\alpha^{-1}(\lambda) + \alpha^{-1}(\mu)\},\\
\alpha - subtraction &\rightarrow \lambda\dot{-}\mu = \alpha\{\alpha^{-1}(\lambda) - \alpha^{-1}(\mu)\},\\
\alpha - multiplication &\rightarrow \lambda\dot{\times}\mu = \alpha\{\alpha^{-1}(\lambda) \times \alpha^{-1}(\mu)\},\\
\alpha - division &\rightarrow \lambda\dot{/}\mu = \alpha\{\alpha^{-1}(\lambda) \div \alpha^{-1}(\mu)\} = \frac{\lambda}{\mu}\mathcal{N},\\
\alpha - order &\rightarrow \lambda\dot{<}\mu = \alpha\{\alpha^{-1}(\lambda) < \alpha^{-1}(\mu)\}.
\end{aligned}$$

Specifically, selecting $\alpha-$generator I, which is the identity function $\alpha(t) = t$ for all $t \in \mathbb{R} \Rightarrow \alpha^{-1}(t) = t$, makes it evident that $\alpha-$arithmetic is indeed classical arithmetic. Assuming that the $\alpha-$generator is *exp* and that $\alpha(k) = e^k$ for $k \in \mathbb{R}$, $\alpha^{-1}(k) = \ln k$, $\alpha-$arithmetic transforms into geometric arithmetic as follows:

$$\begin{aligned}
Geometric \quad addition &\rightarrow \lambda\dot{+}\mu = \alpha\{\alpha^{-1}(\lambda) + \alpha^{-1}(\mu)\} = e^{\{\ln\lambda + \ln\mu\}} = \lambda\cdot\mu,\\
Geometric \quad subtraction &\rightarrow \lambda\dot{-}\mu = \alpha\{\alpha^{-1}(\lambda) - \alpha^{-1}(\mu)\} = e^{\{\ln\lambda - \ln\mu\}} = \frac{\lambda}{\mu} \quad (\mu \neq 0),\\
Geometric \quad multiplication &\rightarrow \lambda\dot{\times}\mu = \alpha\{\alpha^{-1}(\lambda) \times \alpha^{-1}(\mu)\} = e^{\{\ln\lambda \times \ln\mu\}} = \lambda^{\ln\mu} = \mu^{\ln\lambda},\\
Geometric \quad division &\rightarrow \lambda\dot{/}\mu = \alpha\{\alpha^{-1}(\lambda) \div \alpha^{-1}(\mu)\} = e^{\{\ln\lambda \div \ln\mu\}} = \lambda^{\{1\div\ln\mu\}} \quad (\mu \neq 1).
\end{aligned}$$

These operations define α-arithmetic, where α is typically the exponential function in this context.
Now, we create the non-Newtonian real field $\mathbb{R}(\mathcal{N})$ and provide some associated characteristics.
Definition of the dual operations addition and multiplication for the set of non-Newtonian real numbers $\mathbb{R}(\mathcal{N})$ as follows, respectively:

$$\begin{aligned}
\dot{+} :&\mathbb{R}(\mathcal{N}) \times \mathbb{R}(\mathcal{N}) \rightarrow \mathbb{R}(\mathcal{N})\\
&(\lambda,\mu) \longmapsto \lambda\dot{+}\mu = \alpha\{\alpha^{-1}(\lambda) + \alpha^{-1}(\mu)\},\\
\dot{\times} :&\mathbb{R}(\mathcal{N}) \times \mathbb{R}(\mathcal{N}) \rightarrow \mathbb{R}(\mathcal{N})\\
&(\lambda,\mu) \longmapsto \lambda\dot{\times}\mu = \alpha\{\alpha^{-1}(\lambda) \times \alpha^{-1}(\mu)\}.
\end{aligned}$$

It is demonstrable that $\left(\mathbb{R}(\mathcal{N}), \dot{+}, \dot{\times}\right)$ is an complete field by normal checking, so we omit out the specifics. Let $A \subset \mathbb{R}(\mathcal{N})$ be a set of integers in the extended real numbers [3].
The $v-$th $\alpha-$power of $\lambda \in \mathbb{R}(\mathcal{N})$ for a given integer v is represented by

$$\lambda^{v_{\mathcal{N}}} = \underbrace{\lambda\dot{\times}\lambda\dot{\times}\ldots\dot{\times}\lambda}_{v \quad \text{terms}}.$$

The α-factorial of a given positive integer v is represented by

$$\dot{v}!_{\mathcal{N}} = \dot{v}\dot{\times}(\dot{v}\dot{-}\dot{1})\dot{\times}(\dot{v}\dot{-}\dot{2})\dot{\times}\ldots\dot{\times}\dot{2}\dot{\times}\dot{1}.$$

The α-binomial of a given positive integer u and v is represented by

$$\binom{\dot{u}}{\dot{v}}_{\mathcal{N}} = \frac{\dot{u}!_{\mathcal{N}}}{\dot{v}!_{\mathcal{N}} \dot{\times} (\dot{u} \dot{-} \dot{v})!_{\mathcal{N}}} \mathcal{N}.$$

The α-binomial sum of a given integer λ, μ and u is represented by

$$(\dot{\lambda} \dot{+} \dot{\mu})^{u_{\mathcal{N}}} =_{\mathcal{N}} \sum_{v=0}^{u} \binom{\dot{u}}{\dot{v}}_{\mathcal{N}} \dot{\times} \dot{\lambda}^{v_{\mathcal{N}}} \dot{\times} \dot{\mu}^{(u-v)_{\mathcal{N}}}. \tag{1}$$

The notation $\sqrt{\lambda}^{\mathcal{N}}$ will be utilized for $s = \alpha\{\sqrt{\alpha^{-1}(\lambda)}\}$ where every s is $\alpha-$nonnegative integer. This indicates that $s^{2_{\mathcal{N}}} = \lambda$ is the only $\alpha-$nonnegative integer whose $\alpha-$square equals λ. Additionally, $\alpha(-\lambda) = \alpha\{-\alpha^{-1}(\dot{\lambda})\} = \dot{-}\dot{\lambda}$ all $\lambda \in \mathbb{R}$.

The Padovan and Perrin sequences are defined as follows. The Padovan sequence $\{P_v\}_{v\geq 0}$ and Perrin sequence $\{R_v\}_{v\geq 0}$ are defined by the third order recurrences, respectively,

$$P_{v+3} = P_{v+1} + P_v, \tag{2}$$

$$R_{v+3} = R_{v+1} + R_v, \tag{3}$$

with the initial conditions $P_0 = P_1 = P_2 = 1$ and $R_0 = 3$, $R_1 = 0$, $R_2 = 2$, respectively [8, 9]. The Padovan and Perrin sequences appear as sequences A000931 and A001608 on the On-Line Encyclopedia of Integer Sequences (OEIS), respectively [10]. The first few values of these sequences are $1, 1, 1, 2, 2, 3, 4, 5, 7, 9, 12, 16, 21, 28, 37$ and $3, 0, 2, 3, 2, 5, 5, 7, 10, 12, 17, 22$, respectively. The unique real root of the characteristic equation of these sequences is known as the plastic number:

$$t^3 - t - 1 = 0$$

with a value of

$$\sqrt[3]{\frac{1}{2} + \frac{1}{6}\sqrt{\frac{23}{3}}} + \sqrt[3]{\frac{1}{2} - \frac{1}{6}\sqrt{\frac{23}{3}}} \approx 1.324718.$$

By designating its roots as δ, η, and γ, the subsequent equalities can be obtained

$$\delta + \eta + \gamma = 0,$$

$$\delta\eta + \delta\gamma + \eta\gamma = -1,$$

$$\delta\eta\gamma = 1.$$

In addition, the Binet-like formulas for the Padovan and Perrin sequences are as follows:

$$P_v = a\delta^v + b\eta^v + c\gamma^v, \tag{4}$$

$$R_v = \delta^v + \eta^v + \gamma^v, \tag{5}$$

respectively, where

$$a = \frac{(\eta - 1)(\gamma - 1)}{(\delta - \eta)(\delta - \gamma)}, \quad b = \frac{(\delta - 1)(\gamma - 1)}{(\eta - \delta)(\eta - \gamma)}, \quad c = \frac{(\delta - 1)(\eta - 1)}{(\gamma - \delta)(\gamma - \eta)}.$$

It is commonly known that the following identities are recognized based on [11, 12]:

$$P_{-v-7} = P_v^2 - P_{v+1}P_{v-1}, \tag{6}$$

$$P_v = P_{v-1} + P_{v-5}, \tag{7}$$

$$R_v = P_{v-10} + P_{v+1}, \tag{8}$$

$$P_{v-5}P_{-v-5} + P_{v-3}P_{-v-4} + P_{v-4}P_{-v-3} = 1, \tag{9}$$

$$P_v = P_{u-1}P_{v-u-4} + P_{u+1}P_{v-u-3} + P_uP_{v-u-2}, \tag{10}$$

$$\sum_{v=1}^{u} P_v = P_{u+5} - 3, \tag{11}$$

$$\sum_{v=1}^{u} R_v = R_{u+5} - 5, \tag{12}$$

$$\sum_{v=0}^{\infty} P_v x^v = \frac{1 + x}{1 - x^2 - x^3}, \tag{13}$$

$$\sum_{v=0}^{\infty} R_v x^v = \frac{3 - x^2}{1 - x^2 - x^3}, \tag{14}$$

$$\sum_{v=0}^{\infty} \frac{P_v}{v!} x^v = ae^{\delta x} + be^{\mu x} + ce^{\gamma x}, \tag{15}$$

$$\sum_{v=0}^{\infty} \frac{R_v}{v!} x^v = e^{\delta x} + e^{\mu x} + e^{\gamma x}. \tag{16}$$

In recent years, numerous studies on Padovan numbers have been published. For further information, please refer to the works cited in [13–19].

Some Properties of the Non-Newtonian Padovan and Non-Newtonian Perrin Numbers

This section provides a novel interpretation of the definitions of a non-Newtonian Padovan number and a non-Newtonian Perrin number from a different perspective. Along with dealing with the non-Newtonian versions of various formulas and identities, we also demonstrate their links by comparing them in an analogy with several well-known identities and formulas for their classical equivalents.

Definition 1. The non-Newtonian Padovan and non-Newtonian Perrin numbers are defined by

$$\mathcal{N}P_v = \dot{P}_v = \alpha(P_v) \quad \text{and} \quad \mathcal{N}R_v = \dot{R}_v = \alpha(R_v),$$

respectively, where the $v-$th Padovan and Perrin numbers are P_v and R_v, respectively. The $\mathcal{N}P$ and $\mathcal{N}R$ represent the set of the non-Newtonian Padovan and non-Newtonian Perrin numbers, respectively. That is,

$$\mathcal{N}P = \{\mathcal{N}P_v : v \in \mathbb{N}\} = \{\dot{1}, \dot{1}, \dot{1}, \dot{2}, \dot{2}, \dot{3}, \dot{4}, \dot{5}, \dot{7}, \dot{9}, \dot{12}, \dot{16}, ..., \dot{P}_v, ...\}$$

and

$$\mathcal{N}R = \{\mathcal{N}R_v : n \in \mathbb{N}\} = \{\dot{3}, \dot{0}, \dot{2}, \dot{3}, \dot{2}, \dot{5}, \dot{5}, \dot{7}, \dot{10}, \dot{12}, \dot{17}, \dot{22}, ..., \dot{R}_v, ...\}$$

Regarding classical arithmetic, we obtain Padovan and Perrin numbers if we utilize the generator I specified by $\alpha(x) = x$ for any $x \in \mathbb{R}$.

Additionally, by selecting the generator *exp*, which is defined as $\alpha(x) = e^x$ for any $x \in \mathbb{R}$, we may derive the following Padovan and Perrin numbers in terms of geometric arithmetic:

$$\begin{aligned} \mathcal{N}GP &= \{\alpha(P_v) : v \in \mathbb{N}\} \\ &= \{e^{P_v} : v \in \mathbb{N}\} \\ &= \{e^1, e^1, e^1, e^2, e^2, e^3, e^4, e^5, e^7, e^9, e^{12}, e^{16}, ..., e^{P_v}, ...\} \end{aligned}$$

and

$$\begin{aligned} \mathcal{N}GR &= \{\alpha(R_v) : v \in \mathbb{N}\} \\ &= \{e^{R_v} : v \in \mathbb{N}\} \\ &= \{e^3, e^0, e^2, e^3, e^2, e^5, e^5, e^7, e^{10}, e^{12}, e^{17}, e^{22}, ..., e^{R_v}, ...\}. \end{aligned}$$

Now, we emphasize on a few relations concerning non-Newtonian Padovan and non-Newtonian Perrin numbers, as well as their respective relationships.

Theorem 1. For $v, u \geq 0$, the following identities valid:

i) $\mathcal{N}P_v \dot{+} \mathcal{N}P_{v+1} = \mathcal{N}P_{v+3}$,

ii) $\mathcal{N}P_{v-1}\dot{+}\mathcal{N}P_{v-5}=\mathcal{N}P_{v}$,

iii) $\mathcal{N}R_{v}\dot{+}\mathcal{N}R_{v+1}=\mathcal{N}R_{v+3}$,

iv) $\mathcal{N}P_{v-10}\dot{+}\mathcal{N}P_{v+1}=\mathcal{N}R_{v}$,

v) $\mathcal{N}P_{v}^{2}\dot{-}\mathcal{N}P_{v+1}\dot{\times}\mathcal{N}P_{v+1}=\mathcal{N}P_{-v-7}$,

vi) $\mathcal{N}P_{v-5}\dot{\times}\mathcal{N}P_{-v-5}\dot{+}\mathcal{N}P_{v-3}\dot{\times}\mathcal{N}P_{-v-4}\dot{+}\mathcal{N}P_{v-4}\dot{\times}\mathcal{N}P_{-v-3}=1$,

vii) $\mathcal{N}P_{v-1}\dot{\times}\mathcal{N}P_{u-v}\dot{+}\mathcal{N}P_{v+1}\dot{\times}\mathcal{N}P_{u-v+1}\dot{+}\mathcal{N}P_{v}\dot{\times}\mathcal{N}P_{u-v+2}=\mathcal{N}P_{u}$.

Proof. The proofs of i, ii, iii, iv, v and vi are obvious based on the addition and subtraction properties of non-Newtonian real numbers by using expressions (2), (7), (3), (8), (6) and (9), respectively. The proof of equality vii is shown by using expression (10) as follows:

$$
\begin{aligned}
&\mathcal{N}P_{v-1}\dot{\times}\mathcal{N}P_{u-v}\dot{+}\mathcal{N}P_{v+1}\dot{\times}\mathcal{N}P_{u-v+1}\dot{+}\mathcal{N}P_{v}\dot{\times}\mathcal{N}P_{u-v+2}\\
&=\alpha(P_{v-1})\dot{\times}\alpha(P_{u-v})\dot{+}\alpha(P_{v+1})\dot{\times}\alpha(P_{u-v+1})\dot{+}\alpha(P_{v})\dot{\times}\alpha(P_{u-v+2})\\
&=\alpha\{\alpha^{-1}\alpha(P_{v-1})\times\alpha^{-1}\alpha(P_{u-v})\}\dot{+}\alpha\{\alpha^{-1}\alpha(P_{v+1})\times\alpha^{-1}\alpha(P_{u-v+1})\}\\
&\dot{+}\alpha\{\alpha^{-1}\alpha(P_{v})\times\alpha^{-1}\alpha(P_{u-v+2})\}\\
&=\alpha\{\alpha^{-1}\alpha\{\alpha^{-1}\alpha(P_{v-1})\times\alpha^{-1}\alpha(P_{u-v})\}+\alpha^{-1}\alpha\{\alpha^{-1}\alpha(P_{v+1})\times\alpha^{-1}\alpha(P_{u-v+1})\}\}\\
&\dot{+}\alpha\{\alpha^{-1}\alpha(P_{v})\times\alpha^{-1}\alpha(P_{u-v+2})\}\\
&=\alpha\{\alpha^{-1}\alpha\{\alpha^{-1}\alpha\{\alpha^{-1}\alpha(P_{v-1})\times\alpha^{-1}\alpha(P_{u-v})\}+\alpha^{-1}\alpha\{\alpha^{-1}\alpha(P_{v+1})\times\alpha^{-1}\alpha(P_{u-v+1})\}\}\\
&+\alpha^{-1}\alpha\{\alpha^{-1}\alpha(P_{v})\times\alpha^{-1}\alpha(P_{u-v+2})\}\}\\
&=\alpha(P_{v-1}P_{u-v}+P_{v+1}P_{u-v+1}+P_{v}P_{u-v+2})\\
&=\alpha(P_{u})\\
&=\mathcal{N}P_{u}.
\end{aligned}
$$

Remark 1. The non-Newtonian characteristic equation of the recurrence relation in the i-th item of the above theorem is as follows:

$$\dot{t}^{3_{\mathcal{N}}}=\dot{t}\dot{+}\dot{1}. \tag{17}$$

If $\mathcal{N}P_{v}=\dot{t}^{v_{\mathcal{N}}}$ is taken in the recurrence relation in the i-th

$$\dot{t}^{v+3_{\mathcal{N}}}=\dot{t}^{v+1_{\mathcal{N}}}\dot{+}\dot{t}^{v_{\mathcal{N}}}$$

is obtained.
Thus, we get the result by simplifying the $\dot{t}^{v_{\mathcal{N}}}$'s.

Theorem 2. For all $v\geq 0$, the Binet-like formulas for $\mathcal{N}P_{v}$ and $\mathcal{N}R_{v}$ are given by

$$\mathcal{N}P_{v}=\dot{a}\dot{\times}\dot{\delta}^{v_{N}}\dot{+}\dot{b}\dot{\times}\dot{\eta}^{v_{N}}\dot{+}\dot{c}\dot{\times}\dot{\gamma}^{v_{N}} \tag{18}$$

and

$$\mathcal{N}R_v = \dot{\delta}^{v_N} \dot{+} \dot{\eta}^{v_N} \dot{+} \dot{\gamma}^{v_N}, \tag{19}$$

respectively, where

$$\dot{a} = \frac{(\dot{\eta} \dot{-} \dot{1}) \dot{\times} (\dot{\gamma} \dot{-} \dot{1})}{(\dot{\delta} \dot{-} \dot{\eta}) \dot{\times} (\dot{\delta} \dot{-} \dot{\gamma})}\mathcal{N}, \quad \dot{b} = \frac{(\dot{\delta} \dot{-} \dot{1}) \dot{\times} (\dot{\gamma} \dot{-} \dot{1})}{(\dot{\eta} \dot{-} \dot{\delta}) \dot{\times} (\dot{\eta} \dot{-} \dot{\gamma})}\mathcal{N} \quad \text{and} \quad \dot{c} = \frac{(\dot{\delta} \dot{-} \dot{1}) \dot{\times} (\dot{\eta} \dot{-} \dot{1})}{(\dot{\gamma} \dot{-} \dot{\delta}) \dot{\times} (\dot{\gamma} \dot{-} \dot{\eta})}\mathcal{N}.$$

Also, $\dot{\delta}$, $\dot{\eta}$ and $\dot{\gamma}$ are roots of the characteristic equation $\dot{t}^{3_N} \dot{-} \dot{t} \dot{-} \dot{1} = \dot{0}$.

Proof. By using the equation (4) for Padovan numbers, we obtain

$$\begin{aligned}
&\dot{a} \dot{\times} \dot{\delta}^{v_N} \dot{+} \dot{b} \dot{\times} \dot{\eta}^{v_N} \dot{+} \dot{c} \dot{\times} \dot{\gamma}^{v_N} \\
&= \alpha\{\alpha^{-1}(\dot{a}) \times \alpha^{-1}(\alpha\{(\alpha^{-1}(\dot{\delta}))^v\})\} \dot{+} \alpha\{\alpha^{-1}(\dot{b}) \times \alpha^{-1}(\alpha\{(\alpha^{-1}(\dot{\eta}))^v\})\} \\
&\dot{+} \alpha\{\alpha^{-1}(\dot{c}) \times \alpha^{-1}(\alpha\{(\alpha^{-1}(\dot{\gamma}))^v\})\} \\
&= \alpha\{\alpha^{-1}(\alpha\{\alpha^{-1}(\dot{a}) \times \alpha^{-1}(\alpha\{(\alpha^{-1}(\dot{\delta}))^v\})\}) + \alpha^{-1}(\alpha\{\alpha^{-1}(\dot{b}) \times \alpha^{-1}(\alpha\{(\alpha^{-1}(\dot{\eta}))^v\})\}) \\
&+ \alpha^{-1}(\alpha\{\alpha^{-1}(\dot{c}) \times \alpha^{-1}(\alpha\{(\alpha^{-1}(\dot{\gamma}))^v\})\})\} \\
&= \alpha\{\alpha^{-1}(\dot{a}) \times (\alpha^{-1}(\dot{\delta}))^v + \alpha^{-1}(\dot{b}) \times (\alpha^{-1}(\dot{\eta}))^v + \alpha^{-1}(\dot{c}) \times (\alpha^{-1}(\dot{\gamma}))^v\} \\
&= \alpha\{a\delta^v + b\eta^v + c\gamma^v\} \\
&= \alpha\{P_v\} = \mathcal{N}P_v.
\end{aligned}$$

On the other hand, by performing the equation (5) for the Perrin numbers, one can easily observe that

$$\begin{aligned}
\dot{\delta}^{v_N} \dot{+} \dot{\eta}^{v_N} \dot{+} \dot{\gamma}^{v_N} &= \alpha\{(\alpha^{-1}(\dot{\delta}))^v\} \dot{+} \alpha\{(\alpha^{-1}(\dot{\eta}))^v\} \dot{+} \alpha\{(\alpha^{-1}(\dot{\gamma}))^v\} \\
&= \alpha\{\alpha^{-1}(\alpha\{\alpha^{-1}(\alpha\{(\alpha^{-1}(\dot{\delta}))^v\}) + \alpha^{-1}(\alpha\{(\alpha^{-1}(\dot{\eta}))^v\})\}) + \alpha^{-1}(\alpha\{(\alpha^{-1}(\dot{\gamma}))^v\})\} \\
&= \alpha\{\delta^v + \eta^v + \gamma^v\} \\
&= \alpha\{R_v\} = \mathcal{N}R_v.
\end{aligned}$$

Theorem 3. The generating functions for $\mathcal{N}P_v$ and $\mathcal{N}R_v$ are as follows, respectively,

i.

$${}_{\mathcal{N}}\sum_{v=0}^{\infty}(\mathcal{N}P_v \dot{\times} t^{v_{\mathcal{N}}}) = \frac{\dot{1} \dot{+} t}{\dot{1} \dot{-} t^{2_{\mathcal{N}}} \dot{-} t^{3_{\mathcal{N}}}}\mathcal{N},$$

ii.

$${}_{\mathcal{N}}\sum_{v=0}^{\infty}(\mathcal{N}R_v \dot{\times} t^{v_{\mathcal{N}}}) = \frac{\dot{3} \dot{-} t^{2_{\mathcal{N}}}}{\dot{1} \dot{-} t^{2_{\mathcal{N}}} \dot{-} t^{3_{\mathcal{N}}}}\mathcal{N},$$

where the notation ${}_{\mathcal{N}}\sum_{v=0}^{\infty}$ denotes the non-Newtonian real number series as elaborated in [20].

Proof. $i.$ Let $g_{\mathcal{N}P}(t) =_{\mathcal{N}} \sum_{v=0}^{\infty}(\mathcal{N}P_v \dot{\times} t^{v_{\mathcal{N}}})$. We have

$$\begin{aligned} g_{\mathcal{N}P}(t) &= \dot{1} \dot{+} t \dot{+} t^{2_{\mathcal{N}}} \dot{+}_{\mathcal{N}} \sum_{v=3}^{\infty}(\mathcal{N}P_v \dot{\times} t^{v_{\mathcal{N}}}) \\ &= \dot{1} \dot{+} t \dot{+} t^{2_{\mathcal{N}}} \dot{+}_{\mathcal{N}} \sum_{v=3}^{\infty}(\mathcal{N}P_{v-2} \dot{\times} t^{v_{\mathcal{N}}}) \dot{+}_{\mathcal{N}} \sum_{v=3}^{\infty}(\mathcal{N}P_{v-3} \dot{\times} t^{v_{\mathcal{N}}}) \end{aligned}$$

$$t^{2_{\mathcal{N}}} \dot{\times} g_{\mathcal{N}P}(t) =_{\mathcal{N}} \sum_{v=0}^{\infty}(\mathcal{N}P_v \dot{\times} t^{(v \dot{+} 2)_{\mathcal{N}}}) = t^{2_{\mathcal{N}}} \dot{+}_{\mathcal{N}} \sum_{v=3}^{\infty}(\mathcal{N}P_{v-2} \dot{\times} t^{v_{\mathcal{N}}})$$

$$t^{3_{\mathcal{N}}} \dot{\times} g_{\mathcal{N}P}(t) =_{\mathcal{N}} \sum_{v=0}^{\infty}(\mathcal{N}P_v \dot{\times} t^{(v \dot{+} 3)_{\mathcal{N}}}) =_{\mathcal{N}} \sum_{v=3}^{\infty}(\mathcal{N}P_{v-3} \dot{\times} t^{v_{\mathcal{N}}})$$

Therefore, it follows that

$$\begin{aligned} (\dot{1} \dot{-} t^{2_{\mathcal{N}}} \dot{-} t^{3_{\mathcal{N}}}) \dot{\times} g_{\mathcal{N}P}(t) &= g_{\mathcal{N}P}(t) \dot{-} t^{2_{\mathcal{N}}} \dot{\times} g_{\mathcal{N}P}(t) \dot{-} t^{3_{\mathcal{N}}} \dot{\times} g_{\mathcal{N}P}(t) \\ &= \dot{1} \dot{+} t. \end{aligned}$$

Thus, we obtain the function $g_{\mathcal{N}P}(t) = \frac{\dot{1} \dot{+} t}{\dot{1} \dot{-} t^{2_{\mathcal{N}}} \dot{-} t^{3_{\mathcal{N}}}}\mathcal{N}$ as the intended outcome.

$ii.$ The proof can be obtained in a manner similar to the proof above.

Theorem 4. The exponential generating functions for $\mathcal{N}P_v$ and $\mathcal{N}R_v$ are, respectively,

i.

$${}_{\mathcal{N}}\sum_{v=0}^{\infty}(\mathcal{N}P_v \dot{\times} \dot{x}^{v_{\mathcal{N}}}) \dot{/} \dot{v}!^{\mathcal{N}} = \dot{a} \dot{\times} \dot{e}^{\dot{\delta} \dot{\times} \dot{x}_{\mathcal{N}}} \dot{+} \dot{b} \dot{\times} \dot{e}^{\dot{\eta} \dot{\times} \dot{x}_{\mathcal{N}}} \dot{+} \dot{c} \dot{\times} \dot{e}^{\dot{\gamma} \dot{\times} \dot{x}_{\mathcal{N}}},$$

ii.

$${}_{\mathcal{N}}\sum_{v=0}^{\infty}(\mathcal{N}R_v \dot{\times} x^{v_{\mathcal{N}}}) \dot{/} \dot{v}!^{\mathcal{N}} = \dot{e}^{\dot{\delta} \dot{\times} \dot{x}_{\mathcal{N}}} \dot{+} \dot{e}^{\dot{\eta} \dot{\times} \dot{x}_{\mathcal{N}}} \dot{+} \dot{e}^{\dot{\gamma} \dot{\times} \dot{x}_{\mathcal{N}}},$$

where the notation ${}_{\mathcal{N}}\sum_{v=0}^{\infty}$ denotes the non-Newtonian real number series as elaborated.

Proof. $i.$ Using the identity (15), we get

$$\begin{aligned} &{}_{\mathcal{N}}\sum_{v=0}^{\infty}(\mathcal{N}P_v \dot{\times} \dot{x}^{v_{\mathcal{N}}}) \dot{/} \dot{v}! \\ &=_{\mathcal{N}} \sum_{v=0}^{\infty}(\alpha(P_v) \dot{\times} \alpha\{(\alpha^{-1}(\dot{x}))^{v}\}) \dot{/} \dot{v}! \end{aligned}$$

$$
\begin{aligned}
&= \alpha\{\alpha^{-1}(\alpha\{\alpha^{-1}(\alpha\{\alpha^{-1}(\alpha(P_0)) \times \alpha^{-1}(\alpha\{(\alpha^{-1}(\alpha(x)))^0\})\}) \div \alpha^{-1}(\alpha(0!))\}) \\
&+ \alpha^{-1}(\alpha\{\alpha^{-1}(\alpha\{\alpha^{-1}(\alpha(P_1)) \times \alpha^{-1}(\alpha\{(\alpha^{-1}(\alpha(x)))^1\})\}) \div \alpha^{-1}(\alpha(1!))\}) \\
&+ \alpha^{-1}(\alpha\{\alpha^{-1}(\alpha\{\alpha^{-1}(\alpha(P_2)) \times \alpha^{-1}(\alpha\{(\alpha^{-1}(\alpha(x)))^2\})\}) \div \alpha^{-1}(\alpha(2!))\}) + \dots\} \\
&= \alpha\{(P_0 \times x^0) + (P_1 \times x^1) + (P_2 \times x^2) \div 2 + \dots\} \\
&= \alpha\{\sum_{v=0}^{\infty}(P_v x^v) \div v!\} \\
&= \alpha\{ae^{\delta x} + be^{\eta x} + ce^{\gamma x}\} \\
&= \alpha\{\alpha\{\alpha^{-1}(\alpha(a)) \times \alpha\{(\alpha^{-1}(\alpha(e)))^{\alpha\{\alpha^{-1}(\alpha(\delta))\times\alpha^{-1}(\alpha(x))\}}\}\} \\
&+ \alpha\{\alpha^{-1}(\alpha(b)) \times \alpha\{(\alpha^{-1}(\alpha(e)))^{\alpha\{\alpha^{-1}(\alpha(\eta))\times\alpha^{-1}(\alpha(x))\}}\}\} \\
&+ \alpha\{\alpha^{-1}(\alpha(c)) \times \alpha\{(\alpha^{-1}(\alpha(e)))^{\alpha\{\alpha^{-1}(\alpha(\gamma))\times\alpha^{-1}(\alpha(x))\}}\}\}\} \\
&= \alpha\{\alpha^{-1}(\dot{a}) \times \alpha\{(\alpha^{-1}(\dot{e}))^{\alpha\{\alpha^{-1}(\dot{\delta})\times\alpha^{-1}(\dot{x})\}}\}\} \\
&\dot{+}\alpha\{\alpha^{-1}(\dot{b}) \times \alpha\{(\alpha^{-1}(\dot{e}))^{\alpha\{\alpha^{-1}(\dot{\eta})\times\alpha^{-1}(\dot{x})\}}\}\} \\
&\dot{+}\alpha\{\alpha^{-1}(\dot{c}) \times \alpha\{(\alpha^{-1}(\dot{e}))^{\alpha\{\alpha^{-1}(\dot{\gamma})\times\alpha^{-1}(\dot{x})\}}\}\} \\
&= \dot{a}\dot{\times}\dot{e}^{\dot{\delta}\dot{\times}\dot{x}_{\mathcal{N}}}\dot{+}\dot{b}\dot{\times}\dot{e}^{\dot{\eta}\dot{\times}\dot{x}_{\mathcal{N}}}\dot{+}\dot{c}\dot{\times}\dot{e}^{\dot{\gamma}\dot{\times}\dot{x}_{\mathcal{N}}}.
\end{aligned}
$$

$ii.$ The proof can be obtained in a manner similar to the proof above by using the identity (16).

Theorem 5. The partial sum formulas for $\mathcal{N}P_v$ and $\mathcal{N}R_v$ are, respectively,

i.

$$
{}_{\mathcal{N}}\sum_{v=1}^{u}\mathcal{N}P_v = \mathcal{N}P_{u+5}\dot{-}\dot{3},
$$

ii.

$$
{}_{\mathcal{N}}\sum_{v=1}^{u}\mathcal{N}R_v = \mathcal{N}R_{u+5}\dot{-}\dot{5},
$$

where the notation ${}_{\mathcal{N}}\sum_{v=1}^{u}$ represents a finite sum based on $\alpha-$arithmetic, and u is a non-negative integer.

Proof. $i.$ Using the formula (11), we find

$$
\begin{aligned}
{}_{\mathcal{N}}\sum_{v=1}^{u}\mathcal{N}P_v &= {}_{\mathcal{N}}\sum_{v=1}^{u}\alpha(P_v) \\
&= \alpha\{\alpha^{-1}(\alpha(P_1)) + \alpha^{-1}(\alpha(P_2)) + \cdots + \alpha^{-1}(\alpha(P_u))\} \\
&= \alpha\{P_1 + P_2 + \cdots + P_u\} \\
&= \alpha\{\sum_{v=1}^{u} P_v\} \\
&= \alpha\{P_{u+5} - 3\}
\end{aligned}
$$

$$
\begin{aligned}
&= \alpha\{\alpha^{-1}(\alpha(P_{u+5})) - \alpha^{-1}(\alpha(3))\}\\
&= \mathcal{N}P_{u+5} \dot{-} \dot{3}.
\end{aligned}
$$

$ii.$ The proof can be obtained in a manner similar to the proof above by using the formula (12).

Theorem 6. The binomial sum formulas for $\mathcal{N}P_v$ and $\mathcal{N}R_v$ are, respectively,

i.

$$
{}_{\mathcal{N}}\sum_{v=0}^{u} \binom{\dot{u}}{\dot{v}}_{\mathcal{N}} \dot{\times} \mathcal{N}P_v = \mathcal{N}P_{3u},
$$

ii.

$$
{}_{\mathcal{N}}\sum_{v=0}^{m} \binom{\dot{u}}{\dot{v}}_{\mathcal{N}} \dot{\times} \mathcal{N}R_v = \mathcal{N}R_{3u},
$$

where the notation ${}_{\mathcal{N}}\sum_{v=0}^{u}$ represents a finite sum based on $\alpha-$arithmetic, and v is a non-negative integer.

Proof. $i.$ Using the equalities (18), (17) and (1), we obtain

$$
\begin{aligned}
&{}_{\mathcal{N}}\sum_{v=0}^{u} \binom{\dot{u}}{\dot{v}}_{\mathcal{N}} \dot{\times} \mathcal{N}P_v\\
&= {}_{\mathcal{N}}\sum_{v=0}^{u} \binom{\dot{u}}{\dot{v}}_{\mathcal{N}} \dot{\times} (\dot{a} \dot{\times} \dot{\delta}^{v_N} \dot{+} \dot{b} \dot{\times} \dot{\eta}^{v_N} \dot{+} \dot{c} \dot{\times} \dot{\gamma}^{v_N})\\
&= \dot{a} \dot{\times} {}_{\mathcal{N}}\sum_{v=0}^{u} \binom{\dot{u}}{\dot{v}}_{\mathcal{N}} \dot{\times} \dot{\delta}^{v_N} \dot{+} \dot{b} \dot{\times} {}_{\mathcal{N}}\sum_{v=0}^{u} \binom{\dot{u}}{\dot{v}}_{\mathcal{N}} \dot{\times} \dot{\eta}^{v_N} \dot{+} \dot{c} \dot{\times} {}_{\mathcal{N}}\sum_{v=0}^{u} \binom{\dot{u}}{\dot{v}}_{\mathcal{N}} \dot{\times} \dot{\gamma}^{v_N}\\
&= \dot{a} \dot{\times} {}_{\mathcal{N}}\sum_{v=0}^{u} \binom{\dot{u}}{\dot{v}}_{\mathcal{N}} \dot{\times} \alpha\{(\alpha^{-1}(\dot{\delta}))^{v}\} \dot{+} \dot{b} \dot{\times} {}_{\mathcal{N}}\sum_{v=0}^{u} \binom{\dot{u}}{\dot{v}}_{\mathcal{N}} \dot{\times} \alpha\{(\alpha^{-1}(\dot{\eta}))^{v}\}\\
&\dot{+} \dot{c} \dot{\times} {}_{\mathcal{N}}\sum_{v=0}^{u} \binom{\dot{u}}{\dot{v}}_{\mathcal{N}} \dot{\times} \alpha\{(\alpha^{-1}(\dot{\gamma}))^{v}\}\\
&= \dot{a} \dot{\times} {}_{\mathcal{N}}\sum_{v=0}^{u} \binom{\dot{u}}{\dot{v}}_{\mathcal{N}} \dot{\times} \alpha\{\delta^{v}\} \dot{+} \dot{b} \dot{\times} {}_{\mathcal{N}}\sum_{v=0}^{u} \binom{\dot{u}}{\dot{v}}_{\mathcal{N}} \dot{\times} \alpha\{\eta^{v}\} \dot{+} \dot{c} \dot{\times} {}_{\mathcal{N}}\sum_{v=0}^{u} \binom{\dot{u}}{\dot{v}}_{\mathcal{N}} \dot{\times} \alpha\{\gamma^{v}\}\\
&= \dot{a} \dot{\times} {}_{\mathcal{N}}\sum_{v=0}^{u} \binom{\dot{u}}{\dot{v}}_{\mathcal{N}} \dot{\times} \alpha\{\delta^{v} \dot{\times} 1^{u-v}\} \dot{+} \dot{b} \dot{\times} {}_{\mathcal{N}}\sum_{v=0}^{u} \binom{\dot{u}}{\dot{v}}_{\mathcal{N}} \dot{\times} \alpha\{\eta^{v} \dot{\times} 1^{u-v}\}\\
&\dot{+} \dot{c} \dot{\times} {}_{\mathcal{N}}\sum_{v=0}^{u} \binom{\dot{u}}{\dot{v}}_{\mathcal{N}} \dot{\times} \alpha\{\gamma^{v} \dot{\times} 1^{u-v}\}\\
&= \dot{a} \dot{\times} {}_{\mathcal{N}}\sum_{v=0}^{u} \binom{\dot{u}}{\dot{v}}_{\mathcal{N}} \dot{\times} \alpha\{(\alpha^{-1}(\dot{\delta}))^{v} \times (\alpha^{-1}(\dot{1}))^{u-v}\}\\
&\dot{+} \dot{b} \dot{\times} {}_{\mathcal{N}}\sum_{v=0}^{m} \binom{\dot{u}}{\dot{v}}_{\mathcal{N}} \dot{\times} \alpha\{(\alpha^{-1}(\dot{\eta}))^{v} \times (\alpha^{-1}(\dot{1}))^{u-v}\}
\end{aligned}
$$

$$
\begin{aligned}
&\dot{+}\dot{c}\dot{\times}_{\mathcal{N}}\sum_{v=0}^{u}\binom{u}{v}_{\mathcal{N}}\dot{\times}\alpha\{(\alpha^{-1}(\dot{\gamma}))^{v}\times(\alpha^{-1}(\dot{1}))^{u-v}\}\\
&=\dot{a}\dot{\times}_{\mathcal{N}}\sum_{v=0}^{u}\binom{\dot{u}}{\dot{v}}_{\mathcal{N}}\dot{\times}\dot{\delta}^{v_N}\dot{\times}\dot{1}^{u-v_N}\dot{+}\dot{b}\dot{\times}_{\mathcal{N}}\sum_{v=0}^{u}\binom{\dot{u}}{\dot{v}}_{\mathcal{N}}\dot{\times}\dot{\eta}^{v_N}\dot{\times}\dot{1}^{u-v_N}\\
&\dot{+}\dot{c}\dot{\times}_{\mathcal{N}}\sum_{v=0}^{u}\binom{\dot{u}}{\dot{v}}_{\mathcal{N}}\dot{\times}\dot{\gamma}^{v_N}\dot{\times}\dot{1}^{u-v_N}\\
&=\dot{a}\dot{\times}_{\mathcal{N}}(\dot{\delta}\dot{+}\dot{1})^{u_{\mathcal{N}}}\dot{+}\dot{b}\dot{\times}_{\mathcal{N}}(\dot{\eta}\dot{+}\dot{1})^{u_{\mathcal{N}}}\dot{+}\dot{c}\dot{\times}_{\mathcal{N}}(\dot{\gamma}\dot{+}\dot{1})^{u_{\mathcal{N}}}\\
&=\dot{a}\dot{\times}_{\mathcal{N}}\dot{\delta}^{3u_{\mathcal{N}}}\dot{+}\dot{b}\dot{\times}_{\mathcal{N}}\dot{\eta}^{3u_{\mathcal{N}}}\dot{+}\dot{c}\dot{\times}_{\mathcal{N}}\dot{\gamma}^{3u_{\mathcal{N}}}\\
&=\mathcal{N}P_{3u}
\end{aligned}
$$

$ii.$ The proof can be obtained in a manner similar to the proof above by using the the equalities (19), (17) and (1).

Conclusions

In this work, we have introduced a novel perspective on Padovan and Perrin numbers, termed as non-Newtonian Padovan and non-Newtonian Perrin numbers. We have explored various properties of these new numbers and provided a range of identities and formulas. These include Binet-like formulas, generating functions, partial sum formulas, and binomial sum formulas.

Important conclusions from our research include:

Recurrence relations and recursive formulations for non-Newtonian Padovan and non-Newtonian Perrin numbers. Derivation and proof of several formulas applicable in the analysis of these new numbers. In-depth investigation into the analytic and combinatorial properties of these numbers. In conclusion, this study aims to enhance understanding of the mathematical structures of non-Newtonian Padovan and non-Newtonian Perrin numbers, potentially opening new avenues for advanced mathematical research and applications. Future work could explore further applications of these new numbers in different fields and investigate extended properties.

By contributing an innovative perspective to the classical theories of Padovan and Perrin numbers, this work encourages further exploration and utilization of these new types within those working in this field.

Acknowledgments The author would like to thank the editors and reviewers for their careful reading and suggestions.

Funding/Financial Disclosure The author has no received any financial support for the research, authorship, or publication of this study.

Ethics Committee Approval and Permissions The work does not require ethics committee approval and any private permission.

Conflict of Interests The author stated that there are no conflict of interest in this article.

Authors Contribution -

References

[1] Grossman, M. & Katz, R. (1972). *Non-Newtonian calculus*, Lee Press: Pigeon Cove, MA, USA.

[2] Grossman, M. (1979). An introduction to non-Newtonian calculus. *International Journal of Mathematical Educational in Science and Technology 10*(4), 525–528. https://doi.org/10.1080/0020739790100406

[3] Çakmak, A. F. & Başar, F. (2012). Some new results on sequence spaces with respect to non-Newtonian calculus. *Journal of Inequalities and Applications*, 1–17. https://doi.org/10.1186/1029-242X-2012-228

[4] Duyar, C., & Sağır, B. (2017). Non-Newtonian Comment of Lebesgue Measure in Real Numbers. *Journal of Mathematics 2017*(1), 6507013. https://doi.org/10.1155/2017/6507013

[5] Erdogan, M., & Duyar, C. (2018). Non-Newtonian improper integrals. *Journal of Science and Arts 18*(1), 49–74.

[6] Degirmen, N. & Duyar, C. (2023). A new perspective on Fibonacci and Lucas numbers. *Filomat*, *37*(28), 9561–9574. https://doi.org/10.2298/FIL2328561D

[7] Yağmur, T. (2024). Non-Newtonian Pell and Pell-Lucas numbers. *Journal of New Results in Science*, *13*(1), 22–35. https://doi.org/10.54187/jnrs.1447678

[8] Shannon, A. G., Horadam, A. F., & Anderson, P. R. (2006). The Auxiliary Equation Associated with the Plastic Numbers, *Notes Number Theory Discrete Mathematics*, *12*(1), 1–12.

[9] Shannon, A. G., Anderson, P. R. & Horadam, A. F. (2006). Properties of Cordonnier, Perrin and Van der Laan numbers, *International Journal of Mathematical Education in Science and Technology*, *37*(7), 825–831. https://doi.org/10.1080/00207390600712554

[10] Sloane, N. J. A. (1973). A Handbook of Integer Sequences, Academic Press, NY.

[11] Dişkaya, O. (2023). Padovan sayılarının genellemeleri ve uygulamaları . (Tez no. 826990) [Doktora Tezi, Mersin Üniversitesi].

[12] Adegoke, K. (2022). Summation identities involving Padovan and Perrin numbers.*Palestine Journal of Mathematics*, *11*(1), 633—650.

[13] Yilmaz, N. & Taskara, N. (2013). Matrix sequences in terms of Padovan and Perrin numbers. *Journal of Applied Mathematics*, *2013*(1), 941673. https://doi.org/10.1155/2013/941673

[14] Dişkaya, O. & Menken, H. (2021). Some properties of the plastic constant. *Journal of Science and Arts 21*(4), 883–894. https://doi.org/10.46939/J.Sci.Arts-21.4-a01

[15] Diskaya, O., & Menken, H. (2020). On the Padovan Triangle. *Journal of Contemporary Applied Mathematics 10*(2), 77–83.

[16] Diskaya, O., & Menken, H. (2024). On the pulsating Padovan sequence. *Notes on Number Theory and Discrete Mathematics 30*(1), 1–7. https://doi.org/10.7546/nntdm.2024.30.1.1-7

[17] Diskaya, O., & Menken, H. (2023). Padovan Polynomials Matrix. *Bulletin of The International Mathematical Virtual Institute 13*(3), 499–509. https://doi.org/10.7251/BIMVI2303499D

[18] Diskaya, O., & Menken, H. (2020). Some Identities of Gadovan Numbers. *Journal of Science and Arts*, *20*(2), 317–322.

[19] Deveci, O., & Karaduman, E. (2017). On the Padovan p-numbers. *Hacettepe Journal of Mathematics and Statistics 46*(4), 579–592.

[20] Duyar, C. & Erdogan, M. (2016). On non-Newtonian real number series. *IOSR Journal of Mathematics*, *12*(6), 34–48.

Sinopfbd, 2024; 9(2): 516-533 **https://doi.org/10.33484/sinopfbd.1587996**

Sinop Üniversitesi Fen Bilimleri Dergisi
Sinop Uni J Nat Sci

E-ISSN: 2564-7873

https://dergipark.org.tr/tr/pub/sinopfbd

Determination of the Phytochemical, Antioxidant, and Antimicrobial Properties of *Smilax excelsa* L. Extracted with Different Solvents

Elif Fatma TOPKARA[1] Beyza KABA[2] Hayrettin SAYGIN[3] Eda TURGUT UĞURTAY[1] and Hojjat PASHAZADE[4]

How to cite: Topkara, E. F., Kaba, B., Saygın, H., Turgut Ugurtay, E., & Pashazade, H. (2024). Determination of the phytochemical, antioxidant, and antimicrobial properties of *Smilax excelsa* L. extracted with different solvents. *Sinop Üniversitesi Fen Bilimleri Dergisi, 9*(2), 516-533. https://doi.org/10.33484/sinopfbd.1587996

Research Article

Corresponding Author
Elif Fatma TOPKARA
topkaraelif@hotmail.com

ORCID of the Authors
E.F.T: 0000-0002-4743-2914
B.K: 0000-0001-7954-8025
H.S: 0000-0002-8642-5872
E.T.U: 0000-0001-9793-2872
H.P: 0000-0001-8932-8165

Received: 19.11.2024
Accepted: 17.12.2024

Abstract

Smilax excelsa L., an edible wild plant whose leaves and shoots are frequently consumed in the daily diet and used to treat various diseases in traditional medicine, grows in certain regions of Türkiye, especially in the Black Sea Region. This study aims to determine the phytochemical properties, antioxidant and antimicrobial activities of *S. excelsa* with different solvents. In this study, the shoots of *S. excelsa* were extracted with water, 70% ethanol, and 80% methanol solvents and an ultrasound-assisted extraction method was used. It was found that the total phenolic contents of the extracts obtained from the plant were higher in the ethanol (75.09 mg/g) and methanol (74.72 mg/g) extracts compared to the water extract (49.62 mg/g). While the water extract had the highest amount of flavonoids (22.96 mg/g), the 80% methanol extract had the highest amount of total anthocyanins (0.52 mg/g). The efficacy of the extracts against various pathogens was also investigated. It was determined that in the Petri dish in which *Enterococcus faecalis* ATCC 29212 pathogen was cultivated, a clear zone was formed around the disc into which only the water extract was impregnated. The zone diameter was 2.10 ± 0.08 cm. As a result of the study, it can be said that especially the ethanol and methanol extracts were effective in terms of both the phytochemical properties and antioxidant activities and therefore they exhibited high antioxidant properties.

Keywords: *Smilax excelsa*, edible wild plants, phenolic compound, antioxidant activity

Farklı Çözücülerle Ekstrakte Edilen *Smilax excelsa* L.'nin Fitokimyasal, Antioksidan ve Antimikrobiyal Özelliklerinin Belirlenmesi

[1]Ondokuz Mayıs University, Black Sea Advanced Technology Research and Application Center, Biotechnology Unit, Samsun, Türkiye

[2]Ondokuz Mayıs University, Faculty of Engineering, Department of Food Engineering, Samsun, Türkiye

Öz

Yaprak ve sürgünleri günlük diyette sıklıkla tüketilen ve geleneksel tıpta çeşitli hastalıkların tedavisinde kullanılan, yenilebilir yabani bir bitki olan *Smilax excelsa* L. başta Karadeniz Bölgesi olmak üzere Türkiye'nin belirli bölgelerinde yetişmektedir. Bu çalışmanın amacı, farklı çözücülerle hazırlanan *S. excelsa* ekstraktlarının fitokimyasal özelliklerini, antioksidan ve antimikrobiyal aktivitelerini belirlemektir. Çalışmada, *S. excelsa* sürgünleri su, %70 etanol ve %80 metanol çözücüleriyle ekstrakte edilmiş ve ultrason destekli ekstraksiyon metodu uygulanmıştır. Bitkiden elde edilen ekstraktların toplam fenolik madde miktarının etanol (75.09 mg/g) ve metanol (74.72 mg/g) ekstraktlarında su ekstraktına (49.62

[3]Ondokuz Mayis University, Faculty of Science, Department of Molecular Biology and Genetics, Samsun, Türkiye

[4]Istanbul Nişantaşı University, Art and Design Faculty, Department of Gastronomy and Culinary Arts, İstanbul, Türkiye

mg/g) kıyasla yüksek olduğu bulunmuştur. Su ekstraktı en yüksek flavonoid (22.96 mg/g) miktarına sahipken, %80'lik metanol ekstraktı en yüksek toplam antosiyanin miktarına (0.52 mg/g) sahiptir. *S. excelsa* ekstraktlarının çeşitli patojenlere karşı etkinliği de araştırılmıştır. *Enterococcus faecalis* ATCC 29212 patojeninin ekili olduğu Petride, yalnızca su ekstraktının emdirildiği diskin etrafında açık zon oluşumu meydana geldiği belirlenmiştir. Zon çapı 2.10 ± 0.08 cm'idi. Çalışma sonucunda, özellikle etanol ve metanol ekstraktlarının hem fitokimyasal özellikler hem de antioksidan aktiviteler bakımından etkin olduğu ve bu nedenle yüksek antioksidan özellikler sergiledikleri söylenebilir.

Anahtar Kelimeler: *Smilax excelsa*, yenilebilir yabani bitkiler, fenolik bileşik, antioksidan aktivite

Introduction

Wild edible plants (WEPs) are found in various agroecosystems and offer both direct and indirect resources for human nutrition and health [1]. In addition to being a potential source of income, these plants are crucial for the traditional food, fodder, medicine, socio-cultural, and general well-being of rural dwellers, especially in mountainous areas [2, 3]. WEPs are an inexpensive source of minerals, vitamins, and antioxidants and a cultural heritage that should be protected worldwide [4]. In addition to their nutritional content, these plants are increasingly attracting people's attention due to diversifying dietary habits and promoting ecological and biodiversity sustainability [5]. Recently, a new trend in some developed countries and Europe is using local edible wild plants in modern cuisines, both for their health benefits and as an element of cultural identity [6, 4]. WEPs are an alternative raw material for clean-label food production in the food industry thanks to their bioactive compounds [7]. Due to their medicinal functions, many edible wild plants are believed to have positive effects on human health. Due to their medicinal functions, many edible wild plants are believed to have positive effects on human health. These plants are also known as "nutraceutical plants" because they offer nutritional and pharmaceutical benefits [8]. WEPs, which have many properties such as antioxidants, antimicrobial, anticarcinogenic, antidiabetic, anti-inflammatory, and anti-obesity effects, are the focus of studies in pharmacology and food science [7]. *Smilax* (Smilacaceae), including edible wild plants, is a genus of about 350 species in tropical, temperate, and subtropical regions worldwide. This genus contains plants in America, Europe, Asia, and Oceania. Species of the genus *Smilax*, commonly called sarsaparilla, have long, slender spiny stems and are characterized as climbers. They climb by clinging to other plants or objects with their tendrils, which grow continuously upwards [9]. The leaves, stems, roots, and rhizomes of sarsaparilla are consumed as food and used in traditional medicine. The genus *Smilax* has pharmacological properties with antioxidant, antibacterial, antifungal, and immunomodulatory effects. It is used in the treatment of diabetes, different types of cancer, ulcers, and various skin diseases as well as gout, fever, and eye diseases [10]. These plants, which have saponins in their roots, are also utilized as diuretics and tranquilizers [11]. *S. excelsa*, a species belonging to the genus *Smilax*, is a climbing, perennial and shrubby wild plant. It grows up to 800 m in height in shrubby and forested areas [12] and grows in temperate regions, especially in North and South America, and East Asia [13]. In Türkiye, it is distributed in the Black Sea, Mediterranean, Aegean, and western Marmara regions including Samsun, Sinop, Artvin, Zonguldak, Trabzon, Tekirdağ, İstanbul, Bolu, Antalya, Muğla, Aydın, and Hatay provinces [14-17]. Locally known as "kırçan, dikenucu, melocan, saparna, merülcen, and melevcan" [18], the leaves and shoots of this plant are frequently consumed in the daily diet. Due to its antioxidant, antimutagenic, antiviral, and antimicrobial properties [19], this plant is used in traditional medicine in Türkiye to treat stomach pain, breast cancer, and indigestion [9]. In addition, it is of great importance in the field of pharmacology as it is actively used in treating rheumatism, diabetes, ulcers, and various skin diseases [20, 13]. In this study, it was aimed to determine the phytochemical properties (leaf properties, the total phenolic, flavonoid, and anthocyanin contents) of shoots of *S. excelsa*, which is frequently consumed in Türkiye, extracted with different solvents (water, ethanol, and methanol) and prepared by ultrasound-assisted extraction. In addition, the antioxidant [(DPPH (1,1-diphenyl-2-picrylhydrazyl), FRAP (ferric-reducing antioxidant power), and ABTS (2,2'-azino-bis(3-ethylbenzothiazoline-6-sulfonic acid)] and antimicrobial activities of the *S. excelsa* extracts were also determined.

Materials and Methods

Sampling

The shoots of *S. excelsa* were collected from the Dikbıyık District of Çarşamba, in 2024 (41.221082° N 36.608975° E). Species identification was made by Prof. Dr. Hamdi Güray Kutbay from the Department of Botany, Department of Biology, Ondokuz Mayıs University. The weeds were removed from *S. excelsa* in the laboratory (Figure 1).

Figure 1. *The shoots of Smilax excelsa*

The shoots were washed with distilled water, and the water was removed. Some of the fresh shoots were separated for color determination. The remaining shoot samples were kept in a lyophilizer (Labconco Freezone 12 plus, USA) at 85°C and 0.020 mbar pressure for 24 hours to remove the water. After 24 hours, the samples taken from the device were pulverized with the help of a grinder (Sinbo, Scm 2934, Istanbul, Türkiye).

Preparation of the Extracts of *Smilax excelsa*

The method reported by Raghunath et al. [21] was modified and used to prepare extracts. A certain amount of the lyophilized *S. excelsa* powder was weighed and pure water, 70% ethyl alcohol, and 80% methyl alcohol were added as three different solvent with a solid: solvent ratio of 1:25. First, it was left to macerate in an ultrasonic water bath at 20°C for 30 minutes, then at room temperature for 2 hours. Then, it was centrifuged at 4000 rpm for 15 minutes and the obtained extracts were analyzed for antioxidant and phenolic compound composition by passing through a 0.45 µm pore teflon filter.

Color Measurement

Color measurement of *S. excelsa* leaves was made with the MiniScan EZ 4500 (Reston, Virginia, USA) color measuring device. L* (light/darkness), a* (redness/greenness), and b* (yellowness/blueness) values were measured.

Determination of Dry Matter

The fresh samples were weighed in a certain amount in tarred nickel containers. Then, they were dried in a vacuum oven at 70°C and 100 mm Hg pressure until they reached constant weight [22].

Total Phenolic Compound Analysis

The method reported by Singleton and Rossi [23] was modified and used to determine the total phenolic compound content. The total phenolic content of the *S. excelsa* was determined using the Folin-Ciocalteu reagent. For this, 150 µl of the diluted sample was mixed with 750 µl of 10% Folin-Ciocalteu reagent (5 minutes) and 600 µl of 7.5% Na_2CO_3. The mixture was kept in the dark for 2 hours, and then its absorbance was determined at 760 nm. Results are expressed as mg gallic acid equivalent/g (mg GAE/g).

Determination of Total Flavonoid Content (TFC)

1 ml of the diluted sample was taken, 0.3 ml of 5% $NaNO_2$ was added and then the mixture was left for 5 minutes. Then, 0.5 ml of 5% $AlCl_3$ was added. After the mixture was left for 6 minutes, 0.5 ml of 1 M NaOH was added. After 10 minutes, the absorbance was read at 510 nm. TFC was calculated based on a calibration curve created using the epicatechin standard. Results are given as mg epicatechin equivalent (ECE)/g dry weight [24].

Total Anthocyanin Analysis

The total anthocyanin contents of the extracts were determined by the pH differential method. The absorbances of the extracts mixed with pH 1 and 4.5 buffers were determined at 510 and 700 nm. Expressed as mg cyanidin-3-glucoside equivalent (mg CGE/g) per g of total anthocyanin [25].

Determination of Individual Phenolic Compounds

The samples were extracted with different solvents and the phenolic compound compositions were determined through LC-MS/MS. Liquid chromatography and Tandem MS mass spectroscopy were used in the study. MS/MS conditions, operating conditions, and Gradient program are given in Tables 1 and 2. A total of 10 phenolic compounds (prigallol, procateutic acid, procateutic aldehyde, catechin, chlorogenic acid, epicatechin, caffeic acid, taxifolin, luteolin-7-glycoside, and rutin) could be identified in *S. excelsa*.

Table 1. *MS/MS instrument conditions*

Capillary temperature	300 °C
Vaporizer temperature	350 °C
Sheat gas pressure (Arb)	30
Aux gas pressure (Arb)	13
Spray voltage (V) (Positive polarity)	4000
Spray voltage (V) (Negative polarity)	2500
Discharge current (μA)	4.0

Table 2. *Sample information and analysis test conditions.*

	Minute	**%A (0.1% Formic acid water)**	**%B (Methanol)**
Solvent Program	0	100	0
	1	100	0
	22	5	95
	25	5	95
	30	0	100
Solvent flow rate	0.7 ml/minute		
Column oven temperature	30 °C		
Column properties	ODS HYPERSIL 4,6*250 mm 5 μm colon		
Injection volume	20 μl		
Analysis time	34 Minutes		

Determination of DPPH (1,1-diphenyl-2-picrylhydrazyl) Radical Scavenging Effect

The method reported by Tural and Koca [26] was modified to determine the scavenging effect of DPPH radical (2,2-diphenyl-1 picrylhydrazyl). A solution of 50 μl of the extract was prepared and prepared and then mixed with 1 ml of a solution of 0.06 mM DPPH. The mixture was shaken and left in the dark for 2 hours until the reaction was complete. At the end of the reaction, the absorbance at 517 nm was recorded. The same process was repeated without extract and only solvents, and the DPPH free radical scavenging effect was determined using the following formula:

$$\text{Reduction (\%)} = \left(\frac{\text{A control sample} - \text{A sample}}{\text{A control sample}}\right) \text{x } 100$$

The DPPH radical scavenging effect was calculated by a calibration curve using Trolox as the standard. Results are given in mmol Trolox equivalent (TE)/g.

Determination of Iron Reducing Antioxidant Power (FRAP)

50 µl of the extract was mixed with 950 µl of FRAP solution containing 100 mM acetate buffer, 10 mM $FeCl_3$, and 10 mM TPTZ (2,4,6-tri-pyridyl-s-triazine). The mixture was shaken for approximately 5 minutes and the absorbance was read against the blank solution at 593 nm. FRAP values of the extracts were calculated with the help of a calibration curve prepared using Trolox as a standard. Results are given as mmol Trolox equivalents (mmol TE/g dry weight) [27].

ABTS Radical Scavenging Capacity

0.2 ml of the extract was mixed with 2 ml of $ABTS^+$ radical cation solution. Then, the mixture was left in the dark for 2 hours and measurements were made using a spectrophotometer at 734 nm. Results are expressed as mmol of Trolox equivalents per gram (mmol TE/g) [28].

Disc Diffusion Test Method

The antimicrobial activities of the extracts were determined by the disc diffusion method by Bauer et al. [29]. Five of the human and plant pathogens kept at -80°C in the Microbiology Laboratory at Ondokuz Mayis University were selected and cultivated with the help of a loop. Nutrient agar (NA) and Sabouraud dextrose agar (SDA) [30] media were used for incubation of pathogenic bacteria and fungus, respectively. The pathogen strains used in the study are given in Table 3.

Table 3. *Pathogenic strains were used in the study.*

Pathogenic strain	Group/Host	Medium	Incubation temperature
Aspergillus niger ATCC 16404	Fungus/Plant	SDA	30
Bacillus subtilis ATCC 6633	Bacteria/Human	Nutrient Agar	37
Enterococcus faecalis ATCC 29212	Bacteria/Human	Nutrient Agar	37
Klebsiella pneumoniae ATCC 700603	Bacteria/Human	Nutrient Agar	37
Staphylococcus aureus ATCC 25923	Bacteria/Human	Nutrient Agar	37

The Petri dishes were allowed to briefly dry at room temperature, then bagged and inverted, and incubated at 37°C for *A. niger* and 30°C for bacteria with an incubation period of 48 hours. At the end of 48 hours, the microbial growth and purity of the Petri dishes were checked. Cotton wool was placed in the mouth of the flasks and the cotton wool was covered and wrapped with aluminium foil. The flasks were autoclaved to sterilize the media before the bacterial and fungal inoculation. At the end of autoclaving, each of the pathogens was transferred to 20 ml Nutrient broth medium in 50 ml Erlenmeyer flasks. Then, each flask was placed in a shaking incubator running at 150 rpm and incubated at the specified temperature given above for both fungus and bacteria for 48 hours. After incubation period, the turbidity was checked in the media. Microbial suspensions were prepared as equivalent to 0.5 McFarland standard (approximately 1.5×10^8 cfu/ml for bacteria and 1.0×10^6 cfu/ml for fungi) within glass tubes containing 10 ml Nutrient and Sabouraud dextrose broth using a spectrophotometer. Then, 200 µl of each solution was taken and the pathogens were cultivated on a Nutrient agar and Sabouraud dextrose media by spreading plate method. Petri dishes were allowed to dry in a sterile cabinet for 30 minutes. Meanwhile, the empty discs were held with a sterile clamp and 20 µl of the plant extracts to be tested for antimicrobial activity and the solutions to be used as negative controls were drawn with a pipette and impregnated on these discs. Then, the discs were carefully placed on the Petri dishes where the pathogens were cultivated with the help of forceps. As negative controls, 70% ethanol, 80% methanol or water was used as appropriate for each extract. Discs containing the appropriate antibiotic to be used as a positive control were also placed in the Petri dishes (Table 4). For each pathogen, the study was performed in 3 replicates. A total of 7 discs were placed on each Petri dish. After placing the discs, the Petri dishes were bagged and inverted and incubated at 30°C and 37°C for 48 hours. At the end of the incubation period, each Petri dish was examined to see whether a clear zone formed around the discs. The diameter of the zone was measured with a ruler in the Petri dishes in which zone formation was observed and recorded [31].

Table 4. *Antibiotics used according to pathogenic strains in the disc diffusion method*

Pathogenic strain	**Antibiotics as positive control**
Aspergillus niger ATCC 16404	Amphotericin B (10 µg/disc)
Bacillus subtilis ATCC 6633	Amoxycillin (10 µg/disc)
Enterococcus faecalis ATCC 29212	Penicillin G (10 µg/disc)
Klebsiella pneumoniae ATCC 700603	Amoxycillin (10 µg/disc)
Staphylococcus aureus ATCC 25923	Penicillin G (10 µg/disc)

Minimum Inhibition Concentration (MIC) Test

MIC test was performed to determine the lowest concentration at which the inhibitory effect of the water extract, which gave positive results in the disc diffusion test, on E. faecalis ATCC 29212. For this purpose, a 96-well plate was used. Cells of the pathogen previously grown on Nutrient agar were removed with a toothpick and transferred to glass tubes containing 10 ml Nutrient Broth. Then, a Nutrient Broth solution with a McFarland value of 0.5 was obtained by diluting the solution in this glass tube. Then, 500 µl of distilled water was aseptically added to each of the 9 sterile centrifuge tubes. Using a pipette, 500 µl of the water extract in the capped glass tube was taken and transferred to the centrifuge tube containing 500 µl of distilled water. Thus, the concentration of the main extract was halved. Then, 500 µl was taken from this tube and transferred to the next tube in the same way and the process was continued until the 9th centrifuge tube. 200 µl of sterile Nutrient broth was added to the 12th well of the 96-well plate and 200 µl of bacterial solution was added to the 11th well. 100 µl of the bacterial solution was added to wells 1-10. 100 µl of the master stock of the water extract (undiluted) was added at the 1st well. In the 2nd-10th wells, 100 µl of the extracts diluted from high concentrated to low concentrated were added. The study was carried out in 3 replicates in each well. Then, the plate was covered with a sterile lid and incubated at 37°C for 24 hours. At the end of the incubation, the turbidity in the wells was evaluated with the naked eye.

Statistical Analysis

The data were evaluated according to one-way analysis of variance (ANOVA) in the SPSS 22.0 package program (licensed by Ondokuz Mayıs University). The differences between the averages were determined by Duncan's multiple comparison. All measurements were performed in triplicate.

Results and Discussion

Phytochemical Contents

In this study, the shoots as edible parts of *S. excelsa* were extracted with different solvents and the phytochemical properties, and the antioxidant and antimicrobial activities of the extracts prepared by ultrasound-assisted extraction were determined. In the study, it was determined that the water content of fresh plants was 88.57±0.67% and the water content of plant powder was 8.93%. The mean *L** (brightness) value was 24.83± 4.84, *a** (redness) value was 5.41±1.03, and *b** (yellowness) value was 31.85±1.85. Topdas et al. [32] measured the color of lyophilized green (LY) and lyophilized reddish (LK) *S. excelsa* samples. As a result of their study, they determined the brightness (*L**) value as 50.01 in the LY sample and 40.93 in the LK sample; redness (*a**) value as -7.75 in the LY sample and 7.17 in the LK sample; yellowness (*b**) value as 30.03 in the LY sample and 14.00 in the LK sample. The brightness and redness values determined by the researchers are higher than our findings, while the yellowness value is lower. This situation indicates that our samples have a more intense yellowness tone. The main reason for the difference in color values from literature is the difference in water content between the samples [33]. The total phenolic, flavonoid, and anthocyanin contents and the antioxidant activities (DPPH, FRAP, and ABTS) of *S. excelsa* extracts are given in Table 5.

Table 5. *The phytochemical and antioxidant properties of the extracts from different solvents*

Solvent	**Total phenolic content, mg/g**	**Total flavonoid content, mg/g**	**Total antosiyanin content, mg/g**	**DPPH, mmol/g**	**FRAP, mmol/g**	**ABTS, mmol/g**
Water	49.62±0.53^b	22.96±0.81^a	0.19±0.01^b	807.54±198.07^b	918.05±226.11^b	322.17±38.10^b
Ethanol	75.09±0.73^a	22.50±0.59 ^{a}	0.11±0.07^c	1868.38±282.35^a	2000.46±92.70^a	326.66±39.38^b
Methanol	74.72±2.51^a	21.40±0.96 ^{a}	0.52±0.07^a	1701.51±63.21^a	2030.84±67.83^a	684.10±120.66^a

There is no statistical difference between the averages indicated with the same letter in the same column ($P>0.05$)

The total phenolic content of the *S. excelsa* varied significantly according to the solvent ($P<0.05$). The total phenolic content of the extract prepared with water was lower than the others. The extracts prepared with 70% ethanol and 80% methanol had higher phenolic contents (75.09 mg/g and 74.72 mg/g, respectively). There was no statistically significant difference between the ethanol and methanol extract groups (*P*>0.05). Different results were obtained in various studies. For example, Miser-Salihoglu et al. [34] found the total phenolic content of the extract obtained from shoots and roots of *S. excelsa* to be 645.38 µg/ml gallic acid. Yılmaz-Sarıaltın et al. [18] investigated the total phenolic content of *S. excelsa* extracts prepared with different solvents by HPLC. The authors determined phenolic amounts as 402.94 mg GAE/g in the methanol extract and 366.46 mg GAE/g in the water extract of *S. excelsa*. As can be seen, the phenolic content obtained from the methanol extract was higher than that of the water extract. These findings are compatible with the results obtained in our study. However, when analyzed quantitatively, it was determined that the total phenolic content obtained from our study was lower than that determined by Yılmaz-Sarıaltın et al. [18]. Demir [12] determined the total phenolic contents in the ethanol, methanol, and water extracts of fresh shoots of *S. excelsa* as 4.96, 4.94, and 4.71 mg/g, respectively, which were considerably lower than the results obtained from our study. Şahin [35] proved that the total phenolic contents in the ethanol extract of *S. excelsa* leaves varied between 53.57-61.68 mg gallic acid/g depending on the solvent concentration and time, which was close to the results of our study. According to our results, the total flavonoid content did not change much depending on the solvent. The extracts prepared with water (22.96 mg/g) and ethanol (22.50 mg/g) solvents had the highest flavonoid contents, but there was no statistically significant difference (*P*>0.05). Yılmaz-Sarıaltın et al. [18] determined the total flavonoid content as 191.42 mg QE/g in the methanol extract and 109.96 mg QE/g in the water extract of *S. excelsa*. The authors also noted the high flavonoid contents in parallel with the high total phenolic contents, which are higher than our findings. When the anthocyanin contents were compared, it was determined that the extract prepared with 80% methanol gave higher results (0.52 mg/g) than the other extracts. Ozsoy et al. [19] found that the passage of antioxidant compounds was different depending on the solvent and preparation technique in the extraction of water, ethanol, and ethyl acetate of the leaves of *S. excelsa*. The researchers found that the total phenolic contents of the water and ethanol extracts (30.6 mg/g and 30.1 mg/g, respectively) were higher than that of ethyl acetate (8.8 mg/g). They found the highest flavonoid content in the ethanol extract (28.7 mg/g), which is almost similar to the results obtained in our study. Ozsoy et al. [19] determined the total anthocyanin content in leaves as 0.32 mg/g, which is much higher than the total anthocyanin content obtained in the methanol extract in our study. Al Yassine et al. [36] determined that the total phenolic content in the water extract of stems and leaves of *S. excelsa* was significantly higher than the ethanol extract. The results of our study do not coincide with the results of this study because the water extract gave the lowest result. Significant differences were found in the phenolic compound compositions of the *S. excelsa* extracted in different solvents (Table 6).

Table 6. *Phenolic compound composition of Smilax excelsa (µg/g).*

	Parent	Product	Collision energy	Polarity	Water	Methanol	Ethanol
Pyrogallol	124.86	69.31 79.28	20 23	– –	7.93±0.00^{b}	11.80±8.35^{a}	5.62±0.00^{c}
Procatechuic acid	155.01	65.40 93.20	22 13	+ +	2.75±0.00^{b}	Nd	5.75±0.66^{a}
Procatechuic aldehyde	136.9	92.25 108.20	25 25	– –	nd	Nd	3.04±1.25
Catechin	289.2	203.90 245.70	22 17	– –	nd	1250.77±31.75^{a}	1116.14±20.87^{b}
Chlorogenic acid	353.4	86.50 192.10	43 21	– –	nd	2246.13±0.86	2253.17±34.62
Epicatechin	291.5	123.30 139.30	15 16	+ +	3.12±2.21^{b}	124.38±4.63^{a}	106.26±12.83^{a}
Caffeic acid	179.7	135.20 136.20	27 18	– –	nd	0.42±0.04^{a}	0.21±0.15^{b}
Taxifolin	303	126.20 285.50	23 15	– –	0.21±0.00^{c}	3.31±0.09^{a}	2.95±0.06^{b}
Luteolin-7-glucoside	446.89	284.00 285.00	45 40	– –	0.14±0.05	0.12±0.01	0.17±0.06
Rutin	609.37	300.60 301.70	38 34	– –	4.95±0.50^{b}	494.06±26.53^{a}	500.31±3.07^{a}

nd: not detected. There is no statistical difference between the means indicated with the same letter on the same line (P>0.05).

Among all compounds, the highest values were found for chlorogenic acid in the methanol and ethanol extracts (2246.13 µg/g and 2253.17 µg/g, respectively). This situation indicates that both solvents provide high yields in the extraction of chlorogenic acid. Chlorogenic acid is an important compound with multiple pharmacological properties such as antioxidant, anti-inflammatory, hypoglycemic, hypolipidemic [37], anti-hypertensive, anti-viral, neuroprotective, hepatoprotective, central nervous system stimulant, anti-proliferative, cardioprotective, and anti-obesity. Al Yassine et al. [36] examined the phenolic compound profile of *S. excelsa* and found protocatechuic acid (5.35 mg/100 g), chlorogenic acid (5.91 mg/100 g), and chlorogenic acid derivatives (9.76 mg/100 g) as the main phenolic acids. In particular, chlorogenic acid and its derivatives are known as compounds that increase the antioxidant capacity of the plant. Compounds such as protocatechuic acid and chlorogenic acid contribute significantly to the antioxidant potential of the plant since they contribute to cell protection with their free radical scavenging activities. In our study, especially chlorogenic acid is dominant. In this respect, the results of our study are consistent with the results of Al Yassine et al. [36]. In the present study, catechin, a flavonoid, was found at high levels in the methanol and ethanol extracts (1250.77 µg/g and 1116.14 µg/g, respectively). Catechin prevents cell damage and reduces oxidative stress by fighting free radicals [38]. Rutin is an important flavonoid that supports the antioxidant capacity. The amount of rutin was found to be 500.31 µg/g in the ethanol extract and 494.06 µg/g in the methanol extract. It was reported that rutin can effectively eliminate free radicals and inhibit lipid peroxidation [39]. Cellat et al. [40] determined that protocatechuic acid was 0.416 mg/g, protocatechuic aldehyde was 0.072 mg/g, catechin was 2.203 mg/g, chlorogenic acid was 3.218 mg/g, epicatechin was 1.720 mg/g, caffeic acid was 0.043 mg/g, and luteolin was 0.15 mg/g in the ethanol extract obtained from the leaves of *S. excelsa*, but they could not detect rutin. Yılmaz-Sarıaltın et al. [18] showed that chlorogenic acid (2.78 mg/g) and caffeic acid (0.22 mg/g) were particularly high in the methanol extract of S. excelsa. The researchers also detected rutin (0.126 mg/g) in the *S. excelsa* extract. In the present study, it was also found that *S. excelsa* contains rutin and is rich in chlorogenic acid. On the other hand, luteolin-7 glycoside and taxifolin were found at the lowest amounts. Taxifolin is one of the flavonols, a subclass of flavonoids. They are potent phenolic compounds and are a food and dietary supplement. Taxifolin is a powerful antioxidant and fights against antiradical activities. It is used to minimize or prevent lipid oxidation in food products, delay the formation of toxic oxidation products and maintain nutritional quality [41]. Furthermore, this compound has been reported to show promising inhibitory activity against oxidative stress, microbial infection, inflammation, cardiovascular disease, and liver disease [42]. As a result of our study, it was recorded that the amounts of taxifolin varied between 0.21-3.31 µg/g. Luteolin-7-glycoside was very low in all extracts, 0.14 µg/g in the water extract, 0.12 µg/g in the methanol extract, and 0.17 µg/g in the ethanol extract. Similarly, the amounts of caffeic acid were also found at very low levels in the methanol and ethanol extracts (0.42 µg/g and 0.21 µg/g, respectively). These results showed that methanol and ethanol were more effective in the extraction of some phenolic compounds, while water provided low extraction efficiency, especially for compounds other than chlorogenic acid and catechin. Different information on the phenolic compound composition of *S. excelsa* was found in literature. For example, Demir [12] investigated the phenolic compound composition of S. excelsa and identified six phenolic acids. These were gallic acid (117.33 µg/g), vanillic acid (33.89 µg/g), caffeic acid (4.55 µg/g), ferulic acid (93.78 µg/g), rosmarinic acid (0.33 µg/g), and hydroxycinnamic acid (0.33 µg/g). The researcher reported that gallic acid, vanillic acid, and ferulic acid were the dominant phenolic acids in *S. excelsa*. The phenolic compound composition determined in the present study is different from the findings of Demir [12]. In another study, Khaligh et al. [13] reported the presence of five major compounds in *S. excelsa*, namely solanesol, violasterol A, trans-resveratrol, 5-O-caffeoylchikimic acid, and 6-O-caffeoyl-β-d-fructofuranosyl-(2-1)-α-d-glucopyranoside. Cellat et al. [40] reported the presence of twenty-four different phytochemicals, including phenolic acids and flavonoids, in the ethanol extract of *S. excelsa*. The phenolic compound composition determined by the researchers overlaps with the compounds detected in our study. The results obtained from both our study and other studies explain the differences in the total phenolic, flavonoid, and anthocyanin contents as well as the differences in the phenolic compounds composition as affected by many factors such as growing conditions, soil structure and geographical region, collection time, climatic conditions, solvent type, and genetics.

Antioxidant Activity

According to the antioxidant activity (DPPH, FRAP, and ABTS) results, it was determined that the extracts prepared with 70% ethanol and 80% methanol solvents showed high antioxidant activities, especially in the DPPH and FRAP tests. The 70% ethanol extract had the highest value (1868.38 mmol/g) in the DPPH test, while the 80% methanol extract gave the highest value (2030.84 mmol/g) in the FRAP test. At the ABTS value, the 80% methanol extract exhibited a higher antioxidant capacity (684.10 mmol/g) compared to the others. In various studies, the antioxidant activities in the *S. excelsa* extracts prepared with different solvents were investigated. Yılmaz-Sarıaltın et al. [18] determined that in the DPPH test, the methanol extract of *S. excelsa* showed the strongest effect with an IC_{50} value of 45.81 µg/ml, while the water extract had a lower effect with an IC_{50} value of 57.49 µg/ml. These results reveal that the methanol extract is stronger than the water extract in terms of antioxidant capacity. In the ABTS test, the authors recorded the IC50 value of the methanol extract as 17.16 µg/ml and the value of the water extract as 21.31 µg/ml [17]. These results are consistent with the findings of our study, where we found that both the DPPH and FRAP values of the methanol extract were higher than those of the water extract. Ozsoy et al. [19] noted that the DPPH free radical scavenging value of the water extract of S. excelsa was higher than that of the ethanol extract, which does not coincide with the findings of our study. These researchers attributed the antioxidant activity of Smilax rhizomes to different compounds such as proanthocyanidins, trans-resveratrol, naringenin, 1-O-trans-p-coumarolglycerol, etc. [19]. In the current study, it has been proven that the most effective extract in terms of DPPH free radical scavenging effect was obtained with ethanol, and in terms of FRAP and ABTS-reducing activities, the most effective extract was obtained with methanol. Oğuz Akın et al. [43] found that the fruit extract of *S. aspera* exhibited 61% DPPH radical scavenging activity. Yıldız et al. [44] examined the characteristics of two different Smilax species growing in Hatay and its surroundings, and they found that the FRAP value of *S. excelsa* was 62.28-64.07 mmol Fe+2/kg in the leaves, which are much lower than our findings. As the researchers reported, these differences may result from climatic conditions or genotypes. Demir [12] prepared the extracts with different solvents from the fresh shoots of *S. excelsa* growing in Düzce and compared the antioxidant properties of the extracts. As a result of the study, the DPPH activities were listed as methanol>ethanol>water, while the ABTS activities were listed as ethanol≥ methanol>water. The fact that the water extract showed the lowest activities in both cases coincides with our study. The shoots and leaves of *S. excelsa* are sources of biologically active phytochemicals, including various phenolic compounds [45], and it has been proven that the main chemical components responsible for antioxidant activity consist of flavonoids and anthocyanins [19]. In our study, it has been proven that the extracts are rich in phenolic and flavonoid contents, and especially the ethanol and methanol extracts with high phenolic amounts show high DPPH and FRAP values, which is attributed to the fact that phenolic compounds may have a strong antioxidant effect.

Results of Antimicrobial Activity and Minimum Inhibition Concentration (MIC)

In this study, the efficacy of different solvent extracts of S. *excelsa* against one fungus, three gram (+) bacteria, and one gram (-) bacteria was investigated. As a result of the disc diffusion test, a clear zone was observed around all discs used as positive controls. In the Petri dish in which the *E. faecalis* ATCC 29212 pathogen was cultivated, a clear zone formation was observed around the disc in which only the water extract was impregnated (Figure 2). The zone diameter for this Petri dish was measured with the help of a ruler (Table 7). Apart from this, no zones were formed in the other Petri dishes.

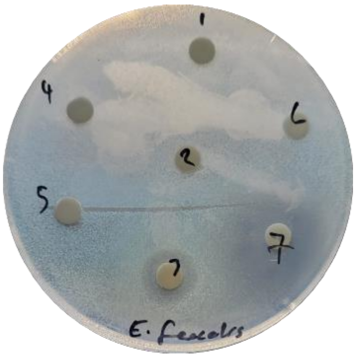

Figure 2. *Antibacterial activity of the Smilax excelsa extracts against Enterococcus faecalis* ATCC 29212*. 1, methanol extract (80%); 2, ethanol extract (70%); 3, water; 4-6, negative control for methanol extract (80%), ethanol extract (70%) and water, respectively; 7, positive control*

Table 7. *Zone diameters of the water extract giving positive results in the disc diffusion test.*

Extract	**Pathogen**	**Average zone diameter in positive control (cm) ± SD**	**Average zone diameter in extract (cm) ± SD**
Water extract	*Enterococcus faecalis* ATCC 29212	2.10 ± 0.08	1.17 ± 0.05

SD: standard deviation

MIC test was performed to determine the lowest concentration at which the inhibitory effect of the water extract, which gave positive results in the disc diffusion test, on *E. faecalis* ATCC 29212 was achieved. At the end of incubation, the turbidity in the wells was evaluated with the naked eye. Accordingly, it was observed that there was no turbidity in the 12th well containing sterile medium, and therefore the study was carried out aseptically. In the wells containing the extract, an increased turbidity was observed in the 4th-11th wells compared to the previous 24 hours, but no such change was detected in the first 3 wells. As a result, it was found that the concentration of the extract in the 3rd well was the lowest concentration required for the inhibition of the pathogen. The minimum inhibitory concentration (MIC) of the water extract against *E. faecalis* ATCC 29212 was determined to be 10 mg/mL (Figure 3).

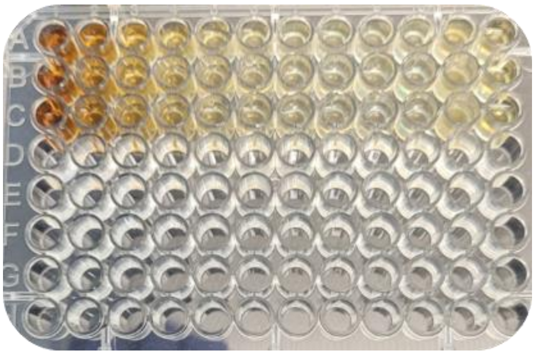

Figure 3. *Minimum inhibition concentration tests of the water extract against Enterococcus faecalis using a 96-well plate assay (conducted in triplicate)*

It was documented in a study that the extracts made from the fresh shoots of *S. excelsa* exhibited the antibacterial and antifungal activities [46]. Efe et al. [47] proved that the fruit extract of *S. excelsa* has an inhibitory effect against *Staphylococcus aureus, Escherichia coli, Klebsiella pneumonia, Pseudomonas aeruginosa, Staphylococcus epidermidis, Candida krusei, Candida albicans,* and *Streptococcus mutans*. Researchers have determined different antimicrobial activities against all tested microorganisms; the maximum antimicrobial effect was recorded with a 16 mm inhibition zone against *E. coli*, while the lowest antimicrobial effect was reported to be obtained with an 11 mm inhibition zone against *S. aureus*. Khaligh et al. [13] reported that the compounds violasterol A and trans-resveratrol (3), obtained from the ethyl acetate extract of S. excelsa, showed activity against *S. aureus* with MIC values of 142.5 and 136.9 µM, respectively. Oğuz Akın et al. [43] found the MIC values of the ethanol extracts of *S. aspera* fruits against *E. coli* and *C. albicans* as 31.25 µg/ml. On the other hand, no antimicrobial activity of the methanol and ethanol extracts of *S. excelsa* was observed in this study, and the activity against *E. faecalis* ATCC 29212 strain was only found in the water extract. This situation reveals the effect of the choice of solvent. In addition, it is thought that the necessity of a synergistic effect in the antimicrobial activities of the *S. excelsa* extracts or the lack of stability of the compounds enabled these results to be obtained.

Conclusion

As a result of this study, it was determined that different solvent extracts of shoots, which are the edible parts of *S. excelsa*, differ in terms of phytochemical properties, and antioxidant and antimicrobial activities. In this context, it can be said that the ethanol and methanol extracts are more effective in terms of both phytochemical properties and antioxidant activities compared to the water extract. In particular, the high amounts of phenolic compounds in the ethanol and methanol extracts brought about high antioxidant activities. According to this result, it can be concluded that the edible parts of *S. excelsa* have an essential potential in terms of health and food. Plants are used in the treatment of various diseases. In addition, secondary compounds obtained from plants also have deterrent or toxic effects on pests. For this reason, it is recommended to determine the effects of the extracts that can be obtained from the edible wild plant or the secondary compounds that can be isolated from the plant on different organisms. In line with the results obtained, it is suggested that, due to the antioxidant properties exhibited by *S. excelsa*, this plant can be an important source for different medicines and can be integrated into many treatment methods in modern medicine.

Acknowledgement We would like to thank Assoc. Prof. Dr. Kadir Mert DÖLEKER for providing laboratory usage support. We also thank Nejdet AYCAN for his help in collecting the plant used the study.

Funding/Financial Disclosure -

Ethics Committee Approval and Permissions The study does not require ethics committee approval or any special permission.

Conflicts of Interest The authors declared no conflict of interest.

Authors Contribution All authors read and approved the final manuscript.

References

[1] Ferreira, I. C. F. R., Morales, P., & Barros, L. (2017). *Wild Plants, Mushrooms and Nuts: Functional Properties and Food Applications*. John Wiley & Sons, Ltd.

[2] Gangwar, K. K., Deepali, G. R. & Gangwar, R. S. (2010). Ethnomedicinal plant diversity in Kumaun Himalaya of Uttarakhand, India. *Natural Sciences, 8*(5), 66-78.

[3] Kumari, S., & Sahu, C. (2015). Food habits and its socio-cultural values among the tribals of Jharkhand and Hindus of Bihar. *Asian Man (The)-An International Journal, 9*(1), 87-91.

[4] Harumi Iyda, J., Fernandes, Â., Calhelha, R. C., Alves, M. J., Ferreira, F. D., Barros, L., Amaral, J. S., & Ferreira, I. C. F. R. (2019). Nutritional composition and bioactivity of *Umbilicus rupestris* (Salisb.) Dandy: an underexploited edible wild plant. *Food Chemistry, 295*, 341-349. https://doi.org/10.1016/j.foodchem.2019.05.139

[5] Brito, C., Bertotti, T., Primitivo, M. J., Neves, M., Pires, C. L., Cruz, P. F., Martins, P. A. T., Rodrigues, A. C., Moreno, M. J., Brito, R. M. M., Campos, M. J., Vaz, D. C., Pessoa, M. F., Lidon, F., Reboredo, F., & Ribeiro, V. S. (2021). *Corema album* spp: edible wild crowberries with a high content in minerals and organic acids. *Food Chemistry, 345*, 128732. https://doi.org/10.1016/j.foodchem.2020.128732

[6] Geraci, A., Amato, F., Di Noto, G., Bazan, G., & Schicchi, R. (2018). The wild taxa utilized as vegetables in Sicily (Italy): a traditional component of the Mediterranean diet. *Journal of Ethnobiology and Ethnomedicine, 14*(1), 14. https://doi. org/10.1186/s13002-018-0215-x

[7] Gündüz, M., & Karabıyıklı Çiçek, Ş. (2023). Some edible weeds grown in the Black Sea Region and their bioactive properties. *Toros University Journal of Nutrition and Gastronomy, 2*, 183-195. https://doi.org/10.58625/jfng-2321

[8] Wondimu, T., Asfaw, Z., & Kelbessa, E. (2006). Ethnobotanical study of food plants around "Dheeraa" town, Arsi, Ethiopia. *SINET: Ethiopian Journal of Science, 29*, 71-80. https://doi.org/10.4314/sinet.v29i1.18261

[9] Raul, S. C., Beatriz, H. C., Joseoziel, L. G., & Francenia, S. S. N. (2017). Phenolic Compounds in Genus *Smilax* (Sarsaparilla). In M. Soto-Hernandez, M. Palma-Tenango, & M.D.R. Garcia-Mateos, (Eds.), *Phenolic Compounds - Natural Sources, Importance and Applications*, (pp. 233-260). IntechOpen. https://doi.org/10.5772/66896

[10] Zubair, M., Rizwan, K., Rashid, U., Saeed, R., Saeed, A. A., Rasool, N., & Riaz, M. (2013). GC/MS profiling, *in vitro* antioxidant, antimicrobial and haemolytic activities of *Smilax macrophylla* leaves. *Arabian Journal of Chemistry, 10*(1), 1460-1468. https://doi.org/10.1016/j.arabjc.2013.04.024

[11] Yıldız, Ö. Ş., Ayanoğlu, F., & Bahadırlı, N. P. (2018). Some morphological and chemical characteristics of Sarsaparilla (*Smilax aspera* L., *Smilax excelsa* L.). *Mustafa Kemal Üniversitesi Ziraat Fakültesi Dergisi*, *23*(2), 254-261.

[12] Demir, E. (2023). The fatty acid composition, phytochemicals and antioxidabt potential of wild edible *Smilax excelsa* L. shoots. *Acta Scientiarum Polonorum Hortorum Cultus, 22*(1), 27-35. https://doi.org/10.24326/asphc.2023.4566

[13] Khaligh, P., Salehi, P., Farimani, M. M., Ali-Asgari, S., Esmaeili, M. A., & Nejad-Ebrahimi, S. (2016). Bioactive compounds from *Smilax excelsa* L. *Journal of the Iranian Chemical Society*, *13*, 1055-1059. https://doi.org/10.1007/s13738-016-0819-9

[14] Baytop, T. (1984). *Türkiye'de Bitkiler ile Tedavi (Geçmiste ve Bugün)*. İstanbul Üniversitesi Yayınları.

[15] Davis, P. H. (1984). *Smilax* L. In P. H. Davis, (Ed.), *Flora of Turkey and the East Aegean Islands*, (pp. 70-72). Edinburgh, Edinburgh University Press.

[16] Güner, A., Aslan, S., Ekim, T., Vural, M., & Babaç, M. T. (2012). *Türkiye Bitkileri Listesi (Damarlı Bitkiler)*. Nezahat Gökyiğit Botanik Bahçesi ve Flora Araştırmaları Derneği Yayını.

[17] Eminağaoğlu, Ö., & Aksu, G. (2018). *Smilax* L. In Ü. Akkemik (Ed), *Türkiye'nin Doğal-Egzotik Ağaç ve Çalıları*, (pp. 613-614). Orman Genel Müdürlüğü Yayınları.

[18] Yılmaz-Sarıaltın, S., Çiçek-Polat, D., & Yalçın, C. Ö. (2023). Cytotoxic and antioxidant activities and phytochemical analysis of *Smilax excelsa* L. and *Aegopodium podagraria* L. *Food Bioscience*, *52*, 102359. https://doi.org/10.1016/j.fbio.2023.102359

[19] Ozsoy, N., Can, A., Yanardag, R., & Akev N. (2008). Antioxidant activity of *Smilax excelsa* L. leaf extracts. *Food Chemistry, 110*, 571-583. https://doi.org/10.1016/j.foodchem.2008.02.037

[20] Wu, L. S., Wang, X, J., Wang, H., Yang, H. W., Jia, A. Q., & Ding, Q. (2010). Cytotoxic polyphenols against breast tumor cell in *Smilax china* L. *Journal of Ethnopharmacology*, *130*(3), 460-464. https://doi.org/10.1016/j.jep.2010.05.032

[21] Raghunath, S., Budaraju, S., Gharibzahedi, S. M. T., Koubaa, M., Roohinejad, S., & Mallikarjunan, K. (2023). Processing technologies for the extraction of value-added bioactive compounds from tea. *Food Engineering Reviews, 15*, 276-308. https://doi.org/10.1007/s12393-023-09338-2

[22] AOAC (2010). *Association of Official Analytical Chemists Official Methods of Analysis of the Association of Official Analytical Chemists*, 18th edn. AOAC International, Washington DC.

[23] Singleton, V., & Rossi, J. (1965). Colorimetry of total phenolic compounds with phosphomolybdic-phosphotungstic acid reagents. *American Journal of Enology and Viticulture, 16*, 144-158.

[24] Zannou, O., & Koca, I. (2020). Optimization and stabilization of the antioxidant properties from Alkanet (*Alkanna tinctoria*) with natural deep eutectic solvents. *Arabian Journal of Chemistry, 13*(8), 6437-6450. https://doi.org/10.1016/j.arabjc.2020.06.002

[25] Zannou, O., & Koca, I. (2022). Greener extraction of anthocyanins and antioxidant activity from blackberry (*Rubus* spp) using natural deep eutectic solvents. *Lwt, Food Science and Technology, 158*, 113184. https://doi.org/10.1016/j.lwt.2022.113184

[26] Tural, S., & Koca, I. (2008). Physico-chemical and antioxidant properties of cornelian cherry fruits (*Cornus mas* L.) grown in Turkey. *Scientia Horticulturae*, *116*, 362-366.

[27] Gao, X., Ohlander, M., Jeppsson, N., Björk, L., & Trajkovski, V. (2000). Changes in antioxidant effects and their relationship to phytonutrients in fruits of sea buckthorn (*Hippophae rhamnoides* L.) during maturation. *Journal of Agricultural and Food Chemistry, 48*(5), 1485-90. https://doi.org/10.1021/jf991072g

[28] Zannou, O., Pashazadeh, H., Ghellam, M., Koca, I., Kaddour, A. A., & Leriche, F. (2024). Appraisal of phenolic compounds, antioxidant activity and in vitro gastrointestinal digestion of borage (*Echium amoenum*) flowers using natural deep eutectic solvent (NADES). *Biomass Conversion and Biorefinery, 14*(7), 8523-8535. https://doi.org/10.1007/s13399-022-02739-z

[29] Bauer, A. W., Kirby, W. M., Sherris, J. C., & Turck, M. (1966). Antibiotic susceptibility testing by a standardized single disk method. *American Journal of Clinical Pathology, 45*(4), 493-496.

[30] Sabouraud, R. (1892). Contribution a l'etude de la trichophytie humaine. Etude clinique, microscopique et bacterioloqique sur la pluralité des trichophytons de l'homme. *Ann Dermatol Syphil*, *3*, 1061-1087.

[31] Balouiri, M., Sadiki, M., & Ibnsouda, S. K. (2016). Methods for in vitro evaluating antimicrobial activity: a review. *Journal of Pharmaceutical Analysis, 6*(2), 71-79. https://doi.org/10.1016/j.jpha.2015.11.005

[32] Topdas, E. F., Demirbaş, M., Şengül, M., & Şat, İ. G. (2021). Farklı kurutma tekniklerinin *Smilax excelsa* genç sürgünlerinin antioksidan aktivitesi ve bazı fizikokimyasal özellikleri üzerine etkisi. *Atatürk Üniversitesi Ziraat Fakültesi Dergisi*, *52*(3), 314-324. https://doi.org/10.17097/ataunizfd.816887

[33] Özkan, M., Kırca, A., & Cemeroğlu, B. (2003). Effect of moisture content on CIE color values in dried apricots. *European Food Research and Technology, 216,* 217-219. https://doi.org/10.1007/s00217-002-0627-6

[34] Miser-Salihoglu, E., Akaydin, G., Caliskan-Can, E., Yardim-Akaydin, S., Tatiparthi, R., Duraiswamy, D., Bannoth, C. K., Ozdamar, E. D., Eke, B. C., & Gokbulut, A. (2010). Evaluation of antioxidant activity of various herbal folk evaluation medicine. *Fabad Journal of Pharmaceutical Sciences*, *35*, 59-67.

[35] Şahin, Ö. (2019). *Melocan (Smilax excelsa L.) bitkisinin farklı kısımlarının ultrason ve mikrodalga destekli ekstraksiyon ile elde edilen bileşenlerinin tanımlanması*. (Tez no. 547224). [Yüksek lisans tezi, Hacettepe Üniversitesi].

[36] Al Yassine, D., El Massri, N., Demircan, G., Bulut, G., Akin, D., & Tacer-Caba, Z. (2023). Total antioxidant potential, total phenolic profile and cytotoxic activity against brain cancer: melocan and galdirik. *Food Technology and Biotechnology, 61*(4), 475-484. https://doi.org/10.17113/ftb.61.04.23.8071

[37] Yan, Y., Zhou, X., Guo, K., Zhou, F., & Yang, H. (2020). Use of chlorogenic acid against diabetes mellitus and its complications. *Journal of Immunology Research, 2020,* 9680508. https://doi.org/10.1155/2020/9680508

[38] Ganeshpurkar, A., & Saluja, A. (2020). The pharmacological potential of catechin. *Indian Journal of Biochemistry and Biophysics*, *57*(5), 505-511.

[39] Yang, J., Guo, J., & Yuan, J. (2008). In vitro antioxidant properties of rutin. *LWT-Food Science and Technology, 41*(6), 1060-1066. https://doi.org/10.1016/j.lwt.2007.06.010

[40] Cellat, M., İşler, C. T., Uyar, A., Kuzu, M., Aydın, T., Etyemez, M., Türk, E., Yavas, I., & Güvenç M. (2022). Protective effect of *Smilax excelsa* L. pretreatment via antioxidant, anti-inflammatory effects, and activation of Nrf-2/HO-1 pathway in testicular torsion model. *Journal of Food Biochemistry, 46*(8), e14161. https://doi.org/10.1111/jfbc.14161

[41] Topal, F., Nar, M., Gocer, H., Kalin, P., Kocyigit, U. M., Gülçin, İ., & Alwasel, S. H. (2016). Antioxidant activity of taxifolin: an activity-structure relationship. *Journal of Enzyme Inhibition and Medicinal Chemistry*, *31*(4), 674-683. https://doi.org/10.3109/14756366.2015.1057723

[42] Das, A., Baidya, R., Chakraborty, T., Samanta, A. K., & Roy, S. (2021). Pharmacological basis and new insights of taxifolin: a comprehensive review. *Biomedicine & Pharmacotherapy*, *142*, 112004. https://doi.org/10.1016/j.biopha.2021.112004

[43] Oğuz Akın, S., Yesil Celiktas, O., & Sevimli Gür, C. (2022). Anticancer, antioxidant and antimicrobial activities of some Mediterranean plants extracts. *Journal of the Institute of Science and Technology, 12*(3), 1550-1557. https://doi.org/10.21597/jist.1099409

[44] Yıldız, Ö. Ş., Ayanoğlu, F., & Bahadırlı, N. P. (2018). Some morphological and chemical characteristics of Sarsaparilla (*Smilax aspera* L., *Smilax excelsa* L.). *Mustafa Kemal Üniversitesi Ziraat Fakültesi Dergisi*, *23*(2), 254-261.

[45] Ozsoy, N., Okyar, A., Arda-Pirincci, P., Can, A., Bolkent, S., & Akev, N., 2013. Evaluation of *Smilax excelsa* L. use in experimentally induced nephrotoxicity. *Kafkas Universitesi Veteriner Fakültesi Dergisi, 19*, 807. https://doi.org/10.9775/kvfd.2013.9253

[46] Gürbüz, İ., Özçelik, B., Günbatan, T., Akkol, E. K., Şahinöz, M., & Akaydın, G. (2021). Antibacterial, antifungal and enzyme inhibitory effects of selected plants from Turkey. *Pakistan Journal of Pharmaceutical Sciences, 34*(3), 1011-1017. https://doi.org/10.36721/PJPS.2021.34.3.REG.1011-1017.1

[47] Efe, E., Yalçın, E., & Çavuşoğlu, K. (2019). Antimutagenic and multi-biological activities of *Smilax excelsa* L. fruit extract. *Cumhuriyet Science Journal*, *40*(*2*), 440-446. https://doi.org/10.17776/csj.513469

Sinopfbd, 2024; 9(2): 534-550 **https://doi.org/10.33484/sinopfbd.1526629**

Sinop Üniversitesi Fen Bilimleri Dergisi
Sinop Uni J Nat Sci

E-ISSN: 2564-7873

https://dergipark.org.tr/tr/pub/sinopfbd

Ekivaryant CW Kompleksler Üzerine Kompakt Grup Etkileri İçin Conner'in Sanısı

Mehmet ONAT

How to cite: Onat, M. (2024). Ekivaryant CW kompleksler üzerine kompakt grup etkileri için Conner'in Sanısı. *Sinop Üniversitesi Fen Bilimleri Dergisi*, *9*(2), 534-550. https://doi.org/10.33484/sinopfbd.1526629

Araştırma Makalesi

Sorumlu Yazar
Mehmet ONAT
monat@sinop.edu.tr

Yazarlara ait ORCID
M.O: 0000-0002-6538-6624

Received: 01.08.2024
Accepted: 27.12.2024

Öz

X, Λ ($\mathbb{Z}$, $\mathbb{Z}_p$ veya $\mathbb{Q}$) üzerinde sonlu kohomolojik boyuta sahip bir parakompakt uzay ve G, X üzerine sonlu sayıda orbit tipi ile etki eden kompakt bir Lie grubu olsun. R. Oliver tarafından kanıtlandı ki eğer X, Λ üzerinde asiklik bir uzay ise X/G orbit uzayı da Λ üzerinde asiklik bir uzaydır. Bu çalışmada, sonlu sayıda bağlantılı orbit tipli, sonlu boyutlu ekivaryant CW kompleksler üzerine sonlu boyutlu kompakt grup (Lie grubu olmayabilir) etkileri için bu sonuç kanıtlanacaktır. Ayrıca, bazı koşullar altında parakompakt uzaylar üzerine etki eden kompakt bağlantılı grup (Lie grubu olmayabilir) etkileri için rasyonel sayılar üzerinde bir asiklik uzayın sabit nokta uzayının asiklik olduğu gösterilecektir.

Anahtar Kelimeler: Conner'in sanısı, Asiklik uzaylar, Kompakt grup etkileri

The Conner Conjecture For Compact Group Actions On Equivariant CW Complexes

Sinop Üniversitesi, Fen-Edebiyat Fakültesi, Matematik Bölümü, Sinop, Türkiye

Abstract

Let X be a paracompact space of finite cohomological dimension over Λ ($\mathbb{Z}$, $\mathbb{Z}_p$ or $\mathbb{Q}$) and G be a compact Lie group acting on X with finite many orbit types. It has been proven by R. Oliver that if X is acyclic over Λ, then the orbit space X/G is also acyclic over Λ. In this study, for rational coefficients, this result will be proven for finite-dimensional compact (non-Lie) group actions on finite dimensional equivariant CW complexes with finitely many connective orbit types. Furthermore, it will be showen that the fixed point space of an acyclic space over rationals is acyclic for compact connected (non-Lie) group actions on paracompact spaces under certain conditions.

Keywords: Conner conjecture, Acyclic spaces, Compact group actions

Giriş

G, bir X topolojik uzayı üzerine sürekli bir şekilde etki eden bir topolojik grup olsun. Kompakt dönüşüm gruplarının çalışmasında ilginç ve önemli bir problem X uzayının kohomolojik yapısı ile X^G sabit nokta kümesi veya X/G orbit uzayının kohomolojik yapısı arasındaki ilişkileri incelemektir. Bu şekilde bir çok sonuç literatürde bulunabilir (Allday ve Puppe [1], Borel [2], Bredon [3], Bredon [4], Conner [5], Conner

[6], Deo [7], Deo ve ark. [8], Ku [9], Ku [10], Oliver [11]). Bu biçimdeki bazı sonuçları hatırlayarak işe başlayalım.

H^* bir kohomoloji teorisi olmak üzere eğer $H^0(X;\Lambda) = \Lambda$ ve $n \geq 1$ iken $H^n(X;\Lambda) = 0$ ise X topolojik uzayına asiklik (acyclic) uzay veya Λ-asiklik uzay denir.

Teorem 1. (Conner'in Sanısı) G kompakt bir Lie grup ve X sonlu sayıda orbit tipli, sonlu boyutlu bir G-CW kompleks olsun. O zaman eğer X bir Λ-asiklik uzay ise X/G orbit uzayı da Λ-asiklik uzaydır, burada Λ herhangi bir abelyen gruptur.

Teoremde X'in sonlu boyutlu olması gerekli bir koşuldur. Evrensel serbest (free) G-uzay E_G, sonsuz boyutlu bir G-CW komplekstir (G aşikar değilse) ve asiklik bir uzaydır fakat $B_G = E_G/G$ orbit uzayı sıfırdan farklı kohomoloji cebirine sahiptir.

Bu teoremin Conner'in sanısının özel bir durumu olduğunu not edelim. Teorem bazı koşullar altında Conner [6] tarafından kanıtlandı. Daha sonra Oliver [11] gösterdi ki eğer G, sonlu sayıda orbit tipi ile sonlu kohomolojik boyutlu, parakompakt bir X uzayı veya kompakt bir X uzayı üzerine etki eden kompakt bir Lie grubu ise Λ-asiklik ($\Lambda = \mathbb{Z}$, $\mathbb{Z}_p$ veya $\mathbb{Q}$) X uzayının X/G orbit uzayı da Λ-asiklik bir uzaydır. X uzayının kompakt olması durumunda sonlu sayıda orbit tipi hipotezine gerek yoktur. Bu sonuçlar aynı zamanda Bredon'un kitabında bulunabilir [4, IV, §14].

Bununla birlikte Deo ve ark. [8] gösterdi ki eğer G, sonlu sayıda orbit tipi ile finitistik (her zaman parakompakt) bir X uzayı üzerine etki eden kompakt bir Lie grubu ise Λ-asiklik bir uzayın X/G orbit uzayı da Λ-asiklik bir uzaydır.

Şimdi Euler karakteristiğinin tanımı hatırlansın. $\chi(X)$ Euler karakteristiği herhangi bir katsayı halkası için

$$\chi(X) = \sum_{i=0}^{\infty} (-1)^i \dim H^i(X)$$

biçiminde tanımlanır. Aşağıdaki teorem Borel-Hsiang-Quillen lokalizasyon teoreminin önemli bir sonucudur.

Teorem 2. G bir torus (kompakt, bağlantılı, abelyen Lie grubu, yani $G = \mathbb{S}^1 \times \cdots \times \mathbb{S}^1$) ve X sonlu sayıda bağlantılı orbit tipli ve sonlu kohomolojik boyutlu parakompakt bir G-uzay olsun. Eğer $\sum_{i\geq 0} rkH^i(X;\mathbb{Q}) < \infty$ ise $\sum_{i\geq 0} rkH^i\left(X^G;\mathbb{Q}\right) < \infty$ ve $\chi(X) = \chi\left(X^G\right)$ olur. Özellikle eğer $\chi(X) \neq 0$ ise $X^G \neq \emptyset$ olur. Ayrıca, X bir $\mathbb{Q}$-asiklik uzay ise X^G sabit nokta kümesi de $\mathbb{Q}$-asiklik uzaydır.

Kanıt. Allday ve Puppe [1, Corollary 3.1.13 ve Remark 3.10.5]'de bulunabilir.

Bundan sonra Λ katsayısına göre X uzayının kohomolojik boyutu $\dim_\Lambda X$ ile gösterilecektir, tanım için bkz. Bredon [4] veya Quillen [12].

Teorem 3. (Borel [2, p. 60], Conner [5]) G kompakt bir Lie grup ve X, kompakt bir G-uzay olsun. Eğer $\dim_\Lambda X < \infty$ ve her $x \notin X^G$ için $H^*\left(B_{G_x};\Lambda\right) = 0$ ve her $i \geq N$ için $H^i(X;\Lambda) = 0$ ise o zaman aşağıdakiler sağlanır.

a. Her $i \geq N$ için $H^i(X/G;\Lambda) = 0$'dır.

b. Eğer G sonsuz ise her $i \geq N$ için $H^i\left(X^G; \Lambda\right) = 0$'dır.

Aşağıdaki koşul kısaca (I_0) olarak adlandırılacaktır.
G_x izotropi alt grubunun birim bağlantılı bileşeni G_x^0, verilen etki altında sabit olmayan her $x \in X$ noktası için G'nin merkezi $Z(G)$'de içerilir, yani her $x \in X \setminus X^G$ için $G_x^0 \subset Z(G)$'dir.
Aşağıdaki sonuç Hofmann ve Mostert [13] tarafından kanıtlandı.

Teorem 4. G, kompakt, $\mathbb{Q}$-asiklik bir X uzayı üzerine etki eden kompakt, bağlantılı bir grup olsun. Eğer (I_0) koşulu sağlanıyorsa X^G sabit nokta kümesi boştan farklıdır ve $\mathbb{Q}$-asiklik uzaydır.

Aşağıdaki sonuçlar Ku [10] tarafından kanıtlandı.

Teorem 5. G, kompakt, $\mathbb{Q}$-asiklik bir X uzayı üzerine etki eden kompakt, bağlantılı bir grup olsun. Eğer (I_0) koşulu sağlanıyor ve her $i \geq N$ için $H^i(X; \mathbb{Q}) = 0$ ise her $i \geq N$ için $H^i\left(X^G; \mathbb{Q}\right) = 0$ olur.

Teorem 6. G, kompakt, $\mathbb{Q}$-asiklik bir X uzayı üzerine etki eden kompakt bir grup olsun ve (I_0) koşulu sağlansın. Eğer G'nin birim bileşeni G_0, $Z(G)$'de içerilmiyor ve her $i \geq N$ i çin $H^i(X; \mathbb{Q}) = 0$ ise her $i \geq N$ için $H^i\left(X^G; \mathbb{Q}\right) = 0$ olur.

Teorem 7. G, kompakt bir X uzayı üzerine etki eden sonlu boyutlu kompakt bir grup olsun ve (I_0) koşulu sağlansın. Eğer her $i \geq N$ için $H^i(X; \mathbb{Q}) = 0$ ise her $i \geq N$ için $H^i(X/G; \mathbb{Q}) = 0$ olur. Özel olarak X, $\mathbb{Q}$-asiklik bir uzay ise X/G orbit uzayı da $\mathbb{Q}$-asiklik uzaydır.

Teorem 8. X kompakt bir uzay ve G, X üzerine etki eden abelyen ve sonlu boyutlu kompakt bir grup olsun. Eğer her $i \geq N$ için $H^i(X; \mathbb{Q}) = 0$ ise her $i \geq N$ için $H^i(X/G; \mathbb{Q}) = 0$ olur.

Deo [7] uzayın (I_0) koşulunu sağlaması ile sonlu sayıda orbit tipine sahip olması koşulunu yer değiştirdi ve sonraki teoremi kanıtladı. Bu iki koşulun birbirinden bağımsız olduğunu not edelim.

Teorem 9. G, $\mathbb{Q}$ üzerinde sonlu kohomolojik boyuta sahip yerel kompakt Hausdorff bir X uzayı üzerine etki eden sonlu boyutlu, kompakt bir grup olsun. Eğer X sonlu sayıda orbit tipine sahip ve her $i \geq N$ için $H_c^i(X; \mathbb{Q}) = 0$ ise her $i \geq N$ için $H_c^i(X/G; \mathbb{Q}) = 0$ olur. Burada H_c^*, kompakt destekli sheaf kohomolojiyi gösterir ve X kompakt uzay ise alışılmış H^* kohomolojisine eşit olur.

G-CW kompleksler ile ilgili aşağıdaki sonuç Allday ve Puppe [1, Corollary 3.10.12]'de bulunabilir.

Teorem 10. G bir torus ve X, sonlu sayıda bağlantılı orbit tipli, sonlu boyutlu bir G-CW kompleks olsun. Eğer her $i \geq N$ için $H^i(X; \mathbb{Q}) = 0$ ise her $i \geq N$ için $H^i(X/G; \mathbb{Q}) = 0$ ve $H^i\left(X^G; \mathbb{Q}\right) = 0$ olur.

Yukarıdaki teoremlerde G kompakt grubunun etki ettiği topolojik uzaylar kompakt ya da yerel kompakt uzaylardır.
Bu makalede bu uzayların sonlu boyutlu G-CW kompleksler (parakompakt uzayların bir alt sınıfıdır) ile yer değiştirilebileceği gösterilecektir.
Daha açık yazılacak olursa aşağıdaki teoremler ve sonlu boyutlu G-CW kompleksler üzerine etki eden sonlu boyutlu kompakt gruplar için lokalizasyon teoreminin doğru olduğu kanıtlanacaktır.
Bu sonuçların önemi topolojik grup etkileri teorisinde Hilbert-Smith sanısı olarak bilinen hala cevaplanamamış bir problemin var olmasıdır. Bu sanı, bir sonlu boyutlu manifold üzerine efektif olarak etki eden bir kompakt topolojik grubun bir Lie grubu olması gerektiğini iddia eder.

Teorem 11. G, sonlu boyuta sahip kompakt bir grup ve X sonlu boyutlu G-CW kompleks olsun. Eğer X, $\mathbb{Q}$-asiklik bir uzay ise X/G orbit uzayı da $\mathbb{Q}$-asiklik uzaydır.

Teorem 12. G, sonlu boyutlu bağlantılı, kompakt, abelyen bir grup ve X sonlu boyutlu bir G-CW kompleks olsun. Eğer X, $\mathbb{Q}$-asiklik bir uzay ve X sonlu sayıda bağlantılı orbit tipine sahip ise X^G sabit nokta kümesi de $\mathbb{Q}$-asiklik uzaydır.

Teorem 13. G, kompakt, bağlantılı bir grup ve X, $\mathbb{Q}$-asiklik, parakompakt bir uzay olsun. Eğer (I_0) koşulu sağlanıyorsa X^G sabit nokta kümesi boş değildir ve $\mathbb{Q}$-asiklik uzaydır.

Ön Bilgiler

Bu bölümde bazı temel kavram ve sonuçlar ifade edilecektir. Topolojik gruplar da dahil tüm topolojik uzayların Hausdorff olduğu kabul edilecektir.

Açıklanmamış notasyon ve kavramları okuyucuyu Allday ve Puppe [1], Borel [2], Bredon [3], Hofmann ve Morris [14], veya Onat [19] kaynaklarında bulabilir.

Şimdi X herhangi bir topolojik uzay ve G herhangi bir topolojik grup olsun. Aşağıdaki koşulları sağlayan $\Theta : G \times X \longrightarrow X$ sürekli dönüşümüne G'nin X üzerine bir etkisi ve X uzayına da G-uzay denir.

a. Her $x \in X$ ve $g, h \in G$ için $(gh)\, x = g\,(hx)$'dir.

b. Her $x \in X$ için $ex = x$'dir, burada e , G'nin birimidir.

Bir $x \in X$ noktasının izotropi alt grubu G'nin $G_x = \{g \in G : gx = x\}$ (kapalı) alt grubudur. Bir $x \in X$ noktasının orbiti X'in $G\,(x) = \{gx \in X : g \in G\}$ alt uzayıdır. Daha genel olarak bir $H \subset G$ alt grubu ve $Y \subset X$ alt uzayı için $H\,(Y) = \{hy : h \in H, y \in Y\}$ olarak tanımlanır. Eğer $G\,(Y) = Y$ ise $Y \subset X$ alt uzayına G-invaryant alt uzay denir.

G-etkiler ile uyumlu (yani her $g \in G$ ve $x \in X$ için $f\,(gx) = gf\,(x)$) G-uzaylar arasında sürekli bir $f : X \longrightarrow Y$ dönüşümüne G-ekivaryant bir dönüşüm denir. Eğer X Hausdorff bir uzay ve G kompakt bir grup ise $G\,(x)$, G/G_x homojen uzayına G-izomorfiktir.

Eğer $G_x = G$ (veya denk olarak $G\,(x) = \{x\}$) ise $x \in X$ noktasına G-etkisinin sabit noktası (fixed or stationary point) denir. Etkinin sabit noktalarının kümesi X^G veya $F\,(G, X)$ ile gösterilecektir.

Her bir $x \in X$ noktasını $G\,(x)$ orbiti ile özdeşleştirerek elde edilen bölüm uzayı X 'in orbit uzayı olarak adlandırılır ve X/G ile gösterilir. Böylece $X/G = \{G\,(x) : x \in X\}$ olur ve bölüm topoloji ile verilir.

G, bir X uzayı üzerine etki eden bir topolojik grup olsun. Eğer $\{[G_x] : x \in X\}$ sonlu bir küme ise X sonlu sayıda orbit tipine sahiptir (finitely many orbit types) veya G, X üzerine sonlu sayıda orbit tipi ile etki eder denir, burada $[G_x]$, G_x izotropi alt grubunun G'de konjuge sınıfını gösterir. Eğer $\left\{\left[G_x^0\right] : x \in X\right\}$ sonlu bir küme ise X sonlu sayıda bağlantılı orbit tipine sahiptir (finitely many connective orbit types) veya G, X üzerine sonlu sayıda bağlantılı orbit tipi ile etki eder denir, burada G_x^0, G_x izotropi alt grubunun birim bağlantılı bileşenidir. Aşağıdaki lokalizasyon teoreminde eğer katsayılar halkası karakteristiği sıfır olan bir cisim ise sonlu sayıda bağlantılı orbit tipine sahip olması varsayımı yeterlidir (Allday ve Puppe [1, p.131]). Sonlu sayıda orbit tipine sahip olma, sonlu sayıda bağlantılı orbit tipine sahip olma özelliğini gerektirir. Eğer $G = \mathbb{S}^1$ ise herhangi bir G-uzayının sonlu sayıda bağlantılı orbit tipine sahip olduğu açıktır.

G kompakt bir grup ve X herhangi bir G-uzay olsun. Eğer H, G'nin kapalı ve normal bir alt grubu ise G/H bölüm grubunun X/H orbit uzayı üzerine etkisi $(gH) * (Hx) = H\,(gx)$ ile verilir ve H'nin X üzerine etkisi G'nin kısıtlanmış etkisidir. Ayrıca $i\,(Gx) = (G/H) * (Hx) = Gx/H$ ile tanımlanan $i : X/G \longrightarrow (X/H)\,/\,(G/H)$ dönüşümü bir homeomorfizmdir (Bredon [3] veya Hofmann ve Morris [14]).

İyi bilinen başka bir gerçek şudur:

Lemma 14. (Bredon ve ark. [15], Ku [10]) Eğer G, bir X uzayı üzerine etki eden bağlantılı bir grup ve N tamamen bağlantısız (totally disconnected) bir alt grup ise o zaman $(X/N)^{G/N} \approx X^G$ olur.

Bu gerçekler gösterir ki kompakt grup etkileri ile ilgili problemler Lie grubu etkilerine indirgenebilirler. Yukarıdaki verilen grup etkisi ile bölüm grubu etkisinin izotropi alt grupları ve bağlantılı bileşenleri arasında aşağıdaki ilişkiler vardır.

Not 15. G, bir X uzayı üzerine etki eden kompakt bir grup ve N, G'nin kapalı ve normal bir alt grubu olsun. Her $x \in X$ için

$$(G/N)_{N(x)} = NG_x/N$$

(Hofmann ve Morris [14, Proposition 10.31] veya Conner [6]) ve

$$(G/N)^0_{N(x)} = \left(NG^0_x\right)/N$$

(Hofmann ve Morris [14, Lemma 9.18]) olduğundan kolayca görülebilir ki eğer G, X üzerine sonlu sayıda (sırasıyla bağlantılı) orbit tipi ile etki ediyorsa G/N, X/N üzerine sonlu sayıda (sırasıyla bağlantılı) orbit tipi ile etki eder.

Eğer G bir torus ve X sonlu sayıda bağlantılı orbit tipli herhagi bir G-uzay ise $X^G = X^{\mathbb{S}^1}$ olacak şekilde bir $\mathbb{S}^1 \subset G$ alt çember grubu vardır (Allday ve Puppe [1, Lemma 4.2.1]). Bu gerçek gösterir ki sonlu sayıda bağlantılı orbit tipine sahip bir uzay üzerine etki eden torus etkilerinin sabit noktaları ile ilgili sonuçları yalnızca çember grubu etkisi için kanıtlamak yeterlidir.

Şimdi kompakt gruplar ile ilgili bazı gerçekler ifade edilecektir.

Öncelikle bir normal uzayın boyutunu hatırlayalım. X bir küme ve $\mathcal{A}$, X'in alt kümelerinin sonlu bir ailesi olsun. Her $x \in X$ için x noktasını içeren $\mathcal{A}$'nın elemanlarının sayısını $r\,(x)$ ile gösterelim. X üzerinde tanımlanan $r\,(x)$ fonksiyonunun maksimumu $\mathcal{A}$'nın derecesi (order) olarak adlandırılır.

$\mathcal{A}$ ve $\mathcal{B}$, bir X uzayının örtüleri olsun. Eğer her $B \in \mathcal{B}$ için $B \subset A$ olacak şekilde bir $A \in \mathcal{A}$ varsa $\mathcal{B}$'ye $\mathcal{A}$'nın bir incelmişi (refinement) denir.

Şimdi $X \neq \emptyset$ normal bir uzay olsun. X'in örtü boyutu negatif olmayan bir tamsayı ya da ∞ olarak aşağıdaki şekilde tanımlanır ve $\dim X$ ile gösterilir.

1. Eğer X uzayının her sonlu açık örtüsü, derecesi n'den küçük ya da eşit olan bir sonlu açık incelmişe sahip ise $\dim X \leq n$'dir, burada $n = 0, 1, \cdots$ şeklindedir.

2. Eğer $\dim X \leq n$ ve $\dim X > n - 1$ ise $\dim X = n$'dir.

3. Eğer $n = 0, 1, \cdots$ için $\dim X > n$ ise $\dim X = \infty$'dur.

Bir kompakt grubun sıfır boyutlu olması için gerek ve yeter şart tamamen bağlantısız olmasıdır.

İyi bilinir ki her kompakt gruba Lie grupları ile yaklaşılabilir, yani her kompakt grup kompakt Lie gruplarının ters (projektif) limitidir. G kompakt bir grup ve $\mathcal{N}$, G'nin normal, kapalı ve tamamen bağlantısız alt gruplarının bir filtre bazı olsun öyle ki her $N \in \mathcal{N}$ için G/N sonlu boyuta sahip kompakt bir Lie gruptur ve $\bigcap \mathcal{N} = \{1\}$'dir. O zaman G, $\varprojlim_{N \in \mathcal{N}} G/N$ ters limitine homeomorfiktir. Eğer G sonlu boyutlu, kompakt bir grup ise her $N \in \mathcal{N}$ için $\dim G = \dim G/N$ olduğu kabul edilebilir.

Eğer G, n-boyutlu torusların bir ters limiti ise G sonlu boyutlu pro-torus olarak adlandırılır, yani G sonlu boyutlu kompakt, bağlantılı, abelyen bir gruptur. 1-boyutlu pro-torus solenoid olarak adlandırılır. Daha fazla detay, Montgomery ve Zippin [16], Pontryagin [17] veya Hofmann ve Morris [18] kaynaklarında bulunabilir.

Teorem 16. [17, Theorem 69] Eğer G sonlu boyutlu kompakt bir grup ise G/N bir Lie grubu olacak şekilde G'nin tamamen bağlantısız kapalı bir N alt grubu vardır.

G-uzayların kohomolojini çalışmak için Borel [2] tarafından bir metod ortaya kondu. Bu metod, topolojik dönüşüm grupları teorisinin temel aracı haline gelmiştir. Bu yapı aşağıdaki şekilde tanımlanır.

Her G topolojik grubu için G'nin serbest etki ettiği bir (büzülebilir, parakompakt) E_G uzayı vardır ve $G \to E_G \to B_G$ bir esas demet uzayı (principal bundle) olup evrensel esas demet uzayı olarak adlandırılır, burada $B_G = E_G/G$ orbit uzayı G'nin sınıf uzayı olarak adlandırılır. (Milnor [20]). Şimdi X herhangi bir G-uzayı ise G'nin $X \times E_G$ çarpım uzayı üzerine $g\,(x, e) = (gx, ge)$ ile tanımlanan bir (serbest) etkisi vardır. Bu etkinin orbit uzayı $X_G = X \times_G E_G = (X \times E_G)\,/G$ ile gösterilir ve X'in Borel yapısı olarak adlandırılır. X_G uzayı üzerinde düşünülmesi gereken iki doğal dönüşüm vardır. $X \times E_G \longrightarrow E_G$, 2. izdüşüm dönüşümü, lifi (fiber) X olan bir $\pi_2 : X_G \to B_G$ demetimsi (fibration) belirler. Bu demetimsi Borel demetimsi olarak adlandırılır (Borel [2]).

Ayrıca $X \times E_G \longrightarrow X$, 1. izdüşüm dönüşümü, bir $\pi_1 : X_G \longrightarrow X/G$ dönüşümü belirler (genelde bir demetimsi değildir) öyle ki bu dönüşümün lifleri $\pi_1^{-1}(x^*) = G\,(x) \times_G E_G = (G/G_x) \times_G E_G = (G \times_G E_G)\,/G_x = E_G/G_x$ olur, burada $x^* \in X/G$ ve $x \in x^*$'dır. Eğer $G \longrightarrow G/G_x$ bir esas G_x-demet ise (örneğin G kompakt Lie grubu ya da G sonlu boyutlu, kompakt bir grup iken bu sağlanır) bu durumda $E_G \longrightarrow E_G/G_x$ bir evrensel esas G_x-demet olur ve $E_G = E_{G_x}$ alınabilir ve E_G/G_x bölüm uzayı B_{G_x} sınıf uzayı olarak seçilebilir.

$H_G^*\,(X; \Lambda) := H^*\,(X_G; \Lambda)$ (burada sağdaki kohomoloji alışılmış kohomoloji teorisidir) ile tanımlanan genelleştirilmiş kohomoloji teorisi Λ katsayılı Borel kohomoloji ya da ekivaryant kohomoloji olarak adlandırılır. $H_G^*\,(X; \Lambda)$ kohomoloji halkası $H^*\,(B_G; \Lambda)$ üzerinde $\pi_2^* : H^*\,(B_G; \Lambda) \to H_G^*\,(X; \Lambda)$ halka homomorfizmi ile belirlenen kanonik bir cebir yapısına sahiptir. Çarpma işlemi $a \in H^*\,(B_G; \Lambda)$ ve $x \in H_G^*\,(X; \Lambda)$ için $ax = \pi_2^*\,(a) \cup x$ ile verilir, burada $\cup$, $H_G^*\,(X; \Lambda)$'deki cup çarpmadır. Bu cebir X'in ekivaryant dereceli kohomoloji cebiri olarak adlandırılır.

Şimdi G ve G' iki topolojik grup ve X ile X', sırasıyla G ve G'-uzaylar olsun. $u : G \to G'$ sürekli bir dönüşüm ve $f : X \to X'$, u-ekivaryant bir dönüşüm (yani her $g \in G$, $x \in X$ için $f\,(gx) = u\,(g)\,f\,(x)$) ise o zaman (u, f) ikilisi $H_{G'}^*\,(X') \to H_G^*\,(X)$ homomorfizmini belirler (Quillen [12]).

Bu makalede rasyonel katsayılı, kapalı destekli sheaf kohomoloji ile çalışılacaktır. Fakat sonuçlar karakteristiği sıfır olan bir cisim durumunda da sağlanır.

Son olarak bu makalenin temel konusu olan sonlu boyutlu G-CW komplekslerin tanımı ve bazı önemli özellikleri verilecektir.

Tanım 17. A/G, Hausdorff bir uzay olmak üzere (X, A), G-uzayların bir çifti olsun. (X, A) üzerinde bir relatif G-CW kompleks yapısı aşağıdakilerden oluşur.

a. $X = \bigcup_{n=-1}^{\infty} X_n$ uzayının $A = X_{-1} \subset X_0 \subset X_1 \subset X_2 \cdots$

şeklinde bir filtrasyonu vardır.

b. Her $n \geq 0$ için aşağıdaki özelliklere sahip X_n'in $e_i^n \subset X_n$, G-alt uzaylarının bir $\{e_i^n : i \in I_n\}$ koleksiyonu vardır.

i. X, $\{X_n : n \geq -1\}$ filtrasyonuna göre zayıf topolojiye sahiptir, yani herhangi bir $n \geq -1$ için $B \subset X$'in kapalı olması için gerek ve yeter şart $B \cap X_n \subset X_n$'nin kapalı olmasıdır.

ii. Her $n \geq 0$ için, $e_i^n = Q_i^n\left(G/H_i \times \operatorname{Int} D^n\right)$ olacak şekilde bir G-pushout diyagramı vardır.

$$\begin{tikzcd}
\coprod_{i\in I_n} G/H_i \times \mathbb{S}^{n-1} \arrow[r, "\coprod_{i\in I_n} q_i^n"] \arrow[d, hook] & X^{n-1} \arrow[d, hook] \\
\coprod_{i\in I_n} G/H_i \times D^n \arrow[r, "\coprod_{i\in I_n} Q_i^n"'] & X^n
\end{tikzcd}$$

Eğer $A = \emptyset$ ise o zaman X uzayı bir G-CW kompleks olarak adlandırılır.

X_n alt uzayları (X, A)'nın $n.$ iskeleti olarak adlandırılır ve e_i^n, G-alt uzayları açık n-hücreler olarak adlandırılır. Eğer $X = X_n$ ve $X \neq X_{n-1}$ sağlanıyorsa bir (X, A) relatif G-CW komplekse n-boyutlu denir. Eğer bir n için bu kompleks n-boyutlu ise bu kompleks sonlu boyutlu olarak adlandırılır. Eğer G kompakt bir grup ise herhangi bir sonlu boyutlu G-CW kompleks hem sonlu kohomolojik boyuta sahip parakompakt uzaydır hem de finitistik bir uzaydır. Aşağıdaki lemmanın kanıtı Lück [21, p. 7]'da bulunabilir.

Lemma 18. (X, A) çifti A/G, Hausdorff bir uzay olacak şekilde bir relatif G-CW kompleks olsun. Eğer H, G'nin bir normal alt grubu ve aşağıdaki koşullardan biri sağlanıyor ise $(X/H, A/H)$ bir kanonik G/H-CW kompleks yapısına sahiptir.

a. H kompakttır.

b. Her $x \in X \setminus A$ için G_x kompakttır.

c. G/H ayrıktır.

Eğer X_n, X'in $n.$ iskeleti ve $\{e_i^n : i \in I_n\}$, X'in açık n-hücreleri ise o zaman X_n/H, X/H'nin $n.$ iskeletidir ve $\{e_i^n/H : i \in I_n\}$, X/H 'nin açık n-hücreleridir.
Ana teoremlerin kanıtlanması için aşağıdaki iyi bilinen lemmalara ihtiyaç vardır.

Lemma 19. [10] Bir kompakt, tamamen bağlantısız grubun sınıf uzayı $\mathbb{Q}$-asiklik uzaydır, yani
$H^*\left(B_G; \mathbb{Q}\right) = \mathbb{Q}$'dur.

Kanıt. Ku [10] veya Onat [22]'da bulunabilir.

Lemma 20. (Vietoris-Begle dönüşüm teoremi) X ve Y parakompakt Hausdorff uzaylar, G bir abelyen grup ve $f : X \longrightarrow Y$ örten, sürekli ve kapalı bir dönüşüm olsun. Her $y \in Y$ ve $q < n$ için $\widetilde{H}^q\left(f^{-1}(y); G\right) = 0$ olacak şekilde bir $n \geq 0$ doğal sayısının var olduğunu kabul edelim. O zaman

$$f^q : \widetilde{H}^q(Y; G) \longrightarrow \widetilde{H}^q(X; G)$$

homomorfizmi $q < n$ için bir izomorfizm ve $q = n$ için bir monomorfizmdir.

Kanıt. Spanier [23, p. 344]'de bulunabilir.

Asiklik Uzayların Orbit Uzayı ve Sabit Nokta Kümesi

Tamamen bağlantısız, kompakt grupların etkileri sonlu boyuta sahip kompakt grupların etkilerinde önemli bir yere sahiptir. İlk olarak kompakt, tamamen bağlantısız grup etkilerinin orbit uzayının kohomolojisi ile ilgili bir sonuç kanıtlanacaktır. Aşağıdaki önermenin X kompakt uzayı için doğru olduğu yukarıdaki ifade edilmişti. Şimdi bu sonucun parakompakt uzaylar için genellemesi kanıtlanacaktır.

Önerme 21. G, parakompakt bir X uzayı üzerine etki eden kompakt, tamamen bağlantısız bir grup olsun. Eğer X, $\mathbb{Q}$-asiklik bir uzay ise X/G orbit uzayı da $\mathbb{Q}$-asiklik uzaydır.

Kanıt. X parakompakt bir uzay olduğundan X_G uzayı da parakompakttır (Allday ve Puppe [1, p.141]) ve B_G sınıf uzayı da parakompakttır. Şimdi $X \to X_G \to B_G$ Borel demetimsisini düşünelim. X, $\mathbb{Q}$-asiklik bir uzay ise Vietoris-Begle dönüşüm teoreminden $H^*(B_G; \mathbb{Q}) \to H^*(X_G; \mathbb{Q})$ homomorfizmi bir izomorfizmdir. Ayrıca B_G, $\mathbb{Q}$-asiklik uzay olduğundan (Lemma 19) X_G uzayının $\mathbb{Q}$-asiklik uzay olduğu elde edilir. Diğer taraftan $\pi_1 : X_G \to X/G$ sürekli bir dönüşüm ve lifleri $\pi_1^{-1}(G(x)) = B_{G_x}$ ve B_{G_x}, $\mathbb{Q}$-asiklik uzaydır çünkü G_x kompakt, tamamen bağlantısız bir uzaydır. Yine Vietoris-Begle dönüşüm teoreminden π_1 dönüşümü $H^*(X/G; \mathbb{Q}) \to H^*(X_G; \mathbb{Q})$ izomorfizmini belirler. Böylece X/G orbit uzayı $\mathbb{Q}$-asiklik bir uzay olur.

Şimdi ana teoremlerimizi kanıtlamak için hazırız.

Teorem 22. G sonlu boyuta sahip kompakt bir grup ve X sonlu boyutlu bir G-CW kompleks olsun. Eğer X, $\mathbb{Q}$-asiklik bir uzay ise X/G uzayı da $\mathbb{Q}$-asikliktir.

Kanıt. G/N kompakt bir Lie grubu olacak biçimde G'nin kapalı, normal, tamamen bağlantısız bir N alt grubu vardır (Teorem 16). X/N orbit uzayı üzerinde G/N kompakt Lie grubunun doğal etkisini göz önüne alalım. Önerme 21 gereği X/N bir $\mathbb{Q}$-asiklik uzaydır. Lemma 18 gereği açıktır ki X/N, sonlu boyutlu bir G/N-CW komplekstir. Ayrıca G/N, X/N üzerine sonlu sayıda orbit tipi ile etki eder (Not 15). Conner'in teoremi (Teorem 1) gereği $X/G \approx (X/N)/(G/N)$ uzayı da $\mathbb{Q}$-asiklik uzaydır.

Teorem 23. G sonlu boyutlu bir pro-torus ve X, sonlu sayıda bağlantılı orbit tipli, sonlu boyutlu bir G-CW kompleks olsun. Eğer X, $\mathbb{Q}$-asiklik bir uzay ise X^G sabit nokta kümesi de $\mathbb{Q}$-asiklik uzaydır.

Kanıt. G/N bölüm grubu torus olacak biçimde G'nin kapalı, normal, tamamen bağlantısız bir N alt grubu vardır (Teorem 16). X/N orbit uzayı üzerinde, G/N torus grubunun kanonik etkisini düşünelim. Bu etki sonlu sayıda bağlantılı orbit tipine sahiptir (Not 15). Ayrıca Önerme 21 gereği X/N, $\mathbb{Q}$-asiklik bir uzaydır ve Lemma 18 gereği X/N, sonlu boyutlu bir G/N-CW komplekstir. Teorem 2 gereği $(X/N)^{G/N} \approx X^G$ sabit nokta kümesi de $\mathbb{Q}$-asiklik uzaydır.

Aşağıdaki teoremler yerel kompakt uzaylar için Ku [9, p. 33] tarafından kanıtlandı fakat parakompakt uzaylar için de sağlanır.

Teorem 24. $\mathbb{S}^1$ çember grubu parakompakt bir X uzayı üzerine etki etsin. Eğer $\dim H^*(X;\mathbb{Q}) < \infty$ ise $\chi(X;\mathbb{Q}) = \chi(F;\mathbb{Q})$ olur. Özel olarak eğer X, $\mathbb{Q}$-asiklik uzay ise X^G sabit nokta kümesi de $\mathbb{Q}$-asiklik uzaydır.

Teorem 25. X, parakompakt bir uzay ve G, X üzerine etki eden kompakt, tamamen bağlantısız olmayan bir grup olsun. Eğer $\dim H^*(X;\mathbb{Q}) < \infty$ ve her $x \notin X^G$ için G_x sonlu ise $\chi(X;\mathbb{Q}) = \chi(F;\mathbb{Q})$ olur.

Hofmann ve Mostert [13, Theorem 3.7] tarafından kullanılan teknikleri kullanarak aşağıdaki teoremi kanıtlayabiliriz.

Teorem 26. G, sonlu boyuta sahip kompakt ve bağlantılı bir grup ve X, $\mathbb{Q}$-asiklik, parakompakt bir G-uzay olsun. Eğer (I_0) koşulu sağlanıyorsa o zaman X^G sabit nokta kümesi boş değildir ve $\mathbb{Q}$-asiklik bir uzaydır.

Kanıt. G/N kompakt ve bağlantılı bir Lie grup olacak biçimde G'nin kapalı, normal, tamamen bağlantısız bir N alt grubu bulunabilir (Teorem 16). Böylece $F(G,X) \approx F(G/N, X/N)$ ve Önerme 21 gereği X/N, $\mathbb{Q}$-asiklik bir uzaydır. Ayrıca

$$(G/N)^0_{N(x)} = \left(NG^0_x\right)/N \subset [NZ(G)]/N \subset Z(G/N)$$

olduğundan G'yi kompakt, bağlantılı bir Lie grubu varsayabiliriz.

İlk olarak G'nin abelyen olduğu varsayılsın. O zaman G bir torus olup iddia G'nin boyutu üzerinden tümevarımla kanıtlanabilir. Eğer G, 1-boyutlu ise o zaman Teorem 24 gereği iddia doğrudur.

Şimdi iddianın $(n-1)$-boyutlu toruslar için doğru olduğu varsayılsın ve kabul edelim ki $\dim G = n$ olsun. N, G'nin bir çember alt grubu olsun. O halde $F(N,X)$ sabit nokta kümesi $\mathbb{Q}$-asiklik bir uzaydır ve N, altında invaryanttır. Böylece G/N, $F(N,X)$ uzayı üzerine etki eder ve $\dim G/N = n-1$'dir. Böylece tümevarım hipotezinden $F(G,X) = F(G/N, F(N,X))$, $\mathbb{Q}$-asiklik bir uzaydır.

Şimdi G herhangi bir kompakt, bağlantılı Lie grup olsun. Z, G'nin $Z(G)$ merkezinin birim bileşenini göstersin. O zaman Z, X üzerine etki eder ve abelyen durumdan dolayı $F(Z,X)$ sabit nokta kümesi $\mathbb{Q}$-asiklik bir uzaydır. Z normal alt grup ve $F(Z,X)$, Z altında invaryant olduğundan G/Z kompakt, bağlantılı Lie grubu $F(Z,X)$ üzerine etki eder. Her $x \in F(Z,X) \setminus F(G/Z, F(Z,X))$ için $(G/Z)_x$ izotropi alt grubu sonludur. Gerçekten $G^0_x \subset Z(G)$ olduğundan $G^0_x = G^0_x \cap Z < G_x \cap Z$ ve $(G/Z)_x = \{gZ : gZx = gx = x\} = \frac{G_x}{G_x \cap Z} < \frac{G_x}{G^0_x}$ olur. $\frac{G_x}{G^0_x}$ sonlu olduğundan $(G/Z)_x$ sonlu olur. Böylece Teorem 25 gereği $F(G,X) = F(G/Z, F(Z,X))$ sabit nokta kümesi $\mathbb{Q}$-asiklik bir uzay olur.

Yukarıdaki teoremi kompakt, bağlantılı gruplara genellemek için aşağıdaki lemmaya (Hofmann ve Mostert [13, p. 332]) ihtiyaç vardır.

Lemma 27. (Hofmann-Mostert) Eğer G kompakt, bağlantılı bir grup ve $\mathcal{A}$ tüm sonlu boyutlu, kompakt, bağlantılı, normal alt grupların kümesi ise alt grupların çarpımı altında $\mathcal{A}$ bir yarılatistir ve birleşimi G'de yoğundur.

Teorem 28. G, parakompakt bir X uzayı üzerine etki eden kompakt, bağlantılı bir grup olsun. Eğer (I_0) koşulu sağlanıyor ve X, $\mathbb{Q}$-asiklik bir uzay ise X^G sabit nokta kümesi boş değildir ve $\mathbb{Q}$-asiklik bir uzaydır.

Kanıt. G'nin herhangi iki kompakt, normal H, H' alt grupları için $F(HH', X) = F(H, X) \cap F(H', X)$ olur. Lemma 27 gereği G grubu tüm sonlu boyutlu kompakt, bağlantılı, normal H alt grupları tarafından doğurulur ve bunların sabit nokta kümeleri $F(H, X)$, $\mathbb{Q}$-asiklik uzaylardır. Böylece sonuç, sheaf kohomolojinin tautness özelliğinden (Bredon [4, p. 73] veya Spanier [23, p. 316]) elde edilir.

Lokalizasyon Teoremi

Bu bölümde, sonlu boyutlu G-CW kompleksler üzerine sonlu sayıda orbit tipi ile etki eden sonlu boyuta sahip kompakt grup etkileri için Borel-Hsiang-Quillen lokalizasyon teoremini çalışacağız.
Kabul edelim ki $S \subset H^*(B_G;\ \mathbb{Q}) = R$ çarpımsal kapalı bir alt küme olsun. Lokalizasyon teoremi, çarpımsal kapalı bir alt kümeye göre $H_G^*(X;\ \mathbb{Q})$, R-modulünün lokalizasyonu ile ilgilidir. $i_x : G_x \longrightarrow G$ kanonik içerme dönüşümü ve $i_x^* : H^*(B_G;\ \mathbb{Q}) \to H^*(B_{G_x};\ \mathbb{Q})$ olsun.

$X^S = \{x \in X :$ Her $s \in S$ için $i_x^*(s) \neq 0\}$

olarak tanımlansın. $X^G \subset X^S$ olduğu açıktır. Eğer X bir G-CW kompleks ise kohomolojinin tautness özelliğinden X^S, X uzayının G-invaryant kapalı bir alt uzayı ve X'in bir G-CW alt kompleksidir.

Teorem 29. (Borel-Hsiang-Quillen-Deo ve ark.) Kabul edelim ki G kompakt bir Lie grup ve X, aşağıdaki koşullardan birini sağlayan bir G-uzay olsun. Eğer $S \subset H^*(B_G)$ çarpımsal kapalı bir alt küme ise o zaman $X^S \to X$ içerme dönüşümü tarafından belirlenen $S^{-1}H_G^*(X) \to S^{-1}H_G^*(X^S)$ lokal kısıtlanmış homomorfizm bir izomorfizmdir.

1. X bir kompakt uzaydır (Hsiang [24]).
2. X sonlu sayıda orbit tipli, sonlu kohomolojik boyuta sahip bir parakompakt uzaydır (Hsiang [24] veya Quillen [12]).
3. X sonlu sayıda orbit tipli parakompakt finitistik bir uzaydır (Deo ve ark. [8]).

Dikkat edilsin ki katsayı halkası olarak karakteristiği sıfır olan bir cisim kullanıldığında 2. ve 3. durumda sonlu sayıda bağlantılı orbit tipli uzay varsayımı yapmak yeterlidir (Allday ve Puppe [1, s.131]).
Sonlu boyuta sahip kompakt grupların kompakt uzaylar üzerine etkileri için lokalizasyon teoremi, Özkurt ve Onat [25] tarafından çalışıldı. Şimdi 2. durumun özel bir hali olan G-CW kompleksler için lokalizasyon teoreminin doğruluğunu inceleyeceğiz.

Teorem 30. G, sonlu boyutlu, kompakt bir grup ve X, sonlu sayıda bağlantılı orbit tipine sahip sonlu boyutlu bir G-CW kompleks olsun. Kabul edelim ki her $x \in X \setminus X^G$ ve her $n \geq 1$ için $H^i(B_{G_x}; \mathbb{Q}) = 0$ olsun. Eğer $S \subset H^*(B_G; \mathbb{Q})$ çarpımsal kapalı bir alt küme ise $X^S \to X$ içerme dönüşümü

$$S^{-1}H_G^*(X; \mathbb{Q}) \longrightarrow S^{-1}H_G^*(X^S; \mathbb{Q})$$

izomorfizmini belirler.

Kanıt. G/N kompakt bir Lie grubu olacak biçimde G'nin kapalı, normal, tamamen bağlantısız bir N alt grubu bulunabilir (Teorem 16).
İlk olarak $X^S = \emptyset$ olduğu varsayılsın. O zaman X^G sabit nokta kümesi de boş olur. $\pi_1 : X_G \longrightarrow X/G$ dönüşümünü düşünelim. Böylece $\pi_1^{-1}\left(G\left(x\right)\right)$, B_{G_x} sınıf uzayına homeomorfiktir. Hipotezden her $x \in X$ için B_{G_x}, $\mathbb{Q}$-asiklik bir uzay olduğundan Vietoris-Begle dönüşüm teoremi gereği

$$\pi_1^* : H^*\left(X/G; \mathbb{Q}\right) \longrightarrow H_G^*\left(X; \mathbb{Q}\right)$$

izomorfizmi elde edilir. Diğer taraftan Özkurt ve Onat [25, Remark 3.5] tarafından

$$H^*\left(B_{(G/N)_{N(x)}}; \mathbb{Q}\right) \longrightarrow H^*\left(B_{G_x}; \mathbb{Q}\right)$$

dönüşümünün bir izomorfizm olduğu kanıtlandı. Böylece $N\left(x\right)$ noktası X/N orbit uzayında G/N etkisinin sabit bir noktası değildir ve $B_{(G/N)_{N(x)}}$, $\mathbb{Q}$-asiklik bir uzaydır.
Benzer şekilde

$$\left(X/N\right)_{G/N} \longrightarrow \left(X/N\right)/\left(G/N\right) \approx X/G$$

kanonik dönüşümünün lifi $B_{(G/N)_{N(x)}}$ sınıf uzayına homeomorfik olduğundan

$$H^*\left(X/G; \mathbb{Q}\right) \longrightarrow H_{G/N}^*\left(X/N; \mathbb{Q}\right)$$

izomorfizmini elde ederiz.
Böylece

$$H_{G/N}^*\left(X/N; \mathbb{Q}\right) \longrightarrow H_G^*\left(X; \mathbb{Q}\right)$$

izomorfizmi elde edilir. Ayrıca Özkurt ve Onat [25, Lemma 3.3] tarafından $\pi : G \to G/N$ bölüm dönüşümünün

$$\pi^* : H^*\left(B_{G/N}; \mathbb{Q}\right) \longrightarrow H^*\left(B_G; \mathbb{Q}\right)$$

izomorfizmini belirlediği gösterildi. Şimdi $R = (\pi^*)^{-1}(S) \subset H^*(B_{G/N}; \mathbb{Q})$ çarpımsal kapalı alt kümesini düşünelim, açıktır ki R, S'nin bir kopyasıdır. Böylece

$$R^{-1}H_{G/N}^*\left(X/N; \mathbb{Q}\right) \cong S^{-1}H_G^*\left(X; \mathbb{Q}\right)$$

izomorfizmi elde edilir. Özkurt ve Onat [25, Corollary 3.6] tarafından $X^S/N \approx \left(X/N\right)^R$ olduğu gösterildi. Böylece $\left(X/N\right)^R = \emptyset$ elde edilir. X/N, sonlu sayıda bağlantılı orbit tipine sahip sonlu boyutlu bir G/N-CW kompleks olduğundan sonlu boyutlu G-CW kompleksler üzerine kompakt Lie grup etkileri için lokalizasyon teoreminden (Allday ve Puppe [1, Theorem 3.1.6])

$$R^{-1}H_{G/N}^*\left(X/N; \mathbb{Q}\right) \longrightarrow R^{-1}H_{G/N}^*\left(\left(X/N\right)^R; \mathbb{Q}\right)$$

homomorfizminin bir izomorfizm olduğu elde edilir. Buradan ise $R^{-1}H_{G/N}^*\left(X/N; \mathbb{Q}\right) = 0$ ve $S^{-1}H_G^*\left(X; \mathbb{Q}\right) =$

0 olduğu görülür.

Genel durum $S^{-1}H_G^*\left(X, X^S;\mathbb{Q}\right) = 0$ olduğunu göstermeye denktir. Her $x \in H_G^*\left(X, X^S;\mathbb{Q}\right)$ için $s \cdot x = 0$ olacak şekilde bir $s \in S$ olduğunu göstermek bunun için yeterlidir. Şimdi eğer B_G^k, B_G sınıf uzayının k. iskeleti ve $X_G^k = \pi_2^{-1}\left(B_G^k\right)$ ise o zaman

$$H^i\left(X_G^{k+1};\mathbb{Q}\right) \longrightarrow H^i\left(X_G^k;\mathbb{Q}\right)$$

kısıtlanmış homomorfizminin her $i < k$ için bir izomorfizm olduğu biliniyor (Allday ve Puppe [1, p. 130]). O halde

$$k > n \text{ için } x \in H^n\left(X_G, X_G^S;\mathbb{Q}\right) = H^n\left(X_G^k, X_G^S \cap X_G^k;\mathbb{Q}\right)$$

olduğunu kabul edebiliriz. Şimdi X_G^k, parakompakt, Hausdorff bir uzay ve X_G^k uzayında $X_G^S \cap X_G^k$'nın $\left\{V_G \cap X_G^k : V,\, X^S\text{'nin bir invaryant komşuluğudur}\right\}$ formundaki komşulukları cofinal'dır. H_G^*-kohomoloji teorisinin tautness özelliğinden (Quillen [12, p. 552])

$$x \in Im\left\{H_G^*\left(X, V;\mathbb{Q}\right) \longrightarrow H_G^*\left(X, X^S;\mathbb{Q}\right)\right\}$$

olacak şekilde X^S'nin invaryant bir V komşuluğu vardır. Ayrıca $X = V \cup \operatorname{Int} Y$ olacak şekilde G altında invaryant olan parakompakt bir $Y \subset X \setminus X^S$ alt uzayı vardır. $Y^S = \emptyset$ olacağından ilk durumdan ve H_G^*-teori için (X, Y) çiftinin Mayer-Vietoris uzun tam dizisinden

$$\pi_2^*\left(s\right) \in Im\left\{H_G^*\left(X, Y;\mathbb{Q}\right) \longrightarrow H_G^*\left(X, \operatorname{Int} Y;\mathbb{Q}\right) \longrightarrow H_G^*\left(X;\mathbb{Q}\right)\right\}$$

olacak şekilde bir $s \in S$ vardır. Böylece

$$\pi_2^*\left(s\right) \in Im\left\{H_G^*\left(X, \operatorname{Int} Y;\mathbb{Q}\right) \longrightarrow H_G^*\left(X;\mathbb{Q}\right)\right\}$$

olur. Bu ise $\pi_2^*\left(s\right)x$ elemanının

$$0 = H_G^*\left(X, V \cup \operatorname{Int} Y;\mathbb{Q}\right) \longrightarrow H_G^*\left(X, X^S;\mathbb{Q}\right)$$

dönüşümünün görüntüsünde olduğu anlamına gelir. O halde $s \cdot x = \pi_2^*\left(s\right)x = 0$ olduğu elde edilmiş olur.

Sonuç 31. G bir solenoid ve X, sonlu sayıda bağlantılı orbit tipli, sonlu boyutlu bir G-CW kompleks olsun. Eğer $S \subset H^*\left(B_G;\mathbb{Q}\right)$ çarpımsal kapalı bir alt küme ise $X^S \to X$ içerme dönüşümü

$$S^{-1}H_G^*\left(X;\mathbb{Q}\right) \longrightarrow S^{-1}H_G^*\left(X^S;\mathbb{Q}\right)$$

izomorfimini belirler.

Kanıt. G, çember gruplarının ters limtidir, yani her $N \in \mathcal{N}$ için $G/N = \mathbb{S}^1$ olmak üzere $G = \varprojlim_{N\in\mathcal{N}} G/N$ şeklindedir. Burada tekrar hatırlayalım ki $\mathcal{N}$, $G/N = \mathbb{S}^1$ olacak biçimde G'nin kapalı, normal, tamamen bağlantısız alt gruplarının ailesini gösterir. O zaman Hofmann ve Morris [26, Theorem

2.2] tarafından kanıtlanan kapalı alt grup teoremine göre

$$G_x = \varprojlim_{N\in\mathcal{N}} G_x N/N = \varprojlim_{N\in\mathcal{N}} \left(G/N\right)_{N(x)}$$

olduğu elde edilir. Böylece Hofmann ve Mostert [27, III, Corollary 1.12] gereği

$$H^n\left(B_{G_x};\mathbb{Q}\right) = \varinjlim_{N\in\mathcal{N}} H^n\left(B_{(G/N)_{N(x)}};\mathbb{Q}\right)$$

elde edilir. Eğer $x \in X$ sabit bir nokta değilse o zaman $N(x) \in X/N$ noktası da X/N üzerine G/N etkisinin bir sabit noktası değildir. Buradan $\left(G/N\right)_{N(x)}$, $G/N = \mathbb{S}^1$ çember grubunun sonlu bir alt grubu olacağından her $n \geq 1$ için $H^n\left(B_{(G/N)_{N(x)}};\mathbb{Q}\right) = 0$ olduğu elde edilir (Borel [2, p. 51]). Böylece her $n \geq 1$ için

$$H^n\left(B_{G_x};\mathbb{Q}\right) = 0$$

bulunur. Böylece sonuç, Teorem 30 gereği açıktır.

Sabit nokta olmayan her $x \in X$ noktası ve her $n \geq 1$ için $H^n\left(B_{G_x};\mathbb{Q}\right) = 0$ olmasının kanıtı Özkurt [28, Theorem 3.2] tarafından farklı tekniklerle gösterildi.
Eğer G, herhangi bir X uzayı üzerine etki eden kompakt, bağlantılı, abelyen bir grup ise $S = H^*(B_G;\mathbb{Q}) - \{0\} \subset H^*(B_G;\mathbb{Q})$ çarpımsal kapalı alt kümesi için $X^S = X^G$ olur (Özkurt ve Onat [25, Remark 3.10]). Bu gerçekle birlikte Borel'in sabit noktanın varlığı için kriterinin sonlu boyutlu pro-torus etkiler için bir genellemesi elde edilmiş olur.

Önerme 32. G, sonlu boyutlu bir pro-torus ve X, sonlu sayıda orbit tipli, sonlu boyutlu bir G-CW kompleks olsun. Eğer her $x \in X \setminus X^G$ ve her $n \geq 1$ için $H^n\left(B_{G_x};\mathbb{Q}\right) = 0$ ise $S = H^*(B_G;\mathbb{Q}) - \{0\}$ çarpımsal kapalı alt kümesi için $X^S = X^G \to X$ içerme dönüşümü

$$S^{-1}H_G^*\left(X;\mathbb{Q}\right) \longrightarrow S^{-1}H_G^*\left(X^G;\mathbb{Q}\right) = H^*\left(X^G;\mathbb{Q}\right) \otimes_{\mathbb{Q}} \left(S^{-1}H^*\left(B_G;\mathbb{Q}\right)\right)$$

izomorfizmini belirler.

Sonuç 33. (Borel'in sabit nokta kriteri) G, sonlu boyutlu bir pro-torus ve X, sonlu sayıda bağlantılı orbit tipli, sonlu boyutlu bir G-CW kompleks olsun. Eğer her $x \in X \setminus X^G$ ve her $n \geq 1$ için $H^n\left(B_{G_x};\mathbb{Q}\right) = 0$ ise $X^G \neq \emptyset$ olması için gerek ve yeter şart $H^*\left(B_G;\mathbb{Q}\right) \to H_G^*\left(X;\mathbb{Q}\right)$ homomorfizminin injektif olmasıdır.

Kanıt. Hsiang [24, p. 45]'de bulunabilir.

Not edelim ki bu sonuç B_{G_x}, $\mathbb{Q}$-asiklik bir uzay olmasa da doğrudur (Onat [22, Theorem 3.9]).
Aşağıdaki soruların cevapları yazar tarafından bilinmiyor.
Soru 1: G kompakt (bağlantılı, abelyen, sonlu boyutlu) bir grup ve X, parakompakt bir G-uzay olsun. Bu durumda Teorem $5-8$ sağlanır mı?
Soru 2: G sonlu boyuta sahip kompakt bir grup ve X aşağıdaki koşullardan birini sağlayan bir G-uzay olsun. Bu durumda lokalizasyon teoremi doğru mudur?

a. X sonlu sayıda bağlantılı orbit tipli ve sonlu kohomolojik boyuta sahip parakompakt bir uzaydır.

b. X sonlu sayıda bağlantılı orbit tipli parakompakt, finitistik bir uzaydır.

Şimdi bazı özel durumlarda lokalizasyon teoreminin daha basit kanıtlarını vereceğiz. Daha önce bahsettiğimiz gibi daha genel olarak sonlu boyuta sahip kompakt grupların kompakt uzaylar üzerine etkileri için lokalizasyon teoremi Özkurt ve Onat [25] tarafından elde edildi. Orada açık bir şekilde ifade edilmesede X kompakt uzayının bağlantılı olmasına ihtiyaç vardır, bu koşul iki demetimsinin lif, baz ve total uzaylarının kohomoloji gruplarının karşılaştırılması için gereklidir. Burada uzayın bağlantılı olması koşulundan da kurtulmuş olacağız.

Kanıtı vermeden önce iyi bilinen bir gerçeği hatırlayarak işe başlayalım. Kompakt bir X uzayının Čech kohomoloji cebirinde (bu sheaf kohomoloji cebirine izomorfiktir) pozitif dereceli her eleman nilpotenttir, yani eğer bir $m \geq 1$ için $a \in H^m(X;\mathbb{Q})$ ise o zaman her $n \geq n_0$ için $a^n = 0 \in H^*(X;\mathbb{Q})$ olacak şekilde bir n_0 doğal sayısı vardır. Bu gerçek daha genel olarak herhangi bir finitistik X uzayı için Deo ve ark. [8] tarafından kanıtlandı. Şimdi teoremimizi kanıtlayabiliriz.

Teorem 34. Kabul edilsin ki G, kompakt bir X uzayı üzerine etki eden bir solenoid olsun. O zaman $S = H^*(B_G;\mathbb{Q}) - \{0\}$ çarpımsal kapalı alt kümesi için $X^S = X^G \to X$ içerme dönüşümü

$$S^{-1}H_G^*(X;\mathbb{Q}) \longrightarrow S^{-1}H_G^*\left(X^G;\mathbb{Q}\right)$$

izomorfizmini belirler.

Kanıt. İlk olarak $X^G = \emptyset$ olduğu varsayılsın. O halde her $x \in X$ için $i_x^*(s) = 0$ olacak şekilde bir $s \in S$ vardır. B_G (yol) bağlantılı olduğundan $i_x^* : H^0(B_G;\mathbb{Q}) \to H^0(B_{G_x};\mathbb{Q})$ bir izomorfizmdir ve böylece s, pozitif dereceli bir elemandır, yani bir $n \geq 1$ için $s \in H^n(B_G;\mathbb{Q})$ olur. O halde $\pi_2^*(s)$, $H_G^*(X;\mathbb{Q})$ cebirinde pozitif dereceli bir elemandır. Yukarıda gösterildiği gibi $H^*(X/G;\mathbb{Q}) \to H_G^*(X;\mathbb{Q})$ bir izomorfizm olur. X/G kompakt olduğundan $H^*(X/G;\mathbb{Q})$'de ve böylece $H_G^*(X;\mathbb{Q})$'de pozitif dereceli her eleman nilpotent olur. Sonuç olarak bir $n_0 \in \mathbb{N}$ için $(\pi_2^*(s))^{n_0} = 0 \in H_G^*(X;\mathbb{Q})$ olur. Buradan $s^{n_0} \in S$ ve $\pi_2^*(s^{n_0}) = 0$ olur. Bu ise $S^{-1}H_G^*(X;\mathbb{Q}) = 0$ olması demektir.

Eğer $X^G \neq \emptyset$ ise kanıt Teorem 30'da olduğu gibi yapılır.

Sonuç 35. G, kompakt bir X uzayı üzerine etki eden bir solenoid olsun. O halde $X^G \neq \emptyset$ olması, $H^*(B_G;\mathbb{Q}) \to H_G^*(X;\mathbb{Q})$ homomorfizminin injektif olması için gerek ve yeter koşuldur.

Teorem 36. G, finitistik bir X uzayı üzerine etki eden bir çember grubu olsun. O zaman $S = H^*(B_G;\mathbb{Q}) - \{0\}$ çarpımsal kapalı alt kümesi için $X^S = X^G \to X$ içerme dönüşümü

$$S^{-1}H_G^*(X;\mathbb{Q}) \longrightarrow S^{-1}H_G^*\left(X^G;\mathbb{Q}\right)$$

izomorfizmini belirler.

Kanıt. Eğer G, finitistik bir X uzayı üzerine etki eden kompakt bir Lie grup ise o zaman X/G orbit uzayı da finitistiktir (Deo ve Tripathi [29]). Ayrıca bir finitistik uzayın sheaf kohomolojisinde pozitif dereceli her eleman nilpotenttir. Böylece kanıt Teorem 34'de olduğu gibi yapılır.

Bu teoremin, Deo ve ark. [8] tarafından herhangi bir kompakt Lie grup etkisi için kanıtlandığını tekrarlayalım. Şimdi yukarıdaki $1-3$ koşullarından herhangi birini sağlayan iki uzayın çarpımı için Borel'in sabit nokta kriteri sonucunu inceleyeceğiz.

Teorem 37. Kabul edilsin ki X ve Y uzayları yukarıdaki $1-3$ koşullarından birini sağlayan iki G-uzay olsun. G, $X \times Y$ çarpım uzayı üzerine $g(x,y) = (gx, gy)$ ile etki eden kompakt bir Lie grubu olsun. O zaman $(X \times Y)^G \neq \emptyset$ olması, $H^*(B_G;\mathbb{Q}) \to H_G^*(X \times Y;\mathbb{Q})$ homomorfizminin injektif olması için gerek ve yeter şarttır.

Kanıt. Eğer $(X \times Y)^G \neq \emptyset$ ise $H^*(B_G;\mathbb{Q}) \to H_G^*(X \times Y;\mathbb{Q})$ homomorfizminin injektif olması açıktır. Şimdi kabul edelim ki $(X \times Y)^G = \emptyset$ olsun. $(X \times Y)^G = X^G \times Y^G$ olduğu kolayca görülür. Eğer $X^G = \emptyset$ ise $H^*(B_G;\mathbb{Q}) \to H_G^*(X;\mathbb{Q})$ homomorfizmi injektif değildir. $X \times Y \to X$ izdüşüm dönüşümü G-invaryant olduğundan $H_G^*(X;\mathbb{Q}) \to H_G^*(X \times Y;\mathbb{Q})$ dönüşümü belirlenir ve aşağıdaki diyagram değişmelidir. Diyagramdan $H^*(B_G;\mathbb{Q}) \to H_G^*(X \times Y;\mathbb{Q})$ homomorfizminin injektif olmadığı elde edilir.

$$\begin{tikzcd}
H^*(B_G;\mathbb{Q}) \arrow[r] \arrow[d] & H_G^*(X \times Y;\mathbb{Q}) \\
H_G^*(X;\mathbb{Q}) \arrow[ur] &
\end{tikzcd}$$

Benzer şekilde $Y^G = \emptyset$ olması $H^*(B_G;\mathbb{Q}) \to H_G^*(X \times Y;\mathbb{Q})$ homomorfizminin injektif olmamasını gerektirir. Böylece kanıt tamamlanır.

Dikkat edilsin ki finitistik bir uzay ile kompakt bir uzayın ya da sonlu kohomolojik boyuta sahip parakompakt bir uzayın çarpımı finitistik olmak zorunda değildir (Deo ve Singh [30]).

Teşekkür Yazar, yorumları ve önerileri ile bu makalenin geliştirilmesine ve netleştirilmesine yardımcı olan hakemlere teşekkür etmeyi bir borç bilir.

Fon/Finansman bilgileri -

Etik Kurul Onayı ve İzinler Çalışma, etik kurul izni ve herhangi bir özel izin gerektirmemektedir.

Çıkar çatışmaları/Çatışan çıkarlar -

Yazarların Katkısı Yazar makalenin son halini okumuş ve onaylamıştır.

Kaynaklar

[1] Allday, C., Puppe, V. (1993). *Cohomological Methods in Transformation Groups.* Cambridge, UK: Cambridge University Press.

[2] Borel, A. (1960). *Seminar on Transformation Groups.* Princeton, NJ, USA: Princeton University Press.

[3] Bredon, G. E. (1972). *Introduction to Compact Transformation Groups.* Academic Press, New York.

[4] Bredon, G. E. (1997). *Sheaf Theory. 2nd ed.* Graduate Texts in Mathematics 170. New York, NY, USA: Springer.

[5] Conner, P. E. (1957). On the action of the circle group. *Michigan Mathematical Journal, 4*, 241-247. https://doi.org/10.1307/mmj/1028997955

[6] Conner, P. E. (1960). Retraction properties of the orbit space of a compact topological transformation group. *Duke Mathematical Journal, 27*, 341-57. https://doi.org/10.1215/S0012-7094-60-02732-0

[7] Deo, S. (1983). On some local and global cohomological properties which pass on to the orbit space. *Indian Journal of Pure and Applied Mathematics, 14*, 1319-1326.

[8] Deo, S., Singh, T. B., & Shukla, R. A. (1982). On an extension of localization theorem and generalized Conner conjecture. *Transactions of the American Mathematical Society, 269*, 395-402. https://doi.org/10.1090/S0002-9947-1982-0637697-0

[9] Ku, H. T. (1967). *Cohomology structure of compact transformation groups.* PhD, Tulane University.

[10] Ku, M. C. (1967). *Some topics in compact transformation groups.* (Publication No. 6717927) [Doctoral dissertation, Tulane University].

[11] Oliver, R. (1976). A proof of the Conner conjecture. *Annals of Mathematics, 103*, 637-644. https://doi.org/10.2307/1970955

[12] Quillen, D. (1971). The spectrum of an equivariant cohomology ring I. *Annals of Mathematics, 94*(2), 549-572. https://doi.org/10.2307/1970770

[13] Hofmann, K. H., & Mostert, P. S. (1966). *Elements of Compact Semigroups*. Charles E. Merrill, Columbus, Ohio.

[14] Hofmann, K. H., & Morris, S. A. (2013). *The Structure of Compact Groups. 3rd ed.* Berlin, Germany: de Gruyter.

[15] Bredon, G. E., Raymond, F., & Williams, R. F. (1961). p-Adic Groups of Transformations. *Transactions of the American Mathematical Society, 99*(3), 488-498. https://doi.org/10.2307/1993558

[16] Montgomery, D., & Zippin, L. (1955). *Topological transformation groups.* Interscience Publishers, New York.

[17] Pontryagin, L. S. (1986). *Topological Groups. 3rd ed.* Gordon and Breach Science Publishers, New York.

[18] Hofmann, K. H., & Morris, S. A. (2007). *The Lie Theory of Connected Pro-Lie Groups.* European Mathematical Society, Zürich.

[19] Onat, M. (2018). *Kompakt Grup Etkilerinin Kohomoloji Teorisi.* (Tez no. 531232) [Doktora Tezi, Çukurova Üniversitesi]

[20] Milnor, J. (1956). Construction of universal bundles II. *Annals of Mathematics, 63*, 430–436.

[21] Lück, W. (1989). *Transformation groups and algebraic K-theory*. Springer-Verlag, Berlin, Heidelberg, New York.

[22] Onat, M. (2022). The Borsuk-Ulam Type Theorems for Finite-Dimensional Compact Group Actions. *Bulletin of the Iranian Mathematical Society, 48*, 1339-1349. https://doi.org/10.1007/s41980-021-00581-z

[23] Spanier, E. (1966). *Algebraic Topology.* McGraw–Hill, New York.

[24] Hsiang, W. Y. (1975). *Cohomology Theory of Topological Transformation Groups.* Springer-Verlag, Berlin-Heidelberg-New York.

[25] Özkurt, A. A., & Onat, M. (2018). The localization theorem for finite-dimensional compact group actions. *Turkish Journal of Mathematics, 42*(4), 1556-1565. https://doi.org/10.3906/mat-1609-47

[26] Hofmann, K. H., & Morris, S. A. (2003). Projective limits of finite dimensional Lie groups. *Proceedings of the London Mathematical Society, 87*(3), 647-676. https://doi.org/10.1112/S0024611503014254

[27] Hofmann, K. H., & Mostert, P. S. (1973). *Cohomology Theories for Compact Abelian Groups.* Springer-Verlag, Berlin, Heidelberg, New York.

[28] Özkurt, A. A. (2014). On the equivariant cohomology algebra for solenoidal actions. *Turkish Journal of Mathematics, 38*(6), 1081-1089. https://doi.org/10.3906/mat-1310-6

[29] Deo, S., & Tripathi, H. S. (1982). Compact Lie Group Actions on Finistic Spaces. *Topology, 21*, 393-399. https://doi.org/10.1016/0040-9383(82)90019-2

[30] Deo, S., & Singh, M. (1983). On certain constructions in finitistic spaces. *International Journal of Mathematics and Mathematical Sciences, 6*, 477-482. https://doi.org/10.1155/S0161171283000423

Sinopfbd, 2024; 9(2): 551-571 **https://doi.org/10.33484/sinopfbd.1485489**

Sinop Üniversitesi Fen Bilimleri Dergisi
Sinop Uni J Nat Sci

E-ISSN: 2564-7873

https://dergipark.org.tr/tr/pub/sinopfbd

The Impact of Prior Based Loss Function For Elliptical Regression Models

Mohammad ARASHI[1], Fatma Sevinç KURNAZ[2] and Naushad MAMODEKHAN[3]

How to cite: Arashi, M., Kurnaz, F. S., & MamodeKhan, N. (2024). The impact of prior based loss function for elliptical regression models. *Sinop Üniversitesi Fen Bilimleri Dergisi*, *9*(2), 551-571. https://doi.org/10.33484/sinopfbd.1485489

Research Article

Corresponding Author
Fatma Sevinç KURNAZ
fskurnaz@yildiz.edu.tr

ORCID of the Authors
M.A: 0000-0002-5881-9241
F.S.K: 0000-0002-5958-7366
N.M: 0000-0002-9125-7121

Received: 16.05.2024
Accepted: 27.12.2024

Abstract

In the paper we consider a multiple regression model with elliptically contoured errors. In the Bayesian view, a prior information is taken for the weight under a prior based balanced-type loss function in order to avoid making redundant assumptions. This is the essence of the Bayesian inference with vague prior information in regression analysis. It directly impacts on the performance of the quasi empirical Bayesian shrinkage estimators through the inclusion of a reciprocal weight related to the dimension of parameter space. The shrinkage factor of the estimator is also robust to outliers and the unknown density generator of elliptical models. Finally, this result is supported by an application.

Keywords: Balanced loss function, Elliptically contoured distribution, Prior based loss function, Quasi-empirical Bayes estimator, Shrinkage estimator

Eliptik Regresyon Modelleri Için Kayıp Fonksiyona Dayalı Önselliğin Etkisi

[1]Ferdowsi University of Mashhad, Department of Statistics, Mashhad, Iran

[2]Yildiz Technical University, Faculty of Mathematical Sciences and Arts, Istanbul, Türkiye

[3]University of Mauritius, Faculty of Mathematical Sciences, Mauritius

Öz

Bu çalışmada eliptik konturlu hatalara sahip olan çoklu regresyon modeli ele alınmıştır. Bayesyen bakıştan, gereksiz varsayımlarda bulunmaktan kaçınmak için, ağırlık için dengeli tipteki kayıp fonksiyonuna dayalı bir önsellik altında önsellik bilgisi gözönüne alınmıştır. Bu, regresyon analizindeki muğlak öncelik bilgisiyle Bayesyen çıkarımın özüdür. Parametre uzayının boyutuyla ilgili karşılıklı ağırlığın dahil edilmesi yoluyla yarı ampirik Bayesyen büzücü tahmincilerin performansı bundan etkilenir. Tahmin edicinin büzülme faktörünün, verilerdeki aykırı değerlere ve eliptik modellerin bilinmeyen yoğunluk yaratıcı fonksiyonuna karşı dayanıklı olduğu gösterilmiştir. Son olarak, bir uygulama ile desteklenmiştir.

Anahtar Kelimeler: Dengeli kayıp fonksiyonu, Eliptik konturlu dağılım, Kayıp fonksiyona dayalı önsellik, Yarı-ampirik Bayes tahmin edici, Büzücü tahmin edici

Introduction

Multiple regression model is commonly used statistical tool applied in many disciplines of the modern area. The estimation of parameters of the multiple regression model is a common interest in many studies. Let us consider the following multiple regression model

$$\boldsymbol{y} = \boldsymbol{X}\boldsymbol{\beta} + \boldsymbol{\epsilon}, \tag{1}$$

where

- $\boldsymbol{y}$ is an $n \times 1$ response vector, representing the observed outcomes or dependent variable.
- $\boldsymbol{X}$ is an $n \times p$ design matrix, which contains the independent variables or predictors. It is assumed to be non-stochastic (i.e., not random) and of full rank p with $n > p$ (meaning the number of observations is greater than the number of predictors).
- $\boldsymbol{\beta} = (\beta_1, \cdots, \beta_p)'$ is a $p \times 1$ vector of unknown regression coefficients.
- $\boldsymbol{\epsilon} = (\epsilon_1, \cdots, \epsilon_n)'$ is the $n \times 1$ error vector, representing the random disturbances or noise in the model. The errors are assumed to follow an elliptically contoured distribution (ECD), specifically $\boldsymbol{\epsilon} \sim \mathcal{E}_n(\mathbf{0}, \sigma^2\mathbf{V}, g_n)$, where: σ^2 is the variance of the error; $\mathbf{V} \in S(n)$ is a known, positive definite matrix (i.e., all its eigenvalues are positive) that defines the covariance structure of the errors; g_n is the density generator function, which specifies the shape of the distribution.

Precisely the density of $\boldsymbol{\epsilon}$ is given by

$$f(\boldsymbol{\epsilon}) = \phi|\sigma^2\mathbf{V}|^{-\frac{1}{2}} g_n\left[\frac{1}{2\sigma^2}\boldsymbol{\epsilon}'\mathbf{V}^{-1}\boldsymbol{\epsilon}\right], \tag{2}$$

where ϕ is the normalizing constant given by

$$\phi^{-1} = \frac{\pi^{\frac{n}{2}}}{\Gamma\left(\frac{n}{2}\right)} \int_{\mathbb{R}+} y^{\frac{n}{2}-1} g_n(y) \mathrm{d}y \tag{3}$$

for some density generator function $g_n(.)$. Here, $\Gamma\,(.)$ is the Gamma function, which generalizes the factorial function to continuous values. The integral ensures that the distribution is properly normalized. The condition in [1]

$$\int_0^\infty x^{\frac{n}{2}-1} g_n(x) \mathrm{d}x < \infty \tag{4}$$

guarantees that $g_n(x)$ is a density generator. If the function $g_n(.)$ does not depend on n, we use the notation g instead of $g_n(x)$.

Lower risk improves the performance of the estimator. In such a case, the loss function plays as a decision mechanism. It is quite significant to work with reasonable and practical losses in order to improve the performance of the estimator.

Let $\boldsymbol{\beta}^*$ be any estimator of $\boldsymbol{\beta}$, then the quadratic loss function is described by $(\boldsymbol{X}\boldsymbol{\beta}^* - \boldsymbol{y})'(\boldsymbol{X}\boldsymbol{\beta}^* - \boldsymbol{y})$, which shows the goodness of fit. Then, the precision of the estimator $\boldsymbol{\beta}^*$ is computed using the weighted loss function $(\boldsymbol{\beta}^* - \boldsymbol{\beta})'\boldsymbol{X}'\boldsymbol{X}(\boldsymbol{\beta}^* - \boldsymbol{\beta})$. In order to show the performances of an estimator, both of the above criteria are taken into consideration. In this paper, we take into consideration the issue of the estimator with following *balanced loss function* (BLF)

$$L^{\boldsymbol{W}}_{\omega,\boldsymbol{\delta}_0}(\boldsymbol{\beta}^*;\boldsymbol{\beta}) = \omega r\left(\|\boldsymbol{\beta}\|^2\right)(\boldsymbol{\beta}^* - \boldsymbol{\delta}_0)'\boldsymbol{W}(\boldsymbol{\beta}^* - \boldsymbol{\delta}_0) + (1-\omega)r\left(\|\boldsymbol{\beta}\|^2\right)(\boldsymbol{\beta}^* - \boldsymbol{\beta})'\boldsymbol{W}(\boldsymbol{\beta}^* - \boldsymbol{\beta}), \qquad (5)$$

where the weight shows with $\omega \in [0,1]$, $\boldsymbol{W}$ shows the matrix including weights, a pd weight function is $r(.)$ and $\boldsymbol{\delta}_0$ is the estimation of unknown vector $\boldsymbol{\beta}$. This loss function was proposed by Jozani [2] based on Zellner's balanced loss function [3]. Gómez-Déniz called it as weighted balanced loss function (WBLF) and generalized that idea to the credibility theory [4]. Both measures for goodness of fit and estimator error are taken using the WBLF. The first term in Eq. (5), $\omega r\left(\|\boldsymbol{\beta}\|^2\right)(\boldsymbol{\beta}^* - \boldsymbol{\delta}_0)'(\boldsymbol{\beta}^* - \boldsymbol{\delta}_0)$, is similar to the penalty term for being without smoothness in non-parametric regression. The weight ω in Eq. (5) calibrates the relative importance of these two measures. Dey et al. [5] worked the issues of admissibility and dominance under the loss function in Eq. (5) with $r = 1$ and $\boldsymbol{W} = \boldsymbol{I}_p$. For $\omega = 0$, $L^{\boldsymbol{W}}_0(\boldsymbol{\delta};\boldsymbol{\beta})$ shows the quadratic loss function. Bayesian context is used to explain the the weight function $r(.)$. To the best of our knowledge, the studies that use vague prior information (roughly speaking, objective Bayesian) for the parameter space seem to provide no more than a classical approach. A possible idea to solve this issue is to consider a prior information for the weight function in the loss function in Eq. (5). This approach is different from the recent study of Evans and Jang [6], where they derived the least relative surprise Bayes estimator using a prior based loss function.

The main focus of this study is to improve objective Bayesian inference considering a prior based loss function. We estimate the unknown regression coefficients $\boldsymbol{\beta} = (\beta_1, \cdots, \beta_p)'$ under the condition that we may not know whether $\boldsymbol{\beta}$ belongs to the subspace defined by $\boldsymbol{H}\boldsymbol{\beta} = \boldsymbol{h}$. This implies the presence of certain restrictions on the parameter space, which may influence the estimation process. Specifically, the matrix $\boldsymbol{H}$ shows a $q \times p$ matrix of constants, and $\boldsymbol{h}$ is a q-dimensional vector containing known constants. These restrictions imply that certain linear combinations of the regression coefficients $\boldsymbol{\beta}$ are fixed or constrained, and this affects how the coefficients are estimated.

The study pays special attention to the use of Stein-type shrinkage estimators and the preliminary test (PT) estimator of $\boldsymbol{\beta}$. The key restriction here is that the prior information regarding the weights in the balanced loss function (Eq. (3)) directly influences the risk associated with these estimators. By incorporating prior knowledge about the relationship between $\boldsymbol{\beta}$ and $\boldsymbol{H}\boldsymbol{\beta} = \boldsymbol{h}$, the shrinkage estimator is able to reduce the risk, but the extent of this reduction depends on both the dimensionality of the parameter vector and the specific choice of prior models. Saleh [7] provides an overview for this issue under normal and non-parametric theory covering many standard models. For more information, see [8–19].

Our contribution has the following specific highlights:

1. We propose shrinkage estimators with robust performance concerning.
2. We introduce a flexible prior-based balanced loss function that can calibrate variability and risk.
3. We propose a class of minimax estimators under the balanced loss function.
4. We proposed the preliminary and Stein-type estimators for the class of elliptically contoured

distribution.

Apart from the highlights mentioned above, as an advantage of the proposed shrinkage estimators, they outperform the Bayes estimator using the BLF, under some mild conditions.

The summary of this paper is here: In the next section we take the vague prior on the entire parameter space $\boldsymbol{\Theta} = (\boldsymbol{\beta}, \sigma^2) \in \mathbb{R}^p \times \mathbb{R}^+$, in order to show that the results are not unrelated to the Bayesian analysis, and then introduce the prior information that plays a key role for enabling a real Bayesian analysis. The following section introduces various estimators. The bias function and the risk function for the estimators are obtained in the next section. Then the performances of the five estimators are compared theoretically and then supported the results with a numerical example Last section presents out conclusions and remarks.

The Bayesian Setup

Under standard assumptions, the least squares (LS) estimator of $\boldsymbol{\beta}$ is

$$\tilde{\boldsymbol{\beta}} = (\mathbf{X}'\mathbf{V}^{-1}\mathbf{X})^{-1}\mathbf{X}'\mathbf{V}^{-1}\boldsymbol{y} = \boldsymbol{C}^{-1}\mathbf{X}'\boldsymbol{V}^{-1}\boldsymbol{y}, \text{ where } \boldsymbol{C} = \mathbf{X}'\mathbf{V}^{-1}\mathbf{X}. \tag{6}$$

Similarly the LS estimator of σ^2 is

$$\tilde{\sigma}^2 = \frac{1}{n}(\boldsymbol{y} - \mathbf{X}\tilde{\boldsymbol{\beta}})'\mathbf{V}^{-1}(\boldsymbol{y} - \mathbf{X}\tilde{\boldsymbol{\beta}}). \tag{7}$$

It is straightforward to show that

$$S^2 = \frac{1}{n-p}\left[(\boldsymbol{y} - \mathbf{X}\tilde{\boldsymbol{\beta}})'\mathbf{V}^{-1}(\boldsymbol{y} - \mathbf{X}\tilde{\boldsymbol{\beta}})\right] \tag{8}$$

is an unbiased estimator of the true error variance $\sigma_{\boldsymbol{\epsilon}}^2$. Under the assumption of elliptical errors, the true error variance $\sigma_{\boldsymbol{\epsilon}}^2$ is related to the characteristic generator $\psi'(0)$ of the elliptical distribution:

$$\sigma_{\boldsymbol{\epsilon}}^2 = -2\psi'(0)\sigma^2 \tag{9}$$

where $\psi'(0)$ denotes the first derivative of the characteristic generator of the elliptical distribution at zero. Thus, the estimator S^2, derived from the residuals weighted by $\mathbf{V}^{-1}$, provides an unbiased estimate of the error variance $\sigma_{\boldsymbol{\epsilon}}^2$, which is consistent with the true variance structure of the model. See Chapt. 4 of [1] for more details.

From the Bayesian perspective, firstly, it is assumed to be a little about the parameters and further the elements of $\boldsymbol{\beta}$ are independent of σ^2. Therefore, the joint prior distribution has form

$$\pi(\boldsymbol{\beta}, \sigma^2) = \pi(\boldsymbol{\beta})\pi(\sigma^2), \tag{10}$$

where $\pi(\cdot)$ is a prior density. At this stage, it is important to consider invariant theory, which ensures that the accuracy of the models is preserved regardless of linear transformations applied to the dataset. Using the invariant theory as in [20], we take the prior knowledge about the parameter space as follows:

$$\pi(\boldsymbol{\beta}) \propto \text{constant}, \quad \pi(\sigma^2) \propto \sigma^{-2} \text{ (that is } \pi(\boldsymbol{\beta}, \sigma^2) \propto \sigma^{-2}), \tag{11}$$

where $\boldsymbol{\beta}$ and σ^2 are regression model parameters. Additionally, invariant theory enhances the reliability of estimators by ensuring that the error variance remains unchanged under transformations, particularly in special models such as elliptical distributions.

Lemma 1. (Arashi, 2010) Assume that $\boldsymbol{\epsilon} \sim \mathcal{E}_n(\mathbf{0}, \sigma^2\boldsymbol{V}, \boldsymbol{g})$, where $\boldsymbol{V} \in S(n)$ in the *multiple regression* model (1). Then, with respect to the prior distribution defined by (11), the posterior distribution of $\boldsymbol{\beta}$ follows a multivariate Student's t-distribution, denoted as $\boldsymbol{\beta}|(\mathbf{X}, \boldsymbol{y}) \sim t_p(\tilde{\boldsymbol{\beta}}, \boldsymbol{\Sigma}, m)$, where $\boldsymbol{\Sigma} = S^2\boldsymbol{C}^{-1}$, with the following density

$$f(\boldsymbol{\beta}|\mathbf{X}, \boldsymbol{y}) = \frac{|\boldsymbol{\Sigma}|^{-\frac{1}{2}}}{C(m,p)\pi^{\frac{p}{2}}} \left[1 + \frac{1}{m}\,(\boldsymbol{\beta} - \tilde{\boldsymbol{\beta}})'\boldsymbol{\Sigma}^{-1}(\boldsymbol{\beta} - \tilde{\boldsymbol{\beta}})\right]^{-\frac{n}{2}}, \tag{12}$$

where the normalizing constant $C(m,p)$ is given by

$$C(m,p) = \frac{m^{\frac{p}{2}}\Gamma\left(\frac{m}{2}\right)}{\Gamma\left(\frac{n}{2}\right)}, \text{ with } \quad m = n - p. \tag{13}$$

Using Lemma 2 of Jozani et al. [2], the Bayes estimator under the BLF in Eq. (5) is given by

$$\begin{aligned}\hat{\boldsymbol{\beta}}^B &= \omega\boldsymbol{\delta}_0 + (1-\omega)\frac{E_\pi\left[\boldsymbol{\beta} r\left(\|\boldsymbol{\beta}\|^2\right)|(\boldsymbol{X}, \boldsymbol{y})\right]}{E_\pi\left[r\left(\|\boldsymbol{\beta}\|^2\right)|(\boldsymbol{X}, \boldsymbol{y})\right]} \\ &= \omega\tilde{\boldsymbol{\beta}} + (1-\omega)\frac{E_\pi\left[\boldsymbol{\beta} r\left(\|\boldsymbol{\beta}\|^2\right)|(\boldsymbol{X}, \boldsymbol{y})\right]}{E_\pi\left[r\left(\|\boldsymbol{\beta}\|^2\right)|(\boldsymbol{X}, \boldsymbol{y})\right]},\end{aligned} \tag{14}$$

where $\boldsymbol{\delta}_0$ refers to any estimator of $\boldsymbol{\beta}$ according to [2]. ω is a weight factor between 0 and 1 that controls the balance between the prior and posterior components. $E_\pi\left[.|(\boldsymbol{X}, \boldsymbol{y})\right]$ presents the posterior expectation given the data. $r\left(\|\boldsymbol{\beta}\|^2\right)$ is a function of the squared norm of $\boldsymbol{\beta}$. Let $\tilde{\boldsymbol{\beta}}$ be the target estimator. Here the LS estimator of $\boldsymbol{\beta}$ as the target estimator, and ω, r, and δ_0 are defined in Eq. (5). When $r\left(\|\boldsymbol{\beta}\|^2\right) = 1$, the Bayes estimator reduces to $\hat{\boldsymbol{\beta}}^B = \tilde{\boldsymbol{\beta}}$, which is similar to considering the Bayes estimator under the quadratic error loss (QEL) function. In this case, since the Bayes estimator is nothing more than the classical LS estimator of β, one may ask ***what would be the benefit of putting prior on the model?*** As a response, we suggest to take a prior based loss function and consider the role of the prior distribution in the loss function in the form of $r(\|\boldsymbol{\beta}\|^2)$.

For the ECDs, let us take the form of the $r(.)$ function as follows

$$r(\|\boldsymbol{\beta}\|^2) = g_p(\|\boldsymbol{\beta}\|^2), \tag{15}$$

where g_p is defined in Eq. (2). Under the above assumption, the loss function relates to the density generator of the base model and therefore the prior information has direct impact on the model understudy. One should note that $r(.)$ can be independent of the function $g(.)$.

In order to recompute the Bayes estimator, we need to use invariant theory, which refers to computing expectations in two steps: first, calculating the conditional expectation of a quantity given the data

$(\boldsymbol{X}, \boldsymbol{y})$, and then taking the expectation of that conditional expectation with respect to the posterior distribution of the parameters $\boldsymbol{\beta}$. This process ensures that the estimator accounts for both the prior knowledge (through the prior distribution) and the data (through the posterior distribution).

Therefore, using double expectation property and Lemma 1, we have

$$\begin{aligned}\hat{\boldsymbol{\beta}}^B &= \omega\tilde{\boldsymbol{\beta}} + (1-\omega)\frac{E_\pi\left[\boldsymbol{\beta} r\left(\|\boldsymbol{\beta}\|^2\right)|(\boldsymbol{X},\boldsymbol{y})\right]}{E_\pi\left[r\left(\|\boldsymbol{\beta}\|^2\right)|(\boldsymbol{X},\boldsymbol{y})\right]}\\ &= \omega\tilde{\boldsymbol{\beta}} + (1-\omega)\frac{E_g\left\{E_\pi\left[\boldsymbol{\beta} r\left(\|\boldsymbol{\beta}\|^2\right)|(\boldsymbol{X},\boldsymbol{y})\right]\Big| r\left(\|\boldsymbol{\beta}\|^2\right)\right\}}{E_g\left\{E_\pi\left[r\left(\|\boldsymbol{\beta}\|^2\right)|(\boldsymbol{X},\boldsymbol{y})\right]\Big| r\left(\|\boldsymbol{\beta}\|^2\right)\right\}}\\ &= \omega\tilde{\boldsymbol{\beta}} + (1-\omega)\frac{\phi^{-1}\tilde{\boldsymbol{\beta}}}{\phi^{-1}} = \tilde{\boldsymbol{\beta}}, \end{aligned} \tag{16}$$

where we computed $E_g\left\{r(\|\boldsymbol{\beta}\|^2)\right\}$ by making use of (11) for fixed constant (to 1) as follows

$$\begin{aligned}E_g\left\{r(\|\boldsymbol{\beta}\|^2)\right\} &= \int_{\mathbb{R}^p} g_p(\|\boldsymbol{\beta}\|^2)\mathrm{d}\boldsymbol{\beta}\\ &= \frac{\pi^{\frac{p}{2}}}{\Gamma\left(\frac{p}{2}\right)}\int_{\mathbb{R}^+} y^{\frac{p}{2}-1} g_p(y)\mathrm{d}y\\ &= \phi^{-1},\end{aligned} \tag{17}$$

where ϕ corresponds to the normalizing constant as in (2) when n is replaced by p.

Note that the Bayes estimator we obtained with the prior based loss function may also be obtained by using the QEL function. The advantage of using the risk function relative to the prior based loss function will be benefited from the effect of prior in Eq. (17). In other words, the prior based BLF enables us to evaluate the risk functions based on this loss, whereas the Bayes estimator is the QEL derived in reality.

Shrinkage Estimators

For testing $H_0 : \boldsymbol{H\beta} = \boldsymbol{h}$ (where $q < p$) against $H_a : \boldsymbol{H\beta} \neq \boldsymbol{h}$, let us consider the restricted estimator (RE) under H_0 designated $\hat{\boldsymbol{\beta}}$ given by

$$\hat{\boldsymbol{\beta}} = \hat{\boldsymbol{\beta}}^B - \boldsymbol{C}^{-1}\boldsymbol{H}'\boldsymbol{V}_1(\boldsymbol{H}\tilde{\boldsymbol{\beta}} - \boldsymbol{h}), \tag{18}$$

where $\boldsymbol{V}_1 = [\boldsymbol{H}\boldsymbol{C}^{-1}\boldsymbol{H}']^{-1}$, $\boldsymbol{H}$ is a q x p constant matrix of row rank $q(q \leq p)$ and $\boldsymbol{h}$ is a q-vector of pre-specified values. $\boldsymbol{C} = \mathbf{X}'\mathbf{V}^{-1}\mathbf{X}$, $\tilde{\boldsymbol{\beta}}$ is the LS estimator in (6), and $\hat{\boldsymbol{\beta}}^B$ is the Bayes estimator.

From the definition of the elliptical model in Eq. (1), $\hat{\boldsymbol{\beta}} \sim \mathcal{E}_p\left(\boldsymbol{\beta} - \boldsymbol{\Delta}, \sigma^2\boldsymbol{V}_2, \boldsymbol{g}\right)$ for $\boldsymbol{\Delta} = \boldsymbol{C}^{-1}\boldsymbol{H}'\boldsymbol{V}_1(\boldsymbol{H\beta} - \boldsymbol{h})$ and $\boldsymbol{V}_2 = \boldsymbol{C}^{-1}(\boldsymbol{I}_p - \boldsymbol{H}'\boldsymbol{V}_1\boldsymbol{H}\boldsymbol{C}^{-1})$. Similarly, the following estimator is unbiased for $\sigma^2_{\boldsymbol{\epsilon}}$ under $H_0 : \boldsymbol{H\beta} = \boldsymbol{h}$,

$$S^{*2} = \frac{1}{n-p+q}\left[(\boldsymbol{y} - \boldsymbol{X}\hat{\boldsymbol{\beta}})'\boldsymbol{V}^{-1}(\boldsymbol{y} - \boldsymbol{X}\hat{\boldsymbol{\beta}})\right]. \tag{19}$$

In this part, we calculate the test statistic for testing the linear null hypothesis $H_0 : \boldsymbol{H\beta} = \boldsymbol{h}$.

Direct computations using Corollary 1 [21], gives the likelihood ratio test statistic as follows

$$\mathcal{L}_n = \frac{(\boldsymbol{H}\tilde{\boldsymbol{\beta}} - \boldsymbol{h})'\boldsymbol{V}_1(\boldsymbol{H}\tilde{\boldsymbol{\beta}} - \boldsymbol{h})}{qS^2}. \tag{20}$$

where $\tilde{\boldsymbol{\beta}}$ and S^2 are given respectively by Eq. (6), Eq. (8). $\boldsymbol{V}_1 = [\boldsymbol{H}\boldsymbol{C}^{-1}\boldsymbol{H}']^{-1}$, $\boldsymbol{H}$ is a q x p constant matrix of row rank $q(q \leq p)$ and $\boldsymbol{C} = \mathbf{X}'\mathbf{V}^{-1}\mathbf{X}$.

Under the hypothesis H_0, the pdf of the likelihood ratio test statistic $\mathcal{L}_n$ is given by

$$\boldsymbol{g}^*_{q,m}(\mathcal{L}_n) = \frac{\left(\frac{q}{m}\right)^{\frac{q}{2}} \mathcal{L}_n^{\frac{q}{2}-1}}{B\left(\frac{q}{2}, \frac{m}{2}\right)\left(1 + \frac{q}{m}\mathcal{L}_n\right)^{\frac{1}{2}(q+m)}} \tag{21}$$

where $m = n - p$, $B(\cdot, \cdot)$ is the beta function and q is the rank of $\boldsymbol{H}$ and dimension of vector of constants $\boldsymbol{h}$ in our restriction. Eq. (21) shows that $\mathcal{L}_n$ follows the central F-distribution with (q, m) degrees of freedom (df).

Based on that model, $\boldsymbol{\beta}$ may not belong to the subspace defined by $\boldsymbol{H}\boldsymbol{\beta} = \boldsymbol{h}$. In such a situation one combines the estimators of $\boldsymbol{\beta}$ and the test-statistic in order to obtain shrinkage estimators as in [7]. Firstly, we consider the PT estimator as a convex combination of the LS estimator $\tilde{\boldsymbol{\beta}}$ (designated as unrestricted estimator - UE) and $\hat{\boldsymbol{\beta}}$ (designated as RE) which are defined by Eq. (18) as follows:

$$\hat{\boldsymbol{\beta}}^{PT} = \tilde{\boldsymbol{\beta}} I(\mathcal{L}_n \geq F_\alpha) + \hat{\boldsymbol{\beta}} I(\mathcal{L}_n < F_\alpha), \tag{22}$$

where $I(A)$ is an indicator function of the set A and F_α is the upper α^{th} percentile of the central F-distribution with (q, m) df. The PT estimator has disadvantage since it is defined with α $(0 < \alpha < 1)$, the significance level. In addition to this, it yields the extreme results. Therefore, $\hat{\boldsymbol{\beta}}$ or $\tilde{\boldsymbol{\beta}}$ depends on the outcome of the test. To overcome this problem, we suggest a Stein-type shrinkage (SS) estimator of $\boldsymbol{\beta}$, as

$$\hat{\boldsymbol{\beta}}^{S} = \hat{\boldsymbol{\beta}} + (1 - d\mathcal{L}_n^{-1})(\tilde{\boldsymbol{\beta}} - \hat{\boldsymbol{\beta}}) = \tilde{\boldsymbol{\beta}} - d\mathcal{L}_n^{-1}(\tilde{\boldsymbol{\beta}} - \hat{\boldsymbol{\beta}}), \tag{23}$$

where $\hat{\boldsymbol{\beta}}$ and $\tilde{\boldsymbol{\beta}}$ are LS and RE estimators given by Eq. (6) and Eq. (18), respectively, and $\mathcal{L}_n$ as in Eq. (20), and

$$d = \frac{(q-2)m}{q(m+2)} \qquad \text{with} \qquad q \geq 3. \tag{24}$$

However, the SS has some drawbacks for small values of $\mathcal{L}_n$ such as the shrinkage factor $(1 - d\mathcal{L}_n^{-1})$ becomes negative for $\mathcal{L}_n < d$. Another estimator is proposed using the positive-rule shrinkage (PRS) estimator as follows

$$\hat{\boldsymbol{\beta}}^{S+} = \hat{\boldsymbol{\beta}} + (1 - d\mathcal{L}_n^{-1}) I(\mathcal{L}_n > d)(\tilde{\boldsymbol{\beta}} - \hat{\boldsymbol{\beta}}), \tag{25}$$

where $I()$ shows the indicator function.

Bias and Risk for the Estimators

For an estimator $\boldsymbol{\beta}^*$, the risk function under the BLF in Eq. (5) is given by

$$\boldsymbol{R}^{\boldsymbol{W}}_{\omega,\boldsymbol{\delta}_0}(\boldsymbol{\beta}^*;\boldsymbol{\beta}) = E\left\{E[L^{\boldsymbol{W}}_{\omega,\boldsymbol{\delta}_0}(\boldsymbol{\beta}^*;\boldsymbol{\beta})]|\boldsymbol{\beta}\right\}. \tag{26}$$

Note that the computation of the risk function in Eq. (26) depends on the balanced-type expectation (inner expectation) w.r.t the sampling distribution. Then the expectation (outer expectation) from the prior information is obtained by equation (15).
This section is dedicated to deriving the bias and the risk function in Eq. (26) for the five different estimators when the target estimator is determined by $\boldsymbol{\delta}_0 = \tilde{\boldsymbol{\beta}}$ and the weight matrix is given by $\boldsymbol{W} = \boldsymbol{C}$, where $\boldsymbol{C}$ is defined in Eq. (6). We will simply write $\boldsymbol{R}^{\boldsymbol{W}}_0(\boldsymbol{\beta}^*;\boldsymbol{\beta})$ for $\omega = 0$.

Computation of bias

The bias of the estimator $\hat{\boldsymbol{\beta}}^B$ in Eq. (14) and RE estimator $\hat{\boldsymbol{\beta}}$ in Eq. (18) are

$$\boldsymbol{b}_1 = E[\hat{\boldsymbol{\beta}}^B - \boldsymbol{\beta}] = \boldsymbol{0}, \text{ and } \boldsymbol{b}_2 = E[\hat{\boldsymbol{\beta}} - \boldsymbol{\beta}] = -\boldsymbol{\Delta}, \tag{27}$$

respectively, where $\boldsymbol{\Delta} = \boldsymbol{C}^{-1}\boldsymbol{H}'\boldsymbol{V}_1(\boldsymbol{H}\boldsymbol{\beta} - \boldsymbol{h})$. Using [22], the bias of the PT is

$$\begin{aligned}\boldsymbol{b}_3 &= E(\hat{\boldsymbol{\beta}}^{PT} - \boldsymbol{\beta}) = E[\tilde{\boldsymbol{\beta}} - I(\mathcal{L}_n \le F_\alpha)(\tilde{\boldsymbol{\beta}} - \hat{\boldsymbol{\beta}}) - \boldsymbol{\beta}]\\ &= -\boldsymbol{C}\boldsymbol{H}'\mathbf{V}_1^{1/2}\, E[I(\mathcal{L}_n \le F_\alpha)\mathbf{V}_1^{1/2}(\boldsymbol{H}\tilde{\boldsymbol{\beta}} - \boldsymbol{h})] = -\boldsymbol{\Delta} G^{(2)}_{q+2,m}\left(F_\alpha;\Delta_*^2\right),\end{aligned} \tag{28}$$

where $\Delta_*^2 = \theta/\sigma_{\boldsymbol{\epsilon}}^2$, $\theta = (\boldsymbol{H}\boldsymbol{\beta} - \boldsymbol{h})'\boldsymbol{V}_1'(\boldsymbol{H}\boldsymbol{\beta} - \boldsymbol{h})$,

$$G^{(2-j)}_{q+2i,m}(l_\alpha,\Delta_*^2) = \sum_{r=0}^{\infty} K_r^{(j)}(\Delta_*^2) I_{l_\alpha}\left[\frac{q+2i}{2} + r, \frac{m}{2}\right], \text{ and } j = 0,1, \tag{29}$$

$l_\alpha = \frac{qF_{q,m}(\alpha)}{m+qF_{q,m}(\alpha)}$, $I_x[a,b] = \frac{1}{B(a,b)}\int_0^x u^{a-1}(1-u)^{b-1}du$ is the incomplete function of beta,

$$K_r^{(j)}(\Delta_*^2) = \frac{[-2\psi'(0)]^r}{r!}\left(\frac{\Delta_*^2}{2}\right)^2 \int_0^\infty t^{r-j} e^{t\psi'(0)\Delta_*^2} W(t)dt, \tag{30}$$

and $W(t)$ is a weight function.
Then, the bias of the SS becomes

$$\begin{aligned}\boldsymbol{b}_4 &= E(\hat{\boldsymbol{\beta}}^S - \boldsymbol{\beta}) = E[\tilde{\boldsymbol{\beta}} - d\mathcal{L}_n^{-1}(\tilde{\boldsymbol{\beta}} - \hat{\boldsymbol{\beta}}) - \boldsymbol{\beta}]\\ &= -d\boldsymbol{C}^{-1}\boldsymbol{H}'\boldsymbol{V}_1^{1/2}E[\mathcal{L}_n^{-1}\boldsymbol{V}_1^{1/2}(\boldsymbol{H}\tilde{\boldsymbol{\beta}} - \boldsymbol{h})] = -dq\boldsymbol{\Delta}E^{(2)}[\chi^{*-2}_{q+2}(\Delta_*^2)],\end{aligned} \tag{31}$$

and here

$$E^{(2-j)}[\chi^{*-2}_{q+s}(\Delta_*^2)] = \sum_{r\ge 0}\frac{1}{r!}K_r^{(j)}(\Delta_*^2)(q+s-2+2r)^{-1}, \text{ for } s = 2,4. \tag{32}$$

Finally, the bias of the PRSE is obtained as follows:

$$\begin{aligned}\boldsymbol{b}_5 &= E(\hat{\boldsymbol{\beta}}^S - \boldsymbol{\beta}) - E[I(\mathcal{L}_n \leq d)(\tilde{\boldsymbol{\beta}} - \hat{\boldsymbol{\beta}})] + dE[\mathcal{L}_n^{-1} I(\mathcal{L}_n \leq d)(\tilde{\boldsymbol{\beta}} - \hat{\boldsymbol{\beta}})] \\ &= -dq\boldsymbol{\Delta} E_N^{(2)}[\chi_{q+2}^{*-4}(\Delta_*^2)] + \boldsymbol{\Delta} G_{q+2,m}^{(2)}\left(d; \Delta_*^2\right) \\ &+ \frac{qd}{q+2}\,\boldsymbol{\Delta} E^{(2)}\left[F_{q+2,m}^{-1}(\Delta_*^2) I\left(F_{q+2,m}(\Delta_*^2) \leq \frac{qd}{q+2}\right)\right],\end{aligned} \tag{33}$$

where

$$\begin{aligned}&E^{(2-j)}[F_{q+s,n-p}^{-k}(\Delta_*^2) I(F_{q+s,n-p}(\Delta_*^2) < d_1)] \\ &= \sum_{r=0}^{\infty} K_r^{(j)}(\Delta_*^2)\left(\frac{q+s}{n-p}\right)^k \frac{B(\frac{q+s+2r-2k}{2}, \frac{m+2k}{2})}{B(\frac{q+s+2r}{2}, \frac{m}{2})} I_{x'}\left[\frac{q+s+2r-2k}{2}, \frac{m+2k}{2}\right],\end{aligned} \tag{34}$$

in which $d_1 = \frac{dq}{q+2}$, and $x' = \frac{dq}{m+dq}$.
Note that for the non-centrality parameter $\Delta_*^2 (= \boldsymbol{\Delta}' \boldsymbol{C} \boldsymbol{\Delta} / \sigma_{\boldsymbol{\epsilon}}^2) \to \infty$, the bias of these estimators are obtained by $\boldsymbol{b}_1 = \boldsymbol{b}_3 = \boldsymbol{b}_4 = \boldsymbol{b}_5 = \boldsymbol{0}$, except for $\boldsymbol{b}_2$ which becomes unbounded. However, under $H_0 : \boldsymbol{H}\boldsymbol{\beta} = \boldsymbol{h}$ hypothesis, because $\boldsymbol{\Delta} = \boldsymbol{0}$, the bias of that estimators is defined as $\boldsymbol{b}_1 = \boldsymbol{b}_2 = \boldsymbol{b}_3 = \boldsymbol{b}_4 = \boldsymbol{b}_5 = \boldsymbol{0}$.

Computation of risk

The risk function of the Bayes estimator $\hat{\boldsymbol{\beta}}^B$, $\boldsymbol{R}_{\omega, \tilde{\boldsymbol{\beta}}}^{\boldsymbol{C}}(.; \boldsymbol{\beta})$ in Eq. (26), is computed as

$$\begin{aligned}\boldsymbol{R}_{\omega, \tilde{\boldsymbol{\beta}}}^{\boldsymbol{C}}(\hat{\boldsymbol{\beta}}^B; \boldsymbol{\beta}) &= (1-\omega) E_{\boldsymbol{\beta}}\left\{r\left(\|\boldsymbol{\beta}\|^2\right) E[(\tilde{\boldsymbol{\beta}} - \boldsymbol{\beta})' \boldsymbol{C} (\tilde{\boldsymbol{\beta}} - \boldsymbol{\beta})] | \boldsymbol{\beta}\right\} \\ &= p\, \sigma_{\boldsymbol{\epsilon}}^2 (1-\omega) E_{\boldsymbol{\beta}}\left\{r\left(\|\boldsymbol{\beta}\|^2\right)\right\} \\ &= p\, \phi^{-1} \sigma_{\boldsymbol{\epsilon}}^2 (1-\omega).\end{aligned} \tag{35}$$

where $\omega \in [0,1]$ (see Eq. (5)), $\sigma_{\boldsymbol{\epsilon}}^2 = -2\psi'(0)\sigma^2$, and

$$\phi = \left(\frac{\pi^{\frac{n}{2}}}{\Gamma\left(\frac{n}{2}\right)} \int_{\mathbb{R}+} y^{\frac{n}{2}-1} g_n(y) \mathrm{d}y\right)^{-1}. \tag{36}$$

Using the fact that (see [8]) $\boldsymbol{V}_1^{\frac{1}{2}}(\boldsymbol{H}\tilde{\boldsymbol{\beta}} - \boldsymbol{h}) \sim \mathcal{E}_q(\boldsymbol{V}_1^{\frac{1}{2}}(\boldsymbol{H}\boldsymbol{\beta} - \boldsymbol{h}), \sigma^2 \boldsymbol{I}_q, \boldsymbol{g})$, the risk of the estimator RE is given by

$$\begin{aligned}\boldsymbol{R}_{\omega, \tilde{\boldsymbol{\beta}}}^{\boldsymbol{C}}(\hat{\boldsymbol{\beta}}; \boldsymbol{\beta}) &= \omega E_{\boldsymbol{\beta}}\left\{r\left(\|\boldsymbol{\beta}\|^2\right) E[(\boldsymbol{H}\tilde{\boldsymbol{\beta}} - \boldsymbol{h})' \boldsymbol{V}_1 (\boldsymbol{H}\tilde{\boldsymbol{\beta}} - \boldsymbol{h})] | \boldsymbol{\beta}\right\} \\ &+ (1-\omega) E_{\boldsymbol{\beta}}\left\{r\left(\|\boldsymbol{\beta}\|^2\right) E[(\hat{\boldsymbol{\beta}} - \boldsymbol{\beta})' \boldsymbol{C} (\hat{\boldsymbol{\beta}} - \boldsymbol{\beta})] | \boldsymbol{\beta}\right\} \\ &= -q\omega\sigma_{\boldsymbol{\epsilon}}^2 E_{\boldsymbol{\beta}}\left\{r\left(\|\boldsymbol{\beta}\|^2\right)\right\} + (1-\omega) E_{\boldsymbol{\beta}}\left\{r\left(\|\boldsymbol{\beta}\|^2\right)\right\} [\sigma_{\boldsymbol{\epsilon}}^2 \mathrm{tr}(\boldsymbol{V}_2 \boldsymbol{C}) + \boldsymbol{\Delta}' \boldsymbol{C} \boldsymbol{\Delta}] \\ &= -q\omega\sigma_{\boldsymbol{\epsilon}}^2 \phi^{-1} + \boldsymbol{R}_{\omega, \tilde{\boldsymbol{\beta}}}^{\boldsymbol{C}}(\tilde{\boldsymbol{\beta}}; \boldsymbol{\beta}) + \phi^{-1}(1-\omega)(-\sigma_{\boldsymbol{\epsilon}}^2 \mathrm{tr}[\boldsymbol{H}' \boldsymbol{V}_1 \boldsymbol{H} \boldsymbol{C}] + \boldsymbol{\Delta}' \boldsymbol{C} \boldsymbol{\Delta}) \\ &= \boldsymbol{R}_{\omega, \tilde{\boldsymbol{\beta}}}^{\boldsymbol{C}}(\tilde{\boldsymbol{\beta}}; \boldsymbol{\beta}) - q\, \phi^{-1} \sigma_{\boldsymbol{\epsilon}}^2 + (1-\omega)\phi^{-1}\theta,\end{aligned} \tag{37}$$

where $\theta = \boldsymbol{\Delta}'\boldsymbol{C}\boldsymbol{\Delta} = (\boldsymbol{H\beta} - \boldsymbol{h})'\boldsymbol{V}_1(\boldsymbol{H\beta} - \boldsymbol{h})$. Note that $\boldsymbol{R} = \boldsymbol{C}^{-1/2}\boldsymbol{H}'\boldsymbol{V}_1\boldsymbol{H}\boldsymbol{C}^{-1/2}$ is a symmetric idempotent matrix of rank $q \leq p$ and $\boldsymbol{C} = \mathbf{X}'\mathbf{V}^{-1}\mathbf{X}$. Thus, there exists an orthogonal matrix $\boldsymbol{Q}$ ($\boldsymbol{Q}'\boldsymbol{Q} = \boldsymbol{I}_p$) such that $\boldsymbol{QRQ}' = \begin{bmatrix} \boldsymbol{I}_q & 0 \\ 0 & 0 \end{bmatrix}$. A random vector is defined by $\boldsymbol{w} = \boldsymbol{Q}\boldsymbol{C}^{1/2}\tilde{\boldsymbol{\beta}} - \boldsymbol{Q}\boldsymbol{C}^{-1/2}\boldsymbol{H}'\boldsymbol{V}_1\boldsymbol{h}$, then $\boldsymbol{w} \sim \mathcal{E}_p(\boldsymbol{\eta}, \sigma^2\boldsymbol{I}_p, \boldsymbol{g})$, where $\boldsymbol{\eta} = \boldsymbol{Q}\boldsymbol{C}^{1/2}\boldsymbol{\beta} - \boldsymbol{Q}\boldsymbol{C}^{-1/2}\boldsymbol{H}'\boldsymbol{V}_1\boldsymbol{h}$. Partitioning the vector $\boldsymbol{w} = (\boldsymbol{w}_1', \boldsymbol{w}_2')'$ and $\boldsymbol{\eta} = (\boldsymbol{\eta}_1', \boldsymbol{\eta}_2')'$, where $\boldsymbol{w}_1$ and $\boldsymbol{w}_2$ are the subvectors of sequence q and $p - q$ respectively, one may rewrite the test statistic $\mathcal{L}_n$ defined in Eq. (17) as

$$\mathcal{L}_n = \frac{\boldsymbol{w}_1'\boldsymbol{w}_1}{qS^2}, \quad \theta = \boldsymbol{\eta}_1'\boldsymbol{\eta}_1. \tag{38}$$

Consequently, the risk of the PT, $\boldsymbol{R}^{\boldsymbol{C}}_{\omega,\tilde{\boldsymbol{\beta}}}(\hat{\boldsymbol{\beta}}^{PT}; \boldsymbol{\beta})$, noting that $\hat{\boldsymbol{\beta}} - \tilde{\boldsymbol{\beta}} = \boldsymbol{C}^{-1}\boldsymbol{H}'\boldsymbol{V}_1\boldsymbol{H}\boldsymbol{C}^{-\frac{1}{2}}\boldsymbol{w}$ as follows:

$$\begin{aligned}
\boldsymbol{R}^{\boldsymbol{C}}_{\omega,\tilde{\boldsymbol{\beta}}}(\hat{\boldsymbol{\beta}}^{PT}; \boldsymbol{\beta}) &= \omega E_{\boldsymbol{\beta}}\left\{r\left(\|\boldsymbol{\beta}\|^2\right) E[I(\mathcal{L}_n < F_\alpha)(\hat{\boldsymbol{\beta}} - \tilde{\boldsymbol{\beta}})'\boldsymbol{C}(\hat{\boldsymbol{\beta}} - \tilde{\boldsymbol{\beta}})]|\boldsymbol{\beta}\right\} \\
&+ (1-\omega)E_{\boldsymbol{\beta}}\left\{r\left(\|\boldsymbol{\beta}\|^2\right) E[(\hat{\boldsymbol{\beta}}^{PT} - \boldsymbol{\beta})'\boldsymbol{C}(\hat{\boldsymbol{\beta}}^{PT} - \boldsymbol{\beta})]|\boldsymbol{\beta}\right\} \\
&= \boldsymbol{R}^{\boldsymbol{C}}_{\omega,\tilde{\boldsymbol{\beta}}}(\tilde{\boldsymbol{\beta}}; \boldsymbol{\beta}) - (1-2\omega)E_{\boldsymbol{\beta}}\left\{r\left(\|\boldsymbol{\beta}\|^2\right) E[\boldsymbol{w}_1'\boldsymbol{w}_1 I(\mathcal{L}_n \leq F_\alpha)]|\boldsymbol{\beta}\right\} \\
&+ 2(1-\omega)E_{\boldsymbol{\beta}}\left\{r\left(\|\boldsymbol{\beta}\|^2\right) \boldsymbol{\eta}_1' E[\boldsymbol{w}_1 I(\mathcal{L}_n \leq F_\alpha)]|\boldsymbol{\beta}\right\} \\
&= \boldsymbol{R}^{\boldsymbol{C}}_{\omega,\tilde{\boldsymbol{\beta}}}(\tilde{\boldsymbol{\beta}}; \boldsymbol{\beta}) - (1-2\omega)q\sigma^2_{\boldsymbol{\epsilon}}\phi^{-1}G^{(1)}_{q+2,m}\left(F_\alpha; \Delta^2_*\right) \\
&+ 2\theta(1-\omega)\phi^{-1}\left[2G^{(2)}_{q+2,m}\left(F_\alpha; \Delta^2_*\right) - G^{(2)}_{q+4,m}\left(F_\alpha; \Delta^2_*\right)\right],
\end{aligned} \tag{39}$$

where we obtain this result by simplifying the expressions.
Similarly, after simplifying the expressions, the risk of the SE $\boldsymbol{R}^{\boldsymbol{C}}_{\omega,\tilde{\boldsymbol{\beta}}}(\hat{\boldsymbol{\beta}}^{S}; \boldsymbol{\beta})$ is obtained by

$$\begin{aligned}
\boldsymbol{R}^{\boldsymbol{C}}_{\omega,\tilde{\boldsymbol{\beta}}}(\hat{\boldsymbol{\beta}}^{S}; \boldsymbol{\beta}) &= \omega d^2 E_{\boldsymbol{\beta}}\left\{r\left(\|\boldsymbol{\beta}\|^2\right) E[\mathcal{L}_n^{-1}\boldsymbol{w}_1'\boldsymbol{w}_1]|\boldsymbol{\beta}\right\} + \boldsymbol{R}^{\boldsymbol{C}}_{\omega,\tilde{\boldsymbol{\beta}}}(\tilde{\boldsymbol{\beta}}; \boldsymbol{\beta}) \\
&- 2d(1-\omega)E_{\boldsymbol{\beta}}\left\{r\left(\|\boldsymbol{\beta}\|^2\right) E[\mathcal{L}_n^{-1}(\boldsymbol{w}_1'\boldsymbol{w}_1 - \boldsymbol{\eta}_1'\boldsymbol{w}_1)]|\boldsymbol{\beta}\right\} \\
&+ d^2(1-\omega)E_{\boldsymbol{\beta}}\left\{r\left(\|\boldsymbol{\beta}\|^2\right) E[\mathcal{L}_n^{-2}\boldsymbol{w}_1'\boldsymbol{w}_1]|\boldsymbol{\beta}\right\} \\
&= \boldsymbol{R}^{\boldsymbol{C}}_{\omega,\tilde{\boldsymbol{\beta}}}(\tilde{\boldsymbol{\beta}}; \boldsymbol{\beta}) + q\,\phi^{-1}\Bigg\{\left[d^2\omega - 2d(1-\omega)\right]E^{(1)}[\chi^{*-2}_{q+2}(\Delta^2_*)] \\
&+ d^2(1-\omega)E^{(1)}[\chi^{*-4}_{q+2}(\Delta^2_*)]\Bigg\} + \theta\,\phi^{-1} \\
&\times \Bigg\{\left[d^2\omega - 2d(1-\omega)\right]E^{(2)}[\chi^{*-2}_{q+4}(\Delta^2_*)] \\
&- 2d(1-\omega)E^{(2)}[\chi^{*-2}_{q+2}(\Delta^2_*)] + d^2(1-\omega)E^{(2)}[\chi^{*-4}_{q+4}(\Delta^2_*)]\Bigg\},
\end{aligned} \tag{40}$$

where

$$E^{(2-j)}[\chi^{*-4}_{q+s}(\Delta^2_*)] = \sum_{r\geq 0}\frac{1}{r!}K^{(j)}_r(\Delta^2_*)(q+s-2+2r)^{-1}(q+s-4+2r)^{-1}, \tag{41}$$

$\omega \in [0,1]$ is the weight used in the BLF, and (24)

$$d = \frac{(q-2)m}{q(m+2)} \qquad \text{with} \qquad q \geq 3, \tag{42}$$

and $\boldsymbol{w}_1$ is the first sub-partition of $\boldsymbol{w}$. Finally, the risk function of the PRSE, $\boldsymbol{R}^{\boldsymbol{C}}_{\omega,\tilde{\boldsymbol{\beta}}}(\hat{\boldsymbol{\beta}}^{S+};\boldsymbol{\beta})$ is found as follows

$$\begin{aligned}
\boldsymbol{R}^{\boldsymbol{C}}_{\omega,\tilde{\boldsymbol{\beta}}}(\hat{\boldsymbol{\beta}}^{S+};\boldsymbol{\beta}) &= \boldsymbol{R}^{\boldsymbol{C}}_{\omega,\tilde{\boldsymbol{\beta}}}(\hat{\boldsymbol{\beta}}^{S};\boldsymbol{\beta}) - E_{\boldsymbol{\beta}}\Big\{ r\left(\|\boldsymbol{\beta}\|^2\right) E[(1-d\mathcal{L}_n^{-1})^2 I(\mathcal{L}_n \leq d) \\
&\quad \times (\tilde{\boldsymbol{\beta}}-\hat{\boldsymbol{\beta}})'\boldsymbol{C}(\tilde{\boldsymbol{\beta}}-\hat{\boldsymbol{\beta}})]|\boldsymbol{\beta}\Big\} - 2E_{\boldsymbol{\beta}}\Big\{ r\left(\|\boldsymbol{\beta}\|^2\right) E\{[(1-d\mathcal{L}_n^{-1}) I(\mathcal{L}_n \leq d) \\
&\quad \times (\hat{\boldsymbol{\beta}}-\boldsymbol{\beta})'\boldsymbol{C}(\tilde{\boldsymbol{\beta}}-\hat{\boldsymbol{\beta}})]\}|\boldsymbol{\beta}\Big\} \\
&= \boldsymbol{R}^{\boldsymbol{C}}_{\omega,\tilde{\boldsymbol{\beta}}}(\hat{\boldsymbol{\beta}}^{S};\boldsymbol{\beta}) - E_{\boldsymbol{\beta}}\left\{ r\left(\|\boldsymbol{\beta}\|^2\right) E[(1-d\mathcal{L}_n^{-1})^2 I(\mathcal{L}_n \leq d)\boldsymbol{w}_1'\boldsymbol{w}_1]|\boldsymbol{\beta}\right\} \\
&\quad - 2E_{\boldsymbol{\beta}}\left\{ r\left(\|\boldsymbol{\beta}\|^2\right) E[(1-d\mathcal{L}_n^{-1}) I(\mathcal{L}_n \leq d)(\boldsymbol{w}_1'\boldsymbol{w}_1 - \boldsymbol{\eta}_1'\boldsymbol{w}_1)]|\boldsymbol{\beta}\right\} \\
&= \boldsymbol{R}^{\boldsymbol{C}}_{\omega,\tilde{\boldsymbol{\beta}}}(\hat{\boldsymbol{\beta}}^{S};\boldsymbol{\beta}) \\
&\quad - \phi^{-1}\sigma_{\boldsymbol{\epsilon}}^2\Bigg\{ qE^{(1)}\left[\left(1-\frac{qd}{q+2}F^{-1}_{q+2,m}(\Delta_*^2)\right)^2 I\left(F_{q+2,m}(\Delta_*^2) \leq \frac{qd}{q+2}\right)\right] \\
&\quad + \frac{\theta}{\sigma_{\boldsymbol{\epsilon}}^2}E^{(2)}\left[\left(1-\frac{qd}{q+2}F^{-1}_{q+2,m}(\Delta_*^2)\right)^2 I\left(F_{q+2,m}(\Delta_*^2) \leq \frac{qd}{q+2}\right)\right]\Bigg\} \\
&\quad - 2\phi^{-1}\theta E^{(2)}\left[\left(1-\frac{qd}{q+2}F^{-1}_{q+2,m}(\Delta_*^2)\right) I\left(F_{q+2,m}(\Delta_*^2) \leq \frac{qd}{q+2}\right)\right].
\end{aligned} \tag{43}$$

Comparison of Risks

Recall that the LS estimator $\tilde{\boldsymbol{\beta}}$ is designated as UE and $\hat{\boldsymbol{\beta}}$ is termed as RE. Then, the risk difference of the estimator RE in Eq. (18) and the estimator UE in Eq. (6) is given by

$$\mathcal{D}_{21} = \boldsymbol{R}^{\boldsymbol{C}}_{\omega,\tilde{\boldsymbol{\beta}}}(\hat{\boldsymbol{\beta}};\boldsymbol{\beta}) - \boldsymbol{R}^{\boldsymbol{C}}_{\omega,\tilde{\boldsymbol{\beta}}}(\tilde{\boldsymbol{\beta}};\boldsymbol{\beta}) = \phi^{-1}\left[(1-\omega)\theta - q\sigma_{\boldsymbol{\epsilon}}^2\right]. \tag{44}$$

It is shown that $\hat{\boldsymbol{\beta}}$ outperforms to $\tilde{\boldsymbol{\beta}}$ ($\hat{\boldsymbol{\beta}} \succeq \tilde{\boldsymbol{\beta}}$) - in other words $\hat{\boldsymbol{\beta}}$ dominates $\tilde{\boldsymbol{\beta}}$ - provided $0 \leq \theta \leq \frac{q\sigma_{\boldsymbol{\epsilon}}^2}{1-\omega}$ for $\omega \neq 1$ since $\phi > 0$.
First, let us start the comparison of risk with $\hat{\boldsymbol{\beta}}^{PT}$ versus $\tilde{\boldsymbol{\beta}}$. We use the risk difference defined by

$$\begin{aligned}
\mathcal{D}_{13} = \boldsymbol{R}^{\boldsymbol{C}}_{\omega,\tilde{\boldsymbol{\beta}}}(\tilde{\boldsymbol{\beta}};\boldsymbol{\beta}) - \boldsymbol{R}^{\boldsymbol{C}}_{\omega,\tilde{\boldsymbol{\beta}}}(\hat{\boldsymbol{\beta}}^{PT};\boldsymbol{\beta}) &= (1-2\omega)q\;\phi^{-1}\sigma_{\boldsymbol{\epsilon}}^2 G^{(1)}_{q+2,m}\left(F_\alpha;\Delta_*^2\right) \\
- 2\theta\;\phi^{-1}(1-\omega)[2G^{(2)}_{q+2,m}\left(F_\alpha;\Delta_*^2\right) - G^{(2)}_{q+4,m}\left(F_\alpha;\Delta_*^2\right)]&.
\end{aligned} \tag{45}$$

where G is defined in Eq. (29), $\omega \in [0,1]$ is the weight under the BLF, q is the rank of matrix $\boldsymbol{H}$,

$$\phi^{-1} = \frac{\pi^{\frac{n}{2}}}{\Gamma\left(\frac{n}{2}\right)}\int_{\mathbb{R}^+} y^{\frac{n}{2}-1}g_n(y)\mathrm{d}y \tag{46}$$

$\sigma_{\boldsymbol{\epsilon}}^2 = -2\psi'(0)\sigma^2$, F_α is the upper α^{th} percentile of the central F-distribution with (q, m) df, and $\Delta_*^2 = \theta/\sigma_{\boldsymbol{\epsilon}}^2$, $\theta = (\boldsymbol{H}\boldsymbol{\beta} - \boldsymbol{h})'\boldsymbol{V}_1'(\boldsymbol{H}\boldsymbol{\beta} - \boldsymbol{h})$. For $\omega \neq 1$, the of Eq. (45) is not negative $\hat{\boldsymbol{\beta}}^{PT} \succeq \tilde{\boldsymbol{\beta}}$ whenever

$$\theta \leq \frac{(1-2\omega)q\sigma_{\boldsymbol{\epsilon}}^2 G_{q+2,m}^{(1)}\left(F_\alpha; \Delta_*^2\right)}{2(1-\omega)\left[2G_{q+2,m}^{(2)}\left(F_\alpha; \Delta_*^2\right) - G_{q+4,m}^{(2)}\left(F_\alpha; \Delta_*^2\right)\right]}. \tag{47}$$

Under the hypothesis $H_0 : \boldsymbol{H}\boldsymbol{\beta} = \boldsymbol{h}$ when $\theta = 0$, $\hat{\boldsymbol{\beta}}^{PT} \succeq \tilde{\boldsymbol{\beta}}$ for ω with $\omega \leq \frac{1}{2}$.
Secondly, the comparison of $\hat{\boldsymbol{\beta}}$ and $\hat{\boldsymbol{\beta}}^{PT}$ using the risk difference is defined as follows

$$\begin{aligned}\mathcal{D}_{23} &= \boldsymbol{R}_{\omega,\tilde{\boldsymbol{\beta}}}^{\boldsymbol{C}}(\hat{\boldsymbol{\beta}}; \boldsymbol{\beta}) - \boldsymbol{R}_{\omega,\tilde{\boldsymbol{\beta}}}^{\boldsymbol{C}}(\hat{\boldsymbol{\beta}}^{PT}; \boldsymbol{\beta}) \\ &= -q\,\phi^{-1}\sigma_{\boldsymbol{\epsilon}}^2[1 - (1-2\omega)G_{q+2,m}^{(1)}\left(F_\alpha; \Delta_*^2\right)] + \theta\,\phi^{-1}(1-\omega)[1 - 2G_{q+2,m}^{(2)}\left(F_\alpha; \Delta_*^2\right) \\ &\quad + G_{q+4,m}^{(2)}\left(F_\alpha; \Delta_*^2\right)],\end{aligned} \tag{48}$$

where G is defined in Eq. (29), $\omega \in [0, 1]$ is the weight used in the BLF, q is the rank of matrix $\boldsymbol{H}$,

$$\phi^{-1} = \frac{\pi^{\frac{n}{2}}}{\Gamma\left(\frac{n}{2}\right)} \int_{\mathbb{R}+} y^{\frac{n}{2}-1} g_n(y) \mathrm{d}y, \tag{49}$$

$\sigma_{\boldsymbol{\epsilon}}^2 = -2\psi'(0)\sigma^2$, F_α is the upper α^{th} percentile of the central F-distribution with (q, m) df, and $\Delta_*^2 = \theta/\sigma_{\boldsymbol{\epsilon}}^2$, $\theta = (\boldsymbol{H}\boldsymbol{\beta} - \boldsymbol{h})'\boldsymbol{V}_1'(\boldsymbol{H}\boldsymbol{\beta} - \boldsymbol{h})$.
Thus $\hat{\boldsymbol{\beta}}^{PT} \succeq \hat{\boldsymbol{\beta}}$ whenever

$$\theta \geq \frac{q\sigma_{\boldsymbol{\epsilon}}^2\left[1 - (1-2\omega)G_{q+2,m}^{(1)}\left(F_\alpha; \Delta_*^2\right)\right]}{(1-\omega)\left[1 - 2G_{q+2,m}^{(2)}\left(F_\alpha; \Delta_*^2\right) + G_{q+4,m}^{(2)}\left(F_\alpha; \Delta_*^2\right)\right]}, \tag{50}$$

and vice versa. Under H_0, the superiority order of $\tilde{\boldsymbol{\beta}}$, $\hat{\boldsymbol{\beta}}$ and $\hat{\boldsymbol{\beta}}^{PT}$ is defined by

$$\hat{\boldsymbol{\beta}} \succeq \hat{\boldsymbol{\beta}}^{PT} \succeq \tilde{\boldsymbol{\beta}}, \quad \text{or} \quad \hat{\boldsymbol{\beta}}^{PT} \succeq \hat{\boldsymbol{\beta}} \succeq \tilde{\boldsymbol{\beta}}, \tag{51}$$

depending on the value α satisfying (5.5).
To demonstrate the superiority of $\hat{\boldsymbol{\beta}}^S$ to $\tilde{\boldsymbol{\beta}}$, we give the following results.

Theorem 1. Let us take into account the model in Eq. (1) with the error vector based on the ECD, $\mathcal{E}_n(\mathbf{0}, \sigma^2\mathbf{V}, \boldsymbol{g})$. Then the SS estimator of $\boldsymbol{\beta}$ is defined by

$$\hat{\boldsymbol{\beta}}^S = \tilde{\boldsymbol{\beta}} - d^*\mathcal{L}_n^{-1}(\tilde{\boldsymbol{\beta}} - \hat{\boldsymbol{\beta}}) \tag{52}$$

where $\tilde{\boldsymbol{\beta}}$ and $\hat{\boldsymbol{\beta}}$ are the UE and RE, respectively. The SS estimator uniformly controls the Bayes estimator $\tilde{\boldsymbol{\beta}}$ with respect to the BLF $L_0^{\boldsymbol{C}}(\boldsymbol{\delta}; \boldsymbol{\beta})$ and it is minimax iff $0 < d^* \leq \frac{2m}{m+2}$. The biggest risk decrease is obtained for $d^* = \frac{m}{m+2}$.

Proof: Let $\left(\frac{mS^2}{\sigma^2}\right)\Big|\tau \sim \tau^{-1}\chi_m^2$ and $\tilde{\boldsymbol{\beta}}'\boldsymbol{H}'\boldsymbol{V}_1\boldsymbol{H}\tilde{\boldsymbol{\beta}} \mid \tau \sim \tau^{-2}\sigma^4\chi_q^2(\dot{\boldsymbol{\Delta}})$. Defining $\dot{\boldsymbol{z}} = \boldsymbol{H}'\boldsymbol{V}_1(\boldsymbol{H}\tilde{\boldsymbol{\beta}} - \boldsymbol{h})$, the SS estimator is as follows

$$\begin{aligned}\hat{\boldsymbol{\beta}}^S &= \tilde{\boldsymbol{\beta}} - qd^*S^2\left[(\boldsymbol{H}\tilde{\boldsymbol{\beta}}-\boldsymbol{h})'\boldsymbol{V}_1(\boldsymbol{H}\tilde{\boldsymbol{\beta}}-\boldsymbol{h})\right]^{-1}\boldsymbol{C}^{-1}\boldsymbol{H}'\boldsymbol{V}_1(\boldsymbol{H}\tilde{\boldsymbol{\beta}}-\boldsymbol{h})\\ &= \tilde{\boldsymbol{\beta}} - qd^*S^2\left(\dot{\boldsymbol{z}}'\boldsymbol{C}^{-1}\dot{\boldsymbol{z}}\right)^{-1}\boldsymbol{C}^{-1}\dot{\boldsymbol{z}}. \end{aligned} \tag{53}$$

Using the result of [23], the weight function $W(t)$ in elliptical models satisfies $\int_0^\infty t^{-1}W^+(dt) < \infty$ and $\int_0^\infty t^{-1}W^-(dt) < \infty$, where $W^+ - W^-$ is the Jordan decomposition of W in positive and negative part.

Therefore, the risk difference between the SS estimator and the Bayes estimator under BLF is then given by

$$\begin{aligned}\mathcal{D}_{41} &= E_{\boldsymbol{\beta}}\left\{E(\hat{\boldsymbol{\beta}}^S-\boldsymbol{\beta})'\boldsymbol{C}(\hat{\boldsymbol{\beta}}^S-\boldsymbol{\beta}) - E(\tilde{\boldsymbol{\beta}}-\boldsymbol{\beta})'\boldsymbol{C}(\tilde{\boldsymbol{\beta}}-\boldsymbol{\beta})|\boldsymbol{\beta}\right\}\\ &= E_{\boldsymbol{\beta}}\left\{(d^*)^2E\left[q^2S^4\left(\dot{\boldsymbol{z}}'\boldsymbol{C}^{-1}\dot{\boldsymbol{z}}\right)^{-1}\right] - 2d^*E\left[qS^2\left(\dot{\boldsymbol{z}}'\boldsymbol{C}^{-1}\dot{\boldsymbol{z}}\right)^{-1}(\tilde{\boldsymbol{\beta}}-\boldsymbol{\beta})'\dot{\boldsymbol{z}}\right]|\boldsymbol{\beta}\right\}\\ &= E_{\boldsymbol{\beta}}\Bigg\{(d^*)^2E_\tau\left\{E_N\left[q^2S^4\left(\dot{\boldsymbol{z}}'\boldsymbol{C}^{-1}\dot{\boldsymbol{z}}\right)^{-1}\Big|\tau\right]\right\}\\ &- 2d^*E_\tau\left\{E_N\left[qS^2\left(\dot{\boldsymbol{z}}'\boldsymbol{C}^{-1}\dot{\boldsymbol{z}}\right)^{-1}(\tilde{\boldsymbol{\beta}}-\boldsymbol{\beta})'\boldsymbol{H}'\boldsymbol{V}_1(\boldsymbol{H}\tilde{\boldsymbol{\beta}}-\boldsymbol{h})\Big|\tau\right]\right\}|\boldsymbol{\beta}\Bigg\}\\ &= \phi^{-1}\left\{\frac{q^2(m+2)}{m}(d^*)^2E_\tau\left(\frac{\tau^{-2}}{\dot{\boldsymbol{z}}'\boldsymbol{C}^{-1}\dot{\boldsymbol{z}}}\right) - 2q^2d^*E_\tau\left(\frac{\tau^{-2}}{\dot{\boldsymbol{z}}'\boldsymbol{C}^{-1}\dot{\boldsymbol{z}}}\right)\right\}, \end{aligned} \tag{54}$$

where $\dot{\boldsymbol{\Delta}} = \boldsymbol{\beta}'\boldsymbol{H}'\boldsymbol{V}_1\boldsymbol{H}\boldsymbol{\beta}$ and E_N means getting expectation with respect to multivariate normal with covariance $\tau^{-1}\sigma^2\boldsymbol{V}$ and E_τ means getting expectation with respect to measure $dW(.)$.

Therefore, $\mathcal{D}_{41} \leq 0$ iff $0 < d^* \leq \frac{2m}{m+2}$ since $\int_0^\infty \frac{\tau^{-2}}{\dot{\boldsymbol{z}}'\boldsymbol{C}^{-1}\dot{\boldsymbol{z}}}\,dW(\tau) > 0$.

Remark 1. Consider the shrinkage coefficient d given by Eq. (24). For $q \geq 3$, we get $0 < d = \frac{(q-2)m}{q(m+2)} < \frac{2m}{m+2}$ and thus using Theorem 1, the $\hat{\boldsymbol{\beta}}^S$ uniformly controls the $\tilde{\boldsymbol{\beta}}$ on the entire parameter space under BLF.

Lemma 2. (Arashi, 2012)

(i) The estimator $\boldsymbol{\delta}_0(\boldsymbol{X})+(1-\omega)\boldsymbol{h}_1(\boldsymbol{X})$ controls $\boldsymbol{\delta}_0(\boldsymbol{X})+(1-\omega)\boldsymbol{h}_2(\boldsymbol{X})$ under the BLF $L^{\boldsymbol{W}}_{\omega,\boldsymbol{\delta}_0}(\boldsymbol{\delta};\boldsymbol{\beta})$ iff $\boldsymbol{\delta}_0(\boldsymbol{X})+\boldsymbol{h}_1(\boldsymbol{X})$ dominates $\boldsymbol{\delta}_0(\boldsymbol{X})+\boldsymbol{h}_2(\boldsymbol{X})$ with respect to the quadratic loss function $L^{\boldsymbol{W}}_0(\boldsymbol{\delta};\boldsymbol{\beta})$.

(ii) Suppose that the estimator $\boldsymbol{\delta}_0(\boldsymbol{X})$ has the constant risk γ with respect to the quadratic loss function $L^{\boldsymbol{W}}_0(\boldsymbol{\delta};\boldsymbol{\beta})$. Then $\boldsymbol{\delta}_0(\boldsymbol{X})$ is minimax under the BLF $L^{\boldsymbol{W}}_{\omega,\boldsymbol{\delta}_0}(\boldsymbol{\delta};\boldsymbol{\beta})$ with constant risk $(1-\omega)\gamma$ iff $\boldsymbol{\delta}_0(\boldsymbol{X})$ is minimax under the quadratic loss function $L^{\boldsymbol{W}}_0(\boldsymbol{\delta};\boldsymbol{\beta})$ with constant risk γ.

Theorem 2. Suppose $\boldsymbol{\epsilon} \sim \mathcal{E}_n(\boldsymbol{0},\sigma^2\boldsymbol{V},\boldsymbol{g})$ in the model (1). Then the SS estimator

$$\hat{\boldsymbol{\beta}}^S_* = \tilde{\boldsymbol{\beta}} - d(1-\omega)\mathcal{L}_n^{-1}(\tilde{\boldsymbol{\beta}}-\hat{\boldsymbol{\beta}}) \tag{55}$$

uniformly dominates the $\tilde{\boldsymbol{\beta}}$ under the BLF $L^{\boldsymbol{C}}_{\omega,\tilde{\boldsymbol{\beta}}}(\tilde{\boldsymbol{\beta}};\boldsymbol{\beta})$.

With Lemma 2(i) and Theorem 1, the theorem is proven easily.

Corollary 1. Let us take into consideration the Eq. (1), $\boldsymbol{\epsilon} \sim \mathcal{E}_n(\boldsymbol{0},\sigma^2\boldsymbol{V},\boldsymbol{g})$. In this case, $\hat{\boldsymbol{\beta}}^S \succeq \tilde{\boldsymbol{\beta}}$ under the BLF $L^{\boldsymbol{C}}_{\omega,\tilde{\boldsymbol{\beta}}}(\tilde{\boldsymbol{\beta}};\boldsymbol{\beta})$.

Using Theorem 5.2 with $\omega = 0$, this corollary is proven, easily.

Lemma 3. Suppose $\boldsymbol{\epsilon} \sim \mathcal{E}_n(\mathbf{0}, \sigma^2 \boldsymbol{V}, \boldsymbol{g})$ in the model (1). Then the estimator $\tilde{\boldsymbol{\beta}}$ of $\boldsymbol{\beta}$ is minimax under the BLF $L^{\boldsymbol{C}}_{\omega,\tilde{\boldsymbol{\beta}}}(\tilde{\boldsymbol{\beta}}; \boldsymbol{\beta})$ given in Eq. (2).

Theorem is proven using the information that $\tilde{\boldsymbol{\beta}}$ is minimax under quadratic loss function and applying Lemma 2 (ii).

Remark 2. Using Corollary 1 and Lemma 2, the SS estimator $\hat{\boldsymbol{\beta}}^S$ of $\boldsymbol{\beta}$ is minimax.

To compare $\hat{\boldsymbol{\beta}}$ and $\hat{\boldsymbol{\beta}}^S$, it is easy to show that

$$\boldsymbol{R}^{\boldsymbol{C}}_0(\hat{\boldsymbol{\beta}}^S; \boldsymbol{\beta}) = \boldsymbol{R}^{\boldsymbol{C}}_0(\hat{\boldsymbol{\beta}}; \boldsymbol{\beta}) + \phi^{-1}\Bigg(q\sigma^2_{\boldsymbol{\epsilon}} - \theta - dq^2\sigma^2_{\boldsymbol{\epsilon}}\Bigg\{(q-2)E[\chi^{*^{-4}}_{q+2}(\Delta^2_*)] \\ + \left[1 - \frac{(q+2)\theta}{2q\sigma^2_{\boldsymbol{\epsilon}}\Delta^2_*}\right](2\Delta^2_*)E[\chi^{*^{-4}}_{q+4}(\Delta^2_*)]\Bigg\}\Bigg). \tag{56}$$

Under the hypothesis H_0, Eq. (56) becomes

$$\boldsymbol{R}^{\boldsymbol{C}}_0(\hat{\boldsymbol{\beta}}^S; \boldsymbol{\beta}) = \boldsymbol{R}^{\boldsymbol{C}}_0(\hat{\boldsymbol{\beta}}; \boldsymbol{\beta}) + qd_n^{-1}\sigma^2_{\boldsymbol{\epsilon}}(1-d) \geq \boldsymbol{R}^{\boldsymbol{C}}_0(\hat{\boldsymbol{\beta}}; \boldsymbol{\beta}), \tag{57}$$

where note that

$$\boldsymbol{R}^{\boldsymbol{C}}_0(\hat{\boldsymbol{\beta}}; \boldsymbol{\beta}) = \boldsymbol{R}^{\boldsymbol{C}}_0(\tilde{\boldsymbol{\beta}}; \boldsymbol{\beta}) - q\phi^{-1}\sigma^2_{\boldsymbol{\epsilon}} \leq \boldsymbol{R}^{\boldsymbol{C}}_0(\tilde{\boldsymbol{\beta}}; \boldsymbol{\beta}). \tag{58}$$

Therefore, under the hypothesis H_0, $\hat{\boldsymbol{\beta}} \succeq \hat{\boldsymbol{\beta}}^S$ with the BLF $L^{\boldsymbol{C}}_0(\boldsymbol{\beta}^*, \boldsymbol{\beta})$. Under the hypothesis H_0, using Lemma 1(i), $\hat{\boldsymbol{\beta}} \succeq \hat{\boldsymbol{\beta}}^S$ with the BLF $L^{\boldsymbol{C}}_{\omega,\tilde{\boldsymbol{\beta}}}(\boldsymbol{\beta}^*; \boldsymbol{\beta})$. As $\boldsymbol{\eta}_1$ moves away from 0, θ increases and the risk of $\hat{\boldsymbol{\beta}}$ becomes unbounded while the risk of $\tilde{\boldsymbol{\beta}}^S$ remains below the risk of $\tilde{\boldsymbol{\beta}}$. $\tilde{\boldsymbol{\beta}}^S$ dominates $\hat{\boldsymbol{\beta}}$ outside an interval around the origin under the BLF $L^{\boldsymbol{C}}_{\omega,\tilde{\boldsymbol{\beta}}}(\boldsymbol{\beta}^*; \boldsymbol{\beta})$. The situation is repeated while comparing $\hat{\boldsymbol{\beta}}^S$ and $\hat{\boldsymbol{\beta}}^{PT}$. Let us consider the risk function under the hypothesis H_0 as follows

$$\boldsymbol{R}^{\boldsymbol{C}}_0(\hat{\boldsymbol{\beta}}^S; \boldsymbol{\beta}) = \boldsymbol{R}^{\boldsymbol{C}}_0(\hat{\boldsymbol{\beta}}^{PT}; \boldsymbol{\beta}) + q\phi^{-1}\sigma^2_{\boldsymbol{\epsilon}}[1 - \alpha - d] \geq \boldsymbol{R}^{\boldsymbol{C}}_0(\hat{\boldsymbol{\beta}}^{PT}; \boldsymbol{\beta}), \tag{59}$$

for all α such that $F^{-1}_{q+2,m}(d, 0) \leq \frac{qF_\alpha}{q+2}$, which means the estimator $\hat{\boldsymbol{\beta}}^S$ does not dominate $\hat{\boldsymbol{\beta}}^{PT}$ under H_0. Under hypothesis H_0 with α holding $F^{-1}_{q+2,m}(d, 0) \leq \frac{qF_\alpha}{q+2}$ with the balanced loss function, $\hat{\boldsymbol{\beta}} \succeq \hat{\boldsymbol{\beta}}^{PT} \succeq \hat{\boldsymbol{\beta}}^S \succeq \tilde{\boldsymbol{\beta}}$ holds.

Afterwards, we compare the risks of $\hat{\boldsymbol{\beta}}^{S+}$ and $\hat{\boldsymbol{\beta}}^S$ with the risk difference given by

$$\mathcal{D}_{54} = \boldsymbol{R}^{\boldsymbol{C}}_{\omega,\tilde{\boldsymbol{\beta}}}(\hat{\boldsymbol{\beta}}^{S+}; \boldsymbol{\beta}) - \boldsymbol{R}^{\boldsymbol{C}}_{\omega,\tilde{\boldsymbol{\beta}}}(\hat{\boldsymbol{\beta}}^S; \boldsymbol{\beta}) = \\ -\phi^{-1}\sigma^2_{\boldsymbol{\epsilon}}\Bigg\{qE^{(1)}\left[\left(1 - \frac{qd}{q+2}F^{-1}_{q+2,m}(\Delta^2_*)\right)^2 I\left(F_{q+2,m}(\Delta^2_*) \leq \frac{qd}{q+2}\right)\right] \\ + \frac{\theta}{\sigma^2_{\boldsymbol{\epsilon}}}E^{(2)}\left[\left(1 - \frac{qd}{q+2}F^{-1}_{q+2,m}(\Delta^2_*)\right)^2 I\left(F_{q+2,m}(\Delta^2_*) \leq \frac{qd}{q+2}\right)\right]\Bigg\} \\ - 2\phi^{-1}\theta E^{(2)}\left[\left(1 - \frac{qd}{q+2}F^{-1}_{q+2,m}(\Delta^2_*)\right) I\left(F_{q+2,m}(\Delta^2_*) \leq \frac{qd}{q+2}\right)\right]. \tag{60}$$

The r.h.s. of the above equality is negative for $F_{q+2,m}(\Delta_*^2) \leq \frac{qd}{q+2}$, $(\frac{qd}{q+2}F_{q+2,m}(\Delta_*^2) - 1) \geq 0$ and the expectation of a positive random variable is also positive. Thus, $\hat{\boldsymbol{\beta}}^{S+} \succeq \hat{\boldsymbol{\beta}}^{S}$.

Remark 3. The positive-rule shrinkage estimator $\hat{\boldsymbol{\beta}}^{S+}$ of $\boldsymbol{\beta}$ is minimax.

Let us extend the comparisons under $L_0^{\boldsymbol{C}}(\boldsymbol{\beta}^*; \boldsymbol{\beta})$. The same results can be obtained for the BLF $L^{\boldsymbol{C}}_{\omega,\tilde{\boldsymbol{\beta}}}(\boldsymbol{\beta}^*; \boldsymbol{\beta})$. For comparison of $\hat{\boldsymbol{\beta}}$ and $\hat{\boldsymbol{\beta}}^{S+}$, let us take the case under the hypothesis H_0 i.e., $\boldsymbol{\eta}_1 = 0$. For this

$$\begin{aligned}\boldsymbol{R}_0^{\boldsymbol{C}}(\hat{\boldsymbol{\beta}}^{S+}; \boldsymbol{\beta}) &= \boldsymbol{R}_0^{\boldsymbol{C}}(\hat{\boldsymbol{\beta}}; \boldsymbol{\beta}) + q\phi^{-1}\sigma_{\boldsymbol{\epsilon}}^2\Bigg\{(1-d) - E\Bigg[(1 - \frac{qd}{q+2}F^{-1}_{q+2,m}(0))^2 \\ &\quad \times I(F_{q+2,m}(0) \leq \frac{qd}{q+2})\Bigg]\Bigg\} \geq \boldsymbol{R}_0^{\boldsymbol{C}}(\hat{\boldsymbol{\beta}}; \boldsymbol{\beta}), \end{aligned} \tag{61}$$

since $E\left[(1 - \frac{qd}{q+2}F^{-1}_{q+2,m}(0))^2 I(F_{q+2,m}(0) \leq \frac{qd}{q+2})\right] \leq E\left[(1 - \frac{qd}{q+2}F^{-1}_{q+2,m}(0))^2\right] = 1 - d$.
Under the hypothesis H_0, $\hat{\boldsymbol{\beta}} \succeq \hat{\boldsymbol{\beta}}^{S+}$. As $\boldsymbol{\eta}_1$ moves away from 0, θ increases and the risk of $\hat{\boldsymbol{\beta}}$ becomes unbounded when the risk of $\tilde{\boldsymbol{\beta}}^{S+}$ stays below the risk of $\tilde{\boldsymbol{\beta}}$. This means that $\tilde{\boldsymbol{\beta}}^{S+}$ predominates $\hat{\boldsymbol{\beta}}$ outside an interval around the origin.

Then, we compare $\hat{\boldsymbol{\beta}}^{S+}$ and $\hat{\boldsymbol{\beta}}^{PT}$. When hypothesis H_0 holds, $G^*_{q+2,m}(F_\alpha, 0) = 1 - \alpha$. The risk is given by

$$\begin{aligned}\boldsymbol{R}_0^{\boldsymbol{C}}(\hat{\boldsymbol{\beta}}^{S+}; \boldsymbol{\beta}) &= \boldsymbol{R}_0^{\boldsymbol{C}}(\hat{\boldsymbol{\beta}}^{PT}; \boldsymbol{\beta}) + q\phi^{-1}\sigma_{\boldsymbol{\epsilon}}^2\Bigg\{1 - \alpha - d - E\Bigg[(1 - \frac{qd}{q+2}F^{-1}_{q+2,m}(0))^2 \\ &\quad \times I(F_{q+2,m}(0) \leq \frac{qd}{q+2})\Bigg]\Bigg\} \geq \boldsymbol{R}_0^{\boldsymbol{C}}(\hat{\boldsymbol{\beta}}^{PT}; \boldsymbol{\beta}) \end{aligned} \tag{62}$$

for $\forall\ \alpha$ $E\left[(1 - \frac{qd}{q+2}F^{-1}_{q+2,m}(0))^2 I(F_{q+2,m}(0) \leq \frac{qd}{q+2})\right] \leq 1 - \alpha - d$.
As a result, $\hat{\boldsymbol{\beta}}^{S+}$ does not always dominate $\hat{\boldsymbol{\beta}}^{PT}$ when the null-hypothesis H_0 holds. Under the null hypothesis, the dominance order of five estimators under the BLF $L^{\boldsymbol{C}}_{\omega,\tilde{\boldsymbol{\beta}}}(\boldsymbol{\beta}^*; \boldsymbol{\beta})$ can be determined under following two categories

$$1.\quad \hat{\boldsymbol{\beta}} \succeq \hat{\boldsymbol{\beta}}^{PT} \succeq \hat{\boldsymbol{\beta}}^{S+} \succeq \hat{\boldsymbol{\beta}}^{S} \succeq \tilde{\boldsymbol{\beta}} \text{ and } 2.\quad \hat{\boldsymbol{\beta}} \succeq \hat{\boldsymbol{\beta}}^{\mathrm{S+}} \succeq \hat{\boldsymbol{\beta}}^{\mathrm{S}} \succeq \hat{\boldsymbol{\beta}}^{\mathrm{PT}} \succeq \tilde{\boldsymbol{\beta}}. \tag{63}$$

To look closely at the dominance relationships above, we examine the risk function of the estimators graphically in Figure 1. Let us suppose the error term in Eq. (1) has the multivariate Student's t (MT) distribution with $\boldsymbol{\epsilon} \sim \mathcal{T}_n(\boldsymbol{0}, \boldsymbol{I}_n, \nu)$. Figure 1 shows the results of the data sets with $n = 30$, $p = 5$, $q = 3$ for different df values $\nu = 5, 10$ and for different values of $\omega \in \{0, 0.5, 0.9\}$ to fulfill possible situations. The equations required for risk functions are considered as in [24], [25], and [26]. For more clarity, equations can be simply obtained from equations (35), (37), (39), (40), (43) and the fact that

$$K_{(r)}^{(\Delta_*^2)} = \frac{\Gamma\left(\frac{\nu}{2}+r\right)\left(\frac{\Delta_*^2}{\nu-2}\right)^r}{\Gamma\left(\frac{\nu}{2}\right)\left(1+\frac{\Delta_*^2}{\nu-2}\right)^{\frac{\nu}{2}+r}},$$

and

$$\begin{aligned}
G_{p,m}^{(j)}(l_\gamma;\Delta_*^2) &= \sum_{r\geq 0}\frac{\Gamma\left(\frac{\nu}{2}+r\right)\left(\frac{\Delta_*^2}{\nu-2}\right)^r I_x\left[\frac{1}{2}(p+2r),\frac{m}{2}\right]}{\Gamma(r+1)\Gamma\left(\frac{\nu}{2}\right)\left(1+\frac{\Delta_*^2}{\nu-2}\right)^{\frac{\nu}{2}+r}},\\
E^{(j)}[\chi_{p+s}^{*-2}(\Delta_*^2)] &= \sum_{r\geq 0}\frac{\Gamma\left(\frac{\nu}{2}+r+j-2\right)}{\Gamma(r+1)\Gamma\left(\frac{\nu}{2}\right)(p+s-2+2r)}\\
&\quad\times\frac{\left(\frac{\Delta_*^2}{\nu-2}\right)^r}{\left(1+\frac{\Delta_*^2}{\nu-2}\right)^{\frac{\nu}{2}+r+j-2}},\\
E^{(j)}[\chi_{p+s}^{*-4}(\Delta_*^2)] &= \sum_{r\geq 0}\frac{\Gamma\left(\frac{\nu}{2}+r+j-2\right)\left(\frac{\Delta_*^2}{\nu-2}\right)^r}{\Gamma(r+1)\Gamma\left(\frac{\nu}{2}\right)\left(1+\frac{\Delta_*^2}{\nu-2}\right)^{\frac{\nu}{2}+r+j-2}}\\
&\quad\times\frac{1}{(q+s-2+2r)(p+s-4+2r)}\\
E^{(j)}[F_{p+s,m}^{-1}(\Delta_*^2)I(F_{p+s,m}(\Delta_*^2)<c_i)] &= \sum_{r\geq 0}\frac{\Gamma\left(\frac{\nu}{2}+r+j-2\right)\left(\frac{\Delta_*^2}{\nu-2}\right)^r}{\Gamma(r+1)\Gamma\left(\frac{\nu}{2}\right)\left(1+\frac{\Delta_*^2}{\nu-2}\right)^{\frac{\nu}{2}+r+j-2}}\\
&\quad\times\frac{(p+s)I_{x'}\left[\frac{p+s-2+2r}{2},\frac{m+2}{2}\right]}{(p+s-2+2r)},\\
E^{(j)}[F_{p+s,m}^{-2}(\Delta_*^2)I(F_{p+s,m}(\Delta_*^2)<c_i)] &= \sum_{r\geq 0}\frac{\Gamma\left(\frac{\nu}{2}+r+j-2\right)\left(\frac{\Delta_*^2}{\nu-2}\right)^r}{\Gamma(r+1)\Gamma\left(\frac{\nu}{2}\right)\left(1+\frac{\Delta_*^2}{\nu-2}\right)^{\frac{\nu}{2}+r+j-2}}\\
&\quad\times\frac{(q+s)^2 I_{x'}\left[\frac{p+s-4+2r}{2},\frac{m+4}{2}\right]}{m(p+s-2+2r)(p+s-4+2r)}.
\end{aligned}$$

The value of ϕ^{-1} as in Eq. (2) is explored for arbitrary selection the arguments using Eq. (17) as

$$\phi^{-1} = \frac{(\pi\nu)^{\frac{p}{2}}\Gamma\left(\frac{\nu}{2}\right)}{\Gamma\left(\frac{p+\nu}{2}\right)}.$$

Application

Table 1 presents specific values of $\phi^{-1} = (\pi\nu)^{\frac{p}{2}}\Gamma\left(\frac{\nu}{2}\right)/\Gamma\left(\frac{p+\nu}{2}\right)$ for various parameter combinations (p,ν). It is important to note that when ϕ^{-1} (for the t-distribution kernel) becomes smaller than 1, it leads to a reduction in risk values. We observe that as the number of parameters p increases while ν remains relatively small, the risk values decrease compared to situations with small p and large ν.

Therefore, as the dimension of the parameter space grows, we recommend using the MT distribution rather than the multivariate normal distribution for the error terms. Note that we eliminated the effect of ϕ^{-1} in the graphs, since it gives the same amount of 54.16 and 679.36 for $\nu = 5$ and $\nu = 10$, respectively, according to each risk value as seen in Table 1.

The dimension p is constrained by the sample size for the results to remain valid, as the theoretical framework assumes $n > p$. Hence, if the model includes a large number of regressors (i.e., a high value of p), the sample size must also be sufficiently large to ensure the validity of the model.

Table 1. *Values of ϕ^{-1} for different parameter values (p, ν)*

(p, ν)	1	2	5	10	100
1	3.14	2.82	2.63	2.56	2.51
2	2π	2π	2π	2π	2π
5	15.56	29.77	54.16	70.95	95.36
10	10.36	81.60	679.36	2023.93	8063.73
100	< 1	< 1	< 1	74883.62	∞

Figure 1 demonstrates the risk function results of the suggested estimators for different numbers of df comparing the risks of the PT, SE, and PRSE for the chosen number of df (here which is 5) with different ω. Two upper frames of Figure 1 illustrate the superiority relationship given in equation (63). The two lower frames of Figure 1 clearly demonstrate that as the w and α decrease, the risk increases. Furthermore, as we deviate from the origin, or the null hypothesis, the risk values increase. From this perspective, Figure 1 supports the results of the analytical comparison covered earlier here. The risk values decrease when ω increases, which means, if the model fit is good under the structure of BLF, then the risk values decrease naturally.

Figure 2 shows how rapidly ϕ^{-1} increases as both the arguments (p, ν) increase. Moreover, the contour plot shows the skewed performance relative to the df, i.e., as the number of df gets larger, the coefficient ϕ^{-1} increases rapidly with two exceptions for the cases $p = 1, 2$.

Conclusions and Remarks

This paper addresses the multiple regression model with elliptically contoured errors, utilizing a Bayesian approach that integrates a prior-based balanced loss function (BLF) applied to the parameter space. This methodology inherently influences the statistical properties of the resulting estimators. Specifically, from a Bayesian standpoint, we introduce a set of shrinkage estimators designed for regression analysis. In this novel framework, we derive key statistical criteria, such as bias and risk, and re-assess the properties of these estimators across various scenarios.

Of particular interest is the fact that the proposed balanced loss shrinkage factor demonstrates robustness to outliers in the data. By adjusting for extreme values, this approach provides a more stable estimation process compared to traditional methods. Furthermore, we examine the conditions under which a broad class of shrinkage estimators can achieve minimax properties—ensuring optimal performance across a range of possible parameter values. This investigation reveals the circumstances under which these estimators minimize both bias and variance simultaneously.

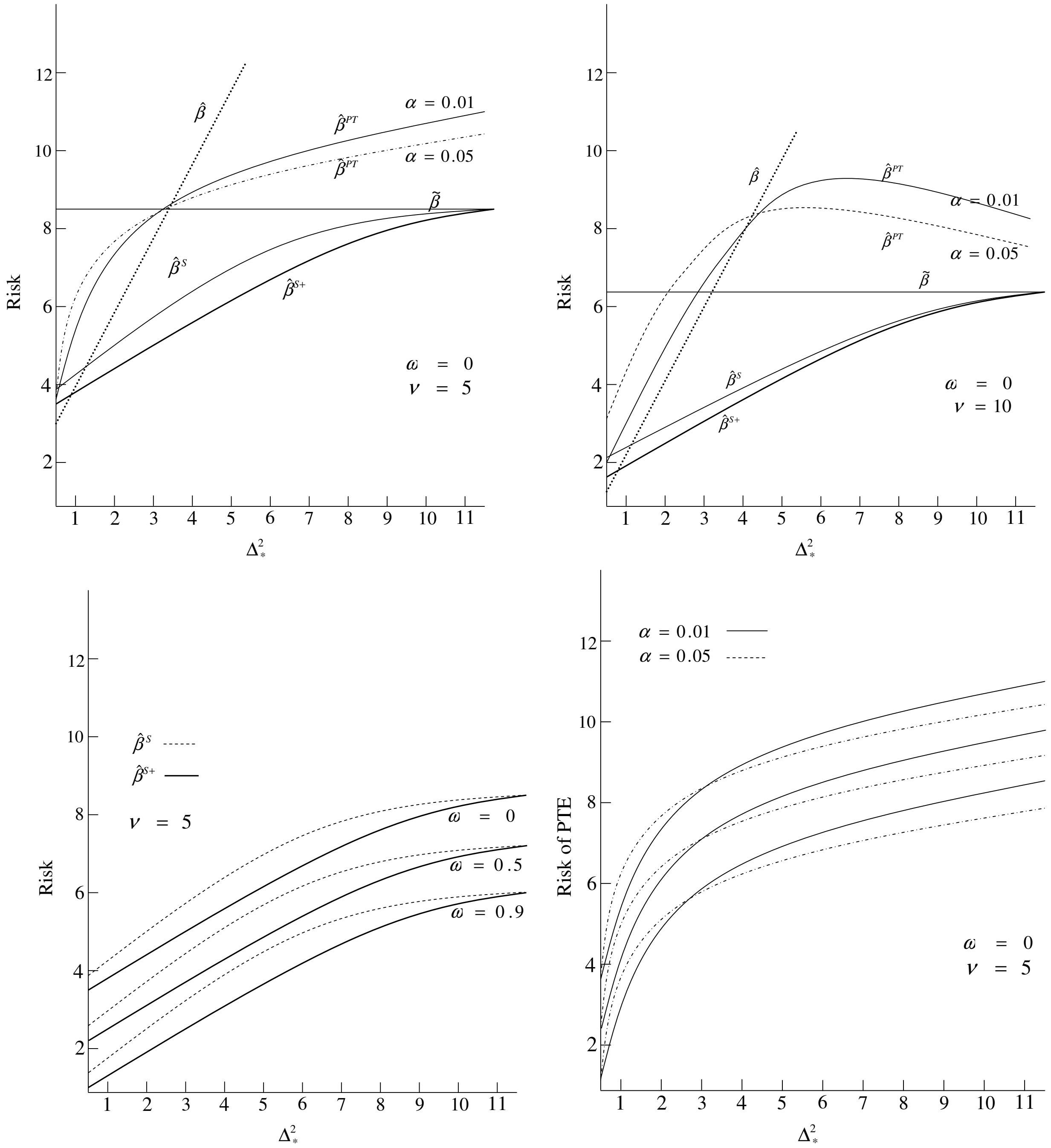

Figure 1. *Risk Performance*

Additionally, we explore the risk performance of the proposed shrinkage estimators, providing a comparison with conventional methods based on the closeness to the null hypothesis. This comparison allows us to highlight the strengths and potential limitations of the shrinkage-based approach in practical applications, offering insights into how the estimators behave under different settings. Ultimately, this paper contributes to the understanding of shrinkage estimators in Bayesian regression, emphasizing their utility in improving model robustness, especially when facing data with irregularities or outliers.

Acknowledgments We would like to thank two anonymous reviewers for their constructive comments that led us to add many details and improve the presentation.

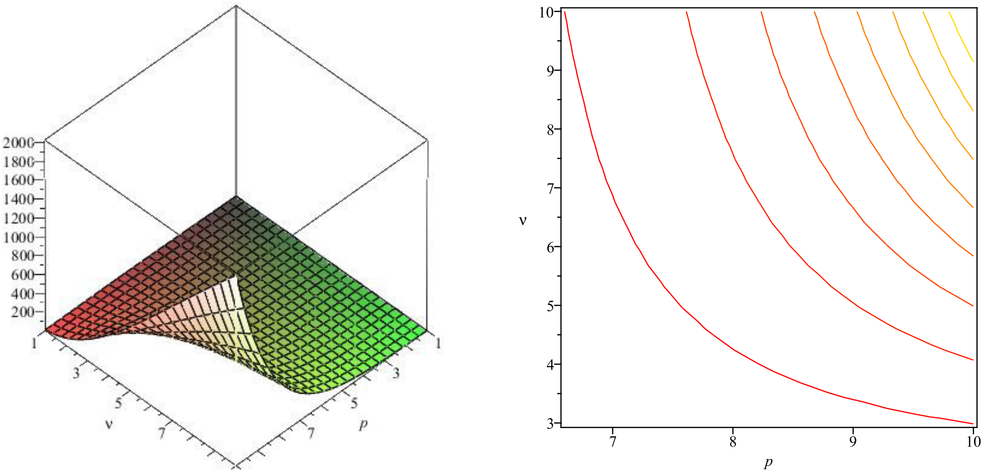

Figure 2. *Visualization of the performance of* ϕ^{-1}

Funding/Financial Disclosure The authors have no received any financial support for the research, authorship, or publication of this study.

Ethics Committee Approval and Permissions The work does not require ethics committee approval and any private permission.

Conflict of Interests The authors stated that there are no conflict of interest in this article.

Authors Contribution Authors contributed equally to the study.

References

[1] Fang, K. T., & Zhang, Y. T. (1990). Generalized Multivariate Analysis. Springer, New York.

[2] Jozani, M. J., Marchand, E., & Parsian, A. (2006). On estimation with weighted balanced-type loss function. *Statistics and Probability Letters*, *76*, 773–780. https://doi.org/10.1016/j.spl.2005.10.026

[3] Zellner, A.(1994). Bayesian and non-Bayesian estimation using balanced loss functions. In: J.O. Berger and S.S. Gupta, (Eds.), Statistical Decision Theory and Methods V, Springer, New York, pp. 337–390.

[4] Gomez-Deniz, E. (2008). A generalization of the credibility theory obtained by using the weighted balanced loss function. *Insurance: Mathematics and Economics*, *42*, 850-854. https://doi.org/10.1016/j.insmatheco.2007.09.002

[5] Dey, D., Ghosh, M., & Strawderman, W. E. (1999). On estimation with balanced loss function. *Statistics and Probability Letters*, *45*, 97–101. https://doi.org/10.1016/S0167-7152(99)00047-4

[6] Evans, M., & Jang, G. H. (2011). Inference from prior-based loss function. Technical report No. 1104, University of Toronto.

[7] Saleh, A. K. Md. E. (2006). Theory of Preliminary Test and Stein-type Estimation with Applications. John Wiley, New York.

[8] Arashi, M., Saleh, A. K., Ehsanes, A. K. Md., & Tabatabaey, S. M. M. (2013). Regression model with elliptically contoured errors. *Statistics*, *47*(6), 1266–1284. https://doi.org/10.1080/02331888.2012.694442

[9] Cellier, D., Fourdrinier, D., and Strawderman, W. E. (1995). Shrinkage positive rule estimators for spherically symmetrical distributions. *Journal of multivariate analysis*, *53*2, 194–209. https://doi.org/10.1006/jmva.1995.1032

[10] Khan, S. & Saleh, A. K. Md. E. (1997). Shrinkage Pre-Test Estimator of the Intercept Parameter for a Regression Model with Multivariate Student-t Errors. *Biometrical Journal*, *39*2, 131–147. https://doi.org/10.1002/bimj.4710390202

[11] Khan, S. & Saleh, A. K. Md. E. (1998). Comparison of estimators of means based on p-samples from multivariate student-t population. *Communications in Statistics-Theory and Methods*, *27*1 193–210. https://doi.org/10.1080/03610929808832660

[12] Khan, S. & Saleh, A. K. Md. E. (2001). On the comparison of the pre-test and shrinkage estimators for the univariate normal mean. *Statistical Papers*, *42*(4), 451–473.

[13] Khan, S., Hoque, Z., & Saleh, A. K. Md. E. (2002). Estimation of the slope parameter for linear regression model with uncertain prior information. *Journal of Statistical Research*, *36*, 55–73.

[14] Khan, S. (2005). Estimation of parameters fo the simple multivariate linear models with Student-t errors. *Journal of Statistical Research*, *39*(2), 71–86.

[15] Khan, S. (2008). Shrinkage Estimators of Intercept Parameters of Two Simple Regression Models with Suspected Equal Slopes. *Communications in Statistics—Theory and Methods*, *37*, 247–260. https://doi.org/10.1080/03610920701648961

[16] Saleh, A. K. Md. E & Kibria, B. M. G. (2011). On Some Ridge Regression Estimators: A Nonparametric Approach. *Journal of Nonparametric Statistics*, *23*3, 819–851. https://doi.org/10.1080/10485252.2011.567335

[17] Saleh, A. K. Md. E & Sen, P. K. (1978). Nonparametric Estimation of Location Parameters after a Preliminary Test on Regression. *The Annals of Statistics*, *6*, 154–168.

[18] Stein, C. (1956). The admissibility of Hotelling's T2-test. *The Annals of Mathematical Statistics*, *27*, 616–623.

[19] Tabatabaey, S. M. M., Saleh, A. K. Md. E.,& Kibria, B. M. G. (2004). Simultaneous estimation of regression parameters with spherically symmetric errors under possible stochastic constrains. *International Journal of Statistical Sciences*, *3*, 1–20.

[20] Jeffreys, H. (1961). Theory of Probability, Oxford: Clarendon, 1961.

[21] Anderson, T. W., Fang, K. T., & Hsu, H. (1986). Maximum-likelihood estimates and likelihood-ratio criteria for multivariate elliptically contoured distributions. *The Canadian Journal of Statistics*, *14*, 55–59. https://doi.org/10.2307/3315036

[22] Arashi, M. (2012). Preliminary test and Stein estimators in simultaneous linear equations. *Linear Algebra and its Applications*, *436*(5), 1195–1211. https://doi.org/10.1016/j.laa.2011.07.036

[23] Srivastava, M., & Bilodeau, M. (1989). Stein estimation under elliptical distribution. *Journal of Multivariate Analysis*, *28*, 247–259. https://doi.org/10.1016/0047-259X(89)90108-5

[24] Khan, S. (2000). Improved estimation of the mean vector for student-t model. *Communications in Statistics-Theory and Methods*, *29*3, 507–527. https://doi.org/10.1080/03610920008832499

[25] Arashi, M., Saleh, A. K. Md. E., & Tabatabaey, S. M. M. (2010). Estimation of parameters of parallelism model with elliptically distributed errors. *Metrika*, *71*, 79-100. https://doi.org/10.1007/s00184-008-0203-6

[26] Saleh, A. K. Md. E., Arashi, M., & Tabatabaey, S. M. M. (2014). Statistical Inference for Models with Multivariate t-Distributed Errors, John Wiley, New Jersey.

Sinopfbd, 2024; 9(2): 572-590 **https://doi.org/10.33484/sinopfbd.1563519**

Sinop Üniversitesi Fen Bilimleri Dergisi
Sinop Uni J Nat Sci
E-ISSN: 2564-7873

https://dergipark.org.tr/tr/pub/sinopfbd

Geospatial Assessment of Trophic Status From a Dam Under Significant Agricultural Drainage at the Mid-Anatolia, Türkiye

Mehmet Ali DERELİ[1], Hüseyin CÜCE[2] and Erkan KALIPCI[1]

How to cite: Dereli M. A., Cüce H. & Kalıpçı, E. (2024). Geospatial assessment of trophic status from a dam under significant agricultural drainage at the mid-Anatolia, Türkiye. *Sinop Üniversitesi Fen Bilimleri Dergisi, 9*(2), 572-590. https://doi.org/10.33484/sinopfbd.1563519

Research Article

Corresponding Author
Hüseyin CÜCE
huseyin.cuce@giresun.edu.tr

ORCID of the Authors
M.A.D: 0000-0003-0575-1316
H.C: 0000-0002-3590-681X
E.K: 0000-0002-1908-5468

Received: 09.10.2024
Accepted: 09.12.2024

Abstract

The population of Anatolia is continuously growing and developing and it is under the deep influence of global warming. It is increasingly evident that more fresh water will be needed for drinking, irrigation and domestic use. This study aims to assess the water quality and trophic status of a dam (Bayramhacılı dam lake) under excessive agricultural irrigation threat using spatial and multivariate statistical analysis. In the study, the periodic changes in the eutrophic state of the dam lake were determined using global index categories, Carlson Trophic Status Index (CTSI = 66.7), Burns Trophic Level Index (BTLI = 6.4), and Shu Trophic State Index (STSI = 65.6). The two periodical averages of total phosphorus (TP), total nitrogen (TN), biological oxygen demand (BOD), (chemical oxygen demand (COD) and chlorophyll a (Chl_a) concentrations, which serve as an indicator of anthropogenic nutrient input, were determined to be 0.23, 31.28, 1.83, 8.99 and 48.1 µg/L, respectively. Trophic index distribution maps demonstrate that the dam's surface water displays considerable alterations, particularly during the dry season. This evidence supports the implementation of a local management model that addresses the issue of eutrophication. It is therefore imperative that on-site measures are taken without delay.

Keywords: Lake quality assessment, trophic index, spatial analysis, Bayramhacılı Dam Lake

Orta Anadolu'da Önemli Tarımsal Drenaj Altındaki Bir Barajın Trofik Durumunun Jeo-Konumsal Değerlendirmesi, Türkiye

[1]Giresun University, Faculty of Engineering, Department of Geomatics Engineering, Giresun, Türkiye

[2]Giresun University, Faculty of Engineering, Department of Environmental Engineering, Giresun, Turkiye

Öz

Küresel ısınmanın derin etkisi altında olan Anadolu'da nüfusun sürekli büyümesi ve gelişmesi içme, sulama ve evsel kullanım için daha fazla tatlı suya ihtiyaç duyulacağını giderek daha belirgin hale getirmektedir. Bu çalışmanın amacı, aşırı tarımsal sulama tehdidi altındaki bir barajın (Bayramhacılı baraj gölü) su kalitesi ve trofik durumunun mekansal ve çok değişkenli istatistiksel analizler kullanılarak değerlendirilmesidir. Araştırmada ötrofiksel durumdaki baraj gölündeki periyodik değişiklikler; global indeks kategorileri, Carlson trofik durum indeksi (CTSI = 66.7), Burns trofik seviye indeksi (BTLI = 6.4) ve Shu trofik durum indeksi (STSI = 65.6) ile belirlenmiştir. Antropojenik besin girdisinin göstergesi olan toplam fosfor (TP), toplam azot (TN), biyolojik oksijen ihtiyacı (BOD), kimyasal oksijen ihtiyacı (COD) ve klorofil a (Chl_a) konsantrasyonlarının iki periyodik ortalaması sırasıyla 0.23, 31.28, 1.83, 8.99 ve 48.1 µg/L olarak belirlenmiştir. Trofik indeks dağılım haritaları, baraj yüzey suyunun özellikle kurak mevsimde önemli değişiklikler gösterdiğini göstermektedir. Bu kanıt, ötrofikasyon sorununu ele alan yerel bir yönetim modelinin uygulanmasını desteklemektedir. Bu nedenle yerinde önlemlerin gecikmeksizin alınması zorunludur.

Anahtar Kelimeler: Göl kalitesi değerlendirme, trofik indeks, konumsal analiz, Bayramhacılı Baraj Gölü

Introduction

Lake and river water pollution is an important ecological issue in developing countries like Türkiye. A substantial body of research has demonstrated that natural processes exerting a considerable influence on water quality encompass mineral oxidation, soil erosion, weathering of bedrock, and climate, especially for dam lakes. The principal causes of the reduction in reservoir quality are human activities, including animal husbandry, irrigation, the inadvertent usage of pesticides and fertilizers in agricultural districts, and the discharge of domestic wastewater. Ensuring the quality of freshwater resources is crucial for promoting both human health and economic progress. Therefore, it is essential that sufficient attention must be paid to their enhancement and preservation. Rivers are the first places where pollutants from home wastewater and solid waste, veterinary and agricultural operations, and industrial discharges merge before moving on to lakes and seas. As dam lakes are continually subjected to new ecosystems, pollution from the surrounding environment offers considerable concern. As a result, to predict and manage possible changes in water quality, thorough evaluations and projections are crucial [1-6]

Nutrients, surfactants and other possible anthropogenic chemicals constitute one of the parameters that provide information about the water quality. The sources of these elements entering surface waters can be natural, domestic or agricultural high levels of trace elements and nutrition-compounds in water can have a toxic effect on aquatic organisms. The inputs of nutrient elements, referred to as nutrients, into aquatic environments typically originate from point and anthropogenic sources known as non-point sources. The quantification of pollutant loads from point sources is generally more controlled and manageable than non-point sources. It is established that the toxic effects of nitrate are less than those of nitrite and ammonium nitrate [7-9]. Controlling point and non-point pollution sources, in particular, is crucial when they are close to dams that provide drinking and utility water. Water contamination in reservoirs must be controlled to effectively regulate water quality. Water quality and availability are equally important, especially for power plants to continue operating [10-13]. Protecting and managing ecosystems (rivers, lakes, and wetlands) fed by water resources requires regular monitoring of the quality of the water at specified intervals, the identification of important variables influencing pollution, and the implementation of appropriate solutions. This is essential for maintaining ecological balance and making effective use of water resources [14, 15].

The sustainable use of dam lakes, which are established for a variety of purposes including the cultivation of plants, the pursuit of leisure activities, and the implementation of strategies for the management and control of eutrophication, should be subject to more precise examination and evaluation. This is necessary for several reasons, including the effects of climate change. A thorough grasp of how atmospheric phenomena, in-lake dynamics, and other environmental elements interact is necessary for the effectiveness of water quality monitoring techniques and systems [16, 17]. The objective of spatial analysis is to identify the factors affecting water quality, thus enabling the development of appropriate strategies to facilitate the effective management of water resources [18-21]. Consequently, in the context of water quality assessment, it is of the utmost importance to conduct a comprehensive, multi-dimensional analysis of the complex interactions between the surface water body and the surrounding region [22-26].

The effects of global warming are becoming increasingly evident in the form of drought, which is drying up Anatolia's water resources. In addition to the impact of human-induced water pollution, the scarcity of water for agricultural use is becoming a significant concern, contributing to the emergence of regional problems. In light of the aforementioned considerations, the study concentrated on the Bayramhacılı dam, which provides irrigation to approximately 3.415 hectares in the Kayseri/Nevşehir Cappadocia region, a pivotal agricultural zone in Anatolia that is grappling with the challenge of excessive irrigation. The purpose of this study is; a periodical, comprehensive and multi-dimensional determination of the physico-chemical parameters of the dam lake water. Also compare of the results with national/international criteria, to analyze the trophic status of the dam lake according to different indices based on GIS, and to discuss the protection of this dam, which is important in terms of sustainable energy needs with climate change oriented agricultural irrigation and hydropower plants.

Materials and Methods

This investigation was conducted at the Bayramhacılı Dam Lake, built along the boundaries of Kayseri and Nevşehir Province. To determine the trophic water quality in the center region of Anatolia, where the effects of drought and agricultural drainage waters are particularly severe, monitoring and evaluation studies were conducted in three stages. First, multidimensional statistical analyses including clustering, correlation, and principal component analysis (PCA) were performed on each outcome, focusing on the periodic dimension of chemical contamination in the water was addressed. Second, the trophic status of the reservoir water was evaluated using various ecological status indices (Carlson [27], Burns et al. [28], Shu [29]). Finally, the trophic status of the reservoirs was further assessed through spatial analysis utilizing geographic information systems (ArcGIS).

Study Area and Sampling

The Bayramhacılı Dam Lake, is located on the Kızılırmak River and falls inside the borders of both Kayseri Province and the Avanos District in Nevşehir Province. The dam lake provides irrigation water that is also used for recreational water and natural activities. Covering a fishing area of 460 hectares, Bayramhacılı Dam Lake is one of the significant inland water resources supporting fish production in addition to its hydropower capabilities. The most commonly caught fish species in the lake include

Leuciscus cephalus and Cyprinus carpio among others. Figure 1 displays the map with the study area and the marked sampling points. The dam features a concrete-capped rock fill and has a lake volume of 218 m³ at normal water height. It irrigates a total of 3.117 hectares of land [30].

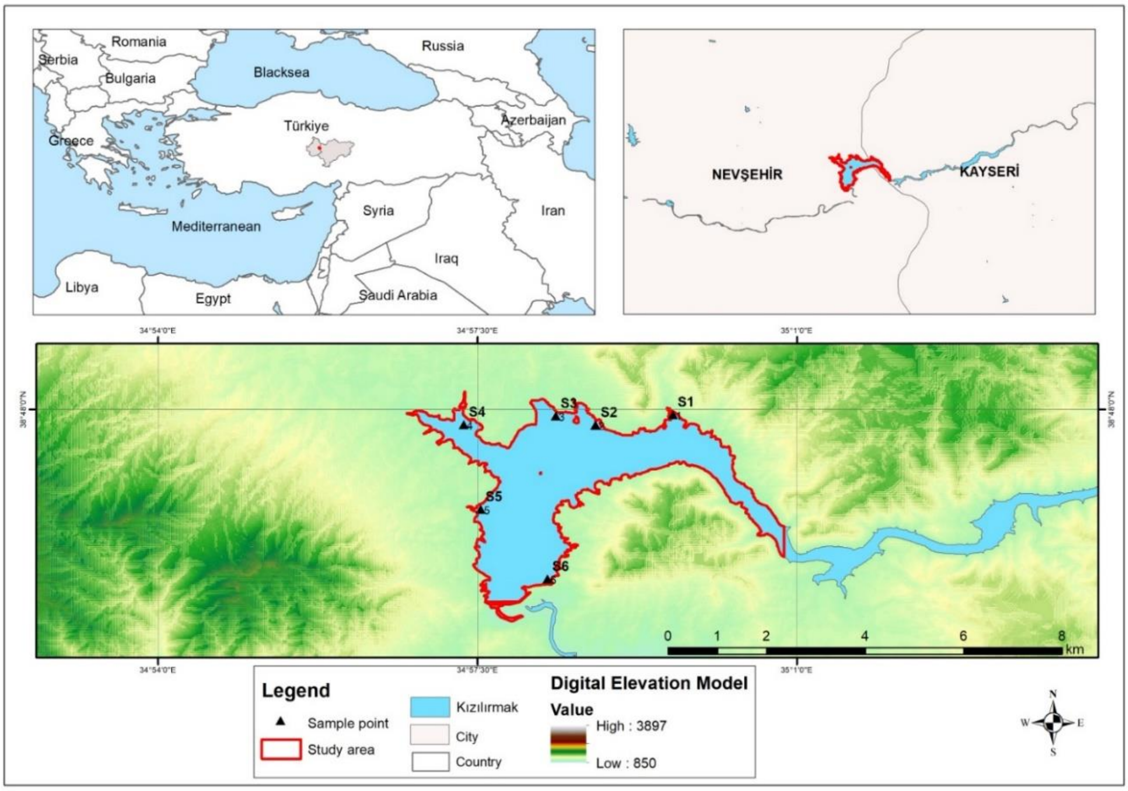

Figure 1. *Sampling points in the dam lake*

Sampling was carried out over two periods (wet and dry seasons/April 2020- July 2021). Seasonal sampling times were selected due to the local population drawing water from the dam lake for irrigation purposes and transporting it from the drainage areas to the lake. A periodic sampling program was established based on the planting and harvest schedules of agricultural products specific to the region, particularly grapes, pumpkins and potatoes. Surface water was collected in plexiglass sample containers from six locations during the two field research periods. The GPS coordinates of each location were recorded using a Magellan Exp710 and processed according to the WGS 1984 coordinate system. The coordinates of the stations where the samples were collected are provided in Table 1. Real-time fieldwork measurements of the water quality parameters including temperature, pH, dissolved oxygen (DO), total suspended solids (TSS), and electrical conductivity (EC) were taken using a portable Hach 40dQ multi-gauge probe. Additionally, fluorometric analysis was conducted to determine chlorophyll-a concentrations in surface water samples. Anionic surfactants, total phosphorus (TP), total nitrogen (TN), biological oxygen demand (BOD), chemical oxygen demand (COD) and Cl^- concentrations in samples stored at +4 ˚C were quantified using laboratory test kits (Hach-Lange) and conventional procedures [31]. All investigations were carried out using analytically pure chemicals, and spectrophotometric measurements were performed in a laboratory setting with the Hach Lange DR3900 thermo-reactor. (Hach Lange LT-200) and analytical scales (BEL).

Table 1. *GPS coordinates of each station*

Sampling Points	Latitude	Longitude
1	38.7991	34.9940
2	38.7972	34.9799
3	38.7988	34.9727
4	38.7972	34.9559
5	38.7817	34.9590
6	38.7690	34.9711

Eutrophical Assessment

In this research, the Carlson Trophic Status Index CTSI [27], Burns Trophic Level Index BTLI [28] and Shu Trophic State Index STSI [29] values were calculated to assess the periodical change in the trophic status of the dam's surface water. The Carlson index is commonly used by government officials and researchers as an indirect measure of algal biomass and serves as a key indicator of the health of aquatic ecosystems for the extent of lentic system eutrophication [32]. It is calculated mathematically based on the relevant equations for three parameters: chlorophyll-*a*, Secchi depth, and total phosphorus. In this study, the Carlson Trophic Status Index was derived from periodic Chl-*a* values. Equation 1 is as follows:

$$TSI(Chl\_a) = 10(6 - \frac{2.04 - 0.68 \ln Chla}{ln2}) \tag{1}$$

The Carlson trophic status index (CTSI) value: A value below 40 indicates oligotrophic water quality, values between 40 and 60 indicate mesotrophic quality, values between 60 and 70 indicate eutrophic quality, and values above 70 indicate hypertrophic quality [33]. Burns et al. [28] developed the Burns Trophic Level Index BTLI to assess the trophic status of lakes in New Zealand. This required modifying the Carlson TSI by removing the total nitrogen (TN) parameter. In this study, the seasonal trophic levels of the dam lakes were determined based on the average Chl-*a* value for the BTLI. Burns Trophic Level Index (BTLI) value: The classification of water quality levels is as follows: levels below 3 are considered oligotrophic, levels 3 - 4 are mesotrophic, levels 4 - 5 are eutrophic, levels 5 - 6 are super-oligotrophic, and levels above 7 are hypertrophic [34].

$$TLI(Chl\_a) = 2.22 + 2.54\log{(Chl_a)} \tag{2}$$

The method developed by Shu [29] to assess the periodic eutrophication of lakes, defined as the Shu model, calculates index values reflecting the current trophic state of the lake based on the algorithm defined below (equation 3), focusing on chlorophyll-a concentration. The unit of chlorophyll a concentration is µg/L. Shu Trophic State Index (STSI) value: ≤20 indicates oligotrophic, ≤40 mesotrophic, ≤70 eutrophic, ≤80 hypertrophic and ≤100 extremely hypertrophic water quality [29].

$$TSI(Chl\_a) = 10(2.46 + \frac{\ln(chl-a)}{\ln(2.5)}) \quad (3)$$

The trophic status of the Bayramhacılı dam lake was established in accordance with the relevant legislation of Türkiye. This legislation, known as the "Surface Water Quality Management Regulations (SWQR)" was published in the Official Gazette of the Republic of Türkiye in 2012. Table 2 shows the trophic classes defined by the SWQR [35]. By using the trophic status classification of lakes and ponds specified by the National SWQ regulations of Türkiye, the trophic level of the irrigation/energy dam has been revealed based on CTSI, BTLI and STSI values.

Table 2. *Trophic Classifications based on SWQR according to the legislation of Türkiye [35]*

Trophic Classes	**TP (µg/L)**	**TN (µg/L)**	**Chl_*a* (µg/L)**	**Secchi Depht (m)**	**DO (mg/L)**
Oligotrophic	<10	<350	<3.5	>4	>7
Mesotrophic	30-50	650-1000	9-15	2.0-1.5	6-4
Eutrophic	100	1500	25	1	3
Hypereutrophic	>100	>1500	>25	<1	<3

Statistical and Geographical Studies

All data computations and statistical analyses were performed using SPSS 22, while spatial analyzes were performed using ArcGIS 10.8. The maps produced to compare the effects of periodic changes on the trophic/water quality of the dam lake were created using the Inverse Distance Weighted (IDW) interpolation technique. Tercan and Dereli [36] noted that the method allows the evaluation of the influence of each point on the other based on the inverse of the distance between the points. In this context, the periodic changes in the physico-chemical quality of pond surface water was evaluated geographically.

Results and Discussions

Physical and Chemical Results of the Dam Lake Water

Figure 2, 3a and 3b, shows the two-period graph for physico-chemical parameters and the regional distribution maps of metrics related to surface water quality, respectively. The analysis of parameter results and preparation of spatial maps represents a rapid and efficacious approach to the assessment of water quality. The application of spatial analysis has revealed significant alterations in water quality, including increases in nutrient and pigment concentrations observed in the southwestern area of the lake during the dry period. These changes are likely a consequence of anthropogenic impacts and land use practices.

During the summer, conductivity rises by an average of 1324.3 µS/cm due to the geological structure of the lake environment (Figure 2). Electrical conductivity (EC) values are in the range of 920-1020 µS/cm during the wet period, while 1220-1414 µS/cm during the dry period, and reaches the highest values as it approaches the southern parts of the dam. According to the Turkish Surface Water Quality (SWQ) Regulation [35], Bayramhacılı Dam is classified as medium-category water quality. In addition, in terms of irrigation water, the dam pond is in the 'high saline water' category and has been determined to have permissible water quality. As seen in Figure 3a, the pH value (>9) reached the highest possible level (highly alkaline) in the northwestern sections of the dam.

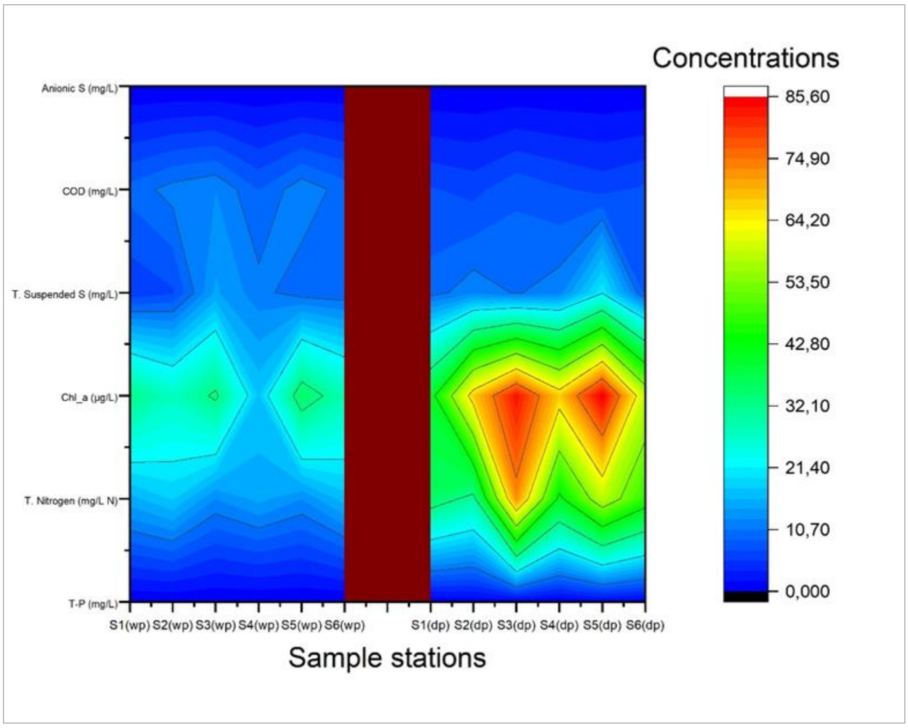

Figure 2. *The distribution of average physico-chemical parameters based on sampling stations during wet (wp) and dry (dp) periods.*

It was established that the mean annual concentration of total suspended solids (TSS) in the lake was 11 mg/L. It is hypothesized that the TSS load is a consequence of agricultural drainage and the erosion of the upper soil layers into the aquatic environment. Because of the heavy precipitation during the dry period, TSS and nutrient concentrations were higher. In Korean reservoirs, the time period has a major impact on the hydrology, nutrients, and suspended solids concentration [37]. The current concentration of dissolved oxygen (DO) in the lake is 7.5 mg/L, which represents the lowest recorded value even during the dry season. This can be considered as an indication that particle pollution in the lake is not a permanent issue.

The periodical average of the surface water temperature ranges from 14.4 to 19.07 °C. The lowest recorded temperature of the surface water in the dam lake was 13.6 °C (during the wet season, at station no. 3) while the maximum temperature of the surface water was 20.2 °C (in dry season, at station no.6). Although the northeast of the dam lake had a low temperature, it was found that temperatures increased in the southern parts (Figure 3a).

During this investigation, the Chl_*a* value was measured and monitored in all samples to evaluate the periodic changes in the TP and TN levels in the lake, as well as stability of the dam lake's trophic state. The mean concentration of chlorophyll-a in the dam lake was 29.07 µg/L throughout the wet period, with a local increase in the dry period, reaching an average of 67.1 µg/L (Figure 3b).

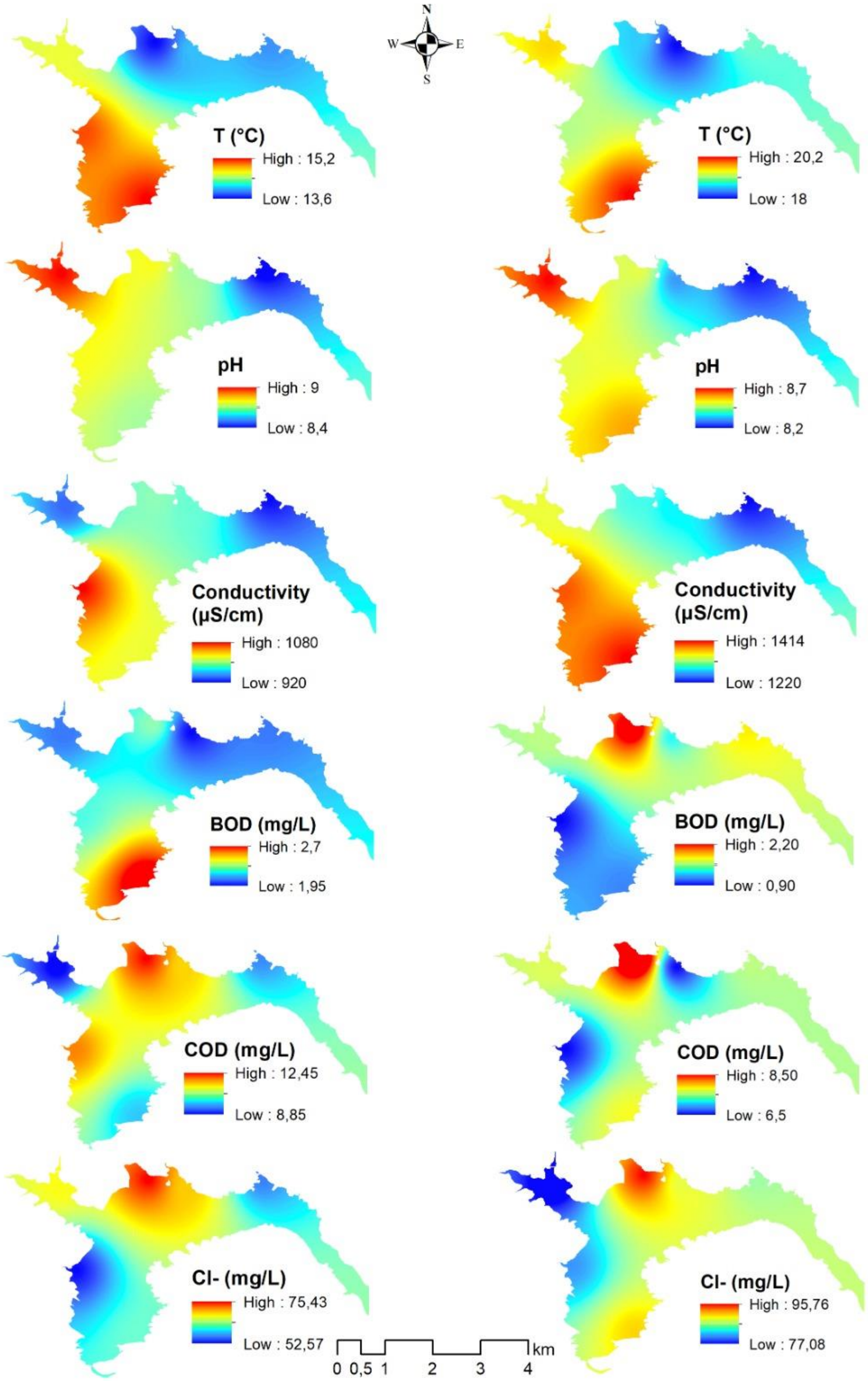

Figure 3a. *Geo-spatial distribution maps of surface water quality parameters (T, pH, EC, BOD, COD, Cl$^-$, DO) over two periods*

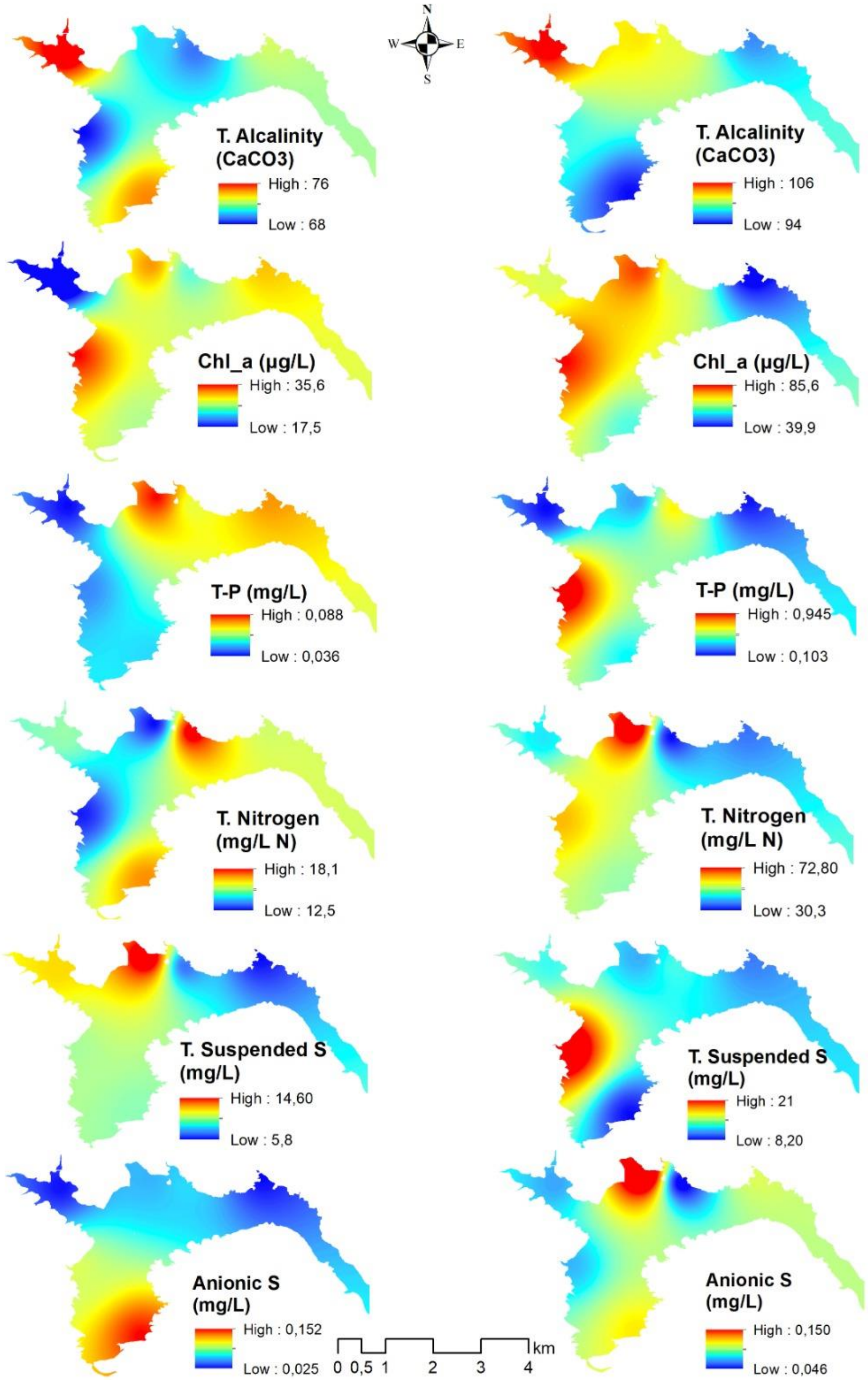

Figure 3b. *Geo-spatial distribution maps of surface water quality parameters (TA, Chl_a, TP, TN, TSS, AS) over two periods*

The periodic effect is a significant factor influencing the alteration of total nitrogen and phosphorus concentrations. In the dam water where the highest TN concentrations were detected during the dry period, the increase in the nutritional input is considered to be the most significant factor influencing the lake's trophic state. An increase in phosphorus was observed at the 3rd station in the wet period and at the 5th point in the dry period (Figure 4). In aquatic environments near agricultural lands, the concentrations of phosphate and nitrogen substances may be considerably increased by agricultural activities and irrigation techniques [38]. Moreover, pollution may arise from sewage, garbage, waste, and the industrial facilities in the area. The mean value in our study has been found to be 0.79 mg/L, which has been considered to be a highly dangerous concentration for aquaculture and aquatic life, potentially resulting in sudden mortality. The sharp rise in the levels recorded at all monitoring stations on the dam is likely a result of the phosphatic fertilisers leaching into the water. Furthermore, it is thought that the influx of water from urban waste and agricultural areas into the lake during the transition from the dry season to the rainy season contributes to the observed increase in nutrient levels in the lake’s surface water.

Similarly, the area is a center for subterranean travel, with the end of fall being the peak population for the city. Although summer-drying streams contribute minimal waste to the lake, rainfall affects this situation. The average total alkalinity (71.5 mg/L) observed at the lowest levels during the rainy season increased to high values (99.5 mg/L) during the dry season, particularly in the lake's northeastern region (Figure 3b).

It was observed that the highest TDS and EC values were concentrated in the western area and at the southern end of the reservoir during the dry period. Especially the COD values in the central-northern parts of the lake are extremely high for an irrigation dam suggesting an attempt. The sources of organic matter (BOD and COD) in reservoirs can be classified as either autochthonous or allochthonous. During rainfall events, runoff from overland water flow is the primary source of allochthonous organic matter entering aquatic systems, whereas phytoplankton and hydrophytes produce autochthonous organic matter through photosynthesis [39]. While COD concentrations have generally been rising, BOD concentrations in the majority of lakes and reservoirs have been steadily declining. This suggests that the biological effluent treatment process may not be effectively breaking down the significant amounts of nonbiodegradable organic matter in the influent [40]. In accordance with the classification standards for inland water resources [41], the surface water quality of the lake can be classified as 'medium' quality.

Evaluation of the Trophic Status of the Dam Lake

The eutrophication index, a key metric in the assessment of lake water quality, reveals a notable shift in trophic levels throughout the year, indicating a considerable degree of pollution in the lake. A description of the classification scale utilized in the Carlson Trophic Status Index (CTSI) ranges from 0 to 100, and the findings of this regional study show that the mean CTSI for periodic Chl_*a* is 63.38 in the wet period and 70.04 in the dry period. The overall annual mean CTSI is 66.7.

The hierarchy of classification for Burns Trophic Level Index (TLI) ranges from 0 to 7. In this regional study, the average BTLI during the wet period was calculated to be 5.91 for Chl_*a*, and increased to 6.83 during the dry period. The annual average BTLI was determined to be 6.37. These results indicate that the lake can reach regional hypereutrophic limits (Figure 4.).

The classification scale of Shu Trophic State Index (STSI) ranges from 0 to 100. The findings of this regional study showed that the average STSI for periodic Chl_a reached 61.1 in the wet period and 70.18 in the dry period, and the annual average STSI was calculated as 65.64. According to these results, while the lake is classified as mesotrophic during the wet period, it becomes eutrophic during the dry period.

The index values (CTSI, BTLI and STSI) indicate that Dam Lake of Bayramhacılı is hypereutrophic, which is evidenced by the elevated levels of phosphorus (P) and nitrogen (N) in the surface water. Similarly, other studies have indicated a notable enhancement in eutrophic state during the late spring-period, when temperature typically rises and precipitation declines [42, 43]. Investigations on the trophic structure of ecosystems in eutrophic lakes [44-47] found that TSI index values determined according to the average of chlorophyll-a concentrations, were higher during the dry period compared to the rainy period. A similar trend was observed in the TSI values calculated in this study (Carlson TSI 70.04/63.08, Burns TLI 6.83/5.91 and Shu TSI 70.18/61.10, Figure 4).

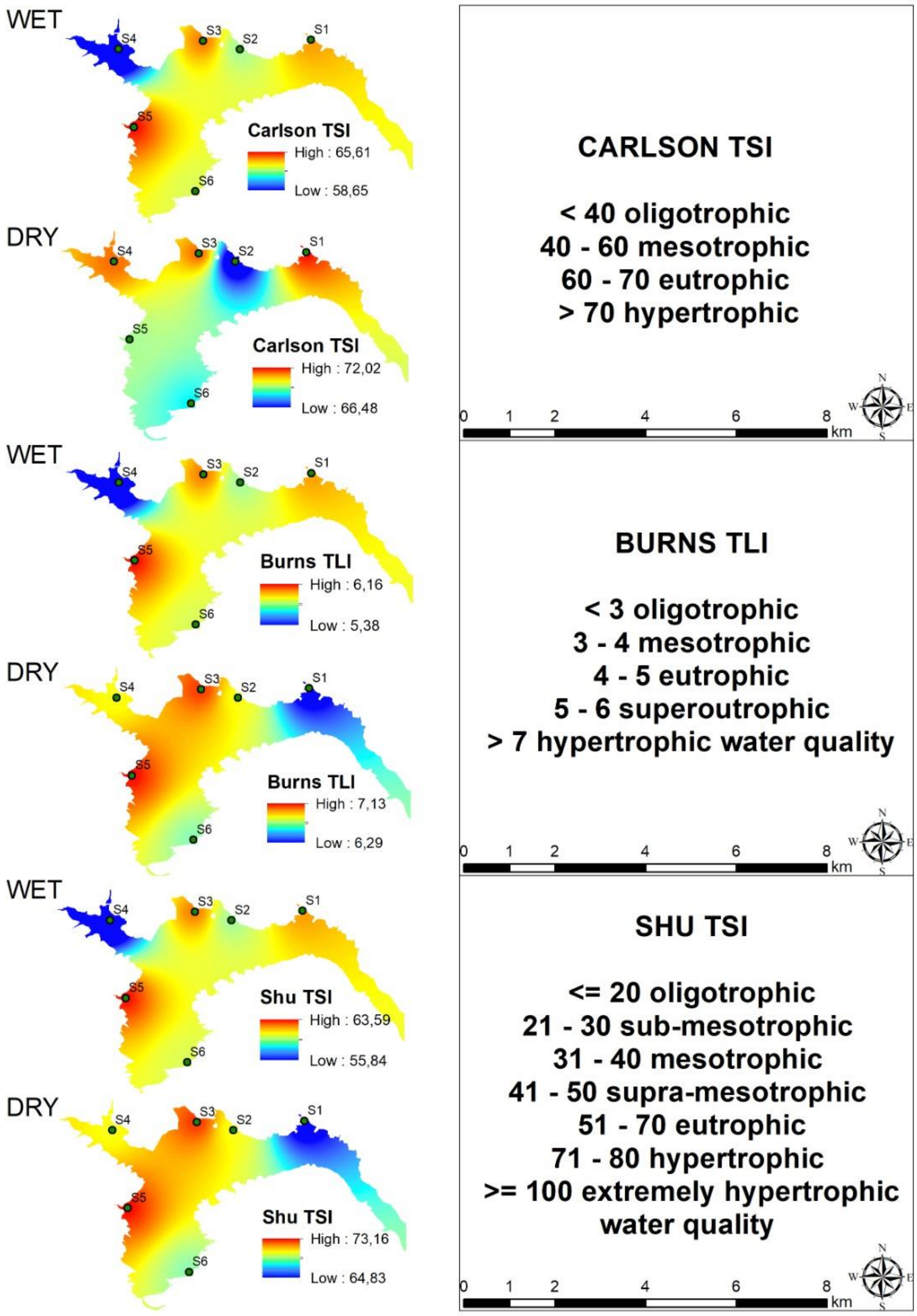

Figure 4. *Geographical analysis of periodic trophic status index values in the dam lake*

Statistical Observations

The principal components analysis (PCA) with varimax rotation yielded two variables with an eigenvalue exceeding one, collectively explaining 64% of the total variance (Figure 6). Based on the loading levels, Liu et al. [48] categorized the factor loadings as "strong (>0.75)," "moderate (0.75 – 0.50)," and "weak (0.50 – 0.30)". TN, Cl-, TP exhibit a markedly positive charge (> 0.75) in varifactor 1 (VF1), which accounts for 45.99% of the total variance. Conductivity, alkalinity and pH are moderately positively charged, while COD and TN are strongly positively charged. Elevated BOD and

COD levels indicate the presence of organic contamination in the reservoir. Nitrogen fertilizers, animal manure and chemical fertilizers/ pesticides are intensively used in the agriculture of the region. The strong link between chlorophyll-a values and COD and total phosphorus/total nitrogen coincides with the high correlation results (Figure 5).

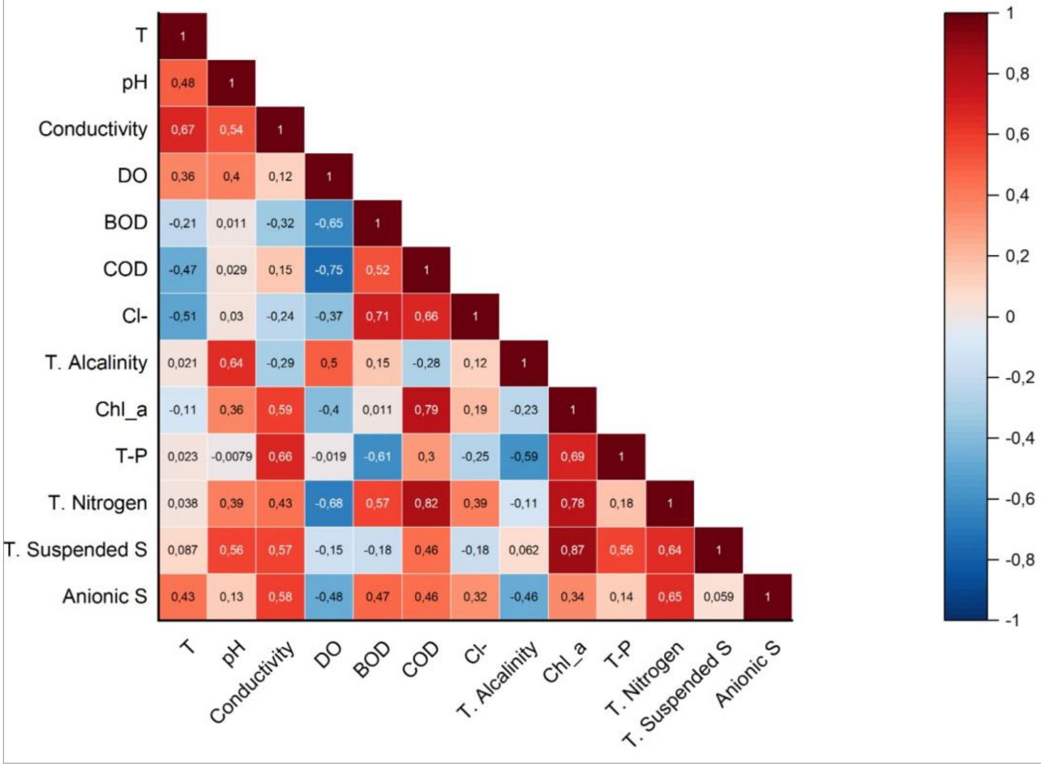

	T	pH	Conductivity	DO	BOD	COD	Cl-	T. Alcalinity	Chl_a	T-P	T. Nitrogen	T. Suspended S	Anionic S
T	1												
pH	0,48	1											
Conductivity	0,67	0,54	1										
DO	0,36	0,4	0,12	1									
BOD	-0,21	0,011	-0,32	-0,65	1								
COD	-0,47	0,029	0,15	-0,75	0,52	1							
Cl-	-0,51	0,03	-0,24	-0,37	0,71	0,66	1						
T. Alcalinity	0,021	0,64	-0,29	0,5	0,15	-0,28	0,12	1					
Chl_a	-0,11	0,36	0,59	-0,4	0,011	0,79	0,19	-0,23	1				
T-P	0,023	-0,0079	0,66	-0,019	-0,61	0,3	-0,25	-0,59	0,69	1			
T. Nitrogen	0,038	0,39	0,43	-0,68	0,57	0,82	0,39	-0,11	0,78	0,18	1		
T. Suspended S	0,087	0,56	0,57	-0,15	-0,18	0,46	-0,18	0,062	0,87	0,56	0,64	1	
Anionic S	0,43	0,13	0,58	-0,48	0,47	0,46	0,32	-0,46	0,34	0,14	0,65	0,059	1

Figure 5. *Spearman's correlation between physicochemical parameters*

The strong positive relationship between anionic surfactants, conductivity and total nitrogen (TN) is typically linked to domestic waste. To identify the possible sources and factors influencing the dam's water quality, a principal component analysis (PCA) and a factor analysis (FA) were carried out. Due to the strong positive correlation between TN/TP and BOD in VF1, it is the object in question represents agricultural drainage (Figure 6). Representing 27.10% of the total variance in VF2, strong positive charges are found in T, DO, and TA, but strong negative charges are found in Chl_*a*, according to the data (Figure 6). In accordance with the findings of VF2, erosion and surface runoffs are on effective the water quality of the Dam Lake of Bayramhacılı. The water quality of a lentic ecosystem was evaluated using FA and CA in a study conducted at Uluabat Lake, Türkiye [49]. Twelve sampling sites were divided into two clusters by CA, and three components accounted for 77.35% of the total variance, according to FA. The results of the dual clustering analysis indicate the formation of two principal stationary clusters, S5 and other stations (Figure 7). Among the chemical parameters measured are pH, alkalinity and DO, which form a cluster among themselves. In contrast, other parameters are clustered. Upon examination of the subclusters of the other main group, small clusters between T (ºC)-conductivity and surfactants, between COD-TN and Chl_*a*-TSS and BOD-Cl$^-$ are distinguished from the others. Anthropogenic activity impacts in the dam are indicated by the geographic variations of these metrics.

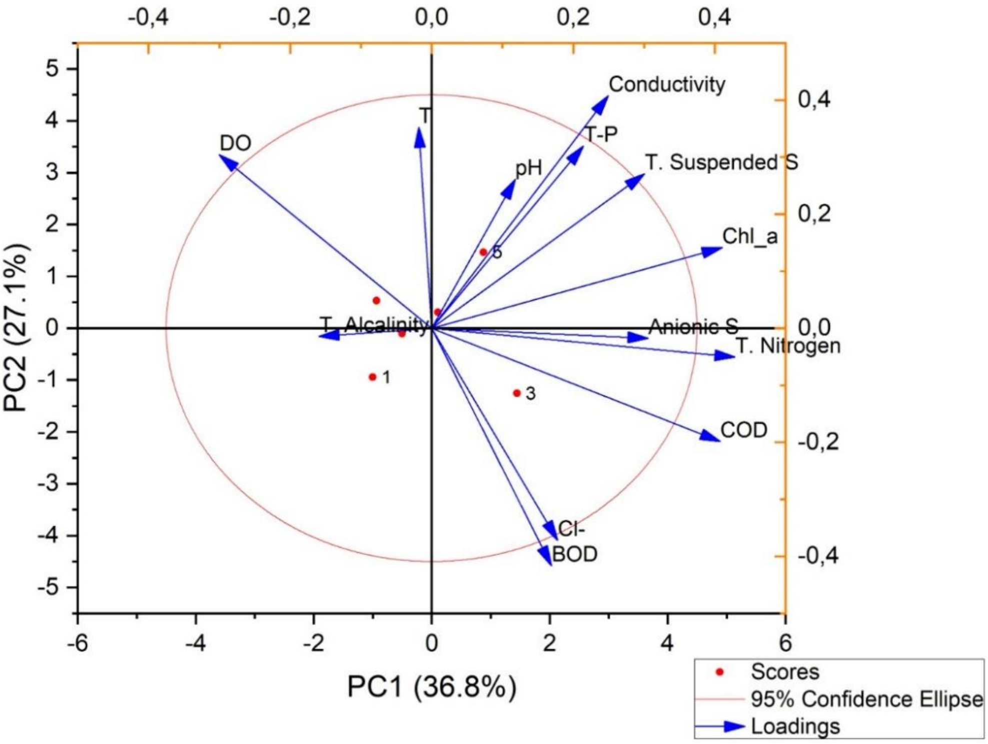

Figure 6. *PCA/FA of measured physico-chemical parameters*

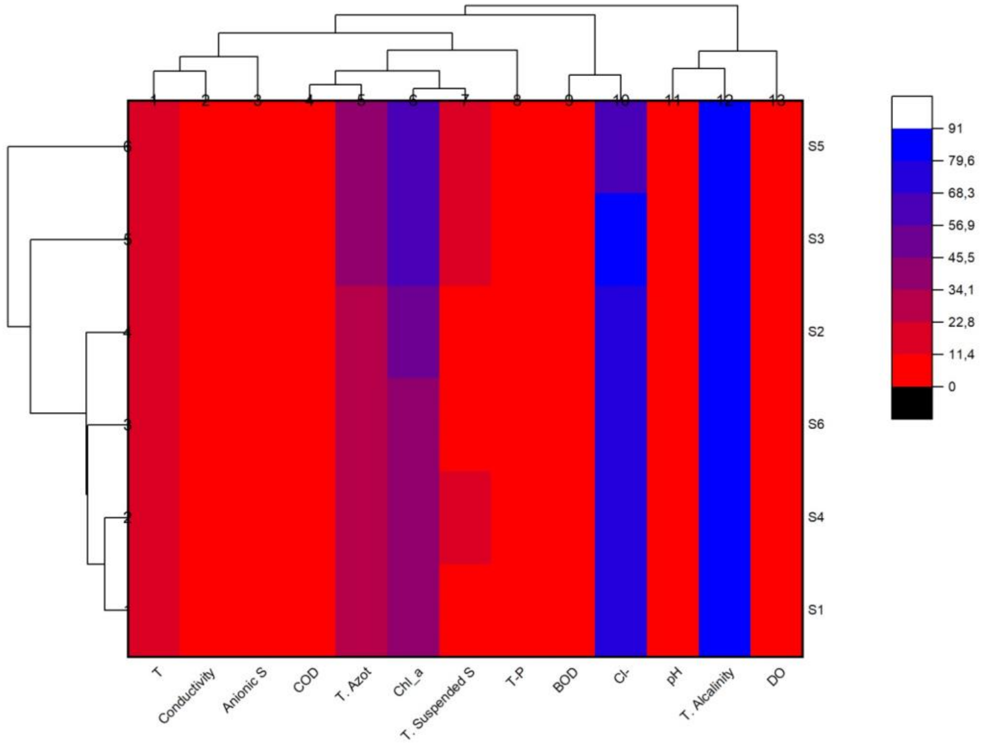

Figure 7. *Cluster analysis of measured physico-chemical parameters*

Conclusions

In this study, the periodic changes in the state of eutrophication and water quality of a HEPP dam lake facing the possibility of a drought and agricultural drainage were evaluated using statistical, ecological indices and geo-spatial analyses. The results of thematic maps and multi-statistical analysis indicate that seasonal and extreme fluctuations in nutrient loadings may be caused by agro-irrigation discharges that directly impact the eutrophication of lakes. The most significant finding indicative of eutrophication in the Dam was the minimum and maximum values of chlorophyll-a (Chl_*a*), which ranged from a minimum of 17.5 µg/L to a maximum of 85.6 µg/L. The average TSI values were determined from the chlorophyll-a measurements obtained during the dry period were found higher compared to the rainy period.

For this reason, some suggestions for decision makers are presented below in order to extend the life of the dam lake in providing both irrigation and HEPP energy.

i. It is necessary to guide the region towards good agricultural activities that will be carried out with reduced use of inorganic chemicals.
ii. The implementation of irrigation water quality controls and the application of right amounts and forms of fertilizer, in accordance with soil analysis, will be an effective strategy for reducing pollution.
iii. It is evident that enhanced pollution control within the dam lake system is imperative to attain optimal chemical and ecological status. This can be accomplished by implementing wastewater treatment facilities while maintaining a minimal level of agricultural pollution within the system. Thus, it is necessary to prevent sewage and solid waste from mixing into streams with effective removal and control techniques, thus preventing possible pollutants from mixing into the dam lake.

As a result, the findings obtained within the scope of this study will guide future studies within the framework of the sustainability of the dam lake in energy and irrigation. It will also contribute to the eutrophic restoration of the dam lake and to make managerial decisions compatible with the drought-based climate, which is expected to improve its regional influence further.

Acknowledgements -

Funding/Financial Disclosure The authors have no received any financial support for the research, authorship, or publication of this study.

Ethics Committee Approval and Permissions The work does not require ethics committee approval and any private permission.

Conflict of Interests The authors stated that there are no conflict of interest in this article.

Authors Contribution M. A. D. performed statistical calculations and provided graphs, worked with GIS to map and interpret the spatial distribution of the data and helped write the manuscript, H. C.

carried out the experimental studies and edited the original draft manuscript, E. K. assisted with the experimental studies, processed all data and helped write the manuscript. All authors read and approved the final version of the manuscript.

References

[1] Gorenflo, L., & Warner, D. B. (2016). Integrating biodiversity conservation and water development: in search of long-term solutions. *Wiley Interdisciplinary Reviews: Water, 3*(3), 301-311. https://doi.org/10.1002/wat2.1142

[2] Wu, Z., Wang, X., Chen, Y., Cai, Y., & Deng, J. (2018). Assessing river water quality using water quality index in Lake Taihu Basin, China. *Science of The Total Environment, 612*, 914-922. https://doi.org/10.1016/j.scitotenv.2017.08.293

[3] Ravikumar, P., Mehmood, M. A., & Somashekar, R. K. (2013). Water quality index to determine the surface water quality of Sankey tank and Mallathahalli lake, Bangalore urban district, Karnataka, India. *Applied Water Science, 3*(1), 247-261. https://doi.org/10.1007/s13201-013-0077-2

[4] Meguid, M. A. (2017). Key Features of the Egypt's Water and Agricultural Resources. In: Negm, A.M. (eds) Conventional Water Resources and Agriculture in Egypt. *The Handbook of Environmental Chemistry, vol 74. Springer, Cham.* (pp. 39-99), Springer https://doi.org/10.1007/698_2017_41

[5] Rao, K. D. (2005). Multi-criteria spatial decision analysis for forecasting urban water requirements: a case study of Dehradun city, India. *Landscape and Urban Planning, 71*(2-4), 163-174. https://doi.org/10.1016/j.landurbplan.2004.03.001

[6] Singh, S., Ghosh, N., Gurjar, S., Krishan, G., Kumar, S., & Berwal, P. (2018). Index-based assessment of suitability of water quality for irrigation purpose under Indian conditions. *Environmental monitoring and assessment, 190*(1), 29. https://doi.org/10.1007/s10661-017-6407-3

[7] Tepe, Y., Ateş, A., Mutlu, E. & Töre, Y. 2006. Water quality of Hasan stream (Erzin-Hatay) and its montly variations. *E.U. Journal of Fisheries & Aquatic Sciences, 23*(1/1), 149-154. https://10.12714/egejfas.2006.23.1.5000156796

[8] Mutlu, E., Yanık, T., & Demir, T. (2014). Horohon Deresi (Hafik-Sivas) Su Kalitesi Özelliklerinin Aylık Değişimleri. *Alinteri Journal of Agriculture Science, 25*(2), 45-57.

[9] Baki, B., & Baki O.G. (2023). *Sea Cage Aquaculture*. In Marine Environments Trophic Index (Trix). Academic Studies in Agriculture, Forestry and Aquaculture, (Ed: Doğanlar B. and Ellialtioglu Ş.), Gece Kitapligi, 79.

[10] Karadavut, I. S., Saydam, A. C., Kalipci, E., Karadavut, S., & Özdemir, C. (2011). A research for water pollution of Melendiz stream in terms of sustainability of ecological balance. *Carpathian Journal of Earth and Environmental Sciences, 6*(1), 65-80.

[11] Kalipci, E., Cüce, H. & Toprak, S. (2017). Evaluation of surface water quality of Mamasin Reservoir by using geographical information system (GIS). *Omer Halisdemir University Journal of Engineering Sciences, 6*(2), 351-361. https://doi.org/10.28948/ngumuh.341144

[12] Töre, Y., Ustaoğlu, F., Tepe, Y., & Kalipci, E. (2021). Levels of toxic metals in edible fish species of the Tigris River (Turkey); Threat to public health. *Ecological Indicators*, 123, 107361. https://doi.org/10.1016/j.ecolind.2021.107361

[13] Cüce, H., Kalipci, E., Ustaoğlu, F., Dereli, M. A., & Türkmen, A. (2022). Integrated spatial distribution and multivariate statistical analysis for assessment of ecotoxicological and health risks of sediment metal contamination, Ömerli Dam (Istanbul, Turkey). *Water, Air, & Soil Pollution, 233*(6), 199. https://doi.org/10.1007/s11270-022-05670-1

[14] Cüce, H., Kalıpcı, E., Tas, B. & Yılmaz, M. (2020). Evaluation of the Impacts on Water Quality from Meteorological Changes Due to Differences in Altitude by GIS: A Comparison for Two Morphologically Different Lakes. *Karadeniz Fen Bilimleri Dergisi, 10*(1), 1-26. https://doi.org/10.31466/kfbd.649297

[15] Kalipci, E., Cüce, H., Ustaoğlu, F., Dereli, M. A., & Türkmen, M. (2023). Toxicological health risk analysis of hazardous trace elements accumulation in the edible fish species of the Black Sea in Türkiye using multivariate statistical and spatial assessment. *Environmental Toxicology and Pharmacology, 97*, 104028. https://doi.org/10.1016/j.etap.2022.104028

[16] Kalipci, E., Cüce, H. & Toprak, S. (2017). Damsa Barajı (Nevşehir) yüzey suyu kalitesinin coğrafi bilgi sistemi ile mekansal analizi. *Karaelmas Science and Engineering Journal, 7*(1), 312-319.

[17] Cüce, H. & Bakan, G. (2017). Spatial assessment of the effect of sediment quality on the nutrient levels in shallow waters: Cernek Lake case. *Turkish Journal of Agriculture - Food Science and Technology, 5*(5), 546-555. https://doi.org/10.24925/turjaf.v5i5.546-555.1104

[18] Lambrakis, N., Antonakos, A., & Panagopoulos, G. (2004). The use of multicomponent statistical analysis in hydrogeological environmental research. *Water Research, 38*(7), 1862-1872.

[19] Mendiguchía, C., Moreno, C., Galindo-Riaño, M. D., & García-Vargas, M. (2004). Using chemometric tools to assess anthropogenic effects in river water: A case study: Guadalquivir River (Spain). *Analytica Chimica Acta, 515*(1), 143-149.

[20] Simeonov, V., Stratis, J. A., Samara, C., Zachariadis, G., Voutsa, D., Anthemidis, A., Sofoniou, M., & Kouimtzis, T. (2003). Assessment of the surface water quality in Northern Greece. *Water Research, 37*(17), 4119-4124. https://doi.org/10.1016/S0043-1354(03)00398-1

[21] Singh, K. P., Malik, A., & Sinha, S. (2005). Water quality assessment and apportionment of pollution sources of Gomti river (India) using multivariate statistical techniques—a case study. *Analytica Chimica Acta, 538*(1-2), 355-374. https://doi.org/10.1016/j.aca.2005.02.006

[22] Akbal, F., Gürel, L., Bahadır, T., Güler, İ., Bakan, G., & Büyükgüngör, H. (2011). Multivariate statistical techniques for the assessment of surface water quality at the mid-black sea coast of Turkey. *Water, Air, & Soil Pollution, 216*, 21-37. https://doi.org/10.1007/s11270-010-0511-0

[23] Rakotondrabe, F., Ngoupayou, J. R. N., Mfonka, Z., Rasolomanana, E. H., Abolo, A. J. N., & Ako, A. A. (2018). Water quality assessment in the Bétaré-Oya gold mining area (East-Cameroon): multivariate statistical analysis approach. *Science of the total environment, 610-611*, 831-844. https://doi.org/10.1016/j.scitotenv.2017.08.080

[24] Varol, M., Ustaoğlu, F., & Tokatlı, C. (2022). Ecological risks and controlling factors of trace elements in sediments of dam lakes in the Black Sea Region (Turkey). *Environmental Research*, 205, 112478. https://doi.org/10.1016/j.envres.2021.112478

[25] Ustaoğlu, F., Taş, B., Tepe, Y., & Topaldemir, H. (2021). Comprehensive assessment of water quality and associated health risk by using physicochemical quality indices and multivariate analysis in Terme River, Turkey. *Environmental science and pollution research, 28*, 62736-62754. https://doi.org/10.1007/s11356-021-15135-3

[26] Aydın, H., Tepe, Y., & Ustaoğlu, F. (2023). A holistic approach to the eco-geochemical risk assessment of trace elements in the estuarine sediments of the Southeastern Black Sea. *Marine Pollution Bulletin,* 189, 114732. https://doi.org/10.1016/j.marpolbul.2023.114732

[27] Carlson, R. E. (1977). A trophic state index for lakes 1. *Limnology and oceanography, 22*(2), 361-369. https://doi.org/10.4319/lo.1977.22.2.0361

[28] Burns, N. M., Rutherford, J. C., & Clayton, J. S. (1999). A monitoring and classification system for New Zealand lakes and reservoirs. *Lake and Reservoir Management, 15*(4), 255-271. https://doi.org/10.1080/07438149909354122

[29] Shu, J. H. (1993). Evaluation of eutrophication degree of main lakes in China. *Journal of Oceanology and Limnology, 6*, 616-620.

[30] SWA, (2020). *General Directorate of State Water Affairs*. http://www.dsi.gov.tr.

[31] APHA, AWWA, WEF: Rice, E. W., Bridgewater, L., & American Public Health Association (Eds.). (2012). *Standard methods for the examination of water and wastewater* (Vol. 10). Washington, DC: American public health association.

[32] Jeppesen, E., Peder Jensen, J., SØndergaard, M., Lauridsen, T., & Landkildehus, F. (2000). Trophic structure, species richness and biodiversity in Danish lakes: changes along a phosphorus gradient. *Freshwater biology, 45*(2), 201-218. https://doi.org/10.1046/j.1365-2427.2000.00675.x

[33] Carlson, R. E., & Havens, K. E. (2005). Simple graphical methods for the interpretation of relationships between trophic state variables. *Lake and Reservoir Management, 21*(1), 107-118. https://doi.org/10.1080/07438140509354418

[34] Burns, N., McIntosh, J., & Scholes, P. (2005). Strategies for managing the lakes of the Rotorua District, New Zealand. *Lake and Reservoir Management, 21*(1), 61-72. https://doi.org/10.1080/07438140509354413

[35] SWQR, (2012). *Surface Water Quality Regulation*. Official Gazette Number: 28483 (Environmental quality standards for some parameters in surface water masses and their usage purposes).

[36] Tercan, E., & Dereli, M. A. (2020). Development of a land suitability model for citrus cultivation using GIS and multi-criteria assessment techniques in Antalya province of Turkey. *Ecological Indicators, 117*, 106549. https://doi.org/10.1016/j.ecolind.2020.106549

[37] Lee, Y., Ha, S. Y., Park, H. K., Han, M. S., & Shin, K. H. (2015). Identification of key factors influencing primary productivity in two river-type reservoirs by using principal component regression analysis. *Environmental Monitoring and Assessment. 187,* 213. https://doi.org/10.1007/s10661-015-4438-1

[38] Manahan, SE., (2011). *Water Chemistry: Green Science and Technology of Nature's Most Renewable Resource*. Taylor & Francis Group, CRC Press, 398 pages.

[39] WPCR (2004). *Water Pollution and Control Regulation*. Official Gazette 25687(Quality Classification of Water Environments).

[40] Mamun, M., Kim, J. Y., & An, K. G. (2021). Multivariate statistical analysis of water quality and trophic state in an artificial dam reservoir. *Water, 13*(2), 186. https://doi.org/10.3390/w13020186

[41] Culha, S. T., & Erdoğuş, M. (2018). Investigations on Some Physicochemical Parameters of Demirköprü Dam Lake (Manisa, Turkey). *Turkish Journal of Agriculture-Food Science and Technology, 6*(9), 1267-1273. https://doi.org/10.24925/turjaf.v6i9.1267-1273.2032

[42] Er, B. A., Ayeri, T., Temel, F. A., Turan, N. G., & Ardalı, Y. (2017). Management Model of Lakes as a tool for planning the remediation of Suat Uğurlu Lake. *Turkish Journal of Agriculture-Food Science and Technology, 5*(7), 732-738. https://doi.org/10.24925/turjaf.v5i7.732-738.1118

[43] Bulut, C., & Kubilay, A. (2018). Eğirdir Gölü su kalitesinin trofik durum indeksleriyle belirlenmesi. *Acta Aquatica Turcica, 14*(4), 324-338. https://doi.org/10.22392/egirdir.415073

[44] Cüce, H. & Bakan, G. (2017). A Evaluation of the effects of sediment quality on trophic status in a shallow lake; The case of Balik Lake (Kizilirmak Delta). *Ordu University Journal of Science and Tecnology, 7*(1), 83-97.

[45] Opiyo, S., Getabu, A. M., Sitoki, L. M., Shitandi, A., & Ogendi, G. M. (2019). Application of the Carlson's trophic state index for the assessment of trophic status of lake Simbi ecosystem, a deep alkaline-saline lake in Kenya. *International Journal of Fisheries and Aquatic Studies, 7*(4), 327-333. https://dx.doi.org/10.2139/ssrn.3451145

[46] Bilgin, A. (2020). Trophic state and limiting nutrient evaluations using trophic state/level index methods: a case study of Borçka Dam Lake. *Environmental monitoring and assessment, 192*, 1-19. https://doi.org/10.1007/s10661-020-08741-0

[47] Liu, C. W., Lin, K. H., & Kuo, Y. M. (2003). Application of factor analysis in the assessment of groundwater quality in a Blackfoot disease area in Taiwan. *Science of the Total Environment, 313*(1-3), 77–89. https://doi.org/10.1016/S0048-9697(02)00683-6

[48] Iscen, C. F., Emiroglu, Ö., Ilhan, S., Arslan, N., Yılmaz, V., Ahiska, S. (2008). Application of multivariate statistical techniques in the assessment of surface water quality in Uluabat Lake, Turkey. *Environmental Monitoring and Assessment, 144*, 269–276. https://doi.org/10.1007/s10661-007-9989-3